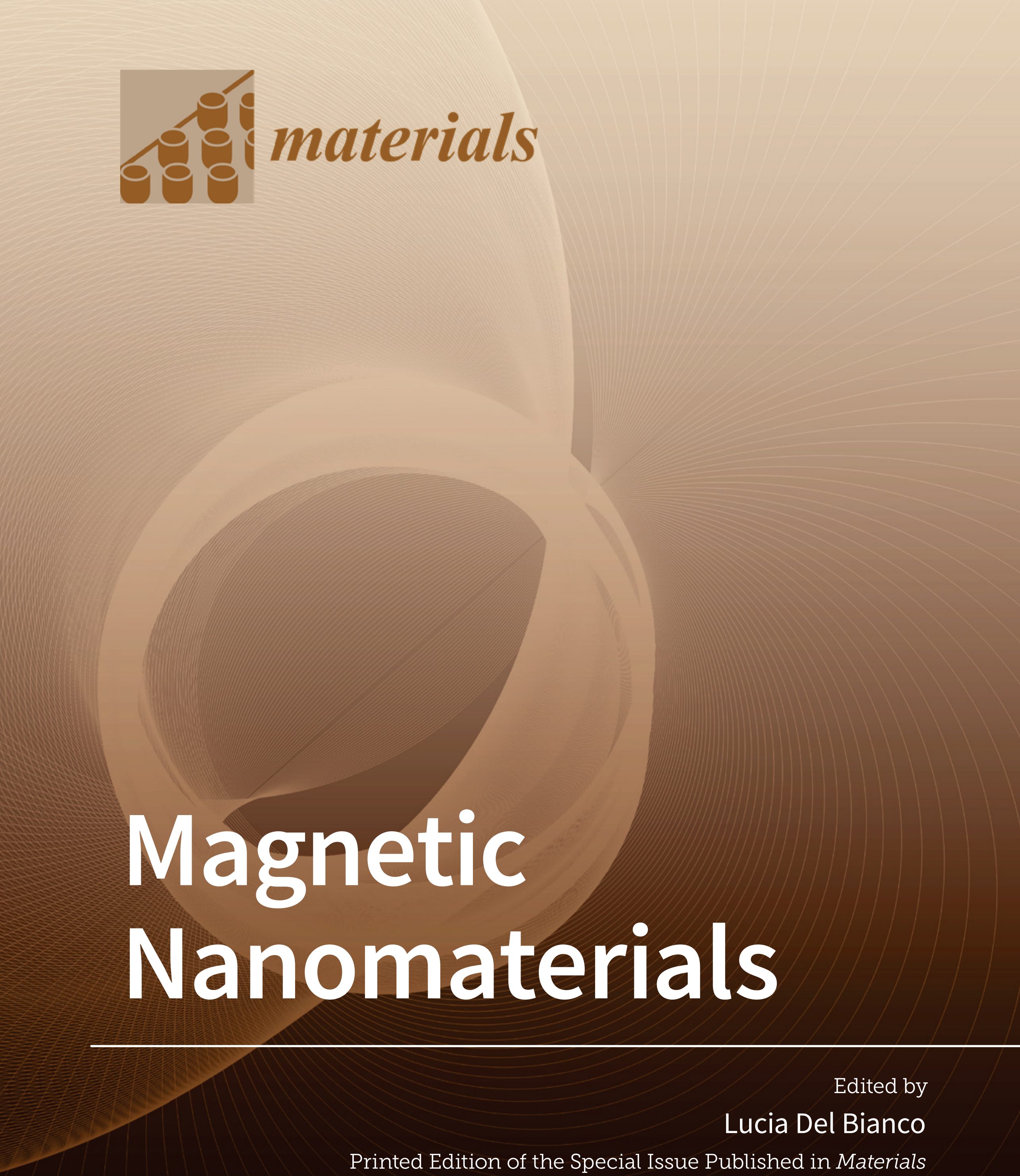

materials

Magnetic Nanomaterials

Edited by

Lucia Del Bianco

Printed Edition of the Special Issue Published in *Materials*

www.mdpi.com/journal/materials

MDPI

Magnetic Nanomaterials

Magnetic Nanomaterials

Editor

Lucia Del Bianco

MDPI • Basel • Beijing • Wuhan • Barcelona • Belgrade • Manchester • Tokyo • Cluj • Tianjin

Editor
Lucia Del Bianco
University of Ferrara
Italy

Editorial Office
MDPI
St. Alban-Anlage 66
4052 Basel, Switzerland

This is a reprint of articles from the Special Issue published online in the open access journal *Materials* (ISSN 1996-1944) (available at: https://www.mdpi.com/journal/materials/special_issues/Magnetic_Nanomaterial).

For citation purposes, cite each article independently as indicated on the article page online and as indicated below:

LastName, A.A.; LastName, B.B.; LastName, C.C. Article Title. *Journal Name* **Year**, *Volume Number*, Page Range.

ISBN 978-3-0365-3104-5 (Hbk)
ISBN 978-3-0365-3105-2 (PDF)

Contents

About the Editor

Lucia Del Bianco is an Associate Professor at the Department of Physics and Earth Science of the University of Ferrara (Italy). Her research activity in the field of Nanomagnetism concerns the experimental study of the magnetic properties of nanostructured magnetic systems: nanocomposite materials and nanoparticles, thin films and multilayers, and nanopatterned structures. Her research interests include finite-size effects (magnetic configuration, magnetization process, thermal stability, and superparamagnetism), magnetic phenomena connected with dipolar and exchange interactions, and disordered magnetism effects. She also has expertise in the study of magnetotransport properties and magnetoelasticity. Currently, she is dedicated, in particular, to the study of magnetic nanoparticles and hybrid magnetic materials for nanomedicine applications (e.g., magnetic hyperthermia, tissue regeneration). She is the author of around 80 articles published in peer-reviewed journals.

Preface to ”Magnetic Nanomaterials”

The constant search for innovative magnetic materials increasingly leads to the creation of highly engineered systems built in different forms (films, wires, particles), structured on a nanometric scale in at least one spatial direction, and often characterized by the coexistence of two or more phases that are magnetically and/or structurally different. The possible coincidence, at the nanoscale, of the typical size of the system with critical magnetic lengths ruling specific magnetic phenomena (for instance, the exchange length, below which a ferromagnetic element becomes single domain, or the exchange-correlation length corresponding to the domain wall thickness) can cause the appearance of unexpected and amazing magnetic effects. Moreover, the magnetic behavior of the nanomaterials crucially depends on the structure and morphology of the constituent elements and on the type and strength of the magnetic interactions between them. Indeed, the study of the magnetic behavior of nanomaterials continues to arouse great interest for their intriguing fundamental properties and prospective technological applications.

The main objective of this Special Issue was to contribute to broadening the knowledge on magnetic nanomaterials, demonstrating the breadth and richness of this research field as well as the growing need to address it through an interdisciplinary approach. The papers collected in this book (two reviews and eight regular articles) fulfill this goal in an excellent way. In fact, they report cutting-edge studies on the production and characterization of a variety of novel magnetic nanomaterials (nanoparticles, nanocomposites, thin films and multilayers), which have the potential to play a key role in different technologically advanced sectors, such as biotechnology, nanomedicine, energy, spintronics, data storage and sensors.

I would like to express my gratitude to all the authors for the remarkable work they have done. Finally, I sincerely thank Dr. Dexin Wang, MDPI Managing Editor of this Special Issue, for the fruitful collaboration and the constant support.

Lucia Del Bianco
Editor

materials

MDPI

Review

Nanoparticles for Magnetic Heating: When Two (or More) Is Better Than One

Jesus G. Ovejero [1,2], Federico Spizzo [3], M. Puerto Morales [1] and Lucia Del Bianco [3,*]

[1] Departamento de Energía, Medio Ambiente y Salud, Instituto de Ciencia de Materiales de Madrid, CSIC, Cantoblanco, E-28049 Madrid, Spain; jesus.g.ovejero@csic.es (J.G.O.); puerto@icmm.csic.es (M.P.M.)
[2] Servicio de Dosimetría y Radioprotección, Hospital General Universitario Gregorio Marañón, E-28007 Madrid, Spain
[3] Dipartimento di Fisica e Scienze della Terra, Università di Ferrara, I-44122 Ferrara, Italy; federico.spizzo@unife.it
* Correspondence: lucia.delbianco@unife.it

Abstract: The increasing use of magnetic nanoparticles as heating agents in biomedicine is driven by their proven utility in hyperthermia therapeutic treatments and heat-triggered drug delivery methods. The growing demand of efficient and versatile nanoheaters has prompted the creation of novel types of magnetic nanoparticle systems exploiting the magnetic interaction (exchange or dipolar in nature) between two or more constituent magnetic elements (magnetic phases, primary nanoparticles) to enhance and tune the heating power. This process occurred in parallel with the progress in the methods for the chemical synthesis of nanostructures and in the comprehension of magnetic phenomena at the nanoscale. Therefore, complex magnetic architectures have been realized that we classify as: (a) core/shell nanoparticles; (b) multicore nanoparticles; (c) linear aggregates; (d) hybrid systems; (e) mixed nanoparticle systems. After a general introduction to the magnetic heating phenomenology, we illustrate the different classes of nanoparticle systems and the strategic novelty they represent. We review some of the research works that have significantly contributed to clarify the relationship between the compositional and structural properties, as determined by the synthetic process, the magnetic properties and the heating mechanism.

Keywords: magnetic hyperthermia; magnetic nanoparticles; magnetic aggregates; magnetic interactions; core/shell nanoparticles; multicore nanoparticles; hybrid systems; mixed nanoparticle systems; chemical synthesis; magnetic heating

Citation: Ovejero, J.G.; Spizzo, F.; Morales, M.P.; Del Bianco, L. Nanoparticles for Magnetic Heating: When Two (or More) Is Better Than One. *Materials* **2021**, *14*, 6416. https://doi.org/10.3390/ma14216416

Academic Editor: Dominique de Caro

Received: 14 September 2021
Accepted: 22 October 2021
Published: 26 October 2021

1. Introduction

The amazing progress made in the last decade in the production of magnetic nanoparticles (NPs) for biomedical applications has been possible thanks to the close operational connection between chemistry, physics and biology. Taking advantage of the unique properties of the magnetic materials at the nanoscale it is possible to prepare colloids that can be remotely manipulated/stimulated/monitored through a magnetic stimulus [1].

Among the possible uses of magnetic NPs in nanomedicine, those based on their ability to produce heat under an alternating magnetic field (AMF) have been the subject of strong research interest for many years. Magnetic NPs can be exploited as heating agents in oncological treatments by taking advantage of the local heat generated in hyperthermia therapies or using this heat to trigger other thermosensitive therapies. The heat produced by NPs delivered at the tumor site can kill the cancer cells [2–9] or inhibit their self-renewal capacity [10]. Magnetic hyperthermia can enhance the effects of radiotherapy on cancer cells [11–13] and activate the immune system to fight metastatic tumors [14]. In a different strategy, magnetic NPs can be incorporated into a biocompatible matrix together with drug molecules (bound to the NPs or loaded separately) and magnetic heating can be used to induce the controlled degradation of the matrix and the targeted release of the drug, maximizing its effect and monitoring the treatment [6,15–23]. Comprehensive review articles can be found in the literature, well illustrating the latest advances and future prospects in biomedical applications of magnetic heating through NPs [24–29].

Novel types of magnetic NPs are continuously being designed with the ultimate goal of improving heating performance and biocompatibility. In this process, the knowledge acquired over time on the magnetism of nanosized structures and on the physics of the heat generation mechanism directs the efforts for the chemical synthesis of NPs with controlled magnetic properties and tuned heating capacity. On the other hand, the preparation of NPs with innovative structural and compositional characteristics offers the possibility to reveal or better elucidate peculiar magnetic behaviors and thus to expand the fundamental comprehension of magnetic phenomena at the nanoscale.

The development of the synthetic methods of colloidal magnetic NPs has achieved a fine control on their size, on the degree of crystallinity and also on their shape [30], which are key parameters that determine the magnetic properties, particularly the anisotropy energy barrier associated with the reversal of the magnetic moment [31,32]. A second important aspect on the development of functional magnetic materials is the effect of the surface chemistry on the colloidal properties and NP reactivity. In most preparations, the NPs are coated with a non-magnetic layer (organic, inorganic, ceramic or metallic) created on purpose or grown as a natural consequence of the synthetic process. The coating (i) confers biocompatibility to the NPs, (ii) determines their hydrophobic or hydrophilic character and colloidal stability and (iii) introduces intermediate moieties for the attachment of drugs or other biofunctional molecules (enzymes, proteins, antibodies) [33]. From the magnetic point of view, the presence of a non-magnetic coating rules the magnetic interactions, preventing the exchange coupling—which only occurs between NPs in close contact—and modulating the strength of dipolar interactions. Furthermore, coatings could even modify the magnetic properties of small magnetic cores if they bind covalently to the surface atoms perturbing the electronic state [34].

Over the last decade, the growing interest for magnetic heating agents has led to the development of new synthesis protocols for the creation of NPs consisting of two magnetic phases, forming a core/shell structure, or of systems comprising several distinguishable magnetic elements arranged in complex architectures. In this review, we present some of the most relevant examples of chemically synthesized systems that exploit the magnetic coupling between two or more constituent magnetic elements (magnetic phases, primary NPs) to enhance and tune the heating efficiency. We will focus on those works that have significantly contributed to clarify the connection between the compositional and structural properties, analyzing in detail the synthetic process, the magnetic properties and the heating mechanism. Since these elements are known to be strictly intertwined, elucidating their relationship is never trivial. In fact, each new material has its own peculiarities and the elements of knowledge acquired for a system cannot be applied directly and uncritically to another, but an in-depth study is needed. For this reason, the aim of the review is to analyze the most common strategies followed to optimize the heating performance of interacting magnetic systems. Thus, after a brief presentation of the fundamental principles underlying the magnetic heating mechanism, highlighting the principal structural and magnetic parameters involved in it, we will address the following classes of magnetic systems (Figure 1):

(a) Core/shell nanoparticles (CS_NPs): NPs with a core/shell structure made of two different magnetic phases, typically iron/iron-oxide and hard/soft ferromagnets. The magnetic properties are ruled by the magnetic exchange coupling between the two phases;

(b) Multicore nanoparticles (MC_NPs): Nanosized isometric (i.e., sphere-like) structures comprising more cores, i.e., primary NPs, of the same magnetic phase. The cores are structurally connected or held together by chemical bonds and are subjected to exchange or dipolar magnetic interactions;

(c) Linear aggregates: Anisometric assemblies of dipolar interacting NPs (chains and columns, namely 1-dimensional and 3-dimensional structures, respectively);

(d) Hybrid systems: Hybrid magnetic materials, i.e., consisting of magnetic NPs incorporated in a matrix with different chemical nature, such as lipid structures, polymers or silica. Attention will be focused on systems structured in such a way that the NPs are confined in a delimited spatial region and thus inevitably form magnetic aggregates;

(e) Mixed NP systems: Assemblies obtained by mixing together two populations of NPs differing in composition and/or shape, which implies a different magnetic anisotropy and possibly different colloidal properties.

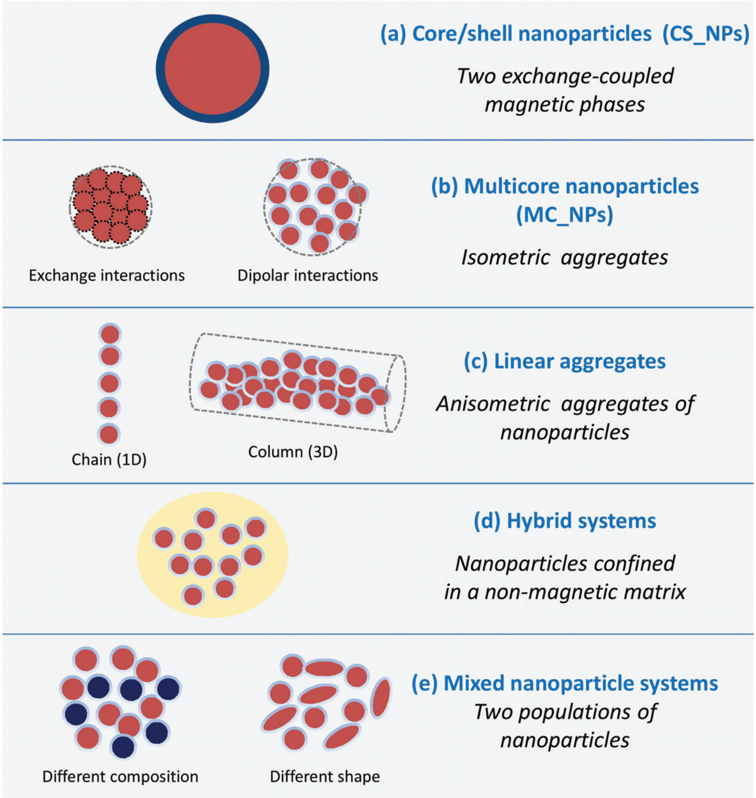

Figure 1. Scheme showing the different classes of magnetic NP systems whose magnetic heating performance is determined by the synergy between two or more constituent magnetic elements.

Most of the systems described in this review are made up, in whole or in part, of iron oxide. The term 'magnetic iron oxide', which is widespread in literature on magnetic NPs, is generally used to indicate the ferrimagnetic iron oxide phases, i.e., magnetite (Fe_3O_4) and maghemite (γ-Fe_2O_3). These phases present a good degree of biocompatibility and iron oxide in the form of NPs is one of the few inorganic nanosystems approved by the U.S. Food and Drug Administration (FDA) for use in human patients. As maghemite can result from the oxidation of magnetite, iron oxide NPs are often reported to consist of a mix of these two phases [35,36]. On the other hand, the two phases have similar inverse spinel structures, which are very difficult to be experimentally distinguished at the nanoscale.

This review does not include all the reported cases of magnetic NPs which show the unwanted and uncontrollable tendency to aggregate during the synthesis or during the magnetic heating process under the action of the AMF. We exclusively focus on designed NP systems for magnetic heating applications, prepared by chemical methods, which possess as strength point the synergistic union of different magnetic components.

2. Basis of the Magnetic Heating Phenomenon

This section summarizes the basic physics concepts on the phenomenon of magnetic heating generated by NPs, in order to highlight the main structural and magnetic parameters involved in it. To deepen the subject, we refer the reader to the article by Carrey et al. [37] and to the review by Perigo et al. [38]. In particular, the article by Carrey et al. is a rigorous presentation of the theory behind the magnetic heating effect, which has also the merit to clearly point out the improper separation, made in several experimental articles, of the mechanisms responsible for the heating between 'hysteresis losses', produced by NPs in the ferromagnetic regime, and 'relaxation losses' produced by NPs in the superparamagnetic regime. This separation is misleading since the heat released by an assembly of magnetic NPs under an AMF, per unit volume and during one cycle, is equal to the area A of the resulting hysteresis loop (magnetization vs. AMF field amplitude). Therefore, the magnetic energy losses are always hysteresis losses. The Specific Absorption Rate (SAR) parameter quantifies the efficiency of the NPs to transform magnetic energy into heat and corresponds to the product between A and the frequency f_m of the applied AMF. According to this definition, SAR is expressed in W/m^3 units (SI system). Usually, the SAR quantity is given in W/kg units, which is obtained by dividing by the mass density ρ of the NPs, namely

$$\mathrm{SAR} = \mathrm{A}f_m/\rho \quad [\mathrm{W/kg}] \tag{1}$$

It is well known that, below a critical size, a magnetic NP becomes single domain, in order to minimize the magnetostatic energy, and its magnetic moment lies along one of the magnetic anisotropy axes (i.e., the easy magnetization directions). In the case of uniaxial anisotropy, the moment has only two stable orientations separated by an energy barrier KV, where K is the magnetic anisotropy coefficient and V is the NP volume. The action of an externally applied field H on the NP is described by the Stoner-Wohlfarth model, which essentially provides the magnetization M vs. H at different values of the angle θ between the anisotropy axis and the applied field [32].

Two limiting cases can be distinguished. (i) When the field is parallel to the anisotropy axis ($\theta = 0$), a perfectly squared hysteresis loop is obtained with maximal area given by

$$\mathrm{A} = 4\mu_0 M_S H_K = 8\mathrm{K} \tag{2}$$

where M_S is the NP saturation magnetization (in this case, M_S coincides with the remanent magnetization M_r) and $\mu_0 H_K$ is the anisotropy field, which corresponds to 2 K/M_S (in this case, anisotropy field, switching field and coercivity H_C coincide). (ii) When the field is perpendicular to the anisotropy axis ($\theta = \pi/2$) no magnetic hysteresis is observed.

In the case of an assembly of non-interacting randomly oriented identical NPs, the hysteresis loop features a remanent magnetization $M_r = 0.5\ M_S$ and a coercivity $H_C = 0.48\ \mu_0 H_K$. Accordingly, the loop area is reduced and it can be approximately estimated as

$$\mathrm{A} \approx 4\mu_0 M_r H_C = 2\mu_0 M_S H_C = 1.92\mathrm{K} \tag{3}$$

The Stoner–Wohlfarth model considers the temperature T = 0 K, i.e., does not take into account thermal effects on the magnetization process. However, temperature activates magnetic relaxation processes, i.e., the thermal energy can assist the magnetic field in promoting the reversal of the NP moment. Therefore, the coercivity decreases on increasing temperature. Moreover, when the anisotropy energy barrier is comparable to the thermal energy or lower, the moment overcomes the energy barrier without the need of an applied field and is free of thermally fluctuating between the two energy minima corresponding to the stable orientations, similarly to the atomic spins of a paramagnetic material. This phenomenon is known as superparamagnetic relaxation. An assembly of superparamagnetic NPs can be brought to magnetic saturation by an external field, but it does not exhibit magnetic hysteresis, i.e M_r and H_C are null.

Magnetic relaxation effects can be dealt with in the framework of the Néel relaxation theory and hence considering the existence of a relaxation time for the moment reversal. Under the assumption that the atomic spins of the NP rotate coherently in the reversal process (macrospin approximation), the Néel expression for the relaxation time of the NP moment is:

$$\tau_N = \tau_0 \exp(KV/k_B T) \tag{4}$$

where k_B is the Boltzmann constant, hence k_BT is the thermal energy, and τ_0 is the flipping time. The latter inversely depends on the gyromagnetic ratio γ_0, usually given in angular frequency [39], and it is generally assumed equal to 10^{-9} s.

The observed magnetic behavior of the NP depends on the value of τ_N with respect to the measuring time t_m characteristic of the used investigating technique ($f_m = 1/t_m$ is the measuring frequency). The NP is in the superparamagnetic regime for $\tau_N < t_m$ (or for $f_m\tau_N < 1$) and in the blocked ferromagnetic regime for $\tau_N > t_m$ ($f_m\tau_N > 1$). Conventionally, the transition between the two regimes occurs at $\tau_N = t_m$ (i.e., $f_m\tau_N = 1$). It follows that the temperature T_B (blocking temperature) that marks the passage between the blocked regime and the superparamagnetic one is expressed by the relation (in which $f_0 = 1/\tau_0$):

$$T_B = KV/k_B \ln(t_m f_0) \tag{5}$$

Therefore, T_B shifts to higher values with reducing t_m, i.e., with increasing f_m. For DC measurements by SQUID (Superconducting Quantum Interference Device) magnetometer, a value t_m = 100 s is usually considered (i.e., measuring frequency f_m = 0.01 Hz).

Accordingly, for a fixed temperature T, the critical volume above which a NP is blocked and below which it is superparamagnetic is:

$$V_P = \ln(t_m f_0) k_B T/K \tag{6}$$

For instance, from the above equation, at t_m = 100 s and T = 300 K, the critical diameter for a spherical magnetite NP is ~26 nm, setting K equal to the magnetocrystalline anisotropy of the bulk phase (1.1×10^5 erg/cm^3).

Regarding the magnetic hysteretic properties of an assembly of NPs subjected to an AMF with amplitude H_{max} and frequency f_m, two principal scenarios can be distinguished, depending on the value of the parameter $\xi = \mu_0 M_S V H_{max}/k_B T$.

The first is described by the so-called Linear Response Theory (LRT), which assumes that the magnetization M is linear with the magnetic field [37,40]. This assumption substantially coincides with the condition $\xi < 1$, which is therefore a fundamental requirement for the applicability of LRT. Hence, for fixed M_S and V, the LRT theory ceases to be valid at sufficiently high H_{max} values. Moreover, it is possible to show that LRT can be more adequately applied to strongly anisotropic NPs [37].

The hysteresis loop area A for randomly oriented NPs, predicted by LRT, is related to the imaginary component of the magnetic susceptibility χ'' through this relation

$$A = \pi\mu_0 H_{max}^2 \chi'' = \frac{\pi\mu_0^2 H_{max}^2 M_S^2 V}{3k_B T} \frac{f_m\tau_N}{1 + \left(f_m\tau_N\right)^2} \tag{7}$$

It is worth noticing that the AC magnetic susceptibility, as obtained from the Casimir–Du Pré model [41], depends on $\varpi\tau_N$ where ϖ corresponds to $2\pi f_m$, actually. However, as observed by Dormann et al. [39,42], if the gyromagnetic ratio γ_0 is given in angular frequency, ϖ has to be replaced by f_m. Accordingly, for AC magnetic measurements, the measuring frequency, that is the reciprocal of the measuring time t_m, coincides with the field frequency (for this we have indicated them both as f_m) [39,42]. Therefore, a resonant phenomenon is essentially observed on varying f_m. In fact, according to Equation (7), A is null for $f_m\tau_N << 1$ (full superparamagnetic regime) and for $f_m\tau_N >> 1$ (full ferromagnetic regime) and reaches a maximum for $f_m\tau_N = 1$ (transition between the two regimes), which is the resonant condition. Apart from a few exceptions [43–46], most studies on the heating properties of magnetic NPs refer to the LRT, even when the criterion $\xi < 1$ is not fulfilled. Indeed, if the condition $\xi < 1$ is not satisfied, a different scenario opens. Regarding the fully superparamagnetic NPs, also in this case they are useless for generating heat because of their null hysteresis. The loop area of single-domain NPs in the full ferromagnetic regime can be predicted by the Stoner–Wohlfarth model, eventually including also the thermal dependence of the coercivity, namely considering $A(T) \sim 4\mu_0 M_r H_C(T)$. This approach is valid under the assumption that the assembly is substantially saturated by H_{max}, which is not always the case, actually. Highest area values are reached by adjusting H_{max} well above the anisotropy field H_K. The loop area increases with increasing H_{max} up to the value at which magnetic saturation is attained. For a fixed H_{max}, the SAR parameter increases with increasing f_m, unlike what occurs in the LRT frame, in which the loop area and hence the SAR are maximized by setting $f_m = 1/\tau_N$.

In magnetic heating experiments, care should be taken to select H_{max} and f_m so that their product does not exceed 5×10^9 A/ms, which is indicated as the criterion to avoid detrimental effects on living organs in medicine applications [47].

Above a critical size, which depends on M_S and K, the description of the NPs as canonical single magnetic domains, whose atomic spins reverse coherently, is no longer valid and therefore the Stoner-Wohlfarth model cannot be applied. In fact, closure magnetization configurations, i.e., vortex-type, and incoherent reversal modes may become energetically favored, resulting in a lower coercivity and hence narrower hysteresis loops [48–51]. Obviously, the same is true for particles with a multi-domain configuration [31,52].

It should be also remarked that neither the Néel relaxation theory nor the Stoner-Wohlfarth model consider the existence of interparticle magnetic interactions. This is exactly one of the main points that we will address in the following, namely how the magnetic heating response of an assembly of magnetic nanoheaters is influenced by magnetic interactions.

When the NPs are dispersed in a fluid, another magnetization mechanism may be active besides the internal rotation of the moments, namely the physical rotation of the NPs due to the torque action exerted by the magnetic field and under the influence of thermal effects [40,53,54]. The process is usually described within the Brownian relaxation theory, by introducing a relaxation time defined as

$$\tau_B = 3\eta\, V_H / k_B T \tag{8}$$

where η is the viscosity of the solvent and V_H is the hydrodynamic volume of the NP [40].

As in the Néel relaxation, the magnetic behavior of a NP subjected to Brownian relaxation depends on the value of τ_B with respect to the measuring time t_m. Hence, the relaxation mechanism that ultimately rules the magnetic reversal behavior of the NP is that with the shortest relaxation time, under the adopted experimental conditions. The hydrodynamic volume V_H is usually larger than the physical one and can be strongly altered by the tendency of the NPs to aggregate during the synthetic process, under the action of electrostatic or magnetic interactions. Moreover, the application of the AMF during the heating tests can result in the formation of chains and agglomerates of NPs [55–58], namely V_H can change in an unpredictable way. Hence, Brownian motion is a quite difficult phenomenon to evaluate and govern in practice.

Operatively, the heating capacity of a NP assembly can be assessed through a calorimetric method, namely by measuring the temperature increase during time of a fluid containing a certain amount of NPs, subjected to the AMF. The SAR parameter is calculated using the relation [59]

$$\mathrm{SAR} = \frac{C}{m_{NPs}} \cdot \frac{\Delta T}{\Delta t} \tag{9}$$

where C is the heat capacity of the sample (taken equal to the heat capacity of the fluid, if that of the NPs is assumed negligible), m_{NPs} is the mass of the magnetic NPs and ΔT is the temperature increase during the time interval Δt. In the initial slope method, which is probably the most often used, $\Delta T/\Delta t$ is calculated as the slope of the linear curve fitting the initial portion of the heating curve.

The SAR parameter estimated by Equation (9) is usually given in W/g units or, in the case of ferrite NPs, in W/g_{Fe} units (i.e., watts per gram of iron). In literature, the same physical quantity expressed by SAR can be found indicated with different names: specific loss power (SLP), specific power loss (SPL), specific heat power (SHP), specific power absorption (SPA).

Another parameter, the intrinsic loss power (ILP), has been also proposed, given by

$$\mathrm{ILP} = \frac{\mathrm{SAR}}{f_m H_{max}^2} \tag{10}$$

ILP is defined on the assumption that SAR depends quadratically on H_{max} and linearly on f_m, namely in the LRT context. Thus, normalizing SAR by these dependences should allow the heating efficiency at different experimental conditions of the applied field to be directly compared [60].

However, at present, the wide variety of customized instruments for magnetic heating tests and the lack of standardized protocols make it very difficult, if not impossible, to compare SAR values measured on different NP systems. In order to be comparable, SAR values estimated using a calorimetric method should not refer just to tests carried out at the same field frequency and amplitude, but also in similar thermodynamic conditions [59]. Moreover, it would be advisable to disperse the NPs at a similar concentration and in the same solvent.

3. Core/Shell Nanoparticles (CS_NPs)

The concept behind CS_NPs, consisting of two different magnetic phases, is to exploit the interface exchange coupling to tune the magnetic anisotropy and therefore the hysteretic properties (coercivity, remanent magnetization). In fact, this magnetic coupling can give rise to an additional source of anisotropy, i.e., exchange anisotropy, for the magnetically softer component, as first observed by Meiklejohn and Bean, decades ago, in ferromagnetic/antiferromagnetic Co/CoO CS_NPs [61]. Since then, the exchange coupling mechanism has been studied in a number of different systems (NPs, films and patterned structures) consisting of at least two magnetic phases with different intrinsic anisotropy and, in many cases, also with different magnetic nature (ferromagnetic, antiferromagnetic, ferrimagnetic). The exchange anisotropy is also responsible for the exchange bias effect [61–65], i.e., the horizontal shift of the hysteresis loop, particularly interesting for technological applications in spintronic devices [66].

In ferromagnetic/antiferromagnetic and ferromagnetic/ferrimagnetic CS_NPs, the exchange anisotropy produces an increase in coercivity, compared to that measured in the single-phase ferromagnetic cores [63,67–69]. Moreover, the exchange bias effect can appear when the assembly is cooled in a static magnetic field across a critical temperature, below which the anisotropy energy of the harder component (antiferromagnetic or ferrimagnetic, possibly showing a spin-glass-like behavior) is larger than the exchange interaction energy at the interface with the soft ferromagnetic phase. This is the case of iron/iron oxide NPs for example, whose exchange coupling has been strongly investigated [70–76]. CS_NPs of this type are particularly interesting because, thanks to the presence of the metallic iron core, the saturation magnetization is higher than that of iron oxide, but the oxide shell guarantees resistance to oxidation and biocompatibility.

In hard/soft ferromagnetic systems, the exchange anisotropy can produce a characteristic reversible demagnetizing curve (exchange-spring behavior) and, most remarkably, the coupling between the hard component, with high coercivity, and the soft component, with high saturation magnetization, results in a high value of the maximum energy product [77–79]. This phenomenon paved the way for the creation of a new generation of high-performance permanent magnets [80].

The chemical routes to produce CS_NPs includes co-precipitation in water [81,82], thermal decomposition in organic media, metal reduction in microemulsions [83], hydrothermal synthesis [84] and electrodeposition [85]. However, the most widely used and most efficient in terms of crystallinity, homogeneity and shape control is the two-step thermal decomposition method in organic media, named as seed-mediated method. On the first step, the core crystals are formed controlling carefully the size and surface orientation. The crystals formed are used in a second step to induce a heterogeneous nucleation of the shell phase to control the growth and avoid secondary nucleation [86–89]. Some examples of the materials explored are: $Fe/CoFe_2O_4$ [90]; $CoFe_2O_4/ZnFe_2O_4$ or $ZnFe_2O_4/CoFe_2O_4$ [91]; $CoFe_2O_4/MnFe_2O_4$ or $MnFe_2O_4/CoFe_2O_4$ [92]; $Mn_xFe_{3-x}O_4/Fe_xMn_{3-x}O_4$ [88]; Mn_3O_4/Fe_3O_4 or Fe_3O_4 $/Mn_3O_4$ [89]. A simpler alternative is the surface treatment of ferromagnetic metallic NPs to produce a thick and stable layer of antiferromagnetic or ferrimagnetic oxide, as is the case for Fe/Fe_3O_4 NPs [93–96]. Although simpler, this route offers a poor control on the shell thickness and low stability of phase composition due to oxygen migration towards the metallic core.

In this context, Zhang et al. were among the first to study iron/iron oxide CS_NPs for prospective biomedical applications (hyperthermia and magnetic resonance imaging) [97]. Their work was particularly focused on the surface engineering of the CS_NPs, in order to make them highly biocompatible. Iron NPs were synthesized by reduction of an iron salt by $NaBH_4$ in a water-in-oil microemulsion solution of n-octane and water, in the presence of two surfactants, cetyl trimethyl ammonium bromide (CTAB) and n-butanol. The volume ratio between oil phase and water phase was increased to decrease the size of the iron NPs from 20 to 8 nm. The passivation procedure generated the core-shell structure of the NPs, with trimethylamine N-oxide ($(CH_3)_3NO$) that worked as a mild oxidant and flowing Ar for two days to improve the stability. Finally, phosphatidylcholine was assembled on the surface of the NPs to make them biocompatible. CS_NPs of ~20 nm in size, subjected to a AMF of 150 Oe at 250 kHz, could produce, in 60 s, a temperature increase higher than that obtained using single-phase iron oxide NPs.

Another interesting core/shell system with high M_S and good air stability was proposed by Meffre et al. [98]. It consisted of Fe(soft)/FeC(hard) NPs, prepared by first obtaining the iron metal cores by thermal decomposition of an iron organometallic compound [99] and then, adding $Fe(CO)_5$ under H_2 and heating at 120–150 °C. Final size of CS_NPs could be finely controlled between 12 and 15 nm by varying the average size of the initial iron(0) nanocrystals or the $Fe(CO)_5$ concentration. To render the CS_NPs water soluble, the organic coating was exchanged with dimercaptosuccinic acid (DMSA). This method allowed the control of the amount of carbon diffused and therefore the tuning of the anisotropy of the CS_NPs. A SLP value of 415 W/g was measured in the best samples (AMF of 20 mT and frequency 96 kHz).

Tsopoe et al. carried out a comparative study on the exchange bias effect in antiferromagnetic/ferrimagnetic CS_NPs, with structure NiO/Fe_3O_4 and Fe_3O_4/NiO [100]. These structures were also synthesized in two steps: first the precipitation in water of the NiO or Fe_3O_4 core; then the precipitation of the other salt in the presence of the core and sodium acetate in ethylene glycol, in an autoclave at 180 °C for 10 h. CS_NPs between 30–35 nm showed colloidal stability thanks to the polyol rests at the surface. Both types showed higher SAR values in comparison to single-phase magnetite NPs, owing to the interface exchange coupling; the system with magnetite as shell exhibited higher exchange bias and SAR.

It is known that the structure of iron/iron oxide CS_NPs can deteriorate due to the interdiffusion of atoms between the core and the shell. This may even lead to a shrink of the core and to the formation of a hollow structure in the so-known Kirkendall effect [101]. The influence of this process on the heating efficiency was investigated by Nemati et al., studying $Fe/\gamma\text{-}Fe_2O_3$ CS_NPs obtained by thermal decomposition of

$Fe(CO)_5$ [102]. They found that with increasing the NP average size from 8 to 14 nm, the core/shell morphology was retained for a longer period of time and the heating efficiency improved. In hollow NPs, obtained by annealing the previous samples at 180 °C for one hour under oxygen, the heating efficiency decreased, rendering them less useful for magnetic hyperthermia application.

Famiani et al. also produced Fe/Fe_xO_y CS_NPs with tunable sizes (12, 15, 18, and 20 nm) by thermal decomposition of $Fe(CO)_5$ and used dopamine molecules to functionalize the iron oxide surface, replacing the native oleylamine groups through the catechol groups [103]. Larger sizes were obtained in this case by increasing the amounts of iron precursor and extending the injection time. The authors evaluated the retention of the stable magnetic α-Fe core upon exposure to air and after ligand exchange and its resulting effect on the magnetic hyperthermia.

Lee et al. exploited the hard/soft coupling mechanism to maximize the heating efficiency of magnetic ferrite NPs, different from magnetite and maghemite [104]. They studied CS_NPs made of a hard core of $CoFe_2O_4$ (9 nm in size) and a soft shell of $MnFe_2O_4$ (3 nm-thick). At T = 5 K, the coercivity was between the values of single-phase $CoFe_2O_4$ and $MnFe_2O_4$ NPs; the CS_NPs were superparamagnetic at room temperature. The SLP (tested in AMF of 37.3 kA/m and 500 kHz) was one order of magnitude larger than that of single-phase $CoFe_2O_4$ and $MnFe_2O_4$ NPs, with size 9 nm and 15 nm respectively. These CS_NPs were prepared by thermal decomposition in organic media, by the seed-mediated method. $CoFe_2O_4$ NP was used as a seed and synthesized by thermal decomposition of Co(acac) with 1,2-hexadecanediol in the presence of oleic acid and oleylamine [86]; $MnFe_2O_4$ was over-grown by thermal decomposition onto the surface of the seed NP, adding $MnCl_2$ and $Fe(acac)_3$ in the presence of oleic acid, oleylamine and trioctylamine, and heating at 365 °C/1 h. As-synthesized CS_NPs were transferred to the aqueous phase by modification of the surface using dimercaptosuccinic acid. Using the same synthetic method, the authors were able to prepare various core/shell combinations, including $CoFe_2O_4/Fe_3O_4$, $MnFe_2O_4/CoFe_2O_4$ and $Fe_3O_4/CoFe_2O_4$, demonstrating the possibility to tune the magnetic anisotropy of the CS_NPs and their SLP, which ranged between 1 and 4 kW/g. These remarkably high SLP values were obtained with the AMF indicated above, i.e., in testing conditions that did not fulfill the safety criterion for medicine applications [47], already mentioned in Section 2. It can easily be verified that the same consideration applies to many of the studies cited in this review, actually.

S. Liebana-Vinas et al. studied ferrite cores of soft $MnFe_2O_4$ or hard $CoFe_2O_4$ prepared by the same method described above, covered by a 2–3 nm Fe_3O_4 shell formed in a second step, with an overall size in the 10 nm range [105,106]. In both types of cores, the addition of the magnetite coating produced an improvement of the heating efficiency, but the effect was definitely more marked in the case of $CoFe_2O_4$, in which an increase of SLP by a factor of 24 was experienced [105]

Fabris et al. reported on the possibility to control the heat generation mechanism of colloids of $Fe_3O_4/Zn_xCo_{1-x}Fe_2O_4$ CS_NPs by changing the shell composition with a similar seed-mediated growth method [107]. In particular, they showed that the effective anisotropy of the whole core–shell structure could be tuned by the substitution of Co^{2+} by Zn^{2+} ions in the shell. Increasing the Zn concentration of the shell, from x = 0 to 1.00, decreased the magnetic anisotropy and, in turn, this effect provided a way to select the magnetic relaxation mechanism, Brown or Néel, which dominated the heating process.

Lavorato et al. synthesized by seed-mediated growth method $Fe_3O_4/Co_xZn_{1-x}Fe_2O_4$ CS_NPs, whose heating properties could be optimized by modulating their shell composition and thickness and, hence, by finely controlling the interface exchange coupling and the resulting effective anisotropy [108]. They reported SLP up to ~2.4 kW/g for water colloids and ~1 kW/g for immobilized particles (AMF of ~63 kA/m and 309 kHz). The authors also showed that a reduction in the shell thickness or Co/Zn ratio favored the appearance of a collective magnetic behavior, arising from the competition between the dipolar and anisotropy energies of the CS_NPs. Such collective behavior led to the formation of chains in the colloid, which, according to the authors, was likely to be responsible for the large heating powers exhibited by their samples (see also Section 5).

Indeed, the magnetic heating mechanism has been studied in several types of CS_NPs, with different core size and/or shell thickness: $Fe_{3\text{-}x}O_4$ core (~4 nm) coated by a $CoFe_2O_4$ shell of variable thickness (1.0, 2.5, 3.5 nm) [109]; soft Fe_3O_4 core (varying between ~6 and 10 nm) and hard $CoFe_2O_4$ shell (varying between ~1 and 4 nm) [110]; Fe_3O_4 core (~6.3 nm) and $CoFe_2O_4$ shell (thickness 0.05, 1.0 and 2.5 nm) [111]; 14 nm sized NPs of Co ferrite core and a Mn-ferrite shell and inverted structure, with shells of varying thicknesses [112]; hard $CoFe_2O_4$ core and soft $Ni_{0.5}Zn_{0.5}Fe_2O_4$ shell (total size ~9 nm) [113]; hard $CoFe_2O_4$ core and soft $AlFe_2O_4$ shell (total size ~14 nm) [114]; Fe_3O_4 core and $ZnCoFe_2O_4$ shell and inverted structure (total size ~10 nm) [115].

CS_NPs with different $CoFe_2O_4$ core size (varying between ~4.4 and 8.4 nm), chemical nature of the shell ($MnFe_2O_4$ and iron oxide), and shell thickness (between ~1.9 and 3 nm) were prepared by Angotzi et al., using a seed-mediated growth strategy in an alcohol media and using an autoclave for heating [116]. In this case, initial cores were obtained by decomposition of metal oleates in a mixture of solvents (pentanol, octanol or toluene and water) in an autoclave at 180 or 220 °C/10 h and the shell was grown on the initial cores in a second reaction in the autoclave, adding the metal oleates in toluene, pentanol and water [117]. For all sets of samples, those with iron oxide shells featured higher heating efficiency and the thicker the soft shell, the better the performance.

In this framework, which highlights a general positive effect of hard/soft coupling in nanoheaters, perhaps the only exception is the article by Pilati et al. [118], dealing with $Zn_xMn_yFe_zO_4/\gamma\text{-}Fe_2O_3$ and $Zn_xCo_yFe_zO_4/\gamma\text{-}Fe_2O_3$ CS_NPs. These CS_NPs were prepared by hydrothermal coprecipitation of metal salts in aqueous alkaline medium at 100 °C and the iron oxide shell was deposited onto them by precipitation of $Fe(NO_3)_3$. The authors elucidated how the chemical composition affected the saturation magnetization, the anisotropy and the heating properties of the CS_NPs. The two different sets of CS_NPs, having either hard or soft ferrite cores and soft maghemite shell, did not present evidence of any interfacial exchange coupling contribution to their power absorption efficiency.

A heating efficiency as high as 10.6 kW/g (AMF of 37.3 kA/m and 500 kHz,) was measured by Noh et al. in cubic CS_NPs of $Zn_{0.4}Fe_{2.6}O_4$ core (50 nm in edge) and $CoFe_2O_4$ shell (5 nm in thickness) [119]. The total size of the CS_NPs was ~60 nm and they did not exhibit superparamagnetic behavior (Figure 2). This high efficiency was attributed not only to the presence of the hard $CoFe_2O_4$ shell, but also to the cubic shape of the CS_NPs that, compared to the spherical shape, allowed to reduce magnetic disorder effects and hence to attain a saturation magnetization of the core closer to the value of the bulk phase.

As a matter of fact, the shape of the NPs has been proved to have a strong impact on the magnetic heating mechanism [120–123] and iron oxide nanocubes are among the best performing materials [52,124–126].

The good synergy between cubic shape and exchange coupling was also demonstrated by Yang et al., who measured SAR = 1.21 kW/g in superparamagnetic CS_NPs composed of a spherical FePt core, of ~4.1 nm in size, embedded inside a cube of Fe_3O_4, so that the total size was ~14.7 nm (AMF of 18.8 kA/m and 630 kHz) (Figure 3) [127]. Again, we should emphasize that all these NPs showing high heating efficiency (SAR larger than 1 kW/g), were prepared by thermal decomposition in organic media, which is a method especially interesting for synthesizing CS_NPs with the low size dispersity, the good surface crystallinity and the homogeneous coating, required to maximize the coupling between the hard and soft phases. This method guarantees a strict control over the composition, structure, and morphology of the NPs. The main drawback of this technique is the difficulty of scaling up and the use of harmful and non-environmentally friendly reagents.

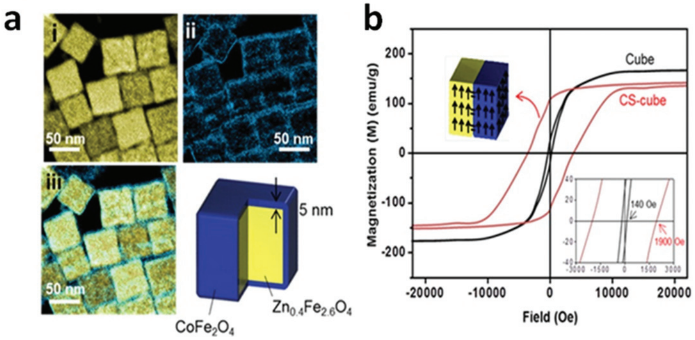

Figure 2. (**a**) Electron energy loss spectroscopy (EELS) mapped images of cubic CS_NPs with $Zn_{0.4}Fe_{2.6}O_4$ core and $CoFe_2O_4$ shell. (i) Yellow and (ii) blue regions represent Fe and Co, respectively, and (iii) the merged image. (**b**) Magnetic hysteresis loops measured at T = 300 K on the CS_NPs and $Zn_{0.4}Fe_{2.6}O_4$ cubic NPs with similar size (~60 nm). The coercivity of the CS_NPs was ~1900 Oe, 14 times larger than that of the single-phase cubes (~140 Oe). Adapted with permission from Ref. [119], Copyright 2012 American Chemical Society.

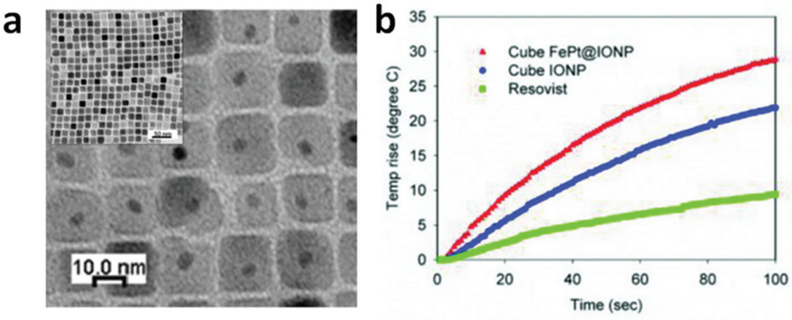

Figure 3. (**a**) Transmission electron microscopy (TEM) image of CS_NPs composed of a spherical FePt core embedded in a cube of Fe_3O_4. (**b**) Heating curves measured on the CS_NPs (sample FePt@IONP) and, for comparison, on single-phase magnetite cubic NPs (sample IONP) and on commercial iron oxide NPs (Resovist). Resovist and IONP showed SAR values of 0.39 and 0.92 kW/g, respectively, while the CS_NPs exhibited a value of 1.21 kW/g (AMF of 18.8 kA/m and 630 kHz). Adapted from Ref. [127] under CC BY_NC 4.0 International License.

4. Multicore Nanoparticles (MC_NPs)

MC_NPs are sphere-like nanosized aggregates of magnetically interacting ‘primary’ NPs (i.e., the cores). Other terms can be found in literature to refer to this type of structures, such as clusters, nanoclusters, nanoassemblies and nanoflowers.

The magnetic interactions between the primary NPs, exchange or dipolar in type, improve their magnetothermal stability. Therefore, MC_NPs can exhibit either ferromagnetic behavior at room temperature or superparamagnetic relaxation, but at higher T_B compared to the constituent NPs (obviously, under the same measuring conditions). These two different possibilities depend on the sizes of the primary NPs and of the final aggregated structure and also on the type and strength of magnetic interactions between the primary NPs, which in turn are determined by their spatial arrangement. All these factors ultimately depend on the chemical synthetic method, which determines the reaction rate and the degree of fusion between the cores [128]. Thus, depending on the viscosity of the media, the temperature and the heating time, multicore structures made of individual random cores or well-oriented cores can be obtained.

In a very large number of articles on magnetic NPs, the absence of magnetic hysteresis, usually ascertained by DC magnetometers (typically SQUID or vibrating sample magnetometer, VSM), is considered as an evidence that the NPs are in the superparamagnetic regime. In our opinion, although the measurement of null values of H_C and M_r strongly supports this interpretation, it does not constitute definitive proof. Using DC magnetometry, a complete study of the magnetic relaxing behavior of the NPs should include the measurement of hysteresis loops at different temperatures and the evaluation of the anisotropy energy barrier distribution, and hence of the T_B distribution, through the analysis of the thermal dependence of the thermoremanent magnetization or of the zero-field-cooled (ZFC) field-cooled (FC) magnetization [39,71]. Particularly in the case of magnetic NPs that tend to form spherical aggregates, it is not uncommon to measure null values of H_C and M_r at a temperature significantly lower than the higher T_B of the assembly assessed by ZFC-FC magnetization measurements [129]. The possible explanation is that the moments of the NPs arrange in low-remanence flux-closure configurations [55,130–132]. This occurs in order to minimize the energy of the aggregate as a whole, reaching a balance between the magnetostatic energy, the anisotropy energy and the contribution of the magnetic interactions between the NPs, all of which vary with temperature due to the thermal dependence of M_S and K. Therefore, one can observe that both M_r and H_C decrease strongly on increasing temperature and possibly become smaller than the measuring experimental error.

As for MC_NPs, the onset of low-remanence magnetic configurations is certainly not favorable as regard the heating efficiency and therefore it would deserve attention. On the other hand, regardless of the real reason behind the absence of magnetic remanence at room temperature, this feature has been considered a point of strength of this type of nanostructures, just as it is for single-core superparamagnetic NPs [133]. In fact, a null or small remanence implies that dipolar interactions between the MC_NPs are suppressed or strongly decreased. This reduces the risk of formation of large agglomerates, in the micrometer range, that may occlude blood vessels of a patient and cause dangerous side effects. Regarding biomedical applications, the relatively large size of MC_NPs favors high cellular uptake and prolonged circulation in the blood stream [134–136].

In general, ascertaining whether the magnetic behavior of MC_NPs is dominated by exchange or dipolar interactions is not simple and in some articles the item is not explored in detail, actually. However, exchange and dipolar interactions may influence the overall magnetic properties of spherical aggregates differently depending on their nature, which is magnetizing and demagnetizing respectively. In Sections 4.1 and 4.2, we will try to better highlight the role of exchange and dipolar interactions and we will present some selected examples taken from literature, also on the basis of the scientific novelty they represented.

Different synthesis methods have been described for the preparation of iron oxide MC_NPs with sizes between 20–250 nm, starting from Fe(II), Fe(III) or a mixture of both, in organic, aqueous and polyol media, using different surfactant to control the reaction rate and finally, using different heating sources, microwave, autoclaves or a heating mantle [128]. It is worth mentioning that, when the synthesis is performed in aqueous media, large aggregates with poor internal order are generally obtained. When the synthesis is in organic media, multicore structures have been reported as intermediate steps, with a certain degree of internal order [137]. However, when the synthesis takes place in polyol media, the adsorption of solvent molecules on the primary cores causes in situ-oriented aggregation [138]. It has been shown that polyol molecules are mainly adsorbed on some specific faces, favoring intermolecular hydrogen bonding from one covered core to another. Interestingly, at high surface coverage, polyol molecules are detached leading to a highly ordered multicore nanostructure.

In fact, one of the most used methods for preparing MC_NPs with internal exchange interactions (Section 4.1) is the synthesis in polyol media because of its versatility and reproducibility [139]. The polyol is a polar media to dissolve the precursors and determine the maximum temperature of heating. Then, there is a biocompatible complexing agent, that can be polyacrylic acid (PAA) or polyethylene glycol (PEG), and a base, sodium hydroxide, sodium acetate or an amine, that initiates the nucleation of the precursors and form the initial cores. Then, these cores are immediately aggregated into three dimensional nanostructures, stabilized with the excess of the complexing molecules.

MC_NPs around 40–50 nm were obtained by the polyol method using iron(III) acetylacetonate as precursor, tri(ethylene glycol) (TREG) and triethanolamine (TREA) heated to reflux and maintained at the refluxing temperature (245–280 °C) under the argon flow for 1 h [140]. Increasing the amount of base concentration, the nucleation of the iron oxide NPs became faster, so that the nucleated particles tried to aggregate to reduce their surface energy. By a similar method, but using diethylene glycol (DEG), Mn-doped iron oxide MC_NPs of 50 nm were prepared [141]. This method allowed the successful incorporation and homogeneous distribution of Mn within the MC_NPs. Slightly smaller sizes, 24–29 nm, were obtained by using a mixture of glycols, diethylene glycol (DEG)/tetraethyleneglycol (TEG) in a heating mantle up to 250 °C [142]. By using a microwave-assisted polyol approach $Fe_2(SO_4)_3$, sodium acetate and PEG in EG, MC_NPs of 27 to 52 nm could be obtained at 200 °C, increasing the size with the increase in reaction time from 10 s to 600 s [143]. Much larger MC_NPs (<250 nm) were be obtained by using an autoclave assisted polyol method, starting from Fe(III) in EG, urea and PAA, composed of many Fe_3O_4 nanocrystals with size < 10 nm [144].

Clustering previously synthesized primary NPs is the preferred route for obtaining MC_NPs with internal dipolar interactions (Section 4.2). First, individual NPs are obtained, either in water or in organic media, coated with oleic acid and then they are aggregated in a second step, using either citric acid, for example for the hydrophilic ones, or an oil in water emulsion, using a surfactant such as CTAB [145]. In general, these methods involving synthesis and aggregation of NPs yield non-uniform and large size distributions, having mainly dipolar magnetic interactions between cores.

4.1. MC_NPs with Internal Exchange Interactions

Exchange interactions are possible in multicore structures when the primary NPs are in a very close contact, substantially fused together. The terms 'grains' or 'nanocrystals' are also used instead of primary NPs. This condition of intimate and extensive structural connection is usually accompanied by a good degree of crystallinity of the grains and hence a high saturation magnetization, comparable to that of bulk materials. In fact, surface and structural/magnetic disorder effects that mostly affect single-core ferrite NPs, such as an alteration of the spinel structure and spin-canting [146–151], are strongly reduced.

In bulk nanocrystalline magnetic materials, the exchange interaction tends to couple ferromagnetically the atomic spins of neighboring nanocrystals, in competition with their local magnetic anisotropy. This can cause a reduction of the effective magnetic anisotropy of the system, compared to that of the individual nanocrystals, and hence of the coercivity. If the size of the nanocrystals is comparable to their ferromagnetic exchange correlation length, the anisotropy decrease is restrained [152]. On the other hand, if the nanocrystal size is lower than the ferromagnetic exchange correlation length, the local magnetic anisotropy is substantially averaged out to zero, which leads to superior soft magnetic properties [153]. Being magnetizing in nature, exchange interactions result in high susceptibility and favor the remanence of the magnetization.

Passing to MC_NPs, it must be considered that the magnetic properties and their thermal evolution, including the magnetization configuration, are determined by the interplay between this exchange-coupling phenomenology and small-size effects, i.e., magnetic relaxation and magnetostatic effects. The examples here below demonstrate that this interplay can actually lead to excellent heating capacity.

In a 2009 article, Dutz and coworkers stressed the suitability of MC_NPs for biomedical applications, particularly magnetic hyperthermia and cell separation [154]. The authors reported about water-based suspensions of aggregates of ~40–80 nm (coated by a carboxymethyldextran shell) consisting of primary iron oxide NPs with mean size of 14 nm

(Figure 4). The synthesis was carried out by coprecipitation in aqueous media (100 °C). The material showed ferrimagnetic behavior owing to the exchange interaction between the cores [133]. The highest SAR ~ 330 W/g was measured in MC_NPs with hydrodynamic size of ~82 nm (AMF of 11 kA/m and 400 kHz).

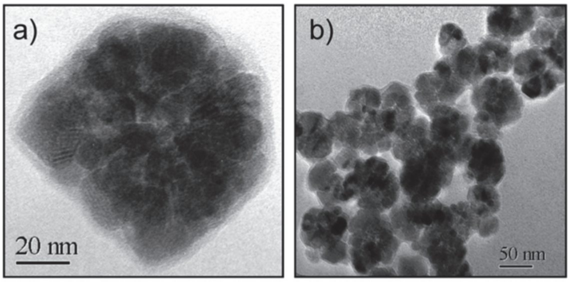

Figure 4. Typical TEM images of (**a**) a MC_NP consisting of exchange-coupled iron oxide cores and (**b**) an ensemble of MC_NPs. Reused with permission from Ref. [154], Copyright 2009 Elsevier B.V. All rights reserved.

In the same year, Barick et al. prepared Fe_3O_4 spherical MC_NPs of ~40 nm in size by the polyol method (EG, 200 °C) [155]. The MC_NPs were porous and composed of highly crystalline primary NPs of ~6 nm, which, as observed by TEM, were pseudoepitaxially fused together. At T = 300 K, the MC_NPs showed a higher magnetic susceptibility, compared to that of 6 nm Fe_3O_4 NPs taken as reference, and a much higher magnetization (~64.3 emu/g under a static field of 20 kOe). This behavior was explained in terms of a collective magnetic behavior of the primary NPs, induced by exchange coupling and dipolar interactions. Although we agree that, due to the porous nature of the MC_NPs, both types of magnetic interactions could be active, the increased susceptibility and magnetization seem more consistent with predominant exchange interactions, in our opinion. No magnetic hysteresis was observed at T = 300 K and the authors concluded that the MC_NPs were superparamagnetic. Although the article was mainly focused on the excellent properties shown by these nanostructures as contrast agents in Magnetic Resonance Imaging (MRI), the ability to generate heat under an AMF was also demonstrated (SAR = 92.62 W/g_{Fe} in AMF of 10 kA/m and 425 kHz).

Lartigue et al. prepared maghemite MC_NPs through a polyol process similar to the previous one (TEG, 220 °C) [156]. In particular, they obtained citrate-stabilized nanostructures ranging from single-core NPs of 10 nm to MC_NPs, with different mean size (19.6, 22.2, 24 and 28.8 nm). Transmission electron microscopy (TEM) techniques revealed that the MC_NPs consisted of merged grains sharing a same facet, namely the grains had the same crystalline orientation and the continuity of the crystal lattice at the grain interfaces could be clearly observed (Figure 5a). The saturation magnetization of the MC_NPs was close to that of bulk maghemite, unlike that of single-core NPs which was 30% lower, while the magnetic anisotropy was reduced ($1.75 \div 2.5 \times 10^4$ J/m^3 for MC_NPs and 2.6×10^4 J/m^3 for single-cores). The MC_NPs were superparamagnetic at room temperature, as observed by SQUID, but the blocking temperature T_B was considerably higher than that of the single-cores. Based on the whole of experimental results, the authors hypothesized that the cores were exchange interacting. Heating tests were carried out for different AMF amplitudes ($9 \div 29$ kA/m) and frequencies ($100 \div 700$ kHz). Under all conditions, a $2 \div 10$-fold SAR increase was observed for MC_NPs with respect to single-cores. In AMF of 29 kA/m and 520 kHz, the largest sized MC_NPs produced the highest SAR (above 1.5 kW/g) (Figure 5b,c). The authors concluded that the combination of reduced anisotropy and enhanced magnetic moment, made possible by magnetic ordering and exchange interactions at the grain interfaces, preserved the superparamagnetic-like behavior of the MC_NPs and simultaneously increased the thermal losses.

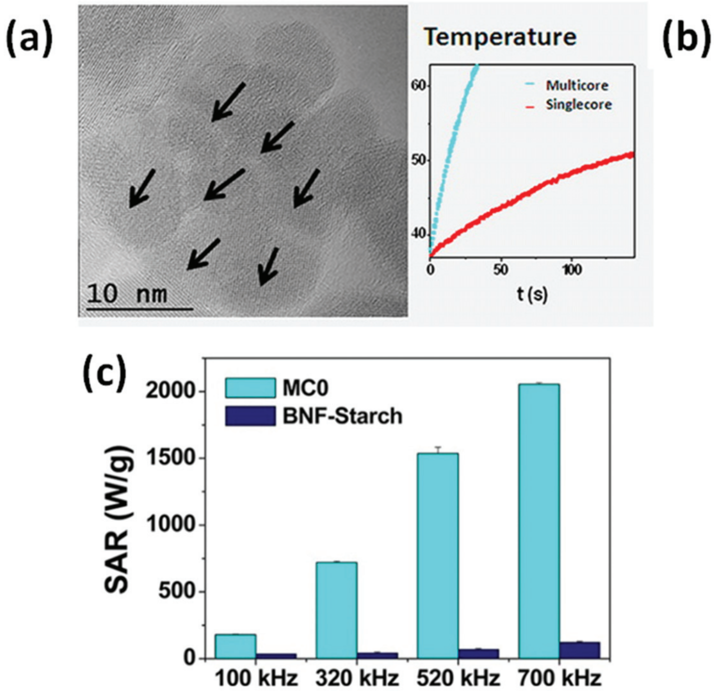

Figure 5. (**a**) High resolution TEM image of a maghemite MC_NP consisting of merged grains with the same crystalline orientation. (**b**) Heating curves measured on the MC_NPs and on single-core NPs (AMF of 29 kA/m and 520 kHz). (**c**) SAR value comparison between the MC_NPs (sample called MC0) and commercial magnetite NPs (BNF_starch) at different frequencies for a magnetic field amplitude of 25 kA/m. Adapted with permission from Ref. [156], Copyright 2012 American Chemical Society.

This work by Lartigue at al. was published shortly after another article by the same group, in which the authors described in detail the polyol synthetic protocol and discussed the formation mechanism of maghemite MC_NPs, with variable size, made up of grains of approximately 11 nm [157]. The article highlighted the great heating capacity of this type of structures and for MC_NPs of 24 nm a SLP value as high as ~2 kW/g was reported (AMF of 21.5 kA/m and 700 kHz). In this article, the authors did not mention the possible role of exchange interactions and the exact heating mechanisms was not delineated, actually. However, they already observed that the MC_NPs were single crystalline and that, probably thanks to the high crystallinity degree, had a high saturation magnetization, close to that of bulk maghemite or, in some samples, even the same.

The polyol method was also used by Gavilán et al. starting from an Fe(III) salt to prepare maghemite MC_NPs of ~60 nm, but with different size of the cores [158]. In fact, on increasing the reaction time, the MC_NPs undertook a crystallization process that increased the core size from ~11 nm to ~23 nm, as well as the saturation magnetization (Figure 6).

An enhanced magnetic susceptibility and a smaller coercivity, compared to that of 36 nm single-core NPs, indicated a collective magnetic behavior of the constituent primary NPs. The highest SLP (~1.13 kW/g_{Fe} in AMF of 23.8 kA/m and 710 kHz) was measured in water suspension of MC_NPs with the largest core size (i.e., 23 nm). This value was 5 times larger than that of MC_NPs with cores of 15 nm and 1.5 times larger than the 36 nm single-core NPs. However, a drastic decrease (~37%) of the heating performance of the MC_NPs tested in a viscous medium (agar 2%) was reported.

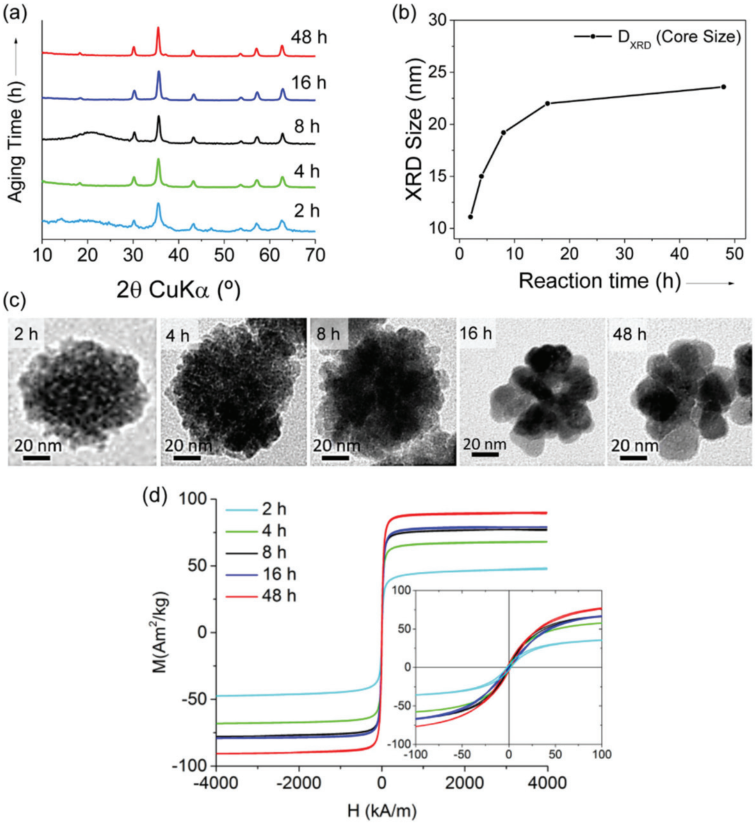

Figure 6. Structure of maghemite MC_NPs at different reaction time (2–48 h) during the synthesis with polyol method: (**a**) X-ray diffraction patterns; (**b**) core size calculated by Scherrer's equation. (**c**) Representative TEM images. (**d**) Magnetization curves measured on the samples at T = 290 K: M_S increased from 48 to 90 Am^2/kg with prolonging the reaction time, as well as H_C (0.5−2 kA/m). Adapted with permission from Ref. [158], Copyright 2017 American Chemical Society (further permissions related to the material excerpted should be directed to the ACS).

Indeed, a similar effect was also observed for 25 nm MC_NPs, similar to those of Refs. [156,157], by comparing heating tests in water and in high viscosity glycerol [159]. The authors reported an even stronger decrease of the heating efficiency (up to 90%) for MC_NPs in cellular environment (i.e., attached to the cell membrane or internalized within intracellular vesicles), though this result seems somewhat contradictory to the previously reported good ability of these nanostructures to kill breast cancer cells under AMF exposition [156]. It was argued that the heating reduction was due to the inhibition of the Brownian mobility in glycerol and in the cells, caused by the high viscosity.

In fact, in MC_NPs, the magnetization by Brownian motion may be relevant due to the large magnetic moment they can acquire in an applied field. However, particularly in the case of dispersion in biological media or confinement in cells, aggregation states can be favored and hence dipolar interactions can come into play, which affect the heating mechanism [160–162]. This point is further addressed in Sections 4.2 and 6.

Bender et al. studied the hyperthermia performance of dextran coated maghemite MC_NPs, of about 39 nm in size, constituted by exchange-coupled 5−15 nm cores and hydrodynamic sizes (z-average) of 56 nm with a polydispersity index of 0.099 [163]. The heating tests were carried out on the colloidal dispersion whose viscosity was changed by adding glycerol (AMF of 8.8 mT and rotational frequency $\varpi = 5.9 \times 10^6$ Hz). Considerably high ILP values were measured (~7 nHm^2/kg_{Fe}) and nearly independent of the viscosity, indicating that, at this high AMF frequency and under the adopted experimental conditions, the heat was generated by internal magnetization processes and not by Brownian relaxation.

Hence, the problem of the efficiency of MC_NPs in highly viscous media, including cells, is complex, somewhat controversial, but certainly can be a concern. It depends in part on the existence of remanence in these multicore structures or on the poor colloidal stability in different media that may lead to agglomeration of the material. On the other hand, several articles have confirmed the excellent suitability of these nanostructures as hyperthermia agents in cancer treatments.

Dutz et al. performed heating tests (AMF of 25 kA/m and 400 kHz) on maghemite MC_NPs of 40–60 nm in size dispersed in fluid (SAR = 400 W/g) and embedded in gelatin, i.e., immobilized as in a tumor tissue (SAR = 262 W/g) [164]. In spite of the SAR reduction, in vivo experiments in mice demonstrated that these MC_NPs heated a tumor of about 100 mg by about 22 °C within the first 60 s of treatment.

Hemery et al. compared the efficiency of iron oxide MC_NPs (29.1 nm) and single-core NPs (14.5 nm) for magnetic hyperthermia treatments on glioblastoma cells [134]. The samples were produced by a polyol method [165] and for this study the authors selected samples with SAR of 265 W/g and 134 W/g for the MC_NPs and for the single-core NPs, respectively (AMF of 10 kA/m and 755 kHz). The study highlighted the superior efficiency of MC_NPs for magnetic hyperthermia, leading to 80% cancer cell death, which was ascribed to the higher SAR and better cellular uptake.

Shaw et al. synthesized MC_NPs with size around 40–60 nm consisting of γ-Fe_2O_3 grains grown over the surface of a $MnFe_2O_4$ core [166]. Microwave-assisted polyol method in two steps was used to obtain first the $MnFe_2O_4$ seed and then the $MnFe_2O_4/\gamma$-Fe_2O_3 structure. The exchange interaction within the MC_NPs led to enhanced M_S and magnetic susceptibility, compared to $MnFe_2O_4$ cores alone. A magnetic hyperthermia treatment carried out for 30 min on HeLa cells, with 0.75 mg/mL ferrofluid of the MC_NPs, induced a temperature rise to 46 °C and decreased the cell viability to 17% (AMF of 250 Oe and 113 kHz).

An original type of 100 nm MC_NPs, made of $Fe_{0.6}Mn_{0.4}O$ (wüstite), were synthesized by Liu et al. by thermal decomposition of acetate precursors in trioctylamine and PEG (Mw = 10,000) to make them hydrophilic by ligand exchange reaction [167]. The MC_NPs exhibited unique room-temperature ferromagnetic behavior, unlike their antiferromagnetic bulk counterpart, thanks to the high iron content and to the exchange coupling between the cores that enhanced the ferromagnetic ordering. Heating tests (AMF of 40 mT and 366 kHz) gave SAR = 535 W/g_{Fe} in aqueous solution and 490 W/g_{Fe} in agarose gel. In vitro and in vivo magnetic hyperthermia experiments demonstrated that these wüstite MC_NPs could induce breast cancer cell apoptosis and a complete tumor regression in tumor-bearing mice without appreciable side effects.

Similar results were obtained for cRGD coated 20 nm manganese iron oxide MC_NPs obtained by similar method, with maximized SAR (680 W/g at moderated AMF of 47 kA/m and 96 kHz,) and very efficient results in a human tumor-derived glioblastoma cell line U87MG (62% cell death) [168].

4.2. MC_NPs with Internal Dipolar Interactions

If the cores forming the MC_NPs are not enough closely packed or if the intimate contact between them is not extended or is prevented by a non-magnetic coating, dipolar interactions predominate.

The influence of dipolar magnetic interactions on the magnetothermal behavior of a NP assembly has been extensively studied in the last decades and different, sometimes conflicting, models have been applied to explain the experimental data [39,169,170]. In general agreement with numerical calculations and theoretical predictions [171,172], we could summarize the role of dipolar magnetic interactions acting on a NP assembly by saying that they produce two main competing magnetic effects, relevant for the magnetic heating mechanism. As formerly indicated by Dormann et al. [39], dipolar magnetic interactions lead to an increase of the anisotropy energy barriers of the NPs. In the case of small and soft NPs, this effect improves the thermal stability of their magnetic moments, shifting to higher temperature or preventing the entrance in the superparamagnetic regime [39,129,149,173–176]. Under the conditions of validity of the LRT (i.e., in the linear regime), dipolar interactions can vary the Néel relaxation time τ_N so as to approach the resonant condition $f_m\tau_N = 1$ or move away from it, which leads to an increase or decrease of the hysteresis loop area, respectively; in the nonlinear regime, increasing τ_N so as to pass from the superparamagnetic state ($f_m\tau_N < 1$) to the blocked one ($f_m\tau_N > 1$) increases more and more the hysteresis loop area, at least until demagnetizing effects become prevalent [172]. In fact, in blocked NPs, magnetic dipolar interactions exert a demagnetizing action and bring about a decrease of remanent magnetization, magnetic susceptibility and possibly of coercivity. Both experimental and modeling results have confirmed this second effect of dipolar interactions, which is clearly detrimental to the heating efficiency [171,177–182].

Hence, the role played by dipolar interactions in the heat generation mechanism is complex: while increasing the effective anisotropy of the NPs can enhance the heating efficiency [175,183–185], their demagnetizing nature is disadvantageous. Therefore, the final heating performance comes from the competition between these different effects, which ultimately depends on the specificities of the system, i.e., size and anisotropy of the individual NPs and aggregation state, and on the measurement conditions (AMF amplitude and frequency) [171]. Some experiments and numerical simulations revealed a non-monotonic evolution of SAR on increasing the concentration of ferrofluids, hence the strength of dipolar interactions, on a wide range of values [176,186–189]. It was highlighted the existence of a SAR peak at an optimal concentration at which dipolar interactions are comparable to the anisotropy field [186,188].

When dipolar interactions give rise to stable aggregates of NPs, configurational effects of magnetostatic nature must be also included in this description. In isometric aggregates of soft NPs (i.e., spherical aggregates, precisely what we call MC_NPs) a low-remanence magnetic state is favored, which implies a decreased heating efficiency (in the case of hard NPs, their individual anisotropy dominates on dipolar interactions); on the opposite, anisometric aggregates (i.e., elongated formations such as chains and columns) exhibit high-remanence magnetic configurations, which can enhance the heating efficiency (see Section 5) [55]. Moreover, a reduced Brownian mobility connected to an increased hydrodynamic size may also enter into this already intricate picture [190].

Therefore, MC_NPs with internal dipolar interactions do not necessarily guarantee better heating efficiency than individual NPs. The main advantage of this type of nanostructures is represented by the possibility of controlling their structural characteristics (such as size of the cores, distance between the cores, size of the aggregates), hence the state of magnetic interaction and the heating capacity. In this regard, some examples are now shown.

Blanco-Andujar et al. reported on the heating properties of citric acid coated iron oxide MC_NPs, obtained by coprecipitation in a microwave reactor and coated in a second step [191]. This particular synthesis method allowed to control the size (varying between 13 and 17 nm) and number of the individual magnetic cores and hence the hydrodynamic size D_H of the aggregated structure (50–125 nm), by changing the time of heating in the second step. The samples did not show magnetic hysteresis at room temperature in SQUID measurement conditions. The existence of inter-cores demagnetizing interactions of dipolar type was verified through the analysis of the field dependence of the remanence (isothermal remanent magnetization, IRM, and direct current demagnetization, DCD) and the construction of the Henkel plots. A better heating efficiency was associated with a lower core-to-core magnetic interaction. The best response (ILP of 4.1 nHm^2/kg) was measured for small MC_NPs (D_H ~ 65 nm) consisting of large cores (~17 nm).

Sakellari et al. studied the heating properties of colloidal MC_NPs of various size (45–98 nm), consisting of 13 nm iron oxide NPs prepared by the polyol process in the presence of PAA. Water content seems to be the parameter to control the multicore size [192]. The packing density of the MC_NPs increased with the size and therefore the saturation magnetization increased too. In spite of the small size of the primary NPs, the samples showed ferrimagnetic behavior at room temperature, which was ascribed to an enhanced blocking temperature T_B due to dipolar interactions [193]. The thermal response of the MC_NPs was higher than that of the individual NPs. The 50 nm MC_NPs showed the best heating capacity (maximum SAR ~ 400 W/g in AMF of 25 kA/m and 765 kHz) as a result of the optimized interplay between structural features, packing density and strength of dipolar interactions.

Ovejero et al. studied the effects of dipolar interactions in iron oxide MC_NPs prepared by thermal decomposition in organic media, transferred to water by ligand exchange with DMSA and controlling aggregation by changing the pH of the dispersion [189]. The primary NPs had a hydrodynamic size D_H = 20 nm. The D_H of the MC_NPs varied between 56 nm and 356 nm. The authors stressed the influence of the polydispersity index (PDI) in the heating mechanism. In fact, the heating capacity was strongly influenced by the dipolar interactions resulting from the aggregation of the NPs, but in a different manner depending on PDI. For low PDI (<0.2), the SAR value slightly increased at small values of D_H (<100 nm) and then showed a 25% drop starting from D_H =139 nm. For high PDI, a progressive but smooth reduction of SAR (~10%) was observed on increasing D_H. Thanks to the analysis of high frequency hysteresis loops, the authors also provided some hints on the causes of such SAR dependence. The increase of dipolar interactions due to the increase of aggregation state resulted in a reduction of the remanent magnetization, though accompanied by an enhancement of coercivity.

Another strategy for controlling the dipolar interactions of MC_NPs was presented by Spizzo et al., who prepared aggregates, of ~25 nm in size, consisting of small iron oxide NPs (5–10 nm) with 2-pyrrolidone as capping agent [151]. Thanks to the presence of 2-pyrrolidone, the MC_NPs were stable in water. Conversely, when dispersed in PEG, the primary NPs tended to separate from each other, although they still formed spherical aggregates (Figure 7a–d). Thus, the strength of the dipolar interactions between the primary NPs varied upon changing the fluid in which they were dispersed. Accordingly, the heating response varied too and, in AMF of 13.5 kA/m and 177 kHz, the best response was measured in the aqueous dispersion of MC_NPs, namely in the more compact structures dominated by stronger dipolar interactions (Figure 7e).

To produce tight clustering of Fe_3O_4 NPs and highlight the importance of the primary NPs in cluster formation for enhanced heat-generation power, Hayashi et al. prepared magnetite NPs (~17 nm in diameter) by precipitation with hydrazine in the presence of a pyrrole polymer that formed multicore structures of ~55 nm, also containing anticancer drug (i.e., doxorubicin, DOX) [194]. NP size was controlled by adjusting the amount of hydrazine and the reaction time. Folic acid and PEG were used to stabilize the multicore structures in suspension, leading to final MC_NPs of (64 ± 6) nm with ferrimagnetic behavior at room temperature (Figure 8a–c). In fact, strong dipolar interaction between the primary NPs influenced the passage to the superparamagnetic regime, which, using SQUID magnetometry, was seen to occur at T_B ~ 400 K. For comparison, in a sample of unclustered Fe_3O_4 NPs, prepared as control material, T_B ~ 350 K (Figure 8d). A maximum SAR value of 353 W/g was measured in the MC_NPs, more than double that of the control NPs (AMF of 8 kA/m and 217 kHz) (Figure 8e). The capacity of the MC_NPs to hold the DOX and the possibility to control its release using the AMF as a trigger was also investigated. This work followed previous articles by Hayashi and co-workers, which were also aimed at demonstrating the suitability of Fe_3O_4 MC_NPs as theranostic agents [23,195].

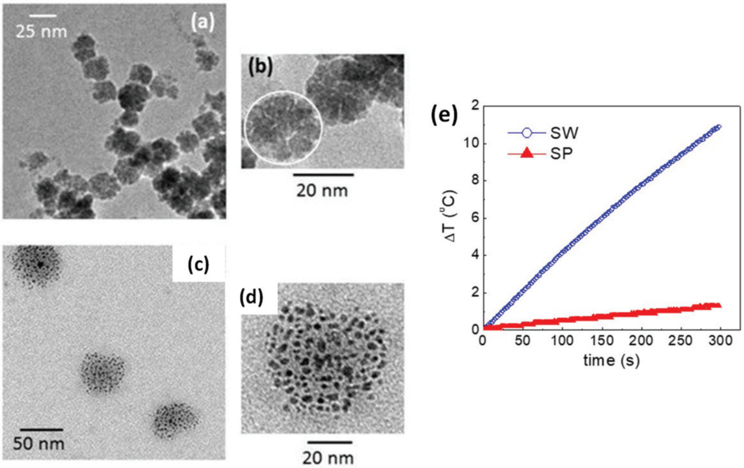

Figure 7. (**a**,**b**) TEM images of iron oxide MC_NPs dispersed in water (sample SW); in (**b**) the white circle highlights one MC_NP consisting of primary NPs capped with 2-pyrrolidone. (**c**,**d**) TEM images of the MC_NPs dispersed in polyethylene glycol 400 (PEG) (sample SP), showing how the primary NPs tended to separate from each other. (**e**) Heating curves for samples SW and SP in an AMF of 13.5 kA7m and 177 kHz. Adapted from Ref. [151] under CC BY 4.0 License.

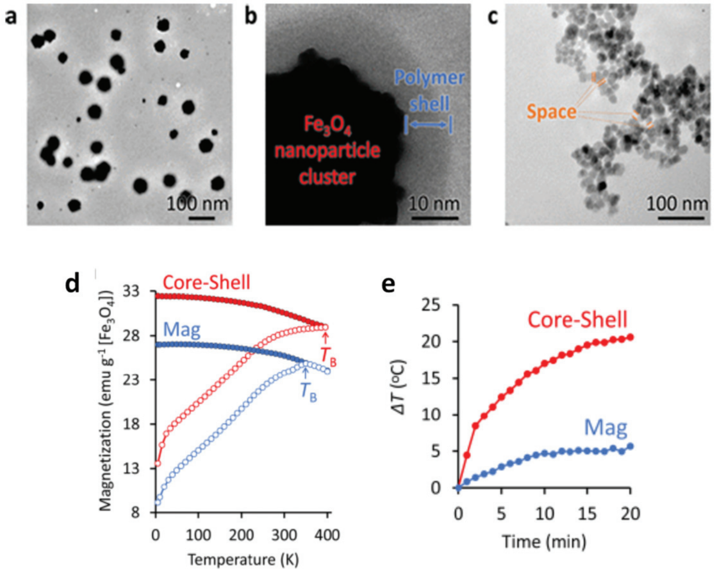

Figure 8. (**a**) TEM image of magnetite MC_NPs (**b**) Magnified view of a MC_NP allowing to distinguish the existence of a 6 nm-thick polymer shell. (**c**) TEM image of unclustered Fe_3O_4 NPs, prepared as control material. (**d**) ZFC-FC magnetization measurements vs. T measured on the MC_NPs (indicated as core-shell sample due to the presence of the polymer coating) and on the control NPs (sample called Mag). (**e**) Changes in the temperature of an aqueous solution containing MC_NPs and the control NPs with AMF application time. Adapted with permission from Ref. [194], Copyright 2016 American Chemical Society (further permissions related to the material excerpted should be directed to the ACS).

Regarding the potential of MC_NPs as multifunctional agents in nanomedicine applications, it is worth highlighting the high efficiency of these nanostructures as MRI contrast agents. The topic has been dealt with in a number of articles and the T_1 and T_2 contrast enhancement by aggregation of iron oxide NPs is a well-established phenomenon [140,196–199], common to MC_NPs dominated both by exchange interactions [155,156,165,167] and dipolar interactions [141,193–195].

5. Linear Aggregates

With the term 'linear aggregates', we refer to anisometric assemblies of NPs, both 1-dimensional (i.e., chains) and 3-dimensional (columnar aggregates), coupled by dipolar interactions. The research interest in the magneto-heating properties of this kind of magnetic structures has been prompted by two main factors: the discovery of the excellent heating performance exhibited by chains of magnetosomes synthesized by magnetotactic bacteria [200–203] and the observation that magnetic NPs in a fluid tend to arrange in linear aggregates under a uniform magnetic field (static or alternating).

Magnetosomes consist of a highly crystalline cubic-shaped core of magnetite/maghemite surrounded by biological materials, in particular lipids and proteins. Typically, the cores have a mean size of ~30 nm, are single magnetic domains and show ferrimagnetic properties at room temperature. The magnetosomes are naturally arranged in chains inside the bacteria thanks to protein filaments that favor their alignment [204]. It must be noted that, in the chain configuration, the dipolar interactions favor the ferromagnetic alignment of the moments of the NPs, i.e., they exert a magnetizing action. This marks a fundamental difference with respect to isometric aggregates of randomly oriented NPs, where dipolar interactions are demagnetizing, as discussed above (Section 4.2).

It was argued that the superior magnetic efficiency of magnetosomes was only in part due to the cubic shape of the individual cores—which implied a higher surface magnetic anisotropy, compared to spherical iron oxide of similar size—and that the chain arrangement was a crucial element [126]. In fact, dipolar interactions between the cores was found to result in an effective magnetic anisotropy of configurational type [204].

The onset of an effective anisotropy, induced by the formation of linear aggregates during heating tests and oriented parallel to the applied field, was also invoked to correctly interpret magnetic heating performance of NPs in fluids [55,58]. This effective uniaxial anisotropy is substantially the shape anisotropy of the whole aggregate and competes with the magnetocrystalline anisotropy of the individual NPs. Therefore, it is more effective in the case of low anisotropy NPs, where it leads to an increase of the hysteresis loop area and hence of the SAR [55].

Excluding a few theoretical studies that reported a decrease in heating efficiency related to NP chain formation [205,206], in general both theoretical analyses and experimental results confirmed that chain-like arrangements of NPs had enhanced heating performance compared to systems of randomly distributed NPs and pointed out a dependence on the features of the linear aggregates (width, length and density as well as the size and shape of the constituent NPs) [57,207–209]. In the latter cited articles, samples of linear aggregates suitable for heating tests were prepared by quenching magnetic NPs in an agarose gel matrix in the presence of a static uniform magnetic field, so as to develop anisotropic dipolar interactions between them. Hence, it was also shown that the heating efficiency of these systems could be modified by changing the viscosity of the agarose matrix and the relative orientation between the aggregate long axis and the direction of the AMF [207–209]. This last item was also theoretically addressed by Valdes et al., who also analyzed the case of randomly oriented NP chains and predicted significantly better heating performance with respect to a system of dispersed non-interacting NPs [210,211].

The better heating capacity of anisometric groups of NPs was also demonstrated by Niculaes et al. who compared the SAR values of individual iron oxide nanocubes (edge length ~20 nm) of dimers and trimers (composed of two and three nanocubes, respectively) and of larger aggregates of more than four nanocubes [212]. The highest SAR was measured in the anisometric dimers and trimers whereas the larger and more isometric structures exhibited the lower thermal response.

Avugadda et al. fabricated aggregates of iron oxide nanocubes, coated with a bioresorbable polymer, that could be disassembled upon exposure to lytic enzymes, thus obtaining 2D assemblies and finally small chain-like clusters, containing just few nanocubes, with improved heating performance [213].

Balakrishnan et al. showed that cubic-shaped cobalt ferrite NPs (mean edge size ~17 nm), injected in tumors developed in mice, spontaneously formed randomly oriented chain-like structures (median of 4 nanocubes/chain), whose length increased (median of 7 nanocubes/chain) after exposure to an AMF during an heating treatment [214].

Fu et al. prepared compact aggregates of magnetite NPs of different sizes, using an emulsion droplet solvent evaporation method [215]. They showed that dipolar interactions between the NPs in the aggregates improved the heating efficiency as long as the latter were small and anisometric, so as to favor the appearance of shape magnetic anisotropy. As the size of the aggregates increases, they became more and more spherical. Thus, the shape anisotropy decreased and this impaired the heating efficiency.

As for the production of long linear aggregates of NPs, excluding the possibility of extracting magnetosome chains from cultured magnetotactic bacteria [201], the adopted methods involve the use of an externally applied magnetic field, as already seen above for immobilization into an agar matrix. In this respect, another example is the work of Hu et al., who inserted linear aggregates of NPs, of 15 nm and 200 nm in size, in a hydrogel matrix [216]. This was obtained by assembling the magnetic NPs in monomers solution and then activating the gelation, in presence of a magnetic field during both processes.

The use of an inorganic shell-like silica to encapsulate linear arrangements was also explored by Andreu et al. [217] to produce small chains of cubic iron oxide NPs mimicking naturally produced magnetosomes and enhance the SAR respect to individual nanocubes. Comparing these chains with individual nanocubes for a fixed AMF of 3 kA/m and 111 kHz, they observed that the heating performance of chains resulted higher at room temperature, but lower at low temperatures (<250 K). These results stress the importance of considering the temperature and AMF conditions for comparing the heating efficiency.

Sanz et al. tested the heating capacity of $MnFe_2O_4$ NPs (~50 nm average size) loaded in cells cultured in a static magnetic field of 650 kA/m and in no field [218]. The application of the magnetic field led to the formation of linear aggregates inside the cells, in contrast with the spherically shaped ones that formed in absence of field; in vitro measurements indicated that the heating efficiency was approximately a factor 2 higher in the first case (Figure 9).

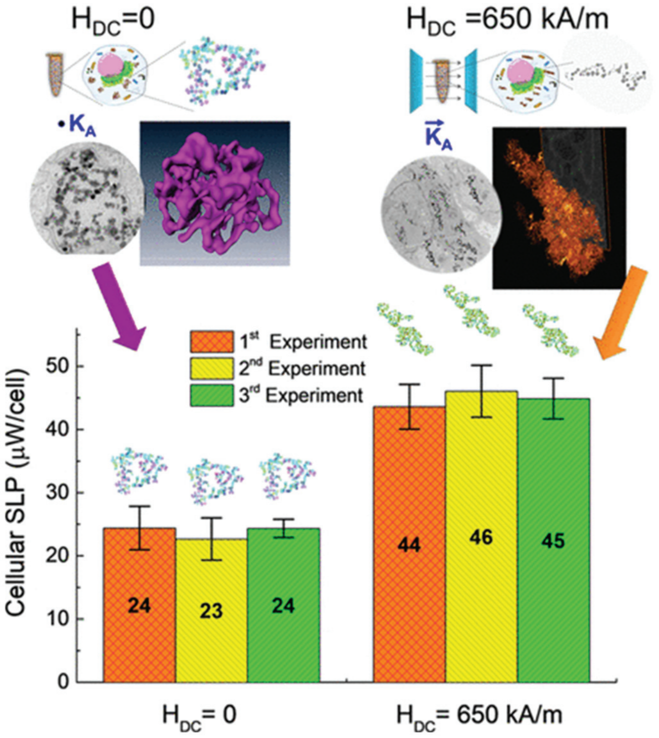

Figure 9. In vitro power absorption experiments for aggregates of $MnFe_2O_4$ NPs within BV2 cells. The aggregates formed overnight without an applied field, resulting in sphere-like shape, and under an applied dc field H = 650 kA/m, resulting in elongated shape. SLP values are given per cell in μW/cell. Adapted with permission from Ref. [218], Copyright 2020 American Chemical Society.

6. Hybrid Systems

Hybrid magnetic materials, consisting of NPs loaded into a non-magnetic organic or inorganic matrix, are generally created to combine different functionalities coming from the magnetic NPs and the matrix. Thus, in addition to the heating capacity and the enhancement of contrast in diagnostic imaging that the NPs provide, the matrix may allow drug transportation (hydrophobic and hydrophilic) and stimuli responsive actions, eventually improving the theranostic concept [16,219–224]. If the containers in which the NPs are encapsulated are also of nanometric dimensions, they are often referred to with the terms 'nanocontainers', 'nanocapsules', 'nanovectors', 'nanocarriers'. Therefore, in this formulation, the magnetic NPs are spatially confined at the nanoscale and generally subjected to interparticle dipolar magnetic interactions, whose strength varies with their concentration. Moreover, the NPs are not free to move and their spatial arrangement depends to some extent on the geometric and chemical-structural features of the carriers into which they are loaded.

The methods for the synthesis of these hybrid systems are numerous and vary mainly according to the type of matrix and the characteristics of the loaded magnetic NPs. Here below, we focus on three types of container: liposomes, polymeric matrix and silica.

From the magnetic point of view, the magnetothermal phenomenology is basically similar to that already described in Section 4.2, i.e., typical of aggregates of dipolar interacting NPs. As we have discussed, dipolar interactions between NPs of a sphere-like aggregate play a complex role in the heating mechanism, not always favorable for SAR. However, it is worth remarking that hybrid systems are intended as multifunctional agents.

If the thermal degradation of the carrier and the release of drug must be induced, the amount of loaded NPs must be high enough to generate the needed heating power, even if their accumulation may determine the onset of strong dipolar interactions and lead to a decrease in their thermal response. Moreover, a high amount of magnetic NPs is needed for efficient imaging and for enhanced magnetophoretic mobility and tissue targeting.

Although this review is devoted to artificial magnetic systems, it is worth noting that also NPs internalized in cells constitutes hybrid systems. In fact, it is now quite well established that inorganic NPs taken up by cells are concentrated within intracellular vesicles having a typical size of some hundreds of nanometers (late endosomes and lysosomes). Cellular internalization leads to a considerably reduction of the NP heating efficiency. Cabrera et al. carried out an in-depth study of this phenomenon and demonstrated that the inhibition of the Brownian relaxation process, caused by the immobilization of the NPs inside the cells, accounted only in part for the heating reduction [162]. The main cause was the intracellular clustering of the NPs, which favored the dipolar interactions. Levy et al. investigated the magnetic outcome of iron oxide NPs, with size below 10 nm, injected intravenously into mice [161]. The superparamagnetic behavior of the NPs was modified following cellular uptake and confinement within intracellular vesicles, due to the dipolar interactions. A different increase in the blocking temperature T_B occurred depending on whether the NPs were internalized in the liver, spleen or adipose tissue, reflecting their different arrangement inside the cells. The authors used the analysis of the dynamical magnetic behavior of the NPs as a tool to gain a fundamental understanding of the local organization of the NPs in the intracellular compartments.

The influence of dipolar interactions on the magnetic heating properties of NPs in lysosomes was also theoretically studied by Tan et al. using Monte Carlo simulations [225]. A spatial repartition of the heating power inside the lysosomes was demonstrated, related to changes in the local concentration of the NPs.

6.1. Liposomes

Liposomes are vesicles formed by a double layer of phospholipids and are used clinically as drug-delivery vehicles. Magnetic NPs can be encapsulated either in the aqueous or in the organic part, between the lipid bilayer, forming magnetoliposomes, which have been extensively investigated as drug-delivery system for targeting tumors and their microenvironment [226]. In addition, liposomes are thermosensitive, so an AMF can stimulate the co-encapsulated internal heating source (iron oxide NPs), for the thermally triggered drug release without increasing the environmental temperature. It should be noted that only an increase of few degrees (2–4 °C) is needed at the NP surface, in close contact with the lipid, to overcome the melting temperature of the liposome, i.e., to change it from the gel to liquid state and release the content. The presence of NPs influences the phase temperature of lipids.

The thin-film hydration method coupled with sequential extrusion is the most versatile and reproducible method for the production of magnetoliposomes. It allows incorporating the NPs, previously synthesized, in the aqueous [227] and the organic phase [228] at the same time that the liposome is formed. Different spatial distribution of the NPs can also be controlled inside or outside the liposome by changing the NP coating (Figure 10). The fact of being encapsulated inside the lipid bilayer can induce a shift of the blocking temperature T_B of the NPs to higher values, indicating an increased aggregation degree in comparison with free NPs. As shown by Forte Brollo et al., the aggregation degree was higher for oleic acid coated NPs, given their confinement at the lipid bilayer. Moreover, T_B increased following internalization of NPs into cells, namely as their intralysosomal density increased [228].

Indeed, the organic confinement can influence significantly the dynamic magnetic response of the NPs. For 9 nm and 7 nm citrated iron oxide NPs densely packed inside liposomes, under high field conditions (AMF of 27 kA/m and 700 kHz), it was observed an increase in SAR values of 438 W/g and 164 W/g compared to 270 W/g and 108 W/g for 9 nm and 7 nm NPs uniformly dispersed in colloidal suspension [219]. These data highlighted the influence of NP size and the noticeable effect of their local confinement in liposomes. The high volume fraction of NPs inside liposomes led to magnetic dipolar interactions, which could be evidenced by ZFC-FC magnetization measurements, in a shift of T_B to higher temperatures and a flattening of the FC curve below T_B.

Even smaller particles (3–5 nm) encapsulated into liposomes can reach the high concentration needed (~10 mg Fe/mL) for an efficient heating (2–4 °C) under high frequency field (750–1150 kHz) [227]. If larger 16–36 nm NPs were encapsulated in liposomes, resulting in 3–6 NPs per liposome, it was observed that lipid cover did not interfere with magnetic response of the NPs (no variation in T_B). SAR values at moderate AMF amplitude and frequency (12 kA/m and 197 kHz) were 34 W/g and 26 W/g as the particle size increased, enough to produce a temperature rise from 37 °C to 42–46 °C [229].

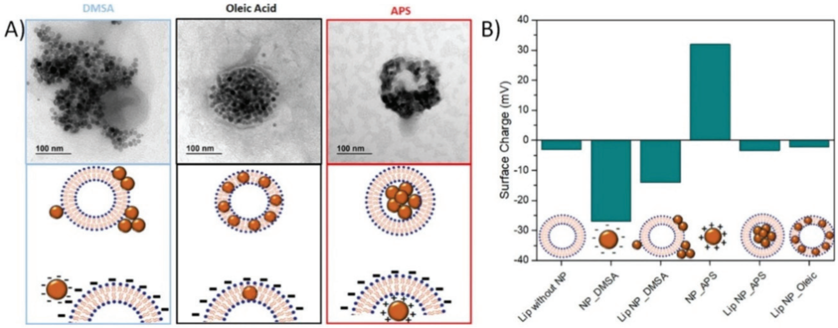

Figure 10. (**A**) TEM images and corresponding schemes of liposomes produced with iron oxide NPs using different coatings as dimercaptosuccinic acid (DMSA), oleic acid and (3-aminopropyl)trimethoxysilane (APS), resulting in different spatial configurations of the NPs. (**B**) Zeta potential measurements at pH 7 for these magnetoliposomes and the comparison with free NPs. Adapted with permission from Ref. [230], Copyright 2020 American Chemical Society.

However, for 8 nm and 15 nm DMSA-coated NPs attached outside liposomes and under mild field conditions (<300 kHz), a slight reduction in heating efficiency for the smallest ones was reported, indicating Néel relaxation regardless being or not physically connected to the liposome; however, for 15 nm NPs, SAR dropped extensively (60%), which reflected that NPs had both Néel and Brownian relaxation [230]. Those NPs were prepared by thermal decomposition in organic media.

Finally, when 4-nm oleic-coated iron oxide NPs were embedded in the lipid membrane, a slight drop in SAR values was reported in an AMF of 20 kA/m at 500 kHz [231]; those magnetoliposomes showed a SAR value of 171.6 W/g.

6.2. Polymeric Matrix

Progress in modern polymer chemistry enables the design of polymeric carriers with a defined chain architectures and controlled sizes. Block copolymer vesicles, also termed polymersomes, offer an attractive structure for drug delivery applications, overcoming the limitations of instability associated with liposomes. By manipulating the co-assembly of amphiphilic co-polymers it is possible to obtain bi- or multilayer structures with an hydrophilic interior or forming stable micelles with an hydrophobic interior. Poly(ethylene oxide)–poly(propyleneoxide)–poly(ethylene oxide) triblock copolymers and poly(N-isopropylacrylamide) homopolymers have a few inherent defects such as limited biodegradability. Poly(l-lactic acid) or poly(lactide-co-glycolide) and poly(ethyleneglycol) or poly(ethylene oxide) as well as thermoreversible hydrogels like PEG-grafted chitosan/glycerophosphate and poly(organophosphazene) gels have been reported to be biodegradable.

Magnetic polymersomes having a hydrophobic internal membrane core made of the biodegradable block poly(trimethylene carbonate) and a polypeptide biocompatible corona of poly(l-glutamic acid, PGA) were loaded with hydrophobic 6.3 nm NPs, embedded into the membrane of dual-loaded vesicles by one-step nanoprecipitation [16]. The simultaneous loading of maghemite NPs and DOX was also achieved by nanoprecipitation. In an AMF of 2.12 kA/m and 500 kHz, the release of DOX was enhanced by a factor 2 compared to the same vesicles with NPs embedded in the membrane but kept away from the coil. In fact, even if the global temperature of the tested suspension remained almost unchanged, the local temperature increased by about 7 °C in the close vicinity of the polymeric membrane (i.e., at the nanometric scale), increasing dramatically the diffusion of the encapsulated DOX.

Oleic acid $MnFe_2O_4$ NPs were embedded within the amphiphilic copolymer (PBMA-g-C12) through a mini-emulsion method and showed that large NP size (here 18 nm) and a low loading ratio were preferable for a high SAR [232]. For 6 and 18 nm $MnFe_2O_4$ NPs, T_B decreased with the polymer immobilization and even more when the loading density was reduced. The results suggested that the polymer matrix was effective at isolating magnetic NPs, thus reducing the magnetic interactions. High SAR values of 330 W/g for 18 nm NPs (AMF of 4 kA/m and 435 kHz) were found for low polymer contents and ascribed to a relatively lower magnetic interaction due to a large amount of polymer isolating the $MnFe_2O_4$ NPs.

Other interesting biodegradable polymeric vesicles for drug delivery are those made up of PEG hydrophilic groups and polyester hydrophobic groups like PLA and PCL, forming a micelle structure with a hydrophobic interior. Sadat et al. synthesized polystyrene nanospheres with average diameter of 100 nm embedding 10 nm Fe_3O_4 NPs, superparamagnetic at room temperature [233]. The magnetic NPs confined in the nanospheres exhibited heating capability (in an AMF of 4.5 kA/m and 13.56 MHz, a maximum SAR ~ 70 W/g was measured), although significantly lower compared to that of free NPs of similar dimensions, mainly due to the effect of dipolar interactions. Note that due to the high field frequency used in the heating tests, Brownian relaxation could not be a dominant heating mechanism in either of the two NP systems.

Hexagon-shaped Co and Mn-doped iron oxide NPs of 14.8 nm were embedded into the hydrophobic interior of a poly(ethylene glycol)-b-poly(ε-caprolactone) (PEG–PCL)-based polymeric particle, prepared by solvent evaporation approach [234]. The developed nanoclusters exhibited enhanced heating efficiency (SAR ~ 1.2 kW/g in AMF of 26.9 kA/m and 420 kHz) when compared to the individual NPs (SAR ~ 1 kW/g), indicating a favorable effect of dipolar interactions between the NPs following their confinement in the polymer. In vivo studies demonstrated that magnetic hyperthermia mediated by the nanoclusters significantly inhibited the growth of tumors.

Similar results were found for smaller NPs immobilized in a similar polymer. Oleic acid coated 8 nm NPs prepared by coprecipitation were encapsulated in a biodegradable polymer poly-ε-caprolactone (PCL) employing the oil-in-water emulsion/solvent evaporation method [235]. As the NP size distribution and anisotropy were reasonably assumed not to vary during the encapsulation into the polymeric capsules, the observed increase in T_B was exclusively ascribed to changes in the dipolar magnetic interactions caused by the particle aggregation state. SAR increased with the loading into the polymer (AMF of 15.9 kA/m and 337−869 kHz). Additionally, the hypothesized ligand exchange with the carboxylic groups of the PCL shell and the higher viscosity of the polymer, compared to water, were proposed to modify the Brownian relaxation time by friction of the surface of the NPs with the carrier matrix, affecting the overall heating transfer mechanism.

Some studies reported about hybrid systems made of magnetic NPs loaded in nanocapsules of poly(lactic-co-glycolic acid) (PLGA)—a copolymer approved for human use and largely employed for drug-delivery applications due to its good biodegradability and biocompatibility—with the aim of realizing highly biocompatible nanovectors, which, by virtue of their magnetic functionality, can be possibly driven to a specific target, where they can release their load, eventually exploiting the heating capacity to promote the degradation of the PLGA matrix [236–240].

Chiang et al. fabricated magnetically responsive hollow microspheres (1–3 µm) from PLGA using a double-emulsion method, with the polymer shell (thickness ~ 250 nm) being doped with both DiO green fluorescent and iron oxide NPs (10–12 nm in size) and the aqueous core containing DOX [238] (Figure 11a,b). Upon exposure to an AMF (2.5 kA/m and 50–100 kHz), the NPs encapsulated in the shell rapidly increased the local temperature above the glass transition temperature of PLGA, so that the PLGA chains became much more mobile. This led to an increase of the permeability of the PLGA shell and thus to a rapid release of DOX molecules. The process was reversible, namely without exposure to AMF, the local temperature relaxed back to 37 °C swiftly and the drug release terminated (Figure 11c,d).

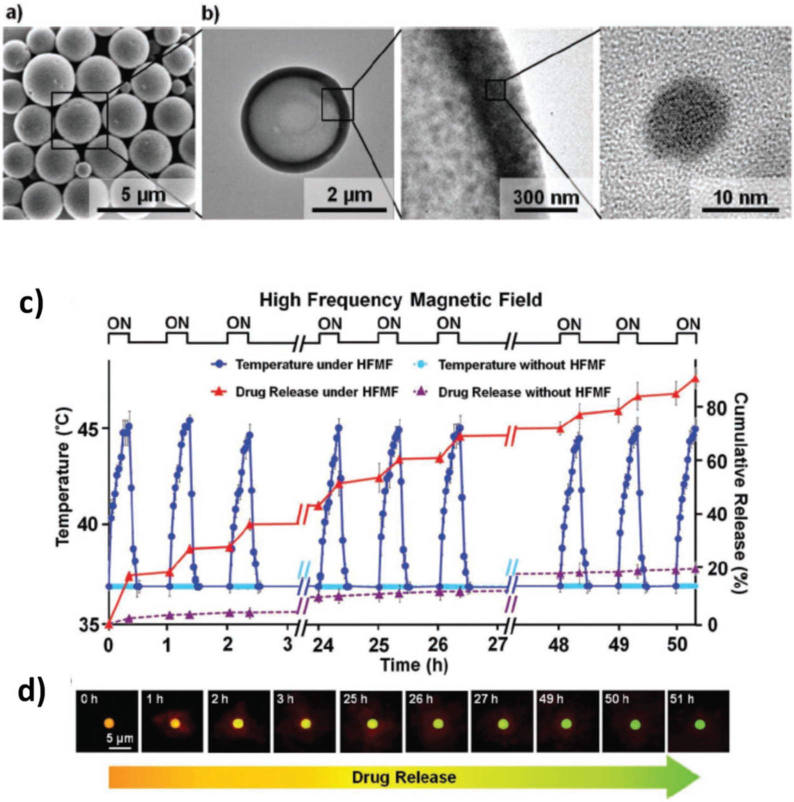

Figure 11. (**a**) SEM image of the PLGA hollow microspheres. (**b**) TEM images revealing the hollow structure of one microsphere and the single crystalline structure of the encapsulated iron oxide NPs. (**c**) Release profiles of DOX from the PLGA hollow microspheres, incubated in PBS, under AMF (2.5 kA/m and 50–100 kHz); the AMF was switched between “ON” and “OFF” modes. Their counterparts, not stimulated by AMF, were used as a control. (**d**) Fluorescence micrographs showing the changes in color of the hollow microspheres during the DOX release. Adapted with permission from Ref. [238], Copyright 2012 WILEY-VCH Verlag GmbH & Co. KGaA, Weinheim.

Del Bianco et al. studied the structural and magnetic properties of PLGA nanocapsules (typical dimension around 200 nm) with a different load of 8 nm oleate-coated Mn-doped magnetite NPs (~5.3 and ~0.72 wt.%), prepared by oil-in-water (o/w) emulsion solvent extraction method [240]. The NPs were not homogeneously distributed into the nanocapsules and tended to form aggregates, which were larger in the case of greater magnetic load (Figure 12a–c). The system was particularly suitable for investigating the effects of the interparticle dipolar interactions on the magneto-heating properties. In fact, the experimental magnetic analyses—which also included the estimation of dipolar interaction strength by the IRM-DCD remanence method (Figure 12d)—well highlighted the effect of stabilization of the NP moments against superparamagnetism, as well as the appearance of low-remanence magnetic configurations of the NP aggregates. Higher heating efficiency was measured in the sample with the lower concentration of magnetic NPs (SAR ~ 68 W/g under an AMF of 18 kA/m and 245 kHz).

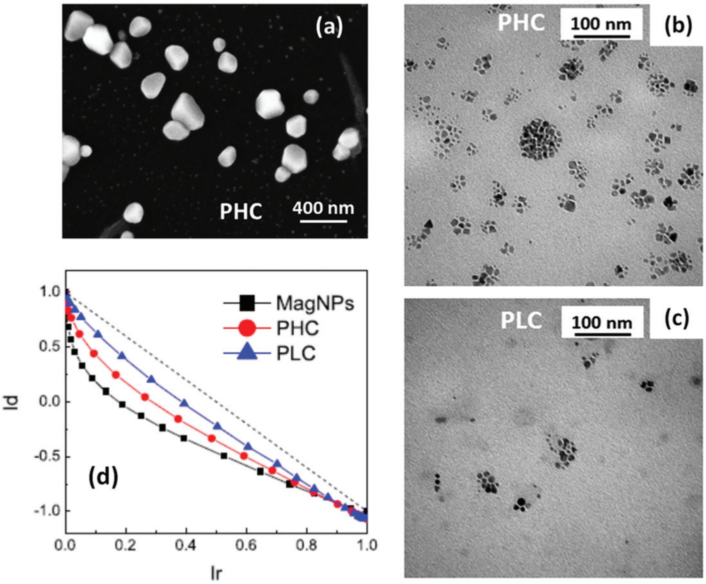

Figure 12. (**a**) SEM image of PLGA nanocapsules loaded with Mn-doped magnetite NPs. (**b**,**c**) Bright-field TEM images of the PLGA nanocapsules with higher (sample PHC) and lower (sample PLC) load of magnetic NPs, which provided the dark contrast. (**d**) Henkel plots for samples PHC, PLC and for the free magnetic NPs (sample MagNPs), obtained by combining the DCD and IRM magnetic remanence, measured by SQUID at T = 5 K. In particular, the normalized DCD values (Id) are plotted as a function of the normalized IRM values (Ir); the observed deviation from the linear trend (dotted line) is a measure of the strength of the dipolar interactions in the samples. Adapted with permission from Ref. [240], Copyright 2019 American Chemical Society.

Finally, magnetic hydrogel nanocomposites are worth mentioning. Hydrogels are crosslinked polymer networks capable of absorbing large amounts of water or biological fluids. Composite materials made of temperature-sensitive hydrogel and magnetic NPs can be used as externally-actuated drug delivery systems. In fact, heat generation by the NPs under an AMF rises the temperature of the hydrogel above a critical temperature at which the hydrogel collapses, causing the expulsion of the imbibed water and of the loaded drug [241–245].

When using citric acid coated iron oxide NPs and copolymer comprising acrylic acid and 2-methacryloylethyl acrylate units as the backbone and poly-(ethylene glycol) and poly(N-isopropylacrylamide) as the grafts, a high amount of NPs (8–10 nm) were incorporated within the thin walls of hollow nanogels (hydrodynamic size DLS ~ 200 nm) [221].

In order to prolong the retention time of magnetic NPs localized within tumor targets and favor repeatable magnetic hyperthermia treatments, poly(organophosphazene) (PPZ) hydrogels were used to encapsulate 9 nm $Zn_{0.47}Mn_{0.53}Fe_2O_4$ NPs, with good heating efficiency (SLP of 150–200 W/g in an AMF of 19.5 kA/m and 389 kHz), synthesized by thermal decomposition. More than three weeks retention of NPs within tumors after a single injection of hydrogel nanocapsules (mean diameter ~ 150 nm) facilitated successful multiple magnetic hyperthermia and four cycles of treatments showed excellent anti-tumor effects on a mouse xenograft model [246].

6.3. Silica

Solid matrices made of inorganic materials, such as silica, are also interesting vehicles for drug delivery. They provide a biocompatible substrate with a well-controlled size dispersion and a polyvalent surface chemistry for functionalization and/or vectorization [247,248]. In contrast to most polymeric matrices, the inorganic matrices are able to protect the cargo to environmental pH or extreme biological conditions. Besides, they can be prepared with an engineered internal structure (mesoporous matrices) that maximizes the cargo capacity and may provide sophisticated methods of dose regulation [249–251]. Magnetic NPs are frequently inserted in this sort of matrices to provide additional functionalities, such as magnetic separation or contactless triggering that can be externally activated even in deep tissues thanks to the deep penetration of magnetic fields [252].

The most common synthesis route for the production of inorganic matrices of silica is the sol–gel condensation of silica precursors (typicaly tetraethylorthosilicate, TEOS) known as Stöber method [253]. This method consists on the hydrolisis of precursor radicals and condensation of O-Si-O groups. In the presence of the proper surfactants (typically CTAB), it is possible to create an internal structure of ordered porous with tunable sizes and shapes [248]. There are three general methods to functionalize this kind of nanostructures with magnetic NPs: (i) encapsulating them on the silica matrix [254], (ii) inserting them in the internal structure of the matrices [255] or (iii) anchoring on their surface [256].

The arrangement of magnetic NPs inside the inorganic matrices results of paramount importance for the thermal activation of the release mechanisms and the magnetic response of the overall nanostructure. The mechanism of immobilization determines how the magnetic NPs will modify their magnetic response after the integration on the silica structure. The encapsulation of NPs inside the silica matrix is generally performed by entrapping few iron oxide nanocrystals in close proximity. Depending on the number of crystals trapped inside the silica matrix, the dipolar interactions may result more or less intense, but generally the presence of a silica shell around the NPs separate the magnetic cores and reduce the effects of dipolar interactions [257].

Inserting NPs in the internal structure of the mesoporous silica is complicated since the pore size are generally ranged between 2–10 nm [258]. Thus, the size of NPs that can be fitted inside the pores is highly restricted and the strategy usually chosen to create these systems is the in situ growth of the magnetic NPs [255]. Virumbrales et al. compared the magnetic response of Zn and Ni ferrite NPs grown inside a mesoporous matrix of 2.6 nm in porous diameter [259] to similar magnetic NPs grown on amorphous matrices and with no matrix. They observed lower M_S, higher H_K and higher T_B. The authors attributed these differences to the reduced dipolar interactions between magnetic cores grown on the porous and to the effect of the matrix on their surface anisotropy. Nevertheless, it is worth noting that the superparamagnetic response of such small cores was weak and difficult to tune.

The third strategy mentioned, in which the magnetic NPs are attached on the surface of silica particles, is one of the most interesting for magnetic harvesting and for the regulation of thermosensitive coatings. In this arrangement, the silica acts as a solid spacer between magnetic NPs decreasing the possible interaction. In this case, the magnetic response can be considered similar to individual NPs, although some authors have observed spin-glass behavior at very low temperatures for silica particles densely coated with iron oxide NPs [260].

7. Mixed NP Systems

Recently, some articles have reported on a promising new strategy that could be undertaken to regulate the heating capacity of magnetic NPs. It basically consists in mixing together NPs with different compositional and/or structural properties and therefore with different magnetic behavior, so as to exploit the synergy arising from their combination.

A first example of this new route is represented by the article by Vamvakidis et al., who, using a microemulsion-based method, were able to incorporate soft ($MnFe_2O_4$) and hard ($CoFe_2O_4$) NPs, at the same weight concentration, into spherical and compact nanoaggregates covered by biocompatible sodium dodecyl sulfate (SSD) polymer molecules [261]. Emulsion droplets are convenient templates to confine NPs into clusters by evaporating the dispersion solvent and the diameter of the colloidal clusters can be controlled by adjustment of the emulsification process. The primary NPs had a similar mean size of ~9 nm, whereas that of the final structures was of ~81 nm. At T = 300 K and under a maximum applied field of 10 kOe, the $CoFe_2O_4$ NPs showed higher magnetization (85 emu/g) and coercivity (250 Oe) than the $MnFe_2O_4$ NPs (66 emu/g, 150 Oe) and both types were coated by oleylamine, which hindered the intimate physical contact among them within each aggregate, thus ruling out exchange interactions. The authors compared the magnetization and coercivity values of the two types of NPs to those of the bi-phasic aggregates and also to those of single-phase $MnFe_2O_4$ and $CoFe_2O_4$ aggregates. Magnetic relaxation effects were not investigated. In our opinion, this study could have helped to better elucidate some puzzling results, such as the fact that the soft $MnFe_2O_4$ did not exhibit superparamagnetic relaxation at room temperature or that the coercivity of the $CoFe_2O_4$ aggregates was ~460 Oe, i.e., considerably higher than in the un-aggregated NPs. However, the authors reached the conclusion that the overall magnetic behavior of the bi-phasic aggregates, featuring magnetization ~90 emu/g and coercivity ~250 Oe at T = 300 K, was the superposition of the properties of each phase, where the soft $MnFe_2O_4$ phase and the hard $CoFe_2O_4$ phase offered moderate coercivity and high magnetization, respectively. The heating properties of the samples were tested by the calorimetric method in a AMF of 25 kA/m and 765 kHz. A strong increase of the heating capacity was observed passing from the single NPs to the single-phase aggregates (SLP increased from 27 W/g to 104 W/g for $MnFe_2O_4$, and from 40 W/g to 223 W/g for $CoFe_2O_4$). Remarkably, a SLP value as high as 525 W/g was measured in the bi-phasic aggregates, which the authors ascribed to the good synergy between the two magnetic phases.

Iglesias et al. studied a mixture of iron oxide NPs of two distinct origins: (i) inorganic, produced by a coprecipitation method and having a mean size of ~18 nm; (ii) biomimetic, i.e., covered by a protein obtained through a bacterial synthesis, with a mean size of ~35 nm [262]. The primary goal of the authors was to provide a composition that could be used as a platform for combining drug delivery and hyperthermia. In fact, the biomimetic NPs presented an isoelectric point below neutrality and could be used for drug transportation and release at the acidic tumor environment; the inorganic iron oxide NPs showed a zero-zeta potential at pH 7 and appeared to be suitable as magnetic hyperthermia agents. Heating tests carried out on the biomimetic and on the inorganic NPs in a AMF of 18 kA/m at three different frequencies (197 kHz, 236 kHz, and 280 kHz) indicated a greater heating efficiency of the latter in all conditions. However, the highest SAR values (up to 96 W/g at 280 kHz) were measured on a mixture containing [25% biomimetic + 75% inorganic] NPs. A different mixture made of [60% biomimetic + 40% inorganic] NPs showed a reduced heating capacity compared to that of inorganic NPs alone, but better than that of biomimetic NPs. The authors associated the best heating performance of the first mixture to an improved colloidal stability of the inorganic NPs, which constituted the larger fraction, thanks to the presence of the biomimetic ones and to the steric and electrostatic repulsion between them due to the protein coating. This explanation disregarded the possible role of magnetic interactions between the two types of NPs in ruling the magneto-heating properties of the mixture. Indeed, the authors reported that both the inorganic and biomimetic NPs showed superparamagnetic behavior at room temperature, being T_B equal to 103 K and 145 K, respectively. However, they also measured a considerably higher T_B (180 K) for the mixture [25% biomimetic + 75% inorganic] NPs, which, in our opinion, was a quite clear clue of the strong influence of interparticle interactions on the magnetothermal behavior of the system.

Ovejero et al. studied an original magnetic system obtained by mixing together iron oxide NPs with different shape: elongated, with aspect ratio ~5.2 and mean volume of the order of 10^3 nm^3 (excluding the silica coating), and spherical, with mean volume one order of magnitude larger (Figure 13a–d) [263]. The first type was produced through a three-step process involving the synthesis of precursor goethite NPs, their dehydration to obtain the hematite phase (after which they were also covered with silica) and, finally, the reduction to magnetite in H_2 atmosphere; the second type was synthesized by a polyol method. The structural features of the prepared NPs determined their intrinsic magnetic anisotropy and their magnetic relaxing behavior. In particular, the spherical NPs were essentially stable against thermal effects at room temperature (i.e., their magnetic moments were blocked), unlike the elongated ones, which, although magnetically harder for T < 100 K, became softer above 100 K and exhibited superparamagnetic relaxation at T = 300 K. The authors showed that mixing the NPs in different proportions allowed to modulate the magnetic hysteretic properties of the system, which did not correspond to the mere superposition of those of the parent NPs, but were affected by their mutual influence, described in terms of a mean field mechanism. This magnetic phenomenology directly impacted on the ability of the mixed samples to generate heat under an alternating magnetic field. In an AMF of 48 kA/m and 96 kHz, the SAR of the mixed samples varied within a wide range of values, between those of the elongated and spherical NPs (~510 W/g_{Fe} and ~890 W/g_{Fe}, respectively) (Figure 13e). In general, the heating efficiency of the mixed samples was larger compared to that obtained as the weighted sum of those of the parent NPs. The highest SAR ~970 W/g_{Fe} was measured in a sample containing an equal fraction of the two types of NPs. In the author's description, this occurred thanks to the mean field produced by the magnetically blocked spherical NPs that stabilized the thermally fluctuating moments of the elongated ones, which therefore contributed more effectively to the heat production. In short, the strategy indicated by the authors exploits one population of NPs, in the specific case the spherical ones, to potentiate the heating ability of the other population of NPs, i.e., the elongated ones. This magnetic interplay between the two types of NPs can be regulated by properly selecting their inherent structural/magnetic features and then varying the composition of the mixed samples. Thus, the creation of mixed NP systems emerges as an effective, still largely unexplored path towards on-demand adjustable magneto-heating performance.

In a completely different approach, the mixture of magnetic NP colloids with different anisotropies (composition or shape) at low concentrations has been recently proposed as a unique strategy to generate multiple local temperatures in a single reactor or biological environment [264]. At low concentrations (<0.1 mg/mL), the interactions between magnetic NPs becomes negligible and each magnetic NP can be independently activated as a local nanoheater. By tuning the field and frequency conditions of the AMF it is possible to optimize the heating performance of one or the other set of magnetic NPs (magnetite NPs with different size and shape), and thus induce an increment of the local temperature in their surrounding media. The proposed general strategy is to combine high frequency-low field vs. high field- low frequency AMF conditions in order to activate magnetic NPs with low and high anisotropy constants, respectively. An effective selective system requires a mix of at least two set of magnetic NPs with well differentiated anisotropies, what can be achieved by combining different sizes, geometries or compositions [264,265].

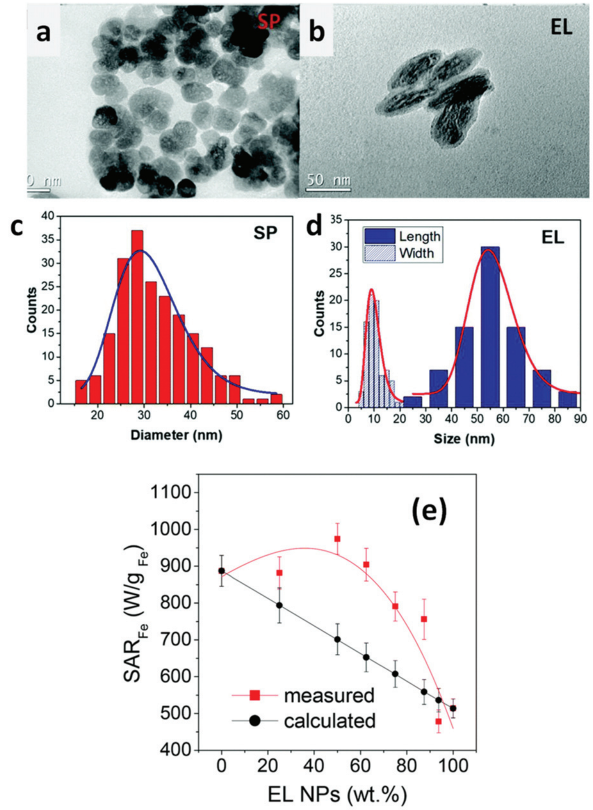

Figure 13. TEM images of (**a**) spherical NPs (SP) and (**b**) silica-coated elongated NPs (EL). Distributions obtained from TEM images of: (**c**) SP diameter, (**d**) length and width of the magnetic core of EL NPs. (**e**) Measured and calculated SAR values for samples obtained by mixing the SP and EL NPs in different proportions (AMF of 48 kA/m and 96 kHz). The values are shown as functions of the fraction of EL NPs in the samples. The calculated values were obtained as the weighted sum of those of the parent SP end EL NPs. Adapted from Ref. [263] under CC BY_NC 3.0 License.

Such selective heating has been only applied to the activation of thermophilic enzymes that generate thermolabile products [266] or to multiplexing activation of thermosensitive membrane channels such as TPRV1 [267], but presents a tremendous potential for multiplexed contactless regulation of temperature dependent processes in biotechnology.

8. Conclusions

We have reviewed the main strategies that exploit the interplay between two or more magnetic elements (magnetic phases or primary NPs) to create nanosized systems with excellent heating performance. Here the term "excellent" does not refer exclusively to the achievement of higher and higher SAR values, but also to the possibility of tuning the thermal response of the nanoheaters according to the specific biomedical function they must fulfill. This is obtained through the control of the compositional and structural features of the system, which in turn determine the magnetic properties, including the nature and strength of magnetic interaction between the constituent elements. In principle, a huge number of different materials may be obtained by spanning all the possible combinations of chemical-physical characteristics. However, biocompatibility and safety constraints reduce the degrees of freedom. This aspect is crucial and, due to the increasing use of NPs in biomedicine, elucidating their interaction with the biological environment, both in vitro and in vivo conditions, as well as their fate in living organisms is currently a hot research topic [268–271], albeit beyond the scope of this review article. It is to be expected that the concerns about biosafety and long-term distribution of the NPs in the patient's body will further push the search for innovative nanoheaters and lead to the creation of increasingly versatile magnetic architectures able to combine tunable heating efficiency with assessed biodegradation and clearance properties.

Author Contributions: Conceptualization, L.D.B.; Data curation, J.G.O., F.S., M.P.M. and L.D.B.; Writing—Original Draft Preparation, J.G.O., F.S., M.P.M. and L.D.B.; Writing—review and editing, J.G.O., F.S., M.P.M. and L.D.B. All authors have read and agreed to the published version of the manuscript.

Funding: J.G.O. and M.P.M. acknowledge funding from the European Commission through the HOTZYMES Project (H2020-FETOPEN-RIA 829162), the Spanish Ministry of Economy and Competitiveness under Grant No. MAT2017-88148-R (AEI/FEDER, UE), the PIE-201960E062 project and Nanotechnology in translational hyperthermia (HIPERNANO)- RED2018-102626-T.

Institutional Review Board Statement: Not applicable.

Informed Consent Statement: Not applicable.

Data Availability Statement: Not applicable.

Conflicts of Interest: The authors declare no conflict of interest.

References

1. Martins, P.M.; Lima, A.C.; Ribeiro, S.; Lanceros-Mendez, S.; Martins, P. Magnetic nanoparticles for biomedical applications: From the soul of the earth to the deep history of ourselves. *ACS Appl. Bio. Mater.* **2021**, *4*, 5839–5870. [CrossRef]
2. Jordan, A.; Scholz, R.; Maier-Hauff, K.; Johannsen, M.; Wust, P.; Nadobny, J.; Schirra, H.; Schmidt, H.; Deger, S.; Loening, S.; et al. Presentation of a new magnetic field therapy system for the treatment of human solid tumors with magnetic fluid hyperthermia. *J. Magn. Magn. Mater.* **2001**, *225*, 118–126. [CrossRef]
3. Wust, P.; Hildebrandt, B.; Sreenivasa, G.; Rau, B.; Gellermann, J.; Riess, H.; Felix, R.; Schlag, P. Hyperthermia in combined treatment of cancer. *Lancet Oncol.* **2002**, *3*, 487–497. [CrossRef]
4. Ortega, D.; Pankhurst, Q.A. Magnetic hyperthermia. In *Nanoscience: Volume 1: Nanostructures through Chemistry*; O'Brien, P., Ed.; RSC Publishing: Cambridge, UK, 2012; pp. 60–88. [CrossRef]
5. Ivkov, R.; DeNardo, S.J.; Daum, W.; Foreman, A.R.; Goldstein, R.C.; Nemkov, V.S.; DeNardo, G.L. Application of high amplitude alternating magnetic fields for heat induction of nanoparticles localized in cancer. *Clin. Cancer Res.* **2005**, *11*, 7093s–7103s. [CrossRef]
6. Kumar, C.S.S.R.; Mohammad, F. Magnetic nanomaterials for hyperthermia-based therapy and controlled drug delivery. *Adv. Drug Deliv. Rev.* **2011**, *63*, 789–808. [CrossRef]
7. Prasad, N.K.; Rathinasamy, K.; Panda, D.; Bahadur, D. Mechanism of cell death induced by magnetic hyperthermia with nanoparticles of γ-$Mn_xFe_{2-x}O_3$ synthesized by a single step process. *J. Mater. Chem.* **2007**, *17*, 5042. [CrossRef]
8. Ito, A.; Matsuoka, F.; Honda, H.; Kobayashi, T. Heat shock protein 70 gene therapy combined with hyperthermia using magnetic nanoparticles. *Cancer Gene Ther.* **2003**, *10*, 918–925. [CrossRef]
9. Engelmann, U.M.; Roeth, A.A.; Eberbeck, D.; Buhl, E.M.; Neumann, U.P.; Schmitz-Rode, T.; Slabu, I. Combining bulk temperature and nanoheating enables advanced magnetic fluid hyperthermia efficacy on pancreatic tumor cells. *Sci. Rep.* **2018**, *8*, 13210. [CrossRef] [PubMed]
10. Moise, S.; Byrne, J.M.; El Haj, A.J.; Telling, N.D. The potential of magnetic hyperthermia for triggering the differentiation of cancer cells. *Nanoscale* **2018**, *10*, 20519–20525. [CrossRef]
11. Attaluri, A.; Kandala, S.K.; Wabler, M.; Zhou, H.; Cornejo, C.; Armour, M.; Hedayati, M.; Zhang, Y.; DeWeese, T.L.; Herman, C.; et al. Magnetic nanoparticle hyperthermia enhances radiation therapy: A study in mouse models of human prostate cancer. *Int. J. Hyperth.* **2015**, *31*, 359–374. [CrossRef]
12. Maier-Hauff, K.; Ulrich, F.; Nestler, D.; Niehoff, H.; Wust, P.; Thiesen, B.; Orawa, H.; Budach, V.; Jordan, A. Efficacy and safety of intratumoral thermotherapy using magnetic iron-oxide nanoparticles combined with external beam radiotherapy on patients with recurrent glioblastoma multiforme. *J. Neurooncol.* **2011**, *103*, 317–324. [CrossRef]
13. Shirvalilou, S.; Khoei, S.; Esfahani, A.J.; Kamali, M.; Shirvaliloo, M.; Sheervalilou, R.; Mirzaghavami, P. Magnetic hyperthermia as an adjuvant cancer therapy in combination with radiotherapy versus radiotherapy alone for recurrent/progressive glioblastoma: A systematic review. *J. Neurooncol.* **2021**, *152*, 419–428. [CrossRef] [PubMed]

14. Datta, N.R.; Ordóñez, S.G.; Gaipl, U.S.; Paulides, M.M.; Crezee, H.; Gellermann, J.; Marder, D.; Puric, E.; Bodis, S. Local hyperthermia combined with radiotherapy and-/or chemotherapy: Recent advances and promises for the future. *Cancer Treat. Rev.* **2015**, *41*, 742–753. [CrossRef] [PubMed]
15. Brulé, S.; Levy, M.; Wilhelm, C.; Letourneur, D.; Gazeau, F.; Ménager, C.; Le Visage, C. Doxorubicin release triggered by alginate embedded magnetic nanoheaters: A combined therapy. *Adv. Mater.* **2011**, *23*, 787–790. [CrossRef]
16. Sanson, C.; Diou, O.; Thévenot, J.; Ibarboure, E.; Soum, A.; Brûlet, A.; Miraux, S.; Thiaudière, E.; Tan, S.; Brisson, A.; et al. Doxorubicin loaded magnetic polymersomes: Theranostic nanocarriers for MR imaging and magneto-chemotherapy. *ACS Nano* **2011**, *5*, 1122–1140. [CrossRef]
17. Oliveira, H.; Pérez-Andrés, E.; Thevenot, J.; Sandre, O.; Berra, E.; Lecommandoux, S. Magnetic field triggered drug release from polymersomes for cancer therapeutics. *J. Control. Release* **2013**, *169*, 165–170. [CrossRef] [PubMed]
18. Thomas, C.R.; Ferris, D.P.; Lee, J.H.; Choi, E.; Cho, M.H.; Kim, E.S.; Stoddart, J.F.; Shin, J.S.; Cheon, J.; Zink, J.I. Noninvasive remote-controlled release of drug molecules in vitro using magnetic actuation of mechanized nanoparticles. *J. Am. Chem. Soc.* **2010**, *132*, 10623–10625. [CrossRef] [PubMed]
19. Ulbrich, K.; Holá, K.; Šubr, V.; Bakandritsos, A.; Tuček, J.; Zbořil, R. Targeted drug delivery with polymers and magnetic nanoparticles: Covalent and noncovalent approaches, release control, and clinical studies. *Chem. Rev.* **2016**, *116*, 5338–5431. [CrossRef]
20. Mertz, D.; Sandre, O.; Bégin-Colin, S. Drug releasing nanoplatforms activated by alternating magnetic fields. *Biochim. Biophys. Acta Gen. Subj.* **2017**, *1861*, 1617–1641. [CrossRef] [PubMed]
21. Hu, S.H.; Liao, B.J.; Chiang, C.S.; Chen, P.J.; Chen, I.W.; Chen, S.Y. Core-shell nanocapsules stabilized by single-component polymer and nanoparticles for magneto-chemotherapy/hyperthermia with multiple drugs. *Adv. Mater.* **2012**, *24*, 3627–3632. [CrossRef]
22. De Alcântara Sica de Toledo, L.; Rosseto, H.C.; dos Santos, R.S.; Spizzo, F.; Del Bianco, L.; Montanha, M.C.; Esposito, E.; Kimura, E.; Bonfim-Mendonça, P.D.S.; Svidzinski, T.I.E.; et al. Thermal magnetic field activated propolis release from liquid crystalline system based on magnetic nanoparticles. *AAPS PharmSciTech* **2018**, *19*, 3258–3271. [CrossRef]
23. Hayashi, K.; Nakamura, M.; Miki, H.; Ozaki, S.; Abe, M.; Matsumoto, T.; Sakamoto, W.; Yogo, T.; Ishimura, K. Magnetically responsive smart nanoparticles for cancer treatment with a combination of magnetic hyperthermia and remote-control drug release. *Theranostics* **2014**, *4*, 834–844. [CrossRef] [PubMed]
24. Wu, K.; Su, D.; Liu, J.; Saha, R.; Wang, J.P. Magnetic nanoparticles in nanomedicine: A review of recent advances. *Nanotechnology* **2019**, *30*, 502003. [CrossRef]
25. Mahmoudi, K.; Bouras, A.; Bozec, D.; Ivkov, R.; Hadjipanayis, C. Magnetic hyperthermia therapy for the treatment of glioblastoma: A review of the therapy's history, efficacy and application in humans. *Int. J. Hyperth.* **2018**, *34*, 1316–1328. [CrossRef] [PubMed]
26. Zhang, H.; Liu, X.L.; Zhang, Y.F.; Gao, F.; Li, G.L.; He, Y.; Peng, M.L.; Fan, H.M. Magnetic nanoparticles based cancer therapy: Current status and applications. *Sci. China Life Sci.* **2018**, *61*, 400–414. [CrossRef] [PubMed]
27. Egea-Benavente, D.; Ovejero, J.G.; Morales, M.P.; Barber, D.F. Understanding MNPs behaviour in response to AMF in biological milieus and the effects at the cellular level: Implications for a rational design that drives magnetic hyperthermia therapy toward clinical implementation. *Cancers* **2021**, *13*, 4583. [CrossRef] [PubMed]
28. Cheng, H.W.; Tsao, H.Y.; Chiang, C.S.; Chen, S.Y. Advances in magnetic nanoparticle-mediated cancer immune-theranostics. *Adv. Healthc. Mater.* **2021**, *10*, 2001451. [CrossRef]
29. Li, X.; Li, W.; Wang, M.; Liao, Z. Magnetic nanoparticles for cancer theranostics: Advances and prospects. *J. Control. Release* **2021**, *335*, 437–448. [CrossRef]
30. Roca, A.G.; Gutiérrez, L.; Gavilán, H.; Fortes Brollo, M.E.; Veintemillas-Verdaguer, S.; Morales, M.P. Design strategies for shape-controlled magnetic iron oxide nanoparticles. *Adv. Drug Deliv. Rev.* **2019**, *138*, 68–104. [CrossRef] [PubMed]
31. Cullity, B.D.; Graham, C.D. *Introduction to Magnetic Materials*, 2nd ed.; Wiley-IEEE Press: Piscataway, NJ, USA, 2009.
32. Stoner, E.C.; Wohlfarth, E.P. A mechanism of magnetic hysteresis in heterogeneous alloys. *IEEE Trans. Magn.* **1991**, *27*, 3475–3518. [CrossRef]
33. Nosrati, H.; Salehiabar, M.; Davaran, S.; Ramazani, A.; Manjili, H.K.; Danafar, H. New advances strategies for surface functionalization of iron oxide magnetic nano particles (IONPs). *Res. Chem. Intermed.* **2017**, *43*, 7423–7442. [CrossRef]
34. Daou, T.J.; Grenèche, J.M.; Pourroy, G.; Buathong, S.; Derory, A.; Ulhaq-Bouillet, C.; Donnio, B.; Guillon, D.; Begin-Colin, S. Coupling agent effect on magnetic properties of functionalized magnetite-based nanoparticles. *Chem. Mater.* **2008**, *20*, 5869–5875. [CrossRef]
35. Schwaminger, S.P.; Bauer, D.; Fraga-García, P.; Wagner, F.E.; Berensmeier, S. Oxidation of magnetite nanoparticles: Impact on surface and crystal properties. *CrystEngComm* **2017**, *19*, 246–255. [CrossRef]
36. Baaziz, W.; Pichon, B.P.; Fleutot, S.; Liu, Y.; Lefevre, C.; Greneche, J.M.; Toumi, M.; Mhiri, T.; Begin-Colin, S. Magnetic iron oxide nanoparticles: Reproducible tuning of the size and nanosized-dependent composition, defects, and spin canting. *J. Phys. Chem. C* **2014**, *118*, 3795–3810. [CrossRef]
37. Carrey, J.; Mehdaoui, B.; Respaud, M. Simple models for dynamic hysteresis loop calculations of magnetic single-domain nanoparticles: Application to magnetic hyperthermia optimization. *J. Appl. Phys.* **2011**, *109*, 083921. [CrossRef]
38. Périgo, E.A.; Hemery, G.; Sandre, O.; Ortega, D.; Garaio, E.; Plazaola, F.; Teran, F.J. Fundamentals and advances in magnetic hyperthermia. *Appl. Phys. Rev.* **2015**, *2*, 041302. [CrossRef]

39. Dormann, J.L.; Fiorani, D.; Tronc, E. Magnetic Relaxation in Fine-Particle Systems. In *Advances in Chemical Physics*; Prigogine, I., Stuart, A.R., Eds.; J. Wiley & Sons, Inc.: New York, NY, USA, 1997; Volume XCVIII, pp. 283–494. [CrossRef]
40. Rosensweig, R.E. Heating magnetic fluid with alternating magnetic field. *J. Magn. Magn. Mater.* **2002**, *252*, 370–374. [CrossRef]
41. Casimir, H.B.G.; du Pré, F.K. Note on the thermodynamic interpretation of paramagnetic relaxation phenomena. *Physica* **1938**, *5*, 507–511. [CrossRef]
42. Dormann, J.; D'Orazio, F.; Lucari, F. Thermal variation of the relaxation time of the magnetic moment of nanoparticles with interparticle interactions of various strengths. *Phys. Rev. B Condens. Matter Mater. Phys.* **1996**, *53*, 14291–14297. [CrossRef] [PubMed]
43. Tong, S.; Quinto, C.A.; Zhang, L.; Mohindra, P.; Bao, G. Size-dependent heating of magnetic iron oxide nanoparticles. *ACS Nano* **2017**, *11*, 6808–6816. [CrossRef]
44. Vallejo-Fernandez, G.; Whear, O.; Roca, A.G.; Hussain, S.; Timmis, J.; Patel, V.; O'Grady, K. Mechanisms of hyperthermia in magnetic nanoparticles. *J. Phys. D Appl. Phys.* **2013**, *46*, 312001. [CrossRef]
45. Coïsson, M.; Barrera, G.; Appino, C.; Celegato, F.; Martino, L.; Safronov, A.P.; Kurlyandskaya, G.V.; Tiberto, P. Specific loss power measurements by calorimetric and thermal methods on γ-Fe_2O_3 nanoparticles for magnetic hyperthermia. *J. Magn. Magn. Mater.* **2019**, *473*, 403–409. [CrossRef]
46. Engelmann, U.M.; Shasha, C.; Teeman, E.; Slabu, I.; Krishnan, K.M. Predicting size-dependent heating efficiency of magnetic nanoparticles from experiment and stochastic Néel-Brown Langevin simulation. *J. Magn. Magn. Mater.* **2019**, *471*, 450–456. [CrossRef]
47. Hergt, R.; Dutz, S. Magnetic particle hyperthermia-biophysical limitations of a visionary tumour therapy. *J. Magn. Magn. Mater.* **2007**, *311*, 187–192. [CrossRef]
48. Hubert, A.; Schäfer, R. *Magnetic Domains*; Springer: Berlin/Heidelberg, Germany, 1983; Volume 18, ISBN 978-3-540-64108-7. [CrossRef]
49. Coey, J.M.D. *Magnetism and Magnetic Materials*; Cambridge University Press: Cambridge, UK, 2010; Volume 9780521816144, ISBN 9780511845000. [CrossRef]
50. Signoretti, S.; Del Bianco, L.; Pasquini, L.; Matteucci, G.; Beeli, C.; Bonetti, E. Electron holography of gas-phase condensed Fe nanoparticles. *J. Magn. Magn. Mater.* **2003**, *262*, 142–145. [CrossRef]
51. López-Conesa, L.; Martínez-Boubeta, C.; Serantes, D.; Estradé, S.; Peiró, F. Mapping the magnetic coupling of self-assembled Fe_3O_4 nanocubes by electron holography. *Materials* **2021**, *14*, 774. [CrossRef]
52. Mehdaoui, B.; Meffre, A.; Carrey, J.; Lachaize, S.; Lacroix, L.M.; Gougeon, M.; Chaudret, B.; Respaud, M. Optimal size of nanoparticles for magnetic hyperthermia: A combined theoretical and experimental study. *Adv. Funct. Mater.* **2011**, *21*, 4573–4581. [CrossRef]
53. Usov, N.A.; Liubimov, B.Y. Dynamics of magnetic nanoparticle in a viscous liquid: Application to magnetic nanoparticle hyperthermia. *J. Appl. Phys.* **2012**, *112*, 023901. [CrossRef]
54. Fortin, J.P.; Wilhelm, C.; Servais, J.; Ménager, C.; Bacri, J.C.; Gazeau, F. Size-sorted anionic iron oxide nanomagnets as colloidal mediators for magnetic hyperthermia. *J. Am. Chem. Soc.* **2007**, *129*, 2628–2635. [CrossRef] [PubMed]
55. Mehdaoui, B.; Tan, R.P.; Meffre, A.; Carrey, J.; Lachaize, S.; Chaudret, B.; Respaud, M. Increase of magnetic hyperthermia efficiency due to dipolar interactions in low-anisotropy magnetic nanoparticles: Theoretical and experimental results. *Phys. Rev. B* **2013**, *87*, 174419. [CrossRef]
56. Mousavi, N.S.S.; Khapli, S.D.; Kumar, S. Direct observations of field-induced assemblies in magnetite ferrofluids. *J. Appl. Phys.* **2015**, *117*, 103907. [CrossRef]
57. Myrovali, E.; Maniotis, N.; Makridis, A.; Terzopoulou, A.; Ntomprougkidis, V.; Simeonidis, K.; Sakellari, D.; Kalogirou, O.; Samaras, T.; Salikhov, R.; et al. Arrangement at the nanoscale: Effect on magnetic particle hyperthermia. *Sci. Rep.* **2016**, *6*, 37934. [CrossRef] [PubMed]
58. Saville, S.L.; Qi, B.; Baker, J.; Stone, R.; Camley, R.E.; Livesey, K.L.; Ye, L.; Crawford, T.M.; Thompson Mefford, O. The formation of linear aggregates in magnetic hyperthermia: Implications on specific absorption rate and magnetic anisotropy. *J. Colloid Interface Sci.* **2014**, *424*, 141–151. [CrossRef]
59. Andreu, I.; Natividad, E. Accuracy of available methods for quantifying the heat power generation of nanoparticles for magnetic hyperthermia. *Int. J. Hyperth.* **2013**, *29*, 739–751. [CrossRef]
60. Kallumadil, M.; Tada, M.; Nakagawa, T.; Abe, M.; Southern, P.; Pankhurst, Q.A. Suitability of commercial colloids for magnetic hyperthermia. *J. Magn. Magn. Mater.* **2009**, *321*, 1509–1513. [CrossRef]
61. Meiklejohn, W.H.; Bean, C.P. New magnetic anisotropy. *Phys. Rev.* **1956**, *102*, 1413–1414. [CrossRef]
62. Nogués, J.; Sort, J.; Langlais, V.; Skumryev, V.; Suriñach, S.; Muñoz, J.S.; Baró, M.D. Exchange bias in nanostructures. *Phys. Rep.* **2005**, *422*, 65–117. [CrossRef]
63. Skumryev, V.; Stoyanov, S.; Zhang, Y.; Hadjipanayis, G.; Givord, D.; Nogués, J. Beating the superparamagnetic limit with exchange bias. *Nature* **2003**, *423*, 850–853. [CrossRef]
64. Spizzo, F.; Bonfiglioli, E.; Tamisari, M.; Gerardino, A.; Barucca, G.; Notargiacomo, A.; Chinni, F.; Del Bianco, L. Magnetic exchange coupling in IrMn/NiFe nanostructures: From the continuous film to dot arrays. *Phys. Rev. B* **2015**, *91*, 064410. [CrossRef]
65. Ovejero, J.G.; Godinho, V.; Lacroix, B.; García, M.A.; Hernando, A.; Fernández, A. Exchange bias and two steps magnetization reversal in porous Co/CoO layer. *Mater. Des.* **2019**, *171*, 107691. [CrossRef]

66. Chappert, C.; Fert, A.; Van Dau, F.N. The emergence of spin electronics in data storage. *Nat. Mater.* **2007**, *6*, 813–823. [CrossRef]
67. Lottini, E.; López-Ortega, A.; Bertoni, G.; Turner, S.; Meledina, M.; Van Tendeloo, G.; Fernández, C.D.J.; Sangregorio, C. Strongly exchange coupled core-shell nanoparticles with high magnetic anisotropy: A strategy toward rare-earth-free permanent magnets. *Chem. Mater.* **2016**, *28*, 4214–4222. [CrossRef]
68. Seto, T.; Akinaga, H.; Takano, F.; Koga, K.; Orii, T.; Hirasawa, M. Magnetic properties of monodispersed Ni/NiO core-shell nanoparticles. *J. Phys. Chem. B* **2005**, *109*, 13403–13405. [CrossRef]
69. Peng, D.L.; Sumiyama, K.; Hihara, T.; Yamamuro, S. Enhancement of magnetic coercivity and macroscopic quantum tunneling in monodispersed Co/CoO cluster assemblies. *Appl. Phys. Lett.* **1999**, *75*, 3856–3858. [CrossRef]
70. Del Bianco, L.; Hernando, A.; Multigner, M.; Prados, C.; Sánchez-López, J.C.; Fernández, A.; Conde, C.F.; Conde, A. Evidence of spin disorder at the surface-core interface of oxygen passivated Fe nanoparticles. *J. Appl. Phys.* **1998**, *84*, 2189–2192. [CrossRef]
71. Del Bianco, L.; Fiorani, D.; Testa, A.M.; Bonetti, E.; Savini, L.; Signoretti, S. Magnetothermal behavior of a nanoscale Fe/Fe oxide granular system. *Phys. Rev. B Condens. Matter Mater. Phys.* **2002**, *66*, 174418. [CrossRef]
72. Del Bianco, L.; Fiorani, D.; Testa, A.M.; Bonetti, E.; Signorini, L. Field-cooling dependence of exchange bias in a granular system of Fe nanoparticles embedded in an Fe oxide matrix. *Phys. Rev. B Condens. Matter Mater. Phys.* **2004**, *70*, 052401. [CrossRef]
73. Fiorani, D.; Del Bianco, L.; Testa, A.M.; Trohidou, K.N. Glassy dynamics in the exchange bias properties of the iron/iron oxide nanogranular system. *Phys. Rev. B Condens. Matter Mater. Phys.* **2006**, *73*, 092403. [CrossRef]
74. Zheng, R.K.; Wen, G.H.; Fung, K.K.; Zhang, X.X. Training effect of exchange bias in γ-Fe_2O_3 coated Fe nanoparticles. *Phys. Rev. B* **2004**, *69*, 214431. [CrossRef]
75. Ong, Q.K.; Wei, A.; Lin, X.-M. Exchange bias in Fe/Fe_3O_4 core-shell magnetic nanoparticles mediated by frozen interfacial spins. *Phys. Rev. B* **2009**, *80*, 134418. [CrossRef]
76. Chandra, S.; Khurshid, H.; Li, W.; Hadjipanayis, G.C.; Phan, M.H.; Srikanth, H. Spin dynamics and criteria for onset of exchange bias in superspin glass Fe/γ-Fe_2O_3 core-shell nanoparticles. *Phys. Rev. B* **2012**, *86*, 014426. [CrossRef]
77. Kneller, E.F.; Hawig, R. The exchange-spring magnet: A new material principle for permanent magnets. *IEEE Trans. Magn.* **1991**, *27*, 3588–3600. [CrossRef]
78. Coehoorn, R.; de Mooij, D.B.; de Waard, C. Meltspun permanent magnet materials containing Fe_3B as the main phase. *J. Magn. Magn. Mater.* **1989**, *80*, 101–104. [CrossRef]
79. Skomski, R.; Coey, J.M.D. Giant energy product in nanostructured two-phase magnets. *Phys. Rev. B* **1993**, *48*, 15812–15816. [CrossRef]
80. Fullerton, E.E.; Jiang, J.S.; Bader, S.D. Hard/soft magnetic heterostructures: Model exchange-spring magnets. *J. Magn. Magn. Mater.* **1999**, *200*, 392–404. [CrossRef]
81. Lee, H.; Yoon, T.J.; Weissleder, R. Ultrasensitive detection of bacteria using core-shell nanoparticles and an NMR-filter system. *Angew. Chem. Int. Ed.* **2009**, *48*, 5657–5660. [CrossRef]
82. Zhang, L.; Li, Z. Synthesis and characterization of $SrFe_{12}O_{19}$/$CoFe_2O_4$ nanocomposites with core-shell structure. *J. Alloys Compd.* **2009**, *469*, 422–426. [CrossRef]
83. Kim, C.W.; Kim, Y.H.; Cha, H.G.; Kim, J.C.; Kang, Y.S. A Study on the exchange-coupling effect of $Nd_2Fe_{14}B$/CoFe forming core/shell shape. *Mol. Cryst. Liq. Cryst.* **2007**, *472*, 155/[545]–160/[555]. [CrossRef]
84. Wang, G.; Chang, Y.; Wang, L.; Liu, C. Synthesis, characterization and microwave absorption properties of Fe_3O_4/Co core/shell-type nanoparticles. *Adv. Powder Technol.* **2012**, *23*, 861–865. [CrossRef]
85. Lamichanne, M.; Rai, B.K.; Mishra, S.R.; Nguyen, V.V.; Liu, J.P. Magnetic properties hard-soft $SmCo_5$-FeNi and $SmCo_5$-FeCo composites prepared by electroless coating technique. *Open J. Compos. Mater.* **2012**, *2*, 119–124. [CrossRef]
86. Sun, S.; Zeng, H.; Robinson, D.B.; Raoux, S.; Rice, P.M.; Wang, S.X.; Li, G. Monodisperse MFe_2O_4 (M = Fe, Co, Mn) nanoparticles. *J. Am. Chem. Soc.* **2004**, *126*, 273–279. [CrossRef]
87. Kudera, S.; Carbone, L.; Carlino, E.; Cingolani, R.; Cozzoli, P.D.; Manna, L. Synthesis routes for the growth of complex nanostructures. *Phys. E Low Dimens. Syst. Nanostruct.* **2007**, *37*, 128–133. [CrossRef]
88. López-Ortega, A.; Estrader, M.; Salazar-Alvarez, G.; Estradé, S.; Golosovsky, I.V.; Dumas, R.K.; Keavney, D.J.; Vasilakaki, M.; Trohidou, K.N.; Sort, J.; et al. Strongly exchange coupled inverse ferrimagnetic soft/hard, $Mn_xFe_{3-x}O_4$/$Fe_xMn_{3-x}O_4$, core/shell heterostructured nanoparticles. *Nanoscale* **2012**, *4*, 5138–5147. [CrossRef] [PubMed]
89. Estrader, M.; López-Ortega, A.; Estradé, S.; Golosovsky, I.V.; Salazar-Alvarez, G.; Vasilakaki, M.; Trohidou, K.N.; Varela, M.; Stanley, D.C.; Sinko, M.; et al. Robust antiferromagnetic coupling in hard-soft bi-magnetic core/shell nanoparticles. *Nat. Commun.* **2013**, *4*, 2960. [CrossRef] [PubMed]
90. Yoon, T.J.; Lee, H.; Shao, H.; Weissleder, R. Highly magnetic core-shell nanoparticles with a unique magnetization mechanism. *Angew. Chem. Int. Ed.* **2011**, *50*, 4663–4666. [CrossRef]
91. Masala, O.; Hoffman, D.; Sundaram, N.; Page, K.; Proffen, T.; Lawes, G.; Seshadri, R. Preparation of magnetic spinel ferrite core/shell nanoparticles: Soft ferrites on hard ferrites and vice versa. *Solid State Sci.* **2006**, *8*, 1015–1022. [CrossRef]
92. Song, Q.; Zhang, Z.J. Controlled synthesis and magnetic properties of bimagnetic spinel ferrite $CoFe_2O_4$ and $MnFe_2O_4$ nanocrystals with core-shell architecture. *J. Am. Chem. Soc.* **2012**, *134*, 10182–10190. [CrossRef] [PubMed]
93. Kaur, M.; McCloy, J.S.; Jiang, W.; Yao, Q.; Qiang, Y. Size dependence of inter- and intracluster interactions in core-shell iron-iron oxide nanoclusters. *J. Phys. Chem. C* **2012**, *116*, 12875–12885. [CrossRef]

94. Wang, D.; Xin, H.L.; Wang, H.; Yu, Y.; Rus, E.; Muller, D.A.; Disalvo, F.J.; Abruña, H.D. Facile synthesis of carbon-supported Pd-Co core-shell nanoparticles as oxygen reduction electrocatalysts and their enhanced activity and stability with monolayer Pt decoration. *Chem. Mater.* **2012**, *24*, 2274–2281. [CrossRef]
95. Suetsuna, T.; Harada, K.; Takahashi, T.; Suenaga, S. Bulk nanocomposite using self-forming core/shell nanoparticles and its magnetic properties for high-frequency applications. *J. Appl. Phys.* **2012**, *111*, 07A307. [CrossRef]
96. Soares, J.M.; Galdino, V.B.; Conceição, O.L.A.; Morales, M.A.; De Araújo, J.H.; MacHado, F.L.A. Critical dimension for magnetic exchange-spring coupled core/shell $CoFe_2O_4/CoFe_2$ nanoparticles. *J. Magn. Magn. Mater.* **2013**, *326*, 81–84. [CrossRef]
97. Zhang, G.; Liao, Y.; Baker, I. Surface engineering of core/shell iron/iron oxide nanoparticles from microemulsions for hyperthermia. *Mater. Sci. Eng. C* **2010**, *30*, 92–97. [CrossRef] [PubMed]
98. Meffre, A.; Mehdaoui, B.; Kelsen, V.; Fazzini, P.F.; Carrey, J.; Lachaize, S.; Respaud, M.; Chaudret, B. A simple chemical route toward monodisperse iron carbide nanoparticles displaying tunable magnetic and unprecedented hyperthermia properties. *Nano Lett.* **2012**, *12*, 4722–4728. [CrossRef] [PubMed]
99. Herman, D.A.J.; Ferguson, P.; Cheong, S.; Hermans, I.F.; Ruck, B.J.; Allan, K.M.; Prabakar, S.; Spencer, J.L.; Lendrum, C.D.; Tilley, R.D. Hot-injection synthesis of iron/iron oxide core/shell nanoparticles for T_2 contrast enhancement in magnetic resonance imaging. *Chem. Commun.* **2011**, *47*, 9221–9223. [CrossRef] [PubMed]
100. Tsopoe, S.P.; Borgohain, C.; Fopase, R.; Pandey, L.M.; Borah, J.P. A comparative investigation of normal and inverted exchange bias effect for magnetic fluid hyperthermia applications. *Sci. Rep.* **2020**, *10*, 18666. [CrossRef] [PubMed]
101. Anderson, B.D.; Tracy, J.B. Nanoparticle conversion chemistry: Kirkendall effect, galvanic exchange, and anion exchange. *Nanoscale* **2014**, *6*, 12195–12216. [CrossRef] [PubMed]
102. Nemati, Z.; Alonso, J.; Khurshid, H.; Phan, M.H.; Srikanth, H. Core/shell iron/iron oxide nanoparticles: Are they promising for magnetic hyperthermia? *RSC Adv.* **2016**, *6*, 38697–38702. [CrossRef]
103. Famiani, S.; Lagrow, A.P.; Besenhard, M.O.; Maenosono, S.; Thanh, N.T.K. Synthesis of fine-tuning highly magnetic $Fe@Fe_xO_y$ nanoparticles through continuous injection and a study of magnetic hyperthermia. *Chem. Mater.* **2018**, *30*, 8897–8904. [CrossRef]
104. Lee, J.H.; Jang, J.T.; Choi, J.S.; Moon, S.H.; Noh, S.H.; Kim, J.W.; Kim, J.G.; Kim, I.S.; Park, K.I.; Cheon, J. Exchange-coupled magnetic nanoparticles for efficient heat induction. *Nat. Nanotechnol.* **2011**, *6*, 418–422. [CrossRef]
105. Liébana-Viñas, S.; Simeonidis, K.; Wiedwald, U.; Li, Z.A.; Ma, Z.; Myrovali, E.; Makridis, A.; Sakellari, D.; Vourlias, G.; Spasova, M.; et al. Optimum nanoscale design in ferrite based nanoparticles for magnetic particle hyperthermia. *RSC Adv.* **2016**, *6*, 72918–72925. [CrossRef]
106. Viñas, S.L.; Simeonidis, K.; Li, Z.A.; Ma, Z.; Myrovali, E.; Makridis, A.; Sakellari, D.; Angelakeris, M.; Wiedwald, U.; Spasova, M.; et al. Tuning the magnetism of ferrite nanoparticles. *J. Magn. Magn. Mater.* **2016**, *415*, 20–23. [CrossRef]
107. Fabris, F.; Lima, E.; De Biasi, E.; Troiani, H.E.; Vásquez Mansilla, M.; Torres, T.E.; Fernández Pacheco, R.; Ibarra, M.R.; Goya, G.F.; Zysler, R.D.; et al. Controlling the dominant magnetic relaxation mechanisms for magnetic hyperthermia in bimagnetic core-shell nanoparticles. *Nanoscale* **2019**, *11*, 3164–3172. [CrossRef] [PubMed]
108. Lavorato, G.C.; Das, R.; Xing, Y.; Robles, J.; Litterst, F.J.; Baggio-Saitovitch, E.; Phan, M.H.; Srikanth, H. Origin and shell-driven optimization of the heating power in core/shell bimagnetic nanoparticles. *ACS Appl. Nano Mater.* **2020**, *3*, 1755–1765. [CrossRef]
109. Yelenich, O.V.; Solopan, S.O.; Greneche, J.M.; Belous, A.G. Synthesis and properties MFe_2O_4 (M = Fe, Co) nanoparticles and core-shell structures. *Solid State Sci.* **2015**, *46*, 19–26. [CrossRef]
110. Robles, J.; Das, R.; Glassell, M.; Phan, M.H.; Srikanth, H. Exchange-coupled $Fe_3O_4/CoFe_2O_4$ nanoparticles for advanced magnetic hyperthermia. *AIP Adv.* **2018**, *8*, 056719. [CrossRef]
111. Solopan, S.O.; Nedelko, N.; Lewińska, S.; Ślawska-Waniewska, A.; Zamorskyi, V.O.; Tovstolytkin, A.I.; Belous, A.G. Core/shell architecture as an efficient tool to tune DC magnetic parameters and AC losses in spinel ferrite nanoparticles. *J. Alloys Compd.* **2019**, *788*, 1203–1210. [CrossRef]
112. Zhang, Q.; Castellanos-Rubio, I.; Munshi, R.; Orue, I.; Pelaz, B.; Gries, K.I.; Parak, W.J.; Del Pino, P.; Pralle, A. Model driven optimization of magnetic anisotropy of exchange-coupled core-shell ferrite nanoparticles for maximal hysteretic loss. *Chem. Mater.* **2015**, *27*, 7380–7387. [CrossRef]
113. Phadatare, M.R.; Meshram, J.V.; Gurav, K.V.; Kim, J.H.; Pawar, S.H. Enhancement of specific absorption rate by exchange coupling of the core-shell structure of magnetic nanoparticles for magnetic hyperthermia. *J. Phys. D Appl. Phys.* **2016**, *49*, 095004. [CrossRef]
114. Choi, H.; An, M.; Eom, W.; Lim, S.W.; Shim, I.B.; Kim, C.S.; Kim, S.J. Crystallographic and magnetic properties of the hyperthermia material $CoFe_2O_4@AlFe_2O_4$. *J. Korean Phys. Soc.* **2017**, *70*, 173–176. [CrossRef]
115. Darwish, M.S.A.; Kim, H.; Lee, H.; Ryu, C.; Lee, J.Y.; Yoon, J. Engineering core-shell structures of magnetic ferrite nanoparticles for high hyperthermia performance. *Nanomaterials* **2020**, *10*, 991. [CrossRef]
116. Sanna Angotzi, M.; Mameli, V.; Cara, C.; Musinu, A.; Sangregorio, C.; Niznansky, D.; Xin, H.L.; Vejpravova, J.; Cannas, C. Coupled hard-soft spinel ferrite-based core-shell nanoarchitectures: Magnetic properties and heating abilities. *Nanoscale Adv.* **2020**, *2*, 3191–3201. [CrossRef]
117. Sanna Angotzi, M.; Musinu, A.; Mameli, V.; Ardu, A.; Cara, C.; Niznansky, D.; Xin, H.L.; Cannas, C. Spinel ferrite core-shell nanostructures by a versatile solvothermal seed-mediated growth approach and study of their nanointerfaces. *ACS Nano* **2017**, *11*, 7889–7900. [CrossRef]

118. Pilati, V.; Cabreira Gomes, R.; Gomide, G.; Coppola, P.; Silva, F.G.; Paula, F.L.O.; Perzynski, R.; Goya, G.F.; Aquino, R.; Depeyrot, J. Core/shell nanoparticles of non-stoichiometric Zn-Mn and Zn-Co ferrites as thermosensitive heat sources for magnetic fluid hyperthermia. *J. Phys. Chem. C* **2018**, *122*, 3028–3038. [CrossRef]
119. Noh, S.H.; Na, W.; Jang, J.T.; Lee, J.H.; Lee, E.J.; Moon, S.H.; Lim, Y.; Shin, J.S.; Cheon, J. Nanoscale magnetism control via surface and exchange anisotropy for optimized ferrimagnetic hysteresis. *Nano Lett.* **2012**, *12*, 3716–3721. [CrossRef]
120. Nemati, Z.; Alonso, J.; Rodrigo, I.; Das, R.; Garaio, E.; García, J.Á.; Orue, I.; Phan, M.H.; Srikanth, H. Improving the heating efficiency of iron oxide nanoparticles by tuning their shape and size. *J. Phys. Chem. C* **2018**, *122*, 2367–2381. [CrossRef]
121. Das, R.; Alonso, J.; Nemati Porshokouh, Z.; Kalappattil, V.; Torres, D.; Phan, M.H.; Garaio, E.; García, J.Á.; Sanchez Llamazares, J.L.; Srikanth, H. Tunable high aspect ratio iron oxide nanorods for enhanced hyperthermia. *J. Phys. Chem. C* **2016**, *120*, 10086–10093. [CrossRef]
122. Simeonidis, K.; Morales, M.P.; Marciello, M.; Angelakeris, M.; De La Presa, P.; Lazaro-Carrillo, A.; Tabero, A.; Villanueva, A.; Chubykalo-Fesenko, O.; Serantes, D. In-situ particles reorientation during magnetic hyperthermia application: Shape matters twice. *Sci. Rep.* **2016**, *6*, 38382. [CrossRef] [PubMed]
123. Walter, A.; Billotey, C.; Garofalo, A.; Ulhaq-Bouillet, C.; Lefèvre, C.; Taleb, J.; Laurent, S.; Elst, L.V.; Muller, R.N.; Lartigue, L.; et al. Mastering the shape and composition of dendronized iron oxide nanoparticles to tailor magnetic resonance imaging and hyperthermia. *Chem. Mater.* **2014**, *26*, 5252–5264. [CrossRef]
124. Guardia, P.; Di Corato, R.; Lartigue, L.; Wilhelm, C.; Espinosa, A.; Garcia-Hernandez, M.; Gazeau, F.; Manna, L.; Pellegrino, T. Water-soluble iron oxide nanocubes with high values of specific absorption rate for cancer cell hyperthermia treatment. *ACS Nano* **2012**, *6*, 3080–3091. [CrossRef]
125. Bae, K.H.; Park, M.; Do, M.J.; Lee, N.; Ryu, J.H.; Kim, G.W.; Kim, C.; Park, T.G.; Hyeon, T. Chitosan oligosaccharide-stabilized ferrimagnetic iron oxide nanocubes for magnetically modulated cancer hyperthermia. *ACS Nano* **2012**, *6*, 5266–5273. [CrossRef]
126. Martinez-Boubeta, C.; Simeonidis, K.; Makridis, A.; Angelakeris, M.; Iglesias, O.; Guardia, P.; Cabot, A.; Yedra, L.; Estradé, S.; Peiró, F.; et al. Learning from nature to improve the heat generation of iron-oxide nanoparticles for magnetic hyperthermia applications. *Sci. Rep.* **2013**, *3*, 1652. [CrossRef] [PubMed]
127. Yang, M.; Ho, C.; Ruta, S.; Chantrell, R.; Krycka, K.; Hovorka, O.; Chen, F.-R.; Lai, P.; Lai, C. Magnetic interaction of multifunctional core–shell nanoparticles for highly effective theranostics. *Adv. Mater.* **2018**, *30*, 1802444. [CrossRef] [PubMed]
128. Gavilán, H.; Kowalski, A.; Heinke, D.; Sugunan, A.; Sommertune, J.; Varón, M.; Bogart, L.K.; Posth, O.; Zeng, L.; González-Alonso, D.; et al. Colloidal flower-shaped iron oxide nanoparticles: Synthesis strategies and coatings. *Part. Part. Syst. Charact.* **2017**, *34*, 1700094. [CrossRef]
129. Del Bianco, L.; Lesci, I.G.; Fracasso, G.; Barucca, G.; Spizzo, F.; Tamisari, M.; Scotti, R.; Ciocca, L. Synthesis of nanogranular Fe_3O_4/biomimetic hydroxyapatite for potential applications in nanomedicine: Structural and magnetic characterization. *Mater. Res. Express* **2015**, *2*, 065002. [CrossRef]
130. Tripp, S.L.; Dunin-Borkowski, R.E.; Wei, A. Flux closure in self-assembled cobalt nanoparticle rings. *Angew. Chem. Int. Ed.* **2003**, *42*, 5591–5593. [CrossRef] [PubMed]
131. Spizzo, F.; Tamisari, M.; Chinni, F.; Bonfiglioli, E.; Gerardino, A.; Barucca, G.; Bisero, D.; Fin, S.; Del Bianco, L. Exchange bias properties of 140 nm-sized dipolarly interacting circular dots with ultrafine IrMn and NiFe layers. *J. Magn. Magn. Mater.* **2016**, *400*, 242–247. [CrossRef]
132. Georgescu, M.; Klokkenburg, M.; Erné, B.H.; Liljeroth, P.; Vanmaekelbergh, D.; Zeijlmans Van Emmichoven, P.A. Flux closure in two-dimensional magnetite nanoparticle assemblies. *Phys. Rev. B Condens. Matter Mater. Phys.* **2006**, *73*, 184415. [CrossRef]
133. Dutz, S. Are magnetic multicore nanoparticles promising candidates for biomedical applications? *IEEE Trans. Magn.* **2016**, *52*, 1–3. [CrossRef]
134. Hemery, G.; Genevois, C.; Couillaud, F.; Lacomme, S.; Gontier, E.; Ibarboure, E.; Lecommandoux, S.; Garanger, E.; Sandre, O. Monocore: Vs. multicore magnetic iron oxide nanoparticles: Uptake by glioblastoma cells and efficiency for magnetic hyperthermia. *Mol. Syst. Des. Eng.* **2017**, *2*, 629–639. [CrossRef]
135. Cabana, S.; Curcio, A.; Michel, A.; Wilhelm, C.; Abou-Hassan, A. Iron oxide mediated photothermal therapy in the second biological window: A comparative study between magnetite/maghemite nanospheres and nanoflowers. *Nanomaterials* **2020**, *10*, 1548. [CrossRef]
136. Muthu, M.S.; Singh, S. Targeted nanomedicines: Effective treatment modalities for cancer, AIDS and brain disorders. *Nanomedicine* **2009**, *4*, 105–118. [CrossRef] [PubMed]
137. Vita, F.; Gavilán, H.; Rossi, F.; De Julián Fernández, C.; Secchi, A.; Arduini, A.; Albertini, F.; Morales, M.P. Tuning morphology and magnetism of magnetite nanoparticles by calix[8]arene-induced oriented aggregation. *CrystEngComm* **2016**, *18*, 8591–8598. [CrossRef]
138. Gaudisson, T.; Sharma, S.K.; Mohamed, R.; Sitamtze Youmbi, B.; Menguy, N.; Calvayrac, F.; Seydou, M.; Ammar-Merah, S. Experimental and theoretical evidence for oriented aggregate crystal growth of CoO in a polyol. *CrystEngComm* **2021**, *23*, 1756–1764. [CrossRef]
139. Ammar, S.; Fiévet, F. Polyol synthesis: A versatile wet-chemistry route for the design and production of functional inorganic nanoparticles. *Nanomaterials* **2020**, *10*, 1217. [CrossRef]
140. Maity, D.; Chandrasekharan, P.; Pradhan, P.; Chuang, K.H.; Xue, J.M.; Feng, S.S.; Ding, J. Novel synthesis of superparamagnetic magnetite nanoclusters for biomedical applications. *J. Mater. Chem.* **2011**, *21*, 14717–14724. [CrossRef]

141. Casula, M.F.; Conca, E.; Bakaimi, I.; Sathya, A.; Materia, M.E.; Casu, A.; Falqui, A.; Sogne, E.; Pellegrino, T.; Kanaras, A.G. Manganese doped-iron oxide nanoparticle clusters and their potential as agents for magnetic resonance imaging and hyperthermia. *Phys. Chem. Chem. Phys.* **2016**, *18*, 16848–16855. [CrossRef]
142. Kandasamy, G.; Khan, S.; Giri, J.; Bose, S.; Veerapu, N.S.; Maity, D. One-pot synthesis of hydrophilic flower-shaped iron oxide nanoclusters (IONCs) based ferrofluids for magnetic fluid hyperthermia applications. *J. Mol. Liq.* **2019**, *275*, 699–712. [CrossRef]
143. Sathya, A.; Kalyani, S.; Ranoo, S.; Philip, J. One-step microwave-assisted synthesis of water-dispersible Fe_3O_4 magnetic nanoclusters for hyperthermia applications. *J. Magn. Magn. Mater.* **2017**, *439*, 107–113. [CrossRef]
144. Ganesan, V.; Lahiri, B.B.; Louis, C.; Philip, J.; Damodaran, S.P. Size-controlled synthesis of superparamagnetic magnetite nanoclusters for heat generation in an alternating magnetic field. *J. Mol. Liq.* **2019**, *281*, 315–323. [CrossRef]
145. Pourmiri, S.; Tzitzios, V.; Hadjipanayis, G.C.; Meneses Brassea, B.P.; El-Gendy, A.A. Magnetic properties and hyperthermia behavior of iron oxide nanoparticle clusters. *AIP Adv.* **2019**, *9*, 125033. [CrossRef]
146. Coey, J.M.D. Noncollinear spin arrangement in ultrafine ferrimagnetic crystallites. *Phys. Rev. Lett.* **1971**, *27*, 1140–1142. [CrossRef]
147. Morales, M.P.; Serna, C.J.; Bødker, F.; Mørup, S. Spin canting due to structural disorder in maghemite. *J. Phys. Condens. Matter* **1997**, *9*, 5461–5467. [CrossRef]
148. Parker, F.T.; Foster, M.W.; Margulies, D.T.; Berkowitz, A.E. Spin canting, surface magnetization, and finite-size effects in γ-Fe_2O_3 particles. *Phys. Rev. B* **1993**, *47*, 7885–7891. [CrossRef]
149. Goya, G.F.; Berquó, T.S.; Fonseca, F.C.; Morales, M.P. Static and dynamic magnetic properties of spherical magnetite nanoparticles. *J. Appl. Phys.* **2003**, *94*, 3520–3528. [CrossRef]
150. Coduri, M.; Masala, P.; Del Bianco, L.; Spizzo, F.; Ceresoli, D.; Castellano, C.; Cappelli, S.; Oliva, C.; Checchia, S.; Allieta, M.; et al. Local structure and magnetism of Fe_2O_3 maghemite nanocrystals: The role of crystal dimension. *Nanomaterials* **2020**, *10*, 867. [CrossRef] [PubMed]
151. Spizzo, F.; Sgarbossa, P.; Sieni, E.; Semenzato, A.; Dughiero, F.; Forzan, M.; Bertani, R.; Del Bianco, L. Synthesis of ferrofluids made of iron oxide nanoflowers: Interplay between carrier fluid and magnetic properties. *Nanomaterials* **2017**, *7*, 373. [CrossRef] [PubMed]
152. Hadjipanayis, G.C.; Gong, W. Magnetic hysteresis in melt-spun Nd-Fe-Al-B-Si alloys with high remanence. *J. Appl. Phys.* **1988**, *64*, 5559–5561. [CrossRef]
153. Herzer, G. Soft magnetic nanocrystalline materials. *Scr. Metall. Mater.* **1995**, *33*, 1741–1756. [CrossRef]
154. Dutz, S.; Clement, J.H.; Eberbeck, D.; Gelbrich, T.; Hergt, R.; Müller, R.; Wotschadlo, J.; Zeisberger, M. Ferrofluids of magnetic multicore nanoparticles for biomedical applications. *J. Magn. Magn. Mater.* **2009**, *321*, 1501–1504. [CrossRef]
155. Barick, K.C.; Aslam, M.; Lin, Y.P.; Bahadur, D.; Prasad, P.V.; Dravid, V.P. Novel and efficient MR active aqueous colloidal Fe_3O_4 nanoassemblies. *J. Mater. Chem.* **2009**, *19*, 7023–7029. [CrossRef]
156. Lartigue, L.; Hugounenq, P.; Alloyeau, D.; Clarke, S.P.; Lévy, M.; Bacri, J.C.; Bazzi, R.; Brougham, D.F.; Wilhelm, C.; Gazeau, F. Cooperative organization in iron oxide multi-core nanoparticles potentiates their efficiency as heating mediators and MRI contrast agents. *ACS Nano* **2012**, *6*, 10935–10949. [CrossRef] [PubMed]
157. Hugounenq, P.; Levy, M.; Alloyeau, D.; Lartigue, L.; Dubois, E.; Cabuil, V.; Ricolleau, C.; Roux, S.; Wilhelm, C.; Gazeau, F.; et al. Iron oxide monocrystalline nanoflowers for highly efficient magnetic hyperthermia. *J. Phys. Chem. C* **2012**, *116*, 15702–15712. [CrossRef]
158. Gavilán, H.; Sánchez, E.H.; Brollo, M.E.F.; Asín, L.; Moerner, K.K.; Frandsen, C.; Lázaro, F.J.; Serna, C.J.; Veintemillas-Verdaguer, S.; Morales, M.P.; et al. Formation mechanism of maghemite nanoflowers synthesized by a polyol-mediated process. *ACS Omega* **2017**, *2*, 7172–7184. [CrossRef]
159. Di Corato, R.; Espinosa, A.; Lartigue, L.; Tharaud, M.; Chat, S.; Pellegrino, T.; Ménager, C.; Gazeau, F.; Wilhelm, C. Magnetic hyperthermia efficiency in the cellular environment for different nanoparticle designs. *Biomaterials* **2014**, *35*, 6400–6411. [CrossRef]
160. Etheridge, M.L.; Hurley, K.R.; Zhang, J.; Jeon, S.; Ring, H.L.; Hogan, C.; Haynes, C.L.; Garwood, M.; Bischof, J.C. Accounting for biological aggregation in heating and imaging of magnetic nanoparticles. *Technology* **2014**, *02*, 214–228. [CrossRef]
161. Levy, M.; Wilhelm, C.; Luciani, N.; Deveaux, V.; Gendron, F.; Luciani, A.; Devaud, M.; Gazeau, F. Nanomagnetism reveals the intracellular clustering of iron oxide nanoparticles in the organism. *Nanoscale* **2011**, *3*, 4402–4410. [CrossRef] [PubMed]
162. Cabrera, D.; Coene, A.; Leliaert, J.; Artés-Ibáñez, E.J.; Dupré, L.; Telling, N.D.; Teran, F.J. Dynamical Magnetic Response of Iron Oxide Nanoparticles Inside Live Cells. *ACS Nano* **2018**, *12*, 2741–2752. [CrossRef]
163. Bender, P.; Fock, J.; Frandsen, C.; Hansen, M.F.; Balceris, C.; Ludwig, F.; Posth, O.; Wetterskog, E.; Bogart, L.K.; Southern, P.; et al. Relating Magnetic Properties and High Hyperthermia Performance of Iron Oxide Nanoflowers. *J. Phys. Chem. C* **2018**, *122*, 3068–3077. [CrossRef]
164. Dutz, S.; Kettering, M.; Hilger, I.; Müller, R.; Zeisberger, M. Magnetic multicore nanoparticles for hyperthermia-influence of particle immobilization in tumour tissue on magnetic properties. *Nanotechnology* **2011**, *22*, 265102. [CrossRef] [PubMed]
165. Hemery, G.; Keyes, A.C.; Garaio, E.; Rodrigo, I.; Garcia, J.A.; Plazaola, F.; Garanger, E.; Sandre, O. Tuning sizes, morphologies, and magnetic properties of monocore versus multicore iron oxide nanoparticles through the controlled addition of water in the polyol synthesis. *Inorg. Chem.* **2017**, *56*, 8232–8243. [CrossRef]
166. Shaw, S.K.; Biswas, A.; Gangwar, A.; Maiti, P.; Prajapat, C.L.; Meena, S.S.; Prasad, N.K. Synthesis of exchange coupled nanoflowers for efficient magnetic hyperthermia. *J. Magn. Magn. Mater.* **2019**, *484*, 437–444. [CrossRef]

167. Liu, X.L.; Ng, C.T.; Chandrasekharan, P.; Yang, H.T.; Zhao, L.Y.; Peng, E.; Lv, Y.B.; Xiao, W.; Fang, J.; Yi, J.B.; et al. Synthesis of ferromagnetic $Fe_{0.6}Mn_{0.4}O$ nanoflowers as a new class of magnetic theranostic platform for in vivo T1-T2 dual-mode magnetic resonance imaging and magnetic hyperthermia therapy. *Adv. Healthc. Mater.* **2016**, *5*, 2092–2104. [CrossRef] [PubMed]
168. Del Sol-Fernández, S.; Portilla-Tundidor, Y.; Gutiérrez, L.; Odio, O.F.; Reguera, E.; Barber, D.F.; Morales, M.P. Flower-like Mn-doped magnetic nanoparticles functionalized with $\alpha_v\beta_3$-integrin-ligand to efficiently induce intracellular heat after alternating magnetic field exposition, triggering glioma cell death. *ACS Appl. Mater. Interfaces* **2019**, *11*, 26648–26663. [CrossRef]
169. Mørup, S.; Tronc, E. Superparamagnetic relaxation of weakly interacting particles. *Phys. Rev. Lett.* **1994**, *72*, 3278–3281. [CrossRef] [PubMed]
170. Allia, P.; Coisson, M.; Tiberto, P.; Vinai, F.; Knobel, M.; Novak, M.A.; Nunes, W.C. Granular Cu-Co alloys as interacting superparamagnets. *Phys. Rev. B Condens. Matter Mater. Phys.* **2001**, *64*, 144420. [CrossRef]
171. Burrows, F.; Parker, C.; Evans, R.F.L.; Hancock, Y.; Hovorka, O.; Chantrell, R.W. Energy losses in interacting fine-particle magnetic composites. *J. Phys. D Appl. Phys.* **2010**, *43*, 474010. [CrossRef]
172. Landi, G.T. Role of dipolar interaction in magnetic hyperthermia. *Phys. Rev. B* **2014**, *89*, 014403. [CrossRef]
173. El-Hilo, M.; O'Grady, K.; Chantrell, R.W. Susceptibility phenomena in a fine particle system. I. Concentration dependence of the peak. *J. Magn. Magn. Mater.* **1992**, *114*, 295–306. [CrossRef]
174. Binns, C.; Maher, M.J.; Pankhurst, Q.A.; Kechrakos, D.; Trohidou, K.N. Magnetic behavior of nanostructured films assembled from preformed Fe clusters embedded in Ag. *Phys. Rev. B Condens. Matter Mater. Phys.* **2002**, *66*, 184413. [CrossRef]
175. Del Bianco, L.; Spizzo, F.; Barucca, G.; Ruggiero, M.R.; Geninatti Crich, S.; Forzan, M.; Sieni, E.; Sgarbossa, P. Mechanism of magnetic heating in Mn-doped magnetite nanoparticles and the role of intertwined structural and magnetic properties. *Nanoscale* **2019**, *11*, 10896–10910. [CrossRef]
176. Coral, D.F.; Mendoza Zélis, P.; Marciello, M.; Morales, M.P.; Craievich, A.; Sánchez, F.H.; Fernández Van Raap, M.B. Effect of nanoclustering and dipolar interactions in heat generation for magnetic hyperthermia. *Langmuir* **2016**, *32*, 1201–1213. [CrossRef] [PubMed]
177. Kechrakos, D.; Trohidou, K. Magnetic properties of dipolar interacting single-domain particles. *Phys. Rev. B Condens. Matter Mater. Phys.* **1998**, *58*, 12169–12177. [CrossRef]
178. Haase, C.; Nowak, U. Role of dipole-dipole interactions for hyperthermia heating of magnetic nanoparticle ensembles. *Phys. Rev. B Condens. Matter Mater. Phys.* **2012**, *85*, 045435. [CrossRef]
179. Serantes, D.; Baldomir, D.; Martinez-Boubeta, C.; Simeonidis, K.; Angelakeris, M.; Natividad, E.; Castro, M.; Mediano, A.; Chen, D.-X.; Sanchez, A.; et al. Influence of dipolar interactions on hyperthermia properties of ferromagnetic particles. *J. Appl. Phys.* **2010**, *108*, 073918. [CrossRef]
180. Usov, N.A.; Serebryakova, O.N.; Tarasov, V.P. Interaction effects in assembly of magnetic nanoparticles. *Nanoscale Res. Lett.* **2017**, *12*, 489. [CrossRef]
181. De La Presa, P.; Luengo, Y.; Velasco, V.; Morales, M.P.; Iglesias, M.; Veintemillas-Verdaguer, S.; Crespo, P.; Hernando, A. Particle interactions in liquid magnetic colloids by zero field cooled measurements: Effects on heating efficiency. *J. Phys. Chem. C* **2015**, *119*, 11022–11030. [CrossRef]
182. Guibert, C.; Dupuis, V.; Peyre, V.; Fresnais, J. Hyperthermia of magnetic nanoparticles: Experimental study of the role of aggregation. *J. Phys. Chem. C* **2015**, *119*, 28148–28154. [CrossRef]
183. Eggemann, A.S.; Majetich, S.A.; Farrell, D.; Pankhurst, Q.A. Size and concentration effects on high frequency hysteresis of iron oxide nanoparticles. *IEEE Trans. Magn.* **2007**, *43*, 2451. [CrossRef]
184. Salas, G.; Camarero, J.; Cabrera, D.; Takacs, H.; Varela, M.; Ludwig, R.; Dähring, H.; Hilger, I.; Miranda, R.; Morales, M.P.; et al. Modulation of magnetic heating via dipolar magnetic interactions in monodisperse and crystalline iron oxide nanoparticles. *J. Phys. Chem. C* **2014**, *118*, 19985–19994. [CrossRef]
185. Dennis, C.L.; Jackson, A.J.; Borchers, J.A.; Ivkov, R.; Foreman, A.R.; Lau, J.W.; Goernitz, E.; Gruettner, C. The influence of collective behavior on the magnetic and heating properties of iron oxide nanoparticles. *J. Appl. Phys.* **2008**, *103*, 07A319. [CrossRef]
186. Martinez-Boubeta, C.; Simeonidis, K.; Serantes, D.; Conde-Leborán, I.; Kazakis, I.; Stefanou, G.; Peña, L.; Galceran, R.; Balcells, L.; Monty, C.; et al. Adjustable hyperthermia response of self-assembled ferromagnetic Fe-MgO core–shell nanoparticles by tuning dipole–dipole interactions. *Adv. Funct. Mater.* **2012**, *22*, 3737–3744. [CrossRef]
187. Lima, E.; De Biasi, E.; Mansilla, M.V.; Saleta, M.E.; Granada, M.; Troiani, H.E.; Effenberger, F.B.; Rossi, L.M.; Rechenberg, H.R.; Zysler, R.D. Heat generation in agglomerated ferrite nanoparticles in an alternating magnetic field. *J. Phys. D. Appl. Phys.* **2013**, *46*, 045002. [CrossRef]
188. Conde-Leboran, I.; Baldomir, D.; Martinez-Boubeta, C.; Chubykalo-Fesenko, O.; Morales, M.P.; Salas, G.; Cabrera, D.; Camarero, J.; Teran, F.J.; Serantes, D. A single picture explains diversity of hyperthermia response of magnetic nanoparticles. *J. Phys. Chem. C* **2015**, *119*, 15698–15706. [CrossRef]
189. Ovejero, J.G.; Cabrera, D.; Carrey, J.; Valdivielso, T.; Salas, G.; Teran, F.J. Effects of inter- and intra-aggregate magnetic dipolar interactions on the magnetic heating efficiency of iron oxide nanoparticles. *Phys. Chem. Chem. Phys.* **2016**, *18*, 10954–10963. [CrossRef] [PubMed]
190. Arteaga-Cardona, F.; Rojas-Rojas, K.; Costo, R.; Mendez-Rojas, M.A.; Hernando, A.; De La Presa, P. Improving the magnetic heating by disaggregating nanoparticles. *J. Alloys Compd.* **2016**, *663*, 636–644. [CrossRef]

191. Blanco-Andujar, C.; Ortega, D.; Southern, P.; Pankhurst, Q.A.; Thanh, N.T.K. High performance multi-core iron oxide nanoparticles for magnetic hyperthermia: Microwave synthesis, and the role of core-to-core interactions. *Nanoscale* **2015**, *7*, 1768–1775. [CrossRef]
192. Sakellari, D.; Brintakis, K.; Kostopoulou, A.; Myrovali, E.; Simeonidis, K.; Lappas, A.; Angelakeris, M. Ferrimagnetic nanocrystal assemblies as versatile magnetic particle hyperthermia mediators. *Mater. Sci. Eng. C* **2016**, *58*, 187–193. [CrossRef]
193. Kostopoulou, A.; Brintakis, K.; Vasilakaki, M.; Trohidou, K.N.; Douvalis, A.P.; Lascialfari, A.; Manna, L.; Lappas, A. Assembly-mediated interplay of dipolar interactions and surface spin disorder in colloidal maghemite nanoclusters. *Nanoscale* **2014**, *6*, 3764–3776. [CrossRef]
194. Hayashi, K.; Sato, Y.; Sakamoto, W.; Yogo, T. Theranostic nanoparticles for MRI-guided thermochemotherapy: "Tight" clustering of magnetic nanoparticles boosts relaxivity and heat-generation power. *ACS Biomater. Sci. Eng.* **2017**, *3*, 95–105. [CrossRef]
195. Hayashi, K.; Nakamura, M.; Sakamoto, W.; Yogo, T.; Miki, H.; Ozaki, S.; Abe, M.; Matsumoto, T.; Ishimura, K. Superparamagnetic nanoparticle clusters for cancer theranostics combining magnetic resonance imaging and hyperthermia treatment. *Theranostics* **2013**, *3*, 366–376. [CrossRef] [PubMed]
196. Larsen, B.A.; Haag, M.A.; Serkova, N.J.; Shroyer, K.R.; Stoldt, C.R. Controlled aggregation of superparamagnetic iron oxide nanoparticles for the development of molecular magnetic resonance imaging probes. *Nanotechnology* **2008**, *19*, 265102. [CrossRef]
197. Yoon, T.J.; Lee, H.; Shao, H.; Hilderbrand, S.A.; Weissleder, R. Multicore assemblies potentiate magnetic properties of biomagnetic nanoparticles. *Adv. Mater.* **2011**, *23*, 4793–4797. [CrossRef] [PubMed]
198. Xu, F.; Cheng, C.; Chen, D.X.; Gu, H. Magnetite nanocrystal clusters with ultra-high sensitivity in magnetic resonance imaging. *ChemPhysChem* **2012**, *13*, 336–341. [CrossRef]
199. Attaluri, A.; Seshadri, M.; Mirpour, S.; Wabler, M.; Marinho, T.; Furqan, M.; Zhou, H.; De Paoli, S.; Gruettner, C.; Gilson, W.; et al. Image-guided thermal therapy with a dual-contrast magnetic nanoparticle formulation: A feasibility study. *Int. J. Hyperth.* **2016**, *32*, 543–557. [CrossRef]
200. Hergt, R.; Hiergeist, R.; Zeisberger, M.; Schüler, D.; Heyen, U.; Hilger, I.; Kaiser, W.A. Magnetic properties of bacterial magnetosomes as potential diagnostic and therapeutic tools. *J. Magn. Magn. Mater.* **2005**, *293*, 80–86. [CrossRef]
201. Alphandéry, E.; Chebbi, I.; Guyot, F.; Durand-Dubief, M. Use of bacterial magnetosomes in the magnetic hyperthermia treatment of tumours: A review. *Int. J. Hyperth.* **2013**, *29*, 801–809. [CrossRef]
202. Alphandéry, E.; Faure, S.; Seksek, O.; Guyot, F.; Chebbi, I. Chains of magnetosomes extracted from AMB-1 magnetotactic bacteria for application in alternative magnetic field cancer therapy. *ACS Nano* **2011**, *5*, 6279–6296. [CrossRef]
203. Gandia, D.; Gandarias, L.; Rodrigo, I.; Robles-García, J.; Das, R.; Garaio, E.; García, J.Á.; Phan, M.H.; Srikanth, H.; Orue, I.; et al. Unlocking the potential of magnetotactic bacteria as magnetic hyperthermia agents. *Small* **2019**, *15*, 1902626. [CrossRef] [PubMed]
204. Alphandéry, E.; Ding, Y.; Ngo, A.T.; Wang, Z.L.; Wu, L.F.; Pileni, M.P. Assemblies of aligned magnetotactic bacteria and extracted magnetosomes: What is the main factor responsible for the magnetic anisotropy? *ACS Nano* **2009**, *3*, 1539–1547. [CrossRef]
205. Branquinho, L.C.; Carrião, M.S.; Costa, A.S.; Zufelato, N.; Sousa, M.H.; Miotto, R.; Ivkov, R.; Bakuzis, A.F. Effect of magnetic dipolar interactions on nanoparticle heating efficiency: Implications for cancer hyperthermia. *Sci. Rep.* **2013**, *3*, 2887. [CrossRef] [PubMed]
206. Zubarev, A.Y. Effect of internal chain-like structures on magnetic hyperthermia in non-liquid media. *Philos. Trans. R. Soc. A Math. Phys. Eng. Sci.* **2019**, *377*, 20180213. [CrossRef]
207. Serantes, D.; Simeonidis, K.; Angelakeris, M.; Chubykalo-Fesenko, O.; Marciello, M.; Morales, M.P.; Baldomir, D.; Martinez-Boubeta, C. Multiplying magnetic hyperthermia response by nanoparticle assembling. *J. Phys. Chem. C* **2014**, *118*, 5927–5934. [CrossRef]
208. Lahiri, B.B.; Ranoo, S.; Philip, J. Effect of orientational ordering of magnetic nanoemulsions immobilized in agar gel on magnetic hyperthermia. *J. Magn. Magn. Mater.* **2018**, *451*, 254–268. [CrossRef]
209. Myrovali, E.; Papadopoulos, K.; Iglesias, I.; Spasova, M.; Farle, M.; Wiedwald, U.; Angelakeris, M. Long-range ordering effects in magnetic nanoparticles. *ACS Appl. Mater. Interfaces* **2021**, *13*, 21602–21612. [CrossRef] [PubMed]
210. Valdés, D.P.; Lima, E.; Zysler, R.D.; De Biasi, E. Modeling the magnetic-hyperthermia response of linear chains of nanoparticles with low anisotropy: A key to improving specific power absorption. *Phys. Rev. Appl.* **2020**, *14*, 014023. [CrossRef]
211. Valdés, D.P.; Lima, E.; Zysler, R.D.; Goya, G.F.; De Biasi, E. Role of anisotropy, frequency, and interactions in magnetic hyperthermia applications: Noninteracting nanoparticles and linear chain arrangements. *Phys. Rev. Appl.* **2021**, *15*, 044005. [CrossRef]
212. Niculaes, D.; Lak, A.; Anyfantis, G.C.; Marras, S.; Laslett, O.; Avugadda, S.K.; Cassani, M.; Serantes, D.; Hovorka, O.; Chantrell, R.; et al. Asymmetric assembling of iron oxide nanocubes for improving magnetic hyperthermia performance. *ACS Nano* **2017**, *11*, 12121–12133. [CrossRef]
213. Avugadda, S.K.; Materia, M.E.; Nigmatullin, R.; Cabrera, D.; Marotta, R.; Cabada, T.F.; Marcello, E.; Nitti, S.; Artés-Ibañez, E.J.; Basnett, P.; et al. Esterase-cleavable 2D assemblies of magnetic iron oxide nanocubes: Exploiting enzymatic polymer disassembling to improve magnetic hyperthermia heat losses. *Chem. Mater.* **2019**, *31*, 5450–5463. [CrossRef] [PubMed]
214. Balakrishnan, P.B.; Silvestri, N.; Fernandez-Cabada, T.; Marinaro, F.; Fernandes, S.; Fiorito, S.; Miscuglio, M.; Serantes, D.; Ruta, S.; Livesey, K.; et al. Exploiting unique alignment of cobalt ferrite nanoparticles, mild hyperthermia, and controlled intrinsic cobalt toxicity for cancer therapy. *Adv. Mater.* **2020**, *32*, 2003712. [CrossRef]
215. Fu, R.; Yan, Y.; Roberts, C.; Liu, Z.; Chen, Y. The role of dipole interactions in hyperthermia heating colloidal clusters of densely-packed superparamagnetic nanoparticles. *Sci. Rep.* **2018**, *8*, 4704. [CrossRef]

216. Hu, K.; Sun, J.; Guo, Z.; Wang, P.; Chen, Q.; Ma, M.; Gu, N. A novel magnetic hydrogel with aligned magnetic colloidal assemblies showing controllable enhancement of magnetothermal effect in the presence of alternating magnetic field. *Adv. Mater.* **2015**, *27*, 2507–2514. [CrossRef] [PubMed]
217. Andreu, I.; Natividad, E.; Solozábal, L.; Roubeau, O. Nano-objects for addressing the control of nanoparticle arrangement and performance in magnetic hyperthermia. *ACS Nano* **2015**, *9*, 1408–1419. [CrossRef] [PubMed]
218. Sanz, B.; Cabreira-Gomes, R.; Torres, T.E.; Valdés, D.P.; Lima, E.; De Biasi, E.; Zysler, R.D.; Ibarra, M.R.; Goya, G.F. Low-dimensional assemblies of magnetic $MnFe_2O_4$ nanoparticles and direct in vitro measurements of enhanced heating driven by dipolar interactions: Implications for magnetic hyperthermia. *ACS Appl. Nano Mater.* **2020**, *3*, 8719–8731. [CrossRef]
219. Béalle, G.; Di Corato, R.; Kolosnjaj-Tabi, J.; Dupuis, V.; Clément, O.; Gazeau, F.; Wilhelm, C.; Ménager, C. Ultra magnetic liposomes for MR imaging, targeting, and hyperthermia. *Langmuir* **2012**, *28*, 11834–11842. [CrossRef]
220. Di Corato, R.; Béalle, G.; Kolosnjaj-Tabi, J.; Espinosa, A.; Clément, O.; Silva, A.K.A.; Ménager, C.; Wilhelm, C. Combining magnetic hyperthermia and photodynamic therapy for tumor ablation with photoresponsive magnetic liposomes. *ACS Nano* **2015**, *9*, 2904–2916. [CrossRef] [PubMed]
221. Chiang, W.H.; Ho, V.T.; Chen, H.H.; Huang, W.C.; Huang, Y.F.; Lin, S.C.; Chern, C.S.; Chiu, H.C. Superparamagnetic hollow hybrid nanogels as a potential guidable vehicle system of stimuli-mediated MR imaging and multiple cancer therapeutics. *Langmuir* **2013**, *29*, 6434–6443. [CrossRef]
222. Materia, M.E.; Guardia, P.; Sathya, A.; Pernia Leal, M.; Marotta, R.; Di Corato, R.; Pellegrino, T. Mesoscale assemblies of iron oxide nanocubes as heat mediators and image contrast agents. *Langmuir* **2015**, *31*, 808–816. [CrossRef]
223. Cervadoro, A.; Cho, M.; Key, J.; Cooper, C.; Stigliano, C.; Aryal, S.; Brazdeikis, A.; Leary, J.F.; Decuzzi, P. Synthesis of multifunctional magnetic nanoflakes for magnetic resonance imaging, hyperthermia, and targeting. *ACS Appl. Mater. Interfaces* **2014**, *6*, 12939–12946. [CrossRef]
224. Jaiswal, M.K.; De, M.; Chou, S.S.; Vasavada, S.; Bleher, R.; Prasad, P.V.; Bahadur, D.; Dravid, V.P. Thermoresponsive magnetic hydrogels as theranostic nanoconstructs. *ACS Appl. Mater. Interfaces* **2014**, *6*, 6237–6247. [CrossRef]
225. Tan, R.P.; Carrey, J.; Respaud, M. Magnetic hyperthermia properties of nanoparticles inside lysosomes using kinetic Monte Carlo simulations: Influence of key parameters and dipolar interactions, and evidence for strong spatial variation of heating power. *Phys. Rev. B Condens. Matter Mater. Phys.* **2014**, *90*, 214421. [CrossRef]
226. Mikhaylov, G.; Mikac, U.; Magaeva, A.A.; Itin, V.I.; Naiden, E.P.; Psakhye, I.; Babes, L.; Reinheckel, T.; Peters, C.; Zeiser, R.; et al. Ferri-liposomes as an MRI-visible drug-delivery system for targeting tumours and their microenvironment. *Nat. Nanotechnol.* **2011**, *6*, 594–602. [CrossRef]
227. Tai, L.A.; Tsai, P.J.; Wang, Y.C.; Wang, Y.J.; Lo, L.W.; Yang, C.S. Thermosensitive liposomes entrapping iron oxide nanoparticles for controllable drug release. *Nanotechnology* **2009**, *20*, 135101. [CrossRef]
228. Fortes Brollo, M.E.; Hernández Flores, P.; Gutiérrez, L.; Johansson, C.; Barber, D.F.; Morales, M.P. Magnetic properties of nanoparticles as a function of their spatial distribution on liposomes and cells. *Phys. Chem. Chem. Phys.* **2018**, *20*, 17829–17838. [CrossRef]
229. Jabalera, Y.; Fernández-Vivas, A.; Iglesias, G.R.; Delgado, Á.V.; Jimenez-Lopez, C. Magnetoliposomes of mixed biomimetic and inorganic magnetic nanoparticles as enhanced hyperthermia agents. *Colloids Surf. B Biointerfaces* **2019**, *183*, 110435. [CrossRef]
230. Fortes Brollo, M.E.; Domínguez-Bajo, A.; Tabero, A.; Domínguez-Arca, V.; Gisbert, V.; Prieto, G.; Johansson, C.; Garcia, R.; Villanueva, A.; Serrano, M.C.; et al. Combined magnetoliposome formation and drug loading in one step for efficient alternating current-magnetic field remote-controlled drug release. *ACS Appl. Mater. Interfaces* **2020**, *12*, 4295–4307. [CrossRef]
231. Guo, Y.; Zhang, Y.; Ma, J.; Li, Q.; Li, Y.; Zhou, X.; Zhao, D.; Song, H.; Chen, Q.; Zhu, X. Light/magnetic hyperthermia triggered drug released from multi-functional thermo-sensitive magnetoliposomes for precise cancer synergetic theranostics. *J. Control. Release* **2018**, *272*, 145–158. [CrossRef] [PubMed]
232. Liu, X.L.; Choo, E.S.G.; Ahmed, A.S.; Zhao, L.Y.; Yang, Y.; Ramanujan, R.V.; Xue, J.M.; Di Fan, D.; Fan, H.M.; Ding, J. Magnetic nanoparticle-loaded polymer nanospheres as magnetic hyperthermia agents. *J. Mater. Chem. B* **2014**, *2*, 120–128. [CrossRef]
233. Sadat, M.E.; Patel, R.; Sookoor, J.; Bud'Ko, S.L.; Ewing, R.C.; Zhang, J.; Xu, H.; Wang, Y.; Pauletti, G.M.; Mast, D.B.; et al. Effect of spatial confinement on magnetic hyperthermia via dipolar interactions in Fe_3O_4 nanoparticles for biomedical applications. *Mater. Sci. Eng. C* **2014**, *42*, 52–63. [CrossRef] [PubMed]
234. Albarqi, H.A.; Wong, L.H.; Schumann, C.; Sabei, F.Y.; Korzun, T.; Li, X.; Hansen, M.N.; Dhagat, P.; Moses, A.S.; Taratula, O.; et al. Biocompatible nanoclusters with high heating efficiency for systemically delivered magnetic hyperthermia. *ACS Nano* **2019**, *13*, 6383–6395. [CrossRef] [PubMed]
235. Grillo, R.; Gallo, J.; Stroppa, D.G.; Carbó-Argibay, E.; Lima, R.; Fraceto, L.F.; Bañobre-López, M. Sub-micrometer magnetic nanocomposites: Insights into the effect of magnetic nanoparticles interactions on the pptimization of SAR and MRI performance. *ACS Appl. Mater. Interfaces* **2016**, *8*, 25777–25787. [CrossRef]
236. Liu, X.; Kaminski, M.D.; Chen, H.; Torno, M.; Taylor, L.T.; Rosengart, A.J. Synthesis and characterization of highly-magnetic biodegradable poly(d,l-lactide-co-glycolide) nanospheres. *J. Control. Release* **2007**, *119*, 52–58. [CrossRef]
237. Jia, Y.; Yuan, M.; Yuan, H.; Huang, X.; Sui, X.; Cui, X.; Tang, F.; Peng, J.; Chen, J.; Lu, S.; et al. Co-encapsulation of magnetic Fe_3O_4 nanoparticles and doxorubicin into biodegradable PLGA nanocarriers for intratumoral drug delivery. *Int. J. Nanomed.* **2012**, *7*, 1697–1708. [CrossRef]

238. Chiang, W.L.; Ke, C.J.; Liao, Z.X.; Chen, S.Y.; Chen, F.R.; Tsai, C.Y.; Xia, Y.; Sung, H.W. Pulsatile drug release from PLGA hollow microspheres by controlling the permeability of their walls with a magnetic field. *Small* **2012**, *8*, 3584–3588. [CrossRef]
239. Fang, K.; Song, L.; Gu, Z.; Yang, F.; Zhang, Y.; Gu, N. Magnetic field activated drug release system based on magnetic PLGA microspheres for chemo-thermal therapy. *Colloids Surf. B Biointerfaces* **2015**, *136*, 712–720. [CrossRef]
240. Del Bianco, L.; Spizzo, F.; Sgarbossa, P.; Sieni, E.; Barucca, G.; Ruggiero, M.R.; Geninatti Crich, S. Dipolar magnetic interactions in Mn-doped magnetite nanoparticles loaded into PLGA nanocapsules for nanomedicine applications. *J. Phys. Chem. C* **2019**, *123*, 30007–30020. [CrossRef]
241. Hu, S.H.; Liu, T.Y.; Liu, D.M.; Chen, S.Y. Controlled pulsatile drug release from a ferrogel by a high-frequency magnetic field. *Macromolecules* **2007**, *40*, 6786–6788. [CrossRef]
242. Satarkar, N.S.; Hilt, J.Z. Magnetic hydrogel nanocomposites for remote controlled pulsatile drug release. *J. Control. Release* **2008**, *130*, 246–251. [CrossRef] [PubMed]
243. Jaiswal, M.K.; Pradhan, L.; Vasavada, S.; De, M.; Sarma, H.D.; Prakash, A.; Bahadur, D.; Dravid, V.P. Magneto-thermally responsive hydrogels for bladder cancer treatment: Therapeutic efficacy and in vivo biodistribution. *Colloids Surf. B Biointerfaces* **2015**, *136*, 625–633. [CrossRef] [PubMed]
244. Zhang, Z.Q.; Song, S.C. Multiple hyperthermia-mediated release of TRAIL/SPION nanocomplex from thermosensitive polymeric hydrogels for combination cancer therapy. *Biomaterials* **2017**, *132*, 16–27. [CrossRef] [PubMed]
245. Turcu, R.; Craciunescu, I.; Garamus, V.M.; Janko, C.; Lyer, S.; Tietze, R.; Alexiou, C.; Vekas, L. Magnetic microgels for drug targeting applications: Physical-chemical properties and cytotoxicity evaluation. *J. Magn. Magn. Mater.* **2015**, *380*, 307–314. [CrossRef]
246. Zhang, Z.Q.; Song, S.C. Thermosensitive/superparamagnetic iron oxide nanoparticle-loaded nanocapsule hydrogels for multiple cancer hyperthermia. *Biomaterials* **2016**, *106*, 13–23. [CrossRef]
247. Baeza, A.; Colilla, M.; Vallet-Regí, M. Advances in mesoporous silica nanoparticles for targeted stimuli-responsive drug delivery. *Expert Opin. Drug Deliv.* **2015**, *12*, 319–337. [CrossRef] [PubMed]
248. Croissant, J.G.; Fatieiev, Y.; Almalik, A.; Khashab, N.M. Mesoporous silica and organosilica nanoparticles: Physical chemistry, biosafety, delivery strategies, and biomedical applications. *Adv. Healthc. Mater.* **2018**, *7*, 1700831. [CrossRef]
249. Lee, K.Y.; Yuk, S.H. Polymeric protein delivery systems. *Prog. Polym. Sci.* **2007**, *32*, 669–697. [CrossRef]
250. Tan, M.L.; Choong, P.F.M.; Dass, C.R. Recent developments in liposomes, microparticles and nanoparticles for protein and peptide drug delivery. *Peptides* **2010**, *31*, 184–193. [CrossRef] [PubMed]
251. Almeida, A.J.; Souto, E. Solid lipid nanoparticles as a drug delivery system for peptides and proteins. *Adv. Drug Deliv. Rev.* **2007**, *59*, 478–490. [CrossRef] [PubMed]
252. Baeza, A.; Guisasola, E.; Ruiz-Hernández, E.; Vallet-Regí, M. Magnetically triggered multidrug release by hybrid mesoporous silica nanoparticles. *Chem. Mater.* **2012**, *24*, 517–524. [CrossRef]
253. Stöber, W.; Fink, A.; Bohn, E. Controlled growth of monodisperse silica spheres in the micron size range. *J. Colloid Interface Sci.* **1968**, *26*, 62–69. [CrossRef]
254. Guisasola, E.; Asín, L.; Beola, L.; De La Fuente, J.M.; Baeza, A.; Vallet-Regí, M. Beyond traditional hyperthermia: In vivo cancer treatment with magnetic-responsive mesoporous silica nanocarriers. *ACS Appl. Mater. Interfaces* **2018**, *10*, 12518–12525. [CrossRef]
255. Yiu, H.H.P.; Keane, M.A.; Lethbridge, Z.A.D.; Lees, M.R.; El Haj, A.J.; Dobson, J. Synthesis of novel magnetic iron metal-silica (Fe-SBA-15) and magnetite-silica (Fe_3O_4-SBA-15) nanocomposites with a high iron content using temperature-programed reduction. *Nanotechnology* **2008**, *19*, 255606. [CrossRef]
256. Lee, J.E.; Lee, N.; Kim, H.; Kim, J.; Choi, S.H.; Kim, J.H.; Kim, T.; Song, I.C.; Park, S.P.; Moon, W.K.; et al. Uniform mesoporous dye-doped silica nanoparticles decorated with multiple magnetite nanocrystals for simultaneous enhanced magnetic resonance imaging, fluorescence imaging, and drug delivery. *J. Am. Chem. Soc.* **2010**, *132*, 552–557. [CrossRef]
257. Tao, C.; Zhu, Y. Magnetic mesoporous silica nanoparticles for potential delivery of chemotherapeutic drugs and hyperthermia. *Dalt. Trans.* **2014**, *43*, 15482–15490. [CrossRef] [PubMed]
258. Miguel-Sancho, N.; Martinez, G.; Sebastian, V.; Malumbres, A.; Florea, I.; Arenal, R.; Ortega-Liebana, M.C.; Hueso, J.L.; Santamaria, J. Pumping netallic nanoparticles with spatial precision within magnetic mesoporous platforms: 3D characterization and catalytic application. *ACS Appl. Mater. Interfaces* **2017**, *9*, 41529–41536. [CrossRef]
259. Virumbrales, M.; Saez-Puche, R.; Torralvo, M.J.; Blanco-Gutierrez, V. Mesoporous silica matrix as a tool for minimizing dipolar interactions in $NiFe_2O_4$ and $ZnFe_2O_4$ nanoparticles. *Nanomaterials* **2017**, *7*, 151. [CrossRef] [PubMed]
260. Chelebaeva, E.; Raehm, L.; Durand, J.O.; Guari, Y.; Larionova, J.; Guérin, C.; Trifonov, A.; Willinger, M.; Thangavel, K.; Lascialfari, A.; et al. Mesoporous silica nanoparticles combining two-photon excited fluorescence and magnetic properties. *J. Mater. Chem.* **2010**, *20*, 1877–1884. [CrossRef]
261. Vamvakidis, K.; Mourdikoudis, S.; Makridis, A.; Paulidou, E.; Angelakeris, M.; Dendrinou-Samara, C. Magnetic hyperthermia efficiency and MRI contrast sensitivity of colloidal soft/hard ferrite nanoclusters. *J. Colloid Interface Sci.* **2018**, *511*, 101–109. [CrossRef] [PubMed]
262. Iglesias, G.R.; Jabalera, Y.; Peigneux, A.; Fernández, B.L.C.; Delgado, Á.V.; Jimenez-Lopez, C. Enhancement of magnetic hyperthermia by mixing synthetic inorganic and biomimetic magnetic nanoparticles. *Pharmaceutics* **2019**, *11*, 273. [CrossRef]
263. Ovejero, J.G.; Spizzo, F.; Morales, M.P.; Del Bianco, L. Mixing iron oxide nanoparticles with different shape and size for tunable magneto-heating performance. *Nanoscale* **2021**, *13*, 5714–5729. [CrossRef]

264. Ovejero, J.G.; Armenia, I.; Serantes, D.; Veintemillas-Verdaguer, S.; Zeballos, N.; López-Gallego, F.; Grüttner, C.; de la Fuente, J.M.; Morales, M.P.; Grazu, V. Selective magnetic nanoheating: Combining iron oxide nanoparticles for multi-hot-spot induction and sequential regulation. *Nano Lett.* **2021**, *21*, 7213–7220. [CrossRef]
265. Christiansen, M.G.; Senko, A.W.; Chen, R.; Romero, G.; Anikeeva, P. Magnetically multiplexed heating of single domain nanoparticles. *Appl. Phys. Lett.* **2014**, *104*, 213103. [CrossRef]
266. Armenia, I.; Grazú Bonavia, M.V.; De Matteis, L.; Ivanchenko, P.; Martra, G.; Gornati, R.; de la Fuente, J.M.; Bernardini, G. Enzyme activation by alternating magnetic field: Importance of the bioconjugation methodology. *J. Colloid Interface Sci.* **2019**, *537*, 615–628. [CrossRef]
267. Moon, J.; Christiansen, M.G.; Rao, S.; Marcus, C.; Bono, D.C.; Rosenfeld, D.; Gregurec, D.; Varnavides, G.; Chiang, P.H.; Park, S.; et al. Magnetothermal multiplexing for selective remote control of cell signaling. *Adv. Funct. Mater.* **2020**, *30*, 2000577. [CrossRef]
268. Kolosnjaj-Tabi, J.; Lartigue, L.; Javed, Y.; Luciani, N.; Pellegrino, T.; Wilhelm, C.; Alloyeau, D.; Gazeau, F. Biotransformations of magnetic nanoparticles in the body. *Nano Today* **2016**, *11*, 280–284. [CrossRef]
269. Feliu, N.; Docter, D.; Heine, M.; Del Pino, P.; Ashraf, S.; Kolosnjaj-Tabi, J.; Macchiarini, P.; Nielsen, P.; Alloyeau, D.; Gazeau, F.; et al. In vivo degeneration and the fate of inorganic nanoparticles. *Chem. Soc. Rev.* **2016**, *45*, 2440–2457. [CrossRef] [PubMed]
270. Feng, Q.; Liu, Y.; Huang, J.; Chen, K.; Huang, J.; Xiao, K. Uptake, distribution, clearance, and toxicity of iron oxide nanoparticles with different sizes and coatings. *Sci. Rep.* **2018**, *8*, 2082. [CrossRef]
271. Zelepukin, I.V.; Yaremenko, A.V.; Ivanov, I.N.; Yuryev, M.V.; Cherkasov, V.R.; Deyev, S.M.; Nikitin, P.I.; Nikitin, M.P. Long-term fate of magnetic particles in mice: A comprehensive study. *ACS Nano* **2021**, *15*, 11341–11357. [CrossRef] [PubMed]

materials

MDPI

Review

A Perspective on Modelling Metallic Magnetic Nanoparticles in Biomedicine: From Monometals to Nanoalloys and Ligand-Protected Particles

Barbara Farkaš [1] and Nora H. de Leeuw [1,2,*]

[1] School of Chemistry, Cardiff University, Cardiff CF10 3AT, UK; FarkasB@cardiff.ac.uk
[2] School of Chemistry, University of Leeds, Leeds LS2 9JT, UK
* Correspondence: N.H.deLeeuw@leeds.ac.uk

Abstract: The focus of this review is on the physical and magnetic properties that are related to the efficiency of monometallic magnetic nanoparticles used in biomedical applications, such as magnetic resonance imaging (MRI) or magnetic nanoparticle hyperthermia, and how to model these by theoretical methods, where the discussion is based on the example of cobalt nanoparticles. Different simulation systems (cluster, extended slab, and nanoparticle models) are critically appraised for their efficacy in the determination of reactivity, magnetic behaviour, and ligand-induced modifications of relevant properties. Simulations of the effects of nanoscale alloying with other metallic phases are also briefly reviewed.

Keywords: nanoparticles; density functional theory; magnetic hyperthermia; magnetic anisotropy

Citation: Farkaš, B.; de Leeuw, N.H. A Perspective on Modelling Metallic Magnetic Nanoparticles in Biomedicine: From Monometals to Nanoalloys and Ligand-Protected Particles. *Materials* **2021**, *14*, 3611. https://doi.org/10.3390/ma14133611

Academic Editor: Lucia Del Bianco

Received: 25 May 2021
Accepted: 21 June 2021
Published: 28 June 2021

1. History of Use and Study of Metal Nanoparticles in Biomedicine

Metal nanoparticles (MNPs) have been attracting researchers' attention for over a century, owing to the diversity in their properties and the unique phenomena that only exist at the nanoscale and have unlocked many new pathways to implement metals as technology materials. However, MNPs have been used, albeit unknowingly, long before modern ages. They were an integral part in the cosmetics of the ancient Egyptians, whereas the Romans were famous for their workmanship of stained glass which evolved from the absorption of light through gold and silver MNPs—the most renowned example being the Lycurgus cup. The trend of dyed glass and metal-resembling glazes on ceramic pottery continued deep into the Middle Ages before the origin of the colouring effects was linked to the presence of optically active colloidal nanosized metallic particles in 1857 by Michael Faraday. Today, efforts to unravel new tuning strategies leading to desired properties of MNPs continue to grow, and utilisation of such nanotechnology has moved a long way from stained glass, reaching an extensive range of confirmed and potential applications in catalysis [1–4], electronics [5–7], optics [8–11], information storage [12–14], and finally, medicine [15–19].

MNPs can exist as common single element structures, constituting alkali/alkaline, transition, or noble metals, or they can be composites of two or more different metals, known as nanoalloys. Their physical and chemical characteristics are determined not only by the chemical composition as in the respective bulk materials, but also by their size and morphology. Therefore, tailoring of the MNP properties depends on the strict control of each of these parameters. Only recently have advances in experimental equipment and methods led to the synthesis of MNPs of a uniform size distribution with directed morphology control of particles synthesised in solution, giving rise to the development of numerous production techniques. Today, procedures to generate MNPs with extensive control over their size and shape are well established, even to the point of reaching atomic-level precision in cluster and MNP synthesis, isolation, and deposition on a support [20,21].

Such progress has enabled the correlation between the MNP properties and size and shape effects, with multiple examples cited in the recent literature [22–28]. Nonetheless, MNPs are principally neither isolated nor clean, rather frequently stabilised by solvent or surfactant molecules or in form of particle aggregates, the presence of which makes the structural determination cumbersome. Consequently, experimental characterisation techniques still face significant challenges in assigning the influence of structural parameters on certain properties over the size distribution of the synthesised MNPs [29], and computational simulations have been shown to significantly contribute to the unravelling of size, morphology, and environmental effects on properties of individual MNPs [30–34].

In recent years, the emerging potential of MNPs with specific magnetic properties (called magnetic metal nanoparticles, mNPs, in the remaining text) has brought further advances in biomedicine. Their response to an externally applied magnetic field, in combination with easy conjugation of the metallic surfaces with various functional groups present in biomolecules, antibodies, and drugs of interest, has opened up a completely new range of biomedical applications, where magnetically induced preconcentration, identification, and separation are merged with targeted medical analytes in a single agent at the nanometre scale. This approach has allowed the development of drug delivery with reduced distribution of medical substances in untargeted tissues and improved contrasts in body scans through magnetic resonance imaging, whereas hyperthermia therapies have progressed from treatments increasing whole-body temperature to treatments with completely localised magnetically induced heat generation, as described in the following text. Initially, the focus was on the use of magnetic nanoparticles of biocompatible metallic oxides, mainly magnetite/maghemite, but upon the failed efforts to sufficiently improve their magnetic moments to fulfil the requirements of the therapies, naturally magnetic metallic counterparts, mNPs, have started to generate an appreciable amount of interest. Many of such mNP agents are already approved for clinical use, but the search for those with superior response and higher efficiencies at safer external field strengths continues, including less obvious material choices, such as Co mNPs, as promising candidates.

A comprehensive, although not by any means complete, summary of magnetic core NPs with protective coatings designed for biomedical purposes can be found in Table 1. There are many reviews on the role of iron oxide magnetic nanoparticles in biomedicine, with details behind the exhaustive efforts to adjust their properties for specific applications [35–41]. However, the topics of the current review are metal nanoparticles, the interplay between their physical and magnetic properties as they relate to the performance in biomedical applications, and how to approach and predict this dependence from a computational modelling perspective, focusing on the example of cobalt mNPs.

1.1. Biomedical Applications of mNPs

1.1.1. MRI

Magnetic resonance imaging (MRI) is a powerful, noninvasive, and sensitive tomographic visualisation technique widely used in biomedicine to obtain high-resolution scans of body cross-sections. An MRI image originates from the measurement of nuclear magnetic resonance (NRM) signals that are collected as responses of abundant water protons present in biological tissues to the applied magnetic field [42–44]. In rare cases, signals are detected from other nuclei, such as C^{13}, P^{31}, or Na^{25}. A strong static magnetic field is first applied to align the magnetic moments of proton nuclei, which are then deflected in the transversal plane upon the application of a short radiofrequency pulse. Magnetic moments spontaneously return to the original longitudinal direction of the magnetic field, and the time necessary for the complete realignment is called relaxation time. One can distinguish between the T1 relaxation time corresponding to the longitudinal recovery and the T2 relaxation time of the transversal decay. Both are sources of tissue contrasts in MRI scans, which depend on the net magnetic effect of a large number of nuclei within a specific voxel of tissue. Contrasting black and white areas of the MRI image correspond to the disproportionate T1 and T2 proton relaxation times of various biological tissues as a consequence of differences in their compositions and proton density, resulting in distanced signal intensities. However, the limited virtue of these differences can sometimes cause low sensitivity of the technique, resulting in inadequate image contrasts for certain clinical objectives.

Table 1. Classification of magnetic NPs based on the core and coating materials and their respective applications.

Magnetic Core	Reported Coating Materials	Application	Ref
Metal			
Fe	polymers	MRI, drug delivery	[45–47]
	iron oxide	MRI, hyperthermia	[48]
	Au	drug delivery, photothermal therapy	[49]
Co	organic acids	drug delivery, hyperthermia	[50]
	polymers	MRI	[51]
	Au	MRI, gene transport, hyperthermia	[52–55]
FeCo	graphite	MRI, optical imaging	[56,57]
	$CoFe_2O_4$	hyperthermia	[58]
	Au	MRI, medical labelling	[59]
FePt	Au	MRI, photothermal therapy	[60,61]
	organic acids/thiols	biosensors, MRI, CT	[62–66]
	$SiW_{11}O_{39}$	hyperthermia	[67]
	polymer + SiO_2	drug delivery	[68]
FeNi	polymers	hyperthermia	[69]
FeNiCo	propylene glycol	hyperthermia	[70]
Oxide			
Fe_3O_4	SiO_2, TiO_2	MRI, photokilling agents	[71–73]
	dextran, DMSA	MRI	[74]
	Au, Ag	MRI, immunosensor, photothermal therapy	[75–78]
Fe_2O_3	SiO_2	MRI, biolabelling	[79,80]
	polymers	MRI, biolabelling, drug delivery, optical imaging	[81,82]
$MnFe_2O_4$	polymers and organic acids	MRI	[83,84]
$CoFe_2O_4$	polymers and organic acids	MRI, drug delivery, hyperthermia	[84–86]
	Au + PNA oligomers	biosensors, genomics	[87]
$NiFe_2O_4$	polymers and organic acids	drug delivery, hyperthermia	[84,88–90]
	polysaccharides	MRI	[91]
MnO	Au	MRI	[92]
	polymers and organic acids	MRI	[81]
	SiO_2	biolabelling	[93]

Because the relaxation process involves an interaction between the protons and their immediate molecular environment, it is possible to administer MRI contrast agents that alter the magnetic characteristics within specific tissues or anatomical regions and improve the image contrast [94–96]. Those contrast agents are individual molecules or particles with unpaired electrons (paramagnetic metal–ligand complexes or magnetic particles) that produce inhomogeneities in the magnetic field causing a rapid dephasing of nearby protons and change in their relaxation rate. Contrast agents can be divided into those that shorten the longitudinal recovery time, resulting in a brighter image, i.e., positive or T1 agents, and those that shorten the transversal decay time, i.e., negative or T2 agents. The principle of MRI and the use of contrast agents is shown in Figure 1. Contrast agents are used in 40–50% of all MRI examinations.

The first paramagnetic complex approved in 1987 for use in cancer patients to detect brain tumours was gadolinium(III) diethylenetetraamine pentaacetic acid (GdDTPA) [97]. With rising concerns over the safety of Gd complexes, which have been found to remain in the body after multiple MRI scans, the World Health Organization (WHO) issued a series of restrictions on their use as contrast agents in 2009 [98,99]. This stimulated intense interest in creating responsive superparamagnetic T2 agents that show higher biocompatibility and safety. Currently, the majority of T2 contrast agents are iron oxide based superparamagnetic NPs (SPIONs) coated with dextran, silicates, or other polymers with variable T2 relaxivities [100–102]. Recent studies investigating the transformation of SPIONs into T1 contrast agents have generated some promising results, but effective contrast enhancement is still lacking, due to the unknown relaxation mechanisms, and nanoparticulate T1 contrast agents have yet to be approved for clinical use [103–106]. This flexibility makes iron oxide NPs attractive for detecting specific biological tissues, but their relatively large sizes still impede cell penetration and delivery, while lower values of their magnetic moments require increased clinical uptake to compensate for the poor contrast obtained when compared to gadolinium-based agents. Low efficacy has led to a discontinuation of a number of prominent iron oxide contrast agents in recent years [107–109], and currently, only ultrasmall particles (USPIONs) remain in clinical use. Superparamagnetic iron–platinum mNPs have been reported to have significantly better T2 relaxivities than SPIONs and USPIONs [110], while iron mNPs offer an order of magnitude greater susceptibility at room temperature [111,112]. As a result, these are currently agents of significant interest and the topic of much investigation, together with cobalt mNPs, whose very high saturation magnetisation (1422 emu/cm^3 for cobalt compared to 395 emu/cm^3 for iron oxide at room temperature) offers a larger effect on proton relaxation, promising improved MRI contrast whilst allowing smaller particle cores to be used without compromising sensitivity [51,55].

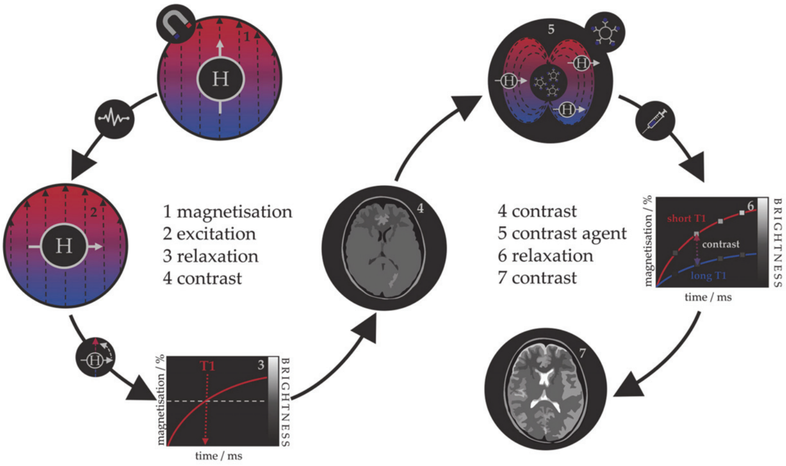

Figure 1. Schematic representation of the principle behind the MRI contrast agents.

1.1.2. Magnetic Hyperthermia

Hyperthermia, in terms of medical treatments, is defined as a moderate increase in temperature (to 40–45 °C) sufficient to cause death of tumorous cells whose vulnerability towards heat originates from the poor blood flow and insufficient oxygenation in the affected region [113–115]. Initially, hyperthermia treatments used water baths; later, conventional therapies proceeded to noncontact external devices for transfer of thermal energy either by irradiation or by electromagnetic waves (microwave, radiofrequency, ultrasound, or laser sources). However, the realisation of the full clinical potential of hyperthermia treatments was limited due to the inability of heat sources to target tumorous cells efficiently and locally. As the effectiveness reduces steeply with the distance from the source, targeted regions were not receiving enough thermal energy, while maximal temperature gradient was obtained on the body's surface. However, the biggest shortcoming was the dissipation of energy that was causing serious damage in the healthy tissue situated near the main path of the radiation beam. Altogether, conventional hyperthermia showed no discrimination between targeted tissue and surrounding environment. The growing usage of magnetic nanosystems initiated an efficient solution, where the problem of an external source could now be circumvented by the intravenous administration of magnetic NPs, followed by the use of an alternating magnetic field that results in the localised transformation of electromagnetic energy into heat by means of NP relaxation mechanisms. This targeted approach allows local heating of tumorous cells with minimal impact on the surrounding tissues. The principle of magnetic nanoparticle hyperthermia is presented in Figure 2.

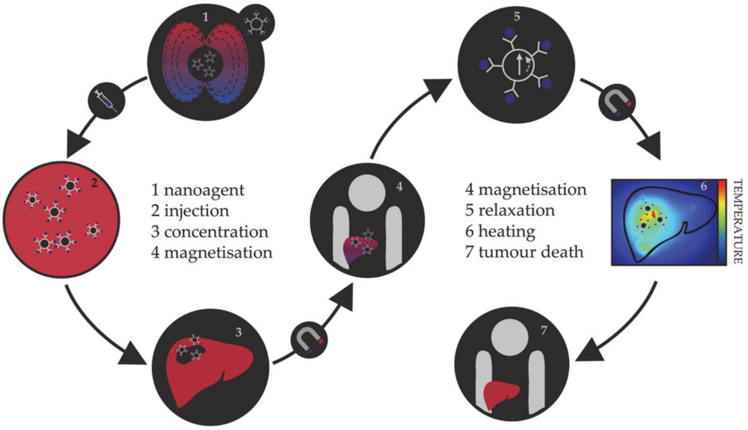

Figure 2. Schematic representation of the principle of magnetic nanoparticle hyperthermia for liver cancer.

The magnetic hyperthermia nanoagents implemented thus far are mostly magnetite and maghemite NPs [116–120]. However, despite the promising results of preclinical trials, there are many ongoing challenges in making magnetic nanoparticle hyperthermia a universal cancer treatment, including the establishment of optimal limits on the strength and frequency of the applied magnetic field, their correlation with the duration of the treatment, and determination of sufficient NP concentrations [121–125]. As the magnetic gradient decreases with the distance from the source of the applied magnetic field, restrictions on the human-safe magnetic field strengths impose challenges in obtaining the necessary gradients to control the residence time of NPs in the desired area. Additionally, estimates of the magnetic field strengths and gradients based on the hydrodynamic conditions of vascular vessels have shown that the highest effectiveness of magnetic targeting is in the regions of slower blood flow, which are usually near the surface [126–128]. Research on the internal magnets implanted in the vicinity of the targeted tissue using minimally invasive surgery is ongoing, and several studies have succeeded in simulating the interaction between an implant and a magnetic agent [129–132]. In terms of the amount of NPs that can be incorporated in a single living cell, the admissible intake is of the order of a few picograms [133–135]. This limit makes it essential that the nanoparticular agents have high magnetic moments, because a relatively small number of particles (between 10^3 and 10^4) has to be capable of increasing the intracellular temperature by several degrees, where mNPs have an important advantage over the relatively weak magnetic moments of iron oxides. There are several excellent reviews in the literature on the principles and requirements of magnetic nanoparticle hyperthermia [136–140].

Nanoparticle hyperthermia can also be combined with other therapies to form multimodality treatments and provide a superior therapy outcome [141]. One possibility is to merge it with chemotherapy, where heat can enhance the cytotoxicity of chemotherapeutic drugs or assist the drug uptake by increasing the local blood supply and tissue oxygenation [142–144]. Besides the synergy with chemotherapy, the combination of unique magnetic and optical properties in a single NP system leads to multimodal photothermal and thermal photodynamic treatments [145–149]. In nano-photodynamic therapy, mNPs act as photosensitiser carriers that under the irradiation with visible (VIS) and/or near-infrared (NIR) light generate reactive oxygen species (ROS) able to cause tumour degradation. Multiple studies on glioblastoma have shown that the combination of nanoparticulate hyperthermia and photodynamic treatments is quite effective to treat this type of cancer [150]. In nano-photothermal therapy, a nanosized photothermal agent is stimulated by both specific band light and vibrational energy/heat release to selectively target abnormal tissues. A number of magnetic nanomaterials with appropriate optical characteristics have been developed by bringing together a magnetic core and, for example, gold coatings, carbon nanotubes, or graphene, all of which show strong optical absorbance in the NIR optical transparency window of biological tissues. The major advantage of the combined electron–phonon and magnetic relaxations is the significant reduction in the laser power density required for efficient therapies [151,152]. Recently, a pilot study on the initial evaluation of nano-photothermal agents based on gold nanoshells in the treatment of prostate cancer confirmed the clinical safety of this combined therapy [153].

1.1.3. Targeted Drug Delivery

One of the most rapidly developing areas of modern pharmacology is targeted drug delivery, with the aim to reduce the drug intake per dose and prevent exposure of healthy tissue to chemically active analytes. In 1906, Paul Ehrlich introduced the term *magic bullet*, describing the drug capable of locating the causative agent of the disease and providing the adequate treatment without further distribution to unaffected areas [154]. Several decades later, the first drug delivery systems were developed, containing active medical substances attached to the surface of a carrier or encapsulated within the carrier which possesses specific cell affinity contained within molecular vectors and would disintegrate and release the capsulated drug upon contact with diseased cells [155–157]. Organic nanosystems (liposomes, micelles, polymer NPs) [158–160] together with carbon nanotubes and fullerene NPs [161–163] are the most often employed drug carriers, while different hormones, enzymes, peptides, antibodies, and viruses often serve as molecular vectors [164–167]. Thus far, the available carriers and capsules for targeted drug delivery have each shown several disadvantages, from limited chemical and mechanical stability of organic NPs, over the questionable toxicity of carbon-based systems, to the general susceptibility to microbiological attack, lack of control over the carrier movement and the rate of drug release, and, finally, high cost [168–171]. Hence, the search for an optimal carrier has shifted direction towards utilising the magnetically induced movement of magnetic nanosystems. Their main advantages are simple visualisation (based on the principles of MRI), easy guidance and retention in the desired area by externally applied magnetic field, and controllable drug detachment triggered by heat released in the variable magnetic field (based on the principles of magnetic hyperthermia). In addition, it is possible to engineer magnetic NPs to either avoid or interact with the immune system in specific ways [172,173].

In common with the previous two applications, most attention has been devoted to iron oxide NPs [174–176]. However, limitations of magnetic drug delivery have promoted the search for materials of higher magnetic moments [177] due to the decrease in the magnetic gradients connected to the distance from the source as well as to the fluid hydrodynamics correlating with the depth of the affected tissue—i.e., the same drawbacks as in hyperthermia treatments. So far, a combination of relatively strong magnetic fields with SPION drug carriers has been shown to reach an effective depth of 10–15 cm in the body [178]. Other restrictions relate to the acceptable size of the NPs; first, they have to be below the critical size for optimal magnetic properties, which is a prerequisite to avoid magnetic memory and agglomeration once the magnetic field is removed, and second, they have to be small enough such that after the attachment of drug molecules on their surface they can still effectively pass through narrow barriers [179,180]. The small size implies a reduced magnetic response and hence requires materials of high magnetisation, such as mNPs, rather than metal oxides. Recently, 5–25 nm diameter cobalt–gold mNPs with a core–shell structure and tailorable morphology were synthesised for the purpose of obtaining high-magnetisation drug carriers [181]. The major advantage of the implementation of cobalt within the mNP core is that it has a magnetic moment nearly twice that of iron oxides.

2. Features of mNPs

2.1. Electronic and Magnetic Properties of mNPs

The proper functionality of mNPs for specific applications depends on their magnetic properties, as well as their biophysical behaviour under physiological conditions. While the latter is most efficiently captured by *in vivo* experiments, insight into the dependence of magnetic properties of nanometre-scale particles on their size, composition, and morphology can be reliably obtained by computer modelling techniques.

Magnetic properties of mNPs can be classified as intrinsic or extrinsic. The former are more important since they are derived from the interactions on an atomic length scale and highly depend on chemical composition and grain size, shape, and crystal microstructure. Additionally, they are much more affected by surface effects and therefore give rise to specific manifestations, such as superparamagnetism, that can only be found at the nanoscale level. These properties include magnetic saturation, anisotropy, and the Curie temperature.

Intrinsically, classification of mNPs based on the ordering of their magnetic moments corresponds to the classes of bulk metallic materials, and hence there are paramagnetic and ferromagnetic mNPs. Those that are paramagnetic exhibit no collective magnetic interactions and they are not magnetically ordered; however, in the presence of a magnetic field, there is a partial alignment of the atomic magnetic moments in the direction of the field, resulting in a net positive magnetisation. mNPs belonging to the ferromagnetic class exhibit long-range magnetic order below a certain critical temperature, resulting in large net magnetisation even in the absence of the magnetic field. If the diameter of the mNP is larger than the critical value, D_C, coupling interactions cause mutual spin alignment of adjacent atoms over large volume regions called magnetic domains. Domains are separated by domain walls, in which the direction of magnetisation of dipoles rotates smoothly from the direction in one domain towards the direction in the next. Once the diameter falls under the critical value (typically between 3 and 50 nm), mNPs can no longer accommodate a wall and each of them becomes a single domain. Additionally, since each domain is also a separate particle, there can be no interactions or ordering of domains within a sample, and particles do not retain any net magnetisation once the external field has been removed. This phenomenon is known as superparamagnetism. Superparamagnetic mNPs are, as the name suggests, much alike paramagnetic mNPs apart from the fact that this property arises from ferromagnetism. Their normal ferromagnetic movements combined with very short relaxation times enable the spins to randomly flip direction under the influence of temperature or to rapidly follow directional changes in the applied field. The temperature above which the thermal energy will be sufficient to suppress ferromagnetic behaviour is called the blocking temperature, T_B. Below T_B, the magnetisation is relatively stable and shows ferromagnetic behaviour, while for $T > T_B$, the spins are as free as in a paramagnetic system and particles behave superparamagnetically. Blocking temperatures for most mNPs are below 100 K [182–185], and their behaviour is therefore paramagnetic, as for most temperatures they are only magnetised in the presence of the external field, but their magnetisation values are in the range of ferromagnetic substances. Moreover, the strength of the external field needed to reach the saturation point of superparamagnetic mNPs is comparable to that of ferromagnetic mNPs.

The highest magnetisation that mNPs can obtain when exposed to a sufficiently large magnetic field is called the saturation magnetisation, M_S. It is the maximum value of the material's permeability curve, where permeability, μ, is the measure of magnetisation that a material obtains in response to an applied magnetic field (total magnetisation of material per volume). It is often correlated with the ratio of magnetisation to the intensity of an applied magnetic field H, which is known as the magnetic susceptibility, χ, and describes whether a material is attracted into or repelled out of a magnetic field. The magnitude of saturation is a function of temperature; once it is reached, no further increase in magnetisation can occur even by increasing the strength of the applied field. The unique temperature limit at which ferromagnetic mNPs can maintain permanent magnetisation is the Curie temperature, T_C. Notably, when the mNP size is reduced from multidomain to a single domain, the magnitude of M_S decreases due to the increment in the spin disorder effect at the surface; thus, the M_S value is also directly proportional to the size of mNPs.

In almost all cases, magnetic materials contain some type of anisotropy that affects their magnetic behaviour. The most common types of anisotropy are (a) magneto-crystalline anisotropy (MCA), (b) surface anisotropy, (c) shape anisotropy, (d) exchange anisotropy, and (e) induced anisotropy (by stress, for example), where MCA and shape anisotropy are the most important in mNPs. Magneto-crystalline anisotropy is the tendency of the magnetisation to align along a specific spatial direction rather than randomly fluctuate over time. It arises from spin–orbit interactions and energetically favours alignment of the magnetic moments along the so-called easy axis. Factors affecting the MCA are the type of material, temperature, and impurities, whereas it does not depend on the shape and size of the mNP. Morphology effects are included in the shape anisotropy. Stress anisotropy implies that magnetisation might change with stress, for example when the surfaces are modified through ligand adsorption, which means that the surface structure can significantly influence the total anisotropy. Hence, due to the large ratio of surface to bulk atoms, the surface anisotropy of mNPs could be very significant, and the coating of mNPs can therefore have a strong influence on their magnetic anisotropies. Different types of anisotropy are often expressed simply as magnetic anisotropy energy (MAE), which determines the stability of the magnetisation by describing the dependence of the internal energy on the direction of spontaneous magnetisation. It has a strong effect on the values of extrinsic properties.

Extrinsic properties of mNPs are not as essential as the intrinsic. They are derived from long-range interactions and include magnetic coercivity and remnant magnetisation (remanence), which are dependent on microstructural factors, such as the orientation of intermetallic phases.

Magnetic coercivity, H_C, can be described as a resistance of a magnetic material to changes in magnetisation, and it is equivalent to the magnitude of the external magnetic field needed to demagnetise material that has previously been magnetised to its saturation point. Ferromagnetic mNPs that have reached saturation cannot return to zero magnetisation in the same direction once the applied field has been removed, and the magnetic field is therefore applied in the opposite direction. This process leads to the creation of a loop known as hysteresis. Hysteresis loops indicate the correlation between the magnetic field and the induced flux density (B/H curves). Superparamagnetic mNPs each have only one domain, and no hysteresis loop is obtained when the applied field is reversed. Remnant magnetisation, M_r, is magnetisation left after the magnetic field has been removed. Once the saturation has occurred and a magnetic field is no longer applied, ferromagnetic mNPs will produce an auxiliary magnetic field and resist sudden change to remain magnetised. In contrast, superparamagnetic mNPs will behave as paramagnets with instant need for demagnetisation and negligible M_r. This property allows for ferromagnetic mNPs to gain magnetic memory.

2.2. Biomedically Desired Properties of mNPs

Specifics of the application of interest govern the desired properties of materials used, as was described briefly for the diagnostics and therapy methods in the previous section. In biomedicine, the safety of the treatment towards a patient is the highest priority, and hence superparamagnetic mNPs are preferred because they are magnetised only under the influence of an external magnetic field and quickly demagnetise otherwise, which makes them safer for the human body. This implies that no coercive forces or remanence exist, preventing magnetic interactions between particles and their aggregation, which could lead to adverse problems derived from the formation of clots in the blood circulation system. Saturation magnetisation is also a substantial factor for two reasons: (1) mNPs with high M_S show a more prominent response to the external magnetic field; (2) high M_S makes the movements of mNPs more controllable and guarantees efficient response to the magnetic field, implying reduced time of residence and lower required dosages of mNPs. M_S is dependent on the mNP magnetic moment, size, and distribution, and it is thus important to take them into consideration. An increase in size yields higher M_S, but above the critical diameter, mNPs become ferromagnetic and show undesired behaviour due to the formation of agglomerates and magnetic memory. Moreover, very small diameter sizes are highly desirable to reach regions of limited access; in order to cross the blood–brain barrier, for example, a magnetic core size of $d \approx 12$ nm or less is required. Thus, a suitable balance should be found between the size distribution and magnetic properties. Since mNP-based therapies work by directing the mNPs to a target site using an external magnetic field, magnetic anisotropy is also a very important factor.

Alongside these general requirements that are applicable to all biomedical applications, to enhance the performance of mNPs within MRI diagnostics and hyperthermia therapy it is essential to gain insight into the inherent mechanisms behind their magnetic processes and assess the properties of mNPs and external magnetic field parameters for optimal treatment results.

2.2.1. Relevant Features in MRI

The mechanism of relaxation enhancement directed by MRI contrast agents arises from the dynamic interactions of water molecules with the magnetic centres. Established classical models have significantly contributed to the correlation between the contrast agents' properties and performance, paving the way to the smarter design of new materials. These models are based on the interpretation of proton–electron interactions between water protons and contrast agents, which is the most important mechanism behind the T1 and T2 contrasts within the contrast-agent-assisted MRI [186–188].

For contrast agents consisting of magnetic centre–ligand complexes, interacting water protons are classified into inner-sphere, second-sphere, and outer-sphere protons, each having distinct interaction mechanisms. The inner-sphere mechanism involves direct magnetic centre–water coordination, whereas the second-sphere mechanism describes interactions between the magnetic centre and water protons situated within the second coordination sphere through hydrogen bonds. The outer sphere includes the influence of the magnetic centre on the translational diffusion and rotational motion of the remaining bulk water protons [97,189]. However, for contrast agents consisting of magnetic particles, the direct coordination of water is atypical, and the largest share of the nuclear magnetic relaxation of water protons in solutions (or suspensions) of magnetic particles arises from pure magnetic interactions at the molecular level. In essence, this amounts to the reformulation of the outer-sphere mechanisms from a single metal atom complex centre to the solution of mNPs.

Superparamagnetic mNPs with large magnetic susceptibility produce local magnetic fields under the influence of an external magnetic field. As a result, the local magnetic field causes a perturbation in the motion and relaxation of nearby water protons. Hence, the relaxation is induced by the fluctuating dipolar interaction between the nuclear magnetic moment of the water proton and the global magnetic moment of the mNP, just as in the case of classical outer-sphere theory. This reformed outer-sphere theory now describes the change in the relaxation of solvent protons as the water molecules diffuse into the neighbourhood of a solute particle and start interacting with its magnetic dipolar moment.

This type of local perturbation shortens the T2 relaxation time, also known as spin–spin relaxation, of water protons during water diffusion. The mNP contrast agent catalytically relaxes water protons at the particle–solvent interface emanating in T2-weighted MRI images. The extent to which the mNP contrast agent affects the relaxation rate of tissue water can be quantitatively characterised by its transversal relaxivity, r_{CA}, and the final relaxation rate of the tissue, r_2, is given by:

$$r_2 = \frac{1}{T_2} = \frac{1}{T_2^{\mathrm{o}}} + r_{\mathrm{CA}}[\mathrm{CA}]. \tag{1}$$

mNP relaxivity is thus defined as a proportionality constant between the induced increase in the relaxation rate of the tissue and the concentration of the contrast agent, [CA]. By definition, low doses of high-relaxivity contrast agents provide an equivalent contrast magnification as higher concentrations of contrast agents with inferior r_{CA}. Every tissue has an inherent relaxation rate, $1/T_2^{\mathrm{o}}$, and in order to generate an observable contrast, the relaxivity of the contrast agent should be at least at 10% of the inherent rate.

Outer-sphere theory for T2 relaxivity has developed an expression for the dependence of relaxivity performance of superparamagnetic mNPs on their intrinsic properties—saturation magnetisation and the effective radius:

$$r_2 = \frac{1}{T_2} = \kappa_\gamma V_{\mathrm{eff}} M_s^2 \frac{r^2}{D(1 + l/r)}, \tag{2}$$

where κ_γ is the constant derived from the gyromagnetic ratio of solvent protons, V_{eff} is the effective volume fraction ($V/$ [CA]), M_s is the saturation magnetisation, r is the radius of the magnetic core, l is the thickness of impermeable mNP coating, and D is the diffusion coefficient of water molecules. Viewed simplistically, an increased M_s value is reflected in the increased response of mNP contrast agents to be magnetised by the external field, resulting in the higher r_2 relaxivity. Similarly, improved relaxivities can be achieved with a larger magnetic core radius. As the proton relaxation occurs mainly at the interface of the mNP and surrounding aqueous environment, nanoparticle coatings also influence the rate of T2 relaxation through the coating thickness.

T2 relaxation processes occur through three mechanisms. The first mechanism, known as Curie spin relaxation, arises from the dipolar interactions between water protons and a large magnetic moment of unpaired mNP electrons. It depends on the strength of the applied magnetic field and is a function of the size and water diffusion time, $r^2/4D$. This mechanism is prominent for small-sized mNP contrast agents under strong fields, while it decreases rapidly for larger mNPs where T2 relaxation is mostly dominated by the remaining two mechanisms: dipole–dipole coupling between metal ions and hydrogen nuclei and scalar or contact relaxation processes. Hence, a primary factor affecting r_2 is the mNP-generated inhomogeneity, which depends largely on the magnetisation of the contrast agent. In general, more efficient inhomogeneity originates from materials with higher saturation magnetisation; such materials can also influence a greater volume of surrounding water. However, the effective magnetisation value of mNPs is often several times lower than that of the bulk counterpart, caused primarily by an increased magnetic anisotropy. Due to the presence of magnetically 'dead' or tilted layers of atoms on the mNP surface, the surface atomic spins are largely canted, thereby enhancing the MAE and reducing overall magnetisation. This effect is especially pronounced in small particles, owing to their high surface-to-volume ratio. Additionally, MAE is also affected by the mNP morphology and surface interactions. For particles of the same volume, a reduced shape and surface anisotropy lead to the spin state similarity between the surface and core, thereby increasing the magnetisation. Contact interfaces between two different magnetic phases, for example in the form of core–shell NPs, often provide an additional source of anisotropy (exchange anisotropy), resulting in a slight reduction but also in stabilisation of magnetisation and improved coercivity. Moreover, changes in the magnetic moments of surface atoms can be enforced through surface functionalisation.

Diffusion dynamics of water molecules in the magnetic field gradients is another important factor for effective r_2 rates. It is characterised by the number of water molecules that have diffused into close proximity of the interface with the contrast agent and their residency time within that region. mNPs with large magnetic moments have a stronger tendency to form dipole interactions with water protons, to form a larger area of influence, and to provide a greater possibility of relaxing the diffused water molecules. Certain coatings can also be beneficial in this matter, while others may hinder water diffusion or prolong water residency within ligand pockets, reducing the image contrast. Coatings forming a hydrophilic mNP surface favour diffusion and retention of water molecules in the mNP outer-sphere. Finally, fine-tuning of the thickness, charge (ligands rich in π-electrons create small magnetic fields increasing inhomogeneity), and porosity of the coating allows for optimised water accessibility and residency.

Hence, the dynamic interactions behind the relaxation mechanisms depend predominantly on the magnetic properties of mNP contrast agents, which, in turn, are attributed to a large extent to the mNP structural features. Relaxivity of superparamagnetic mNPs can be enhanced not only via their magnetic properties, but also through the coating optimisation. The last parameter directly included in the equation, without specifically considering its effect on the magnetic properties, is the diameter of the magnetic core. From the relationship, the r_2 value can be increased by increasing the core size. However, biomedical applications are limited by the superparamagnetic size limit. Within this critical diameter, theoretical studies have identified three mNP size regimes depending on the r_2 rate trends: the motional average regime (MAR), the static dephasing regime (SDR), and the echo-limiting regime (ELR) [190]. With the growing mNP size in the MAR regime, relaxivity increases, reaching a plateau in the SDR regime. With any further size increment, mNPs fall in the ELR regime where r_2 steeply decreases. Accordingly, the highest r_2 is achieved for mNPs within the SDR, but nanoparticulate contrast agents employed thus far have been within the MAR regime to limit the NP aggregation through magnetic interactions [191,192].

Finally, in nanoparticle-based imaging, higher mNP concentrations lead to an improved signal-to-noise contrast, at a cost of a toxicity trade-off. Therefore, even though it does not directly affect the relaxivity constant, mNP concentration is one of the most important parameters in the development of nanoparticulate contrast agents, with the objective of obtaining sufficient contrast at the safest (lowest) mNP concentrations. Studies on SPIONs have consistently shown significant enhancement in the MRI signal when the concentration of Fe progresses from 9 to 100 μg/mL [193–195], and the minimum concentration found to produce marked hypointense signals was evaluated at or above 22.4 μg/mL [196]. Moreover, upon 24 h incubation, Mn-doped SPIONs displayed no appreciable cytotoxicity even at the highest metal ion concentrations, indicating good biocompatibility [193]. Furthermore, the sensitivity of the imaging technique must also be taken into account. So far, the most sensitive detection experiments on mNP imaging have demonstrated sensitivity to particle concentrations in the picomolar and tens of picomolars range. For example, the tissue T2 contrast is clearly distinguished at gold-coated Co mNP concentrations as low as 50 pM [55]. This detection threshold is 7 orders of magnitude better than those for monocrystalline iron oxide particles, whereas the T2 relaxivity per-particle concentration is improved up to 5 orders of magnitude compared to both magnetite and Fe/Au NPs [197,198], which translates into lower mNP concentrations for efficient MRI contrast.

2.2.2. Relevant Features in Hyperthermia

The heating efficiency of the magnetic nanoparticle hyperthermia process depends on the power dissipated by the mNP following the application of an alternating magnetic field, and it is often quantified through the specific absorption rate (SAR). SAR is the rate at which the power is absorbed by a volume of dielectric material, such as biological tissue, exposed to electromagnetic radiation (or another source of energy). It is often mentioned interchangeably with the specific heating power (SHP), which is defined as the thermal power per unit mass dissipated by the magnetic material and accurately describes a material's heating efficiency. The interconversion of magnetic field energy into heat by mNPs can arise through three mechanisms: eddy currents, hysteresis, and relaxation processes. Eddy currents are loops of localised electric current induced by the varying magnetic field. Their existence depends on how resistant the material is towards current heating, and they are usually present in bulk crystals. The prevailing heating mechanism in multidomain mNPs is hysteresis loss, while single-domain superparamagnetic mNPs have high electrical resistivity, and such power loss is thus negligible compared to that originating from relaxation processes. Relaxation mechanisms have two modes: following the removal of the external magnetic field, magnetic moments relax either through the motion of the internal spin (Néel relaxation) or by the rotation of the mNP around its own axis (Brownian relaxation). Either relaxation of the magnetic moment back to the initial position releases thermal energy and induces local heating due to friction. If the mNP undergoes Néel relaxation, heat is dissipated by the rearrangement of atomic dipole moments where internal friction causes phase lagging between the applied field and magnetic moments. If the mNP relaxes through a Brownian relaxation mechanism, the power loss arises from the shear stress in the surrounding medium. Additional power loss can occur due to the physical relaxation of the liquid.

Quantification of the specific heating power of mNPs is derived as:

$$\mathrm{SHP} = \frac{1}{2}\omega\mu_0\chi_0 H^2 \frac{\omega\tau}{1+\omega^2\tau^2} \tag{3}$$

where ω is the angular frequency of the external magnetic field and equals $\omega = 2\pi f$, μ_0 is the magnetic permeability constant of free space, χ_0 is the magnetic susceptibility, and H is the magnitude of the external magnetic field. The fractional term leads to the maximal power at $\omega\tau = 1$; in this case, the matching ω is called a critical frequency. An estimated goal for the material development in this field is an SHP of the order of 1000 Wg^{-1}, based on the amount of mNPs that can be incorporated by a single living cell [16]. The critical factor is hence the relaxation time of mNPs, τ, resulting from prevailing heating mechanisms.

Relaxation time can be defined as the time needed for magnetic moments of mNPs to vanish once the external magnetic field has been shut off. For Néel relaxation, the time constant of the external magnetic field is short enough so that magnetic moment alternates from parallel to antiparallel orientation and back without a change in the physical orientation of the particle. As excitation occurs against the anisotropy energy barrier, the process strongly depends on mNP volume and anisotropic properties, and it is not influenced by the conditions of the surrounding environment. The relaxation time for Néel relaxation, τ_N, can be described by:

$$\tau_N = \frac{\tau_0}{2}\sqrt{\pi\frac{kT}{KV}}e^{KV/kT} \tag{4}$$

where τ_0 is the characteristic relaxation time and equals $\tau_0 = 1/f_0$ ($f_0 = 10^9 - 10^{13}\ \mathrm{s}^{-1}$), k is the Boltzmann constant, T is the temperature, K is the anisotropy constant (includes all sources of anisotropy), and V is the volume of the mNP. KV is somehow equivalent to an activation energy that has to be exceeded by the thermal energy, kT, to overcome the inherent magnetic anisotropy energy barrier. In contrast, Brownian relaxation prevails when magnetic anisotropy is sufficient to overcome inertial resistance, in which case the external magnetic field causes rotation of a whole particle with the magnetic moment remaining fixed relative to the crystal axis. The Brownian relaxation time is highly dependent on the hydrodynamic properties of both mNP and surrounding medium, such as viscosity of the fluid and hydrodynamic volume of mNP, which includes any surfactant layer added for colloidal stability. The equation that describes Brownian relaxation time, τ_B, is:

$$\tau_B = \frac{3\eta V_H}{kt} \tag{5}$$

where η is the viscosity of the medium and V_H is the hydrodynamic volume of mNPs. When these two processes are simultaneously involved, the effective relaxation time, which describes the energy transfer rate, takes both into consideration, and the final expression for the relaxation time is:

$$\frac{1}{\tau} = \frac{1}{\tau_N} + \frac{1}{\tau_B}. \tag{6}$$

Overall, the shorter of the two dominates the effective relaxation time—Néel for small particles in viscous solutions and Brownian for particles with large hydrodynamic volume in an environment of lower viscosity. The exact division between mechanisms depends on the anisotropy constant of each material. In magnetic nanoparticle hyperthermia, mNPs are embedded in a tumorous tissue and internalised by cancer cells, either by adhesion to the cell walls or in the form of the restraint of movement provided by cell plasma. Because of this immobilisation, Brownian mechanism is damped to the maximum and Néel relaxation occurs almost exclusively [199].

mNPs can be remagnetised only after their relaxation is completed; therefore, the frequency of the external field has to match the relaxation time in order to obtain efficient heating rates. SHP is maximised under the condition $\omega\tau = 1$, and since typical Brownian relaxation times in systems where this mechanism dominates over Néel relaxation are around 10^{-5} s, effective frequencies would need to be 10^5 rad s^{-1} (15 kHz), which is much lower than any frequency reported in hyperthermia studies (100–300 kHz range) and therefore favours relaxation times of 10^{-6} s or below [139,200]. This confirms Néel relaxation as the predominant heating mechanism in magnetic nanoparticle hyperthermia and accentuates the need for magnetic anisotropy energies that significantly exceed the thermal energy ($KV \gg kT$); if the anisotropy constant is not satisfactory, no noteworthy heating is expected. Therefore, SHP depends on the size, magnetisation, and anisotropy of mNPs, as well as on the characteristics of the applied external magnetic field.

From the equation for τ_N, MAE is an important factor in enhancing the Néel relaxation time. However, within the limitation of $\omega\tau = 1$ to maximise SHP, an enhancement of the relaxation time may not always yield higher SHP values, and the frequency of the external magnetic field must be chosen accordingly [139]. Only through that correlation can efforts to increase the MAE of mNPs yield a higher heating efficiency and, ultimately, by satisfying the $\omega\tau = 1$ condition, allow for the use of lower frequencies of the applied magnetic field [201].

Magnetic nanoparticle hyperthermia involves the excitation of mNPs suspended in a fluid medium using the external magnetic field, meaning that parameters of the magnetic field itself should also be optimised to obtain the desired results. Changes in frequencies and amplitudes directly and proportionally influence the heating power of mNPs, where SHP increases rapidly with the increase in the strength of the magnetic field. Enough heating power must be generated for the destruction of cancerous tissue, while at the same time the frequency and strength of the applied magnetic field have to be safe for the human body. These requirements force strict limitations on the frequencies to range from 0.05 to 1.2 MHz and the magnetic field strengths to range from 0 to 15 kA m^{-1}. Higher values would lead to serious problems, such as aggregation of mNPs causing embolisms, while lower frequencies would stimulate skeletal, cardiac, and peripheral muscles and trigger arrhythmias. Amplitudes are usually in the range of 5–30 kA m^{-1} and external magnetic fields with $H_0 \times f$ less than 4.85×10^8 A m^{-1} s^{-1} have been approved for successful use in humans [202].

Theoretically, SHP cannot be controlled by the mNP concentration because they show no obvious interdependence; however, higher mNP concentrations provide more efficient hyperthermia performance as less time is required to reach optimal temperatures. The condition of sufficient heat generation by mNPs to sustain tissue temperature of at least 42 °C for ~30 min was achieved in different studies by using SPION concentrations in the 0.1 to 400 mg/mL range, significantly higher than when used as T2 contrast agents [116,203–206]. Nonetheless, according to several recent reports, it was surprisingly observed that SHP and SAR values can be affected by mNP concentration, contrary to the invariance for 6–300 mg/mL measured for mNPs dispersed in water [207]. The physical principle of SHP oscillations was explained by the interparticle magnetic dipole and mutual potential energy interactions, dividing the dependence into four concentration regions. In the region of the lowest concentrations (<0.1 mg(Fe)/mL), the nanofluids showed the highest SHP; in region 0.1–1.0 mg(Fe)/mL, a remarkable drop in SHP was observed; at 1.0–10 mg(Fe)/mL, the SHP was increased again; and at the highest concentrations (10 mg(Fe)/mL or more), the SHP was re-decreased [135,208].

Different combinations of superparamagnetic materials and biocompatible ligands have been investigated, but achieved efficiencies are far from ideal and further efforts are directed to find the best nanocomposites. The most important advance in the last 10 years was the commencement of the first-ever clinical studies of therapeutic hyperthermia induced by magnetic NP heating [121]. The study successfully demonstrated that magnetite NPs can be safely applied in the treatment of brain tumours and that hyperthermic temperatures are achieved. Magnetite and maghemite NPs exhibit (up to this point) medium heating efficiency with little or no control of temperature changes when compared to other magnetic materials, but their biocompatibility, nontoxicity, and ability to escape the reticuloendothelial system makes them preferred candidate NPs for magnetic hyperthermia. However, the relatively low heating rates of conventional SPION hyperthermia agents [137] (less than 100 W g^{-1} for 400 kHz frequency and 10 kA m^{-1} magnetic field strength) unfortunately often require a high mNP concentration, which would not only result in potential toxicity but also complicate the monitoring of the progress of tumor response using imaging tools, thus promoting the implementation of mNPs with higher specific magnetisation. Many efforts have been made in order to improve the properties of magnetite NPs; a valuable strategy was to increase their MAE by the total or partial substitution of Fe^{2+} ions by Co^{2+} ions. Cobalt ferrites have shown comparatively high thermal and oxidative stability with higher suitable MAE and consistently large heating effects with SHP values reaching 720 W g^{-1}, which is significantly higher than the rates reported for the iron oxide NPs (22–200 W g^{-1} [209–211]). The current focus of research is on cobalt mNPs to further improve the heating efficiency in hyperthermia therapy.

2.2.3. Relevant Features in Drug Delivery

Magnetic targeting of drug delivery carriers is based on the attraction of mNPs induced by an external field. For the mNP drug carrier to be efficiently trapped in the magnetic field at the targeted site, the gradient of the magnetic field has to exert a sufficient translational force on the particle–drug complex. This magnetic force, F_{mag}, can be expressed as:

$$F_{mag} = (\chi_2 - \chi_1) V \frac{1}{\mu_0} B(\nabla B) \tag{7}$$

where $\chi_{1,2}$ are the magnetic susceptibilities of the medium and the mNP, V is the volume of mNPs, μ_0 is the magnetic constant, B is the strength of the magnetic field, and ∇B is the field gradient. The susceptibility of the biological medium is usually very small compared to that of mNPs and can be disregarded. From the expression, the effective capture of the mNPs depends on the magnetic properties and volume of the particles, as well as on the parameters of the applied magnetic field. As the magnetisation of the mNP decreases, the ability of the magnetic field to capture and direct them also decreases. Correspondingly, insufficient field strengths and gradients have limited penetration depth and generate weak translational force. Estimations from experimental studies and extended theoretical investigation of the hydrodynamic conditions of mNP drug carrier targeting have indicated that a minimal field strength of 200–700 mT is required at the target site with gradients along the *z*-axis of approximately 8–100 T/m depending on the flow rate [126,127].

3. Computational Modelling of mNPs

For the optimal performance of mNPs in biomedical applications, it is important that they are biocompatible and nontoxic and have colloidal stability, opportune surface modification, an appropriate particle size, and, above all, adequate magnetic properties. The dependence of magnetic properties on the structural parameters of mNPs, namely their size and shape, is well known, with paramount examples in the literature [212–218]. However, the determination of this correlation is by no means easy or exempt from complications. Even with advances in the control over the synthesis and characterisation, an ever-present distribution of mNP sizes ultimately prevents the assignment of specific magnetic features to a particular size or morphology. Furthermore, capping agents increase the complexity of the system, adding even more uncertainty to the assignment of the origin of specific magnetic behaviour. These impediments in the determination of a specific connection between the mNP morphology, coating, and magnetisation are a substantial limitation in the development of property-tuning strategies, which are an ultimate tool in the engineering of mNPs for specific applications. It is in this sense that computational modelling becomes a powerful complementary technique to experiment, by unravelling the connection between the properties of mNPs and their structural factors.

The modelling of isolated monometallic mNPs is only limited by the availability of sufficient computational resources, and quantum mechanical calculations have become the standard technique to obtain properties of clusters and smaller mNPs of up to a few hundred atoms [219–227]. The acquisition of resources for quantum simulations can be problematic for larger mNPs with more realistic diameters that are closer to application-relevant sizes. For simulations of such mNPs with hundreds or thousands of atoms, approximate theoretical models have been designed, based on classical interatomic potentials with parameters that were fitted either to the experimentally captured properties or to the descriptors obtained through quantum density functional theory (DFT) calculations [228–233]. It is the quality of these parameters, as assessed by their ability to estimate closely the values of targeted data, that ultimately determines the accuracy of the results obtained from molecular simulations. Despite the success of classical molecular dynamics (MD) in describing the behaviour of large mNPs, the need to predefine fixed interaction potentials in the form of a force field remains a significant challenge for metallic species and their interaction with different capping agents [234–237]. The lack of the description of bond breaking/forming at the MD level is also hampering any investigation of the mNP reactivity. Additionally, even after the sufficient potentials for a specific system of interest have been elaborated, changing a single species provokes enormous efforts to suitably reparameterise the potential energy function. As a result, systematic studies are a tour de force if consistent potentials are not already available. However, the advent of highly parallelised supercomputers has gone side-by-side with the progress in *ab initio* DFT methods, expanding the initial studies of small gas-phase metal clusters to investigations of large mNPs and their interaction with protective coatings [238–243].

This review focuses on the computational modelling of cobalt mNPs as tackled mostly by means of DFT calculations, which has aided insight into the link between their structural and magnetic properties. It is our aim to show that these studies can provide important information to allow reliable predictions of mNP performance within biomedical applications. They provide a useful gateway before attempting a rational, engineered tuning of the magnetisation of Co mNPs, and they may result in a sound modelling approach for magnetic mNPs of varying compositions as they rely only on *ab initio* inputs of physical constants. Coating and alloying effects are also contemplated, as changes in the magnetic behaviour can be induced by an active interplay between the surfactants and mNPs or between different metallic phases.

A physical description and expressions of observed NP phenomena (magnetic relaxation, heat dissipation, etc.) helped to identify factors affecting material capabilities and the treatment outcomes. Incorporation of *ab initio* models in the research efforts to optimise these factors within magnetic nanosystems could hence facilitate tuning strategies of application-specific properties to acquire the maximum treatment efficacy, and DFT results are often implemented in extended Monte Carlo simulations or analytical and numerical models to quantify magnetic field response, proton relaxation, or heat transfer [244–247]. However, it is important to note that the optimum property settings to generate maximum relaxation or heating through analytically developed expressions cannot ensure clinical suitability, as the optimisation process is often based on a number of assumptions that may deviate in real-life applications [248]. Even *in vivo* and *in vitro* studies sometimes give conflicting results [249–251], and DFT predictions and accompanying optimisation models must hence be verified by clinical data.

3.1. Monometallic mNPs

3.1.1. Cluster Model

The simulation and description of nanosized metallic systems essentially begin by modelling clusters with a small number of atoms. Quite often, exhaustive efforts to define the cluster structure belonging to the global energy minimum of a certain atomic size (note that the number of possible configurations grows exponentially with the number of atoms) can be simplified by implementing a molecular dynamics simulation. Rives et al. [252] and Rodríguez-López et al. [253] have captured corresponding growth structures for small Co clusters using different potential parameters. Both found an icosahedral growth pattern for the global minimum energy structure with hcp and fcc structures dominating in particular sizes, whereas for the second isomer, distorted icosahedral structures were generally obtained. However, MD-based methods lack the electron-level description necessary for the determination of magnetic behaviour and bond forming and breaking, and hence their use beyond the identification of suitably stable structures is rather limited. Hence, knowledge of electronic structures obtainable through quantum mechanical methods, such as those based on the DFT, is required.

DFT results for a number of chosen morphologies will in the majority of cases show good agreement with the MD trends, and the magnetic properties or reactivity behaviour of those structures can be investigated further on the quantum level. The MD-DFT agreement in the stability trends of a convenient number of shapes (convenient in respect of DFT computational cost and exploration of the global minimum well) for each cluster size in the case of Co clusters can be seen in multiple studies, with a few examples shown in Figure 3 [239,253,254]. The second energy difference in the total energy of successive cluster sizes also captures the ability of DFT calculations to reproduce the stable morphologies across the range of cluster sizes (Figure 4).

Small clusters efficiently capture the large surface-to-volume ratio effects on the magnetic and electronic properties, but these observables generally show strong oscillations with the number of atoms per cluster. Such small clusters are known as systems where every atom counts, and an estimation of the properties of a particular cluster size from the characteristics of the neighbouring sized clusters is often misleading. Fortunately, electronic structure features for the couple-atom systems are easily obtainable within the DFT approaches [255–261].

Because of the property oscillations, which are also heavily dependent on the type of metal atoms that constitute the cluster, a universal description of the progression of magnetic moment, or any other property, does not exist. The closest researchers have come to a unifying picture of metal clusters is the closed-shell model, which is manifested through the filling of electronic shells resulting in clusters of extraordinary stability [262–264]. The numbers of electrons corresponding to closed electron shells in metal clusters are 8, 20, 40, 58, etc. This model can often be extended to clusters with geometrically closed shells that often adopt ‘perfect’ structural shapes, such as 13-atom icosahedron. However, the closed-shell model cannot account for a large number of cluster sizes and their structural isomers that are between the clusters with a relevant number of atoms sufficient to form closed electronic or geometric shells. This rich variety of conformational isomers, which often exists within a narrow energy range, and the unique set of properties for each added atom translate into a rather complex issue in the electronic and magnetic structures for small metal clusters [265].

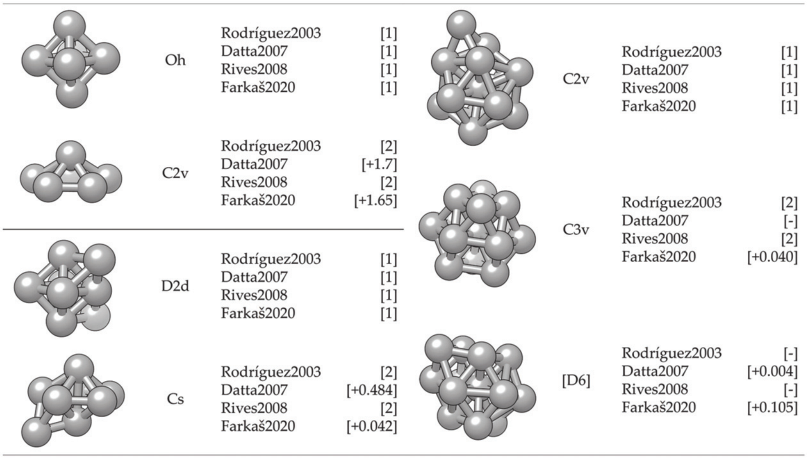

Figure 3. Agreement between most stable cluster structures of 6-, 8-, and 14-atom Co as predicted by DFT [239,254] and MD [252,253] simulations. For DFT studies, energy difference between the structural isomers is given in the square brackets in eV.

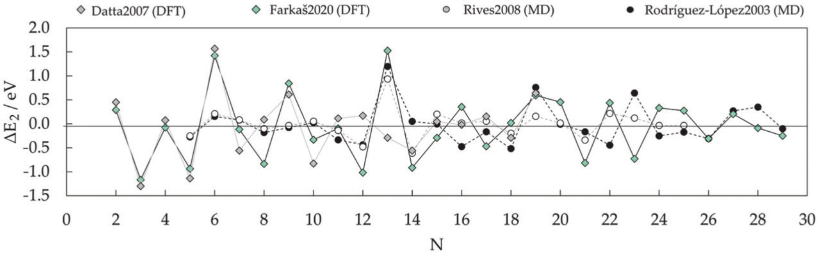

Figure 4. Relative energy stability of successive Co cluster sizes expressed as a second difference in total energy, ΔE_2, as predicted by DFT (Datta (2007) and Farkaš (2020) [239,254]) and MD (Rives (2008) and Rodriguez (2003) [252,253]) simulations.

Magnetic properties, namely magnetic moments per Co atom and magnetic anisotropy energies of small Co clusters ($2 \leq N \leq 30$), are shown in Figure 5. Anything better than a general agreement between experiment and theory is hardly achievable, primarily owing to the deficiency in DFT treatment of the orbital moments, which can be rather large in clusters, in contrast to the bulk metal where they are strongly suppressed [266]. Recent findings of orbital moments in small Co clusters of an order of magnitude higher than those in the bulk further confirm this [267]. Additionally, experimental measurements of magnetic moments also suffer from rapid decrease in the cluster beam intensities, thermalisation, and changes in the direction of magnetisation in response to thermal fluctuations [268–271]. Inconsistencies in the experimental and computed trends can be improved for intermediate sizes ($10 \leq N \leq 25$) by introducing magnetic moments of the second most stable isomer, confirming the possible coexistence of different isomers in the cluster beam, which was proposed experimentally [268].

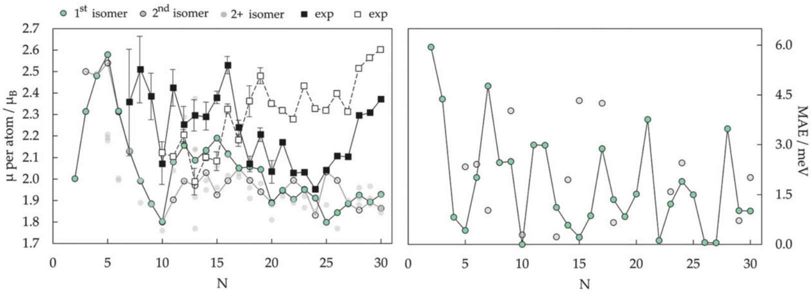

Figure 5. Experimental data are taken from Knickelbein (2006) [270] (■) and Xu (2005) [271] (□), DFT data from Farkaš (2020) [239]. Legend is the same for both graphs.

Generally, clusters in this size range show significantly increased values of the magnetic moment and MAE compared to the bulk counterparts (1.72/1.64 μ_B and 27.2/1.7 μeV MAE per atom for hcp/fcc Co bulk), but the degree of increase is size-dependent. Nevertheless, the differences between magnetic properties of Co clusters and bulk are more a matter of degree than a matter of type, as they are both composed of atoms whose electronic character (i.e., number of unpaired electrons) is responsible for their magnetism. Only in rare instances do metal clusters and metal bulk phases show inverse behaviour [272]. The degree of the cluster's magnetic character depends on the spin coupling of composing atoms, and, as seen in Figure 5, no obvious magnetic moment or MAE trends exist as the cluster size progresses towards a couple of tens of atoms.

In contrast, the chemical properties of small clusters are a combination of the reactivity of bulk and molecular matter, and any general conclusion cannot be simply extrapolated from the bulk behaviour. Similar to the magnetic properties, small and medium clusters show different reactivities that do not vary smoothly with size. Oscillations in the adsorption energies of oxygen on the small Co clusters in the $2 \leq N \leq 30$ range are shown in Figure 6. At instances, groups of cluster sizes with resembling geometries, such as N = 4–7 or N = 15–19, also show similar adsorption behaviour for atomic adsorbates.

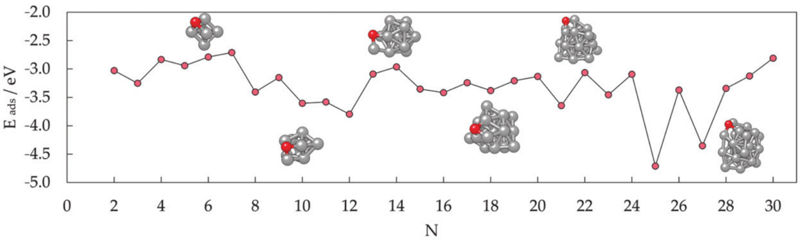

Figure 6. DFT-calculated adsorption energies for single-atom oxygen adsorption on small ($2 \leq N \leq 30$) Co clusters.

However, two different geometric forms of the cluster of a single size often have different reactivities, similarly to the distinct properties of molecules with the same elemental composition but different conformation (chemical isomers). For example, the computed adsorption energy of an oxygen atom on the six-atom cluster with O_h symmetry is −2.79 eV, whereas the same quantity on the six-atom cluster with C_{2v} symmetry is only −1.29 eV. Similarly, 18-atom clusters with icosahedral and hexagonal geometries yielded E_{ads} of −2.88 and −3.38 eV, respectively. It is also not unusual for several cluster sizes and morphologies to induce dissociation of certain molecules, whereas the rest of the cluster systems facilitate plain adsorption [273].

These observations have led to the formulation of what is today known as the non-scalable regime, where chemical and physical properties of clusters cannot be predicted through size-correlated trends but are instead completely independent for each number of atoms. Any system showing such autonomous behaviour and belonging to the series of sizes where trends, if any, are captured with great difficulty, should never be referred to as a metal NP, but rather as a metal cluster or a nanocluster, and as such cannot represent realistic behaviour of nanoparticles.

3.1.2. Surface Model

Metal clusters have, nevertheless, been employed as models for metal surfaces and NPs owing to the confined number of atoms, which was easy to simulate by employing the most sophisticated and accurate quantum methods [274–276]. However, even though these models were useful for insights into the adsorbate–metal atom interactions, a cluster representation results in an increased number of undercoordinated metal sites, which often translates into unrealistic surface or NP electronic properties and chemical activities [277–279]. Consequently, cluster representations have been abandoned, giving place to the extended slab models obtained at the extent of the metal surface periodicity.

The periodic slab model has quickly become the standard for theoretical studies of surface chemistry, and it was believed that a complete description of mNPs can be gained through such simulations if mNPs are considered as a sum of discrete facets [280–285]. For example, for those Co cluster sizes with hexagonal symmetry which showed sufficient surface expansion so that the atomic adsorbate can bind to the cluster solely through the facet sites without interacting with any of the undercoordinated atoms ($22 \leq N \leq 30$), the calculated facet adsorption strength (between -3.06 and -3.54 eV) coincides with the adsorption on the extended slab system ($E_{\text{ads}} = -3.12$ eV). Since the chemical reactivity of facets of relatively small metallic clusters can be envisioned by employing extended slab models, this should also hold for large mNPs with significantly larger surface areas. Nevertheless, there is still a high level of uncertainty when considering these models as reliable representations of the changes in the electronic properties of mNPs upon chemical adsorption.

For cobalt, both fcc- and hcp-bulk phases can be a basis for the mNP construction. Hcp-built mNPs are known to be tiled by the (0001) and $(10\bar{1}1)$ as the most prominent surfaces, while the (111) surface dominates the mNPs of the fcc framework. Average magnetic moments of slab surface models are naturally going to show values closer to the bulk magnetisation than to the moments of cluster systems considering the complete absence of any undercoordinated sites. However, layer-by-layer progression of magnetic moments from the top-most surface atoms towards the bulk-like inner atoms of the slab model is often taken as an indication of the shell-to-core progression of magnetic behaviour of larger, facet-saturated mNPs. Magnetic moments of different layers are shown for the three populated surfaces in Figure 7 (left). A 5–8% reduction in the magnetic moment of Co atoms is captured when going from the surface to the inner, bulk-like atomic layers. An obvious deficiency in slab representation of shell-to-core progression of magnetic moments is the planar contact point between the atoms placed in different atomic layers as opposed to the radial distribution of atoms within the real mNP.

Upon adsorption of a full monolayer (ML) of oxygen (where full monolayer or 1.00 ML is established when the number of interacting atomic adsorbates corresponds to the number of Co atoms in the surface layer), the distribution of magnetic moments between the layers significantly changes (Figure 7, right). Hcp (0001) and fcc (111) surfaces are flat in the sense that the closest Co atoms are levelled within a straight plane and adsorption takes place monotonously on top of the surface, whereas the hcp $(10\bar{1}1)$ surface has a row-like arrangement and allows channel-driven adsorption or even stimulates the subsurface adsorption with minimum energy cost. This significantly influences the induced change in the magnetic moments of surface atoms—for the (0001) and (111) surface, the top-most surface Co atoms experience a reduction in magnetic moments. In the case of the (0001) surface, an 85% decrease in magnetic moment is observed, with a 5–10% reduction in the remaining atomic layers. On the (111) surface with lower packing density, there is a 20% decrease for the first-layer atoms and a 15–30% increase in the inner slab layers. Magnetic moments of the top-most $(10\bar{1}1)$ surface atoms, on the other hand, have 15–40% higher values after adsorption, and a similar rate of increase is observed for the third atomic layer upon the in-channel incorporation of adsorbate atoms.

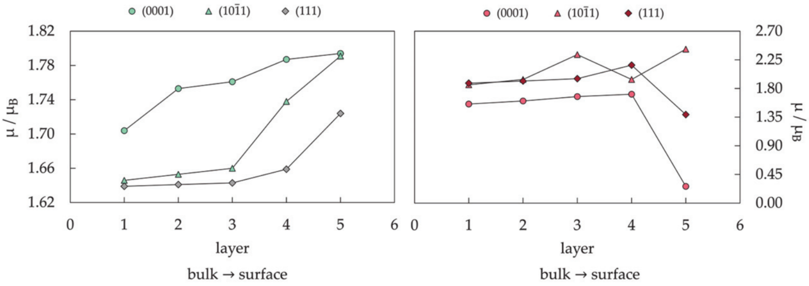

Figure 7. Magnetic moment per Co atom, μ, as a function of the atomic layer within the extended slab models of hcp (0001), hcp $(10\bar{1}1)$, and fcc (111) surfaces of metallic cobalt—**left**: bare surfaces, **right**: oxidised surfaces. Layers are numbered going from bulk to the surface, 1 being the bulk-like inside layer and 5 being the top-most surface layer.

However, the effect of adsorption on the magnetic moments is a complex, site-dependent issue, and different atoms within the same layer might experience varying cumulative effects of adsorbate atoms or molecules [286–288]. Atom-decomposed properties can hence reveal more details on adsorbate–surface coupling and the magnetic nature of the oxidative layer. For oxidative adsorbates, such as atomic oxygen, saturation of the metallic surface can easily lead towards the formation of a metal oxide skin [289–294]. Metal oxides often show significantly distinct magnetic properties from their parent metal materials, which can be unfavourable for many applications.

Experimental studies of cobalt oxidation have observed the growth of cobalt oxides in the (111) direction on the (0001) surface of hcp Co [295]. The top panel of Figure 8 shows optimised magnetic ordering of the (0001) surface with different oxygen coverages and the Co_3O_4 (111) surface as modelled by the Hubbard-corrected generalised gradient approximation, GGA + U (U_{eff} = 3.0 eV) with accompanying densities of state (DOS). GGA + U is known to accurately capture the electronic and magnetic nature of metallic oxides and corresponding metal–oxygen structures, as also shown specifically for cobalt in the literature [296–299]. CoO is known to have antiferromagnetic ordering of type II (AF-II) as the most stable magnetic ordering below its Néel temperature (210 K) [300,301]. Co_3O_4 has magnetically active Co^{2+} ions located in the tetrahedral sites, while octahedral Co^{3+} ions do not have a permanent magnetic moment [302,303]. Bellow the Néel temperature (∼40 K), the antiparallel magnetic ordering within the tetrahedral sublattice of Co_3O_4, due to the lack of magnetic carriers in the octahedral positions, yields a fairly low material magnetisation. Hence, oxidation at room temperature indicates a partial loss of magnetisation upon the formation of magnetically dead cobalt oxide layers on the surface.

Initial oxygen adsorption on the (0001) surface, represented by low adsorbate coverages (0.33 ML), results in a detectable prolongation of Co–Co bonds between the oxygen-interacting and remaining Co atoms without changing the ferromagnetic nature of the cobalt surface. An increase in the magnetic moments of Co atoms that bind to oxygen ($d_{Co\text{–}O}$ = 1.95 Å) is captured at 1.98 to 2.06 μ_B, with 2.37 μ_B calculated for the elevated Co atom. This corresponds well to the experimental suggestions of Co–O formation with CoO character and an expanded intralayer lattice parameter [304], where the Co–O distance at the (111) surface of CoO is approximately 1.85 Å and magnetic moments of Co atoms range from 2.30 to 2.60 μ_B. For medium coverages (0.67 ML), oxygen atoms adsorbed such that three aligned surface Co atoms each formed bonds with three O atoms. Predicted magnetic coupling consists of Co atoms bonded to three O atoms which have spin down antiferromagnetic orientation and significantly reduced magnetic moments of 0.50–0.68 μ_B, whilst the rest are oriented spin up and show values of 1.20–1.85 μ_B. Finally, the optimised structure at full monolayer (1.00 ML) oxygen coverage, including bond lengths, DOS, magnetic moments, and magnetic orderings, implies the initialisation of continuous oxide formation on the (0001) surface. The full first layer is predicted to have minimal magnetisation of 0.35 μ_B with ferromagnetic coupling. The main 2*p* O and 3*d* Co hybridisation peaks are situated between −0.5 and −2.0 eV, and between −4.0 and −5.0 eV, which is consistent with the nonmagnetic Co(III) ions of Co_3O_4. Changes in the magnetic moments of second-layer cobalt atoms are within 0.20 μ_B for any oxygen coverage.

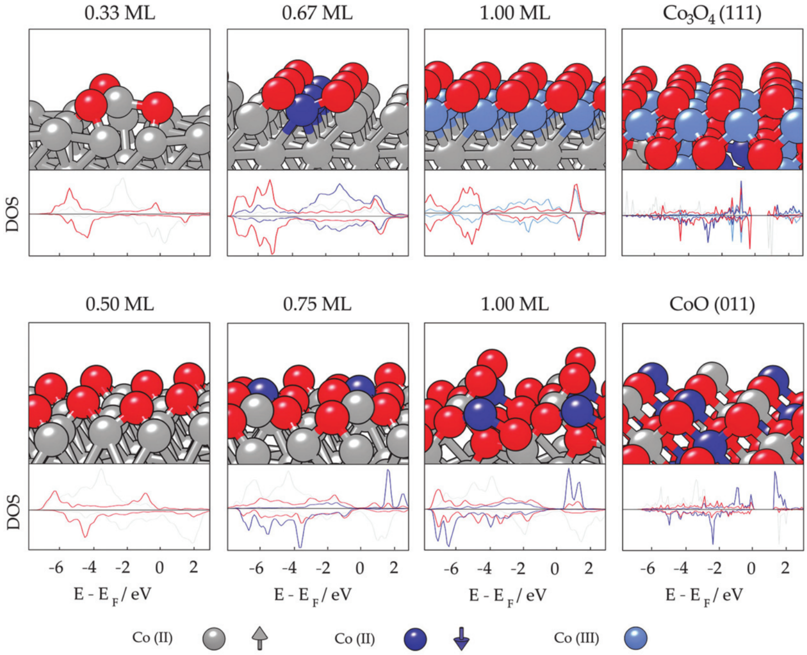

Figure 8. Optimised magnetic orderings for different oxygen coverages on hcp Co (0001) (**top panel**) and $(10\bar{1}1)$ surface (**bottom panel**) as computed by GGA + U; orderings of predicted directions of cobalt oxide growth are provided on the right. Below structures, pDOS in a.u. (range −2.5 to 2.5 states/eV) for 3*d* orbitals of each distinguishable Co surface atom and 2*p* orbitals of O atoms. Grey, dark blue, and light blue spheres represent Co (II) up spin, Co (II) down spin, and Co (III) atoms, respectively, with oxygen shown as red spheres.

Oxidation of the $(10\bar{1}1)$ surface has not as yet been probed experimentally. The bottom panel of Figure 8 shows optimised magnetic ordering of the $(10\bar{1}1)$ surface with different oxygen coverages as modelled by GGA+U (U_{eff} = 3.0 eV) plus accompanying DOS. For coverages of half a monolayer (0.50 ML) or less, no changes in the ferromagnetic coupling of surface cobalt atoms are observed and the calculated magnetic moments are in the range of 1.91–2.23 μ_B. For higher coverages (0.75 ML), the results show changes in the magnetic coupling of certain surface atoms, with a further increase in the magnetic moments to 2.25–2.66 μ_B. At full monolayer coverage (1.00 ML), half of the surface atoms had antiferromagnetic coupling and magnetic moments of 2.38–2.55 μ_B, while the rest experienced ferromagnetic coupling with reduced magnetic moments at values of 1.88–2.20 μ_B. Because of the integration of adsorbate atoms in the structurally arranged rows on the surface, deeper layer Co atoms also feel the presence of oxygen, causing enhancement of the magnetic moments to 1.85–1.95 μ_B.

Reconstruction of the initial row-like geometry of the $(10\bar{1}1)$ surface through the full monolayer oxygen adsorption indicates that the orientation of the cobalt oxide growth would more likely be through the CoO (011) or CoO (100) surfaces compared to the (111) directional growth at the (0001) surface. Experimentally suggested rearrangement of the channel-characterised $(11\bar{2}0)$ hcp Co surface towards the centred lattice of the CoO (100) plane [305] through movement of Co atoms and centring of the adsorbed oxygen between four Co atoms was successfully obtained within the same computational setup. Compared to the $(11\bar{2}0)$ surface, because of the prolonged Co–Co distances, further reconstruction towards the CoO (100) faceting is not to be expected on the $(10\bar{1}1)$ Co surface since already at 1.00 ML certain oxygen atoms were unable to form bonds with more than two surface atoms. Therefore, the (011) surface was suggested as the orientation of CoO growth on the $(10\bar{1}1)$ surface.

Decomposition of oxygen-induced magnetic effects on an atom-to-atom basis thus allows for precise insight into the nature of the oxidised surface layer, which can be used to predict the directional growth of oxide phases as well as further changes in the magnetic moments of slab layers. Similar to the layer progression of magnetic moments for bare slabs, oxygenated surfaces also suffer from the directional aspect of established interactions, where planar adsorption of oxygen cannot account for the morphology-governed adsorption on mNPs.

Following Van Vleck's proposal [306] of spin–orbit coupling induced MCA, calculations of the magnetic anisotropy of metallic bulk phases and slabs have been carried out at different levels of approximation, pioneered by Brooks [307], Fletcher [308], and Daalderop [309,310], which have given satisfactory agreement with experimental methods. An interesting phenomenon of spin reorientation in metallic 2D systems has been observed for supported magnetic films (Fe/Ag(001) [311], Co/Au(111) [312], Ni/Cu(001) [313]). The crucial parameter that affects the direction of magnetisation is the film thickness, as it can induce change in the spontaneous magnetisation axis due to the competition between the interface anisotropy and the effective bulk anisotropy, which includes magneto-crystalline and shape anisotropy energies. It has been recently demonstrated that the electronic states can be responsible for the oscillations of the magnetic anisotropy in Fe(001) thin films with periods of five to nine monolayers since the quantum well states formed by *d* electrons change position in reciprocal space depending on the magnetisation direction [314–316]. Magnetisation-dependent spin–orbit gaps were also observed when the system symmetry was decreased compared to the bulk symmetry. Other factors influencing the interface or bulk terms include temperature conditions (annealing [317]), the presence of surfactants (capping layers [318,319]), and the stacking sequence [320], to name a few, and hence the spin reorientation in the metallic systems also depends on each of these parameters.

The thickness dependence of the MCA energy of cobalt films for different slab arrangements (hcp (0001), fcc (001), and fcc (111), built from the experimental lattice constants) is shown on the left in Figure 9 at the local spin density approximation (LSDA) theory level [321]. In the progression from ultrathin to >10 Å slabs, significant oscillations are captured. For slabs with fewer than three atomic layers, interaction between the layers is more pronounced, resulting in a less systematic behaviour that deviates from the general trend. A certain degree of MCA energy convergence with respect to the slab thickness is also obtained as the number of layers increases, although the oscillations comparable to the total anisotropy values persist even for the thickest slabs considered. Cubic symmetry imposes a minimal barrier for the transition between any of the perpendicular magnetisation directions since its calculated anisotropy is less than a few µeV, meaning that the anisotropies of differently arranged fcc slabs are determined only by the in-plane lattice structure, considering that the bulk anisotropy is negligible. Thus, the converged values are actually the surface anisotropy energies, and their estimations are −0.38 meV for the (001) fcc surface and 0.19 meV for the (111) fcc surface. Note that a positive MCA energy means that the easy magnetisation axis is out-of-plane, whereas a negative MCA energy belongs to slabs with an in-plane easy magnetisation axis. The MCA energy of the hcp (0001) slab shows a slightly negative slope, where the gradient of the linear fit for slabs with more than 10 layers is −0.015 meV. This is in good agreement with the MCA energy of the LSDA hcp bulk Co, which was calculated to be −0.010 meV. The value of the surface anisotropy for the hcp (0001) surface has converged to 0.44 meV.

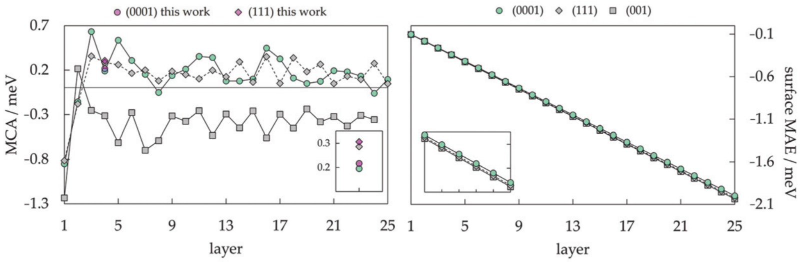

Figure 9. MCA energies for different fcc and hcp Co surfaces of varying thickness calculated at the LSDA level of theory (**left**) and estimated shape anisotropy (**right**). Symbols are the same for both graphs. Data are taken from Zhang (2009) [321]. Legends are the same for both graphs.

Another important contribution to the magnetic anisotropy of the system is the shape anisotropy energy. For 2D films, shape anisotropy can be estimated at $2\mu_B M_s^2$, as shown for Co slabs in Figure 9 on the right. For both fcc and hcp Co slabs, the shape anisotropy energy has almost the same linear dependence with respect to the thickness.

Calculations based on the unrestricted GGA relaxation of the four-layer surface slab models were conducted for comparison, as shown in Figure 9 on the left, and agreement in the results is satisfactory. Predicted anisotropy energies for the (0001), $(10\bar{1}1)$, and (111) Co slabs are hence 81.4 μJ/m^2 or 6.57 μeV/atom, −7.98 μJ/m^2 or −0.70 μeV/atom, and 199.01 μJ/m^2 or 16.63 μeV/atom, respectively. These MCA values arise from the same computational setup that captured the correct order of magnitude for bulk MCA of hcp and fcc cobalt (calculated at 4.16×10^5 J/m^3 or 27.20 μeV/atom and -1.68×10^4 J/m^3 or −1.54 μeV/atom; experiment at 0 K 7–8 $\times 10^5$ J/m^3 or 65 μeV/atom and -2.36×10^4 J/m^3 or −1.6 μeV/atom [322]). Results of other experimental and theoretical studies conducted on self-standing Co films also showed varying values depending on the film thickness. From the anisotropy modelling of close-packed (111) ultrathin transition-metal films, the MAE obtained for the Co (111) film was −0.28 meV [323]. A Néel model of the Co (0001) surface predicted an MAE of 84 μJ/m^2 [324], whereas measurements on the 1000 Å thick Co film resulted in an in-plane anisotropy volume of -7.2×10^2 J/m^3 [325].

2D Co systems deposited on different substrates have received a lot of attention for their unique magnetic properties, both experimentally [320,326,327] and theoretically [328–331]. For a nonmagnetic supporting material, such as a gold surface, measured MAE values correspond well to those calculated for unsupported extended slab models—experimental measurements on the Au/Co interface gave values of 53–70 μJ/m^2 [332]. Another study of the Co/Au(111) system showed 17 μeV/atom out-of-plane magnetic anisotropy [333]. Supported ultrathin Co films are characterised by much higher anisotropy values. When ultrathin films of cobalt atoms were deposited on Rh(111) and Pt(111) surfaces, the MAE values measured were -0.37 ± 0.05 and −0.29 meV per Co atom, respectively [334]. The combination of Co and Ir in a three-layer system gave rise to a similar anisotropy of 0.46 meV per atom, whereas only 0.02 meV MAE per atom was calculated for the Fe–Co–Ir system [335]. Furthermore, significant oscillations were observed in the interlayer exchange coupling for systems of varying numbers of Co and 4*d* transition-metal series layers, and the following quantitative trends of magnetic properties were formulated as a result: across the noble metals and Pd, a ferromagnetic interlayer coupling was found; for the post-noble metals and most 4*d* transition metals (with the exception of Mo), an antiferromagnetic interlayer coupling was obtained, meaning that the choice of the metal can influence the easy axis of magnetisation [336]. The interface magnetic anisotropy of the Co (0001) film was shown to increase by 36 $\mu J/m^2$ upon Co surface oxidation, and follow-up DFT calculations correlated this change with a positive charge increase of $0.54e^-$ per oxidised Co atom [337]. However, the MAE of extended metal slab models is strictly dominated by the surface anisotropy factor, whereas the three-dimensional shape anisotropy that often affects both intensity and easy axis of MAE of mNPs cannot be accounted for through the 2D models.

3.1.3. Nanoparticle Model

A surface representation of mNPs deliberately neglects the role of undercoordinated particle sites, namely edges and vertices, and the effect of the full mNP geometric and electronic structure, which often differs from that of the bulk material. However, converged surface energies obtained by employing surface slab models can be implemented to build NP models using the well-known Wulff construction method [338–340]. The premise of the Wulff construction is that the length of a vector drawn normal to a crystal face from the particle centre is proportional to the surface energy of the corresponding facet, and the crystal equilibrium shape is obtained through the necessary minimisation of the total surface energy of the particle. In practice, there is an infinite number of possible surfaces that can be included in the model. Restraining the surface exploration to a set of those that are experimentally observed is a plausible strategy, whereas taking into consideration only the surfaces with low indices, which in general tend to include the most stable members, is a relatively reliable getaway because such surfaces are the most likely to be expressed in the morphology. Wulff NP construction of low-index facets has become a standard technique to build particle models, as shown in Figure 10. As the contributions from the particle edges are neglected in the Wulff construction method, the shape of small particles might deviate from the predictions, but experimental analysis indicates that particles in the range of a few nanometres are generally consistent with this construction principle [341,342].

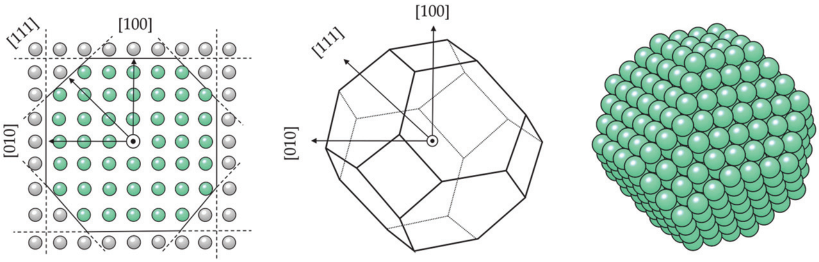

Figure 10. Illustration of the Wulff construction of an fcc particle. Growth direction of crystal facet planes is represented by black arrows, and the centre of the particle is represented by a black dot. Atoms enclosed in the equilibrium shape of the nanoparticle are coloured in teal, while the rest of the bulk atoms are grey. 3D morphology is shown in wire-frame and atomic representation.

More compact, quasispherical NP shapes can be constructed by applying symmetry operations over stable surface members to obtain the highest density of atoms within the NP volume, resulting in the multiple-twinned particle models. These are known as noncrystalline NP models, and the most common is the icosahedron composed of 20 tetrahedra with (111) close-packed facets as their base and the central vertex as their apex, conjoined at 12 boundary vertices with a fivefold rotational axis, as initially proposed by Mackay [343]. The decahedron, on the other hand, is formed of five tetrahedra with (111) close-packed facets, but its sphericity is far from that of the icosahedron, and it was first suggested by Ino [344]. Vertex and edge truncations, suggested by Marks and Ino [345,346], can be implemented to achieve a better surface-to-volume ratio. However, any noncrystalline motif is obtained at the expense of volume contributions for facets to be able to close the intersurface gaps. Some of the possible mNP models, both crystalline and noncrystalline, are represented in Figure 11.

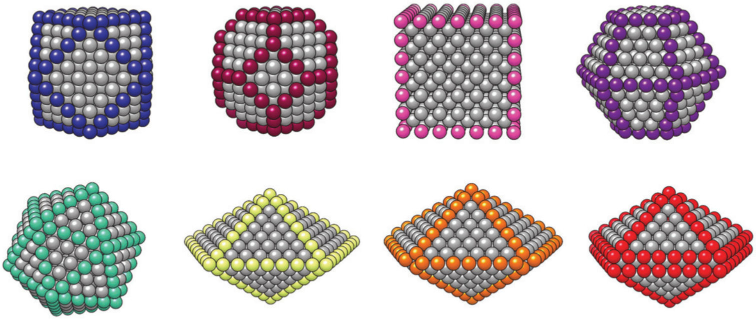

Figure 11. Models of crystalline NPs (left to right: fcc—cuboctahedron and truncated octahedron, bcc, and hcp) in top panel and noncrystalline NPs (left to right: icosahedron, regular, Marks, and Ino decahedron) in bottom panel.

Significant progress in the modelling of mNPs was made when moderately large NP models were implemented in DFT calculations for the simultaneous description of terrace sites of extended surfaces and low-coordinated edge and vertex sites. The NP model strategy is sufficient in providing the influence of the particle size and shape on the properties of interest by defining the so-called scalable regime where many properties (typically nonlocal—independent on the position of different atoms within the cluster, such as cohesive energy per atom) monotonously converge toward the bulk or extended surface limit. Other, more localised properties, which are related to the atoms of a particular region of the NP, such as adsorption energies of simple adsorbates, show invariance with respect to the number of atoms and slowly converge with the increase in the NP size.

Monotonous convergence of the cohesive energy of Co mNPs by applying the NP model is shown in Figure 12 (left) for various morphologies and particle sizes [239]. To limit the exhaustive number of calculations that would be needed if every NP size was considered, the choice of sizes of interest is usually driven by the well-known oft-recurrence of mNPs with a complete, regular outer geometry, designated as full-shell NPs. These numbers, known as magic numbers, are obtained through the mathematical relationships determined individually for each structural motif [347,348].

Size and morphology dependency of the energetic stability of a Co mNP is well represented by linear regression and can be extrapolated to very large mNP sizes. For sizes below 100 atoms, the stability of motifs based on the successive increase in the cohesive energy per atom decreases going from the most stable icosahedron, over fcc truncated octahedron, hcp, fcc cuboctahedron, and decahedron, to bcc as the least stable shape of Co mNPs. Differences in energies for the clusters with the same number of atoms between any two shapes are close to or less than 0.10 eV per atom. The icosahedron is identified as the most stable shape throughout the whole range of small and medium cluster sizes, consistent with the experimentally determined predominance of this noncrystalline shape within particles of up to $N = 800$ atoms [349,350]. The icosahedron-to-hcp transition is predicted to happen at around $N \approx 5500$. An enlarged view of the intersection is represented as an insert in Figure 12 (left).

A linear fitting approach based on the magic-numbered mNPs and a subsequent determination of the stability trends is constrained by the assumption that the stability order is maintained for the remaining, nonmagic particle sizes. Based on the experimental indications of the simultaneous occurrence of more than a single geometrical shape at practically any size, linearly interpolated morphology transitions of magic-numbered clusters serve only as a guideline to the predominating geometry. A promising qualitative agreement was found in recent works that have conducted a full sampling of the energy landscape beyond the magic numbers, where the dominant mNP shape coincides with the one predicted by a 'simple' magic number linear fit [351–353]. The noncrystalline/crystalline distributions thus obtained for Co clusters with magic numbers of atoms represent a good reference point for defining crossover sizes between the structural motifs. Note that shape alternations could occur in reported stability windows, but they should nevertheless be expected to contain the highest proportion of the energetically most favourable structure.

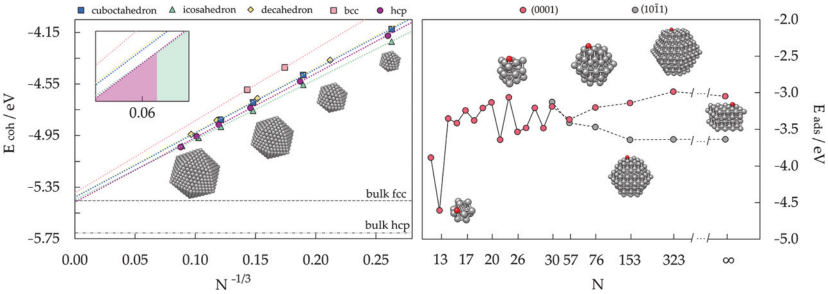

Figure 12. Linear fitting of the cohesive energies of Co NPs of varying morphologies with $55 < N < 1500$ atoms with an insert capturing the crossover between the icosahedral and hexagonal shape (**left**) [239]. Progression of oxygen adsorption energies from nonscalable ($2 < N < 50$) to scalable regime of Co NPs with hexagonal symmetry (**right**); extended slab models are denoted as ∞.

An example of the convergence of more localised properties is the size-dependent progression of the adsorption energy. Calculations of the adsorption behaviour of simple adsorbates, but also of more complex molecules, have captured the nonscalable regime of the smallest metallic cluster models and convergence of adsorption energies for particles composed of approximately 50–60 atoms [273,354–361]. Size dependence of oxygen adsorption on small Co clusters with hexagonal symmetry and large crystalline hcp NP models, as well as on the extended slab models for the hcp (0001) and $(10\bar{1}1)$ surfaces that appear in the hcp mNP morphologies, is depicted in Figure 12 (right) [362]. The 13-atom hcp Co cluster shows by far the most favoured oxygen adsorption, followed by notable oscillations in the adsorption strength established for succeeding cluster sizes. A nonscalable regime extends to the Co clusters with $30 < N < 50$ atoms, similar to what was observed for other metallic systems. For particles with more than 30 atoms, distinctive facet areas can be assigned to the (0001) and $(10\bar{1}1)$ hcp Co surfaces, with each showing unique adsorption behaviour based on their structural arrangements. Nevertheless, adsorption interaction on both constituent hcp mNP surfaces eventually converges to the respective extended slab adsorption energies. The difference in adsorption strengths on the large 323-atom hcp mNPs is insignificant compared to the periodic slab models.

The emergence of the scalable regime occurs at different cluster/NP sizes for distinct properties. The density of states, and, accordingly, the electronic structure, evolves rapidly towards bulk-like behaviour, which enables the use of relatively small mNP models for evaluating the chemical activity of sites characterised by low coordination numbers. The activity toward the adsorption of atomic or molecular species is often evaluated using either the d-band centre as the electronic descriptor or the generalised coordination number as the geometric descriptor, since it was found that the two are linearly correlated [363].

As a general convergence rule, properties are essentially considered converged when the local atomic environment is maintained with the further addition of atoms. For example, the adsorption strength is mostly conditioned by the adsorption site, followed to a substantially decreased extent by the influence of the first atomic neighbours and the second-shell neighbours, whereas neighbours of the third shell have negligible contributions. This approach can be extended to other local or regional properties.

To obtain an optimal description of the mNP properties of interest, it is crucial to choose the particle size that will reliably capture the effects of the studied morphology without accentuating either cluster-dominated behaviour or the monotonicity of the extended slab perspective. This is especially important when investigating the magnetic properties, because they are easily influenced by symmetry factors, directional interactions, and local atomic environment.

Figure 13 represents the core-to-shell progression of magnetic moments in differently sized icosahedral and hcp mNPs. The 13-atom cluster size from the nonscalable regime clearly stands out for both core and shell segments. For larger mNPs, core and inner-most layers show 15–25% lower magnetic moments compared to the surface itself or to the layers in close proximity to the surface. The increase in the magnetisation of surface atoms is hence 3 to 5 times more pronounced than in the case of extended slab models. Additionally, some distinctions in the overall core-to-shell trends have also been captured compared to the layer-to-layer progression of extended slab models.

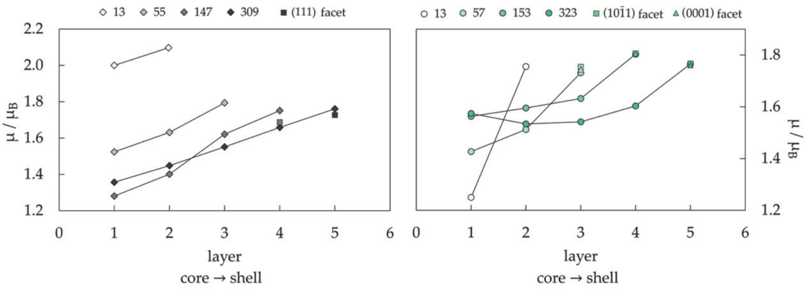

Figure 13. Magnetic moment per Co atom, μ, as a function of the Co NP layers for increasing nanoparticle size—**left**: icosahedral NPs, **right**: hcp NPs. Layers are numbered going from the core to the shell of the NP.

These differences become more pronounced when the effects of oxidation on the magnetic moments are examined for 147-atom icosahedron and 153-atom hcp Co mNP models (Figure 14). Compact organisation of Co atoms within the mNP morphologies allows for less flexible rearrangement to accommodate atomic adsorbates such as oxygen into the structure, in contrast to the frequently observed adsorption-induced reconstruction of the top-most layers of a surface slab [364–370]. For this reason, enhancement of the magnetic moments of the layer placed immediately below the vacuum-exposed outer shell obtained upon oxidation is significantly modified in the absence of surface rearrangement. The increase in the average magnetic moments for Co atoms within this layer is about 8% for both icosahedron and hcp Co mNPs, whereas corresponding slab enhancements for the (111) and $(10\bar{1}1)$ surfaces are 30–40%. The increase in the surface shell magnetic moments is 11–20%. Additionally, elongation of the inner Co–Co distances upon the interaction of surface Co atoms with oxygen adsorbates lessened the volumetric strain and consequently the quenching of the magnetic moment of the central atom. This adsorbate-induced effect could not be captured within extended slab models.

The morphological dependence of the magnetic properties of Co mNPs is captured in Figure 15. Respectable shape deviation of magnetic moment per Co atom is observed only for the smallest mNPs, where each morphology has a unique share of vertex and edge sites. These differences wear off with the increase in the mNP size, when average magnetic moments start rapidly converging towards the bulk Co value. The MAE of mNPs, on the other hand, depends strongly on the shape anisotropy arising from the varying morphologies for all mNP sizes. This is a specific aspect of magnetic nanoparticles, and it is impossible to capture it within the extended slab models. The computational expense of noncollinear DFT calculations limited the determination of MAE to particles with 1–2 nm diameters (50–200 atoms), and the results obtained are shown in Figure 15 (right), together with the experimental data measured for embedded Co mNPs [371].

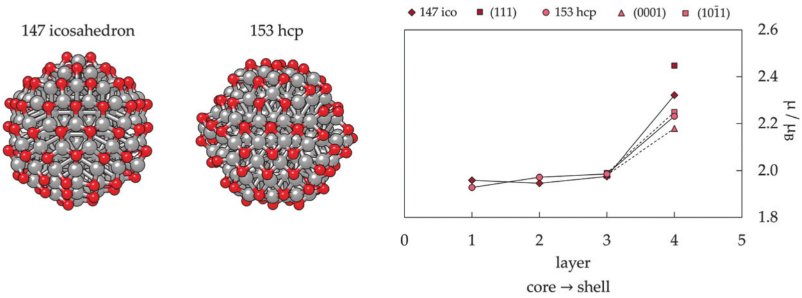

Figure 14. Structures of oxidised 147-atom icosahedron and 153-atom hcp Co mNPs (**left**) and corresponding layer-averaged magnetic moments per Co atom with core-to-surface progression, 1 being the core atom and 4 being the outer shell layer (**right**). Average magnetic moments of (111), (0001), and $(10\bar{1}1)$ facets are also given.

DFT results indicate that the Co mNPs with hexagonal symmetry have the highest MAE values of 1412.5 kJ/m^3 for 0.8 nm and 397.9 kJ/m^3 for 1.3 nm diameter mNPs. Calculated MAE for the 1.5 nm decahedron is 398.2 kJ/m^3, whereas the other noncrystalline icosahedron shape is characterised by very low anisotropies, 30.2 and 65.6 kJ/m^3 for 1.0 and 1.5 nm mNPs, respectively. MAEs of 0.7, 1.0, and 1.4 nm fcc truncated octahedra from DFT calculations are 439.9, 218.0, and 194.5 kJ/m^3 and correspond well to the experimental anisotropy trend. Experimental data have been complemented by the Néel pair modelling to correlate the observed MAE features to the increased importance of the exposed facets, namely those of the (100) and (111) fcc Co surfaces, which is also shown in Figure 15 (right). The addition of a single facet does not contribute significantly to the modifications in the shape, but it is sufficient to break the symmetry and induce a change in the anisotropy of the entire particle. Such increase in the surface area successfully reproduced both experimentally observed effects, the increased MAE values with respect to the bulk for the smallest sizes and the varying trend in MAE with decreasing size. However, even though the addition of a single facet decreases the general enhancement in magnetic anisotropy for larger particles, it is nevertheless possible to obtain very large MAE values because of the shape-induced anisotropy. This means that notably polycrystallinity, which is expected in large particles due to the fabrication mechanism, plays an important role in reducing the contributions of crystal symmetry-breaking to the global anisotropy. Defects have, on the other hand, been proposed as responsible for uniaxial anisotropy in larger cobalt or iron mNPs (8–20 nm) [372,373].

Other experimentally measured MAE energies are reported in the range of 6.0–30.0 kJ/m^3, consistently above the Co bulk values (2.7 kJ/m^3 fcc and 4.4 kJ/m^3 hcp) [374–376]. Geometrical shapes of the particles are not always provided in these studies, but it is suspected that they are mostly crystalline fcc or icosahedral Co mNPs. Moreover, several studies of various mNPs and for different sizes have observed the coexistence of crystallographic structures both in the gas phase and deposited [377–380], especially without further annealing. Comparable strong variations with values of the same order (between 10 and 400 kJ/m^3) have been derived for icosahedral Co mNPs in the 3.1–4.3 nm size range [381]. As hexagonal structures in Co mNPs are expected to compete in stability only at larger sizes above 20 nm [239,382], crystalline structures of fcc features are naturally dominant in any size range up to this critical size, and the general trend obtained in the experiments cannot be specifically assigned to the exact crystalline structure. For a specific case of

3.0 nm truncated octahedral particles, experimentally derived anisotropy constants are in the range of 10–200 kJ/m^3 [383].

A combination of DFT simulations and NP models is hence a very powerful tool in predicting the magnetic behaviour of mNPs, and it corresponds very well to the complexity of the size- and morphology-dependence problem. With improvements in computational power and performance, it has become possible to utilise the advantages of the NP models over couple-atom clusters and extended slabs and to capture reliable values of magnetic moments, anisotropy energies, and adsorbate-induced alternations in the magnetic behaviour of mNPs [384]. These advances are expected to facilitate the research on mNPs with favourable properties for MRI contrast and magnetic nanoparticle hyperthermia agents.

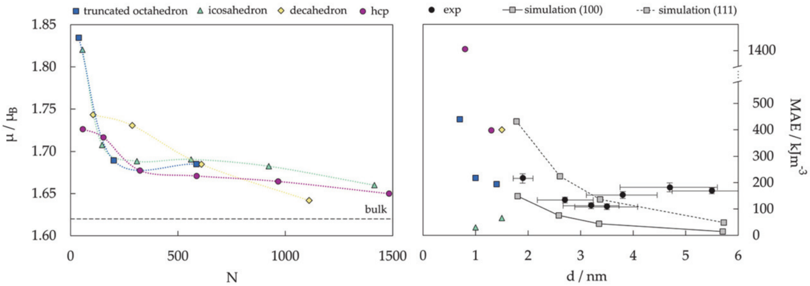

Figure 15. DFT-predicted progression of average magnetic moment per atom, μ, (**left**) and comparison between DFT-calculated, experimentally measured, and Néel pair surface correlated magnetic anisotropy energies, MAE, (**right**) with the increase in the size for Co mNPs of varying morphologies. DFT results are taken from Farkaš (2021) [384], and experimental and Néel pair modelling results are taken from Oyarzún (2005) [371].

3.2. Protected mNPs: Ligand Effects on Magnetic Properties

Two main features dominate the magnetic properties of mNPs: (1) their physical appearance, i.e., size and morphology, and (2) surface effects, i.e., symmetry breaking of the crystal structure at the mNP surface, canted spins of surface atoms, surface oxidation, or chemical effects induced by the bonding of surfactant molecules.

Since gas-phase mNPs have limited stability and can only exist on the order of a few milliseconds, their use in new technologies is based on more practical systems whose longevity is provided through the stabilisation by surface functionalisation [385–387]. Functionalisation molecules also passivate the mNP by forming bonds with the reactive surface metal atoms directly exposed to the environment. Unfortunately, the attachment of surfactants is notoriously correlated with the quenching of mNP magnetic moments [388–391]. In general, the extent of ligand-induced changes in magnetic behaviour depends on the metal–ligand pair in question. The origin of magnetic moment quenching of respective metal atoms in metal–ligand complexes has been linked to two electronic parameters: changes in the *d*-electron count of the metal and changes in the energy level splitting of the metal *d* orbitals through a ligand field effect [392–394]. These ligand-induced changes are indications of the possibly strong ligand effects on magnetic properties of mNPs where ligand-induced changes could scale as a function of the mNP size.

Ligand effects have been recognised as important factors in the implementation of mNPs in biomedicine, since functionalisation often comes at a cost of not only reduced magnetisation, but also changed surface anisotropy. It has been recently demonstrated that the deposition of a self-assembled monolayer of alkanethiolates on an ultrathin Co film grown on Au(111) induces a spin reorientation transition from in-plane to out-of-plane magnetisation, changing the anisotropy values [333]. Computer simulations of these issues have often relied on the representation of mNPs as extended slab models because of the cost of noncollinear calculations. However, this approach causes even more uncertainties when estimating ligand-induced changes in magnetisation than in the simple assessment of the adsorption reactivity, because the neighbouring shells of atoms play a minimal role in the adsorption strength, while their contribution to the global magnetic behaviour is much more prominent.

To make a connection between the impact of ligands on the emergent properties of coordination complexes and in larger ligand-functionalised metallic structures, systematic studies of a combination of varying Co mNP size and a series of ligand shell compositions have been conducted.

Figure 16 shows the linear-like relationship between the total magnetic moment and the Bader charge on the Co core for different ligand shells and two core sizes, a 13-atom Co cluster and a 55-atom Co mNP. In general, there is a net quenching of the total magnetic moment relative to the bare cluster for each system, due to spins being paired in surface–ligand bonds. However, as the charge on the core becomes more positive, the total magnetisation increases. The intensity of the quenching is preserved with the increase in the particle size [395].

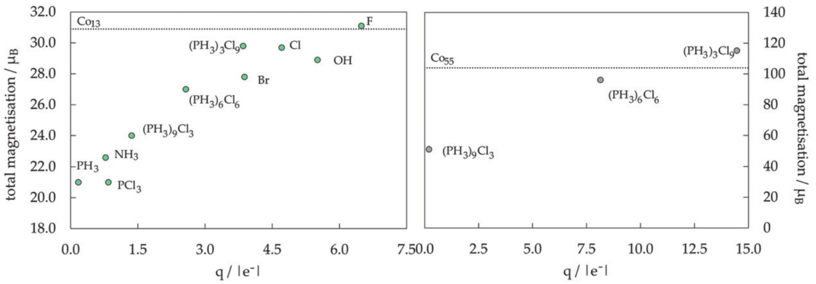

Figure 16. Total magnetic moment as a function of Bader charge for varying ligand shell composition on 13-atom (**left**) and 55-atom (**right**) icosahedral Co mNPs. Dotted lines indicate values of the bare mNPs. Data are taken from Hartmann (2016) [395].

The average local magnetic moments of each Co atom were found to span a wide range of values as a function of the ligand shell composition [396]. The 13-atom cluster-PH_3 ligand system quenches magnetic moments of all Co atoms from the bulk value of 1.72 to 1.61 μ_B, whereas a fluorine ligand shell results in an increased atomic Co magnetic moment of 2.39 μ_B. The 55-atom mNP–PH_3 analogue experiences similar local magnetic moment quenching, even at the mNP centre. The 55-atom mNP–chlorine system also follows the trends of the chlorine-functionalised 13-atom cluster, with the chlorine ligands localising charge and increasing the magnetic moments of surface Co atoms. Analysis of bond lengths and surface–ligand bond angles showed that these alternations in atomic magnetic moments are not driven by geometry modifications due to functionalisation, but depend only on the type of ligand. This provides continuity in the locally induced magnetisation changes over differently sized metallic cores.

The transferability between the core size and magnetic moments of protected Co mNPs was confirmed through investigations of biomedically relevant ligands, namely carboxylic acids. Considering the scaling of ligand-induced changes in the magnetisation as a function of the Co NP size, half and full monolayer coverages of acetic acid have been modelled by DFT with the aim of identifying general trends. Progression of ligand-induced changes in the magnetic moments within the centre, inner, and surface segments of icosahedral Co mNPs with varying sizes (N = 13, 55, 147) upon carboxylic acid functionalisation is shown in Figure 17. Changes in the magnetisation of 55- and 147-atom Co mNPs with the increase in the density of the ligand shell correspond very well for each segment of the two mNP sizes, indicating that the smaller NP model is sufficient to capture the magnetic behaviour of protected Co mNPs.

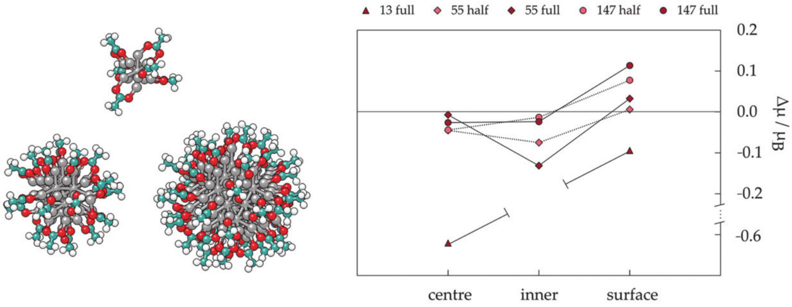

Figure 17. Ligand-induced changes in the magnetic moments of centre, inner, and surface segments of the 13-, 55-, and 147-atom icosahedron Co mNPs functionalised by a half and full acetic acid coating. Δμ is the difference between the average magnetic moment of each segment in unprotected and protected mNPs.

To gain more detailed insight into the coverage-dependent changes in the magnetic properties, average magnetic moments per Co atom are given as a function of the percent ligand coverage for Cl-, PH_3-, and COOH-protected Co mNPs in Figure 18. In the case of each ligand type, there is a strong correlation between ligand coverage and resulting magnetic moment per Co atom, yielding a linear trend as was the case for the total magnetic moments as a function of the core charge. However, different ligand binding types can lead to both an increase and a decrease in the average magnetic moment of varying intensities compared to the moments of the unprotected mNPs. Higher Cl coverage has an enhancing effect on the atomic magnetic moments, where the line of best fit indicates a 0.0043 μ_B increase per percent coverage. However, an increasing magnetic moment arising from the passivating shell composed of acetic acid molecules shows a significantly slower growth of 0.0009 μ_B per percent coverage. In contrast, a PH_3 shell leads to the quenching of the average atomic magnetic moment by 0.0065 μ_B per percent coverage. Taken together, the deviations in average atomic magnetic moment as a function of ligand identity and coverage are evidence that the composition and density of the passivating shell have a stronger impact on magnetisation than the size of the Co core.

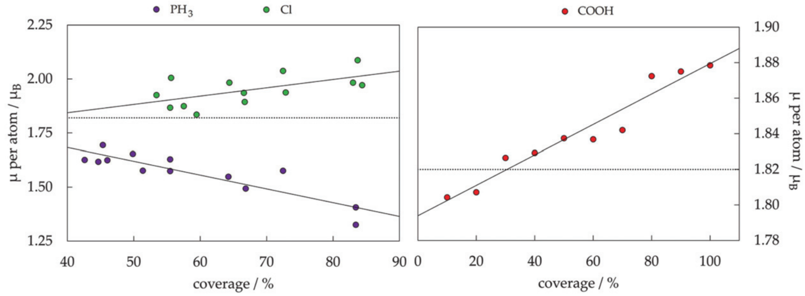

Figure 18. Average magnetic moment per Co atom, μ, as a function of ligand coverage for icosahedron Co mNPs passivated with Cl and PH_3 (**left**) and COOH (**right**). Average magnetic moment per Co atom for unpassivated 55-atom Co icosahedron is added as the dotted line. Data on the left are taken from Hartmann (2018) [396], and data on the right are taken from Farkaš (2021) [384].

To capture ligand effects on the mNP anisotropy, ligand-protected icosahedron Co mNPs with varying coverages of biomedically relevant ligands (carboxylic acid, thiol, amine) were modelled. The calculated anisotropy energies are shown as a function of coverage in Figure 19. Starting from a very low value of 30.2 kJ/m^3 for the unprotected 55-atom Co icosahedron, all three ligand families enhance the MAE with an increase in the coverage density. The rates of this increase are, however, ligand-dependent. Amine passivation resulted in the lowest enhancement of MAE, calculated for a 100% coverage at 531.4 kJ/m^3. A change in the direction of the easy axis of magnetisation was also captured for amine-protected mNPs with coverage densities between 60 and 70%. There is a steady increase in the MAE of acid- and thiol-passivated Co mNPs as the protective coatings become denser, with acidic ligands showing a slightly higher enhancement rate per percent coverage. However, for the maximum coverages of 90 and 100%, MAEs of both acid- and thiol-protected Co mNPs reach similar energies with values between 987.0 and 1087.0 kJ/m^3.

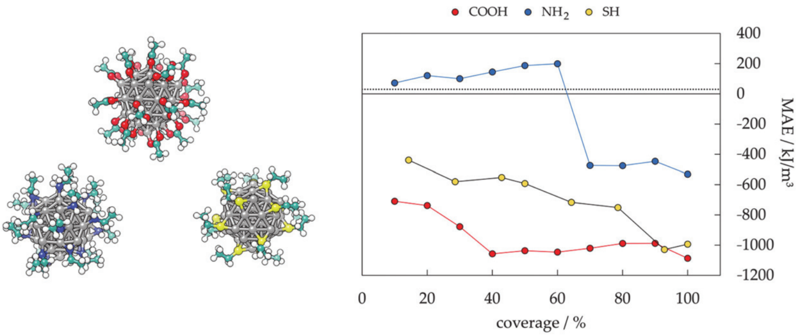

Figure 19. Structures (**left**) and magnetic anisotropy energy, MAE, as a function of ligand coverage (**right**) of COOH-, NH$_2$-, and SH-passivated 55-atom icosahedron Co mNPs. MAE of unpassivated 55-atom Co icosahedron is added as the dotted line. Data are taken from Farkaš (2021) [384].

Overall, ligand binding induces local changes on the atoms of Co cluster and mNP systems, analogous to the effects in the ligand field theory. However, because the local coordination site is a component of a larger nanocluster, the impact of each ligand is observed beyond the metal centre to which it is directly bound. Furthermore, the chemical identity of the ligand within each binding motif provides a fine-tuning mechanism on the exhibited magnetic behaviour through the connection between the electronegativity of the functional group and the amount of electron density withdrawn from the core. Finally, as the size of the mNP increases, ligand-dependent magnetic properties persist, although they are slightly dampened.

3.3. Alloyed mNPs: Effects of Interfaces on Magnetic Properties

The applicability of single-component mNPs is restricted by limited property-tuning possibilities. To overcome this limitation, mNPs can be modified through the construction of bimetallic architectures consisting of two distinct metals, one or both of which should be magnetic [397–402]. Bimetallic (and multimetallic) mNPs, often referred to as magnetic nanoalloys, present properties with a very high degree of tunability owing to the variety of morphologies they can adopt. Their morphology is specified not only by the geometric structure, as in the case of the monometallic systems, but also by the chemical ordering of its components, which corresponds to the arrangement of the two metallic phases within the specified geometry.

The expectations of improved magnetic properties of monometallic mNPs by incorporating additional metallic phases originated from the very large magneto-crystalline anisotropy of the respective bulk and thin-film alloyed materials [403–408]. DFT calculations were shown to be capable of quantitatively describing the MAE and the orbital magnetisation in these alloys [409–412]. For example, in the case of the L1$_0$ CoPt crystal, DFT predicted an MAE of 4290 kJ/m^3 [227], very close to the experimental value of 4000 kJ/m^3 measured by Eurin [413] and much higher than that of the fcc or even hcp Co bulk (23.6 and 700–800 kJ/m^3).

Nevertheless, it was observed that the magnetic properties of alloyed mNPs could become worse than those of bulk metals, in contrast to the monometallic mNPs. The magnetic anisotropy energy of $L1_0$ CoPt NPs was found to be 385 kJ/m^3 [414] or 1700 kJ/m^3 [415], both values much smaller than that measured for the bulk $L1_0$ CoPt crystal. Moreover, a clear reduction in the saturation magnetisation of CoPt mNPs was captured with a decrease in the particle size [416]. Bimetallic mNPs are still promising for many applications because, despite the deterioration in the magnetic behaviour with respect to bulk alloys, which was suggested to be caused by surface effects (surface adsorption and surface spin canting [417]), their anisotropies and magnetic moments substantially exceed those of the monometallic counterparts. For example, distinct $L1_0$ orderings in CoPt mNP systems have already shown how improved MAE can translate into superior catalytic performance in fuel cells [418].

The central difficulty in predicting magnetic properties of bimetallic mNPs lies in the complexity of the possible combinations in composition, geometry, and chemical ordering. Compared to the intermixed $L1_0$ state of CoPt NPs, surface-segregated cuboidal counterparts have shown magnetic moments reduced by 0.52 μ_B and a 19% decrease in MAE. More pronounced, when the cuboctahedral morphology was considered, reductions in the total magnetic moment and CoPt mNP anisotropy were of the order of 4.96 μ_B and 45%, respectively [227].

Finding the optimal bimetallic mNP morphology for a specific composition of two metallic phases by employing MD simulations has shown good agreement with proposed structures of experimentally synthesised systems [419–425]. Owing to the difficulties in assigning magnetic properties to a specific mNP morphology through experimental techniques, DFT simulations are also valuable in predicting the magnetic behaviour of bimetallic mNPs of varying geometries and chemical orderings.

As to their thermodynamic stability, the cuboctahedral shape with $L1_0$ crystal order was obtained as the most stable geometric structure for large CoPt NPs, based on the DFT-calculated surface energies and Wulff construction theorem [426]. Specifically for CoPt mNPs with diameters below 2.5 nm, DFT calculations have directly predicted the multiply twinned icosahedral and decahedral mNPs to be more stable than the $L1_0$ cuboctahedron [238].

For biomedical applications, the alloying of cobalt with more inert metals such as silver or gold has proved to be a valuable strategy to obtain biocompatibility and reduce oxidation. In accordance with the large differences in atomic radii in favour of inert metals, and weak Ag–Co/Au–Co miscibility predicted below 400 °C across all compositional space [427], theoretical studies have reported structures that favour Ag/Au surface segregation and the formation of core–shell orderings [402,428,429]. Experimental synthesis has confirmed theoretical predictions, and core–shell AuCo mNPs were found to have mostly icosahedral structure, although a novel morphology has been recently described consisting of a Co icosahedron surrounded by fcc Au facets [430–432]. In addition, reports have indicated that optical and magnetic properties may both be tuned by tailoring the size of the core and shell of Ag/AuCo mNPs. However, the fact that the surface of the nanoalloy is expected to contain mostly Au (or other noble and inert metals such as Ag or Pt) atoms does not invariably determine the chemical ordering of such systems. The size, structure, and chemical arrangement of bimetallic mNPs can be controlled experimentally throughout the synthesis protocol, allowing metal species to intermix and maximise the synergistic benefits available through their unique combination. For example, physical methods have been reported for the synthesis of AgNi disordered mNPs, which exhibited substantial enhancement in their optical limiting efficiency [433]. Core–shell AuNi NPs with inverted segregation (Au cores covered by Ni) have shown huge magnetisation, which was maintained even after the formation of NiO on the surface [434]. The hybrid AuCo systems are consequently also expected to offer unique properties in different chemical orderings because of the possible magnetoresistance effect and optical–magnetic bifunctionalities [435]. Although the limited literature on AuCo systems is almost exclusively focused on the core–shell structures, Marbella et al. have demonstrated the synthesis of discrete, composition-tuneable alloyed AuCo NPs with random ordering of Au and Co atoms, whose magnetic susceptibility can be tailored while maintaining almost identical particle size and surface chemistry [54]. Finally, a theoretical study has shown that magnetic effects can destabilise core–shell arrangement of AgCo and AuCo systems whose icosahedral structures remain preferential, but peculiar quantum effects reverse the energetics in favour of intermediate compositions, presenting a much more thorough intermixing with cobalt atoms [33].

The magnetic anisotropy of AuCo mNPs was calculated to be an order of magnitude higher for $L1_0$ ordering compared to the core–shell NPs of 1.5–2.0 nm in diameter. Predicted MAE values for cuboctahedron, icosahedron, and decahedron with the $L1_0$ ordering were 928.3, 1038.3, and 1011.7 kJ/m^3, respectively. A corresponding core–shell icosahedron showed MAE of 239.9 kJ/m^3, while the MAE of a decahedron with core–shell structure was found to be 278.2 kJ/m^3. Hence, $L1_0$ bimetallic AuCo mNPs show a 15-fold improvement from the anisotropy of a 1.5 nm monometallic Co icosahedron, which will hopefully trigger improved efforts in the synthesis of these systems and their use in biomedical applications.

4. Conclusions

With the advances in computational power and continuous improvements of DFT methods, the implementation of explicit NP models in simulations of nanoparticle systems should be encouraged, since they are a more realistic representation and able to capture the property dependence on size and morphology. Whilst cluster and extended slab models can often offer valuable insight into the nature of metal–adsorbate interaction, they fail to capture the progression and directional effects of magnetic properties.

DFT simulations of NP models have shown excellent correspondence with experimental measurements of magnetic moments and magnetic anisotropy energies of cobalt mNPs. They are able to properly describe morphology-induced alternations in the magnetic features, calculate ligand effects on both the binding metal centre and the particle as a whole, and predict the outcomes of alloy interfaces of different chemical orderings. It is thus expected that *ab initio* methods can also provide accurate structures and properties of magnetic mono- and bimetallic NPs that do not necessarily have cobalt in their composition.

Incorporation of NP models in research efforts to optimise the magnetic behaviour of metallic magnetic nanosystems for biomedical applications could hence facilitate the smarter design of application-specific properties.

Author Contributions: Conceptualisation, B.F.; Data curation, B.F.; Formal analysis, B.F.; Funding acquisition, N.H.d.L.; Visualization, B.F.; Writing—original draft, B.F.; Writing—review and editing, B.F. and N.H.d.L. Both authors have read and agreed to the published version of the manuscript.

Funding: This study was funded by the Engineering and Physical Sciences Research Council (Grant Nos. EP/R512503/1 and EP/K009567/2). The Cardiff University School of Chemistry has supported BF's PhD studies through a Research Scholarship.

Institutional Review Board Statement: Not applicable.

Informed Consent Statement: Not applicable.

Data Availability Statement: Data sharing is not applicable for this article.

Acknowledgments: Parts of this work were performed using the computational facilities of the Advanced Research Computing @ Cardiff (ARCCA) Division, Cardiff University.

Conflicts of Interest: The authors declare no conflict of interest. The funders had no role in the design of the study; in the collection, analyses, or interpretation of data; in the writing of the manuscript; or in the decision to publish the results.

References

1. Tabor, C.; Narayanan, R.; El-Sayed, M.A. Catalysis with transition metal nanoparticles in colloidal solution: Heterogeneous or homogeneous? *Model Syst. Catal. Single Cryst. Support. Enzym. Mimics* **2010**, 395–414. [CrossRef]
2. Garcia, M.A. Surface plasmons in metallic nanoparticles: Fundamentals and applications. *J. Phys. D Appl. Phys.* **2012**, *45*, 389501. [CrossRef]
3. An, K.; Somorjai, G.A. Size and Shape Control of Metal Nanoparticles for Reaction Selectivity in Catalysis. *ChemCatChem* **2012**, *4*, 1512–1524. [CrossRef]
4. Zhang, L.; Anderson, R.M.; Crooks, R.M.; Henkelman, G. Correlating structure and function of metal nanoparticles for catalysis. *Surf. Sci.* **2015**, *640*, 65–72. [CrossRef]
5. Ko, S.H.; Park, I.; Pan, H.; Grigoropoulos, C.P.; Pisano, A.P.; Luscombe, C.K.; Fréchet, J.M.J. Direct nanoimprinting of metal nanoparticles for nanoscale electronics fabrication. *Nano Lett.* **2007**, *7*, 1869–1877. [CrossRef]
6. Son, Y.; Yeo, J.; Moon, H.; Lim, T.W.; Hong, S.; Nam, K.H.; Yoo, S.; Grigoropoulos, C.P.; Yang, D.Y.; Ko, S.H. Nanoscale electronics: Digital fabrication by direct femtosecond laser processing of metal nanoparticles. *Adv. Mater.* **2011**, *23*, 3176–3181. [CrossRef]
7. Liu, S.; Yuen, M.C.; White, E.L.; Boley, J.W.; Deng, B.; Cheng, G.J.; Kramer-Bottiglio, R. Laser Sintering of Liquid Metal Nanoparticles for Scalable Manufacturing of Soft and Flexible Electronics. *ACS Appl. Mater. Interfaces* **2018**, *10*, 28232–28241. [CrossRef]
8. Sosa, I.O.; Noguez, C.; Barrera, R.G. Optical properties of metal nanoparticles with arbitrary shapes. *J. Phys. Chem. B* **2003**, *107*, 6269–6275. [CrossRef]
9. Murphy, C.J.; Sau, T.K.; Gole, A.M.; Orendorff, C.J.; Gao, J.; Gou, L.; Hunyadi, S.E.; Li, T. Anisotropic metal nanoparticles: Synthesis, assembly, and optical applications. *J. Phys. Chem. B* **2005**, *109*, 13857–13870. [CrossRef]
10. Zijlstra, P.; Orrit, M. Single metal nanoparticles: Optical detection, spectroscopy and applications. *Rep. Prog. Phys.* **2011**, *74*, 106401. [CrossRef]
11. Kelly, K.L.; Coronado, E.; Zhao, L.L.; Schatz, G.C. The Optical Properties of Metal Nanoparticles: The Influence of Size, Shape, and Dielectric Environment. *J. Phys. Chem. B* **2003**, *107*, 668–677. [CrossRef]
12. Wan, D.; Chen, H.L.; Tseng, S.C.; Wang, L.A.; Chen, Y.P. One-shot deep-UV pulsed-laser-induced photomodification of hollow metal nanoparticles for high-density data storage on flexible substrates. *ACS Nano* **2010**, *4*, 165–173. [CrossRef]
13. Sun, X.; Huang, Y.; Nikles, D.E. FePt and CoPt magnetic nanoparticles film for future high density data storage media. *Int. J. Nanotechnol.* **2004**, *1*, 328–346. [CrossRef]
14. Kang, M.; Baeg, K.J.; Khim, D.; Noh, Y.Y.; Kim, D.Y. Printed, flexible, organic nano-floating-gate memory: Effects of metal nanoparticles and blocking dielectrics on memory characteristics. *Adv. Funct. Mater.* **2013**, *23*, 3503–3512. [CrossRef]
15. Liao, H.; Nehl, C.L.; Hafner, J.H. Biomedical applications of plasmon resonant metal nanoparticles. *Nanomedicine* **2006**, *1*, 201–208. [CrossRef]
16. Zeisberger, M.; Dutz, S.; Müller, R.; Hergt, R.; Matoussevitch, N.; Bönnemann, H. Metallic cobalt nanoparticles for heating applications. *J. Magn. Magn. Mater.* **2007**, *311*, 224–227. [CrossRef]
17. Cherukuri, P.; Glazer, E.S.; Curley, S.A. Targeted hyperthermia using metal nanoparticles. *Adv. Drug Deliv. Rev.* **2010**, *62*, 339–345. [CrossRef]
18. Sharma, H.; Mishra, P.K.; Talegaonkar, S.; Vaidya, B. Metal nanoparticles: A theranostic nanotool against cancer. *Drug Discov. Today* **2015**, *20*, 1143–1151. [CrossRef]
19. Rai, M.; Ingle, A.P.; Birla, S.; Yadav, A.; Santos, C.A. Dos Strategic role of selected noble metal nanoparticles in medicine. *Crit. Rev. Microbiol.* **2016**, *42*, 696–719. [CrossRef]
20. Xia, Y.; Xiong, Y.; Lim, B.; Skrabalak, S.E. Shape-controlled synthesis of metal nanocrystals: Simple chemistry meets complex physics? *Angew. Chem. Int. Ed.* **2009**, *48*, 60–103. [CrossRef]
21. Vajda, S.; Pellin, M.J.; Greeley, J.P.; Marshall, C.L.; Curtiss, L.A.; Ballentine, G.A.; Elam, J.W.; Catillon-Mucherie, S.; Redfern, P.C.; Mehmood, F.; et al. Subnanometre platinum clusters as highly active and selective catalysts for the oxidative dehydrogenation of propane. *Nat. Mater.* **2009**, *8*, 213–216. [CrossRef]
22. Grassian, V.H. When size really matters: Size-dependent properties and surface chemistry of metal and metal oxide nanoparticles in gas and liquid phase environments. *J. Phys. Chem. C* **2008**, *112*, 18303–18313. [CrossRef]
23. Carlson, C.; Hussein, S.M.; Schrand, A.M.; Braydich-Stolle, L.K.; Hess, K.L.; Jones, R.L.; Schlager, J.J. Unique cellular interaction of silver nanoparticles: Size-dependent generation of reactive oxygen species. *J. Phys. Chem. B* **2008**, *112*, 13608–13619. [CrossRef]
24. Balamurugan, B.; Maruyama, T. Evidence of an enhanced interband absorption in Au nanoparticles: Size-dependent electronic structure and optical properties. *Appl. Phys. Lett.* **2005**, *87*, 143105. [CrossRef]
25. Xiong, S.; Qi, W.; Cheng, Y.; Huang, B.; Wang, M.; Li, Y. Universal relation for size dependent thermodynamic properties of metallic nanoparticles. *Phys. Chem. Chem. Phys.* **2011**, *13*, 10652–10660. [CrossRef]
26. Haldar, K.K.; Kundu, S.; Patra, A. Core-size-dependent catalytic properties of bimetallic Au/Ag core-shell nanoparticles. *ACS Appl. Mater. Interfaces* **2014**, *6*, 21946–21953. [CrossRef]
27. Neubauer, N.; Palomaeki, J.; Karisola, P.; Alenius, H.; Kasper, G. Size-dependent ROS production by palladium and nickel nanoparticles in cellular and acellular environments - An indication for the catalytic nature of their interactions. *Nanotoxicology* **2015**, *9*, 1059–1066. [CrossRef] [PubMed]

28. Dong, C.; Lian, C.; Hu, S.; Deng, Z.; Gong, J.; Li, M.; Liu, H.; Xing, M.; Zhang, J. Size-dependent activity and selectivity of carbon dioxide photocatalytic reduction over platinum nanoparticles. *Nat. Commun.* **2018**, *9*, 1252. [CrossRef] [PubMed]
29. Mourdikoudis, S.; Pallares, R.M.; Thanh, N.T.K. Characterization techniques for nanoparticles: Comparison and complementarity upon studying nanoparticle properties. *Nanoscale* **2018**, *10*, 12871–12934. [CrossRef] [PubMed]
30. Yan, Z.; Taylor, M.G.; Mascareno, A.; Mpourmpakis, G. Size-, Shape-, and Composition-Dependent Model for Metal Nanoparticle Stability Prediction. *Nano Lett.* **2018**, *18*, 2696–2704. [CrossRef] [PubMed]
31. Taylor, M.G.; Austin, N.; Gounaris, C.E.; Mpourmpakis, G. Catalyst Design Based on Morphology- and Environment-Dependent Adsorption on Metal Nanoparticles. *ACS Catal.* **2015**, *5*, 6296–6301. [CrossRef]
32. Kozlov, S.M.; Kovács, G.; Ferrando, R.; Neyman, K.M. How to determine accurate chemical ordering in several nanometer large bimetallic crystallites from electronic structure calculations. *Chem. Sci.* **2015**, *6*, 3868–3880. [CrossRef]
33. Ferrando, R.; Fortunelli, A.; Rossi, G. Quantum effects on the structure of pure and binary metallic nanoclusters. *Phys. Rev. B Condens. Matter Mater. Phys.* **2005**, *72*, 085449. [CrossRef]
34. Zhu, B.; Xu, Z.; Wang, C.; Gao, Y. Shape Evolution of Metal Nanoparticles in Water Vapor Environment. *Nano Lett.* **2016**, *16*, 2628–2632. [CrossRef]
35. Sangaiya, P.; Jayaprakash, R. A Review on Iron Oxide Nanoparticles and Their Biomedical Applications. *J. Supercond. Nov. Magn.* **2018**, *31*, 3397–3413. [CrossRef]
36. Lima-Tenório, M.K.; Gómez Pineda, E.A.; Ahmad, N.M.; Fessi, H.; Elaissari, A. Magnetic nanoparticles: In vivo cancer diagnosis and therapy. *Int. J. Pharm.* **2015**, *493*, 313–327. [CrossRef]
37. Hervault, A.; Thanh, N.T.K. Magnetic nanoparticle-based therapeutic agents for thermo-chemotherapy treatment of cancer. *Nanoscale* **2014**, *6*, 11553–11573. [CrossRef]
38. Laurent, S.; Dutz, S.; Häfeli, U.O.; Mahmoudi, M. Magnetic fluid hyperthermia: Focus on superparamagnetic iron oxide nanoparticles. *Adv. Colloid Interface Sci.* **2011**, *166*, 8–23. [CrossRef]
39. Singh, A.; Sahoo, S.K. Magnetic nanoparticles: A novel platform for cancer theranostics. *Drug Discov. Today* **2014**, *19*, 474–481. [CrossRef]
40. Périgo, E.A.; Hemery, G.; Sandre, O.; Ortega, D.; Garaio, E.; Plazaola, F.; Teran, F.J. Fundamentals and advances in magnetic hyperthermia. *Appl. Phys. Rev.* **2015**, *2*, 041302. [CrossRef]
41. Hedayatnasab, Z.; Abnisa, F.; Daud, W.M.A.W. Review on magnetic nanoparticles for magnetic nanofluid hyperthermia application. *Mater. Des.* **2017**, *123*, 174–196. [CrossRef]
42. Felder, R.C.; Parker, J.A. Principles of nuclear magnetic resonance imaging. *Med. Instrum.* **1985**, *19*, 248–256. [CrossRef] [PubMed]
43. Geva, T. Magnetic resonance imaging: Historical perspective. *J. Cardiovasc. Magn. Reson.* **2006**, *8*, 573–580. [CrossRef] [PubMed]
44. Grover, V.P.B.; Tognarelli, J.M.; Crossey, M.M.E.; Cox, I.J.; Taylor-Robinson, S.D.; McPhail, M.J.W. Magnetic Resonance Imaging: Principles and Techniques: Lessons for Clinicians. *J. Clin. Exp. Hepatol.* **2015**, *5*, 246–255. [CrossRef]
45. Nattama, S.; Rahimi, M.; Wadajkar, A.S.; Koppolu, B.; Hua, J.; Nwariaku, F.; Nguyen, K.T. Characterization of polymer coated magnetic nanoparticles for targeted treatment of cancer. In Proceedings of the 2007 IEEE Dallas Engineering in Medicine and Biology Workshop, Dallas, TX, USA, 11–12 November 2007; 2007; pp. 35–38. [CrossRef]
46. Rahimi, M.; Wadajkar, A.; Subramanian, K.; Yousef, M.; Cui, W.; Hsieh, J.T.; Nguyen, K.T. In vitro evaluation of novel polymer-coated magnetic nanoparticles for controlled drug delivery. *Nanomed. Nanotechnol. Biol. Med.* **2010**, *6*, 672–680. [CrossRef]
47. Mu, Q.; Yang, L.; Davis, J.C.; Vankayala, R.; Hwang, K.C.; Zhao, J.; Yan, B. Biocompatibility of polymer grafted core/shell iron/carbon nanoparticles. *Biomaterials* **2010**, *31*, 5083–5090. [CrossRef]
48. Zhang, G.; Liao, Y.; Baker, I. Surface engineering of core/shell iron/iron oxide nanoparticles from microemulsions for hyperthermia. *Mater. Sci. Eng. C* **2010**, *30*, 92–97. [CrossRef]
49. Jafari, T.; Simchi, A.; Khakpash, N. Synthesis and cytotoxicity assessment of superparamagnetic iron-gold core-shell nanoparticles coated with polyglycerol. *J. Colloid Interface Sci.* **2010**, *345*, 64–71. [CrossRef]
50. Ansari, S.M.; Bhor, R.D.; Pai, K.R.; Sen, D.; Mazumder, S.; Ghosh, K.; Kolekar, Y.D.; Ramana, C.V. Cobalt nanoparticles for biomedical applications: Facile synthesis, physiochemical characterization, cytotoxicity behavior and biocompatibility. *Appl. Surf. Sci.* **2017**, *414*, 171–187. [CrossRef]
51. Parkes, L.M.; Hodgson, R.; Lu, L.T.; Tung, L.D.; Robinson, I.; Fernig, D.G.; Thanh, N.T.K. Cobalt nanoparticles as a novel magnetic resonance contrast agent-relaxivities at 1.5 and 3 Tesla. *Contrast Media Mol. Imaging* **2008**, *3*, 150–156. [CrossRef]
52. Lu, Y.; Zhao, Y.; Yu, L.; Dong, L.; Shi, C.; Hu, M.J.; Xu, Y.J.; Wen, L.P.; Yu, S.H. Hydrophilic Co@Au yolk/shell nanospheres: Synthesis, assembly, and application to gene delivery. *Adv. Mater.* **2010**, *22*, 1407–1411. [CrossRef]
53. Hrubovčák, P.; Zeleňáková, A.; Zeleňák, V.; Kovác, J. Superparamagnetism in cobalt nanoparticles coated by protective gold layer. *Acta Phys. Pol. A* **2014**, *126*, 216–217. [CrossRef]
54. Marbella, L.E.; Andolina, C.M.; Smith, A.M.; Hartmann, M.J.; Dewar, A.C.; Johnston, K.A.; Daly, O.H.; Millstone, J.E. Gold-cobalt nanoparticle alloys exhibiting tunable compositions, near-infrared emission, and high T2relaxivity. *Adv. Funct. Mater.* **2014**, *24*, 6532–6539. [CrossRef]
55. Bouchard, L.; Anwar, M.S.; Liu, G.L.; Hann, B.; Xie, Z.H.; Gray, J.W.; Wang, X.; Pines, A.; Chen, F.F. Picomolar sensitivity MRI and photoacoustic imaging of cobalt nanoparticles. *Proc. Natl. Acad. Sci. USA* **2009**, *106*, 4085–4089. [CrossRef]
56. Kosuge, H.; Sherlock, S.P.; Kitagawa, T.; Terashima, M.; Barral, J.K.; Nishimura, D.G.; Dai, H.; McConnell, M.V. FeCo/graphite nanocrystals for multi-modality imaging of experimental vascular inflammation. *PLoS ONE* **2011**, *6*, 14523. [CrossRef]

57. Seo, W.S.; Lee, J.H.; Sun, X.; Suzuki, Y.; Mann, D.; Liu, Z.; Terashima, M.; Yang, P.C.; McConnell, M.V.; Nishimura, D.G.; et al. FeCo/graphitic-shell nanocrystals as advanced magnetic-resonance-imaging and near-infrared agents. *Nat. Mater.* **2006**, *5*, 971–976. [CrossRef]
58. Habib, A.H.; Ondeck, C.L.; Chaudhary, P.; Bockstaller, M.R.; McHenry, M.E. Evaluation of iron-cobalt/ferrite core-shell nanoparticles for cancer thermotherapy. *J. Appl. Phys.* **2008**, *103*, 07A307. [CrossRef]
59. Xu, Y.H.; Bai, J.; Wang, J.P. High-magnetic-moment multifunctional nanoparticles for nanomedicine applications. *J. Magn. Magn. Mater.* **2007**, *311*, 131–134. [CrossRef]
60. Chen, C.L.; Kuo, L.R.; Lee, S.Y.; Hwu, Y.K.; Chou, S.W.; Chen, C.C.; Chang, F.H.; Lin, K.H.; Tsai, D.H.; Chen, Y.Y. Photothermal cancer therapy via femtosecond-laser-excited FePt nanoparticles. *Biomaterials* **2013**, *34*, 1128–1134. [CrossRef]
61. Choi, J.S.; Jun, Y.W.; Yeon, S.I.; Kim, H.C.; Shin, J.S.; Cheon, J. Biocompatible heterostructured nanoparticles for multimodal biological detection. *J. Am. Chem. Soc.* **2006**, *128*, 15982–15983. [CrossRef]
62. Yang, H.; Zhang, J.; Tian, Q.; Hu, H.; Fang, Y.; Wu, H.; Yang, S. One-pot synthesis of amphiphilic superparamagnetic FePt nanoparticles and magnetic resonance imaging in vitro. *J. Magn. Magn. Mater.* **2010**, *322*, 973–977. [CrossRef]
63. Liu, Y.; Wu, P.C.; Guo, S.; Chou, P.T.; Deng, C.; Chou, S.W.; Yuan, Z.; Liu, T.M. Low-toxicity FePt nanoparticles for the targeted and enhanced diagnosis of breast tumors using few centimeters deep whole-body photoacoustic imaging. *Photoacoustics* **2020**, *19*, 100179. [CrossRef] [PubMed]
64. Liang, S.Y.; Zhou, Q.; Wang, M.; Zhu, Y.H.; Wu, Q.Z.; Yang, X.L. Water-soluble l-cysteine-coated FePt nanoparticles as dual MRI/CT imaging contrast agent for glioma. *Int. J. Nanomed.* **2015**, *10*, 2325–2333. [CrossRef]
65. Chou, S.W.; Shau, Y.H.; Wu, P.C.; Yang, Y.S.; Shieh, D.B.; Chen, C.C. In vitro and in vivo studies of fept nanoparticles for dual modal CT/MRI molecular imaging. *J. Am. Chem. Soc.* **2010**, *132*, 13270–13278. [CrossRef]
66. Sun, H.; Chen, X.; Chen, D.; Dong, M.; Fu, X.; Li, Q.; Liu, X.; Wu, Q.; Qiu, T.; Wan, T.; et al. Influences of surface coatings and components of FePt nanoparticles on the suppression of glioma cell proliferation. *Int. J. Nanomed.* **2012**, *7*, 3295–3307. [CrossRef]
67. Seemann, K.M.; Luysberg, M.; Révay, Z.; Kudejova, P.; Sanz, B.; Cassinelli, N.; Loidl, A.; Ilicic, K.; Multhoff, G.; Schmid, T.E. Magnetic heating properties and neutron activation of tungsten-oxide coated biocompatible FePt core-shell nanoparticles. *J. Control. Release* **2015**, *197*, 131–137. [CrossRef]
68. Fuchigami, T.; Kawamura, R.; Kitamoto, Y.; Nakagawa, M.; Namiki, Y. A magnetically guided anti-cancer drug delivery system using porous FePt capsules. *Biomaterials* **2012**, *33*, 1682–1687. [CrossRef]
69. Salati, A.; Ramazani, A.; Almasi Kashi, M. Deciphering magnetic hyperthermia properties of compositionally and morphologically modulated FeNi nanoparticles using first-order reversal curve analysis. *Nanotechnology* **2019**, *30*, 025707. [CrossRef]
70. Salati, A.; Ramazani, A.; Almasi Kashi, M. Tuning hyperthermia properties of FeNiCo ternary alloy nanoparticles by morphological and magnetic characteristics. *J. Magn. Magn. Mater.* **2020**, *498*, 166172. [CrossRef]
71. Liu, H.M.; Wu, S.H.; Lu, C.W.; Yao, M.; Hsiao, J.K.; Hung, Y.; Lin, Y.S.; Mou, C.Y.; Yang, C.S.; Huang, D.M.; et al. Mesoporous silica nanoparticles improve magnetic labeling efficiency in human stem cells. *Small* **2008**, *4*, 619–626. [CrossRef]
72. Tanaka, K.; Narita, A.; Kitamura, N.; Uchiyama, W.; Morita, M.; Inubushi, T.; Chujo, Y. Preparation for highly sensitive MRI contrast agents using core/shell type nanoparticles consisting of multiple SPIO cores with thin silica coating. *Langmuir* **2010**, *26*, 11759–11762. [CrossRef]
73. Chen, W.-J.; Tsai, P.-J.; Chen, Y.-C. Functional Fe_3O_4/TiO_2 Core/Shell Magnetic Nanoparticles as Photokilling Agents for Pathogenic Bacteria. *Small* **2008**, *4*, 485–491. [CrossRef]
74. Estelrich, J.; Sánchez-Martín, M.J.; Busquets, M.A. Nanoparticles in magnetic resonance imaging: From simple to dual contrast agents. *Int. J. Nanomed.* **2015**, *10*, 1727–1741. [CrossRef]
75. Liu, W.; Zhang, Y.; Ge, S.; Song, X.; Huang, J.; Yan, M.; Yu, J. Core-shell Fe_3O_4-Au magnetic nanoparticles based nonenzymatic ultrasensitive electrochemiluminescence immunosensor using quantum dots functionalized graphene sheet as labels. *Anal. Chim. Acta* **2013**, *770*, 132–139. [CrossRef]
76. Wang, X.; Wang, M.; Jiang, T.; Wang, F.; Qing, Y.; Bu, S.; Zhou, J. Dual-functional Fe_3O_4@SiO_2@Ag triple core-shell microparticles as an effective SERS platform for adipokines detection. *Colloids Surfaces A Physicochem. Eng. Asp.* **2017**, *535*, 24–33. [CrossRef]
77. Wang, L.; Bai, J.; Li, Y.; Huang, Y. Multifunctional nanoparticles displaying magnetization and near-IR absorption. *Angew. Chem. Int. Ed.* **2008**, *47*, 2439–2442. [CrossRef]
78. Qiu, J.D.; Xiong, M.; Liang, R.P.; Peng, H.P.; Liu, F. Synthesis and characterization of ferrocene modified Fe_3O_4@Au magnetic nanoparticles and its application. *Biosens. Bioelectron.* **2009**, *24*, 2649–2653. [CrossRef]
79. Caizer, C.; Hrianca, I. The temperature dependence of saturation magnetization of γ-Fe2O3/SiO2 magnetic nanocomposite. *Ann. Phys.* **2003**, *12*, 115–122. [CrossRef]
80. Pinho, S.L.C.; Pereira, G.A.; Voisin, P.; Kassem, J.; Bouchaud, V.; Etienne, L.; Peters, J.A.; Carlos, L.; Mornet, S.; Geraldes, C.F.G.C.; et al. Fine tuning of the relaxometry of γ-Fe_2O_3@SiO_2 nanoparticles by tweaking the silica coating thickness. *ACS Nano* **2010**, *4*, 5339–5349. [CrossRef]
81. Park, J.Y.; Choi, E.S.; Baek, M.J.; Lee, G.H.; Woo, S.; Chang, Y. Water-soluble Ultra Small paramagnetic or superparamagnetic metal oxide nanoparticles for molecular MR imaging. *Eur. J. Inorg. Chem.* **2009**, 2477–2481. [CrossRef]
82. Schweiger, C.; Pietzonka, C.; Heverhagen, J.; Kissel, T. Novel magnetic iron oxide nanoparticles coated with poly(ethylene imine)-g-poly(ethylene glycol) for potential biomedical application: Synthesis, stability, cytotoxicity and MR imaging. *Int. J. Pharm.* **2011**, *408*, 130–137. [CrossRef]

83. Zhao, Z.; Sun, C.; Bao, J.; Yang, L.; Wei, R.; Cheng, J.; Lin, H.; Gao, J. Surface manganese substitution in magnetite nanocrystals enhances: T1 contrast ability by increasing electron spin relaxation. *J. Mater. Chem. B* **2018**, *6*, 401–413. [CrossRef]
84. Demirci Dönmez, C.E.; Manna, P.K.; Nickel, R.; Aktürk, S.; Van Lierop, J. Comparative Heating Efficiency of Cobalt-, Manganese-, and Nickel-Ferrite Nanoparticles for a Hyperthermia Agent in Biomedicines. *ACS Appl. Mater. Interfaces* **2019**, *11*, 6858–6866. [CrossRef]
85. Amiri, S.; Shokrollahi, H. The role of cobalt ferrite magnetic nanoparticles in medical science. *Mater. Sci. Eng. C* **2013**, *33*, 1–8. [CrossRef]
86. Dey, C.; Baishya, K.; Ghosh, A.; Goswami, M.M.; Ghosh, A.; Mandal, K. Improvement of drug delivery by hyperthermia treatment using magnetic cubic cobalt ferrite nanoparticles. *J. Magn. Magn. Mater.* **2017**, *427*, 168–174. [CrossRef]
87. Pita, M.; Abad, J.M.; Vaz-Dominguez, C.; Briones, C.; Mateo-Martí, E.; Martín-Gago, J.A.; del Puerto Morales, M.; Fernández, V.M. Synthesis of cobalt ferrite core/metallic shell nanoparticles for the development of a specific PNA/DNA biosensor. *J. Colloid Interface Sci.* **2008**, *321*, 484–492. [CrossRef]
88. Dumitrescu, A.M.; Slatineanu, T.; Poiata, A.; Iordan, A.R.; Mihailescu, C.; Palamaru, M.N. Advanced composite materials based on hydrogels and ferrites for potential biomedical applications. *Colloids Surfaces A Physicochem. Eng. Asp.* **2014**, *455*, 185–194. [CrossRef]
89. Lasheras, X.; Insausti, M.; Gil De Muro, I.; Garaio, E.; Plazaola, F.; Moros, M.; De Matteis, L.; De La Fuente, J.; Lezama, L.M. Chemical Synthesis and Magnetic Properties of Monodisperse Nickel Ferrite Nanoparticles for Biomedical Applications. *J. Phys. Chem. C* **2016**, *120*, 3492–3500. [CrossRef]
90. Menelaou, M.; Georgoula, K.; Simeonidis, K.; Dendrinou-Samara, C. Evaluation of nickel ferrite nanoparticles coated with oleylamine by NMR relaxation measurements and magnetic hyperthermia. *Dalt. Trans.* **2014**, *43*, 3626–3636. [CrossRef] [PubMed]
91. Ahmad, T.; Bae, H.; Iqbal, Y.; Rhee, I.; Hong, S.; Chang, Y.; Lee, J.; Sohn, D. Chitosan-coated nickel-ferrite nanoparticles as contrast agents in magnetic resonance imaging. *J. Magn. Magn. Mater.* **2015**, *381*, 151–157. [CrossRef]
92. Liu, Y.; Lv, X.; Liu, H.; Zhou, Z.; Huang, J.; Lei, S.; Cai, S.; Chen, Z.; Guo, Y.; Chen, Z.; et al. Porous gold nanocluster-decorated manganese monoxide nanocomposites for microenvironment-activatable MR/photoacoustic/CT tumor imaging. *Nanoscale* **2018**, *10*, 3631–3638. [CrossRef] [PubMed]
93. Kim, T.; Momin, E.; Choi, J.; Yuan, K.; Zaidi, H.; Kim, J.; Park, M.; Lee, N.; McMahon, M.T.; Quinones-Hinojosa, A.; et al. Mesoporous silica-coated hollow manganese oxide nanoparticles as positive T1 contrast agents for labeling and MRI tracking of adipose-derived mesenchymal stem cells. *J. Am. Chem. Soc.* **2011**, *133*, 2955–2961. [CrossRef] [PubMed]
94. Caravan, P.; Ellison, J.J.; McMurry, T.J.; Lauffer, R.B. Gadolinium(III) chelates as MRI contrast agents: Structure, dynamics, and applications. *Chem. Rev.* **1999**, *99*, 2293–2352. [CrossRef]
95. Na, H.B.; Song, I.C.; Hyeon, T. Inorganic nanoparticles for MRI contrast agents. *Adv. Mater.* **2009**, *21*, 2133–2148. [CrossRef]
96. Wahsner, J.; Gale, E.M.; Rodríguez-Rodríguez, A.; Caravan, P. Chemistry of MRI contrast agents: Current challenges and new frontiers. *Chem. Rev.* **2019**, *119*, 957–1057. [CrossRef]
97. De Leõn-Rodríguez, L.M.; Martins, A.F.; Pinho, M.C.; Rofsky, N.M.; Sherry, A.D. Basic MR relaxation mechanisms and contrast agent design. *J. Magnet. Reson. Imaging* **2015**, *42*, 545–565. [CrossRef]
98. Moreno-Romero, J.A.; Segura, S.; Mascaró, J.M.; Cowper, S.E.; Julià, M.; Poch, E.; Botey, A.; Herrero, C. Nephrogenic systemic fibrosis: A case series suggesting gadolinium as a possible aetiological factor. *Br. J. Dermatol.* **2007**, *157*, 783–787. [CrossRef]
99. Hasebroock, K.M.; Serkova, N.J. Toxicity of MRI and CT contrast agents. *Expert Opin. Drug Metab. Toxicol.* **2009**, *5*, 403–416. [CrossRef]
100. Khalkhali, M.; Rostamizadeh, K.; Sadighian, S.; Khoeini, F.; Naghibi, M.; Hamidi, M. The impact of polymer coatings on magnetite nanoparticles performance as MRI contrast agents: A comparative study. *DARU J. Pharm. Sci.* **2015**, *23*, 45. [CrossRef]
101. Fernández-Barahona, I.; Muñoz-Hernando, M.; Ruiz-Cabello, J.; Herranz, F.; Pellico, J. Iron oxide nanoparticles: An alternative for positive contrast in magnetic resonance imaging. *Inorganics* **2020**, *8*, 28. [CrossRef]
102. Tromsdorf, U.I.; Bruns, O.T.; Salmen, S.C.; Beisiegel, U.; Weller, H. A highly effective, nontoxic T1 MR contrast agent based on ultrasmall PEGylated iron oxide nanoparticles. *Nano Lett.* **2009**, *9*, 4434–4440. [CrossRef]
103. Iqbal, M.Z.; Ma, X.; Chen, T.; Zhang, L.; Ren, W.; Xiang, L.; Wu, A. Silica-coated super-paramagnetic iron oxide nanoparticles (SPIONPs): A new type contrast agent of T1 magnetic resonance imaging (MRI). *J. Mater. Chem. B* **2015**, *3*, 5172–5181. [CrossRef]
104. Alipour, A.; Soran-Erdem, Z.; Utkur, M.; Sharma, V.K.; Algin, O.; Saritas, E.U.; Demir, H.V. A new class of cubic SPIONs as a dual-mode T1 and T2 contrast agent for MRI. *Magn. Reson. Imaging* **2018**, *49*, 16–24. [CrossRef]
105. Jeon, M.; Halbert, M.V.; Stephen, Z.R.; Zhang, M. Iron Oxide Nanoparticles as T1 Contrast Agents for Magnetic Resonance Imaging: Fundamentals, Challenges, Applications, and Prospectives. *Adv. Mater.* **2020**, *33*, 1906539. [CrossRef]
106. Cao, Y.; Mao, Z.; He, Y.; Kuang, Y.; Liu, M.; Zhou, Y.; Zhang, Y.; Pei, R. Extremely Small Iron Oxide Nanoparticle-Encapsulated Nanogels as a Glutathione-Responsive T1Contrast Agent for Tumor-Targeted Magnetic Resonance Imaging. *ACS Appl. Mater. Interfaces* **2020**, *12*, 26973–26981. [CrossRef]
107. Kiessling, F.; Mertens, M.E.; Grimm, J.; Lammers, T. Nanoparticles for imaging: Top or flop? *Radiology* **2014**, *273*, 10–28. [CrossRef]
108. Wang, Y.-X.J. Superparamagnetic iron oxide based MRI contrast agents: Current status of clinical application. *Quant. Imaging Med. Surg.* **2011**, *1*, 35–40. [CrossRef]
109. Wang, Y.-X.J. Current status of superparamagnetic iron oxide contrast agents for liver magnetic resonance imaging. *World J. Gastroenterol.* **2015**, *21*, 13400. [CrossRef] [PubMed]

110. Taylor, R.M.; Huber, D.L.; Monson, T.C.; Esch, V.; Sillerud, L.O. Structural and magnetic characterization of superparamagnetic iron platinum nanoparticle contrast agents for magnetic resonance imaging. *J. Vac. Sci. Technol. B Nanotechnol. Microelectron. Mater. Process. Meas. Phenom.* **2012**, *30*, 02C101. [CrossRef] [PubMed]
111. Carpenter, E.E. Iron nanoparticles as potential magnetic carriers. *J. Magn. Magn. Mater.* **2001**, *225*, 17–20. [CrossRef]
112. Hadjipanayis, C.G.; Bonder, M.J.; Balakrishnan, S.; Wang, X.; Mao, H.; Hadjipanayis, G.C. Metallic iron nanoparticles for MRI contrast enhancement and local hyperthermia. *Small* **2008**, *4*, 1925–1929. [CrossRef]
113. Bergs, J.W.J.; Franken, N.A.P.; Haveman, J.; Geijsen, E.D.; Crezee, J.; van Bree, C. Hyperthermia, cisplatin and radiation trimodality treatment: A promising cancer treatment? A review from preclinical studies to clinical application. *Int. J. Hyperth.* **2007**, *23*, 329–341. [CrossRef]
114. Chicheł, A.; Skowronek, J.; Kubaszewska, M.; Kanikowski, M. Hyperthermia - Description of a method and a review of clinical applications. *Rep. Pract. Oncol. Radiother.* **2007**, *12*, 267–275. [CrossRef]
115. Saniei, N. Hyperthermia and cancer treatment. *Heat Transf. Eng.* **2009**, *30*, 915–917. [CrossRef]
116. Thomas, L.A.; Dekker, L.; Kallumadil, M.; Southern, P.; Wilson, M.; Nair, S.P.; Pankhurst, Q.A.; Parkin, I.P. Carboxylic acid-stabilised iron oxide nanoparticles for use in magnetic hyperthermia. *J. Mater. Chem.* **2009**, *19*, 6529–6535. [CrossRef]
117. Shah, R.R.; Davis, T.P.; Glover, A.L.; Nikles, D.E.; Brazel, C.S. Impact of magnetic field parameters and iron oxide nanoparticle properties on heat generation for use in magnetic hyperthermia. *J. Magn. Magn. Mater.* **2015**, *387*, 96–106. [CrossRef]
118. Bauer, L.M.; Situ, S.F.; Griswold, M.A.; Samia, A.C.S. High-performance iron oxide nanoparticles for magnetic particle imaging-guided hyperthermia (hMPI). *Nanoscale* **2016**, *8*, 12162–12169. [CrossRef]
119. Abenojar, E.C.; Wickramasinghe, S.; Bas-Concepcion, J.; Samia, A.C.S. Structural effects on the magnetic hyperthermia properties of iron oxide nanoparticles. *Prog. Nat. Sci. Mater. Int.* **2016**, *26*, 440–448. [CrossRef]
120. Jeyadevan, B. Present status and prospects of magnetite nanoparticles-based hyperthermia. *J. Ceram. Soc. Japan* **2010**, *118*, 391–401. [CrossRef]
121. Maier-Hauff, K.; Rothe, R.; Scholz, R.; Gneveckow, U.; Wust, P.; Thiesen, B.; Feussner, A.; Deimling, A.; Waldoefner, N.; Felix, R.; et al. Intracranial thermotherapy using magnetic nanoparticles combined with external beam radiotherapy: Results of a feasibility study on patients with glioblastoma multiforme. *J. Neurooncol.* **2007**, *81*, 53–60. [CrossRef]
122. Johannsen, M.; Gneveckow, U.; Taymoorian, K.; Thiesen, B.; Waldöfner, N.; Scholz, R.; Jung, K.; Jordan, A.; Wust, P.; Loening, S.A. Morbidity and quality of life during thermotherapy using magnetic nanoparticles in locally recurrent prostate cancer: Results of a prospective phase I trial. *Int. J. Hyperth.* **2007**, *23*, 315–323. [CrossRef]
123. Johannsen, M.; Gneveckow, U.; Thiesen, B.; Taymoorian, K.; Cho, C.H.; Waldöfner, N.; Scholz, R.; Jordan, A.; Loening, S.A.; Wust, P. Thermotherapy of Prostate Cancer Using Magnetic Nanoparticles: Feasibility, Imaging, and Three-Dimensional Temperature Distribution. *Eur. Urol.* **2007**, *52*, 1653–1662. [CrossRef]
124. Dutz, S.; Hergt, R. Magnetic nanoparticle heating and heat transfer on a microscale: Basic principles, realities and physical limitations of hyperthermia for tumour therapy. *Int. J. Hyperth.* **2013**, *29*, 790–800. [CrossRef]
125. Nieskoski, M.D.; Trembly, B.S. Comparison of a single optimized coil and a Helmholtz pair for magnetic nanoparticle hyperthermia. *IEEE Trans. Biomed. Eng.* **2014**, *61*, 1642–1650. [CrossRef]
126. Ruuge, E.K.; Rusetski, A.N. Magnetic fluids as drug carriers: Targeted transport of drugs by a magnetic field. *J. Magn. Magn. Mater.* **1993**, *122*, 335–339. [CrossRef]
127. Voltairas, P.A.; Fotiadis, D.I.; Michalis, L.K. Hydrodynamics of magnetic drug targeting. *J. Biomech.* **2002**, *35*, 813–821. [CrossRef]
128. Grief, A.D.; Richardson, G. Mathematical modelling of magnetically targeted drug delivery. *J. Magn. Magn. Mater.* **2005**, *293*, 455–463. [CrossRef]
129. Iacob, G.; Rotariu, O.; Strachan, N.J.C.; Häfeli, U.O. Magnetizable needles and wires - Modeling an efficient way to target magnetic microspheres in vivo. *Biorheology* **2004**, *41*, 599–612. [PubMed]
130. Rosengart, A.J.; Kaminski, M.D.; Chen, H.; Caviness, P.L.; Ebner, A.D.; Ritter, J.A. Magnetizable implants and functionalized magnetic carriers: A novel approach for noninvasive yet targeted drug delivery. *J. Magn. Magn. Mater.* **2005**, *293*, 633–638. [CrossRef]
131. Rotariu, O.; Strachan, N.J.C. Modelling magnetic carrier particle targeting in the tumor microvasculature for cancer treatment. *J. Magn. Magn. Mater.* **2005**, *293*, 639–646. [CrossRef]
132. Yellen, B.B.; Forbes, Z.G.; Halverson, D.S.; Fridman, G.; Barbee, K.A.; Chorny, M.; Levy, R.; Friedman, G. Targeted drug delivery to magnetic implants for therapeutic applications. *J. Magn. Magn. Mater.* **2005**, *293*, 647–654. [CrossRef]
133. Maier-Hauff, K.; Ulrich, F.; Nestler, D.; Niehoff, H.; Wust, P.; Thiesen, B.; Orawa, H.; Budach, V.; Jordan, A. Efficacy and safety of intratumoral thermotherapy using magnetic iron-oxide nanoparticles combined with external beam radiotherapy on patients with recurrent glioblastoma multiforme. *J. Neurooncol.* **2011**, *103*, 317–324. [CrossRef]
134. Asín, L.; Ibarra, M.R.; Tres, A.; Goya, G.F. Controlled cell death by magnetic hyperthermia: Effects of exposure time, field amplitude, and nanoparticle concentration. *Pharm. Res.* **2012**, *29*, 1319–1327. [CrossRef]
135. Skumiel, A.; Kaczmarek, K.; Flak, D.; Rajnak, M.; Antal, I.; Brząkała, H. The influence of magnetic nanoparticle concentration with dextran polymers in agar gel on heating efficiency in magnetic hyperthermia. *J. Mol. Liq.* **2020**, *304*, 112734. [CrossRef]
136. Kumar, B.; Jalodia, K.; Kumar, P.; Gautam, H.K. Recent advances in nanoparticle-mediated drug delivery. *J. Drug Deliv. Sci. Technol.* **2017**, *41*, 260–268. [CrossRef]

137. Hergt, R.; Dutz, S.; Müller, R.; Zeisberger, M. Magnetic particle hyperthermia: Nanoparticle magnetism and materials development for cancer therapy. *J. Phys. Condens. Matter* **2006**, *18*, S2919. [CrossRef]
138. Vallejo-Fernandez, G.; Whear, O.; Roca, A.G.; Hussain, S.; Timmis, J.; Patel, V.; O'Grady, K. Mechanisms of hyperthermia in magnetic nanoparticles. *J. Phys. D Appl. Phys.* **2013**, *46*, 312001. [CrossRef]
139. Deatsch, A.E.; Evans, B.A. Heating efficiency in magnetic nanoparticle hyperthermia. *J. Magn. Magn. Mater.* **2014**, *354*, 163–172. [CrossRef]
140. Dennis, C.L.; Ivkov, R. Physics of heat generation using magnetic nanoparticles for hyperthermia. *Int. J. Hyperth.* **2013**, *29*, 715–729. [CrossRef]
141. Datta, N.R.; Ordóñez, S.G.; Gaipl, U.S.; Paulides, M.M.; Crezee, H.; Gellermann, J.; Marder, D.; Puric, E.; Bodis, S. Local hyperthermia combined with radiotherapy and-/or chemotherapy: Recent advances and promises for the future. *Cancer Treat. Rev.* **2015**, *41*, 742–753. [CrossRef]
142. Issels, R.D. Hyperthermia adds to chemotherapy. *Eur. J. Cancer* **2008**, *44*, 2546–2554. [CrossRef]
143. Orel, V.; Shevchenko, A.; Romanov, A.; Tselepi, M.; Mitrelias, T.; Barnes, C.H.W.; Burlaka, A.; Lukin, S.; Shchepotin, I. Magnetic properties and antitumor effect of nanocomplexes of iron oxide and doxorubicin. *Nanomed. Nanotechnol. Biol. Med.* **2015**, *11*, 47–55. [CrossRef]
144. Hahn, G.M. Potential for therapy of drugs and hyperthermia. *Cancer Res.* **1979**, *39*, 2264–2268.
145. Zhou, Z.; Sun, Y.; Shen, J.; Wei, J.; Yu, C.; Kong, B.; Liu, W.; Yang, H.; Yang, S.; Wang, W. Iron/iron oxide core/shell nanoparticles for magnetic targeting MRI and near-infrared photothermal therapy. *Biomaterials* **2014**, *35*, 7470–7478. [CrossRef]
146. Estelrich, J.; Antònia Busquets, M. Iron oxide nanoparticles in photothermal therapy. *Molecules* **2018**, *23*, 1567. [CrossRef]
147. Lee, C.W.; Wu, P.C.; Hsu, I.L.; Liu, T.M.; Chong, W.H.; Wu, C.H.; Hsieh, T.Y.; Guo, L.Z.; Tsao, Y.; Wu, P.T.; et al. New Templated Ostwald Ripening Process of Mesostructured FeOOH for Third-Harmonic Generation Bioimaging. *Small* **2019**, *15*, 1805086. [CrossRef]
148. De Paula, L.B.; Primo, F.L.; Pinto, M.R.; Morais, P.C.; Tedesco, A.C. Combination of hyperthermia and photodynamic therapy on mesenchymal stem cell line treated with chloroaluminum phthalocyanine magnetic-nanoemulsion. *J. Magn. Magn. Mater.* **2015**, *380*, 372–376. [CrossRef]
149. Di Corato, R.; Béalle, G.; Kolosnjaj-Tabi, J.; Espinosa, A.; Clément, O.; Silva, A.K.A.; Ménager, C.; Wilhelm, C. Combining magnetic hyperthermia and photodynamic therapy for tumor ablation with photoresponsive magnetic liposomes. *ACS Nano* **2015**, *9*, 2904–2916. [CrossRef]
150. De Paula, L.B.; Primo, F.L.; Jardim, D.R.; Morais, P.C.; Tedesco, A.C. Development, characterization, and in vitro trials of chloroaluminum phthalocyanine-magnetic nanoemulsion to hyperthermia and photodynamic therapies on glioblastoma as a biological model. *J. Appl. Phys.* **2012**, *111*, 07B307. [CrossRef]
151. Yang, K.; Wan, J.; Zhang, S.; Tian, B.; Zhang, Y.; Liu, Z. The influence of surface chemistry and size of nanoscale graphene oxide on photothermal therapy of cancer using ultra-low laser power. *Biomaterials* **2012**, *33*, 2206–2214. [CrossRef]
152. Ma, X.; Cheng, Y.; Huang, Y.; Tian, Y.; Wang, S.; Chen, Y. PEGylated gold nanoprisms for photothermal therapy at low laser power density. *RSC Adv.* **2015**, *5*, 81682–81688. [CrossRef]
153. Stern, J.M.; Kibanov Solomonov, V.V.; Sazykina, E.; Schwartz, J.A.; Gad, S.C.; Goodrich, G.P. Initial Evaluation of the Safety of Nanoshell-Directed Photothermal Therapy in the Treatment of Prostate Disease. *Int. J. Toxicol.* **2016**, *35*, 38–46. [CrossRef] [PubMed]
154. Winau, F.; Westphal, O.; Winau, R. Paul Ehrlich - In search of the magic bullet. *Microbes Infect.* **2004**, *6*, 786–789. [CrossRef] [PubMed]
155. Widder, K.; Flouret, G.; Senyei, A. Magnetic microspheres: Synthesis of a novel parenteral drug carrier. *J. Pharm. Sci.* **1979**, *68*, 79–82. [CrossRef]
156. Senyei, A.; Widder, K.; Czerlinski, G. Magnetic guidance of drug-carrying microspheres. *J. Appl. Phys.* **1978**, *49*, 3578–3583. [CrossRef]
157. Mosbach, K.; Schröder, U. Preparation and application of magnetic polymers for targeting of drugs. *FEBS Lett.* **1979**, *102*, 112–116. [CrossRef]
158. Kwon, G.S.; Okano, T. Polymeric micelles as new drug carriers. *Adv. Drug Deliv. Rev.* **1996**, *21*, 107–116. [CrossRef]
159. López-Dávila, V.; Seifalian, A.M.; Loizidou, M. Organic nanocarriers for cancer drug delivery. *Curr. Opin. Pharmacol.* **2012**, *12*, 414–419. [CrossRef]
160. Manatunga, D.C.; Godakanda, V.U.; de Silva, R.M.; de Silva, K.M.N. Recent developments in the use of organic–inorganic nanohybrids for drug delivery. *Wiley Interdiscip. Rev. Nanomed. Nanobiotechnol.* **2020**, *12*, e1605. [CrossRef]
161. Zhang, R.; Olin, H. Carbon nanomaterials as drug carriers: Real time drug release investigation. *Mater. Sci. Eng. C* **2012**, *32*, 1247–1252. [CrossRef]
162. Lim, D.J.; Sim, M.; Oh, L.; Lim, K.; Park, H. Carbon-based drug delivery carriers for cancer therapy. *Arch. Pharm. Res.* **2014**, *37*, 43–52. [CrossRef]
163. Partha, R.; Conyers, J.L. Biomedical applications of functionalized fullerene-based nanomaterials. *Int. J. Nanomed.* **2009**, *4*, 261–275. [CrossRef]
164. Rasheed, A.; Kumar C.K., A.; Sravanthi, V.V.N.S.S. Cyclodextrins as drug carrier molecule: A review. *Sci. Pharm.* **2008**, *76*, 567–598. [CrossRef]

165. Kratz, F. Albumin as a drug carrier: Design of prodrugs, drug conjugates and nanoparticles. *J. Control. Release* **2008**, *132*, 171–183. [CrossRef]
166. MacDiarmid, J.A.; Brahmbhatt, H. Minicells: Versatile vectors for targeted drug or si/shRNA cancer therapy. *Curr. Opin. Biotechnol.* **2011**, *22*, 909–916. [CrossRef]
167. Akash, M.S.H.; Rehman, K.; Parveen, A.; Ibrahim, M. Antibody-drug conjugates as drug carrier systems for bioactive agents. *Int. J. Polym. Mater. Polym. Biomater.* **2016**, *65*, 1–10. [CrossRef]
168. Barbé, C.; Bartlett, J.; Kong, L.; Finnie, K.; Lin, H.Q.; Larkin, M.; Calleja, S.; Bush, A.; Calleja, G. Silica particles: A novel drug-delivery system. *Adv. Mater.* **2004**, *16*, 1959–1966. [CrossRef]
169. Oussoren, C.; Storm, G. Liposomes to target the lymphatics by subcutaneous administration. *Adv. Drug Deliv. Rev.* **2001**, *50*, 143–156. [CrossRef]
170. Städler, B.; Price, A.D.; Zelikin, A.N. A critical look at multilayered polymer capsules in biomedicine: Drug carriers, artificial organelles, and cell mimics. *Adv. Funct. Mater.* **2011**, *21*, 14–28. [CrossRef]
171. Kataoka, K.; Harada, A.; Nagasaki, Y. Block copolymer micelles for drug delivery: Design, characterization and biological significance. *Adv. Drug Deliv. Rev.* **2012**, *64*, 37–48. [CrossRef]
172. Moyano, D.F.; Goldsmith, M.; Solfiell, D.J.; Landesman-Milo, D.; Miranda, O.R.; Peer, D.; Rotello, V.M. Nanoparticle hydrophobicity dictates immune response. *J. Am. Chem. Soc.* **2012**, *134*, 3965–3967. [CrossRef]
173. Corbo, C.; Molinaro, R.; Parodi, A.; Toledano Furman, N.E.; Salvatore, F.; Tasciotti, E. The impact of nanoparticle protein corona on cytotoxicity, immunotoxicity and target drug delivery. *Nanomedicine* **2016**, *11*, 81–100. [CrossRef]
174. Jain, T.K.; Morales, M.A.; Sahoo, S.K.; Leslie-Pelecky, D.L.; Labhasetwar, V. Iron Oxide Nanoparticles for Sustained Delivery of Anticancer Agents. *Mol. Pharm.* **2005**, *2*, 194–205. [CrossRef]
175. Estelrich, J.; Escribano, E.; Queralt, J.; Busquets, M.A. Iron oxide nanoparticles for magnetically-guided and magnetically-responsive drug delivery. *Int. J. Mol. Sci.* **2015**, *16*, 8070–8101. [CrossRef]
176. Wahajuddin, S.A. Superparamagnetic iron oxide nanoparticles: Magnetic nanoplatforms as drug carriers. *Int. J. Nanomed.* **2012**, *7*, 3445–3471. [CrossRef]
177. Khalid, K.; Tan, X.; Mohd Zaid, H.F.; Tao, Y.; Lye Chew, C.; Chu, D.T.; Lam, M.K.; Ho, Y.C.; Lim, J.W.; Chin Wei, L. Advanced in developmental organic and inorganic nanomaterial: A review. *Bioengineered* **2020**, *11*, 328–355. [CrossRef]
178. Neuberger, T.; Schöpf, B.; Hofmann, H.; Hofmann, M.; Von Rechenberg, B. Superparamagnetic nanoparticles for biomedical applications: Possibilities and limitations of a new drug delivery system. *J. Magn. Magn. Mater.* **2005**, *293*, 483–496. [CrossRef]
179. Lockman, P.R.; Mumper, R.J.; Khan, M.A.; Allen, D.D. Nanoparticle technology for drug delivery across the blood-brain barrier. *Drug Dev. Ind. Pharm.* **2002**, *28*, 1–13. [CrossRef]
180. Saraiva, C.; Praça, C.; Ferreira, R.; Santos, T.; Ferreira, L.; Bernardino, L. Nanoparticle-mediated brain drug delivery: Overcoming blood-brain barrier to treat neurodegenerative diseases. *J. Control. Release* **2016**, *235*, 34–47. [CrossRef]
181. Bao, Y.; Krishnan, K.M. Preparation of functionalized and gold-coated cobalt nanocrystals for biomedical applications. *J. Magn. Magn. Mater.* **2005**, *293*, 15–19. [CrossRef]
182. Carpenter, E.E.; Sangregorio, C.; O'Connor, C.J. Effects of shell thickness on blocking temperature of nanocomposites of metal particles with gold shells. *IEEE Trans. Magn.* **1999**, *35*, 3496–3498. [CrossRef]
183. Jung, J.S.; Chae, W.S.; McIntyre, R.A.; Seip, C.T.; Wiley, J.B.; O'Connor, C.J. Preparation and characterization of Ni nanoparticles in an MCM mesoporous material. *Mater. Res. Bull.* **1999**, *34*, 1353–1360. [CrossRef]
184. Lin, X.M.; Sorensen, C.M.; Klabunde, K.J.; Hadjipanayis, G.C. Temperature Dependence of Morphology and Magnetic Properties of Cobalt Nanoparticles Prepared by an Inverse Micelle Technique. *Langmuir* **1998**, *14*, 7140–7146. [CrossRef]
185. Yano, K.; Nandwana, V.; Chaubey, G.S.; Poudyal, N.; Kang, S.; Arami, H.; Griffis, J.; Liu, J.P. Synthesis and Characterization of Magnetic FePt/Au Core/Shell Nanoparticles. *J. Phys. Chem. C* **2009**, *113*, 13088–13091. [CrossRef]
186. Koenig, S.H.; Kellar, K.E. Theory of 1/T1 and 1/T2 NMRD profiles of solutions of magnetic nanoparticles. *Magn. Reson. Med.* **1995**, *34*, 227–233. [CrossRef]
187. Roch, A.; Muller, R.N.; Gillis, P. Theory of proton relaxation induced by superparamagnetic particles. *J. Chem. Phys.* **1999**, *110*, 5403–5411. [CrossRef]
188. Zhou, Z.; Yang, L.; Gao, J.; Chen, X. Structure–Relaxivity Relationships of Magnetic Nanoparticles for Magnetic Resonance Imaging. *Adv. Mater.* **2019**, *31*, 1804567. [CrossRef]
189. Devreux, M.; Henoumont, C.; Dioury, F.; Stanicki, D.; Boutry, S.; Larbanoix, L.; Ferroud, C.; Muller, R.N.; Laurent, S. Bimodal Probe for Magnetic Resonance Imaging and Photoacoustic Imaging Based on a PCTA-Derived Gadolinium(III) Complex and ZW800–1. *Eur. J. Inorg. Chem.* **2019**, *45*, 613–624. [CrossRef]
190. De Haan, H.W. Mechanisms of proton spin dephasing in a system of magnetic particles. *Magn. Reson. Med.* **2011**, *66*, 1748–1758. [CrossRef]
191. Shin, T.H.; Choi, Y.; Kim, S.; Cheon, J. Recent advances in magnetic nanoparticle-based multi-modal imaging. *Chem. Soc. Rev.* **2015**, *44*, 4501–4516. [CrossRef]
192. Kostevšek, N. A review on the optimal design of magnetic nanoparticle-based T2 mri contrast agents. *Magnetochemistry* **2020**, *6*, 11. [CrossRef]

193. Marashdeh, M.W.; Ababneh, B.; Lemine, O.M.; Alsadig, A.; Omri, K.; El Mir, L.; Sulieman, A.; Mattar, E. The significant effect of size and concentrations of iron oxide nanoparticles on magnetic resonance imaging contrast enhancement. *Results Phys.* **2019**, *15*, 102651. [CrossRef]
194. Wabler, M.; Zhu, W.; Hedayati, M.; Attaluri, A.; Zhou, H.; Mihalic, J.; Geyh, A.; DeWeese, T.L.; Ivkov, R.; Artemov, D. Magnetic resonance imaging contrast of iron oxide nanoparticles developed for hyperthermia is dominated by iron content. *Int. J. Hyperth.* **2014**, *30*, 192–200. [CrossRef]
195. Korchinski, D.J.; Taha, M.; Yang, R.; Nathoo, N.; Dunn, J.F. Iron Oxide as an Mri Contrast Agent for Cell Tracking: Supplementary Issue. *Magn. Reson. Insights* **2015**, *8s1*, MRI–S23557. [CrossRef]
196. Labens, R.; Daniel, C.; Hall, S.; Xia, X.R.; Schwarz, T. Effect of intra-articular administration of superparamagnetic iron oxide nanoparticles (SPIONs) for MRI assessment of the cartilage barrier in a large animal model. *PLoS ONE* **2017**, *12*, e0190216. [CrossRef]
197. Lu, J.; Yang, S.; Ng, K.M.; Su, C.H.; Yeh, C.S.; Wu, Y.N.; Shieh, D. Bin Solid-state synthesis of monocrystalline iron oxide nanoparticle based ferrofluid suitable for magnetic resonance imaging contrast application. *Nanotechnology* **2006**, *17*, 5812–5820. [CrossRef]
198. Cho, S.J.; Jarrett, B.R.; Louie, A.Y.; Kauzlarich, S.M. Gold-coated iron nanoparticles: A novel magnetic resonance agent for T1 and T2 weighted imaging. *Nanotechnology* **2006**, *17*, 640–644. [CrossRef]
199. Soukup, D.; Moise, S.; Céspedes, E.; Dobson, J.; Telling, N.D. In situ measurement of magnetization relaxation of internalized nanoparticles in live cells. *ACS Nano* **2015**, *9*, 231–240. [CrossRef]
200. Pearce, J.; Giustini, A.; Stigliano, R.; Jack Hoopes, P. Magnetic Heating of Nanoparticles: The Importance of Particle Clustering to Achieve Therapeutic Temperatures. *J. Nanotechnol. Eng. Med.* **2013**, *4*, 011005. [CrossRef]
201. Carrey, J.; Mehdaoui, B.; Respaud, M. Simple models for dynamic hysteresis loop calculations of magnetic single-domain nanoparticles: Application to magnetic hyperthermia optimization. *J. Appl. Phys.* **2011**, *109*, 083921. [CrossRef]
202. Atkinson, W.J.; Brezovich, I.A.; Chakraborty, D.P. Usable Frequencies in Hyperthermia with Thermal Seeds. *IEEE Trans. Biomed. Eng.* **1984**, *BME 31*, 70–75. [CrossRef]
203. Lemine, O.M.; Omri, K.; Iglesias, M.; Velasco, V.; Crespo, P.; De La Presa, P.; El Mir, L.; Bouzid, H.; Yousif, A.; Al-Hajry, A. γ-Fe_2O_3 by sol-gel with large nanoparticles size for magnetic hyperthermia application. *J. Alloys Compd.* **2014**, *607*, 125–131. [CrossRef]
204. Pilati, V.; Gomide, G.; Gomes, R.C.; Goya, G.F.; Depeyrot, J. Colloidal Stability and Concentration Effects on Nanoparticle Heat Delivery for Magnetic Fluid Hyperthermia. *Langmuir* **2021**, *37*, 1129–1140. [CrossRef]
205. Gamarra, L.; Silva, A.C.; Oliveira, T.R.; Mamani, J.B.; Malheiros, S.M.F.; Malavolta, L.; Pavon, L.F.; Sibov, T.T.; Amaro, E., Jr.; Gamarra, L. Application of hyperthermia induced by superparamagnetic iron oxide nanoparticles in glioma treatment. *Int. J. Nanomed.* **2011**, *6*, 591–603. [CrossRef]
206. Elsherbini, A.A.M.; El-Shahawy, A. Effect of SPIO nanoparticle concentrations on temperature changes for hyperthermia via MRI. *J. Nanomater.* **2013**, *2013*, 467878. [CrossRef]
207. De La Presa, P.; Luengo, Y.; Multigner, M.; Costo, R.; Morales, M.P.; Rivero, G.; Hernando, A. Study of heating efficiency as a function of concentration, size, and applied field in γ-Fe_2O_3 nanoparticles. *J. Phys. Chem. C* **2012**, *116*, 25602–25610. [CrossRef]
208. Kim, J.W.; Wang, J.; Kim, H.; Bae, S. Concentration-dependent oscillation of specific loss power in magnetic nanofluid hyperthermia. *Sci. Rep.* **2021**, *11*, 733. [CrossRef]
209. Zhang, L.Y.; Gu, H.C.; Wang, X.M. Magnetite ferrofluid with high specific absorption rate for application in hyperthermia. *J. Magn. Magn. Mater.* **2007**, *311*, 228–233. [CrossRef]
210. Kekalo, K.; Baker, I.; Meyers, R.; Shyong, J. Magnetic Nanoparticles with High Specific Absorption Rate at Low Alternating Magnetic Field. *Nano Life* **2015**, *05*, 1550002. [CrossRef] [PubMed]
211. Darwish, M.S.A. Effect of carriers on heating efficiency of oleic acid-stabilized magnetite nanoparticles. *J. Mol. Liq.* **2017**, *231*, 80–85. [CrossRef]
212. Lin, X.M.; Sorensen, C.M.; Klabunde, K.J.; Hadjipanayis, G.C. Control of cobalt nanoparticle size by the germ-growth method in inverse micelle system: Size-dependent magnetic properties. *J. Mater. Res.* **1999**, *14*, 1542–1547. [CrossRef]
213. Ibusuki, T.; Kojima, S.; Kitakami, O.; Shimada, Y. Magnetic anisotropy and behaviors of Fe nanoparticles. *IEEE Trans. Magn.* **2001**, *37*, 2223–2225. [CrossRef]
214. Zhang, H.T.; Ding, J.; Chow, G.M. Morphological control of synthesis and anomalous magnetic properties of 3-D branched Pt nanoparticles. *Langmuir* **2008**, *24*, 375–378. [CrossRef]
215. Sinclair, R.; Li, H.; Madsen, S.; Dai, H. HREM analysis of graphite-encapsulated metallic nanoparticles for possible medical applications. *Ultramicroscopy* **2013**, *134*, 167–174. [CrossRef]
216. Skomski, R.; Balamurugan, B.; Manchanda, P.; Chipara, M.; Sellmyer, D.J. Size Dependence of Nanoparticle Magnetization. *IEEE Trans. Magn.* **2017**, *53*, 1–7. [CrossRef]
217. Wang, C.; Han, X.; Zhang, X.; Hu, S.; Zhang, T.; Wang, J.; Du, Y.; Wang, X.; Xu, P. Controlled synthesis and morphology-dependent electromagnetic properties of hierarchical cobalt assemblies. *J. Phys. Chem. C* **2010**, *114*, 14826–14830. [CrossRef]
218. Shao, H.; Huang, Y.; Lee, H.S.; Suh, Y.J.; Kim, C.O. Effect of PVP on the morphology of cobalt nanoparticles prepared by thermal decomposition of cobalt acetate. *Curr. Appl. Phys.* **2006**, *6*, 195–197. [CrossRef]
219. Gruner, M.E.; Rollmann, G.; Entel, P.; Farle, M. Multiply twinned morphologies of FePt and CoPt nanoparticles. *Phys. Rev. Lett.* **2008**, *100*, 087203. [CrossRef] [PubMed]

220. Simeonidis, K.; Martinez-Boubeta, C.; Iglesias, O.; Cabot, A.; Angelakeris, M.; Mourdikoudis, S.; Tsiaoussis, I.; Delimitis, A.; Dendrinou-Samara, C.; Kalogirou, O. Morphology influence on nanoscale magnetism of Co nanoparticles: Experimental and theoretical aspects of exchange bias. *Phys. Rev. B Condens. Matter Mater. Phys.* **2011**, *84*, 144430. [CrossRef]
221. Moghimi, N.; Rahsepar, F.R.; Srivastava, S.; Heinig, N.; Leung, K.T. Shape-dependent magnetism of bimetallic FeNi nanosystems. *J. Mater. Chem. C* **2014**, *2*, 6370–6375. [CrossRef]
222. Yang, L.; Wang, Z.; Ma, L.; Li, A.; Xin, J.; Wei, R.; Lin, H.; Wang, R.; Chen, Z.; Gao, J. The Roles of Morphology on the Relaxation Rates of Magnetic Nanoparticles. *ACS Nano* **2018**, *12*, 4605–4614. [CrossRef]
223. Essajai, R.; Benhouria, Y.; Rachadi, A.; Qjani, M.; Mzerd, A.; Hassanain, N. Shape-dependent structural and magnetic properties of Fe nanoparticles studied through simulation methods. *RSC Adv.* **2019**, *9*, 22057–22063. [CrossRef]
224. Mujica-Martínez, C.A.; Arce, J.C. Mini-bandstructure tailoring in pi-conjugated periodic block copolymers using the envelope crystalline-orbital method. *Int. J. Quantum Chem. J.* **2010**, *110*, 2532–2540. [CrossRef]
225. Liu, Z.; Wang, G. Shape-dependent surface magnetism of Co-Pt and Fe-Pt nanoparticles from first principles. *Phys. Rev. B* **2017**, *96*, 224412. [CrossRef]
226. Di Paola, C.; Baletto, F. Chemical order and magnetic properties in small $M_{x\text{-}2}N_2$ nanoalloys. *Eur. Phys. J. D* **2013**, *67*, 49. [CrossRef]
227. Liu, Z.; Lei, Y.; Wang, G. First-principles computation of surface segregation in L10 CoPt magnetic nanoparticles. *J. Phys. Condens. Matter* **2016**, *28*, 266002. [CrossRef]
228. Baletto, F.; Mottet, C.; Ferrando, R. Growth of Three-Shell Onionlike Bimetallic Nanoparticles. *Phys. Rev. Lett.* **2003**, *90*, 135504. [CrossRef]
229. Lümmen, N.; Kraska, T. Investigation of the formation of iron nanoparticles from the gas phase by molecular dynamics simulation. *Nanotechnology* **2004**, *15*, 525–533. [CrossRef]
230. Zeng, Q.; Jiang, X.; Yu, A.; Lu, G. Growth mechanisms of silver nanoparticles: A molecular dynamics study. *Nanotechnology* **2007**, *18*, 035708. [CrossRef]
231. Grochola, G.; Russo, S.P.; Snook, I.K. On morphologies of gold nanoparticles grown from molecular dynamics simulation. *J. Chem. Phys.* **2007**, *126*, 164707. [CrossRef]
232. Langlois, C.; Li, Z.L.; Yuan, J.; Alloyeau, D.; Nelayah, J.; Bochicchio, D.; Ferrando, R.; Ricolleau, C. Transition from core-shell to Janus chemical configuration for bimetallic nanoparticles. *Nanoscale* **2012**, *4*, 3381–3388. [CrossRef]
233. Safaltın, Ş.; Gürmen, S. Molecular dynamics simulation of size, temperature, heating and cooling rates on structural formation of Ag-Cu-Ni ternary nanoparticles (Ag_{34}-Cu_{33}-Ni_{33}). *Comput. Mater. Sci.* **2020**, *183*, 109842. [CrossRef]
234. Han, Y.; Jiang, D.; Zhang, J.; Li, W.; Gan, Z.; Gu, J. Development, applications and challenges of ReaxFF reactive force field in molecular simulations. *Front. Chem. Sci. Eng.* **2016**, *10*, 16–38. [CrossRef]
235. Deeth, R.J.; Anastasi, A.; Diedrich, C.; Randell, K. Molecular modelling for transition metal complexes: Dealing with d-electron effects. *Coord. Chem. Rev.* **2009**, *253*, 795–816. [CrossRef]
236. Fracchia, F.; Del Frate, G.; Mancini, G.; Rocchia, W.; Barone, V. Force Field Parametrization of Metal Ions from Statistical Learning Techniques. *J. Chem. Theory Comput.* **2018**, *14*, 255–273. [CrossRef]
237. Dasetty, S.; Meza-Morales, P.J.; Getman, R.B.; Sarupria, S. Simulations of interfacial processes: Recent advances in force field development. *Curr. Opin. Chem. Eng.* **2019**, *23*, 138–145. [CrossRef]
238. Entel, P.; Gruner, M.E. Large-scale ab initio simulations of binary transition metal clusters for storage media materials. *J. Phys. Condens. Matter* **2009**, *21*, 064228. [CrossRef]
239. Farkaš, B.; de Leeuw, N.H. Towards a morphology of cobalt nanoparticles: Size and strain effects. *Nanotechnology* **2020**, *31*, 195711. [CrossRef]
240. Souto-Casares, J.; Sakurai, M.; Chelikowsky, J.R. Structural and magnetic properties of large cobalt clusters. *Phys. Rev. B* **2016**, *93*, 174418. [CrossRef]
241. Fernando, A.; Weerawardene, K.L.D.M.; Karimova, N.V.; Aikens, C.M. Quantum Mechanical Studies of Large Metal, Metal Oxide, and Metal Chalcogenide Nanoparticles and Clusters. *Chem. Rev.* **2015**, *115*, 6112–6216. [CrossRef]
242. Mark, L.O.; Zhu, C.; Medlin, J.W.; Heinz, H. Understanding the Surface Reactivity of Ligand-Protected Metal Nanoparticles for Biomass Upgrading. *ACS Catal.* **2020**, *10*, 5462–5474. [CrossRef]
243. de Morais, R.F.; Kerber, T.; Calle-Vallejo, F.; Sautet, P.; Loffreda, D. Capturing Solvation Effects at a Liquid/Nanoparticle Interface by Ab Initio Molecular Dynamics: Pt_{201} Immersed in Water. *Small* **2016**, *12*, 5312–5319. [CrossRef]
244. Kaddi, C.D.; Phan, J.H.; Wang, M.D. Computational nanomedicine: Modeling of nanoparticle-mediated hyperthermal cancer therapy. *Nanomedicine* **2013**, *8*, 1323–1333. [CrossRef]
245. Nabil, M.; Decuzzi, P.; Zunino, P. Modelling mass and heat transfer in nano-based cancer hyperthermia. *R. Soc. Open Sci.* **2015**, *2*, 150447. [CrossRef]
246. Ng, E.Y.K.; Kumar, S.D. Physical mechanism and modeling of heat generation and transfer in magnetic fluid hyperthermia through Néelian and Brownian relaxation: A review. *Biomed. Eng. Online* **2017**, *16*, 36. [CrossRef]
247. Muscas, G.; Trohidou, K.N.; Peddis, D.; Vasilakaki, M.; Yaacoub, N.; Ntallis, N. Optimising the magnetic performance of Co ferrite nanoparticles via organic ligand capping. *Nanoscale* **2018**, *10*, 21244–21253. [CrossRef]
248. Andreu, I.; Natividad, E. Accuracy of available methods for quantifying the heat power generation of nanoparticles for magnetic hyperthermia. *Int. J. Hyperth.* **2013**, *29*, 739–751. [CrossRef]

249. Michalakis, J.; Georgatos, S.D.; De Bree, E.; Polioudaki, H.; Romanos, J.; Georgoulias, V.; Tsiftsis, D.D.; Theodoropoulos, P.A. Short-term exposure of cancer cells to micromolar doses of paclitaxel, with or without hyperthermia, induces long-term inhibition of cell proliferation and cell death in vitro. *Ann. Surg. Oncol.* **2007**, *14*, 1220–1228. [CrossRef]
250. Yang, K.L.; Huang, C.C.; Chi, M.S.; Chiang, H.C.; Wang, Y.S.; Hsia, C.C.; Andocs, G.; Wang, H.E.; Chi, K.H. In vitro comparison of conventional hyperthermia and modulated electro-hyperthermia. *Oncotarget* **2016**, *7*, 84082–84092. [CrossRef]
251. Mohamed, F.; Stuart, O.A.; Glehen, O.; Urano, M.; Sugarbaker, P.H. Docetaxel and hyperthermia: Factors that modify thermal enhancement. *J. Surg. Oncol.* **2004**, *88*, 14–20. [CrossRef]
252. Rives, S.; Catherinot, A.; Dumas-Bouchiat, F.; Champeaux, C.; Videcoq, A.; Ferrando, R. Growth of Co isolated clusters in the gas phase: Experiment and molecular dynamics simulations. *Phys. Rev. B Condens. Matter Mater. Phys.* **2008**, *77*, 085407. [CrossRef]
253. Rodríguez-López, J.L.; Aguilera-Granja, F.; Michaelian, K.; Vega, A. Structure and magnetism of cobalt clusters. *Phys. Rev. B Condens. Matter Mater. Phys.* **2003**, *67*, 174413. [CrossRef]
254. Datta, S.; Kabir, M.; Ganguly, S.; Sanyal, B.; Saha-Dasgupta, T.; Mookerjee, A. Structure, bonding, and magnetism of cobalt clusters from first-principles calculations. *Phys. Rev. B Condens. Matter Mater. Phys.* **2007**, *76*, 014429. [CrossRef]
255. Harada, M.; Dexpert, H. Electronic structure of transition metal clusters from density functional theory. 1. Transition metal dimers. *J. Phys. Chem.* **1996**, *100*, 565–572. [CrossRef]
256. Reddy, B.V.; Nayak, S.K.; Khanna, S.N.; Rao, B.K.; Jena, P. Physics of nickel clusters. 2. Electronic structure and magnetic properties. *J. Phys. Chem. A* **1998**, *102*, 1748–1759. [CrossRef]
257. Derosa, P.A.; Seminario, J.M.; Balbuena, P.B. Properties of small bimetallic Ni-Cu clusters. *J. Phys. Chem. A* **2001**, *105*, 7917–7925. [CrossRef]
258. Jain, P.K. A DFT-based study of the low-energy electronic structures and properties of small gold clusters. *Struct. Chem.* **2005**, *16*, 421–426. [CrossRef]
259. Efremenko, I.; Sheintuch, M. DFT study of small bimetallic palladium-copper clusters. *Chem. Phys. Lett.* **2005**, *401*, 232–240. [CrossRef]
260. Ma, Q.M.; Xie, Z.; Wang, J.; Liu, Y.; Li, Y.C. Structures, binding energies and magnetic moments of small iron clusters: A study based on all-electron DFT. *Solid State Commun.* **2007**, *142*, 114–119. [CrossRef]
261. Zanti, G.; Peeters, D. DFT study of small palladium clusters Pdn and their interaction with a CO ligand (n = 1-9). *Eur. J. Inorg. Chem.* **2009**, 3904–3911. [CrossRef]
262. Katakuse, I.; Ichihara, T.; Fujita, Y.; Matsuo, T.; Sakurai, T.; Matsuda, H. Mass distributions of copper, silver and gold clusters and electronic shell structure. *Int. J. Mass Spectrom. Ion Process.* **1985**, *67*, 229–236. [CrossRef]
263. de Heer, W.A.; Knight, W.D.; Chou, M.Y.; Cohen, M.L. Electronic Shell Structure and Metal Clusters. *Solid State Phys. Adv. Res. Appl.* **1987**, *40*, 93–181. [CrossRef]
264. Martin, T.P.; Bergmann, T.; Göhlich, H.; Lange, T. Shell structure of clusters. *J. Phys. Chem.* **1991**, *95*, 6421–6429. [CrossRef]
265. Jena, P.; Castleman, A.W. Clusters: A bridge across the disciplines of physics and chemistry. *Proc. Natl. Acad. Sci. USA* **2006**, *103*, 10560–10569. [CrossRef]
266. Martins, M.; Wurth, W. Magnetic properties of supported metal atoms and clusters. *J. Phys. Condens. Matter* **2016**, *28*, 503002. [CrossRef]
267. Zamudio-Bayer, V.; Hirsch, K.; Langenberg, A.; Ławicki, A.; Terasaki, A.; Von Issendorff, B.; Lau, J.T. Large orbital magnetic moments of small, free cobalt cluster ions $Co^{+}{}_{n}$ with $n \leq 9$. *J. Phys. Condens. Matter* **2018**, *30*, 464002. [CrossRef]
268. Bucher, J.P.; Douglass, D.C.; Bloomfield, L.A. Magnetic properties of free cobalt clusters. *Phys. Rev. Lett.* **1991**, *66*, 3052–3055. [CrossRef]
269. Jensen, P.J.; Bennemann, K.H. Magnetic properties of free ferromagnetic clusters in a Stern-Gerlach magnet. *Comput. Mater. Sci.* **1994**, *2*, 488–490. [CrossRef]
270. Knickelbein, M.B. Magnetic moments of bare and benzene-capped cobalt clusters. *J. Chem. Phys.* **2006**, *125*, 044308. [CrossRef]
271. Xu, X.; Yin, S.; Moro, R.; de Heer, W.A. Magnetic Moments and Adiabatic Magnetization of Free Cobalt Clusters. *Phys. Rev. Lett.* **2005**, *95*, 237209. [CrossRef]
272. Nealon, G.L.; Donnio, B.; Greget, R.; Kappler, J.P.; Terazzi, E.; Gallani, J.L. Magnetism in gold nanoparticles. *Nanoscale* **2012**, *4*, 5244–5258. [CrossRef]
273. Swart, I.; De Groot, F.M.F.; Weckhuysen, B.M.; Gruene, P.; Meijer, G.; Fielicke, A. H_2 adsorption on 3d transition metal clusters: A combined infrared spectroscopy and density functional study. *J. Phys. Chem. A* **2008**, *112*, 1139–1149. [CrossRef] [PubMed]
274. Sauer, J. Molecular Models in ab Initio Studies of Solids and Surfaces: From Ionic Crystals and Semiconductors to Catalysts. *Chem. Rev.* **1989**, *89*, 199–255. [CrossRef]
275. Wang, G.C.; Jiang, L.; Morikawa, Y.; Nakamura, J.; Cai, Z.S.; Pan, Y.M.; Zhao, X.Z. Cluster and periodic DFT calculations of adsorption and activation of CO_2 on the Cu(hkl) surfaces. *Surf. Sci.* **2004**, *570*, 205–217. [CrossRef]
276. Pessoa, A.M.; Fajín, J.L.C.; Gomes, J.R.B.; Cordeiro, M.N.D.S. Cluster and periodic DFT calculations of adsorption of hydroxyl on the Au(h k l) surfaces. *J. Mol. Struct. THEOCHEM* **2010**, *946*, 43–50. [CrossRef]
277. Psofogiannakis, G.; St-Amant, A.; Ternan, M. Methane oxidation mechanism on Pt(111): A cluster model DFT study. *J. Phys. Chem. B* **2006**, *110*, 24593–24605. [CrossRef]
278. Zhenming, H.; Boyd, R.J. Structure sensitivity and cluster size convergence for formate adsorption on copper surfaces: A DFT cluster model study. *J. Chem. Phys.* **2000**, *112*, 9562–9568. [CrossRef]

279. Dehmani, Y.; Lgaz, H.; Alrashdi, A.A.; Lamhasni, T.; Abouarnadasse, S.; Chung, I.M. Phenol adsorption mechanism on the zinc oxide surface: Experimental, cluster DFT calculations, and molecular dynamics simulations. *J. Mol. Liq.* **2021**, *324*, 114993. [CrossRef]
280. Tafreshi, S.S.; Roldan, A.; De Leeuw, N.H. Density Functional Theory Study of the Adsorption of Hydrazine on the Perfect and Defective Copper (100), (110), and (111) Surfaces. *J. Phys. Chem. C* **2014**, *118*, 26103–26114. [CrossRef]
281. Liu, L.; Yu, M.; Hou, B.; Wang, Q.; Zhu, B.; Jia, L.; Li, D. Morphology evolution of fcc Ru nanoparticles under hydrogen atmosphere. *Nanoscale* **2019**, *11*, 8037–8046. [CrossRef]
282. Zhao, P.; Cao, Z.; Liu, X.; Ren, P.; Cao, D.B.; Xiang, H.; Jiao, H.; Yang, Y.; Li, Y.W.; Wen, X.D. Morphology and Reactivity Evolution of HCP and FCC Ru Nanoparticles under CO Atmosphere. *ACS Catal.* **2019**, *9*, 2768–2776. [CrossRef]
283. Shi, Q.; Sun, R. Adsorption manners of hydrogen on Pt(100), (110) and (111) surfaces at high coverage. *Comput. Theor. Chem.* **2017**, *1106*, 43–49. [CrossRef]
284. Avanesian, T.; Dai, S.; Kale, M.J.; Graham, G.W.; Pan, X.; Christopher, P. Quantitative and Atomic-Scale View of CO-Induced Pt Nanoparticle Surface Reconstruction at Saturation Coverage via DFT Calculations Coupled with in Situ TEM and IR. *J. Am. Chem. Soc.* **2017**, *139*, 4551–4558. [CrossRef] [PubMed]
285. Soon, A.; Wong, L.; Delley, B.; Stampfl, C. Morphology of copper nanoparticles in a nitrogen atmosphere: A first-principles investigation. *Phys. Rev. B Condens. Matter Mater. Phys.* **2008**, *77*, 125423. [CrossRef]
286. Deshlahra, P.; Conway, J.; Wolf, E.E.; Schneider, W.F. Influence of Dipole–Dipole Interactions on Coverage-Dependent Adsorption: CO and NO on Pt(111). *Langmuir* **2012**, *28*, 8408–8417. [CrossRef] [PubMed]
287. Bessarab, P.F.; Uzdin, V.M.; Jónsson, H. Effect of hydrogen adsorption on the magnetic properties of a surface nanocluster of iron. *Phys. Rev. B Condens. Matter Mater. Phys.* **2013**, *88*, 14–16. [CrossRef]
288. Ram, S.; Lee, S.C.; Bhattacharjee, S. Adsorption energy scaling relation on bimetallic magnetic surfaces: Role of surface magnetic moments. *Phys. Chem. Chem. Phys.* **2020**, *22*, 17960–17968. [CrossRef]
289. Pignocco, A.J.; Pellissier, G.E. Leed studies of oxygen adsorption and oxide formation on an (011) iron surface. *Surf. Sci.* **1967**, *7*, 261–278. [CrossRef]
290. Brundle, C.R. Oxygen adsorption and thin oxide formation at iron surfaces: An XPS/UPS study. *Surf. Sci.* **1977**, *66*, 581–595. [CrossRef]
291. Holloway, P.H. Chemisorption and Oxide Formation on Metals: Oxygen-Nickel Reaction. *J. Vac. Sci. Technol.* **1980**, *18*, 653–659. [CrossRef]
292. Li, W.X.; Stampfl, C.; Scheffler, M. Subsurface oxygen and surface oxide formation at Ag(111): A density-functional theory investigation. *Phys. Rev. B Condens. Matter Mater. Phys.* **2003**, *67*, 045408. [CrossRef]
293. Todorova, M.; Reuter, K.; Scheffler, M. Oxygen overlayers on Pd(111) studied by density functional theory. *J. Phys. Chem. B* **2004**, *108*, 14477–14483. [CrossRef]
294. Shi, H.; Stampfl, C. First-principles investigations of the structure and stability of oxygen adsorption and surface oxide formation at Au(111). *Phys. Rev. B* **2007**, *76*, 075327. [CrossRef]
295. Bridge, M.E.; Lambert, R.M. Oxygen chemisorption, surface oxidation, and the oxidation of carbon monoxide on cobalt (0001). *Surf. Sci.* **1979**, *82*, 413–424. [CrossRef]
296. Farkaš, B.; Santos-Carballal, D.; Cadi-Essadek, A.; de Leeuw, N.H. A DFT+U study of the oxidation of cobalt nanoparticles: Implications for biomedical applications. *Materialia* **2019**, *7*, 100381. [CrossRef]
297. Wang, L.; Maxisch, T.; Ceder, G. Oxidation energies of transition metal oxides within the GGA+U framework. *Phys. Rev. B Condens. Matter Mater. Phys.* **2006**, *73*, 195107. [CrossRef]
298. Toroker, M.C.; Kanan, D.K.; Alidoust, N.; Isseroff, L.Y.; Liao, P.; Carter, E.A. First principles scheme to evaluate band edge positions in potential transition metal oxide photocatalysts and photoelectrodes. *Phys. Chem. Chem. Phys.* **2011**, *13*, 16644–16654. [CrossRef]
299. Getsoian, A.B.; Bell, A.T. The influence of functionals on density functional theory calculations of the properties of reducible transition metal oxide catalysts. *J. Phys. Chem. C* **2013**, *117*, 25562–25578. [CrossRef]
300. Roth, W.L. Magnetic structures of MnO, FeO, CoO, and NiO. *Phys. Rev.* **1958**, *110*, 1333–1341. [CrossRef]
301. Wdowik, U.D.; Parlinski, K. Lattice dynamics of CoO from first principles. *Phys. Rev. B Condens. Matter Mater. Phys.* **2007**, *75*, 104306. [CrossRef]
302. Roth, W.L. The magnetic structure of Co_3O_4. *J. Phys. Chem. Solids* **1964**, *25*, 1–10. [CrossRef]
303. Scheerlinck, D.; Hautecler, S. Magnetic Interactions in Co_3O_4. *Phys. Status Solidi* **1976**, *73*, 223–228. [CrossRef]
304. Lee, B.; Ignatiev, A.; Taylor, J.; Rabalais, J. Atomic structure sensitivity of XPS: The oxidation of cobalt. *Solid State Commun.* **1980**, *33*, 1205–1208. [CrossRef]
305. Klingenberg, B.; Grellner, F.; Borgmann, D.; Wedler, G. Oxygen adsorption and oxide formation on Co(1120). *Surf. Sci.* **1993**, *296*, 374–382. [CrossRef]
306. Van Vleck, J.H. On the anisotropy of cubic ferromagnetic crystals. *Phys. Rev.* **1937**, *52*, 1178–1198. [CrossRef]
307. Brooks, H. Ferromagnetic Anisotropy and the Itinerant Electron Model. *Phys. Rev.* **1940**, *58*, 909–918. [CrossRef]
308. Fletcher, G.C. Calculations of the first ferromagnetic anisotropy coefficient, gyromagnetic ratio and spectroscopic splitting factor for nickel. *Proc. Phys. Soc. Sect. A* **1954**, *67*, 505–519. [CrossRef]

309. Daalderop, G.H.O.; Kelly, P.J.; Schuurmans, M.F.H. First-principles calculation of the magnetic anisotropy energy of (Co)$n/(X)m$ multilayers. *Phys. Rev. B* **1990**, *42*, 7270–7273. [CrossRef]
310. Daalderop, G.H.O.; Kelly, P.J.; Den Broeder, F.J.A. Prediction and confirmation of perpendicular magnetic anisotropy in Co/Ni multilayers. *Phys. Rev. Lett.* **1992**, *68*, 682–685. [CrossRef]
311. Berger, A.; Hopster, H. Nonequilibrium Magnetization near the Reorientation Phase Transition of Fe/Ag(100) Films. *Phys. Rev. Lett.* **1996**, *76*, 519–522. [CrossRef]
312. Pütter, S.; Millev, Y.T.; Ding, H.F.; Kirschner, J.; Oepen, H.P. Magnetic susceptibility: An easy approach to the spin-reorientation transition. *Phys. Rev. B Condens. Matter Mater. Phys.* **2001**, *64*, 092409. [CrossRef]
313. O'Brien, W.; Droubay, T.; Tonner, B. Transitions in the direction of magnetism in Ni/Cu(001) ultrathin films and the effects of capping layers. *Phys. Rev. B Condens. Matter Mater. Phys.* **1996**, *54*, 9297–9303. [CrossRef]
314. Młyńczak, E.; Aguilera, I.; Gospodarič, P.; Heider, T.; Jugovac, M.; Zamborlini, G.; Tusche, C.; Suga, S.; Feyer, V.; Blügel, S.; et al. Spin-polarized quantized electronic structure of Fe(001) with symmetry breaking due to the magnetization direction. *Phys. Rev. B* **2021**, *103*, 035134. [CrossRef]
315. Bouhassoune, M.; Zimmermann, B.; Mavropoulos, P.; Wortmann, D.; Dederichs, P.H.; Blügel, S.; Lounis, S. Quantum well states and amplified spin-dependent Friedel oscillations in thin films. *Nat. Commun.* **2014**, *5*, 5558. [CrossRef]
316. Mlynczak, E.; Eschbach, M.; Borek, S.; Minár, J.; Braun, J.; Aguilera, I.; Bihlmayer, G.; Döring, S.; Gehlmann, M.; Gospodaric, P.; et al. Fermi surface manipulation by external magnetic field demonstrated for a prototypical ferromagnet. *Phys. Rev. X* **2016**, *6*, 041048. [CrossRef]
317. Pan, M.; He, K.; Zhang, L.; Jia, J.; Xue, Q.; Kim, W.; Qiu, Z.Q. Structure and magnetism of ultrathin Co film grown on Pt(100). *J. Vac. Sci. Technol. A Vacuum Surf. Film* **2005**, *23*, 790–795. [CrossRef]
318. Yokoyama, T.; Matsumura, D.; Amemiya, K.; Kitagawa, S.; Suzuki, N.; Ohta, T. Spin reorientation transitions of ultrathin Co/Pd(111) films induced by chemisorption: X-ray magnetic circular dichroism study. *J. Phys. Condens. Matter* **2003**, *15*, S537. [CrossRef]
319. Boukari, S.; Beaurepaire, E.; Bulou, H.; Carrière, B.; Deville, J.P.; Scheurer, F.; De Santis, M.; Baudoing-Savois, R. Influence of strain on the magnetocrystalline anisotropy in epitaxial Cr/Co/Pd(111) films. *Phys. Rev. B Condens. Matter Mater. Phys.* **2001**, *64*, 1444311–1444314. [CrossRef]
320. Quirós, C.; Valvidares, S.M.; Robach, O.; Ferrer, S. Low-temperature growth favours hcp structure, flatness and perpendicular magnetic anisotropy of thin (1-5 nm) Co films on Pt(111). *J. Phys. Condens. Matter* **2005**, *17*, 5551–5561. [CrossRef]
321. Zhang, H. Relativistic Density Functional Treatment of Magnetic Anisotropy. Ph.D. Thesis, Technische Universitat Dresden, Dresden, Germany, 2009.
322. Paige, D.M.; Szpunar, B.; Tanner, B.K. The magnetocrystalline anisotropy of cobalt. *J. Magn. Magn. Mater.* **1984**, *44*, 239–248. [CrossRef]
323. Dorantes-Dávila, J.; Dreyssé, H. Magnetic anisotropy of close-packed (111) ultrathin transition-metal films:Role of interlayer packing. *Phys. Rev. B Condens. Matter Mater. Phys.* **1997**, *55*, 15033–15042. [CrossRef]
324. Chappert, C.; Bruno, P. Magnetic anisotropy in metallic ultrathin films and related experiments on cobalt films (invited). *J. Appl. Phys.* **1988**, *64*, 5736–5741. [CrossRef]
325. Suzuki, T.; Weller, D.; Chang, C.A.; Savoy, R.; Huang, T.; Gurney, B.A.; Speriosu, V. Magnetic and magneto-optic properties of thick face-centered-cubic Co single-crystal films. *Appl. Phys. Lett.* **1994**, *64*, 2736–2738. [CrossRef]
326. El Gabaly, F.; Gallego, S.; Muñoz, C.; Szunyogh, L.; Weinberger, P.; Klein, C.; Schmid, A.K.; McCarty, K.F.; De La Figuera, J. Imaging spin-reorientation transitions in consecutive atomic Co layers on Ru(0001). *Phys. Rev. Lett.* **2006**, *96*, 147202. [CrossRef]
327. Przybylski, M.; Yan, L.; Zukrowski, J.; Nyvlt, M.; Shi, Y.; Winkelmann, A.; Barthel, J.; Waśniowska, M.; Kirschner, J. Topology-dependent interface contribution to magneto-optical response from ultrathin Co films grown on the (001), (110), and (111) surfaces of Pd. *Phys. Rev. B Condens. Matter Mater. Phys.* **2006**, *73*, 085413. [CrossRef]
328. Szunyogh, L.; Újfalussy, B.; Blaas, C.; Pustogowa, U.; Sommers, C.; Weinberger, P. Oscillatory behavior of the magnetic anisotropy energy in multilayer systems. *Phys. Rev. B Condens. Matter Mater. Phys.* **1997**, *56*, 14036–14044. [CrossRef]
329. Nicolas, G.; Dorantes-Dávila, J.; Pastor, G.M. Orbital polarization effects on the magnetic anisotropy and orbital magnetism of clusters, films, and surfaces: A comparative study within tight-binding theory. *Phys. Rev. B Condens. Matter Mater. Phys.* **2006**, *74*, 014415. [CrossRef]
330. El Gabaly, F.; McCarty, K.F.; Schmid, A.K.; De La Figuera, J.; Muñoz, M.C.; Szunyogh, L.; Weinberger, P.; Gallego, S. Noble metal capping effects on the spin-reorientation transitions of Co/Ru(0001). *New J. Phys.* **2008**, *10*, 073024. [CrossRef]
331. Buruzs, Á.; Weinberger, P.; Szunyogh, L.; Udvardi, L.; Chleboun, P.I.; Fischer, A.M.; Staunton, J.B. Ab initio theory of temperature dependence of magnetic anisotropy in layered systems: Applications to thin Co films on Cu(100). *Phys. Rev. B Condens. Matter Mater. Phys.* **2007**, *76*, 064417. [CrossRef]
332. Bruno, P. Magnetic surface anisotropy of cobalt and surface roughness effects within Neel's model. *J. Phys. F Met. Phys.* **1988**, *18*, 1291–1298. [CrossRef]
333. Campiglio, P.; Breitwieser, R.; Repain, V.; Guitteny, S.; Chacon, C.; Bellec, A.; Lagoute, J.; Girard, Y.; Rousset, S.; Sassella, A.; et al. Change of cobalt magnetic anisotropy and spin polarization with alkanethiolates self-assembled monolayers. *New J. Phys.* **2015**, *17*, 063022. [CrossRef]

334. Lehnert, A.; Dennler, S.; Błoński, P.; Rusponi, S.; Etzkorn, M.; Moulas, G.; Bencok, P.; Gambardella, P.; Brune, H.; Hafner, J. Magnetic anisotropy of Fe and Co ultrathin films deposited on Rh(111) and Pt(111) substrates: An experimental and first-principles investigation. *Phys. Rev. B Condens. Matter Mater. Phys.* **2010**, *82*, 094409. [CrossRef]
335. Kebaili, A.S.; Blizak, S.; Bihlmayer, G.; Blügel, S. Magnetic properties of ultra-thin (Fe, Co) films coupled by Ir(001) spacers. *Phys. B Condens. Matter* **2020**, *596*, 412395. [CrossRef]
336. Jia, H.; Zimmermann, B.; Hoffmann, M.; Sallermann, M.; Bihlmayer, G.; Blügel, S. Material systems for FM-/AFM-coupled skyrmions in Co/Pt-based multilayers. *Phys. Rev. Mater.* **2020**, *4*, 122405. [CrossRef]
337. Di, N.; Kubal, J.; Zeng, Z.; Greeley, J.; Maroun, F.; Allongue, P. Influence of controlled surface oxidation on the magnetic anisotropy of Co ultrathin films. *Appl. Phys. Lett.* **2015**, *106*, 122405. [CrossRef]
338. Dinghas, A. Über einen geometrischen Satz von Wulff für die Gleichgewichtsform von Kristallen. *Z. Krist. Cryst. Mater.* **1943**, *105*, 304–314. [CrossRef]
339. Herring, C. Some Theorems on the Free Energies of Crystal Surfaces. *Phys. Rev.* **1951**, *82*, 87–93. [CrossRef]
340. Fonseca, I. The Wulff Theorem Revisited. *Proc. R. Soc. A Math. Phys. Eng. Sci.* **1991**, *432*, 125–145. [CrossRef]
341. Marks, L.D. Experimental studies of small particle structures. *Rep. Prog. Phys.* **1994**, *57*, 603–649. [CrossRef]
342. Graoui, H.; Giorgio, S.; Enry, C.R. Effect of the interface structure on the high-temperature morphology of supported metal clusters. *Philos. Mag. B Phys. Condens. Matter. Stat. Mech. Electron. Opt. Magn. Prop.* **2001**, *81*, 1649–1658. [CrossRef]
343. Mackay, A.L. A dense non-crystallographic packing of equal spheres. *Acta Crystallogr.* **1962**, *15*, 916–918. [CrossRef]
344. Ino, S. Epitaxial Growth of Metals on Rocksalt Faces Cleaved in Vacuum. II. Orientation and Structure of Gold Particles Formed in Ultrahigh Vacuum. *J. Phys. Soc. Jpn.* **1966**, *21*, 346–362. [CrossRef]
345. Ino, S. Stability of Multiply-Twinned Particles. *J. Phys. Soc. Jpn.* **1969**, *27*, 941–953. [CrossRef]
346. Howie, A.; Marks, L.D. Multiply Twinned Particles. *Oyobuturi* **1984**, *41*, 388–397. [CrossRef]
347. Teo, B.K.; Sloane, N.J.A. Magic Numbers in Polygonal and Polyhedral. *Inorg. Chem.* **1985**, 4545–4558. [CrossRef]
348. Kaatz, F.H.; Bultheel, A. Magic Mathematical Relationships for Nanoclusters. *Nanoscale Res. Lett.* **2019**, *14*, 150. [CrossRef]
349. Cleveland, C.L.; Landman, U. The energetics and structure of nickel clusters: Size dependence. *J. Chem. Phys.* **1991**, *94*, 7376–7396. [CrossRef]
350. Baletto, F.; Ferrando, R. Structural properties of nanoclusters: Energetic, thermodynamic, and kinetic effects. *Rev. Mod. Phys.* **2005**, *77*, 371–423. [CrossRef]
351. Gafner, Y.Y.; Gafner, S.L.; Golonenko, Z.V.; Redel, L.V.; Khrustalev, V.I. Formation of structure in Au, Cu and Ni nanoclusters: MD simulations. *IOP Conf. Ser. Mater. Sci. Eng.* **2016**, *110*, 012015. [CrossRef]
352. Rahm, J.M.; Erhart, P. Beyond Magic Numbers: Atomic Scale Equilibrium Nanoparticle Shapes for Any Size. *Nano Lett.* **2017**, *17*, 5775–5781. [CrossRef]
353. Garden, A.L.; Pedersen, A.; Jónsson, H. Reassignment of "magic numbers" for Au clusters of decahedral and FCC structural motifs. *Nanoscale* **2018**, *10*, 5124–5132. [CrossRef]
354. Liu, X.; Tian, D.; Meng, C. DFT study on the adsorption and dissociation of H_2 on Pd_n (n = 4, 6, 13, 19, 55) clusters. *J. Mol. Struct.* **2015**, *1080*, 105–110. [CrossRef]
355. Yudanov, I.V.; Genest, A.; Schauermann, S.; Freund, H.J.; Rösch, N. Size Dependence of the adsorption energy of CO on metal nanoparticles: A DFT search for the minimum value. *Nano Lett.* **2012**, *12*, 2134–2139. [CrossRef]
356. Laletina, S.S.; Mamatkulov, M.; Shor, E.A.; Kaichev, V.V.; Genest, A.; Yudanov, I.V.; Rösch, N. Size-Dependence of the Adsorption Energy of CO on Pt Nanoparticles: Tracing Two Intersecting Trends by DFT Calculations. *J. Phys. Chem. C* **2017**, *121*, 17371–17377. [CrossRef]
357. Yang, Y.; Yu, H.; Cai, Y.; Ferrando, R.; Cheng, D. Origin of enhanced stability and oxygen adsorption capacity of medium-sized Pt-Ni nanoclusters. *J. Phys. Condens. Matter* **2018**, *30*, 285503. [CrossRef]
358. Verga, L.G.; Aarons, J.; Sarwar, M.; Thompsett, D.; Russell, A.E.; Skylaris, C.K. DFT calculation of oxygen adsorption on platinum nanoparticles: Coverage and size effects. *Faraday Discuss.* **2018**, *208*, 497–522. [CrossRef]
359. Zhang, X.; Liu, J.-X.; Zijlstra, B.; Filot, I.A.W.; Zhou, Z.; Sun, S.; Hensen, E.J.M. Optimum Cu nanoparticle catalysts for CO_2 hydrogenation towards methanol. *Nano Energy* **2018**, *43*, 200–209. [CrossRef]
360. Zhang, R.; Xue, M.; Wang, B.; Ling, L. Acetylene selective hydrogenation over different size of Pd-modified Cu cluster catalysts: Effects of Pd ensemble and cluster size on the selectivity and activity. *Appl. Surf. Sci.* **2019**, *481*, 421–432. [CrossRef]
361. Xia, Z.; Zhang, S.; Liu, F.; Ma, Y.; Qu, Y.; Wu, C. Size-Dependent Adsorption of Styrene on Pd Clusters: A Density Functional Theory Study. *J. Phys. Chem. C* **2019**, *123*, 2182–2188. [CrossRef]
362. Farkaš, B.; Terranova, U.; de Leeuw, N.H. Binding modes of carboxylic acids on cobalt nanoparticles. *Phys. Chem. Chem. Phys.* **2020**, *22*, 985–996. [CrossRef]
363. Calle-Vallejo, F.; Martínez, J.I.; García-Lastra, J.M.; Sautet, P.; Loffreda, D. Fast Prediction of Adsorption Properties for Platinum Nanocatalysts with Generalized Coordination Numbers. *Angew. Chemie Int. Ed.* **2014**, *53*, 8316–8319. [CrossRef]
364. Simmons, G.W.; Wang, Y.N.; Marcos, J.; Klier, K. Oxygen adsorption on palladium(100) surface: Phase transformations and surface reconstruction. *J. Phys. Chem.* **1991**, *95*, 4522–4528. [CrossRef]
365. Koch, R.; Schwarz, E.; Schmidt, K.; Burg, B.; Christmann, K.; Rieder, K.H. Oxygen adsorption on Co(1010): Different reconstruction behavior of hcp (1010) and fcc(110). *Phys. Rev. Lett.* **1993**, *71*, 1047–1050. [CrossRef]

366. Besenbacher, F.; Nørskov, J.K. Oxygen chemisorption on metal surfaces: General trends for Cu, Ni and Ag. *Prog. Surf. Sci.* **1993**, *44*, 5–66. [CrossRef]
367. Jensen, F.; Besenbacher, F.; Laegsgaard, E.; Stensgaard, I. Surface reconstruction of Cu(110) induced by oxygen chemisorption. *Phys. Rev. B* **1990**, *41*, 10233–10236. [CrossRef]
368. Merrick, I.; Inglesfield, J.E.; Ishida, H. Electronic structure and surface reconstruction of adsorbed oxygen on copper(001). *Surf. Sci.* **2004**, *551*, 158–170. [CrossRef]
369. Deskins, N.A.; Lauterbach, J.; Thomson, K.T. Lifting the Pt{100} surface reconstruction through oxygen adsorption: A density functional theory analysis. *J. Chem. Phys.* **2005**, *122*, 184709. [CrossRef]
370. Ciobîcă, I.M.; van Santen, R.A.; van Berge, P.J.; van de Loosdrecht, J. Adsorbate induced reconstruction of cobalt surfaces. *Surf. Sci.* **2008**, *602*, 17–27. [CrossRef]
371. Oyarzún, S.; Tamion, A.; Tournus, F.; Dupuis, V.; Hillenkamp, M. Size effects in the magnetic anisotropy of embedded cobalt nanoparticles: From shape to surface. *Sci. Rep.* **2015**, *5*, 16–21. [CrossRef]
372. Wernsdorfer, W.; Thirion, C.; Demoncy, N.; Pascard, H.; Mailly, D. Magnetisation reversal by uniform rotation (Stoner-Wohlfarth model) in FCC cobalt nanoparticles. *J. Magn. Magn. Mater.* **2002**, *242–245*, 132–138. [CrossRef]
373. Balan, A.; Derlet, P.M.; Rodríguez, A.F.; Bansmann, J.; Yanes, R.; Nowak, U.; Kleibert, A.; Nolting, F. Direct observation of magnetic metastability in individual iron nanoparticles. *Phys. Rev. Lett.* **2014**, *112*, 107201. [CrossRef]
374. Chen, J.P.; Sorensen, C.M.; Klabunde, K.J. Enhanced Magnetization of Nanoscale Colloidal Cobalt Particles. *Phys. Rev. B* **1995**, *51*, 527–533. [CrossRef] [PubMed]
375. Jamet, M.; Dupuis, V.; Mélinon, P.; Guiraud, G.; Pérez, A.; Wernsdorfer, W. Structure and magnetism of well defined cobalt nanoparticles embedded in a niobium matrix. *Phys. Rev. B Condens. Matter Mater. Phys.* **2000**, *62*, 493–499. [CrossRef]
376. He, L.; Chen, C. Effect of temperature-dependent shape anisotropy on coercivity for aligned Stoner-Wohlfarth soft ferromagnets. *Phys. Rev. B Condens. Matter Mater. Phys.* **2007**, *75*, 184424. [CrossRef]
377. Wang, Z.W.; Palmer, R.E. Determination of the ground-state atomic structures of size-selected Au nanoclusters by electron-beam-induced transformation. *Phys. Rev. Lett.* **2012**, *108*, 245502. [CrossRef]
378. Tournus, F.; Sato, K.; Epicier, T.; Konno, T.J.; Dupuis, V. Multi-$L1_0$ domain CoPt and FePt nanoparticles revealed by electron microscopy. *Phys. Rev. Lett.* **2013**, *110*, 055501. [CrossRef]
379. Masini, F.; Hernández-Fernández, P.; Deiana, D.; Strebel, C.E.; McCarthy, D.N.; Bodin, A.; Malacrida, P.; Stephens, I.; Chorkendorff, I. Exploring the phase space of time of flight mass selected Pt_xY nanoparticles. *Phys. Chem. Chem. Phys.* **2014**, *16*, 26506–26513. [CrossRef]
380. Barke, I.; Hartmann, H.; Rupp, D.; Flückiger, L.; Sauppe, M.; Adolph, M.; Schorb, S.; Bostedt, C.; Treusch, R.; Peltz, C.; et al. The 3D-architecture of individual free silver nanoparticles captured by X-ray scattering. *Nat. Commun.* **2015**, *6*, 6187. [CrossRef]
381. Morel, R.; Brenac, A.; Portemont, C.; Deutsch, T.; Notin, L. Magnetic anisotropy in icosahedral cobalt clusters. *J. Magn. Magn. Mater.* **2007**, *308*, 296–304. [CrossRef]
382. Sato, H.; Kitakami, O.; Sakurai, T.; Shimada, Y.; Otani, Y.; Fukamichi, K.; Introduction, I. Structure and magnetism of hcp-Co fine particles. *J. Appl. Phys.* **1997**, *81*, 1858. [CrossRef]
383. Jamet, M.; Wernsdorfer, W.; Thirion, C.; Mailly, D.; Dupuis, V.; Mélinon, P.; Pérez, A. Magnetic Anisotropy of a Single Cobalt Nanocluster. *Phys. Rev. Lett.* **2001**, *86*, 4676–4679. [CrossRef]
384. Farkaš, B.; De Leeuw, N.H. Effect of coverage on the magnetic properties of -COOH, -SH, and -NH_2 ligand-protected cobalt nanoparticles. *Nanoscale* **2021**. [CrossRef]
385. Pachón, L.D.; Rothenberg, G. Transition-metal nanoparticles: Synthesis, stability and the leaching issue. *Appl. Organomet. Chem.* **2008**, *22*, 288–299. [CrossRef]
386. Cao, A.; Lu, R.; Veser, G. Stabilizing metal nanoparticles for heterogeneous catalysis. *Phys. Chem. Chem. Phys.* **2010**, *12*, 13499–13510. [CrossRef]
387. Albrecht, W.; Bladt, E.; Vanrompay, H.; Smith, J.D.; Skrabalak, S.E.; Bals, S. Thermal Stability of Gold/Palladium Octopods Studied in Situ in 3D: Understanding Design Rules for Thermally Stable Metal Nanoparticles. *ACS Nano* **2019**, *13*, 6522–6530. [CrossRef]
388. Respaud, M.; Broto, J.M.; Rakoto, H.; Fert, A.R.; Thomas, L.; Barbara, B.; Verelst, M.; Snoeck, E.; Lecante, P.; Mosset, A.; et al. Surface effects on the magnetic properties of ultrafine cobalt particles. *Phys. Rev. B* **1998**, *57*, 2925–2935. [CrossRef]
389. van Leeuwen, D.A.; van Ruitenbeek, J.M.; de Jongh, L.J.; Ceriotti, A.; Pacchioni, G.; Häberlen, O.D.; Rösch, N. Quenching of Magnetic Moments by Ligand-Metal Interactions in Nanosized Magnetic Metal Clusters. *Phys. Rev. Lett.* **1994**, *73*, 1432–1435. [CrossRef]
390. Chen, W.; Zhou, W.; He, L.; Chen, C.; Guo, L. Surface magnetic states of Ni nanochains modified by using different organic surfactants. *J. Phys. Condens. Matter* **2010**, *22*, 126003. [CrossRef]
391. Jo, C.; Il Lee, J. Spin polarization and charge transfer of Co nanoclusters coated with CO molecules. *J. Magn. Magn. Mater.* **2009**, *321*, 47–51. [CrossRef]
392. Cotton, F.A.; Meyers, M.D. Magnetic and Spectral Properties of the Spin-Free $3d^6$ Systems Iron(II) and Cobalt(III) in Cobalt(III) Hexafluoride Ion: Probable Observation of Dynamic Jahn–Teller Effects. *J. Am. Chem. Soc.* **1960**, *82*, 5023–5026. [CrossRef]
393. Cotton, F.A.; Goodgame, D.M.L.; Goodgame, M. The Electronic Structures of Tetrahedral Cobalt(II) Complexes. *J. Am. Chem. Soc.* **1961**, *83*, 4690–4699. [CrossRef]

394. Aakesson, R.; Pettersson, L.G.M.; Sandstroem, M.; Wahlgren, U. Ligand Field Effects in the Hydrated Divalent and Trivalent Metal Ions of the First and Second Transition Periods. *J. Am. Chem. Soc.* **1994**, *116*, 8691–8704. [CrossRef]
395. Hartmann, M.J.; Millstone, J.E.; Häkkinen, H. Surface Chemistry Controls Magnetism in Cobalt Nanoclusters. *J. Phys. Chem. C* **2016**, *120*, 20822–20827. [CrossRef]
396. Hartmann, M.J.; Millstone, J.E.; Häkkinen, H. Ligand mediated evolution of size dependent magnetism in cobalt nanoclusters. *Phys. Chem. Chem. Phys.* **2018**, *20*, 4563–4570. [CrossRef]
397. Kuznetsov, A.A.; Leontiev, V.G.; Brukvin, V.A.; Vorozhtsov, G.N.; Kogan, B.Y.; Shlyakhtin, O.A.; Yunin, A.M.; Tsybin, O.I.; Kuznetsov, O.A. Local radiofrequency-induced hyperthermia using CuNi nanoparticles with therapeutically suitable Curie temperature. *J. Magn. Magn. Mater.* **2007**, *311*, 197–203. [CrossRef]
398. Wijaya, A.; Brown, K.A.; Alper, J.D.; Hamad-Schifferli, K. Magnetic field heating study of Fe-doped Au nanoparticles. *J. Magn. Magn. Mater.* **2007**, *309*, 15–19. [CrossRef]
399. Liu, H.L.; Wu, J.H.; Min, J.H.; Kim, Y.K. Synthesis of monosized magnetic-optical AuFe alloy nanoparticles. *J. Appl. Phys.* **2008**, *103*, 07D529. [CrossRef]
400. Srinoi, P.; Chen, Y.T.; Vittur, V.; Marquez, M.D.; Lee, T.R. Bimetallic nanoparticles: Enhanced magnetic and optical properties for emerging biological applications; 2018; Vol. 8; ISBN 1713743272. *Appl. Sci.* **2018**, *8*, 1106. [CrossRef]
401. Farkaš, B.; Perry, C.B.; Jones, G.; De Leeuw, N.H. Adsorbate-Induced Segregation of Cobalt from PtCo Nanoparticles: Modeling Au Doping and Core AuCo Alloying for the Improvement of Fuel Cell Cathode Catalysts. *J. Phys. Chem. C* **2020**, *124*, 18321–18334. [CrossRef]
402. Wu, X.; Sun, Y.; Wei, Z.; Chen, T. Influence of noble metal dopants (M = Ag, Au, Pd or Pt) on the stable structures of bimetallic Co-M clusters. *J. Alloys Compd.* **2017**, *701*, 447–455. [CrossRef]
403. Hall, R.C. Magnetic anisotropy and magnetostriction of ordered and disordered Cobalt-iron alloys. *J. Appl. Phys.* **1960**, *157*, 10–12. [CrossRef]
404. Weller, D.; Brändle, H.; Gorman, G.; Lin, C.J.; Notarys, H. Magnetic and magneto-optical properties of cobalt-platinum alloys with perpendicular magnetic anisotropy. *Appl. Phys. Lett.* **1992**, *61*, 2726–2728. [CrossRef]
405. Weller, D.; Brändle, H.; Chappert, C. Relationship between Kerr effect and perpendicular magnetic anisotropy in $Co_{1-x}Pt_x$ and $Co_{1-x}Pd_x$ alloys. *J. Magn. Magn. Mater.* **1993**, *121*, 461–470. [CrossRef]
406. Huang, J.C.A.; Hsu, A.C.; Lee, Y.H.; Wu, T.H.; Lee, C.H. Influence of crystal structure on the perpendicular magnetic anisotropy of an epitaxial CoPt alloy. *J. Appl. Phys.* **1999**, *85*, 5977–5979. [CrossRef]
407. Lin, C.J.; Gorman, G.L. Evaporated CoPt alloy films with strong perpendicular magnetic anisotropy. *Appl. Phys. Lett.* **1992**, *61*, 1600–1602. [CrossRef]
408. Hashimoto, S.; Ochiai, Y.; Aso, K. Perpendicular magnetic anisotropy in sputtered copd alloy films. *Jpn. J. Appl. Phys.* **1989**, *28*, 1596–1599. [CrossRef]
409. Shick, A.B.; Mryasov, O.N. Coulomb correlations and magnetic anisotropy in ordered (formula presented) CoPt and FePt alloys. *Phys. Rev. B Condens. Matter Mater. Phys.* **2003**, *67*, 172407. [CrossRef]
410. Staunton, J.B.; Ostanin, S.; Razee, S.S.A.; Gyorffy, B.; Szunyogh, L.; Ginatempo, B.; Bruno, E. Long-range chemical order effects upon the magnetic anisotropy of FePt alloys from an ab initio electronic structure theory. *J. Phys. Condens. Matter* **2004**, *16*, S5623. [CrossRef]
411. Burkert, T.; Nordström, L.; Eriksson, O.; Heinonen, O. Giant magnetic anisotropy in tetragonal FeCo alloys. *Phys. Rev. Lett.* **2004**, *93*, 027203. [CrossRef]
412. Turek, I.; Kudrnovský, J.; Carva, K. Magnetic anisotropy energy of disordered tetragonal Fe-Co systems from ab initio alloy theory. *Phys. Rev. B Condens. Matter Mater. Phys.* **2012**, *86*, 174430. [CrossRef]
413. Eurin, P.; Pauleve, J. Influence of thermomagnetic treatments on the magnetic properties of Co-Pt 50-50 alloy. *IEEE Trans. Magn.* **1969**, *5*, 216–219. [CrossRef]
414. Tournus, F.; Blanc, N.; Tamion, A.; Dupuis, V.; Epicier, T. Coalescence-free L10 ordering of embedded CoPt nanoparticles. *J. Appl. Phys.* **2011**, *109*, 2009–2012. [CrossRef]
415. Sun, X.; Jia, Z.Y.; Huang, Y.H.; Harrell, J.W.; Nikles, D.E.; Sun, K.; Wang, L.M. Synthesis and magnetic properties of CoPt nanoparticles. *J. Appl. Phys.* **2004**, *95*, 6747–6749. [CrossRef]
416. Shevchenko, E.V.; Talapin, D.V.; Schnablegger, H.; Kornowski, A.; Festin, Ö.; Svedlindh, P.; Haase, M.; Weller, H. Study of nucleation and growth in the organometallic synthesis of magnetic alloy nanocrystals: The role of nucleation rate in size control of CoPt3 nanocrystals. *J. Am. Chem. Soc.* **2003**, *125*, 9090–9101. [CrossRef]
417. Nairan, A.; Khan, U.; Iqbal, M.; Khan, M.; Javed, K.; Riaz, S.; Naseem, S.; Han, X. Structural and magnetic response in bimetallic core/shell magnetic nanoparticles. *Nanomaterials* **2016**, *6*, 72. [CrossRef]
418. Li, J.; Sharma, S.; Liu, X.; Pan, Y.T.; Spendelow, J.S.; Chi, M.; Jia, Y.; Zhang, P.; Cullen, D.A.; Xi, Z.; et al. Hard-Magnet $L1_0$ -CoPt Nanoparticles Advance Fuel Cell Catalysis. *Joule* **2019**, *3*, 124–135. [CrossRef]
419. Li, G.; Wang, Q.; Li, D.; Lü, X.; He, J. Structure evolution during the cooling and coalesced cooling processes of Cu-Co bimetallic clusters. *Phys. Lett. Sect. A Gen. At. Solid State Phys.* **2008**, *372*, 6764–6769. [CrossRef]
420. Mejía-Rosales, S.J.; Fernández-Navarro, C.; Pérez-Tijerina, E.; Blom, D.A.; Allard, L.F.; José-Yacamán, M. On the structure of Au/Pd bimetallic nanoparticles. *J. Phys. Chem. C* **2007**, *111*, 1256–1260. [CrossRef]

421. Rodríguez-López, J.L.; Montejano-Carrizales, J.M.; José-Yacamán, M. Molecular dynamics study of bimetallic nanoparticles: The case of Au x Cu y alloy clusters. *Appl. Surf. Sci.* **2003**, *219*, 56–63. [CrossRef]
422. Yeo, S.C.; Kim, D.H.; Shin, K.; Lee, H.M. Phase diagram and structural evolution of Ag-Au bimetallic nanoparticles: Molecular dynamics simulations. *Phys. Chem. Chem. Phys.* **2012**, *14*, 2791–2796. [CrossRef]
423. Rodríguez-Proenza, C.A.; Palomares-Báez, J.P.; Chávez-Rojo, M.A.; García-Ruiz, A.F.; Azanza-Ricardo, C.L.; Santoveña-Uribe, A.; Luna-Bárcenas, G.; Rodríguez-López, J.L.; Esparza, R. Atomic surface segregation and structural characterization of PdPt bimetallic nanoparticles. *Materials* **2018**, *11*, 1882. [CrossRef]
424. Rojas-Nunez, J.; Gonzalez, R.I.; Bringa, E.M.; Allende, S.; Sepúlveda, P.; Arancibia-Miranda, N.; Baltazar, S.E. Toward Controlled Morphology of FeCu Nanoparticles: Cu Concentration and Size Effects. *J. Phys. Chem. C* **2018**, *122*, 8528–8534. [CrossRef]
425. Kumar, S. Structural Evolution of Iron-Copper (Fe-Cu) Bimetallic Janus Nanoparticles during Solidification: An Atomistic Investigation. *J. Phys. Chem. C* **2019**, *124*, 1053–1063. [CrossRef]
426. Dannenberg, A.; Gruner, M.E.; Hucht, A.; Entel, P. Surface energies of stoichiometric FePt and CoPt alloys and their implications for nanoparticle morphologies. *Phys. Rev. B Condens. Matter Mater. Phys.* **2009**, *80*, 245438. [CrossRef]
427. Okamoto, H.; Massalski, T.B.; Nishizawa, T.; Hasebe, M. The Au-Co (Gold-Cobalt) system. *Bull. Alloy Phase Diagrams* **1985**, *6*, 449–454. [CrossRef]
428. Bochicchio, D.; Ferrando, R. Morphological instability of core-shell metallic nanoparticles. *Phys. Rev. B Condens. Matter Mater. Phys.* **2013**, *87*, 165435. [CrossRef]
429. Nelli, D.; Ferrando, R. Core-shell: Vs. multi-shell formation in nanoalloy evolution from disordered configurations. *Nanoscale* **2019**, *11*, 13040–13050. [CrossRef]
430. Bao, Y.; Calderon, H.; Krishnan, K.M. Synthesis and characterization of magnetic-optical Co-Au core-shell nanoparticles. *J. Phys. Chem. C* **2007**, *111*, 1941–1944. [CrossRef]
431. Mandal, S.; Krishnan, K.M. Co core Au shell nanoparticles: Evolution of magnetic properties in the displacement reaction. *J. Mater. Chem.* **2007**, *17*, 372–376. [CrossRef]
432. Mayoral, A.; Llamosa, D.; Huttel, Y. A novel Co@Au structure formed in bimetallic core@shell nanoparticles. *Chem. Commun.* **2015**, *51*, 8442–8445. [CrossRef]
433. Zhang, Z.; Nenoff, T.M.; Huang, J.Y.; Berry, D.T.; Provencio, P.P. Room temperature synthesis of thermally tmmiscible Ag-Ni nanoalloys. *J. Phys. Chem. C* **2009**, *113*, 1155–1159. [CrossRef]
434. Kuo, C.C.; Li, C.Y.; Lee, C.H.; Li, H.C.; Li, W.H. Huge inverse magnetization generated by faraday induction in nano-sized Au@Ni Core@Shell nanoparticles. *Int. J. Mol. Sci.* **2015**, *16*, 20139–20151. [CrossRef]
435. Zhang, D.F.; Zhang, Q.; Huang, W.F.; Guo, L.; Chen, W.M.; Chu, W.S.; Chen, C.; Wu, Z.Y. Low-temperature fabrication of Au-Co cluster mixed nanohybrids with high magnetic moment of Co. *ACS Appl. Mater. Interfaces* **2012**, *4*, 5643–5649. [CrossRef]

materials

Communication

Rapid Magneto-Sonoporation of Adipose-Derived Cells

Miriam Filippi [1,*], Boris Dasen [2] and Arnaud Scherberich [2,3,*]

[1] Soft Robotics Laboratory, ETH Zurich, Tannenstrasse 3, 8092 Zurich, Switzerland
[2] Department of Biomedicine, University Hospital Basel, University of Basel, Hebelstrasse 20, 4031 Basel, Switzerland; boris.dasen@usb.ch
[3] Department of Biomedical Engineering, University of Basel, Gewerbestrasse 14, 4123 Allschwil, Switzerland
* Correspondence: miriam.filippi@srl.ethz.ch (M.F.); arnaud.scherberich@usb.ch (A.S.)

Abstract: By permeabilizing the cell membrane with ultrasound and facilitating the uptake of iron oxide nanoparticles, the magneto-sonoporation (MSP) technique can be used to instantaneously label transplantable cells (like stem cells) to be visualized via magnetic resonance imaging in vivo. However, the effects of MSP on cells are still largely unexplored. Here, we applied MSP to the widely applicable adipose-derived stem cells (ASCs) for the first time and investigated its effects on the biology of those cells. Upon optimization, MSP allowed us to achieve a consistent nanoparticle uptake (in the range of 10 pg/cell) and a complete membrane resealing in few minutes. Surprisingly, this treatment altered the metabolic activity of cells and induced their differentiation towards an osteoblastic profile, as demonstrated by an increased expression of osteogenic genes and morphological changes. Histological evidence of osteogenic tissue development was collected also in 3D hydrogel constructs. These results point to a novel role of MSP in remote biophysical stimulation of cells with focus application in bone tissue repair.

Keywords: magneto-sonoporation; magnetic nanoparticles; stem cells; superparamagnetic iron oxide particles; cell labelling; ultrasounds; osteogenesis; bone tissue engineering

Citation: Filippi, M.; Dasen, B.; Scherberich, A. Rapid Magneto-Sonoporation of Adipose-Derived Cells. *Materials* **2021**, *14*, 4877. https://doi.org/10.3390/ma14174877

Academic Editor: Lucia Del Bianco

Received: 2 July 2021
Accepted: 24 August 2021
Published: 27 August 2021

1. Introduction

Due to their responsiveness to externally applied magnetic fields, magnetic nanoparticles (MNPs) are extremely attractive materials used in a number of biomedical applications [1]. Iron oxide-based nanoparticles (IONPs) are composed of cores of magnetite (Fe_3O_4) and its oxidized form maghemite (γ–Fe_2O_3), further surrounded by external coatings that increase the stability and biocompatibility of the suspension. The IONPs have been extensively exploited as contrast agents for magnetic resonance imaging (MRI), but thanks to their highly versatile superparamagnetic nature, they have become relevant also in biosensing, gene and drug delivery, engineering of biological tissues, and theranostics, a discipline that combines treatment and diagnosis of various pathologies [2]. The labeling of cells via IONPs enables not only their visualization and real-time monitoring, but also their magnetization. Magnetization of cells allows for the remote control of their functions and spatial localization. As such, this technique has become of great interest for the delivery of therapeutic cells (cell therapy) and manufacturing of transplantable tissue (tissue engineering) [3]. Indeed, magnetizing the cells with multidirectional differentiation potential and self-renewal capabilities, such as stem cells, holds potential in mediating the structural repair and functional recovery of biological tissues. In fact, the IONPs can be used to stimulate the signaling pathways and regulate the cell functions involved in regeneration (magnetic actuation), as well as to spatially guide the cells through magnetic forces (magnetic targeting and printing) [4–7].

However, regenerative and stem cells are non-phagocytic cells. As such, conventional labeling procedures require long times of incubation and lead to moderate uptake efficiency. Cytotoxicity often occurs at high dosages and long exposure times [8–12]. To enhance the

IONP internalization and improve stem cell magnetization, methodological optimization has been widely tested. For instance, since subjecting the cells to physical forces can assist the delivery of bioactive molecules, various techniques based on biophysical cell stimulation have been proposed, including: microinjection, electroporation, laser irradiation, magnetofection, and electric field-induced molecular vibration [13–16]. However, issues of cytotoxicity are still present.

Mechanical waves, such as ultrasound (US), transiently enhance the permeability of biological membranes (like endothelial layers and cell membranes) and thus facilitate the passage of drugs based on small molecules, plasmidic DNA, and also nanomaterials across layers and barriers. The use of US waves to temporarily permeabilize the cell membrane and elicit the intracellular uptake of exogenous compounds is known as sonoporation, and can be achieved by applying sonication at low frequency (kilohertz), lithotripter shockwaves, high-frequency ultrasound (HIFU), or even diagnostic ultrasound (megahertz frequencies) [17–19]. Sonication allows for safe, effective drug and gene delivery, which can be further enhanced by ultrasonically activated microbubbles (MBs) that pulsate in the close proximity of the cells and augment their membrane permeability [18–21]. Simple and inexpensive, sonoporation also offers the following advantages: minimal requirement in terms of instrumentation; temporal and spatial specificity based on the site of insonation; low risk of immuno-pathogenesis; existing extensive characterization of the approach in vitro and in mammalians; need for moderate energy transfer and easy implementation into clinical approaches; as well as rapid kinetics comparable to those of electroporation (i.e., instant labeling) [18,19]. Moreover, whereas current physical methods allow for instant labeling of limited number of cells, large quantities of cells can be labeled by sonoporation [22,23].

Due to these advantages, sonoporation has emerged among physical cell labeling methods, and it has been extensively used to deliver pharmaceuticals and genetic material [17,19]. During the transient perforation of the membrane, bioactive compounds enter the cells with tunable kinetics which are strongly determined by both acoustic driving parameters and MB-to-cell relative parameters [24–26]. Interestingly, in order to enhance the internalization of biochemicals, sonoporation has been applied also in combination with nanomaterials [27]. Liposomes, polymeric nanoparticles, micelles and nanoemulsions enhanced the gene transfection and drug loading efficiency by acting as nanocarriers, stimuli-responsive delivery systems, or co-adjuvant agents [27–29]. Some of these works demonstrated that nanosized materials could cross the cell membrane during its permeabilization. However, the use of sonoporation to increase the internalization of IONPs (magneto-sonoporation, MSP) has been tested through only few studies [22,23,30–32], which were carried out on progenitor cells with circumscribed regenerative potential and applicability, like neural stem cells and osteosarcoma cell lines [22,23,32].

The adipose-derived stem cells (ASCs) display low immunogenicity and can differentiate into multiple cell types [33]. Furthermore, they can be easily harvested with limited morbidity and then rapidly expanded. As such, they have already been involved in a vast plethora of therapeutic applications at both the pre-clinical and clinical levels. Importantly, ASCs stimulate tissue repair by releasing growth factors [34,35] and undergoing differentiation into muscle, endothelial, bone, cartilage, adipose and nerve tissue [36–39]. Due to their versatility and potency, these cells hold promise for developing effective cellular therapies in various types of damaged tissues [40–42]. Intriguingly, they respond to physical stimuli by activating specific signaling pathways (such as those involved in the differentiation) [43,44], which allows for remote control of their functions [45].

Thereby, the quick and efficient magnetization of ASCs would substantially improve their traceability by MRI and their use in regenerative medicine. In order to enhance the internalization of IONPs and achieve rapid cell magnetization, we thus treated human ASCs with MSP and then characterized the effects of this procedure on the IONP uptake, viability, metabolic activity and differentiation of those cells.

2. Materials and Methods

2.1. Adipose-Derived Stem Cells (ASC) Culture

The ASCs were isolated from the stromal vascular fraction (SVF) cells extracted from the adipose tissue, as previously reported [46,47]. Liposuctions were obtained from six healthy donors after informed consent and according to a protocol approved by the Ethical Committee of the Canton of Basel (Ethikkommission beider Basel [EKKB], Ref. 78/07). The human adipose tissue biopsies were enzymatically digested (37 °C, 45 min) with 0.075% collagenase type II (Worthington Biochemical Corp., Lakewood, NJ, USA) and centrifuged (1700 rpm, 10 min). Finally, a complete medium (CM) consisting of alpha-modified Eagle's medium (α-MEM) supplemented with 10% fetal bovine serum (FBS) (Sigma-Aldrich, Schaffausen, Switzerland), 1% HEPES (Sigma-Aldrich, Schaffausen, Switzerland), 1% sodium pyruvate(Sigma-Aldrich, Schaffausen, Switzerland), and 1% penicillin (10,000 U/mL) (Sigma-Aldrich, Schaffausen, Switzerland), streptomycin (10,000 µg/mL) (Sigma-Aldrich, Schaffausen, Switzerland) and L-glutamine (29.2 mg/mL) solution (PSG solution, Thermo Fischer Scientific, Waltham, MA, USA) was used to suspend the cells before they were filtered through a 100 µm strainer (BD Biosciences, Eysins, Vaud, Switzerland) and counted. SVF cells were plated and then, the ASCs were isolated by adherence to plastic during the culture into CM. Cells were incubated in 5% CO_2 at 37 °C and maintained at sub-confluent levels onto poly-D-lysine (Sigma-Aldrich, Schaffausen, Switzerland)-coated 75 cm^2 flasks, with medium changes every 72 h. When flasks were confluent, cells were detached with trypsin-EDTA (Thermo Fischer Scientific, Waltham, MA, USA), split and re-plated.

2.2. Magneto-Sonoporation

To perform sonoporation, cells were suspended in phosphate-buffered saline (PBS) at a density of approximately 1.5×10^6 cells/mL and mixed with PEG-functionalized iron oxide (II,III) nanoparticles with an average particle size of 15 nm (1 mg/mL in aqueous suspension) purchased from Sigma Aldrich, Schaffausen, Switzerland. MBs of 2.3–2.9 µm of diameter (membrane composition: polyethylene-glycol, phospholipids, and fatty acids; gas mixture: perfluorobutane and nitrogen) used as untargeted US contrast agents (SonoVue) were purchased from BRACCO Research SA (Geneva, Switzerland). After adding the MBs, the plastic tubes containing the mixture were then readily transferred to a custom cup-like container for sonication, which was installed on the top of an ultrasonic transducer connected to an ultrasonic liquid processor sonicator (S4000, Misonix Inc., Farmingdale, NY, USA). To optimize the procedure, the crucial parameters were considered: ultrasonic intensity, duty cycle, and exposure time, which could be adjusted through the digital panel of the ultrasound generator. Water served as transmission medium between the acoustic probe and the specimens, with acoustic powers being tuned as 0.5–2.0 W/cm^2. First, viability of ASCs alone was evaluated by Trypan Blue exclusion test, upon variable power intensities (0.5, 1.0, 2.0 W/cm^2), exposure times (5, 10, 30, 60, 120, 300 s), and duty cycles (20%, 50%). Those parameters that elicited high cell viability (>90%) were selected as the sub-optimal parameters for optimizing the procedure in the presence of IONPs (50 µg/mL). The second round of optimization was conducted by comparing the cell viability among various groups by Student's *t*-test in order to select the setting providing the highest viability and intracellular uptake of iron. The following parameters were selected: 20% duty cycle, 1 W/cm^2 and 30 s.

2.3. Iron Content

The amount of iron in the supernatants of gel cultures was determined by assessing the spectrophotometric properties of SPIO using a 96-well multiplate reader and a standard protocol to obtain spectra from 200–750 nm. The iron was quantified by absorbance at 370 nm, i.e., the one of oxybridged iron (i.e., Fe–O–Fe), found in the SPIO crystal core [48,49]. The spectral analysis of 1× PBS was used as a blank for signal normalization. In this study, the limit of quantification for Fe was 0.20 µg/mL.

2.4. Stability of Nanoparticles

In order to assess the overall stability of MNPs in biological media and the effects possibly caused by the US exposure, MNPs were incubated in cell culture medium (dilution ratio, 1:50) and maintained in cell culture conditions (37 °C, 5% CO_2, pH 7.4) for two days. Dynamic light scattering (DLS, Zetasizer Nano 90 ZS, Malvern, UK) allowed for the determination of the mean hydrodynamic diameter of particles and their polydispersity index (PDI). During the monitoring time, the level of NP aggregation was evaluated in terms of size and PDI changes. In order to calculate the particle size, a scattering angle of 90 degrees was used. All measurements were performed in triplicate at 25 °C.

2.5. Prussian Blue Staining of Cells

Following IONP incubation or MSP treatment, the cells were washed twice with PBS and fixed with 4% paraformaldehyde solution (30 min at room temperature). After washing again twice with PBS, cells were exposed to the Prussian blue staining solution, consisting of a 1:1 mixture of 4% hydrochloric acid (Sigma-Aldrich, Schaffausen, Switzerland) and 4% potassium ferrocyanide (Sigma-Aldrich, Schaffausen, Switzerland) for 15 min at room temperature. Cells were washed with distilled water three times, before the counterstaining for cytoplasm with eosin (Panreac Química S.L.U, Barcelona, Spain) for 5 min at room temperature. After washing, the cells were observed using inverted light microscopy (Olympus IX83, Life Science Solutions, Hamburg, Germany). All experiments were carried out in triplicate.

2.6. Cell Viability and Proliferation

In order to determine whether the magneto-sonoporation would adversely affect the functions of the ASCs, cell viability and proliferation (metabolic assimilation rate) were evaluated. Cell viability was determined using Trypan Blue exclusion, with subsequent cell counting using a hemocytometer.

2.7. Morphology Analysis

Light microscopy and fluorescent phalloidin staining of cells were undertaken at the experimental endpoint. Briefly, 5000 cells per well were plated in order to better visualize individual cell morphology. At the endpoint, cells were washed with phosphate buffer saline (PBS) solution and fixed with 4% (*w/v*) paraformaldehyde for 15 min at room temperature. Following permeabilization with 0.2% (*v/v*) Triton X-100 (Sigma-Aldrich, Schaffausen, Switzerland) for 20 min, cells were stained for 20 min in the dark with Alexa 488-conjugated phalloidin (1:40, Life Technologies, Carlsbad, CA, USA). After PBS washes, cells were imaged using an Olympus IX51 fluorescent microscope at 40× magnification. Fifteen images of cells in each experimental condition were taken, and aspect ratio (AR) for each cell (longest cell length/narrowest cell width) was determined using Image J (National Institutes of Health, Bethesda, MD, USA).

2.8. Evaluation of the Membrane Resealing Time

The Methylene Blue dye (Sigma-Aldrich, Schaffausen, Switzerland) (2.5 mM, for 5 min) was added to cells at different time points after the US application. Stained cells were considered as owing a permeable membrane due to sonoporation, and their percentage on the total population was reported.

2.9. Gene Expression Analysis

Total RNA was extracted with RNeasy® Mini kit protocol (#74104, Qiagen, Hilden, Germany). All RNAs were treated by Deoxyribonuclease I (DNAse I; Invitrogen, Waltham, MA, USA) and total RNA was reverse-transcribed into cDNA with the Omniscript Reverse Transcription kit (#205111, Qiagen, Hilden, Germany) at 37 °C for 60 min. Quantitative real-time PCR assays were performed with ABIPrism 77000 Sequence Detection System (Perkin Elmer, Schwerzenbach, Switzerland) and utilizing Taqman Universal PCR Master

Mix (#4304437, Applied Biosystems, Waltham, MA, USA). The cycling parameters were: 50 °C for 2 min, followed by 95 °C for 10 min and 40 cycles of denaturation at 95 °C for 15 s and annealing/extension at 60 °C for 1 min. Reactions were performed in triplicate for each sample and specific gene expression was evaluated using the 2ΔΔCT method. Gene expression levels were normalized to the glyceraldehyde 3-phosphate dehydrogenase GAPDH mRNA. Primers and probes for GAPDH (Hs02758991_g1), Osterix SP7 (Hs00541729_m1), runt-related transcription factor 2 Runx2/Cbfa1 (Hs00231692_m1), ALPI (Hs00357579_g1), and mitogen-activated protein kinase 8 MAPK8 (also known as JNK1, Hs01548508_m1) were all provided by Assays-on-Demand, Gene Expression Products (Applied Biosystems, Waltham, MA, USA).

2.10. Magnetized Hydrogel Preparation

Fibrin gel for cell embedding was prepared by mixing PBS-diluted fibrinogen and thrombin at the final concentration of 20 mg/mL and 5 U/mL, respectively. The cells were suspended in PBS (5×10^6/mL) and quickly added to the mixture. Then, 10 µL of mixture were laden on to sterilized glass coated with hydro-repellant coating (SigmaCoat, Sigma-Aldrich, Schaffausen, Switzerland) to form a drop. The gel was then placed into the incubator (37 °C, 5% CO_2) to allow the crosslinking to occur (in about 5 min).

2.11. Histological Staining

After in vitro culture, the 3D constructs were fixed overnight in a 4% paraformaldehyde solution, before being embedded into paraffin. Histological sections (4.5 µm thickness) were stained with Hematoxylin-Eosin (#GHS116 and #HT110116, respectively from Sigma-Aldrich, Schaffausen, Switzerland), and Alizarin Red S (#A5533, Sigma-Aldrich, Schaffausen, Switzerland). The primary antibody for anti-OCN was purchased from Abcam (ab198228, Cambridge, UK) and used at 1:500 dilution, before the sections were stained with the secondary antibody (1:300 dilution) coupled to Alexa488 (Life Technologies, Carlsbad, CA, USA) and 4′,6-diamidino-2-phenylindole (DAPI, Sigma-Aldrich, Schaffausen, Switzerland).

3. Results

3.1. Magneto-Sonoporation (MSP) Optimization

In order to magnetize the ASCs, we perform MSP in the presence of a commercial formulation of IONPs, composed of pegylated magnetite nanoparticles with an average particle size of 15 nm. The sonoporation procedure was optimized across power intensity, exposure time, and duty cycle (i.e., exposure interval) in order select a combination of parameters that eventually led to high iron internalization rate with well-preserved cell viability. The intracellular uptake of IONPs, expected as a result of the membrane permeabilization (Figure 1A), was assessed by the spectrophotometric method. The highest iron uptake (≈14 pg/cell) was achieved in the cell group treated for 30 s with 20% duty cycle at 1.0 W/cm^2 in the presence of MBs (Figure 1B). The iron content of cells incubated for 15 min with IONPs after 30 s sonication (10.35 pg/cell) was similar to that of cells exposed to US for only 20 s in the presence of MBs (10.4 pg/cell) (Figure 1C). IONPs accumulated in similar amounts also in the non-sonicated cells, but only after 6 h of incubation, whereas for short incubation times (30 s to 15 min) the internalization was minimal. The resealing time of the cell membrane after sonication was assessed by staining with the Methylene Blue, a dye that does not cross intact cell membranes and is employed as an indicator of altered membrane permeability (Figure 1D). During the recovery phase following the stimulation, the blue cells were counted at different time points. Their amount decreased from 73.1 ± 2.3% to 2.2 ± 0.2% in 15 min, revealing a decay constant of 4.5 min, which suggests a rapid return of the cell membrane to its physiological state. To assess whether the MNPs maintain the colloidal stability upon sonication, we used dynamic light scattering (DLS) to monitor the hydrodynamic diameter and polydispersity index (PDI) of particles diluted in the cell culture media and kept in cell culture conditions for two days (Figure 1E).

The PDI values below 0.2 and the small variations in the particle diameter suggested a good stability of the suspension with no evidence of particle aggregation. Moreover, the MNPs internalized in the cells were detected by Prussian Blue staining (Figure 1F). The uptake of the nano-formulation mostly occurred via endocytosis, since the addition of the endocytosis-inhibitor chlorpromazine (CPZ) reduced the MNP internalization during conventional incubation, as shown by the weak staining. However, the endocytosis inhibition affected the internalization poorly when the cells were subjected to MSP.

3.2. Biological Effects of MSP

In order to understand if the MSP could affect the biology of ASCs, changes in their morphology were investigated. One day after MSP in the presence or absence of MBs, elongated cells and some rounded cells were observed by phase contrast microscopy (Figure 2A). Rounded cells were, however, mostly absent in sonicated cultures or in the untreated controls. Most of rounded cells were detached and most likely dead. One week after MSP, the cells displayed evident changes in the overall morphology with an augmented aspect ratio as compared to the other conditions (Figure 2A,B). Some cells with stellated morphology were also sporadically noticed (Figure 2A). Magneto-sonoporated cells also showed reduced proliferation ability as compared to the unsonicated ones (Figure 2C) and augmented metabolic activity with respect to all other controls (Figure 2D). Even if to a minor extent, their metabolic rate increased also in response to the sole presence of MNPs. Finally, the analysis of the gene expression profile revealed increased expression of osteogenesis marker genes (Osterix, ALP, Runx 2), and activation of a mechano-transduction signaling pathway (JNK1).

3.3. Ultrasound (US)-Activated 3D Matrices

In order to understand whether certain biological effects mediated by MSP could be also observed into 3D cell culture environments, a hydrogel-based tissue construct was generated from the co-assembly of fibrin, MNPs and cells (Figure 3A,B), and then sonicated under the experimental conditions selected from the previous experiments. The histological analysis showed that, one week after treatment, the construct was densely populated by cells (Figure 3C), with some localized areas featuring calcium deposition and cells slightly positive for osteocalcin (OCN) expression, as shown by Alizarin Red staining and immuno-fluorescent staining, respectively (Figure 3D,E). Small clusters of aggregated MNPs were also visible in few sites of gels stained with Alizarin Red (Figure 3F).

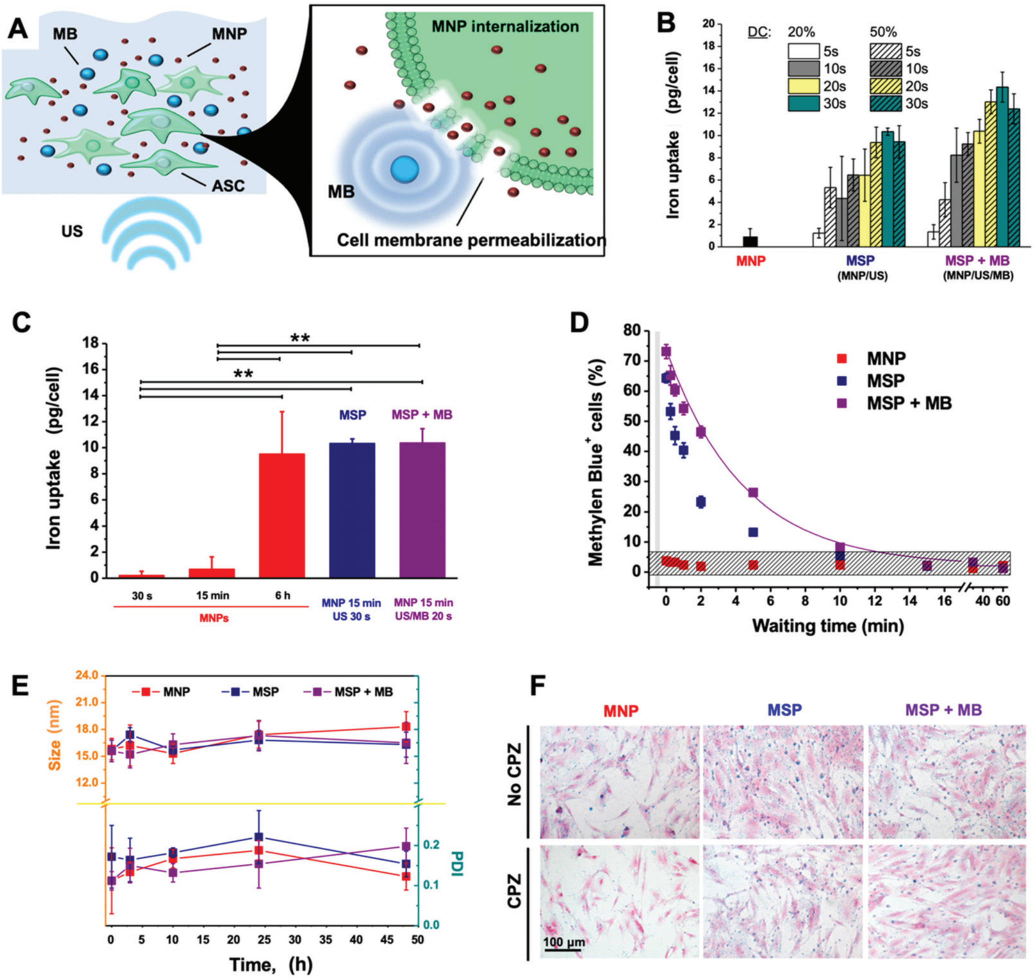

Figure 1. Iron uptake in sonoporated cells. (**A**) Diagram of the working principle of magneto-sonoporation (MSP) using ultrasound (US) in combination or not with microbubbles (MBs) to increase cell membrane permeability. (**B**) To optimize the sonoporation procedure, the cells underwent sonication with different duty cycles for different time ranges at 1.0 W/cm^2. Other power intensities were also tested (data not shown). (**C**) The magnetic nanoparticles (MNP) uptake was compared among cells undergoing simple incubation for different time ranges (30 s, 15 min, 6 h), or upon sonication in the presence or absence of MBs (MSP and MSP + MB, respectively). ** $p < 0{:}01$. (**D**) In order to estimate the resealing time of the cell membrane after sonication, the cells were subjected to the Methylene Blue Permeability assay. Cells positive for the dye were considered to have altered membrane permeability and their fraction over the total population was plotted against time. (**E**) The stability of MNPs in culture media following MSP in the presence or absence of MBs was assessed by monitoring the mean hydrodynamic diameter (size, nm) and polydispersity index (PDI) via dynamic light scattering (DLS) over time, after dilution into cell culture media and maintenance in cell incubation (37 °C, 5% CO_2 and pH 7.4). (**F**) Internalization of MNPs shown by Prussian Blue staining of ASCs after conventional incubation (6 h), MSP or MSP with MBs (15 min) in the presence or absence of the endocytosis-inhibitor chlorpromazine (CPZ). Equivalent volumes of phosphate-buffered saline (PBS) in the culture medium were used as controls (unlabeled).

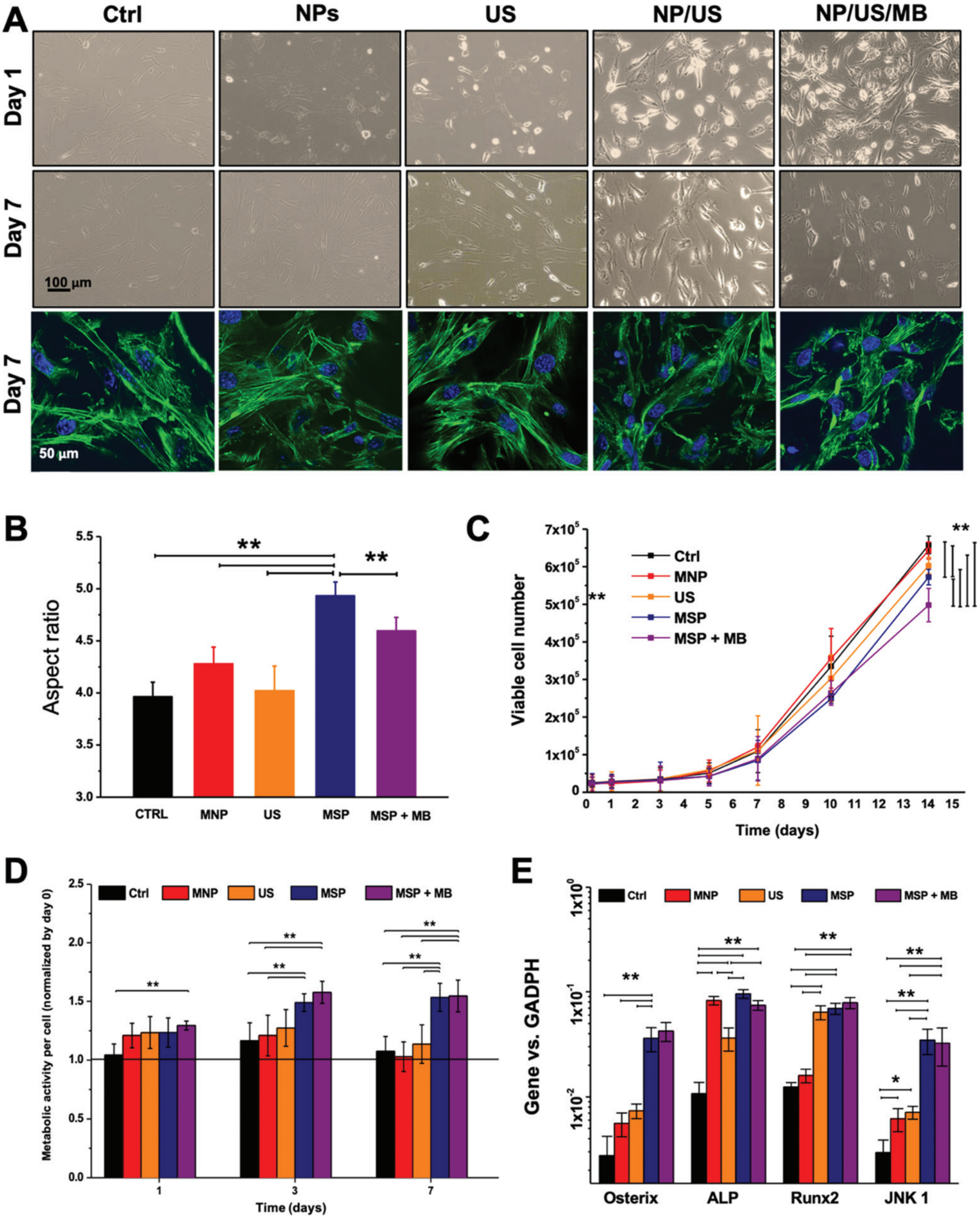

Figure 2. Biological effects. (**A**) Cell morphology was observed in phase contrast microscopy and in fluorescence microscopy (actin displayed in green, nuclei in blue). (**B**) Aspect ratio of cells was calculated one week after the various treatments. (**C**) Proliferation rate of ASCs measured as viable cell numbers over time. (**D**) Metabolic activity per cell in the different conditions, normalized to the DNA content, relative to day 0. (**E**) Gene expression of ASCs one week after sonoporation, focused on the expression of genes involved in osteogenesis and mechanical transduction. Asterisks indicate significant difference (by two-way analysis of variance (ANOVA)): * $p < 0:05$; ** $p < 0:01$. MNP = magnetic nanoparticles; US = ultrasounds; MB = microbubbles. MSP = magneto-sonoporation.

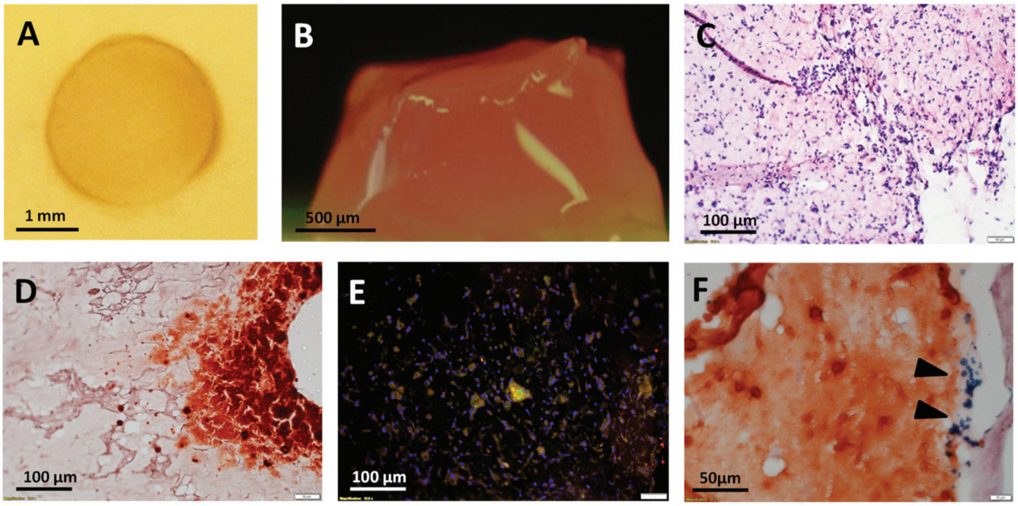

Figure 3. Sonoporation of magnetized 3D tissue constructs. A fibrin-based magnetized 3D tissue construct in top (in cell culture well) and lateral views ((**A**,**B**), respectively). Histological analysis of magnetized tissue, 7 days after sonoporation: hematoxilin and eosin (**C**), Alizarin Red (**D**) and osteocalcin (OCN) immunofluorescent staining (**E**). Nuclear staining (DAPI) and OCN staining are shown in blue and green, respectively. In Alizarin Red, clusters of MNPs were sporadically observed, as a result of aggregation (black arrows, (**F**)).

4. Discussion

Biocompatible nanoscale materials have introduced outstanding innovation in biomedicine, finding use in the controlled delivery of biomolecules, manipulation of cell phenotype and behavior, and improvement of structural or biological features of substrates used for cell growth [50–52]. Key biological applications include non-invasive imaging and drug delivery in living organisms, as well as tissue engineering and wound healing [52–58]. In many instances, the nanomaterial internalization within cells is a mandatory step that can be achieved via various routes. In regards to IONPs, basic labeling procedures relying on the simple cell-nanoparticles co-incubation are conventionally applied because of their technical simplicity [10]. Some transfection agents, especially cationic compounds [8], can possibly be added, which include lipofectamine [9], poly-L-lysine [10,11] and protamine sulfate [12] among others. These substances coat the MRI contrast agents converting them from negatively to positively-charged. This facilitates the binding to the anionic cell membrane, and the subsequent cell internalization. However, such a process often takes a long time and requires high nanomaterial dosage that is detrimental when the exposure to the nano-formulation is associated with time- and dose-dependent decrease of cell viability [59]. The IONP-related cytotoxicity is often mediated by the production of reactive oxygen species [59,60]. In biological systems, the Haber–Weiss reaction is the major responsible mechanism for the generation of highly reactive hydroxyl radicals, and this process can be iron-catalyzed in response to exposure of ferric cores of IONPs let into unstable conditions (e.g., long-lasting permanence in biological milieu) [61–63]. In such conditions, the cells present gross structural alterations (for instance, at the level of the cytoskeleton) that eventually lead to functional impairment and also physical disruption [64]. In our study, we noticed a dramatic decrease in viability when the cells were incubated with IONPs not only together with lipofectamin, but also in presence of the positively-charged linear polymer polyethyleneimine (PEI) (data not shown) that is conventionally used for DNA transfection, but that also widely applied as IONP-coating agent [59]. This observation is in accordance with previous studies demonstrating that certain transfection agents hampered cell viability [59].

To overcome these issues, methods for instant labeling in the absence of additional chemicals have been given a lot of consideration [65]. In "magneto-electroporation" [13–15], electrical pulses induce electromechanical permeability changes in the cell membrane, eliciting the internalization of IONPs [14], or other metal-oxide based particles [15] with treatment duration in the time range of seconds. MSP also enables a fast cell magnetization by inducing a transient membrane perforation. In our experiments, we found that sonicating the cells for 30 s (or 20 s in the presence of MBs) led to IONP uptake yields that could be achieved only after 6 h of standard incubation. In contrast to magneto-electroporation, MSP relies on the convection of ultrasound waves originating from short electrical pulses [19,23]. The energy transfer involved is moderate [66], which implies safe technical settings that can be easily implemented into clinical applications. In the present study, substantial IONP internalization was achieved within a few seconds of sonication, but the treatment was not entirely inert to the cell biology. A short time after MSP, cell death was observed but only to a limited extent. However, even if dramatic cytotoxicity did not occur, sonoporated cells presented slightly decreased proliferation rates and increased metabolic activity. The alterations in the morphology and the genetic expression that we noticed in the treated cells might be the result of cell behavior modulation triggered by mechanical or chemical (iron-related) cues. This functional deviation is congruent to the potential evolution of the ASCs towards the osteogenic profile. In fact, we noticed that a morphology shift occurred in the magneto-sonoporated ASCs. In one week, they lost their conventional fibroblast-like morphology with flattened cell body and acquired instead more spindle-shaped or even stellate-shaped phenotypes, which are typical of the osteoblastic lineage. Congruently, the gene expression was altered by activation of genes involved in the osteogenic differentiation and mechano-transduction signaling pathways.

MBs are typical mediators of acoustic cavitation, a non-thermal US-induced bioeffect which is already widely used for intracellular-delivery [18–20,67]. We performed some of the experiments in the presence of MBs to understand whether they render the MSP more efficient and can modulate the cell behavior. It was found that the presence of MBs could influence some of the cellular processes under investigation (such as the proliferation and the internalization of MNPs), but only scarcely affected others (like the gene expression). This suggests that they play a role in the MNP-cell interaction and can affect the cellular behavior but only to a limited extent.

Methods for bio-physical cell stimulation have started to be integrated into 3D cell culture models, in order to explore their applicability into systems that more faithfully resemble the native tissue configuration as compared to cell monolayers grown in plastic dishes. Matrices activated by sonoporation have also been presented [68–72], which were intended to augment the cell internalization of genetic material on demand. In our study, we have obtained a matrix for ASC culture by co-assembling the MNPs and a common biomedical hydrogel. Our preliminary data show that such culture material can mediate acoustic stimulation of cell functions. The biological effects that we observed also included the deposition of calcium, a feature that points to an osteogenic switch of the ASC phenotype. It is worth noting that the previously reported sono-activated matrices were also developed to enhance the osteogenic potential of progenitors but they relied on direct genetic cell modification [70–72], while in our work we demonstrated that similar results can be achieved by using the mechanical action conveyed by applied forces and small scaled materials. However, the main limitation of the present study is that the biomolecular mechanisms underlying the observed biological effects are not well elucidated. In particular, deeper investigations are needed to differentiate the biochemical effects of the sole MNPs from those of the mechanical stress induced by the MSP procedure. To such a purpose, future studies should focus on the comparison of the MSP with conventional incubation conditions that allow to internalize similar amounts of IONPs, as well as on the assessment of variations in the iron metabolism. Moreover, a complete characterization of the specific formulation of MNPs used as sonoporation agents is also necessary in order to identify the relation between the chemo-physical properties of the nanomaterials, the applied forces, and the reaction triggered in the stimulated biological system. Nevertheless, although observational, the results here reported reveal clear biological alterations that might impact on the proper use of the cells and represent a novel method for biophysical modulation of cell functions.

In the past research, MSP was demonstrated in a few types of stem cell, some of which are endowed with limited potency and can treat only specific pathological tissues [22,23,32]. For instance, it was shown that neural stem cells labeled with superparamagnetic IONPs through focused US maintained key biological features, such as differentiation potential and migration ability to the diseased tissue sites [22,23]. In our study, we performed MSP on ASCs, stem cells characterized by accessible extraction sites, multipotency, and simple culture, that can serve in the regenerative therapy of various tissue types [33–39]. However, we discovered morphological and biochemical alterations suggesting that magneto-sonoporated ASCs were committed towards the osteoblastic profile, thus highlighting a more precise applicative direction in the bone tissue repair.

As the MSP technical settings herein tested allowed for biosafe treatment of cells in vitro, the future pre-clinical research will benefit from our technical optimization of the procedure, while focusing on the mechanisms causing the observed biological alterations. We performed our experiments in a closed apparatus where focused ultrasounds were delivered to cell suspensions collected in plastic tubes, as described in previous works [22,23]. In such a setting, a large number of cells can be easily and safely labeled immediately after the potential extraction from patients, with a reduced contamination risk. The US emission powers were included in the typical value ranges for biocompatible sonoporation, already employed in previous works where MSP demonstrated high capability to preserve cell viability and integrity [22,23,30–32]. The translatability of the present MSP setting mostly concerns the possibility to enhance and accelerate the cell magnetization process, and to control the cell functional profile in vitro, before the potential re-implantation of cells in vivo. Nevertheless, a direct use of MSP in patients can be prospectively imagined following crucial achievements that include:

i. a better definition of the mechanobiological activity of sonicated MNPs and the mechanisms triggering the biological alterations observed in the cells;
ii. the influence of the biophysical properties of the specific MNP formulation on the MSP process;
iii. the understanding of the interaction of US-mediated physical forces with human tissues and bodies;
iv. the inherent optimization of the sonication setting.

The technical implementation of such a knowledge might render it possible to design direct applications of MSP in vivo or to engineer implantable sonoactivated matrices. In this regard, our preliminary test on 3D hydrogel matrices might represent the basis for future investigations enabling the transition of the MSP from a cell pre-conditioning technique to an imaging and therapeutic method applicable in vivo.

5. Conclusions

As a rapid and convenient technique for stem cell labeling, MSP has good prospects for clinical investigations, and the optimization of parameters and experimental settings will allow the MNP-cell interactions to be ameliorated [22]. However, an important consideration arising from our study is that the safety of MSP as applied to stem cell imaging and therapy results in being challenging to decipher and must be evaluated by distinguishing the effects occurring at two different levels. On the one hand, the US waves can have high mechanical compliance with biological materials, rendering the MSP relatively safe to use with cells. Therefore, its application to biological systems is sustainable, and preserves their integrity and survival. On the other hand, the impact of the biophysical stimulation on the intracellular processes has to be carefully assessed. As demonstrated in this work, US and/or micro/nano-materials can strongly affect the cell phenotype in both monolayer and tissue-like configurations. Despite raising questions in regard to the labeling of transplantable cells, this aspect also opens intriguing perspectives in strategies for remote control over cell functions.

Author Contributions: Conceptualization, M.F.; methodology, M.F. and B.D.; validation, M.F.; formal analysis, M.F.; investigation, M.F. and B.D.; data curation, M.F.; writing—original draft preparation, M.F.; writing—review and editing, M.F. and A.S.; supervision, A.S.; project administration, M.F.; funding acquisition, A.S. All authors have read and agreed to the published version of the manuscript.

Funding: This research received no external funding.

Institutional Review Board Statement: The study was conducted according to procedures approved by the Ethical Committee of the Canton of Basel (Ethikkommission beider Basel [EKKB], Ref. 78/07).

Informed Consent Statement: Primary cells used in this study were extracted from biopsies after informed consent of the patients.

Data Availability Statement: Data sharing is not applicable.

Conflicts of Interest: The authors declare no conflict of interest.

References

1. Ajinkya, N.; Yu, X.; Kaithal, P.; Luo, H.; Somani, P.; Ramakrishna, S. Magnetic iron oxide nanoparticle (IONP) synthesis to applications: Present and future. *Materials* **2020**, *13*, 4644. [CrossRef]
2. Ni, J.S.; Li, Y.; Yue, W.; Liu, B.; Li, K. Nanoparticle-based cell trackers for biomedical applications. *Theranostics* **2020**, *10*, 1923–1947. [CrossRef]
3. Farzamfar, S.; Nazeri, N.; Salehi, M.; Valizadeh, A.; Marashi, S.M.; Savari Kouzehkonan, G.; Ghanbari, H. Will nanotechnology bring new hope for stem cell therapy? *Cells Tissues Organs* **2018**, *206*, 229. [CrossRef]
4. Sun, J.H.; Zhang, Y.L.; Qian, S.P.; Yu, X.B.; Xie, H.Y.; Zhou, L.; Zheng, S.S. Assessment of biological characteristics of mesenchymal stem cells labeled with superparamagnetic iron oxide particles in vitro. *Mol. Med. Rep.* **2012**, *5*, 317.
5. Nakamae, T.; Adachi, N.; Kobayashi, T.; Nagata, Y.; Nakasa, T.; Tanaka, N.; Ochi, M. The effect of an external magnetic force on cell adhesion and proliferation of magnetically labeled mesenchymal stem cells. *Sports Med. Arthrosc. Rehabil. Technol.* **2010**, *2*, 5. [CrossRef]
6. Farrell, E.; Wielopolski, P.; Pavljasevic, P.; van Tiel, S.; Jahr, H.; Verhaar, J.; Weinans, H.; Krestin, G.; O'Brien, F.J.; van Osch, G.; et al. Effects of iron oxide incorporation for long term cell tracking on MSC differentiation in vitro and in vivo. *Biochem. Biophys. Res. Commun.* **2008**, *369*, 1076. [CrossRef]
7. Huang, D.M.; Hsiao, J.K.; Chen, Y.C.; Chien, L.Y.; Yao, M.; Chen, Y.K.; Ko, B.S.; Hsu, S.C.; Tai, L.A.; Cheng, H.Y.; et al. The promotion of human mesenchymal stem cell proliferation by superparamagnetic iron oxide nanoparticles. *Biomaterials* **2009**, *30*, 3645. [CrossRef] [PubMed]
8. Suzuki, Y.; Zhang, S.; Kundu, P.; Yeung, A.C.; Robbins, R.C.; Yang, P.C. In vitro comparison of the biological effects of three transfection methods for magnetically labeling mouse embryonic stem cells with ferumoxides. *Magn. Reson. Med.* **2007**, *57*, 1173–1179. [CrossRef]
9. Hoehn, M.; Kustermann, E.; Blunk, J.; Wiedermann, D.; Trapp, T.; Wecker, S.; Focking, M.; Arnold, H.; Hescheler, J.; Fleischmann, B.K.; et al. Monitoring of implanted stem cell migration in vivo: A highly resolved in vivo magnetic resonance imaging investigation of experimental stroke in rat. *Proc. Natl. Acad. Sci. USA* **2002**, *99*, 16267–16272. [CrossRef]
10. Daldrup-Link, H.E.; Meier, R.; Rudelius, M.; Piontek, G.; Piert, M.; Metz, S.; Settles, M.; Uherek, C.; Wels, W.; Schlegel, J.; et al. In vivo tracking of genetically engineered, anti-HER2/neu directed natural killer cells to HER2/neu positive mammary tumors with magnetic resonance imaging. *Eur. Radiol.* **2005**, *15*, 4–13. [CrossRef]
11. Arbab, A.S.; Yocum, G.T.; Kalish, H.; Jordan, E.K.; Anderson, S.A.; Khakoo, A.Y.; Read, E.J.; Frank, J.A. Efficient magnetic cell labeling with protamine sulfate complexed to ferumoxides for cellular MRI. *Blood* **2004**, *104*, 1217–1223. [CrossRef]
12. Daldrup-Link, H.E.; Rudelius, M.; Oostendorp, R.A.; Settles, M.; Piontek, G.; Metz, S.; Rosenbrock, H.; Keller, U.; Heinzmann, U.; Rummeny, E.J.; et al. Targeting of hematopoietic progenitor cells with MR contrast agents. *Radiology* **2003**, *228*, 760–767. [CrossRef]
13. Walczak, P.; Kedziorek, D.A.; Gilad, A.A.; Lin, S.; Bulte, J.W. Instant MR labeling of stem cells using magnetoelectroporation. *Magn. Reson. Med.* **2005**, *54*, 769–774. [CrossRef]
14. Tai, J.H.; Foster, P.; Rosales, A.; Feng, B.; Hasilo, C.; Martinez, V.; Ramadan, S.; Snir, J.; Melling, C.W.; Dhanvantari, S.; et al. Imaging islets labeled with magnetic nanoparticles at 1.5 tesla. *Diabetes* **2006**, *55*, 2931–2938. [CrossRef]
15. Gilad, A.A.; Walczak, P.; McMahon, M.T.; Na, H.B.; Lee, J.H.; An, K.; Hyeon, T.; van Zijl, P.C.; Bulte, J.W. MR tracking of transplanted cells with "positive contrast" using manganese oxide nanoparticles. *Magn. Reson. Med.* **2008**, *60*, 1–7. [CrossRef] [PubMed]

16. Mellott, A.J.; Forrest, M.L.; Detamore, M.S. Physical non-viral gene delivery methods for tissue engineering. *Ann. Biomed. Eng.* **2013**, *41*, 446–468. [CrossRef]
17. Du, X.; Wang, J.; Zhou, Q.; Zhang, L.; Wang, S.; Zhang, Z.; Yao, C. Advanced physical techniques for gene delivery based on membrane perforation. *Drug Deliv.* **2018**, *25*, 1516–1525. [CrossRef] [PubMed]
18. Delalande, A.; Postema, M.; Mignet, N.; Midoux, P.; Pichon, C. Ultrasound and microbubble-assisted gene delivery: Recent advances and ongoing challenges. *Ther. Deliv.* **2012**, *3*, 1199–1215. [CrossRef] [PubMed]
19. Bouakaz, A.; Zeghimi, A.; Doinikov, A.A. Sonoporation: Concept and mechanisms. *Adv. Exp. Med. Biol.* **2016**, *880*, 175–189.
20. Sun, R.R.; Noble, M.L.; Sun, S.S.; Song, S.; Miao, C.H. Development of therapeutic microbubbles for enhancing ultrasound-mediated gene delivery. *J. Control. Release* **2014**, *182*, 111–120. [CrossRef]
21. Delalande, A.; Leduc, C.; Midoux, P.; Postema, M.; Pichon, C. Efficient gene delivery by sonoporation is associated with microbubble entry into cells and the clathrin-dependent endocytosis Pathway. *Ultrasound Med. Biol.* **2015**, *41*, 1913–1926. [CrossRef] [PubMed]
22. Lei, H.; Nan, X.; Wang, Z.; Gao, L.; Xie, L.; Zou, C.; Wan, Q.; Pan, D.; Beauchamp, N.; Yang, X.; et al. Stem cell labeling with superparamagnetic iron oxide nanoparticles using focused ultrasound and magnetic resonance imaging tracking. *J. Nanosci. Nanotechnol.* **2015**, *15*, 2605–2612. [CrossRef]
23. Qiu, B.; Xie, D.; Walczak, P.; Li, X.; Ruiz-Cabello, J.; Minoshima, S.; Bulte, J.W.; Yang, X. Magnetosonoporation: Instant magnetic labeling of stem cells. *Magn. Reson. Med.* **2010**, *63*, 1437–1441. [CrossRef]
24. Qin, P.; Xu, L.; Han, T.; Du, L.; Yu, A.C. Effect of non-acoustic parameters on heterogeneous sonoporation mediated by single-pulse ultrasound and microbubbles. *Ultrason. Sonochem.* **2016**, *31*, 107–115. [CrossRef]
25. Lentacker, I.; De Cock, I.; Deckers, R.; De Smedt, S.C.; Moonen, C.T. Understanding ultrasound induced sonoporation: Definitions and underlying mechanisms. *Adv. Drug Deliv. Rev.* **2014**, *72*, 49–64. [CrossRef]
26. Wang, M.; Zhang, Y.; Cai, C.; Tu, J.; Guo, X.; Zhang, D. Sonoporation-induced cell membrane permeabilization and cytoskeleton disassembly at varied acoustic and microbubble-cell parameters. *Sci. Rep.* **2018**, *8*, 3885. [CrossRef] [PubMed]
27. Husseini, G.A.; Pitt, W.G. Micelles and nanoparticles for ultrasonic drug and gene delivery. *Adv. Drug Deliv. Rev.* **2008**, *60*, 1137–1152. [CrossRef]
28. Awad, N.S.; Paul, V.; AlSawaftah, N.M.; Ter Haar, G.; Allen, T.M.; Pitt, W.G.; Husseini, G.A. Ultrasound-responsive nanocarriers in cancer treatment: A review. *ACS Pharm. Transl. Sci.* **2021**, *4*, 589–612. [CrossRef]
29. Wu, P.; Jia, Y.; Qu, F.; Sun, Y.; Wang, P.; Zhang, K.; Xu, C.; Liu, Q.; Wang, X. Ultrasound-responsive polymeric micelles for sonoporation-assisted site-specific therapeutic action. *ACS Appl. Mater. Interfaces* **2017**, *9*, 25706–25716. [CrossRef]
30. Qiu, B.; Yang, X. Molecular MRI of hematopoietic stem-progenitor cells: In vivo monitoring of gene therapy and atherosclerosis. *Nat. Clin. Pr. Cardiovasc. Med.* **2008**, *5*, 396–404. [CrossRef] [PubMed]
31. Mo, R.; Lin, S.; Wang, G.; Wang, Y.; Wu, E.X. Preliminary in vitro study of ultrasound sonoporation cell labeling with superparamagnetic iron oxide particles for MRI cell tracking. *Annu. Int. Conf. IEEE Eng. Med. Biol. Soc.* **2008**, *2008*, 367–370.
32. Wang, Y.X.; Leung, K.C.; Cheung, W.H.; Wang, H.H.; Shi, L.; Wang, D.F.; Qin, L.; Ahuja, A.T. Low-intensity pulsed ultrasound increases cellular uptake of superparamagnetic iron oxide nanomaterial: Results from human osteosarcoma cell line U2OS. *J. Magn. Reson. Imaging* **2010**, *31*, 1508–1513. [CrossRef]
33. Zhang, J.; Liu, Y.; Chen, Y.; Yuan, L.; Liu, H.; Wang, J.; Liu, Q.; Zhang, Y. Adipose-derived stem cells: Current applications and future directions in the regeneration of multiple tissues. *Stem Cells Int.* **2020**, *2020*, 8810813. [CrossRef]
34. Farinazzo, A.; Turano, E.; Marconi, S.; Bistaffa, E.; Bazzoli, E.; Bonetti, B. Murine adipose-derived mesenchymal stromal cell vesicles: In vitro clues for neuroprotective and neuroregenerative approaches. *Cytotherapy* **2015**, *17*, 571–578. [CrossRef]
35. Kalbermatten, D.F.; Schaakxs, D.; Kingham, P.J.; Wiberg, M. Neurotrophic activity of human adipose stem cells isolated from deep and superficial layers of abdominal fat. *Cell Tissue Res.* **2011**, *344*, 251–260. [CrossRef]
36. Erba, P.; Terenghi, G.; Kingham, P.J. Neural differentiation and therapeutic potential of adipose tissue derived stem cells. *Curr. Stem. Cell Res. Ther.* **2010**, *5*, 153–160. [CrossRef]
37. Mantovani, C.; Terenghi, G.; Shawcross, S.G. Isolation of adult stem cells and their differentiation to Schwann cells. *Methods Mol. Biol.* **2012**, *916*, 47–57.
38. Faroni, A.; Terenghi, G.; Reid, A.J. Adipose-derived stem cells and nerve regeneration: Promises and pitfalls. *Int. Rev. Neurobiol.* **2013**, *108*, 121–136.
39. Kingham, P.J.; Kolar, M.K.; Novikova, L.N.; Novikov, L.N.; Wiberg, M. Stimulating the neurotrophic and angiogenic properties of human adipose-derived stem cells enhances nerve repair. *Stem Cells Dev.* **2014**, *23*, 741–754. [CrossRef]
40. Kappy, N.S.; Chang, S.; Harris, W.M.; Plastini, M.; Ortiz, T.; Zhang, P.; Hazelton, J.P.; Carpenter, J.P.; Brown, S.A. Human adipose-derived stem cell treatment modulates cellular protection in both in vitro and in vivo traumatic brain injury models. *J. Trauma Acute Care Sur* **2018**, *84*, 745–751. [CrossRef]
41. Ciccocioppo, R.; Cangemi, G.C.; Kruzliak, P.; Corazza, G.R. Concise review: Cellular therapies: The potential to regenerate and restore tolerance in immune-mediated intestinal diseases. *Stem Cells* **2016**, *34*, 1474–1486. [CrossRef] [PubMed]
42. Salgado, A.J.; Reis, R.L.; Sousa, N.J.; Gimble, J.M. Adipose tissue derived stem cells secretome: Soluble factors and their roles in regenerative medicine. *Curr. Stem Cell Res.* **2010**, *5*, 103–110. [CrossRef]

43. Tomás, A.R.; Gonçalves, A.I.; Paz, E.; Freitas, P.; Domingues, R.M.A.; Gomes, M.E. Magneto-mechanical actuation of magnetic responsive fibrous scaffolds boosts tenogenesis of human adipose stem cells. *Nanoscale* **2019**, *11*, 18255–18271. [CrossRef] [PubMed]
44. Filippi, M.; Dasen, B.; Guerrero, J.; Garello, F.; Isu, G.; Born, G.; Ehrbar, M.; Martin, I.; Scherberich, A. Magnetic nanocomposite hydrogels and static magnetic field stimulate the osteoblastic and vasculogenic profile of adipose-derived cells. *Biomaterials* **2019**, *223*, 119468. [CrossRef]
45. Labusca, L.; Herea, D.D.; Danceanu, C.M.; Minuti, A.E.; Stavila, C.; Grigoras, M.; Gherca, D.; Stoian, G.; Ababei, G.; Chiriac, H.; et al. The effect of magnetic field exposure on differentiation of magnetite nanoparticle-loaded adipose-derived stem cells. *Mater. Sci. Eng. C Mater. Biol. Appl.* **2020**, *109*, 110652. [CrossRef]
46. Papadimitropoulos, A.; Scherberich, A.; Güven, S.; Theilgaard, N.; Crooijmans, H.J.; Santini, F.; Scheffler, K.; Zallone, A.; Martin, I. A 3D in vitro bone organ model using human progenitor cells. *Eur. Cell Mater.* **2011**, *21*, 445–458. [CrossRef] [PubMed]
47. Guerrero, J.; Pigeot, S.; Müller, J.; Schaefer, D.J.; Martin, I.; Scherberich, A. Fractionated human adipose tissue as a native biomaterial for the generation of a bone organ by endochondral ossification. *Acta Biomater.* **2018**, *77*, 142–154. [CrossRef]
48. Kim, S.J.; Lewis, B.; Steiner, M.S.; Bissa, U.V.; Dose, C.; Frank, J.A. Superparamagnetic iron oxide nanoparticles for direct labeling of stem cells and in vivo MRI tracking. *Contrast Media Mol. Imaging* **2016**, *11*, 55–64. [CrossRef]
49. Schugar, H.J.; Rossman, G.R.; Thibeault, J.; Gray, H.B. Simultaneous pair electronic excitations in a binuclear iron(III) complex. *Chem. Phys. Lett.* **1970**, *6*, 26–28. [CrossRef]
50. Mabrouk, M.; Das, D.B.; Salem, Z.A.; Beherei, H.H. Nanomaterials for biomedical applications: Production, characterisations, recent trends and difficulties. *Molecules* **2021**, *26*, 1077. [CrossRef]
51. Abdollahiyan, P.; Oroojalian, F.; Mokhtarzadeh, A. The triad of nanotechnology, cell signalling, and scaffold implantation for the successful repair of damaged organs: An overview on soft-tissue engineering. *J. Control. Release* **2021**, *332*, 460–492. [CrossRef] [PubMed]
52. Kim, S.W.; Im, G.B.; Kim, Y.J.; Kim, Y.H.; Lee, T.J.; Bhang, S.H. Bio-application of inorganic nanomaterials in tissue engineering. *Adv. Exp. Med. Biol.* **2020**, *1249*, 115–130.
53. Clasky, A.J.; Watchorn, J.D.; Chen, P.Z.; Gu, F.X. From prevention to diagnosis and treatment: Biomedical applications of metal nanoparticle-hydrogel composites. *Acta Biomater.* **2021**, *122*, 1–25. [CrossRef]
54. Han, X.; Li, Y.; Liu, W.; Chen, X.; Song, Z.; Wang, X.; Deng, Y.; Tang, X.; Jiang, Z. The applications of magnetic particle imaging: From cell to body. *Diagnostics* **2020**, *10*, 800. [CrossRef]
55. Pala, R.; Pattnaik, S.; Busi, S.; Nauli, S.M. Nanomaterials as novel cardiovascular theranostics. *Pharmaceutics* **2021**, *13*, 348. [CrossRef] [PubMed]
56. Siemer, S.; Wünsch, D.; Khamis, A.; Lu, Q.; Scherberich, A.; Filippi, M.; Krafft, M.P.; Hagemann, J.; Weiss, C.; Ding, G.B.; et al. Nano meets micro-translational nanotechnology in medicine: Nano-based applications for early tumor detection and therapy. *Nanomaterials* **2020**, *10*, 383. [CrossRef] [PubMed]
57. Hassanzadeh, P. The biomedical significance of multifunctional nanobiomaterials: The key components for site-specific delivery of therapeutics. *Life Sci.* **2021**, *277*, 119400. [CrossRef]
58. Filippi, M.; Born, G.; Felder-Flesch, D.; Scherberich, A. Use of nanoparticles in skeletal tissue regeneration and engineering. *Histol. Histopathol.* **2020**, *35*, 331–350. [PubMed]
59. Feng, Q.; Liu, Y.; Huang, J.; Chen, K.; Huang, J.; Xiao, K. Uptake, distribution, clearance, and toxicity of iron oxide nanoparticles with different sizes and coatings. *Sci. Rep.* **2018**, *8*, 2082. [CrossRef]
60. Kanagesan, S.; Hashim, M.; Tamilselvan, S.; Alitheen, N.B.; Ismail, I.; Hajalilou, A.; Ahsanul, K. Synthesis, characterization, and cytotoxicity of iron oxide nanoparticles. *Adv. Mater. Sci. Eng.* **2013**, *2013*, 710432. [CrossRef]
61. Kehrer, J.P. The Haber-Weiss reaction and mechanisms of toxicity. *Toxicology* **2000**, *149*, 43–50. [CrossRef]
62. Apopa, P.L.; Qian, Y.; Shao, R.; Guo, N.L.; Schwegler-Berry, D.; Pacurari, M.; Porter, D.; Shi, X.; Vallyathan, V.; Castranova, V.; et al. Iron oxide nanoparticles induce human microvascular endothelial cell permeability through reactive oxygen species production and microtubule remodeling. *Part. Fibre Toxicol.* **2009**, *6*, 1. [CrossRef]
63. Videla, L.A.; Fernández, V.; Tapia, G.; Varela, P. Oxidative stress-mediated hepatotoxicity of iron and copper: Role of Kupffer cells. *Biometals* **2003**, *16*, 103–111. [CrossRef]
64. Wu, X.; Tan, Y.; Mao, H.; Zhang, M. Toxic effects of iron oxide nanoparticles on human umbilical vein endothelial cells. *Int. J. Nanomed.* **2010**, *5*, 385–399. [CrossRef]
65. Nejadnik, H.; Jung, K.O.; Theruvath, A.J.; Kiru, L.; Liu, A.; Wu, W.; Sulchek, T.; Pratx, G.; Daldrup-Link, H.E. Instant labeling of therapeutic cells for multimodality imaging. *Theranostics* **2020**, *10*, 6024–6034. [CrossRef] [PubMed]
66. Deng, C.X.; Sieling, F.; Pan, H.; Cui, J. Ultrasound-induced cell membrane porosity. *Ultrasound Med. Biol.* **2004**, *30*, 519–526. [CrossRef] [PubMed]
67. Miller, D.L.; Pislaru, S.V.; Greenleaf, J.E. Sonoporation: Mechanical DNA delivery by ultrasonic cavitation. *Somat. Cell Mol. Genet.* **2002**, *27*, 115–134. [CrossRef]
68. Nomikou, N.; Feichtinger, G.A.; Saha, S.; Nuernberger, S.; Heimel, P.; Redl, H.; McHale, A.P. Ultrasound-responsive gene-activated matrices for osteogenic gene therapy using matrix-assisted sonoporation. *J. Tissue Eng. Regen. Med.* **2018**, *12*, e250–e260. [CrossRef]

69. Nomikou, N.; Feichtinger, G.A.; Redl, H.; McHale, A.P. Ultrasound-mediated gene transfer (sonoporation) in fibrin-based matrices: Potential for use in tissue regeneration. *J. Tissue Eng. Regen. Med.* **2016**, *10*, 29–39. [CrossRef]
70. Feichtinger, G.A.; Hofmann, A.T.; Slezak, P.; Schuetzenberger, S.; Kaipel, M.; Schwartz, E.; Neef, A.; Nomikou, N.; Nau, T.; van Griensven, M.; et al. Sonoporation increases therapeutic efficacy of inducible and constitutive BMP2/7 in vivo gene delivery. *Hum. Gene Methods* **2014**, *25*, 57–71. [CrossRef]
71. Kaipel, M.; Schützenberger, S.; Hofmann, A.T.; Ferguson, J.; Nau, T.; Redl, H.; Feichtinger, G.A. Evaluation of fibrin-based gene-activated matrices for BMP2/7 plasmid codelivery in a rat nonunion model. *Int. Orthop.* **2014**, *38*, 2607–2613. [CrossRef] [PubMed]
72. D'Mello, S.; Atluri, K.; Geary, S.M.; Hong, L.; Elangovan, S.; Salem, A.K. Bone regeneration using gene-activated matrices. *AAPS J.* **2017**, *19*, 43–53. [CrossRef] [PubMed]

materials

MDPI

Article

Magnetic Properties of Electrospun Magnetic Nanofiber Mats after Stabilization and Carbonization

Nadine Fokin [1], Timo Grothe [2], Al Mamun [2], Marah Trabelsi [2,3], Michaela Klöcker [2], Lilia Sabantina [2], Christoph Döpke [2], Tomasz Blachowicz [4], Andreas Hütten [1] and Andrea Ehrmann [2,*]

[1] Department of Physics, Center for Spinelectronic Materials and Devices, Bielefeld University, 33615 Bielefeld, Germany; nfokin@physik.uni-bielefeld.de (N.F.); andreas.huetten@uni-bielefeld.de (A.H.)

[2] Faculty of Engineering and Mathematics, Bielefeld University of Applied Sciences, 33619 Bielefeld, Germany; timo.grothe@fh-bielefeld.de (T.G.); al.mamun@fh-bielefeld.de (A.M.); marah.trabelsi@enis.tn (M.T.); michaela.kloecker@fh-bielefeld.de (M.K.); lilia.sabantina@fh-bielefeld.de (L.S.); christoph.doepke@fh-bielefeld.de (C.D.)

[3] Ecole Nationale d'Ingénieurs de Sfax (ENIS), Sfax 3038, Tunisia

[4] Institute of Physics–CSE, Silesian University of Technology, 44-100 Gliwice, Poland; tomasz.blachowicz@polsl.pl

* Correspondence: andrea.ehrmann@fh-bielefeld.de

Received: 5 March 2020; Accepted: 24 March 2020; Published: 27 March 2020

Abstract: Magnetic nanofibers are of great interest in basic research, as well as for possible applications in spintronics and neuromorphic computing. Here we report on the preparation of magnetic nanofiber mats by electrospinning polyacrylonitrile (PAN)/nanoparticle solutions, creating a network of arbitrarily oriented nanofibers with a high aspect ratio. Since PAN is a typical precursor for carbon, the magnetic nanofiber mats were stabilized and carbonized after electrospinning. The magnetic properties of nanofiber mats containing magnetite or nickel ferrite nanoparticles were found to depend on the nanoparticle diameters and the potential after-treatment, as compared with raw nanofiber mats. Micromagnetic simulations underlined the different properties of both magnetic materials. Atomic force microscopy and scanning electron microscopy images revealed nearly unchanged morphologies after stabilization without mechanical fixation, which is in strong contrast to pure PAN nanofiber mats. While carbonization at 500 °C left the morphology unaltered, as compared with the stabilized samples, stronger connections between adjacent fibers were formed during carbonization at 800 °C, which may be supportive of magnetic data transmission.

Keywords: ferrimagnetic materials; superparamagnetism; magnetic hysteresis; magnetic materials; magnetic nanoparticles; nanocomposites; nanowires

---

1. Introduction

Electrospinning makes it possible to create nanofiber mats from diverse materials, such as pure polymers [1–3], polymers blends, composite fibers from polymers and ceramics or metals [4,5], and cyclodextrins [6]. These can be used in diverse applications such as filters [7–9], biotechnology and tissue engineering [10–12], for energy harvesting and storage [13,14], or other "smart" functions [15]. Recently, a strong focus of diverse research groups has been related to electrospinning magnetic nanofibers, either as composites [16–18] or, after calcination of the composites to remove polymers, as pure metal nanofibers [19–21]. Such magnetic nanofiber mats can be used, e.g., as catalysts [22], for magnetic hyperthermia [23], or electromagnetic shielding [24]. In contrast to other methods, such as electrodeposition [25,26], seed-mediated growth [27], magnetic field patterning of magnetic precursor inks printed on a substrate [28], or electrochemical deposition [29], electrospinning has the advantage of enabling preparation of large-scale nanofiber networks in short times without the necessity to use a cleanroom, highly sophisticated equipment, or highly toxic material, and is thus often used to prepare magnetic nanofibers [30–34]. Notably, polyacrylonitrile (PAN) can be spun from the low-toxic solvent DMSO [3], making the whole process relatively easy to handle and avoiding unnecessary environmental pollution.

In contrast to other methods of producing magnetic nanofibers, electrospinning usually creates nanofibers with different bending radii and forms a nanofiber mat without or with only low-fiber orientation [35–37], resulting in much more complicated magnetic anisotropies than straight, even nanofibers [38–40]. This makes electrospun nanofiber mats challenging for some applications, e.g., in racetrack memory, which usually consists of an array of parallel arranged magnetic nanowires and can theoretically store data series in some ten- to hundred-domain walls per nanowire [41].

On the other hand, chaotic nanofiber mats or fiber networks with low orientation are interesting for other research areas; e.g., for bio-inspired neuromorphic computing [42]. This relatively new research area aims at reaching high-performance computing at low power consumption, avoiding the von Neumann bottleneck due to the separation of processor and memory in modern computers built according to the von Neumann architecture by integrating both parts, i.e., storing and calculating data in a structure inspired by the human brain. Recently, many attempts have been reported to implement neural networks, imitating the biological function of the brain, with conventional computers [43–45]. Much better performance in terms of speed and reduced power consumption, however, can be expected if physical networks of connected components are created to enable massive parallel computing [46–49].

Quasistatic and dynamic studies of the magnetic properties of bent nanofibers have been performed by different research groups, using simulations or experimental investigations which have underlined the aforementioned influence of diameter and curvature distributions [50–52]. For example, Alejos et al. showed that a local longitudinal field could be used to control the current-induced magnetization reversal in ferromagnetic strips. They used two bit-lines, above and below a ferromagnetic line sandwiched between a heavy metal and an oxidized layer. In such a heavy metal/ferromagnet/oxide triple layer, current-induced switching due to a global in-plane field is well-known [53–55], while the local field created domain walls at defined positions—which is necessary for racetrack applications [52].

For potential application in neuromorphic computing, memristors or other elements are often integrated in statistic fiber networks [56–58], an approach which cannot be realized with a single-step electrospinning process. Here, instead, we report on a combination of magnetic nanofibers with beads, tailored by a reduction of the polymer content in the spinning solution, as evaluated in detail in a former study [59]. This combination of long, thin nanofibers with beads along the fibers allows for combining data processing and storage, as shown in former studies [18,60–63].

2. Materials and Methods

2.1. Electrospinning

For the spinning solution, 14% polyacrylonitrile (PAN) (X-PAN, Dralon, Dormagen, Germany) was dissolved in dimethyl sulfoxide (DMSO, min 99.9%, purchased from S3 chemicals, Bad Oeynhausen, Germany) by stirring at room temperature for 2 h with a magnetic stirrer. PAN was chosen due to the possibility of stabilizing and carbonizing it after electrospinning, making it conductive [64].

To make the fibers magnetic, nanoparticles from Fe_3O_4 (magnetite, particle size 50–100 nm) and Fe_2O_3/NiO (diiron nickel tetraoxide or nickel ferrite, particle size <50 nm) were added (both purchased from Merck KGaA, Darmstadt, Germany) by stirring manually for 10 min and dispersing the nanoparticles in an ultrasonic bath for 40 min at 35 °C at a frequency of 37 kHz. Both materials are ferrimagnetic in bulk form and become superparamagnetic for very small nanoparticles [65,66]. The polymer: nanoparticle weight ratio used here was 1:1.8, identical to the highest nanoparticle concentration used in a previous study [18].

The needleless electrospinning machine Nanospider Lab (Elmarco, Liberec, Czech Republic) was used to prepare nanofiber mats on a polypropylene nonwoven substrate. Electrospinning was performed using a high voltage of 80 kV, a nozzle diameter of 0.9 mm, a carriage speed of 150 mm/s, a ground-substrate distance of 240 mm, and an electrode-substrate distance of 50 mm. The temperature in the chamber was held at 22 °C, while the relative humidity was set to 32%.

2.2. Stabilization and Carbonization

Parts of the samples were afterwards stabilized in a B150 muffle furnace (Nabertherm, Germany), approaching a temperature of 280 °C with a heating rate of 0.5 K/min, followed by isothermal treatment for 1 h. This step was necessary to enable carbonization, since pure PAN is not thermally stable at temperatures far above 300 °C, while carefully stabilized PAN is not degraded by high temperatures. Subsequent carbonization was performed in a CTF 12/TZF 12 furnace (Carbolite Gero Ltd., Neuhausen, Germany), approaching temperatures of 500 and 800 °C, respectively, with a heating rate of 10 K/min in a nitrogen flow of 150 mL/min (STP), again followed by isothermal treatment for 1 h.

2.3. Experimental Investigations

Magnetic measurements were performed with an alternating gradient magnetometer (AGM) Princeton MicroMag (LakeShore Cryotronics, Westerville, OH, USA). The surface morphology of the nanofiber mats was investigated using a scanning electron microscope (SEM), the Zeiss 1450VPSE, and an atomic force microscope (AFM), the FlexAFM Axiom (Nanosurf, Liestal, Switzerland). For the chemical investigations, a Fourier-transform infrared (FTIR) spectrometer, Excalibur 3100 (Varian, Inc., Palo Alto, CA, USA), was used. Fiber diameters were evaluated using the software ImageJ 1.51j8 (from National Institutes of Health, Bethesda, MD, USA).

2.4. Simulations

For comparison with the experimental investigations of the magnetic properties, the micromagnetic simulation software OOMMF (Object-Oriented MicroMagnetic Framework) was used [67], applying finite differences for meshing and solving the Landau–Lifshitz–Gilbert equation of motion [68]. The following material parameters were chosen for Fe_3O_4 (Fe_2O_3/NiO) according to typical literature values [69–73]: $M_{S,magnetite} = 500 \times 10^3$ A/m ($M_{S,nickel\text{-}ferrite} = 270 \times 10^3$ A/m), exchange constant $A_{magnetite} = 12 \times 10^{-12}$ J/m ($A_{nickel\text{-}ferrite} = 12 \times 10^{-12}$ J/m), magneto-crystalline anisotropy constant $K_{1,magnetite} = 11 \times 10^3$ J/m^3 ($K_{1,nickel\text{-}ferrite} = -6.9 \times 10^3$ J/m^3). Since the electrospinning process can be expected to produce arbitrarily oriented crystallographic orientations of the nanoparticles, random orientations of the simulated grains of 5 nm diameter were chosen. While this approach would lead to strong modifications of the simulation results due to arbitrary crystallographic orientations in subsequent simulations, in case of cobalt or other materials with large magneto-crystalline anisotropy [74], here the influence of the shape anisotropy dominated the relatively small magneto-crystalline anisotropy, as usual in iron or permalloy samples of similar dimensions [75]. Setting the Gilbert damping constant to $\alpha = 0.5$, a quasi-static case was modeled. Field sweeps were performed in the range of ±300 mT to reach saturation.

The simulated shapes—a branched and a single fiber, respectively—were taken arbitrarily from an SEM image as an example of possible parts of such nanofiber mats (Figure 1). Fiber thickness was assumed as 120 nm, as according to the chosen part of a real magnetic nanofiber mat. Generally, the fiber thickness and thus the shape of the cross-section can be modified by a hot-pressing treatment [76]; this possibility was not further investigated here.

Figure 1. Simulated structures of dimensions 800 nm × 800 nm: (**a**) branched fiber; (**b**) single fiber.

The simulated hysteresis loops shown here were superposed of 7 hysteresis loops each, simulated for external magnetic field sweeps in the range of ±3000 Oe with the field axis applied along 0° (horizontal in Figure 1), 15°, . . . 90° (vertical in Figure 1). This was equivalent to averaging over different nanofiber orientations in a constant external magnetic field, as it was applied during the AGM measurements on the magnetic nanofiber mats.

3. Results and Discussion

3.1. Morphological Investigations

Figure 2 depicts SEM images of the magnetite samples under examination; Figure 3 shows SEM images of the nickel-ferrite samples. As mentioned in Section 2, magnetic nanofiber mats with beads along the fibers were produced to test the combination of structures for data storage and transport for possible application in neuromorphic computing [18].

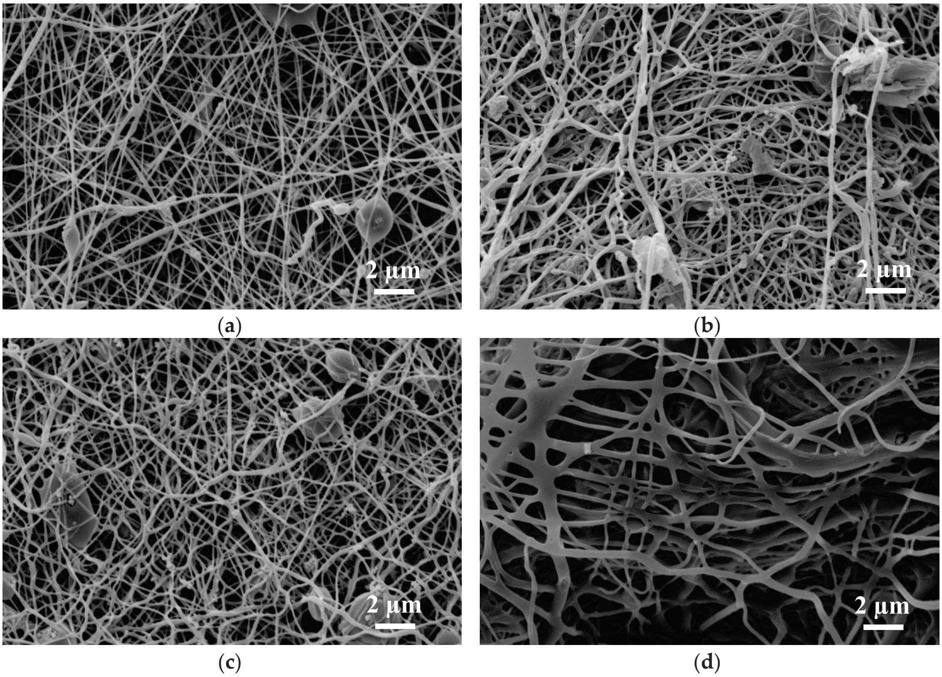

Figure 2. SEM images of polyacrylonitrile (PAN)/magnetite nanofiber mats: (**a**) after electrospinning; (**b**) after stabilization; (**c**) after carbonization at 500 °C; (**d**) after carbonization at 800 °C.

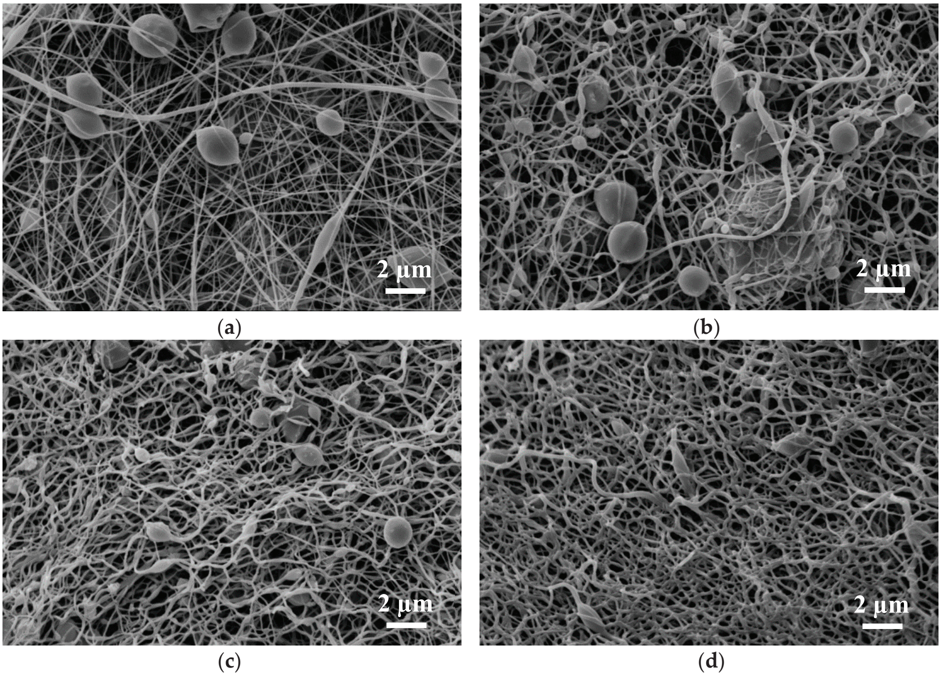

(**a**) (**b**) (**c**) (**d**)

Figure 3. SEM images of PAN/nickel-ferrite nanofiber mats: (**a**) after electrospinning; (**b**) after stabilization; (**c**) after carbonization at 500 °C; (**d**) after carbonization at 800 °C.

It should be mentioned that the aim of our recent study was not optimization of the numbers and dimensions of the beads, but investigation of the magnetic properties of nanofiber mats directly after electrospinning, as well as after stabilization and carbonization at different temperatures. Based on recent results and corresponding micromagnetic simulations, a further morphological optimization of the bead dimensions and quantities will be carried out.

In both nanofiber mats depicted in Figures 2 and 3, the typical increase of the fiber diameter is visible due to relaxation of the internal stress in the nanofibers caused by the severe stretching during electrospinning [77]. Since the nanofiber mats were not mechanically fixed or even actively stretched during stabilization, this behavior can be expected, as discussed in detail in [77].

The diameter distributions of the nanofibers after the different treatments are depicted in Figures 4 and 5. In PAN/magnetite as well as PAN/nickel-ferrite nanofiber mats, stabilization resulted in a larger average as well as in a broader distribution of the nanofiber diameters, the latter especially in case of PAN/magnetite. While the average diameter of PAN/magnetite nanofibers after carbonization at 500 °C was again smaller than after stabilization, both values were nearly identical for PAN/nickel-ferrite. Carbonization at 800 °C resulted in both material blends in the largest diameters.

It should be mentioned, nevertheless, that these differences are not statistically significant due to the broad distributions of the measured fiber diameters and may partly be based on the arbitrary choice of the sample areas under investigation.

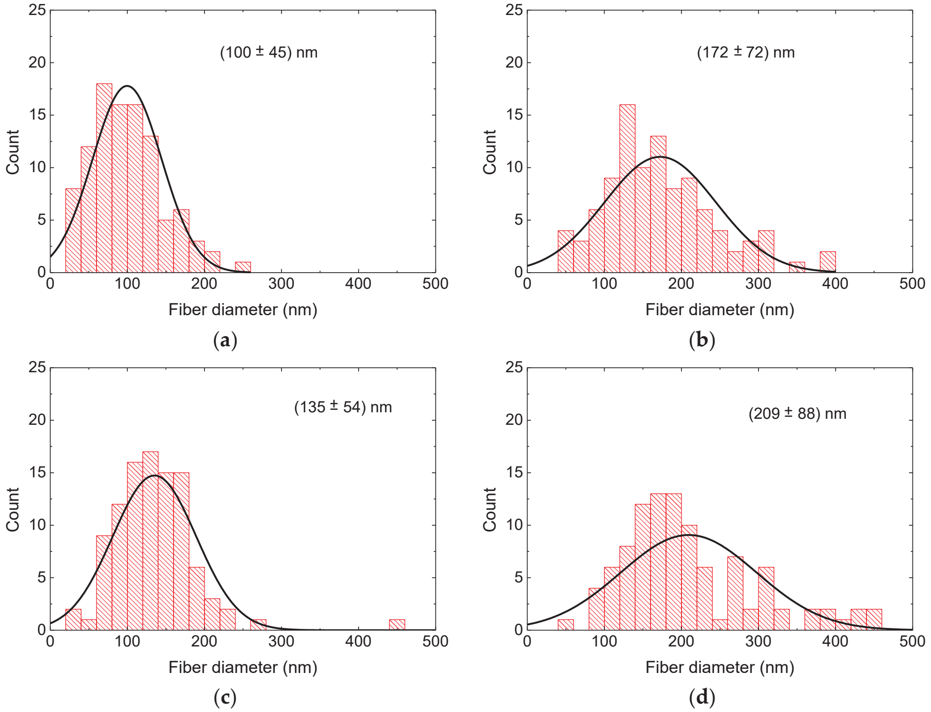

Figure 4. Distributions of the diameters of PAN/magnetite nanofibers: (**a**) after electrospinning; (**b**) after stabilization; (**c**) after carbonization at 500 °C; (**d**) after carbonization at 800 °C.

Both magnetic nanofiber mats showed the desired beads after electrospinning, with a larger number of relatively large beads in the case of PAN/nickel-ferrite. Future micromagnetic simulations are necessary to investigate which bead sizes are advantageous for data storage or use as switches, as shown in [18]. The fibrous structure of the beads stayed similar after stabilization due to the slow heating process, which was optimized in former studies for pure PAN nanofibers and PAN with integrated metal-oxide nanoparticles [78,79]. After carbonization at 500 °C, however, the beads in the PAN/nickel-ferrite nanofiber mats became smaller, an effect which has to be investigated in detail in the future. At 800 °C, the fiber structure of the PAN/magnetite nanofiber mats changed unexpectedly, which was not the case for PAN/TiO_2 nanofiber mats [79] or PAN/gelatin nanofiber mats [80]. While this pure nanofiber structure is of great interest for data transport in magnetic networks, it cannot be used any more for date storage. Similarly, the beads were nearly lost in the PAN/nickel-ferrite nanofiber mat carbonized at 800 °C.

Apparently, it is necessary to either find a compromise between conductivity—which usually increases with increasing carbonization temperature and would support current-driven domain-wall transport—and the beads which could be used for data storage and manipulation. On the other hand, the carbonization parameters used here, especially the heating rate, were optimized for PAN, PAN/gelatin, and PAN/TiO_2, and can possibly be further optimized in the cases of PAN/magnetite, and PAN/nickel-ferrite, respectively, to maintain the desired structure.

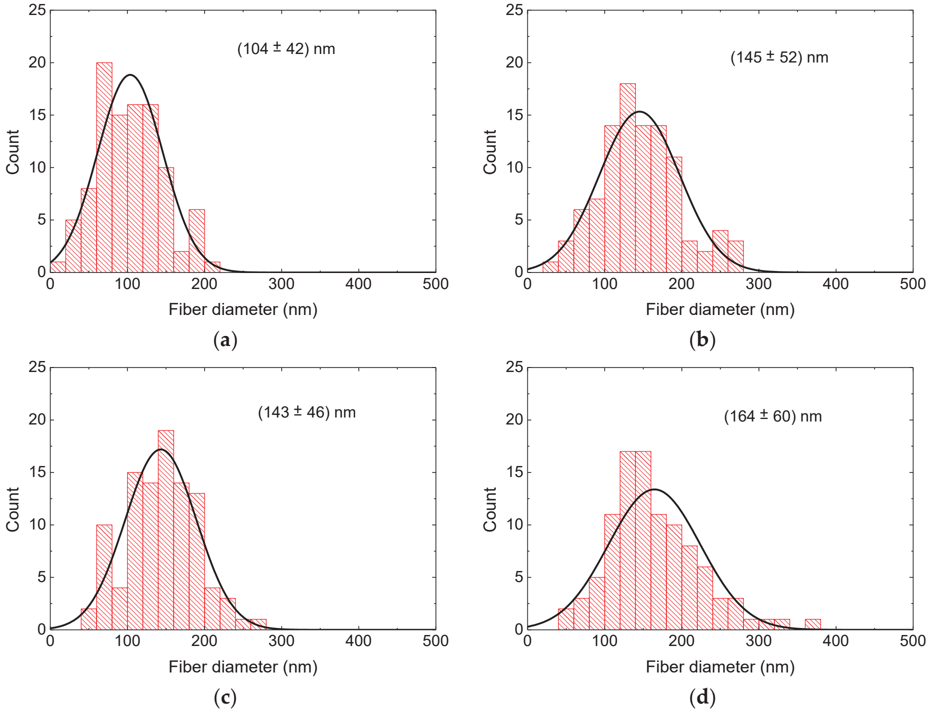

(**a**) (**b**)

(**c**) (**d**)

Figure 5. Distributions of the diameters of PAN/nickel-ferrite nanofibers: (**a**) after electrospinning; (**b**) after stabilization; (**c**) after carbonization at 500 °C; (**d**) after carbonization at 800 °C.

3.2. Chemical Investigations

Next, Figure 6 depicts FTIR spectra of PAN/magnetite samples; spectra measured for PAN/nickel-ferrite are approximately identical and are thus not shown here.

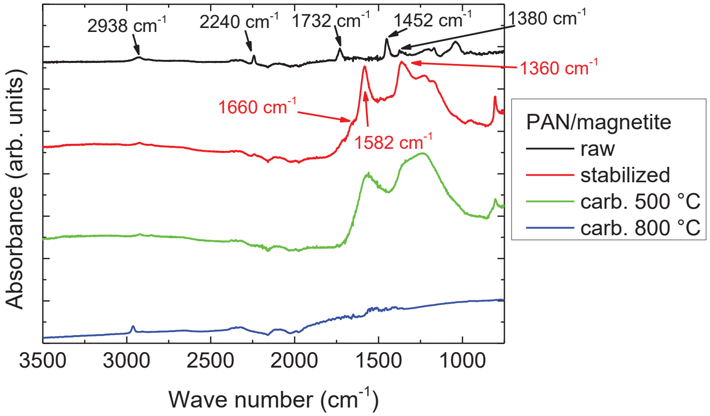

Figure 6. FTIR measurements of PAN/magnetite samples after electrospinning, stabilization, and carbonization at 500 and 800 °C. The lines are vertically offset for clarity.

As described in detail in previous studies [78–80], the raw PAN/magnetite nanofiber mat was characterized by stretching vibrations of the C≡N nitrile functional group at 2240 cm^{-1}, the carbonyl

(C=O) stretching peak at 1732 cm^{-1}, and bending and stretching vibrations of CH_2 visible at 2938 cm^{-1}, 1452 cm^{-1}, and 1380 cm^{-1}. In the raw nanofiber mat, no residues of the solvent DMSO were visible, underlining that only very small amounts of DMSO were left in these nanofiber mats.

In the stabilized nanofiber mats, the most prominent peaks were those of C=N stretching vibrations at 1582 cm^{-1}, C=C stretching vibrations at 1660 cm^{-1}, and C-H bending and C-H_2 wagging around 1360 cm^{-1}. After carbonization at 800 °C, the peaks nearly fully vanished since few functional groups were left after carbonization, resulting in the typical high absorbance of carbon. Temperature treatment at 500 °C was apparently not sufficient for a full carbonization process; instead, the FTIR spectrum still looked very similar to the stabilized sample.

Comparing the FTIR measurements with those performed on pure PAN nanofiber mats or PAN blends with gelatin, TiO_2, etc. [78–80], no significant difference was visible due to the embedded magnetic nanoparticles.

3.3. Magnetic Investigations

The magnetic characteristics of the magnetic nanofibers with magnetite and nickel-ferrite nanoparticles, respectively, are depicted in Figure 7.

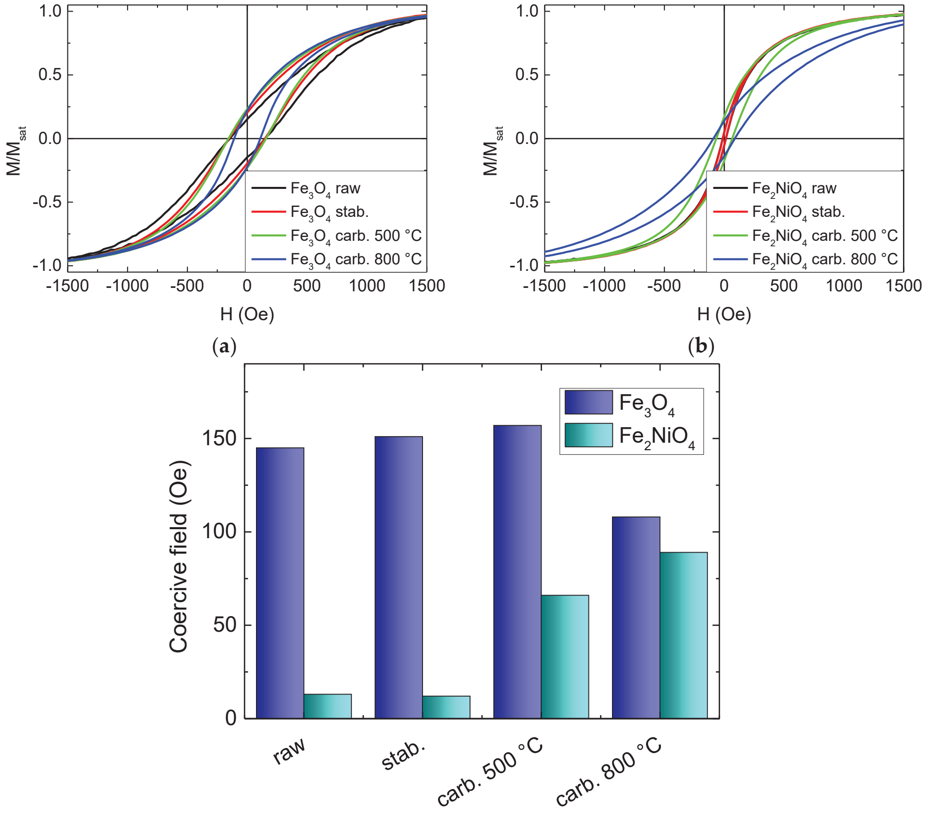

(**a**) (**b**)

(**c**)

Figure 7. Alternating gradient magnetometer (AGM) measurements of hysteresis loops, performed on magnetic nanofibers including nanoparticles from (**a**) magnetite; (**b**) nickel-ferrite; and (**c**) coercive fields measured on these samples.

Firstly, it is clearly visible that the coercive fields of the magnetite-based nanofibers were significantly larger than those of the nickel-ferrite-based nanofibers. For the PAN/magnetite nanofiber mats, the coercive fields did not change strongly with temperature treatments, while the PAN/nickel-ferrite nanofiber mats showed a soft magnetic behavior with only a very small coercive field at low temperature and much larger coercive fields after carbonization processes. Since both materials have similar magnetic properties, this difference can be attributed to the different nanoparticle dimensions—while the magnetite nanoparticles with diameters of 50–100 nm were large enough to show ferrimagnetic characteristics even without agglomerations, the nickel-ferrite nanoparticles with diameters below 50 nm were partly small enough for superparamagnetic behavior. Only after carbonization, when the nanofibers started forming conglutinations, were the neighboring nickel-ferrite nanoparticles near enough to overcome the superparamagnetic limit.

It must be mentioned that the highest carbonization temperature of 800 °C was above the Curie temperatures of both magnetic materials, which is approx. 570 °C for both bulk samples and 517 °C [81] or only 495 °C [82] for nanocrystalline nickel-ferrite. Similarly, in Fe_3O_4 nanocrystals, strongly reduced Curie temperatures down to 440 °C were reported [83]. In addition, a cation reordering was reported to occur in magnetite above 427 °C, corresponding to a gradual transformation from disordered to partially ordered configuration of magnetite [84]. These structural and magnetic effects may also have influenced the hysteresis loop shapes, in addition to the strong mass and volume loss; the latter resulting from an overproportioned shortening of the fibers as compared to the diameter increase, depicted in Figures 4 and 5, of the fibers during stabilization and carbonization [78–80], which automatically reduced the distances between neighboring nanoparticles and thus influenced their collective magnetic characteristics [85].

Figure 8 shows a comparison of nanofiber mats and thin films, prepared from PAN with both magnetic nanoparticles used in this study. It is clearly visible that the magnetic properties were quite similar for both shapes, indicating that in both cases the nanoparticles were not near enough to each other to be subject to the magnetic shape anisotropy of the nanofibers, but were dominated by the single particle magnetic shape anisotropy. Whether there was any magnetic anisotropy of the particles inside the fibers, induced by electrospinning, has to be examined in future magnetic force microscope (MFM) investigations.

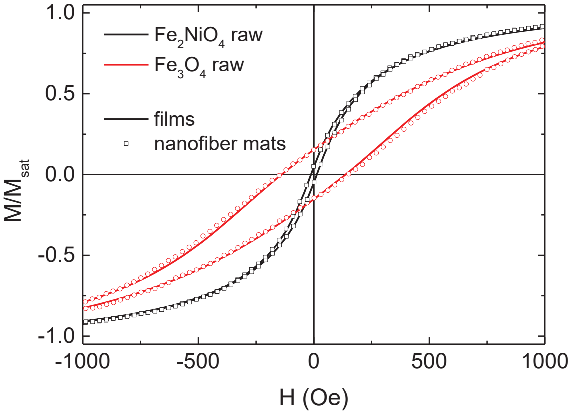

Figure 8. Hysteresis loops of as-prepared nanofiber mats and films from PAN with magnetite or nickel-ferrite nanoparticles, respectively.

3.4. Micromagnetic Simulations

This finding is underlined by the micromagnetic simulations depicted in Figure 9, showing hysteresis loops averaged over simulations along 0°, 15°, … 90° for magnetite and nickel-ferrite branched and single fibers, in this way simulating the expected results of macroscopic measurements on stochastically distributed pure magnetic nanofibers with or without branches.

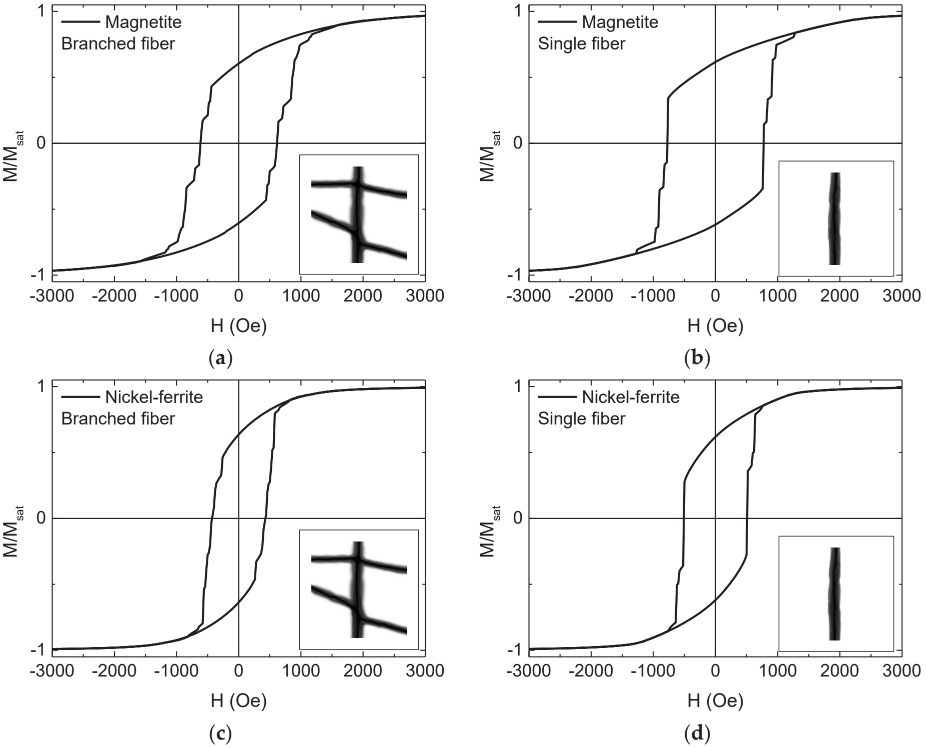

(**a**) (**b**) (**c**) (**d**)

Figure 9. Simulated hysteresis loops of (**a**) magnetite branched fiber; (**b**) magnetite single fiber; (**c**) nickel-ferrite branched fiber; (**d**) nickel-ferrite single fiber.

The finding that coercive fields of nickel-ferrite nanofibers were generally smaller than those of magnetite nanofibers corresponds to the experimental results. The absolute values, however, were significantly larger in the simulation, underlining that the magnetic nanofibers prepared by electrospinning contained distributed magnetic nanoparticles which showed different magnetization reversal processes than the completely magnetic simulated nanoparticles. Apparently, simulations of stochastically distributed nanoparticle networks in the nanofiber shells are necessary to investigate in more detail the influence of inter-particle distances and the overall fiber shell, building a matrix in which the magnetic nanoparticles are distributed, on static and dynamic magnetization characteristics of the nanofiber network.

4. Conclusions

Magnetic nanofibers were prepared by electrospinning PAN nanofibers filled with magnetite or nickel-ferrite nanoparticles. While raw and stabilized fibers were relatively even and straight, more and more conglutinations between neighboring fibers occurred with increasing carbonization temperature, in case of magnetite leading to a deformation of the fiber shape from round fibers into flat ribbons. The magnetic properties were, especially in case of the smaller nickel-ferrite nanoparticles, strongly influenced by the thermal post-treatments, indicating that magnetization reversal is dominated by single-particle characteristics rather than by clusters of strongly interacting nanoparticles. Comparison with micromagnetic simulations of full-metal oxide nanofibers underlined this finding. It should be mentioned that care must be taken in the evaluation of magnetic properties after heating the nanofiber mats above the Curie temperatures of the magnetic nanoparticles; these thermal influences may have caused modifications of the magnetic properties in addition to the well-known structural changes of the nanoparticles due to a high-temperature treatment.

Future simulations of randomly distributed nanoparticles of different sizes inside a nanofiber matrix are necessary to fully understand the magnetic behavior of electrospun, stabilized, and carbonized magnetic nanofibers. To tailor research according to the necessities of data storage and transport for neuromorphic computing and other novel applications, additional MFM investigations on magnetization reversal and dynamics in these random nanofiber networks are necessary to produce reliable neuromorphic computing systems.

Additionally, on the materials science side, tailoring of the dimensions and quantities of the beads according to the afore-simulated necessities should be carried out, as well as an investigation of the stabilization and carbonization process in more detail, including examination of high-resolution images of the inner structures of the fibers by transmission electron microscopy (TEM). In this study, the optimum stabilization and carbonization parameters for pure electrospun PAN nanofibers were applied; however, it cannot be excluded that due to the embedded metallic nanoparticles, a new optimization study is necessary to avoid the unexpected formation of ribbon-like structures in the PAN/magnetite nanofiber mats after carbonization at 800 °C.

Author Contributions: Conceptualization, A.E.; methodology, N.F., T.G., A.E., T.B., A.H.; validation, A.E., T.B., A.H.; formal analysis, A.E.; investigation, N.F., T.G., A.M., M.T., M.K., L.S., C.D.; writing—original draft preparation, T.B. and A.E.; writing—review and editing, all authors; visualization, A.E. All authors have read and agreed to the published version of the manuscript.

Funding: This research was funded by a Volkswagen Foundation grant "Adaptive Computing with Electrospun Nanofiber Networks" no. 93679, the Erasmus+ program of the European Union, the internal PhD funds of Bielefeld University of Applied Sciences and the internal HiF funds of Bielefeld University of Applied Sciences. The APC is funded by the Open Access Publication Fund of Bielefeld University of Applied Sciences and the Deutsche Forschungsgemeinschaft (DFG, German Research Foundation)–414001623.

Conflicts of Interest: The authors declare no conflict of interest. The funders had no role in the design of the study; in the collection, analyses, or interpretation of data; in the writing of the manuscript, or in the decision to publish the results.

References

1. Greiner, A.; Wendorff, J.H. Electrospinning: A fascinating method for the preparation of ultrathin fibers. *Angew. Chem. Int. Ed.* **2007**, *46*, 5670–5703. [CrossRef] [PubMed]
2. Klinkhammer, K.; Seiler, N.; Grafahrend, D.; Gerardo-Nava, J.; Mey, J.; Brook, G.A.; Möller, M.; Dalton, P.D.; Klee, D. Deposition of electrospun fibers on reactive substrates for in vitro investigations. *Tissue Eng. Part C Methods* **2009**, *15*, 77–85. [CrossRef] [PubMed]
3. Grothe, T.; Wehlage, D.; Böhm, T.; Remche, A.; Ehrmann, A. Needleless electrospinning of PAN nanofibre mats. *Tekstilec* **2017**, *60*, 290–295. [CrossRef]
4. Che Othman, F.E.; Yusof, N.; Hasbullah, H.; Jaafar, J.; Ismai, A.F.; Abdullah, N.; Nordin, N.A.H.M.; Aziz, F.; Salleh, W.N.W. Polyacrylonitrile/magnesium oxide-based activated carbon nanofibers with well-developed microporous structure and their adsorption performance for methane. *J. Ind. Eng. Chem.* **2017**, *51*, 281–287. [CrossRef]
5. García-Mateo, F.J.; Cordero-Lanzac, T.; Berenguer, R.; Morallón, E.; Cazorla-Amorós, D.; Rodríguez-Mirasol, J.; Cordero, T. Lignin-derived Pt supported carbon (submicron)fiber electrocatalysts for alcohol electro-oxidation. *Appl. Catal. B Environ.* **2017**, *211*, 18–30. [CrossRef]
6. Yoshida, H.; Sakuragi, K. Elicitation of crystallinity in cyclodextrin electrospinning. *Bull. Chem. Soc. Jpn.* **2019**, *92*, 927–929. [CrossRef]
7. Yalcinkaya, F.; Boyraz, E.; Maryska, J.; Kucerova, K. A review on membrane technology and chemical surface modification for the oily wastewater treatment. *Materials* **2020**, *13*, 493. [CrossRef]
8. Kozior, T.; Trabelsi, M.; Mamun, A.; Sabantina, L.; Ehrmann, A. Stabilization of electrospun nanofiber mats used for filters by 3D printing. *Polymers* **2019**, *11*, 1618. [CrossRef]

9. Boyraz, E.; Yalcinkaya, F.; Hruza, J.; Maryska, J. Surface-modified nanofibrous PVDF membranes for liquid separation technology. *Materials* **2019**, *12*, 2702. [CrossRef]
10. Mamun, A. Review of possible applications of nanofibrous mats for wound dressings. *Tekstilec* **2019**, *62*, 89–100. [CrossRef]
11. Gao, S.T.; Tang, G.S.; Hua, D.W.; Xiong, R.; Han, J.; Jiang, S.; Zhang, Q.; Huang, C. Stimuli-responsive bio-based polymeric systems and their applications. *J. Mater. Chem. B* **2019**, *7*, 709–729. [CrossRef]
12. Wehlage, D.; Blattner, H.; Mamun, A.; Kutzli, I.; Diestelhorst, E.; Rattenholl, A.; Gudermann, F.; Lütkemeyer, D.; Ehrmann, A. Cell growth on electrospun nanofiber mats from polyacrylonitrile (PAN) blends. *Aims Bioeng.* **2020**, *7*, 43–54. [CrossRef]
13. Xue, Y.Y.; Guo, X.; Zhou, H.F.; Zhou, J. Influence of beads-on-string on Na-Ion storage behavior in electrospun carbon nanofibers. *Carbon* **2019**, *154*, 219–229. [CrossRef]
14. Kohn, S.; Wehlage, D.; Juhász Junger, I.; Ehrmann, A. Electrospinning a dye-sensitized solar cell. *Catalysts* **2019**, *9*, 975. [CrossRef]
15. Xue, J.J.; Wu, T.; Dai, Y.Q.; Xia, Y.N. Electrospinning and electrospun nanofibers: Methods, materials, and applications. *Chem. Rev.* **2019**, *119*, 5298–5415. [CrossRef]
16. Peer, P.; Stenicka, M.; Filip, P.; Pizurova, N.; Babayan, V. Magnetorheological characterization and electrospinnability of ultrasound-treated polymer solutions containing magnetic nanoparticles. *Colloid Polym. Sci.* **2018**, *296*, 1849–1855. [CrossRef]
17. Darwish, M.S.A.; Bakry, A.; Kolek, O.; Martinova, L.; Stibor, I. Electrospun functionalized magnetic polyamide 6 composite nanofiber: Fabrication and stabilization. *Polym. Compos.* **2019**, *40*, 296–303. [CrossRef]
18. Döpke, C.; Grothe, T.; Steblinski, P.; Klöcker, M.; Sabantina, L.; Kosmalska, D.; Blachowicz, T.; Ehrmann, A. Magnetic nanofiber mats for data storage and transfer. *Nanomaterials* **2019**, *9*, 92. [CrossRef]
19. Murillo-Ortíz, R.; Mirabal-García, M.; Martínez-Huerta, J.M.; Cabal Velarde, J.G.; Castaneda-Robles, I.E.; Lobo-Guerrero, A. Analysis of the magnetic properties in hard-magnetic nanofiber composite. *J. Appl. Phys.* **2018**, *123*, 105108. [CrossRef]
20. Ghazi, N.; Chenari, H.M.; Ghodsi, F.E. Rietveld refinement, morphology analysis, optical and magnetic properties of magnesium-zinc ferrite nanofibers. *J. Magn. Magn. Mater.* **2018**, *468*, 132–140. [CrossRef]
21. Blachowicz, T.; Ehrmann, A. Most recent developments in electrospun magnetic nanofibers: A review. *J. Eng. Fibers Fabr.* **2020**, *15*, 1558925019900843. [CrossRef]
22. Lin, K.-Y.A.; Yang, M.-T.; Lin, J.-T.; Du, Y.C. Cobalt ferrite nanoparticles supported on electrospun carbon fiber as a magnetic heterogeneous catalyst for activating peroxymonosulfate. *Chemosphere* **2018**, *208*, 502–511. [CrossRef] [PubMed]
23. Matos, R.J.R.; Chaparro, C.I.P.; Silva, J.C.; Valente, M.A.; Borges, J.P.; Soares, P.I.P. Electrospun composite cellulose acetate/iron oxide nanoparticles non-woven membranes for magnetic hyperthermia applications. *Carbohydr. Polym.* **2018**, *198*, 9–16. [CrossRef]
24. Zhan, Y.Q.; Long, Z.H.; Wan, X.Y.; Zhang, J.M.; He, S.J.; He, Y. 3D carbon fiber mats/nano-Fe_3O_4 hybrid material with high electromagnetic shielding performance. *Appl. Surf. Sci.* **2018**, *444*, 710–720. [CrossRef]
25. Li, X.R.; Song, G.J.; Ma, L.C.; Peng, Q.H.; Li, H.Y.; Ji, Z.J.; Cong, H.L. Structural and Magnetic Properties of Rare Earth Doped Multilayer Nanocable Arrays. *J. Nanosci. Nanotechnol.* **2020**, *20*, 1873–1877. [CrossRef] [PubMed]
26. Agarwal, S.; Pohl, D.; Patra, A.K.; Nielsch, K.; Khatri, M.S. Preparation and nanoscale characterization of electrodeposited CoFe-Cu multilayer nanowires. *Mater. Chem. Phys.* **2019**, *230*, 231–238. [CrossRef]
27. Yu, Q.L.; Zhang, Y.M.; Liu, Y.H.; Liu, Y. Magnetic supramolecular nanofibers of gold nanorods for photothermal therapy. *Adv. Ther.* **2019**, *2*, 1800137. [CrossRef]
28. Mahajan, C.G.; Alfadhel, A.; Irving, M.; Kahn, B.E.; Borkholder, D.A.; Williams, S.A.; Cormier, D. Magnetic Field Patterning of Nickel Nanowire Film Realized by Printed Precursor Inks. *Materials* **2019**, *12*, 928. [CrossRef]
29. Yu, Y.L.; Li, J.P.; Wang, J.; Wu, X.G.; Yu, C.Y.; Xu, T.; Chang, B.D.; Sun, H.Y.; Arandiyan, H. Orientation Growth and Magnetic Properties of Electrochemical Deposited Nickel Nanowire Arrays. *Catalysts* **2019**, *9*, 152. [CrossRef]
30. Dolbashian, C.; Chavez, B.L.; Bauer, M.; Budi, M.; Andrew, J.S.; Crawford, T.M. Magnetic properties of aligned multiferroic Janus nanofiber agglomerates measured with the scattered magneto-optical Kerr effect. *J. Phys. D Appl. Phys.* **2020**, *53*, 195002. [CrossRef]

31. Mei, L.Y.; Chen, H.Y.; Shao, Y.P.; Wang, J.Y.; Liu, Y.Q. Highly aligned magnetic composite nanofibers fabricated by magnetic-field-assisted electrospinning PAN/FeCo solution. *High Perform. Polym.* **2019**, *31*, 230–237. [CrossRef]
32. Cai, N.; Chen, M.; Liu, M.M.; Wang, J.Z.; Shen, L.; Wang, J.Y.; Feng, X.J.; Yu, F.Q. Meso-microporous carbon nanofibers with in-situ embedded Co nanoparticles for catalytic oxidization of azo dyes. *J. Mol. Liq.* **2019**, *289*, 111060. [CrossRef]
33. Erfan, N.A.; Barakat, N.; Müller-Borer, B.J. Preparation and characterization of beta-lactoglobulin/poly (ethylene oxide) magnetic nanofibers for biomedical applications. *Colloids Surf. Physicochem. Eng. Asp.* **2019**, *576*, 63–72. [CrossRef]
34. Jiang, P.; Lu, J.F.; Li, K.; Chen, X.Q.; Dan, R.Q. Research on hydrophobicity of electrospun Fe_3O_4/PVDF nanofiber membranes under different preparation conditions. *Fuller. Nanotub. Carbon Nanostructures* **2020**, *28*, 381–386. [CrossRef]
35. Roche, R.; Yalcinkaya, F. Incorporation of PVDF nanofibre multilayers into functional structure for filtration applications. *Nanomaterials* **2018**, *8*, 771. [CrossRef]
36. Kurecic, M.; Smole, M.S. Electrospinning: Nanofibre production method. *Tekstilec* **2013**, *56*, 4–12. [CrossRef]
37. Storck, J.L.; Grothe, T.; Mamun, A.; Sabantina, L.; Klöcker, M.; Blachowicz, T.; Ehrmann, A. Orientation of electrospun magnetic nanofibers near conductive areas. *Materials* **2020**, *13*, 47. [CrossRef]
38. Blachowicz, T.; Ehrmann, A. Magnetization reversal in bent nanofibers of different cross sections. *J. Appl. Phys.* **2018**, *124*, 152112. [CrossRef]
39. Gaididei, Y.; Goussev, A.; Kravchuk, V.P.; Pylypovskyi, O.V.; Robbins, J.M.; Sheka, D.D.; Slastikov, V.; Vasylkevych, S. Magnetization in narrow ribbons: Curvature effects. *J. Phys. Math. Theor.* **2017**, *50*, 385401. [CrossRef]
40. Moreno, R.; Carvalho-Santos, V.L.; Espejo, A.P.; Laroze, D.; Chubykalo-Fesenko, O.; Altbir, D. Oscillatory behavior of the domain wall dynamics in a curved cylindrical magnetic nanowire. *Phys. Rev. B* **2017**, *96*, 184401. [CrossRef]
41. Parkin, S.S.P.; Hayashi, M.; Thomas, L. Magnetic domain-wall racetrack memory. *Science* **2008**, *320*, 190–194. [CrossRef] [PubMed]
42. Grollier, J.; Querlioz, D.; Stiles, M.D. Spintronic Nanodevices for Bioinspired Computing. *Proc. IEEE* **2016**, *104*, 2024–2039. [CrossRef] [PubMed]
43. LeCun, Y.; Bengio, Y.; Hinton, G. Deep learning. *Nature* **2015**, *521*, 7553. [CrossRef] [PubMed]
44. Hinton, G.E.; Salakhutdinov, R.R. Reducing the dimensionality of data with neural networks. *Science* **2006**, *313*, 504–507. [CrossRef]
45. Masquelier, T.; Thorpe, S.J. Unsupervised learning of visual features through spike timing dependent plasticity. *PLoS Comput. Biol.* **2007**, *3*, e31. [CrossRef]
46. Indiveri, G.; Liu, S.C. Memory and information processing in neuromorphic systems. *Proc. IEEE* **2015**, *103*, 1379–1397. [CrossRef]
47. Querlioz, D.; Bichler, O.; Vincent, A.F.; Gamrat, C. Bioinspired programming of memory devices for implementing an inference engine. *Proc. IEEE* **2015**, *103*, 1398–1416. [CrossRef]
48. Meier, K. A mixed-signal universal neuromorphic computing system. In Proceedings of the 2015 IEEE International Electron Devices Meeting (IEDM), Washington, DC, USA, 7–9 December 2015.
49. Merolla, P.A.; Arthur, J.V.; Alvarez-Icaza, R.; Cassidy, A.S.; Sawada, J.; Akopyan, F.; Jackson, B.L.; Imam, N.; Guo, C.; Nakamura, Y.; et al. A million spiking-neuron integrated circuit with a scalable communication network and interface. *Science* **2014**, *345*, 668–673. [CrossRef]
50. Ryu, K.-S.; Thomas, L.; Yang, S.-H.; Parkin, S.S.P. Current induced tilting of domain walls in high velocity motion along perpendicularly magnetized micron-sized Co/Ni/Co racetracks. *Appl. Phys. Express* **2012**, *5*, 093006. [CrossRef]
51. Yang, S.-H.; Ryu, K.-S.; Parkin, S.S.P. Domain-wall velocities of up to 750 m s^{-1} driven by exchange-coupling torque in synthetic antiferromagnets. *Nat. Nanotechnol.* **2015**, *10*, 221–226. [CrossRef]
52. Alejos, O.; Raposo, V.; Tejerina, L.S.; Martinez, E. Efficient and controlled domain wall nucleation for magnetic shift registers. *Sci. Rep.* **2017**, *7*, 11909. [CrossRef]
53. Liu, L.Q.; Lee, O.J.; Gudmundsen, T.J.; Ralph, D.C.; Buhrman, R.A. Current-Induced Switching of Perpendicularly Magnetized Magnetic Layers Using Spin Torque from the Spin Hall Effect. *Phys. Rev. Lett.* **2012**, *109*, 096602. [CrossRef]

54. Liu, L.; Pai, C.-F.; Li, Y.; Tseng, H.W.; Ralph, D.C.; Buhrman, R.A. Spin-torque switching with the giant spin Hall effect of tantalum. *Science* **2012**, *336*, 555–558. [CrossRef]
55. Martinez, E.; Torres, L.; Perez, N.; Hernandez, M.A.; Raposo, V.; Moretti, S. Universal chiral-triggered magnetization switching in confined nanodots. *Sci. Rep.* **2015**, *5*, 10156. [CrossRef]
56. Allwood, D.A.; Xiong, G.; Cowburn, R.P. Domain wall cloning in magnetic nanowires. *J. Appl. Phys.* **2007**, *101*, 024308. [CrossRef]
57. Yao, P.; Wu, H.; Gao, B.; Tang, J.S.; Zhang, Q.T.; Zhang, W.Q.; Yang, J.J.; Qian, H. Fully hardware-implemented memristor convolutional neural network. *Nature* **2020**, *577*, 641–646. [CrossRef]
58. Lequeux, S.; Sampaio, J.; Cros, V.; Yakushiji, K.; Fukushima, A.; Matsumoto, R.; Kubota, H.; Yuasa, S.; Grollier, J. A magnetic synapse: Multilevel spin-torque memristor with perpendicular anisotropy. *Sci. Rep.* **2016**, *6*, 31510. [CrossRef] [PubMed]
59. Sabantina, L.; Rodríguez Mirasol, J.; Cordero, T.; Finsterbusch, K.; Ehrmann, A. Investigation of needleless electrospun PAN nanofiber mats. Secunderabad, India, Dec. 22–23, 2017. *AIP Conf. Proc.* **2018**, *1952*, 020085.
60. Ehrmann, A.; Blachowicz, T. Vortex and double-vortex nucleation during magnetization reversal in Fe nanodots of different dimensions. *J. Magn. Magn. Mater.* **2019**, *475*, 727–733. [CrossRef]
61. Kukuchi, N.; Okamoto, S.; Kitakami, O.; Shimada, Y.; Kim, S.G.; Otani, Y.; Fukamichi, K. Vertical bistable switching of spin vortex in a circular magnetic dot. *J. Appl. Phys.* **2001**, *90*, 6548. [CrossRef]
62. Van Waeyenberge, B.; Puzic, A.; Stoll, H.; Chou, K.W.; Tyliszczak, T.; Hertel, R.; Fähnle, M.; Brückl, H.; Rott, K.; Reiss, G.; et al. Magnetic vortex core reversal by excitation with short bursts of an alternating field. *Nature* **2006**, *444*, 461–464. [CrossRef] [PubMed]
63. Weigand, M.; van Waeyenberge, B.; Vanseenkiste, A.; Curcic, M.; Sackmann, V.; Stoll, H.; Tyliszczak, T.; Kaznatcheev, K.; Woltersdorf, G.; Back, C.H.; et al. Vortex Core Switching by Coherent Excitation with Single In-Plane Magnetic Field Pulses. *Phys. Rev. Lett.* **2009**, *102*, 077201. [CrossRef] [PubMed]
64. Arbab, S.; Teimoury, A.; Mirbaha, H.; Adolphe, D.C.; Noroozi, B.; Nourpanah, P. Optimum stabilization processing parameters for polyacrylonitrile-based carbon nanofibers and their difference with carbon (micro) fibers. *Polym. Degrad. Stab.* **2017**, *142*, 198–208. [CrossRef]
65. Wei, Y.; Han, B.; Hu, X.Y.; Lin, Y.H.; Wang, X.Z.; Deng, X.L. Synthesis of Fe_3O_4 nanoparticles and their magnetic properties. *Proc. Eng.* **2012**, *27*, 632–637. [CrossRef]
66. Duque, J.G.S.; Souza, E.A.; Meneses, C.T.; Kuobta, L. Magnetic properties of $NiFe_2O_4$ nanoparticles produced by a new chemical method. *Phys. B* **2007**, *398*, 287–290. [CrossRef]
67. Donahue, M.J.; Porter, D.G. *OOMMF User's Guide, Version 1.0*; Interagency Report NISTIR 6376; National Institute of Standards and Technology: Gaithersburg, MD, USA, 1999.
68. Gilbert, T.L. A phenomenological theory of damping in ferromagnetic materials. *IEEE Trans. Magn.* **2004**, *40*, 3443. [CrossRef]
69. Dantas, C.C.; Garna, A.M. Micromagnetic simulations of spinel ferrite particles. *J. Magn. Magn. Mater.* **2010**, *322*, 2824–2833. [CrossRef]
70. Kamble, R.B.; Varade, V.; Ramesh, K.P.; Prasad, V. Domain size correlated magnetic properties and electrical impedance of size dependent nickel ferrite nanoparticles. *AIP Adv.* **2015**, *5*, 017119. [CrossRef]
71. Mirgorod, Y.A.; Borshch, N.A.; Fedosyuk, V.M.; Yurkov, G.Y. Magnetic properties of nickel ferrite nanoparticles prepared using flotation extraction. *Inorg. Mater.* **2013**, *49*, 109–113. [CrossRef]
72. Zhao, S.F.; Sun, Q.; Wang, R.M.; Han, Y.N. Growth and micromagnetic simulation of magnetite nanoparticles. *Sci. China* **2011**, *54*, 1208–1212. [CrossRef]
73. Yani, A.; Kurniawan, C.; Djuhana, D. Investigation of the ground state domain structure transition on magnetite (Fe_3O_4). Univ. Indonesia, Bali, Indonesia. *AIP Conf. Proc.* **2018**, *2023*, 020020-1.
74. Blachowicz, T.; Kosmalska, D.; Döpke, C.; Leiste, H.; Hahn, L.; Ehrmann, A. Varying steps in hysteresis loops of Co square nano-frames. *J. Magn. Magn. Mater.* **2019**, *491*, 165619. [CrossRef]
75. Sudsom, D.; Juhász Junger, I.; Döpke, C.; Blachowicz, T.; Hahn, L.; Ehrmann, A. Micromagnetic simulation of vortex development in magnetic bi-material bow-tie structures. *Condens. Matter* **2020**, *5*, 5. [CrossRef]
76. Blachowicz, T.; Döpke, C.; Ehrmann, A. Micromagnetic simulations of electrospun nanofiber networks. *Phys. Rev. B* **2020**, submitted.

77. Sabantina, L.; Rodríguez-Cano, M.Á.; Klöcker, M.; García-Mateos, F.J.; Ternero-Hidalgo, J.J.; Mamun, A.; Beermann, F.; Schwakenberg, M.; Voigt, A.-L.; Rodríguez Mirasol, J.; et al. Fixing PAN nanofiber mats during stabilization for carbonization and creating novel metal/carbon composites. *Polymers* **2018**, *10*, 735. [CrossRef]
78. Sabantina, L.; Klöcker, M.; Wortmann, M.; Rodríguez-Mirasol, J.; Cordero, T.; Moritzer, E.; Finsterbusch, K.; Ehrmann, A. Stabilization of polyacrylonitrile nanofiber mats obtained by needleless electrospinning using dimethyl sulfoxide as solvent. *J. Ind. Text.* **2019**, online first. [CrossRef]
79. Sabantina, L.; Böttjer, R.; Wehlage, D.; Grothe, T.; Klöcker, M.; García-Mateos, F.J.; Rodríguez-Mirasol, J.; Cordero, T.; Ehrmann, A. Morphological study of stabilization and carbonization of polyacrylonitrile/TiO_2 nanofiber mats. *J. Eng. Fibers Fabr.* **2019**, *14*, 1558925019862242. [CrossRef]
80. Sabantina, L.; Wehlage, D.; Klöcker, M.; Mamun, A.; Grothe, T.; García-Mateos, F.J.; Rodríguez-Mirasol, J.; Cordero, T.; Finsterbusch, K.; Ehrmann, A. Stabilization of electrospun PAN/gelatin nanofiber mats for carbonization. *J. Nanomater.* **2018**, *2018*, 6131085. [CrossRef]
81. Nabiyouni, G.; Fesharaki, M.J.; Mozafari, M.; Amighian, J. Characterization and magnetic properties of nickel ferrite nanoparticles prepared by ball milling technique. *Chin. Phys. Lett.* **2010**, *27*, 126401. [CrossRef]
82. Iqbal, Y.; Bae, H.S.; Rhee, I.; Hong, S.W. Control of the saturation temperature in magnetic heating by using polyethylene-glycol-coated rod-shaped nickel-ferrite ($NiFe_2O_4$) nanoparticles. *J. Korean Phys. Soc.* **2016**, *68*, 587–592. [CrossRef]
83. Manohar, A.; Krishnamoorthi, C. Low Curie-transition temperature and superparamagnetic nature of Fe_3O_4 nanoparticles prepared by colloidal nanocrystal synthesis. *Mater. Chem. Phys.* **2017**, *192*, 235–243.
84. Levy, D.; Giustetto, R.; Hoser, A. Structure of magnetite (Fe_3O_4) above the Curie temperature: A cation ordering study. *Phys. Chem. Miner.* **2012**, *39*, 169–176. [CrossRef]
85. Ehrmann, A.; Blachowicz, T. Influence of the distance between nanoparticles in clusters on the magnetization reversal process. *J. Nanomater.* **2017**, *2017*, 5046076. [CrossRef]

materials

MDPI

Article

Glassy Magnetic Behavior and Correlation Length in Nanogranular Fe-Oxide and Au/Fe-Oxide Samples

L. Del Bianco [1,*], F. Spizzo [1], G. Barucca [2], G. Marangoni [3] and P. Sgarbossa [3]

[1] Dipartimento di Fisica e Scienze della Terra, Università di Ferrara, I-44122 Ferrara, Italy; federico.spizzo@unife.it
[2] Dipartimento SIMAU, Università Politecnica delle Marche, I-60131 Ancona, Italy; g.barucca@staff.univpm.it
[3] Dipartimento di Ingegneria Industriale, Università di Padova, I-35131 Padova, Italy; giovanni.marangoni@unipd.it (G.M.); paolo.sgarbossa@unipd.it (P.S.)
* Correspondence: lucia.delbianco@unife.it

Received: 3 November 2019; Accepted: 26 November 2019; Published: 29 November 2019

Abstract: In nanoscale magnetic systems, the possible coexistence of structural disorder and competing magnetic interactions may determine the appearance of a glassy magnetic behavior, implying the onset of a low-temperature disordered collective state of frozen magnetic moments. This phenomenology is the object of an intense research activity, stimulated by a fundamental scientific interest and by the need to clarify how disordered magnetism effects may affect the performance of magnetic devices (e.g., sensors and data storage media). We report the results of a magnetic study that aims to broaden the basic knowledge of glassy magnetic systems and concerns the comparison between two samples, prepared by a polyol method. The first can be described as a nanogranular spinel Fe-oxide phase composed of ultrafine nanocrystallites (size of the order of 1 nm); in the second, the Fe-oxide phase incorporated non-magnetic Au nanoparticles (10–20 nm in size). In both samples, the Fe-oxide phase exhibits a glassy magnetic behavior and the nanocrystallite moments undergo a very similar freezing process. However, in the frozen regime, the Au/Fe-oxide composite sample is magnetically softer. This effect is explained by considering that the Au nanoparticles constitute physical constraints that limit the length of magnetic correlation between the frozen Fe-oxide moments.

Keywords: disordered magnetism; super-spin glass; glassy correlation length; magnetic freezing; nanogranular Au/Fe-oxide; Fe-oxide nanocrystallites

---

1. Introduction

Magnetic systems classifiable as ‘disordered’ have the common property that the constituent magnetic moments undergo, at a critical temperature, a collective freezing along essentially random directions, giving rise to a low-temperature quasi-degenerate frozen state. This phenomenology requires basic ingredients, which are topological disorder, mixed and competing magnetic interactions, and random local anisotropy.

For instance, in amorphous magnetic materials the atomic spins may give rise to a non-collinear magnetic structure (speromagnetic or asperomagnetic) as a result of the competition between magnetic anisotropy and exchange interaction and depending on the distribution in sign of the exchange coupling constants [1].

In dilute magnetic alloys of noble metals (e.g., Au, Ag, Cu, and Pt) with 3d transition metal impurities (e.g., Fe or Mn), the randomness of site occupancy of the atomic spins and the frustration of competing magnetic interactions (RKKY and dipolar) result in a canonical spin glass behavior, characterized by the transition from a high-temperature paramagnetic state of the spins to a low-temperature frozen regime [2–4]. In the spin glass description, an important parameter is the length on which the spins are rigidly coupled together under the action of competitive magnetic interactions [5]. In a canonical spin glass, this magnetic correlation length increases more and more on reducing temperature across the freezing one, and in principle, it reaches an infinite extension in the final, low-temperature frozen regime. It is worth mentioning that, depending on the specific system, the frozen regime can also develop out of a ferromagnetic state of the spins (re-entrant behavior) [5–8].

The advent of nanoscience has led to the creation of engineered magnetic materials (nanoparticles, nanogranular materials, nanocrystalline thin films, and multilayers), showing novel magnetic effects of huge relevance in strategic technological sectors (e.g., energy, spintronics, data storage, sensors, biotechnology, and nanomedicine). This intense research activity on nanostructured magnetic systems has also disclosed the existence of a variety of disordered magnetism phenomena.

It is now quite well established that a random assembly of dipolar interacting magnetic nanoparticles may undergo a collective freezing, resulting in a low-temperature glassy magnetic regime [9–17]. The frozen regime is often termed "super-spin glass" (SSG), in order to stress that the magnetic entities that undergo the freezing process are not atomic spins, but the nanoparticle moments [18–20].

Canting and glassy dynamics of surface spins were observed in ferrite [21–25] and antiferromagnetic nanoparticles [26,27], as a result of reduced atomic coordination and altered super-exchange bonds. A spin glass like freezing was reported for the spins located at the grain boundaries of ball-milled antiferromagnetic FeRh [28], pure nanocrystalline Fe [29], and Fe thin films [30], due to the combination of structural disorder and distributed (in magnitude and sign) exchange interactions.

Disordered magnetism effects were found to dominate the magnetic properties of two-phase nanogranular systems. For instance, pellets obtained by the high-pressure compaction of core-shell Fe/Fe-oxide nanoparticles were described as being composed of a structurally disordered Fe-oxide matrix embedding Fe nanoparticles [31]. The magnetic study revealed a magnetic freezing of net Fe-oxide moments, a behavior which was termed "cluster-glass like." In nanogranular samples consisting of Ni nanoparticles embedded in a NiO matrix, the presence of a structurally disordered NiO components at the interface between the ferromagnetic (FM) and antiferromagnetic (AFM) phases and showing a glassy magnetic behavior, ruled the magnetic properties of the whole composite system [32]. In materials of this type, the observation of the exchange bias effect allowed valuable information to be obtained on the disordered magnetism phenomenology. It is worth recalling that the exchange bias effect is the horizontal shift of the hysteresis loop that may be observed in nanostructured FM/AFM systems after field-cooling through the Néel temperature of the AFM, so that the AFM spins couple to the FM ones, minimizing the interface exchange interaction [33,34]. The loop shift reveals the existence of a unidirectional anisotropy for the FM spins, due to the torque action exerted on them by the AFM ones. It was found out that the role of the AFM in this exchange coupling mechanism may also be played by a glassy magnetic phase whose magnetization dynamics ends up ruling the magnetic behavior of the whole composite system [35–40].

Due to the strategic importance of the exchange bias effect in the technology of spintronic devices [41,42], the exchange coupling mechanism is mainly investigated in FM/AFM samples in the form of films or nanopatterned structures [43]. Disordered magnetism phenomena emerge also in systems with this configuration [44–49]. For instance, in NiFe/IrMn bilayers, the existence of a structurally disordered IrMn region with spin glass like behavior, interposed between the NiFe layer and the bulk of the IrMn layer, well accounted for the thermal evolution of the exchange bias effect and for its disappearance at a temperature much lower than expected, namely, much lower than the Néel temperature of the AFM [46]. However, for this glassy phase, the onset of an infinite magnetic correlation length below the freezing temperature was not experimentally observed. This was explained considering that the interface region was inherently inhomogeneous, both from the structural and magnetic point of view, and that this hindered the formation of an infinite correlated frozen state [50]. In the case of NiFe/IrMn nanodots, a dependence of the exchange bias effect on the ratio between the dot size and the glassy correlation length was demonstrated [50,51]. Moreover, it was shown that the exchange bias effect of NiFe/IrMn bilayers could be tuned by varying the correlation length in the IrMn spin glass like region, through the insertion of non-magnetic nanosized Cu elements at the FM/AFM interface [52].

Thus, these findings indicate that a modulation of the correlation length in a glassy magnetic material may be achieved by controlling the structural and/or compositional features. Despite the described extensive research work on the disordered magnetism phenomenology, this specific topic has rarely been addressed. In order to better elucidating it, suitable samples would be needed, with a dominant and well detectable glassy magnetic nature. Composite materials like those described above, in which the glassy magnetic phase is interfaced to a FM one or interposed at the FM/AFM interface, are not particularly suitable, actually. In fact, it is almost invariably observed that, above the freezing temperature, the spins in the FM and AFM components exert a polarizing action on the thermally fluctuating spins of the disordered component, influencing their relaxation dynamics and preventing their passage to the (super)-paramagnetic regime (effect reminiscent of the re-entrant behavior) [29,32,50].

In this context, we have succeeded in preparing two nanogranular samples with peculiar structural properties, extremely favorable for the appearance of disordered magnetism effects. The first is made of ultrafine spinel Fe-oxide nanocrystallites, with sizes of the order of 1 nm. The second sample consists of the same Fe-oxide phase and of Au nanoparticles of 10–20 nm in size. We will show that both samples possess an SSG magnetic character and that the freezing of the Fe-oxide nanocrystallite moments occurrs following a very similar dynamics. However, in the frozen regime, the Au/Fe-oxide composite exhibits a softer magnetic behavior. This effect is discussed considering how the presence of the Au nanoparticles affects the glassy state and highlighting the role of the magnetic correlation length.

2. Experimental

2.1. Synthesis of the Fe-Oxide and Au/Fe-Oxide Nanogranular Samples

The samples are synthesized by a polyol method [53]. All reagents and solvents are purchased from Sigma-Aldrich and used without further purification.

To prepare the Fe-oxide sample, a solution, obtained dissolving 2.0 g of iron(III) chloride hexahydrate ($FeCl_3{\cdot}6H_2O$) in 5.0 mL of ethylene glycol and 1.5 mL of water, is injected quickly and under vigorous stirring in 25 mL of an oleylamine (10 g) solution in ethylene glycol, at 190 °C in inert atmosphere (nitrogen). The reaction mixture is heated at reflux for 6 h. After cooling at room temperature, the black suspension is poured into 200 mL of acetone to precipitate the Fe-oxide phase, which is separated magnetically, washed several times with acetone (3 × 50 mL), and dried under vacuum.

The Au/Fe-oxide sample is obtained by introducing the gold precursor into the previously prepared Fe-oxide. To this end, 10 mg of the Fe-oxide phase is dispersed in 1 mL of octylamine and 5 mL of ethylene glycol under magnetic stirring, and heated at 150 °C. The black suspension is then treated with 1 mL of gold(III) chloride hydrate ($HAuCl_4$, 30 mg) solution in ethylene glycol, followed by 100 μL of a 50% solution of tetramethylammonium hydroxide in water. The dark-reddish suspension is stirred at room temperature for 45 min and then poured into 250 mL of acetone for magnetic separation. After washing with acetone (4 × 25 mL), the solid precipitate is dried under vacuum.

The Fe-oxide and the Au/Fe-oxide samples are in powder form and labelled MNP and AuMNP, respectively.

2.2. Characterization Techniques

The inner structure of the MNP and AuMNP samples is investigated by transmission electron microscopy (TEM) techniques by using a Philips CM200 microscope (Philips, Amsterdam, The Netherlands) operating at 200 kV and equipped with a LaB6 filament. For TEM observations, a small quantity of powder is dispersed in ethanol and subjected to ultrasonic agitation for approximately one minute. A drop of suspension is deposited on a commercial TEM grid covered with a thin carbon film; finally, the grid is kept in air until complete evaporation of ethanol.

The magnetic properties of the samples are investigated by a superconducting quantum interference device (SQUID) magnetometer (Quantum Design, San Diego, USA) operating in the range 5–300 K (maximum applied field $H_{appl} = 50$ kOe, sensitivity 10^{-7} emu). The powder to be measured is inserted into a suitable holder and slightly pressed to avoid any movement during the measurement.

3. Results

3.1. Structural Properties Investigated by TEM

The morphology and structure of the MNP and AuMNP samples are analyzed by TEM techniques. A bright-field TEM image of MNP is shown in Figure 1a. The powder is composed of large agglomerates, which appear as a quite compact medium. Regions with different thickness (with respect to the electron beam direction), consequently providing a different contrast, can be distinguished.

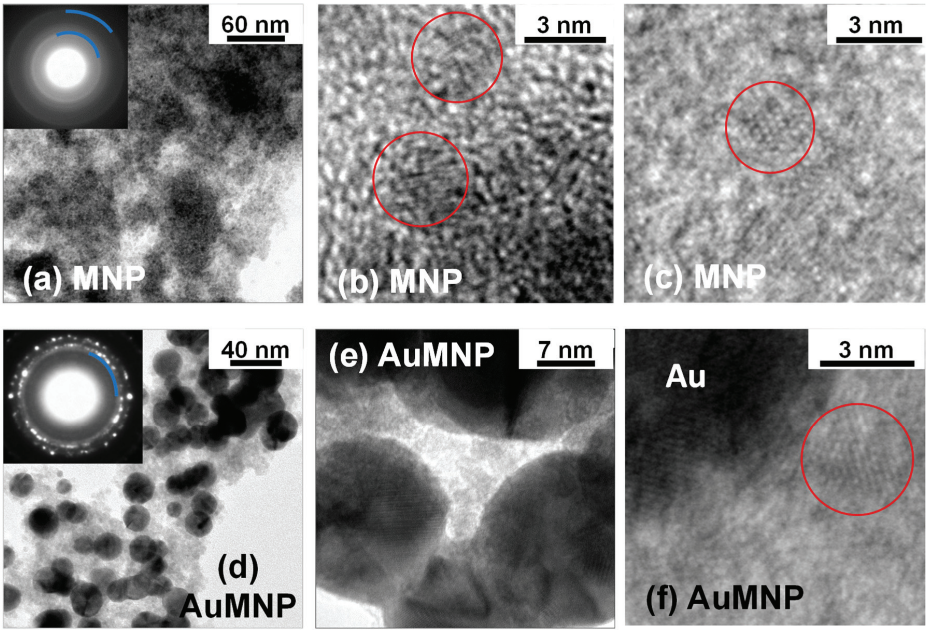

Figure 1. Sample MNP: (**a**) bright field TEM image and corresponding SAED pattern (inset; the blu lines mark the diffraction rings discussed in text); (**b**,**c**) HR-TEM images showing ultrafine Fe-oxide nanocrystallites (red circles). In particular, the circle in frame (**c**) encloses a small Fe-oxide nanocrystallite in [114] zone axis. Sample AuMNP: (**d**) bright field TEM image and corresponding SAED pattern (inset); (**e**) HR-TEM image showing Au nanoparticles in contact with each other and with the Fe-oxide phase; (**f**) HR-TEM image showing a portion of a gold nanoparticle and an ultrafine Fe-oxide nanocrystallite (red circle).

By increasing the magnification and performing high-resolution (HR) TEM observations, it turns out that the sample structure is characterized by a high degree of structural disorder. Typical HR-TEM images, such as those shown in Figure 1b,c, reveal the presence of randomly oriented crystals of about 2–5 nm in size (circled regions). Thus, we model the sample as a nanogranular material made of ultrafine nanocrystallites. The distance between the fringes highlighted in Figure 1b is estimated by the fast Fourier transform (FFT) of the image, performed by using the Gatan Microscopy Suite GMS3 software [54]. The value obtained is d = (0.251 ± 0.05) nm, compatible with the (311) atomic planes of the spinel Fe-oxide structure.

Due to the TEM experimental error, it is not possible to distinguish between magnetite Fe_3O_4 (in which $d_{(311)}$ = 0.253 nm) and maghemite γ-Fe_2O_3 ($d_{(311)}$ = 0.252 nm). The selected area electron diffraction (SAED) pattern of the sample region imaged in Figure 1a is shown in the inset of the same figure. It features broad and diffuse diffraction rings, confirming the poor crystallinity of MNP. The interplanar distances associated to the two most visible rings (evidenced in the image) are d_1 = 0.25(2) nm and d_2 = 0.14(8) nm, corresponding to the family of planes (311) and (440) of the spinel Fe-oxide structure, respectively.

Passing to sample AuMNP, a typical bright field TEM image is shown in Figure 1d. The Fe-oxide phase, which gives the light-grey contrast, incorporates black, roughly spherical elements with sizes between 10 and 20 nm, which correspond to Au nanoparticles. The nature of these two phases is confirmed by SAED measurements. In fact, the SAED pattern (inset of Figure 1d) shows well-defined and speckled diffraction rings, consistent with a crystalline Au phase composed of large grains; in the inner part of the pattern, a diffuse diffraction ring is visible (marked in the figure), which is attributed to the spinel Fe-oxide structure; in particular, to the (311) family of planes.

The HR-TEM analysis further confirms the good crystallinity of the Au nanoparticles, whereas the Fe-oxide phase has a poorly crystalline structure, perfectly similar to that observed in MNP (Figure 1e–f). In most cases the Au nanoparticles are in contact with each other and act so as to spatially confine the Fe-oxide phase, as shown in Figure 1e.

3.2. Magnetic Properties

3.2.1. Hysteresis Loops

Magnetic hysteresis loops measured on MNP and AuMNP at T = 5 K are shown in Figure 2a. In particular, the specific magnetization M is reported, obtained by normalizing the magnetic moment to the mass of the sample. The loops show a non-saturating tendency, more pronounced in MNP. The values of the saturation magnetization M_S at T = 5 K are extrapolated from the loops for 1/H tending to zero and are reported in Table 1. By comparing the M_S of MNP with that measured in AuMNP, we estimate that the fractions of Fe-oxide and Au in the latter sample are (55 ± 1) wt.% and (45 ± 1) wt.%, respectively. In that calculation, the diamagnetic contribution of Au to the total magnetization is neglected. Since the mass magnetic susceptibility of Au is (-1.42×10^{-7}) emu/g Oe [55], the diamagnetic contribution to the magnetization at H = 50 kOe is much smaller than the experimental error associated to the M_S value. In Table 1, we report the values of coercivity H_C and of the irreversibility field H_{irr}. The latter parameter is the field at which the ascending and descending branches of the hysteresis loop join together, and it may be considered a measure of the anisotropy field of the system, i.e., $H_{irr} = 2\,K_{eff}/M_S$, where K_{eff} is the effective anisotropy [56,57]. In order to calculate K_{eff} from this relationship, M_S must be expressed in (emu/cm^3); namely, the value of M_S for MNP must be multiplied by the density of the Fe oxide phase, which we conventionally take to be 5 g/cm^3, corresponding to the average of bulk Fe_3O_4 and γ-Fe_2O_3. The values of K_{eff}, also shown in Table 1, and of H_C, indicate a softer magnetic behavior of sample AuMNP, compared to MNP.

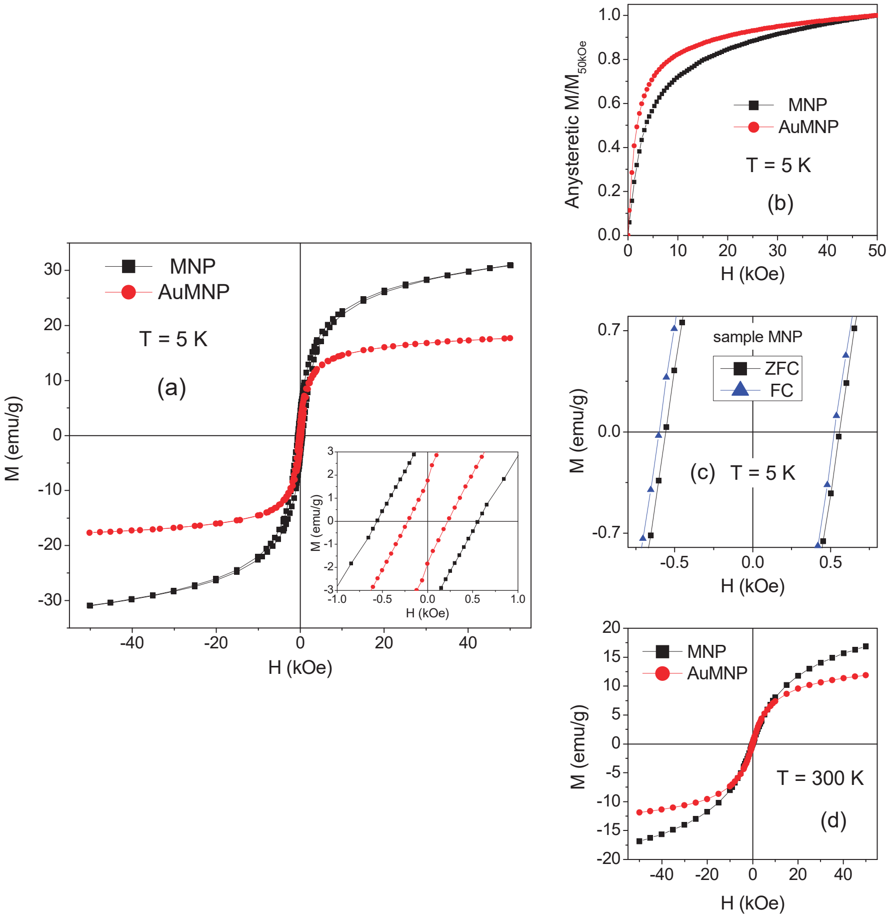

Figure 2. (**a**) Magnetic hysteresis loops measured on the MNP and AuMNP samples at T = 5 K. Inset: close-up of the central region of the loops. (**b**) Anhysteretic magnetization curves for MNP and AuMNP obtained from the loops in (**a**); they are shown as normalized to their value at H = 50 kOe (M_{50kOe}). (**c**) Central region of the hysteresis loops measured on sample MNP in zero-field-cooling (ZFC) and field-cooling (FC) mode. (**d**) Magnetization curves measured on MNP and AuMNP at T = 300 K.

Table 1. The data refer to the MNP and AuMNP samples, as indicated in column 1, measured at T = 5 K. Column 2: saturation magnetization M_S. Column 3: Coercivity H_C. Columns 4 and 5: irreversibility field H_{irr} and effective magnetic anisotropy K_{eff}. Column 6. Parameter H_{shift}, which quantitatively expresses the shift of the FC loop. Column 7: demagnetization remanence coercivity, H_{C_DCD}.

Sample	M_S (emu/g) ±1%	H_C (Oe) ±1%	H_{irr} (Oe) ±2%	K_{eff} (erg/cm^3) ±2%	H_{shift} (Oe)	H_{C_DCD} (Oe) 2%
MNP	34.8	559	21300	1.82×10^6	38 ± 3	1300
AuMNP	19.0	221	6300	5.4×10^5	11 ± 2	618

In Figure 2b, we show the anhysteretic magnetization curves, obtained from the loops at T = 5 K and normalized to their value at H = 50 kOe (M_{50kOe}), in order to deal with comparable values. A higher initial magnetic susceptibility (i.e., slope dM/dH at low field) and a lower high-field magnetic susceptibility (i.e., slope dM/dH in the field range 30–50 kOe) characterize the anhysteretic magnetization curve of AuMNP, both features indicating that this sample is more easily magnetized, compared to MNP.

Hysteresis loops are also measured at T = 5 K after cooling the samples from room temperature in a field H_{appl} = 50 kOe (field-cooling mode, FC). Compared to the loops in Figure 2a, measured in zero-field-cooling mode (ZFC), the FC loops appear shifted to the left. The effect is shown for sample MNP in Figure 2c, where the central region of the ZFC and FC loops is displayed. The shift can be quantitatively expressed by the positive parameter $H_{shift} = -(H_{right} + H_{left})/2$, where H_{right} and H_{left} are the points where the loop intersects the field axis. For MNP, H_{shift} = (38 ± 3) Oe, whereas H_{shift} = (11 ± 2) Oe for AuMNP (Table 1).

Hysteresis loops are also measured on the two samples at temperature T = 20, 50, and 300 K. With increasing temperature, H_C decreases strongly and no magnetic hysteresis is observed at T = 50 K and 300 K. The loops measured at T = 300 K are shown in Figure 2d.

The DC demagnetization remanence (DCD) is measured on MNP and AuMNP at T = 5 K, in order to obtain the demagnetization remanence coercivity H_{C_DCD}. In the DCD measurement procedure, the sample is initially brought to saturation by a negative magnetic field and then progressively magnetized by a positive field increasing from 0 Oe up to 50 kOe. The recorded remanence values are plotted as a function of the previously applied magnetic field, and the curve so-obtained is normalized to its initial value. The parameter H_{C_DCD} corresponds to the field at which the DCD curve intercepts the x-axis, and therefore, it is a measure of the difficulty of demagnetizing the system [58]. In particular, H_{C_DCD} depends only on the irreversible part of the demagnetization process, unlike the coercivity H_C, which includes both reversible and irreversible changes. The values of H_{C_DCD}, obtained from the DCD curves displayed in Figure 3, are reported in Table 1: the parameter is twice higher in MNP than in AuMNP, which confirms the different magnetic hardness of the two samples at T = 5 K.

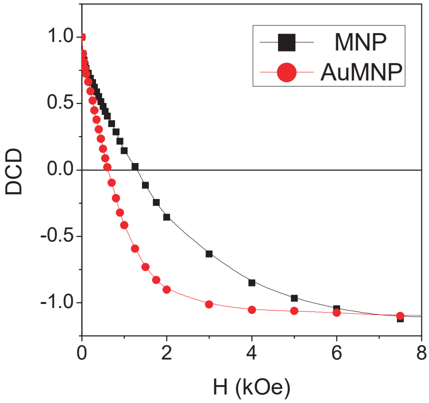

Figure 3. DC demagnetization remanence (DCD) curves, measured at T = 5 K on MNP and AuMNP. The field at which the DCD curve intercepts the x-axis corresponds to the demagnetization remanence coercivity, H_{C_DCD}.

3.2.2. Magnetothermal Behavior

To gain information on magnetic relaxation processes in the two samples, the magnetization is measured for increasing temperature (heating rate = 3 K/min) in a static magnetic field H_{appl} after cooling the samples from room temperature down to T = 5 K with no applied field (ZFC mode) and in H_{appl} (FC mode). The analysis is carried out at different values of H_{appl}, in the 20 Oe–5 kOe range (a higher number of measurements is performed on AuMNP, actually). The curves of M_{ZFC_FC} versus T (each normalized to the respective value of H_{appl}) are shown in Figure 4. Their shapes are similar for the two samples. At the lowest values of H_{appl} (20–50 Oe), M_{ZFC} increases on rising temperature from 5 K to about 30 K and then decreases following a 1/T dependence, giving rise to a sharp cusp (in the inset of Figure 4a, the M_{ZFC} versus T curve, at H_{appl} = 50 Oe, is shown for T ≥ 35 K, together with the 1/T fit line). In the same temperature interval, M_{FC} is higher than M_{ZFC}, namely, an effect of magnetic irreversibility is visible. The M_{ZFC} and M_{FC} branches join together at the irreversibility temperature T_{irr}, which is just slightly higher than that corresponding to the M_{ZFC} peak. A difference between the two samples concerns the trend of the M_{FC} curve in the temperature range where magnetic irreversibility exists. In fact, below T~30 K, M_{FC} in AuMNP increases with decreasing T, whereas the curve of MNP shows a dip, particularly well visible at H_{appl} = 50 Oe.

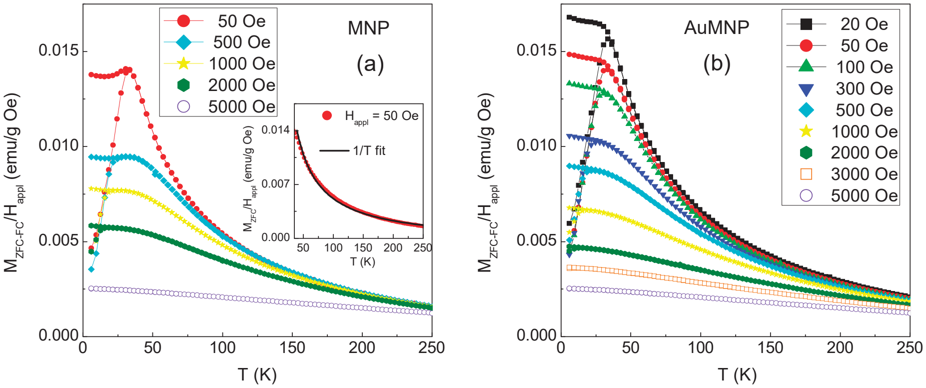

Figure 4. (**a**) Magnetization measured on sample MNP and sample AuMNP (**b**) for increasing temperature (T), at the indicated values of the applied magnetic field H_{appl}, after zero-field-cooling (M_{ZFC}, lower branch of each displayed curve) and after field-cooling (M_{FC}, upper branch). For a better view, the values of M_{ZFC_FC}/H_{appl} are displayed, actually. The inset in frame (**a**) shows the M_{ZFC} versus T curve, at H_{appl} = 50 Oe, for T ≥ 35 K (red circular symbols), together with the 1/T fit line (black line).

On increasing H_{appl}, T_{irr} reduces as well as the extent of the irreversibility effect. The latter is still visible at H_{appl} = 5 kOe, even if it is not appreciable on the scale of the graph shown in Figure 4, and it is erased at a higher field.

The magnetization in applied field H_{appl} = 50 kOe (M_{50kOe}) is measured on MNP and AuMNP as a function of temperature, in the 5–300 K range (Figure 5). A weaker thermal dependence of M_{50kOe} is observed in AuMNP.

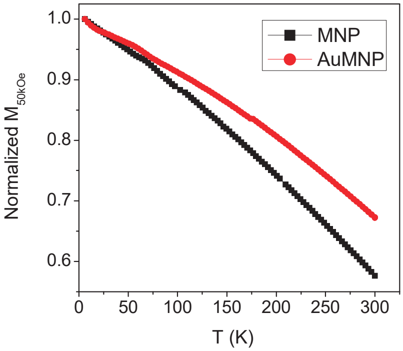

Figure 5. Thermal dependence of the magnetization measured in H_{appl} = 50 kOe (M_{50kOe}) on the MNP and AuMNP samples. The curves are normalized to their initial values at T = 5 K.

Finally, we report the results of magnetic relaxation measurements carried out on MNP and AuMNP according to the following procedure. The sample is cooled from T = 300 K down to T = 5 K; once this temperature is reached, we allow a 30 s elapse (waiting time, t_W) before the application of a magnetic field H_{appl} = 50 Oe, and the time variation of the magnetization is recorded. Then, the field is removed, the temperature is raised to 300 K, lowered at T = 5 K, and after t_W = 10,800 s (i.e., 3 h), H_{appl} is applied and M versus time is measured again.

The results are shown in Figure 6. Both for MNP and for AuMNP, the two curves are not superposed, which reveals the existence of an aging effect, namely, a dependence of the magnetic relaxation phenomenon on t_W.

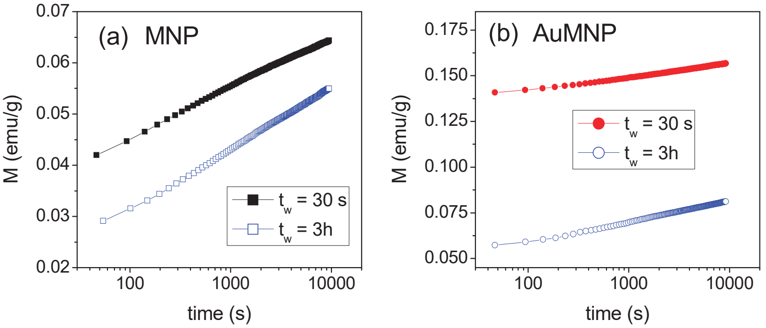

Figure 6. Time dependence of the magnetization measured at T = 5 K, in H_{appl} = 50 Oe, on MNP (**a**) and AuMNP (**b**), for two different waiting times, t_W = 30 s and t_W = 10,800 s (i.e., 3 h).

4. Discussion

Both the samples investigated show a magnetic behavior typical of the disordered magnetism phenomenology. A clear indication of this is the shape of the M_{ZFC-FC} curves (Figure 4), which is consistent with the onset of a low-temperature frozen collective magnetic regime at T_{irr} (i.e., T_{irr} corresponds to the freezing temperature). This magnetic behavior is certainly prompted by the high structural disorder of the Fe-oxide phase, which is also expected to bring about a marked spin canting effect. In fact, the value M_S~34.8 emu/g measured at T = 5 K in MNP (Table 1) is definitely lower than that of bulk spinel iron oxide phases (at T = 0 K, Ms~83 emu/g for maghemite and Ms~98 emu/g for magnetite), which reveals a strong lack of spin collinearity [31,59,60]. In this regard, it should be noted that ferrimagnetic iron oxide nanoparticles are often reported to consist of a mix of maghemite and magnetite [61]. The former can appear following the oxidation of the latter, and thus the two phases have a very similar spinel structure, which makes them difficult to be experimentally distinguished.

As observed by TEM (Figure 1), the Fe-oxide phase consists of large agglomerates of randomly oriented, ultrafine nanocrystallites, forming a quite compact, though inhomogeneous, nanogranular material. Hence, the nanocrystallite magnetic moments can magnetically interact both through super-exchange and dipolar interactions, both being ferromagnetic and antiferromagnetic in type. Thus, the following picture can be drawn. At T = 300 K, the magnetic moments are free to thermally fluctuate, i.e., exhibit superparamagnetic relaxation, in line with the absence of magnetic hysteresis (Figure 2d). Evidence that the fluctuating moments at T = 300 K are larger than single atomic spins—which is the reason why we refer to a superparamagnetic state rather than to purely paramagnetic state—is provided by the S-shape of the magnetization curves at this temperature, showing an approach to saturation in the high-field region (Figure 2d). With decreasing temperature, the effective magnetic anisotropy acting on the magnetic moments increases more and more. Below T_{irr}, the combination of structural disorder and mix of competing magnetic interactions brings about a collective freezing of the moments along locally varying anisotropy axes, giving rise to a disordered magnetic state, essentially describable as an SSG. The existence of a low-temperature collective frozen magnetic state of the

Fe-oxide moments in MNP and AuMNP is definitely confirmed by the observation of the aging effect, i.e., the dependence of the relaxing magnetization on t_w (Figure 6). In fact, that is typical of magnetic moment systems governed by glassy dynamics and it reveals the existence of a multidegenerate ground state (multivalley energy structure) [14,35,62–64].

This behavior is reminiscent of that shown by the poorly crystalline Fe-oxide phase (mean grain size~2 nm) in the Fe/Fe-oxide system, already recalled in the Introduction (in this respect, it is worth noting that also the value of M_S of the Fe-oxide phase was close to that measured in MNP) [31,35]. However, in that case, above the freezing temperature (~20 K), the Fe-oxide moments were not seen to enter the superparamagnetic state, due to the polarizing action of the Fe moments. On the contrary, for MNP and AuMNP, the passage from the frozen to the superparamagnetic regime with increasing temperature above T_{irr} is clearly revealed by the 1/T trend of the M_{ZFC-FC} curves (Figure 4).

Let us consider these curves in more detail. In canonical spin glasses, T_{irr} follows a $(H_{appl})^{2/3}$ dependence, corresponding to the so-called AT line [65]. In the case of the samples investigated, we find that the evolution of T_{irr} with H_{appl} is better described by a $\frac{1}{2}$ power law dependence. This is shown in Figure 7, where the T_{irr} values are reported as a function of $(H_{appl})^{1/2}$ and the solid lines are the best linear fit. This trend is generally observed in systems where the increase of H_{appl} favors the appearance of a ferromagnetic state, for instance, in re-entrant spin glasses [66]. In our samples, we expect that the Fe-oxide moments align more and more on increasing H_{appl}, producing a sort of mean field that adds to H_{appl}. This may account for the weaker dependence of T_{irr} on H_{appl}, compared to the AT line behavior. As regards the best fit lines in Figure 7, the slope is (-0.28 ± 0.01) K/Oe$^{1/2}$ in both samples and the intercept with the y-axis, which corresponds to T_{irr} for $H_{appl} = 0$, is (34.3 ± 0.5) K for MNP and (34.2 ± 0.4) K for AuMNP, i.e., is the same within the error. Hence, as far as the analysis of the M_{ZFC-FC} curves is concerned, the two samples are seen to behave in a very similar way.

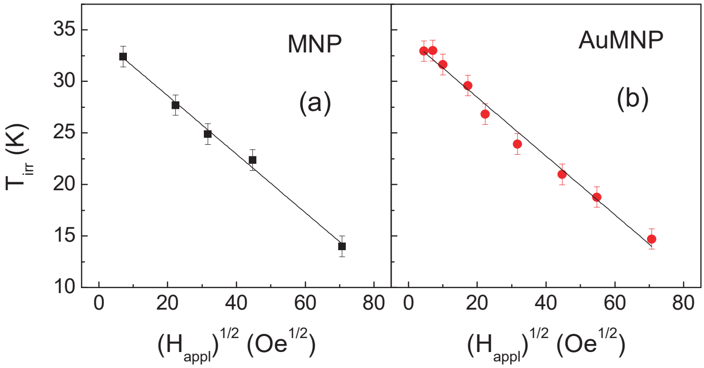

Figure 7. Dependence of the irreversibility temperature T_{irr} on $(H_{appl})^{1/2}$ in MNP (**a**) and AuMNP (**b**). The continuous black lines are the linear fitting curves.

The horizontal shift of the FC hysteresis loops, observed in both samples and quantitatively expressed by the parameter H_{shift} (Figure 2c), recalls the exchange-bias effect observed in a FM/spin glass system [32,35,67]. When this type of system is field-cooled across the freezing temperature, a spin configuration of the glassy phase is selected through the interface exchange coupling with the FM spins, which in turn favors the FM magnetization to be aligned in the FC direction (unidirectional anisotropy). However, a shift of the FC loop has been also observed in canonical spin glasses, such as the CuMn alloy [68]. The effect is explained considering the presence of chemical inhomogeneities bearing net magnetic moments that freeze along a preferred direction induced by the FC process. Thus, a unidirectional anisotropy arises, which manifests itself in the loop shift. In the case of MNP and AuMNP, the presence of net magnetic moments is intrinsic to their SSG nature, and therefore, the observation of the FC loop shift at T = 5 K is in full agreement with their glassy magnetic behavior.

The pronounced non-saturating tendency of the hysteresis loops measured on MNP and AuMNP at T = 5 K (Figure 2a) and the value of K_{eff} (Table 1)—which, in both samples, is higher than the magnetic anisotropy of bulk magnetite (1.1×10^5 ergs/cm^3) and maghemite (5×10^4 erg/cm^3)—are consistent with the collective frozen state of the Fe-oxide moments, implying the existence of high effective anisotropy energy barriers.

The inherent magnetic hardness of the frozen regime is the point on which MNP and AuMNP show their main differences. In fact, K_{eff} is definitely lower in AuMNP than in MNP and the same is true for H_C and H_{C_DCD} and H_{shift} (Table 1). The higher initial susceptibility and the lower high-field susceptibility revealed by the anhysteretic curve of AuMNP definitely confirm its reduced magnetic hardness, compared to MNP (Figure 2b). This behavior must be necessarily ascribed to the presence of the Au nanoparticles, which are substantially embedded in the Fe-oxide nanogranular matrix, as shown by TEM (Figure 1d–f). In an ideal spin glass, all the atomic spins that compose the frozen system are magnetically correlated, so as to give rise to a spatially infinite magnetic aggregate [5]. It is to be expected that the same occurs in SSG systems, and therefore, we can schematically hypothesize the existence of an infinite glassy correlation length in MNP. On the contrary, in AuMNP, the Au nanoparticles tend to spatially confine the Fe-oxide phase, and their presence reduces the possibility of direct contact between the magnetic nanocrystallites, hindering the super-exchange coupling and weakening the dipolar magnetic interactions. In other words, in AuMNP, the Au nanoparticles act so as to break the infinite magnetic aggregate, which implies a reduced correlation length, certainly shorter than that in MNP. As a consequence, in AuMNP, the Fe-oxide moments are less firmly frozen and react more easily to the external field, which is in agreement with the lower K_{eff} and with the overall softer magnetic behavior, compared to that of MNP.

Referring again to the $M_{ZFC\text{-}FC}$ curves in Figure 4, the dip at very low temperature in the M_{FC} branch of the MNP sample is a feature that can be observed exclusively, but not necessarily, in spin glasses and in SSG systems [69,70]. In AuMNP, you do not actually see it. Based on our description, we infer that the appearance of this feature below T_{irr} is connected to the extension of the glassy correlation length; namely, a slight decrease of the FC magnetic susceptibility in the glassy regime is the hint that largely extended magnetic correlations between the frozen moments are established.

The different trend of M_{50kOe} versus T in MNP and AuMNP (Figure 5) is also attributable to the presence of the Au nanoparticles in the latter sample. In this type of measurement, the sample is subjected to a field H_{appl} = 50 kOe, which erases the low-temperature glassy state and favors the ferromagnetic alignment of the magnetic moments. It is known that the thermal dependence of the magnetization in a saturated ferromagnetic system is due to the collective excitation of the aligned spins [71]. The presence of the Au nanoparticles in AuMNP may modify the spin vibrational modes, compared to those active in MNP. In particular, the thermal dependence of the magnetization is weaker in sample AuMNP, in which the spatial extension of the ferromagnetic order is limited due to the Au nanoparticles.

5. Conclusions

We have studied and compared the magnetic behavior of the MNP and AuMNP samples. Both samples possess a glassy magnetic nature. The passage from a high-temperature superparamagnetic regime to a low-temperature SSG regime of the Fe-oxide moments has been revealed by the analysis of the $M_{ZFC\text{-}FC}$ versus T curves and by the observation of an aging effect at T = 5 K. The temperature T_{irr}, which marks the onset of the freezing process, is similar in the two samples (~34 K, for H_{appl} = 0) as well as its dependence on H_{appl}. However, the AuMNP sample is magnetically softer than MNP. This effect has been ascribed to a reduction of the glassy correlation length of the Fe-oxide phase in AuMNP, compared to that in MNP, imposed by the physical constraints represented by the Au nanoparticles.

These findings expand the basic knowledge on disordered magnetism phenomena and glassy magnetic behavior in nanostructured systems, enlightening, in particular, the crucial role of the magnetic correlation length.

Author Contributions: G.M. and P.S. prepared the samples. G.B. carried out the HR-TEM characterization. L.D.B. and F.S. carried out the magnetic study. L.D.B. wrote the manuscript that was discussed and finally approved by all the authors.

Funding: This work has been partially supported by a grant 'Investimento Strategico di Dipartimento—SID' of the Department of Industrial Engineering, Padova University (Progetto SGAR_SID17_01).

Conflicts of Interest: The authors declare no conflict of interest. The funders had no role in the design of the study; in the collection, analyses, or interpretation of data; in the writing of the manuscript, or in the decision to publish the results.

References

1. Coey, J.M.D. Amorphous magnetic order. *J. Appl. Phys.* **1978**, *49*, 1646–1652. [CrossRef]
2. Mulder, C.A.M.; van Duyneveldt, A.J.; Mydosh, J.A. Susceptibility of the CuMn spin glass: Frequency and field dependences. *Phys. Rev. B* **1981**, *23*, 1384–1396. [CrossRef]
3. Cannella, V.; Mydosh, J.A. Magnetic ordering in gold-iron alloys. *Phys. Rev. B* **1972**, *6*, 4220–4237. [CrossRef]
4. Tholence, J.; Tournier, R. Susceptibility and remanent magnetization of a spin glass. *J. Phys. Colloq.* **1974**, *35*, C4-229–C4-235. [CrossRef]
5. Mydosh, J.A. *Spin Glasses: An Experimental Introduction*; Taylor and Francis: London, UK, 1993.
6. Aeppli, G.; Shapiro, S.M.; Birgeneau, R.J.; Chen, H.S. Spin correlations and reentrant spin glass behavior in amorphous Fe-Mn alloys. II. Dynamics. *Phys. Rev. B* **1984**, *29*, 2589–2605. [CrossRef]
7. Del Bianco, L.; Spizzo, F.; Tamisari, M.; Bonetti, E.; Ronconi, F.; Fiorani, D. Changing the magnetism of amorphous FeSiB by mechanical milling. *J. Phys. Condens. Matter.* **2010**, *22*, 296010. [CrossRef]
8. Luo, Q.; Shen, J. Reentrant spin glass ordering in an Fe-based bulk metallic glass. *J. Appl. Phys.* **2015**, *117*, 053909. [CrossRef]
9. Luo, W.; Nagel, S.R.; Rosenbaum, T.F.; Rosensweig, R.E. Dipole interactions with random anisotropy in a frozen ferrofluid. *Phys. Rev. Lett.* **1991**, *67*, 2721–2724. [CrossRef]
10. Dormann, J.L.; Cherkaoui, R.; Spinu, L.; Nogués, M.; Lucari, F.; D'Orazio, F.; Fiorani, D.; Garcia, A.; Tronc, E.; Jolivet, J.P. From pure superparamagnetic regime to glass collective state of magnetic moments in γ-Fe_2O_3 nanoparticle assemblies. *J. Magn. Magn. Mater.* **1998**, *187*, L139–L144. [CrossRef]
11. Sahoo, S.; Petracic, O.; Binek, C.; Kleemann, W.; Sousa, J.B.; Cardoso, S.; Freitas, P.P. Superspin glass nature of discontinuous $Co_{80}Fe_{20}/Al_2O_3$ multilayers. *Phys. Rev. B* **2002**, *65*, 134406. [CrossRef]
12. Jonsson, T.; Svedlindh, P.; Hansen, M.F. Static scaling on an interacting magnetic nanoparticle system. *Phys. Rev. Lett.* **1998**, *81*, 3976–3979. [CrossRef]
13. Alonso, J.; Fdez-Gubieda, M.L.; Barandiarán, J.M.; Svalov, A.; Fernández Barquín, L.; Alba Venero, D.; Orue, I. Crossover from superspin glass to superferromagnet in FexAg100−x nanostructured thin films ($20 < x < 50$). *Phys. Rev. B* **2010**, *82*, 054406. [CrossRef]
14. Parker, D.; Dupuis, V.; Ladieu, F.; Bouchaud, J.-P.; Dubois, E.; Perzynski, R.; Vincent, E. Spin glass behavior in an interacting γ-Fe_2O_3 nanoparticle system. *Phys. Rev. B* **2008**, *77*, 104428. [CrossRef]
15. Mørup, S.; Bødker, F.; Hendriksen, P.V.; Linderoth, S. Spin glass-like ordering of the magnetic moments of interacting nanosized maghemite particles. *Phys. Rev. B* **1995**, *52*, 287–294. [CrossRef]
16. De Toro, J.A.; Lee, S.S.; Salazar, D.; Cheong, J.L.; Normile, P.S.; Muñiz, P.; Riveiro, J.M.; Hillenkamp, M.; Tournus, F.; Tamion, A.; et al. A nanoparticle replica of the spin glass state. *Appl. Phys. Lett.* **2013**, *102*, 183104. [CrossRef]
17. Vasilakaki, M.; Margaris, G.; Peddis, D.; Mathieu, R.; Yaacoub, N.; Fiorani, D.; Trohidou, K. Monte Carlo study of the superspin glass behavior of interacting ultrasmall ferrimagnetic nanoparticles. *Phys. Rev. B* **2018**, *97*, 094413. [CrossRef]
18. Mørup, S.; Madsen, M.B.; Franck, J.; Villadsen, J.; Koch, C.J.W. A new interpretation of Mössbauer spectra of microcrystalline goethite: "Super-ferromagnetism" or "super-spin glass" behaviour? *J. Magn. Magn. Mater.* **1983**, *40*, 163–174. [CrossRef]
19. Bedanta, S.; Kleemann, W. Supermagnetism. *J. Phys. D: Appl. Phys.* **2009**, *42*, 013001. [CrossRef]
20. Andersson, M.S. Nanoparticle magnetism: Superspin glasses. *J. Nanosci. Nanotechnol.* **2019**, *19*, 4903–4910. [CrossRef]
21. Coey, J.M.D. Noncollinear spin arrangement in ultrafine ferrimagnetic crystallites. *Phys. Rev. Lett.* **1971**, *27*, 1140–1142. [CrossRef]

22. Aquino, R.; Depeyrot, J.; Sousa, M.H.; Tourinho, F.A.; Dubois, E.; Perzynski, R. Magnetization temperature dependence and freezing of surface spins in magnetic fluids based on ferrite nanoparticles. *Phys. Rev. B* **2005**, *72*, 184435. [CrossRef]
23. Kodama, R.H.; Berkowitz, A.E.; McNiff, E.J.; Foner, S. Surface spin disorder in $NiFe_2O_4$ nanoparticles. *Phys. Rev. Lett.* **1996**, *77*, 394–397. [CrossRef] [PubMed]
24. Martinez, B.; Obradors, X.; Balcells, L.; Rouanet, A.; Monty, C. Low temperature surface spin glass transition in γ-Fe_2O_3 nanoparticles. *Phys. Rev. Lett.* **1997**, *80*, 181–184. [CrossRef]
25. Peddis, D.; Cannas, C.; Piccaluga, G.; Agostinelli, E.; Fiorani, D. Spin glass-like freezing and enhanced magnetization in ultra-small $CoFe_2O_4$ nanoparticles. *Nanotechnology* **2010**, *21*, 125705. [CrossRef]
26. Kodama, R.H.; Makhlouf, S.A.; Berkowitz, A.E. Finite size effects in antiferromagnetic NiO nanoparticles. *Phys. Rev. Lett.* **1997**, *79*, 1393–1396. [CrossRef]
27. Winkler, E.; Zysler, R.D.; Vasquez Mansilla, M.; Fiorani, D. Surface anisotropy effects in NiO nanoparticles. *Phys. Rev. B* **2005**, *72*, 132409. [CrossRef]
28. Hernando, A.; Navarro, E.; Multigner, M.; Yavari, A.R.; Fiorani, D.; Rosenberg, M.; Filoti, G.; Caciuffo, R. Boundary spin disorder in nanocrystalline FeRh alloys. *Phys. Rev. B* **1998**, *58*, 5181–5184. [CrossRef]
29. Bonetti, E.; Del Bianco, L.; Fiorani, D.; Rinaldi, D.; Caciuffo, R.; Hernando, A. Disordered magnetism at the grain boundary of pure nanocrystalline Iron. *Phys. Rev. Lett.* **1999**, *83*, 2829–2832. [CrossRef]
30. Sefrioui, Z.; Menéndez, J.L.; Navarro, E.; Cebollada, A.; Briones, F.; Crespo, P.; Hernando, A. Correlation between magnetic and transport properties in nanocrystalline Fe thin films: A grain-boundary magnetic disorder effect. *Phys. Rev. B* **2001**, *64*, 224431. [CrossRef]
31. Del Bianco, L.; Fiorani, D.; Testa, A.M.; Bonetti, E.; Savini, L.; Signoretti, S. Magnetothermal behavior of nanoscale Fe/Fe-oxide granular system. *Phys. Rev. B* **2002**, *66*, 174418. [CrossRef]
32. Del Bianco, L.; Boscherini, F.; Fiorini, A.L.; Tamisari, M.; Spizzo, F.; Vittori Antisari, M.; Piscopiello, E. Exchange bias and structural disorder in the nanogranular Ni/NiO system produced by ball-milling and hydrogen reduction. *Phys. Rev. B* **2008**, *77*, 094408. [CrossRef]
33. Meiklejohnn, W.H.; Bean, C.P. New Magnetic Anisotropy. *Phys. Rev.* **1957**, *102*, 1413–1414. [CrossRef]
34. Nogues, J.; Schuller, I.K. Exchange bias. *J. Magn. Magn. Mater.* **1999**, *192*, 203–232. [CrossRef]
35. Fiorani, D.; Del Bianco, L.; Testa, A.M.; Trohidou, K.N. Glassy dynamics in the exchange bias properties of the iron /iron oxide nanogranular system. *Phys. Rev. B* **2006**, *73*, 092403. [CrossRef]
36. Del Bianco, L.; Spizzo, F.; Tamisari, M.; Castiglioni, A. Coexistence of exchange bias effect and giant magnetoresistance in a Ni/NiO nanogranular sample. *J. Appl. Phys.* **2011**, *110*, 043922. [CrossRef]
37. Del Bianco, L.; Spizzo, F.; Tamisari, M.; Calbucci, M.; Allia, P. Study of the magnetic microstructure of Ni/NiO nanogranular samples above the electric percolation threshold by magnetoresistance measurements. *J. Phys. Condens. Matter* **2012**, *24*, 306004. [CrossRef]
38. Cabreira-Gomes, R.; Silva, F.G.; Aquino, R.; Bonville, P.; Tourinho, F.A.; Perzynski, R.; Depeyrot, J. Exchange bias of $MnFe_2O_4$@γFe_2O_3 and $CoFe_2O_4$ @ γFe_2O_3 core/shell nanoparticles. *J. Magn. Magn. Mater.* **2014**, *368*, 409–414. [CrossRef]
39. He, X.; Xu, Y.; Yao, X.; Zhang, C.; Pu, Y.; Wang, X.; Mao, W.; Du, Y.; Zhong, W. Large exchange bias and enhanced coercivity in strongly-coupled Ni/NiO binary nanoparticles. *RSC Adv.* **2019**, *9*, 30195–30206. [CrossRef]
40. Fernández-García, M.P.; Gorria, P.; Blanco, J.A.; Fuertes, A.B.; Sevilla, M.; Boada, R.; Chaboy, J.; Schmool, D.; Grenèche, J.-M. Microstructure and magnetism of nanoparticles with γ-Fe core surrounded by α-Fe and iron oxide shells. *Phys. Rev. B* **2010**, *81*, 094418. [CrossRef]
41. Prejbeanu, I.L.; Kerekes, M.; Sousa, R.C.; Sibuet, H.; Redon, O.; Dieny, B.; Nozieres, J.P. Thermally assisted MRAM. *J. Phys. Condens. Matter* **2007**, *19*, 165218. [CrossRef]
42. Chappert, C.; Fert, A.; Van Dau, F.N. The emergence of spin electronics in data storage. *Nat. Mater.* **2007**, *6*, 813–823. [CrossRef] [PubMed]
43. Nogués, J.; Sort, J.; Langlais, V.; Skumryev, V.; Suriñach, S.; Muñoz, J.S.; Barò, M.D. Exchange bias in nanostructures. *Phys. Rep.* **2005**, *422*, 65–117. [CrossRef]
44. Takano, K.; Kodama, R.H.; Berkowitz, A.E.; Cao, W.; Thomas, G. Interfacial uncompensated antiferromagnetic spins: Role in unidirectional anisotropy in polycrystalline $Ni_{81}Fe_{19}$/CoO bilayers. *Phys. Rev. Lett.* **1997**, *79*, 1130–1133. [CrossRef]

45. Baltz, V.; Rodmacq, B.; Zarefy, A.; Lechevallier, L.; Dieny, B. Bimodal distribution of blocking temperature in exchange-biased ferromagnetic/antiferromagnetic bilayers. *Phys. Rev. B* **2010**, *81*, 052404. [CrossRef]
46. Spizzo, F.; Tamisari, M.; Bonfiglioli, E.; Del Bianco, L. Detection of the dynamic magnetic behaviour of the antiferromagnet in exchange-coupled NiFe/IrMn bilayers. *J. Phys. Condens. Matter* **2013**, *25*, 386001.
47. O'Grady, K.; Fernandez-Outon, L.E.; Vallejo-Fernandez, G. A new paradigm for exchange bias in polycrystalline thin films. *J. Magn. Magn. Mater.* **2010**, *322*, 883–899. [CrossRef]
48. Yu, T.; Chen, Q.L.P.; Zhou, L.; Li, H.; Ning, X.; Qiu, C.; He, H. Interfacial spin glass-like state and exchange bias in epitaxial iridate-manganite heterostructure. *J. Alloys Compd.* **2019**, *789*, 351–356. [CrossRef]
49. Gruyters, M. Interacting magnetic defects in a random antiferromagnetic matrix: A spin glass-like model of exchange bias. *Phys. Rev. B* **2009**, *79*, 134415. [CrossRef]
50. Spizzo, F.; Bonfiglioli, E.; Tamisari, M.; Gerardino, A.; Barucca, G.; Notargiacomo, A.; Chinni, F.; Del Bianco, L. Magnetic exchange coupling in IrMn/NiFe nanostructures: From the continuous film to dot arrays. *Phys. Rev. B.* **2015**, *91*, 064410. [CrossRef]
51. Spizzo, F.; Tamisari, M.; Chinni, F.; Bonfiglioli, E.; Gerardino, A.; Barucca, G.; Bisero, D.; Fin, S.; Del Bianco, L. Exchange bias properties of 140nm-sized dipolarly interacting circular dots with ultrafine IrMn and NiFe layers. *J. Magn. Magn. Mater.* **2016**, *400*, 242–247. [CrossRef]
52. Spizzo, F.; Tamisari, M.; Chinni, F.; Bonfiglioli, E.; Del Bianco, L. Interface adjustment and exchange coupling in the IrMn/NiFe system. *J. Magn. Magn. Mater.* **2017**, *421*, 234–240. [CrossRef]
53. Fievet, F.; Lagier, J.; Blin, B.; Beaudoin, B.; Figlarz, M. Homogeneous and heterogeneous nucleations in the polyol process for the preparation of micron and submicron size metal particles. *Solid State Ion.* **1989**, *32/33*, 198–205. [CrossRef]
54. Gatan Microscopy Suite Software Version 3.x. Available online: www.gatan.com/products/tem-analysis/gatan-microscopy-suite-software (accessed on 28 October 2019).
55. Trudel, S. Unexpected magnetism in gold nanostructures: Making gold even more attractive. *Gold Bull.* **2011**, *44*, 3–13. [CrossRef]
56. Fiorani, D.; Testa, A.M.; Lucari, F.; D'Orazio, F.; Romero, H. Magnetic properties of maghemite nanoparticle systems: Surface anisotropy and interparticle interaction effects. *Phys. B* **2002**, *320*, 122–126. [CrossRef]
57. Del Bianco, L.; Spizzo, F.; Barucca, G.; Ruggiero, M.R.; Geninatti Crich, S.; Forzan, M.; Sieni, E.; Sgarbossa, P. Mechanism of magnetic heating in Mn-doped magnetite nanoparticles and role of the intertwined structural and magnetic properties. *Nanoscale* **2019**, *11*, 10896–10910. [CrossRef]
58. Fearon, M.; Chantrell, R.W.; Wohlfarth, E.P. A theoretical study of interaction effects on the remanence curves of particulate dispersions. *J. Magn. Magn. Mater.* **1990**, *86*, 197–206. [CrossRef]
59. Morales, M.P.; Serna, C.J.; Bødker, F.; Mørup, S. Spin canting due to structural disorder in maghemite. *J. Phys. Condens. Matter* **1997**, *9*, 5461–5467. [CrossRef]
60. Spizzo, F.; Sgarbossa, P.; Sieni, E.; Semenzato, A.; Dughiero, F.; Forzan, M.; Bertani, R.; Del Bianco, L. Synthesis of ferrofluids made of iron oxide nanoflowers: Interplay between carrier fluid and magnetic properties. *Nanomaterials* **2017**, *7*, 373. [CrossRef]
61. Kim, W.; Suh, C.Y.; Cho, S.W.; Roh, K.M.; Kwon, H.; Song, K.; Shon, I.J. A new method for the identification and quantification of magnetite-maghemite mixture using conventional X-ray diffraction technique. *Talanta* **2012**, *94*, 348–352. [CrossRef]
62. Jonsson, T.; Mattsson, J.; Djurberg, C.; Khan, F.A.; Nordblad, P.; Svedlindh, P. Aging in a magnetic particle system. *Phys. Rev. Lett.* **1995**, *75*, 4138–4141. [CrossRef]
63. Djurberg, C.; Svedlindh, P.; Nordblad, P.; Hansen, M.F.; Bødker, F.; Mørup, S. Dynamics of an interacting particle system: Evidence of critical slowing down. *Phys. Rev. Lett.* **1997**, *79*, 5154–5157. [CrossRef]
64. Del Bianco, L.; Lesci, I.G.; Fracasso, G.; Barucca, G.; Spizzo, F.; Tamisari, M.; Scotti, R.; Ciocca, L. Synthesis of nanogranular Fe_3O_4/biomimetic hydroxyapatite for potential applications in nanomedicine: Structural and magnetic characterization. *Mater. Res. Express* **2015**, *2*, 065002. [CrossRef]
65. de Almeida, J.R.L.; Thouless, D.J. Stability of the Sherrington-Kirkpatrick solution of a spin glass model. *J. Phys. A* **1978**, *11*, 983–990. [CrossRef]
66. Maletta, H.; Zinn, W. Spin glasses. In *Handbook on the Physics and Chemistry of Rare Earths*; Gschneidner, K.A., Jr., Eyring, L., Eds.; Elsevier Science Publishers, B.V.: Amsterdam, The Netherlands, 1989; Volume 12, pp. 213–356.
67. Del Bianco, L.; Spizzo, F.; Tamisari, M.; Laureti, S. Dependence of exchange bias on the field-cooled remanent magnetic state in Ni/NiO nanogranular samples. *Solid State Commun.* **2011**, *151*, 351–353. [CrossRef]

68. Monod, P.; Préjean, J.J.; Tissier, B. Magnetic hysteresis of CuMn in the spin glass state. *J. Appl. Phys.* **1979**, *50*, 7324–7329. [CrossRef]
69. Petracic, O.; Chen, X.; Bedanta, S.; Kleemann, W.; Sahoo, S.; Cardoso, S.; Freitas, P.P. Collective states of interacting ferromagnetic nanoparticles. *J. Magn. Magn. Mater.* **2006**, *300*, 192–197. [CrossRef]
70. Sasaki, M.; Jönsson, P.E.; Takayama, H.; Mamiya, H. Aging and memory effects in superparamagnets and superspin glasses. *Phys. Rev. B* **2005**, *71*, 104405. [CrossRef]
71. Coey, J.M.D. *Magnetism and Magnetic Materials*; Cambridge University Press: Cambridge, UK, 2010; pp. 161–167.

materials

MDPI

Article

Structural and Optical Characteristics of Highly UV-Blue Luminescent ZnNiO Nanoparticles Prepared by Sol–Gel Method

Ashraf H. Farha [1,2], Abdullah F. Al Naim [1], Javed Mazher [1,*], Olfa Nasr [1] and Mohamed Helmi Hadj Alouane [1]

[1] Department of Physics, College of Science, King Faisal University, P.O. Box: 400, Al-Ahsa 31982, Saudi Arabia; afarha@kfu.edu.sa (A.H.F.); anaim2@kfu.edu.sa (A.F.A.N.); onasr@kfu.edu.sa (O.N.); malouane@kfu.edu.sa (M.H.H.A.)

[2] Semiconductors Technology Lab, Physics Department, Faculty of Science, Ain Shams University, 11566 Cairo, Egypt

* Correspondence: jkhan@kfu.edu.sa

Received: 17 December 2019; Accepted: 9 February 2020; Published: 15 February 2020

Abstract: A simple single pot sol–gel method is used to prepare ZnNiO nanoparticles at assorted Ni doping levels, 1, 3, 7 and 10 wt.%. Structural and optical properties of nanoparticles are studied by X-ray diffraction (XRD), UV–visible diffuse reflection spectroscopy (DRS), photoluminescence (PL) measurements, scanning electron microscopy (SEM), μ-Raman and X-ray photoelectron-spectroscopy (XPS). A single substitutional solid solution phase is detected in the wurtzite ZnNiO nanoparticles at various doping levels. XRD peak splitting and shifting is ascribed to reduced wurtzite character and presence of crystalline strain in nanoparticles at higher level of Ni doping. The Kubelka-Munk function of DRS data reveals the presence of the Burstein-Moss effect in the optical absorption of ZnNiO nanoparticles. Photoluminescence studies show intense UV-blue emission from ZnNiO nanoparticles. The UV PL also exhibits the Burstein-Moss blue shift in the ZnNiO luminescence. Raman analyses also confirms the wurtzite structure of ZnNiO nanoparticles; however, crystal structural defects and bond stiffness increase with Ni doping. The optical and structural studies presented in this work are pointing towards a multivalent Ni substitution in the nanoparticles.

Keywords: nanoparticles; sol-gel; Raman spectroscopy; UV-blue photoluminescence; ZnNiO; Kubelka-Munk function; Burstein-Moss shift; substitutional doping

---

1. Introduction:

The presence of intense luminescence in diluted magnetic semiconductor (DMS) materials has been a focus of current research interest owing to potential applications in spin-based all-optical switching, opto-spintronics and opto-spin-based computation [1–6]. Fabrication of miniaturized smart devices requires both better optoelectronic and magneto-opto-electronic efficiencies through better incorporation of dopant in nanocrystalline ZnO-based DMS systems [7–11]. The metal (TM) atom incorporation achieved from Ni doping materials in the ZnO lattice has been shown to improvise the integration of both semiconducting and magnetic properties for efficient opto-spintronics applications [12–16]. The success of TM ion doping in ZnO has been evident from observations of room temperature ferromagnetic (FM) ordering in ZnO and Fe atom induced bandgap tuning proved from the diffused reflectance spectroscopy of ZnFeO nanocrystals [17,18]. Moreover, novel phenomena such as poloronic magneto-resistance (MR), superior surface catalysis and super-capacitive behaviors, thermal activation of carriers, and lowering of electrical resistance are also expected in the ZnNiO systems [19–22].

It is crucial to better understand the mechanisms of incorporation of TM dopant in the host lattice because opto-electronic and magneto-electronic properties significantly depend on the synthesis methods used in preparation of TM doped ZnO nanoparticles [14,18,23]. Jlassi et al. estimated that up to 2% Ni incorporation in ZnO prepared by spray pyrolysis technique can increase n-type carriers through O-vacancy defects [20]. Meanwhile, the free carriers are less likely generated in the sol–gel prepared ZnNiO due to large presence of interstitial Ni ions [24]. However, the single-pot sol–gel synthesis of ZnNiO nanoparticles can give different results due to simultaneous formation of cationic sub-lattice and higher photoluminescence yield can be expected due to presence of higher carrier concentrations [8].

A successful incorporation of Ni dopant in the nanocrystalline ZnO particles can also make them deployable in varisters, as battery electrode, as oxidative catalytic thin-films, super-capacitor electrodes, and so on [25–28]. Additional synthesis-dependent variables, such as the level of oxygen vacancies and higher dopant-to-dopant near-neighbor interactions, also play a significant role in the enhancement of optoelectronic and opto-spintronic properties of TM doped metal oxides [13,18,29–31]. A steep decrease in ferromagnetic behavior of ZnNiO was observed on increasing the Ni concentrations beyond 15% due to anti-ferromagnetic (AFM) ordering of Ni^{2+} ions [17,31].

On a similar note, Ni doping also brings significant changes in the ZnO's crystal symmetry, local chemical environments and charge transfer mechanisms in addition to disorder and local polarizability, which are correspondingly proved from the XPS studies and the Raman scattering analysis [32,33]. Russo et al., using Raman analysis, successfully predicted presence of local structural strain in doped ZnO nanoparticles [34]. Similarly, oxidation states of the as-incorporated Ni atom in ZnO host affect carrier density, mobility and opto-spintronic transport processes. [35,36]. The XPS studies show that Ni^{2+} ion replaces Zn^{2+} ion in the ZnO cationic sub-lattice [35,37]. Ni ions' incorporation in ZnO nanoparticles can produce large amounts of surface defects on the nanoparticle surface resulting in the band gap tuning [33]. Fabbiyola et al. found that ≈5–20% Ni concentration reduces ZnO nanoparticles' size, causing a blue shift in the energy gap observed using optical absorption derived from the Kubelka-Mulk's function of DRS data [19].

Nevertheless, the functional aspects of doped ZnO ternaries, especially optoelectronic and spintronic properties, depend not only on the type of synthesis method used but also on level of control over dopant substitution in host-lattice [20,35,37–39]. It is very important to check the oxidation states of the dopants incorporated in the host lattice to study the doping effects on the carrier density, mobility and other transport and optical properties [40]. Oxidation states of the dopant may vary depending on precursor composition, synthesis method, and annealing treatments [37]. Consequently, different synthesis methods may give contradictory trends of free carrier concentration. Despite many reports being available on TM atom doped ZnO powders, most of them fail to properly describe the effects of dopant oxidation states on optical and structural changes [41]. Here, we attempt to investigate the effects of Ni doping on optical and structural properties of ZnNiO nanoparticles.

In this report, we present a simpler method of ZnNiO nanoparticles synthesis using a single pot sol–gel technique. Our choice of the Ni doping range is based on an observable optical absorption shift owing to expected doping induced band structure modifications. It has been reported that significant optical and structural variations are possible in ZnNiO nano-powders prepared by solid-state reaction technique at 0%, 3%, 5%, 7% and 10% Ni doping levels [29]. Similarly, changes in optical processes in ZnNiO nanoparticles have also been reported for Ni concentration in the range of 5%–20% [19]. In this report, effects of dopant substitution are studied in respect to variations of structural, morphological and optical traits of ZnNiO nanoparticles. Any enhancement in the UV-blue emission from ZnNiO nanoparticles can bring a new functionality among the ZnO-based DMS materials. It would be interesting to see the effects of Ni doping on the wurtzite symmetry of ZnNiO nanoparticles or presence of any doping induced crystalline phase transformations. Moreover, the knowledge of chemical states of dopant in the host lattice would be imperative in determining the mechanism of optical processes such as Burstein-Moss shift vis-à-vis Ni doping percentage.

2. Experimental Details

2.1. Synthesis of ZnNiO Nanoparticles

ZnNiO nanoparticles are prepared by single-pot sol–gel method, in which precursors like Nickel (II) nitrate hexahydrate (Sigma-Aldrich, USA, 99.5% purity) and Zinc (II) acetate dihydrate (Sigma-Aldrich, USA, 99.8% purity) are mixed in assorted molar ratios of Ni source, 1%, 3%, 7% and 10%. Isopropyl alcohol (Sigma-Aldrich, 99.5% purity), is used as a solvent in the bath reactor. An aqueous stock solution of zinc precursor (0.5 M), 3.5 g of $Zn(II)\cdot(CH_3COO)_2\cdot 2H_2O$ powder, is first dissolved in 32 mL of isopropyl alcohol to initiate the hydrolysis. Then assorted weights, 0.047 g, 0.14 g, 0.33 g and 0.47 g of Ni precursor, $Ni(II)\cdot(NO_3).6H_2O$, are correspondingly added to the respective Zn stock solutions and the mixtures are stirred for 10 min at room temperature. Furthermore, a suitable rate of hydrolysis is achieved by alkalization with drop-wisely addition of 1.3 mL of mono ethanolamine (MEA) in the solution. Throughout the ZnNiO synthesis, the molar ratio between isopropyl alcohol, zinc precursor and MEA is kept constant ≈200:10:1. Afterwards, the temperature of the solution is raised to 60 °C with continuous stirring for 2 h to complete the alcoholic condensation reaction, and finally a gel is obtained in the form of a fine white colored powder. The obtained gel is dried for 1 h at 250 °C temperature in the oven leading to water and alcohol evaporation and subsequently calcined in air at 600 °C for 5 h. For the assorted weight percentages of Ni, 1% to 10%, different colors of ZnNiO powders are obtained ranging from off-white to grayish-white with respect to increasing Ni concentration.

2.2. Characterization of ZnNiO Nanoparticles

XRD technique is employed for structure examination of as-prepared ZnNiO in powder form. Powder X-ray diffractometer (Ultima-4, Rigaku, Japan) is used for XRD analysis of powdered samples. XRD measurements are obtained in a 2θ range from 20°–80° using CuK_α (λ = 1.5406 Å) radiation source. Evaluation of microstructure and morphology of ZnNiO powders is performed using high-resolution scanning electron microscope (JSM-7600F, Jeol, Japan) and recorded at 100,000× and 25,000× scan magnifications. XPS technique is used to quantitatively probe chemical species and oxidation states. Mg-kα radiation (1253.6 eV) radiation source is used in XPS instrument (ESCA-II, Omicron, Germany) to record spectra at 0.05 eV spectral resolution and at 50-μm X-ray beam spot-size. Raman Spectroscopy, a useful method for understanding lattice vibration energies, is used to study characteristic and disorder phonons present in nanoparticles. Raman spectra are recorded in confocal Raman microscope (Horiba spectrometer, Labram HR Evolution, France) at ultra-low frequency compatible scans in 50 to 800 cm^{-1} range using the 633 nm He-Ne laser excitation source. Diffusion reflectance spectroscopy is performed in spectral range of 190-1100nm at ±0.5 nm spectral accuracy using the UV-Vis spectrometer (UV1800, Shimadzu, Japan). The DRS data is collected on pelleted ZnNiO powders hydraulically pressed at 3.5-tons pressure. Photoluminescence (PL) measurements are also performed in the Horiba Labram PL spectrophotometer using 325 nm He-Cd laser excitation source.

3. Results and Discussion

XRD patterns of ZnNiO powders are shown in Figure 1a. For the sake of clarity, a vertical offset of XRD patterns with Ni doping is shown in the figure. All samples exhibit characteristic ZnO peaks at (100), (200) and (101) XRD reflections confirming the wurtzite structure of ZnNiO. Additionally, the sharper and more intense nature of XRD peaks at lower Ni concentrations indicates a strong wurtzite character of ZnNiO nanoparticles. However, on further doping, the XRD peaks become broader and less intense, indicating decay in the wurtzite character. Nonetheless, the wurtzite structure remains a dominant phase, during compositional variation of ZnNiO nanoparticles, indicating a substitutional solid solution formation. Furthermore, absence of any new XRD peaks on Ni doping implies absence of secondary structural phases. Nevertheless, upon careful examination of the XRD patterns, the XRD peaks are found to be dividing into a doublet peak structure; a smaller XRD peak originates nearby each major XRD peak, reflecting a systematic development of structural changes in ZnNiO at higher

Ni doping. The observation is further clarified from the XRD peak profiles of 101-reflections plotted in Figure 1b, which clearly show shifted and less intense peaks, reflecting a decay in the wurtzite nature of ZnNiO. The (101)-peak becomes a clear doublet peak at 10% Ni content, $\Delta 2\theta \approx 0.61$ for ZnNiO-10, apparently indicating reduction in wurtzite symmetry or a weaker lattice strain induced zinc-blende symmetry at higher doping. The nano phase ZnNiO has already been reported to grow in both wurtzite and zinc-blende metastable phases owing to similarity in their anionic coordination [17]. During the doublet development on doping, as shown in Figure 1b, the lower peak at $2\theta \approx 35.5°$ can best be attributed to a weaker zinc-Blend symmetry of ZnNiO nanoparticles. Herewith, we reject the possibility of any secondary oxide phase formation on doping in the light of absence of NiO's XRD peaks. It should be noted that NiO crystals typically adopt hexoctahedral cubic system (XRD card number: RRUFFID-R080121 [42]) and a major XRD reflection of NiO (111) is positioned at $2\theta \approx 37.45$. The XRD peaks related to NiO cubic phase are completely absent in the ZnNiO XRD patterns at all doping levels implying absence of new phases. Moreover, the XRD peak shift value of $\Delta 2\theta$ in the present studies can be best ascribed either to uniform crystalline strains present in ZnNiO lattice as a result of ionic radii mismatch between Zn^{2+} (0.74 Å) and Ni^{2+} ions (0.69 Å) or to reduced symmetry defects in the crystal structure [20]. The results of the observed crystalline strain behavior in ZnNiO nanocrystals are also summarized in Table 1. Typically, the strain increases in ZnNiO nanoparticles with increasing Ni, and its behavior agrees very well with the increase in unit cell volume.

Table 1. Summary of structural properties present in the assorted samples ZnNiO powders calculated by XRD data fitting. Columns from left represent Ni content (weight percentage), average crystallite size (D) in nanometers (nm), lattice constants (a, c) and their ratio (c/a), bulk strain (Δd/d) present in ZnNiO nanoparticles and their unit cell volume (V).

Doping-Percent	D, nm	a, Å	c, Å	c/a	Strain	V, Å^3
1%	29.8 ± 1.57	3.23 ± 0.01	5.22 ± 0.01	1.600 ± 0.01	0.19	47.99
3%	32.2 ± 2.41	3.23 ± 0.01	5.21 ± 0.01	1.597 ± 0.01	0.01	47.88
7%	18.1 ± 1.37	3.28 ± 0.02	5.22 ± 0.02	1.594 ± 0.01	0.36	48.57
10%	14.1 ± 0.80	3.30 ± 0.02	5.24 ± 0.04	1.586 ± 0.02	0.68	49.54

Crystallite size (D) for nanoparticles in spherical approximation can be easily calculated by measuring the (101)-peak broadening (β) and applying Scherrer's formula, $D = K/\beta$, where constant K depends on the x-ray source and θ-position of the peak used [43]. The Scherrer's particle sizes for ZnNiO nanoparticles are summarized in Table 1. ZnNiO particle sizes were found to systematically decrease from 32 to 14 nm with increasing Ni concentration, as shown in the table. The lower nanoparticle size at higher Ni doping also indicates higher doping related defects affecting the growth of crystallites. Lattice parameters and unit cell volume of ZnNiO were also found to be increasing with Ni content in nanoparticles, as shown in Table 1. Change in the unit cell volume can also be ascribed to the presence of uniform crystalline strain and difference in the ionic radii of the substituted Ni ions in comparison to Zn^{2+} cations [43].

Electron microscopic images of ZnNiO nanoparticles with different Ni ion concentrations are shown in Figures 2 and 3 at 25,000× and 100,000× magnifications, respectively. In the wider area scan of Figure 2, a surface morphology consisting of nanoparticles is distinctively apparent within the rounded shaped regions of larger agglomerations. Moreover, uniformly distributed nanoparticulate morphology is also obvious among all the sol–gel prepared ZnNiO powders. The clusters are characteristically formed in comparable sizes and shapes, which confirms a uniform sol–gel procedure is adopted during the ZnNiO syntheses. SEM images for ZnNiO samples with higher magnification scanning are shown in Figure 3, depicting a granular morphology of nanoparticles. The grains are seemingly hexagonally faceted, indicating conservation of wurtzite structure of ZnNiO during Ni doping. Sharply hexagonally faceted grains can even be observed for nanoparticles at 3% and 7% Ni doping percentages. The higher magnification electron microscopy confirms the identical nature of as-formed grain sizes, along with uniform size distributions among all samples. Comparatively higher porosity and intragranular spacing is observed in the granular morphology of ZnNiO with lower Ni content—1%. On increasing Ni content in remaining ZnNiO samples, the particle sizes remain constant at ≈52 nm; nonetheless, the morphological compactness increases along with reduction in the intragranular voids.

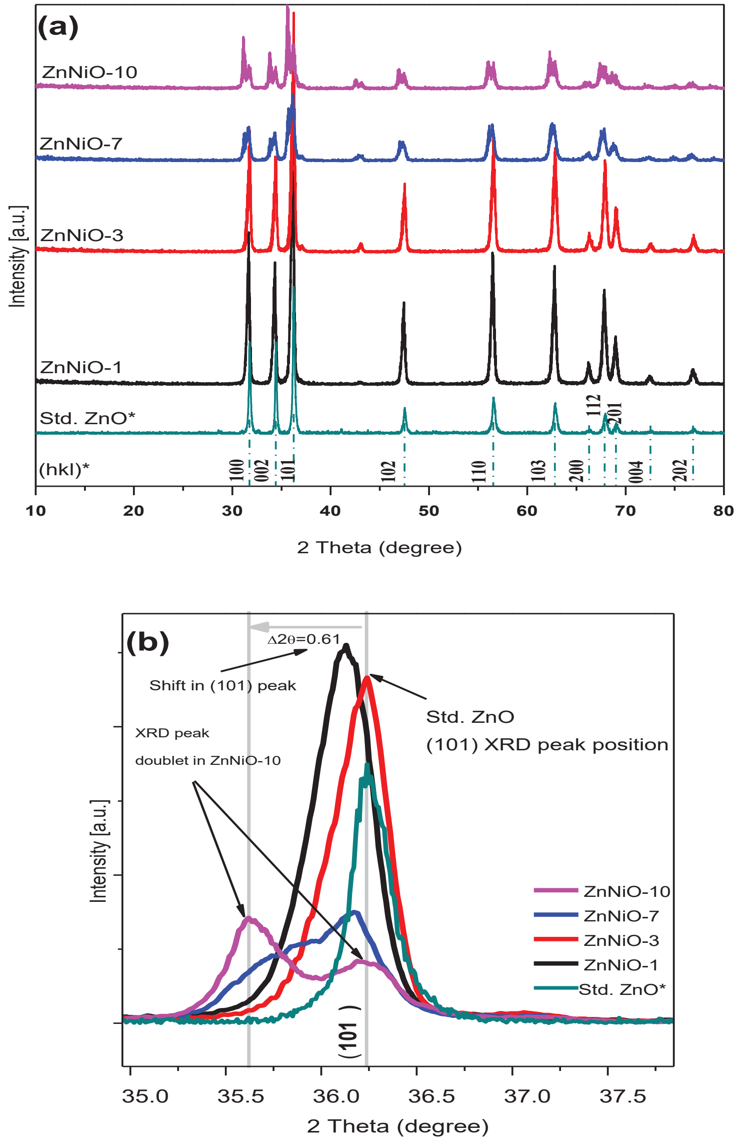

Figure 1. (**a**) XRD patterns of ZnNiO nanoparticles are presented in vertically aligned mode in increasing doping percentages. The Ni doping increases in samples ZnNiO-1, -3, -7 and -10. Asterix sign (*) shows the standard ZnO's XRD pattern and its (hkl) reflection positions as adopted from the XRD card, RRUFFID-R050492. (**b**) shows (101) -peak profiles of most intense XRD reflection in ZnNiO indicating a 2θ shift upon doping and a gradual development of 101-doublet peaks.

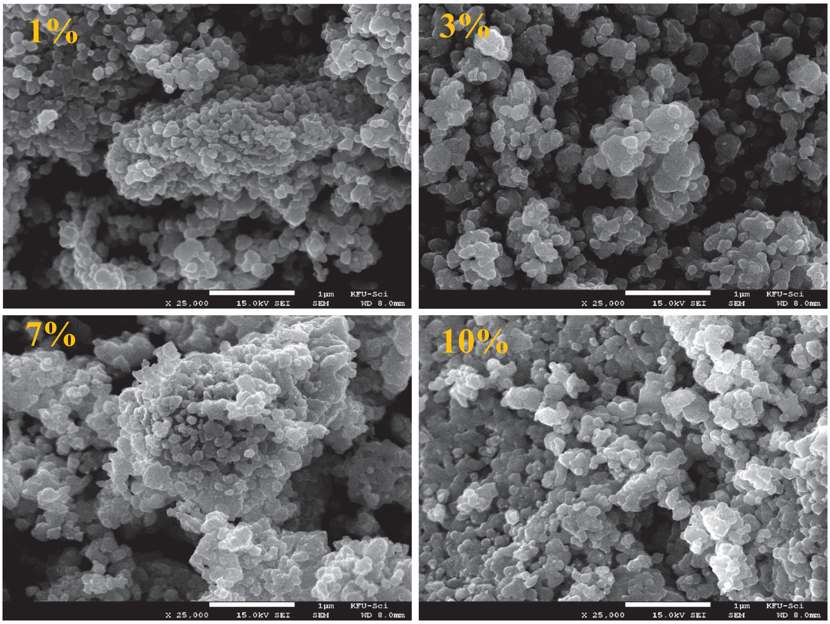

Figure 2. SEM images recorded at 25,000× magnification showing surface morphology of ZnNiO powders at 1%, 3%, 7% and 10% Ni doping percentages. The white colored bar-scale in the bottom of each image represents 1 µm.

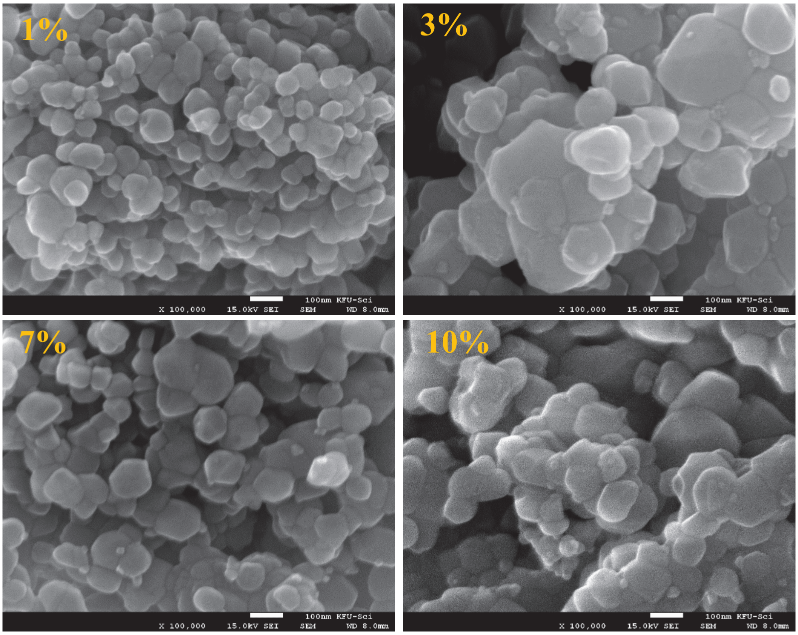

Figure 3. SEM images recorded at higher magnifications (100,000×) showing the granular morphology of ZnNiO powders at 1%, 3%, 7% and 10% doping percentages. The white colored bar-scale in the bottom of each image represents 100 nm.

Optical absorption properties and electronic bandgap are determined using a straight-line fit on Kubelka-Munk function calculated from the diffused reflectance data. The DRS data, as shown in Figure 4a, is plotted in the UV-Vis range for ZnNiO nanoparticles with vertically decreasing Ni concentration. The DR values recorded at different compositions of ZnNiO show a rapid decrease at wavelengths lower than 400 nm. The observed reflectance feature is the most common feature among ZnNiO nanoparticles in UV light range due to fundamental absorption onset involving opto-electronic transition from valance band (VB) to conduction band (CB) [1,44]. In general, the optical reflectivity gradually decreases with Ni doping owing to an upsurge in the dopant related internal light scattering events [19]. Indeed, the Ni doping-induced increase in bond-polarizability in ZnNiO can also lead to higher internal light scattering and low DRS intensity [45,46].

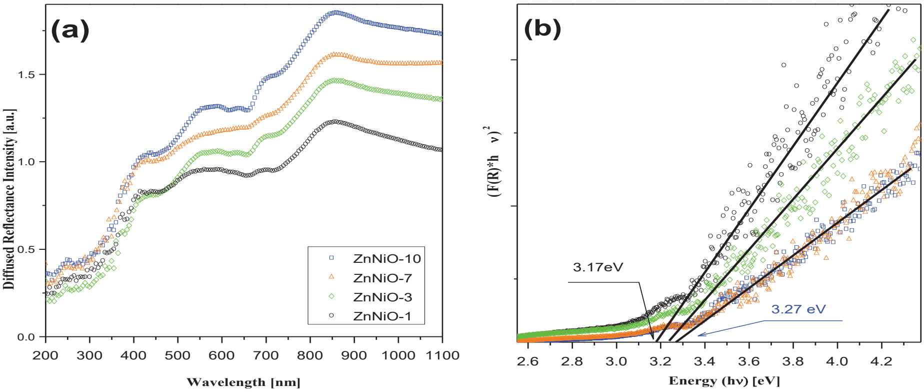

Figure 4. (**a**) The UV-VIS diffuse reflectance spectra for ZnNiO pellets are vertically stacked and plotted in the increasing Ni doping order. The doping percentages in samples, ZnNiO-1, -3, -7 and -10%, are correspondingly plotted in black, green, red and blue colored spectral lines. (**b**) Kubelka-Munk fittings of the DRS are plotted in the right-hand side figure.

The Kubelka-Munk (KM) function, $F(R) = \frac{K}{S} = (1-R)^2/2R$; where K, S and R denote absorption, scattering and reflection coefficients, respectively, is a direct measure of the absorbance from the sample's reflectivity data. The KM function of the diffused reflection spectrum can be used in the calculation of electronic bandgap using the onset of the fundamental absorption edge [47]. The function [(F(R)×hν]^2, which is a direct measure of the absorbance in the material, is plotted with respect to the photon energy (hν, eV) in Figure 4b. A straight-line fit is performed in a linear region of the KM function and extrapolated to baseline absorbance on the hν-axis to find the Tauc's optical bandgap, as shown in the figure. A slightly blue-shifted bandgap ($\Delta \approx 0.1$ eV) is observed in ZnNiO-7 and -10 samples in comparison to the ZnNiO-1 and -3 samples. The bandgaps in the latter two samples with lower Ni concentrations are closer to the reported band gap (~3.1 eV) of standard ZnO [20]. A small blue shift of ~0.1 eV observed with Ni doping is understandably not related to quantum size confinement effects owing to non-variance of ZnNiO particle sizes during Ni doping. Fabbiyola et al., have attributed enhancements in the KM function in ZnNiO to Ni doping due to the formation of surface states which significantly increase the optical absorption [19]. However, we believe the increased $F(R)$ in this study is due to doping induced Burstein-Moss effect. In comparison to bivalent dopant (Ni^{2+}) substitution, the trivalent dopant (Ni^{3+}) substitution in the ZnO lattice replacing the divalent Zn^{2+} has been reported to provide an additional electron for conduction [47]. The Ni atom donating electrons to the conduction band suggestively increase the Fermi level and itinerant related absorption toward the higher energy [48]. Moreover, the KM function value in the UV-blue region is typically higher for ZnNiO with higher Ni doping, and that also indicates an increase in the overall number of optical absorption processes. Furthermore, the Ni doping-related increase in ZnNiO bandgap has also been ascribed to increase in excitonic density and excitonic mediated optical transitions resulting in highly diffused nature of DRS [49].

A possible mechanism of the Burstein-Moss-mediated optical absorption process is depicted in Figure 5 (right), illustrating itinerant related optical absorption and electron transfer from the trivalent dopant (Ni^{3+}) to the conduction band (CB) resulting in upshifting of the Fermi-level. Our XPS studies, which are discussed later in the manuscript, also indicate presence of trivalent Ni doping. Thus, the trivalent substitution of Ni atom in the inherently divalent cationic sub-lattice of Zn^{2+} ions could give electron donating character to nickel atom resulting in the higher carrier concentration effectively lifting the Fermi energy position in the band structure. While the electron transfer is proscribed in the divalent Ni substitution, as shown in Figure 5 (left).

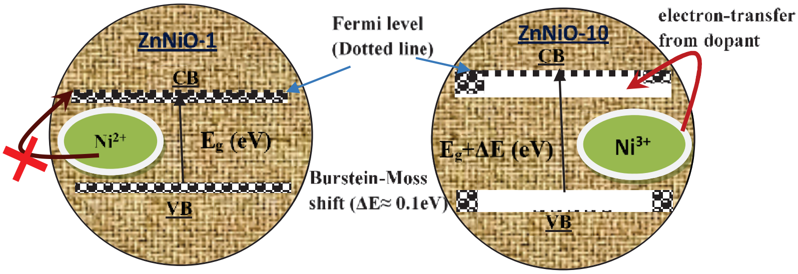

Figure 5. Optical transition processes taking place differently in ZnNiO nanoparticles with 1% and 10% Ni doping levels. Higher Kubelka-Munk function values F(R) are expected in UV-blue region for the optical transition shown in right-side schematic of the figure.

To study the intrinsic and extrinsic defects, photoluminescence (PL) spectroscopy was carried out. Figure 6 shows room temperature PL spectra of ZnNiO nanoparticles excited at 325 nm. It can be seen from the pure ZnO (reference sample) that the PL spectra are mainly comprised of UV emission peaks at 3.34 eV (370 nm) followed by a high-intensity broad visible band with multiple sub-peaks in the range of 2.1–2.75 eV (450–590 nm). The UV emission is attributed to the recombination of free excitons in the near band edge (NBE) of ZnO, whereas the visible band is generally interpreted as the reason for the defects [8,50–53]. Meanwhile, the origins of different visible emissions are still not fully assumed and different controversial hypotheses have been offered [8,50–53]. In our case, the emission features at 2.43 eV (510 nm) and 2.21 eV (560 nm) are related to antisite oxide (OZn) and to transmission from conduction band to vacancy, respectively.

It is shown in Figure 6a that with Ni incorporation, the UV emission intensity typically increases and is shifted to the higher energy, while the intensities of the visible peaks decreases. The results show that Ni doping increases the electron concentration, and that there is a concomitant decrease in the OZn and vacancy defects. On the other hand, additional broad band emissions start becoming apparent at low energy (1.8–2.2 eV) in ZnNiO samples. The broad band is deconvoluted for two different peaks, as shown in Figure 6b. The emission peak at 2.04 eV (607 nm) corresponds to Ni-related defects, and the peaks at 2.13 eV (582 nm) correspond to donor–acceptor pair recombination [52]. For more details, Figure 6c shows changes in the integrated PL intensity of the UV band (I_{UV}), the wide defect-related band (I_{def}) and the relative PL peak intensities ratio R (I_{UV}/I_{def}). From our PL observation, it is evident that Ni doping results in enhancement of luminescence arising in the UV band. Meanwhile, the wide defect-related band decreases in comparison to that of the pure ZnO luminescence, as observed in the same plot. Furthermore, the intensity ratio R increases with increasing Ni content and gets saturated at 7% and 10% Ni concentration, showing higher enhancement of UV emission. It is interesting to note that the UV emission is also blue-shifted when the Ni concentration increases from 1% to 10% due to the Burstein-Moss effect [8]. The electron-doped ZnNiO with a high concentration of n-type states populated within the conduction band moves the Fermi level to higher energies. The filling of the conduction band by electrons will generally result in a blue shift [8].

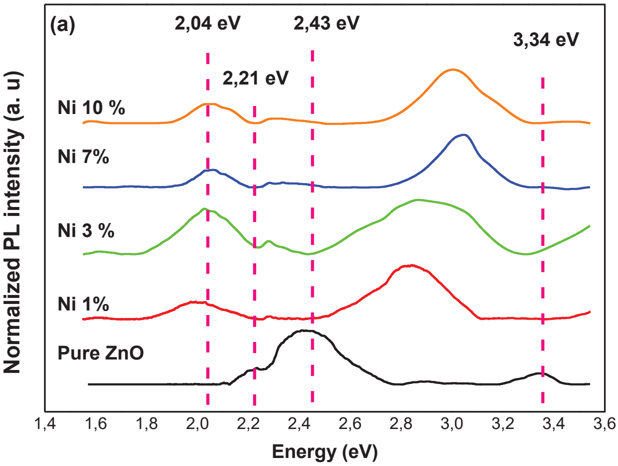

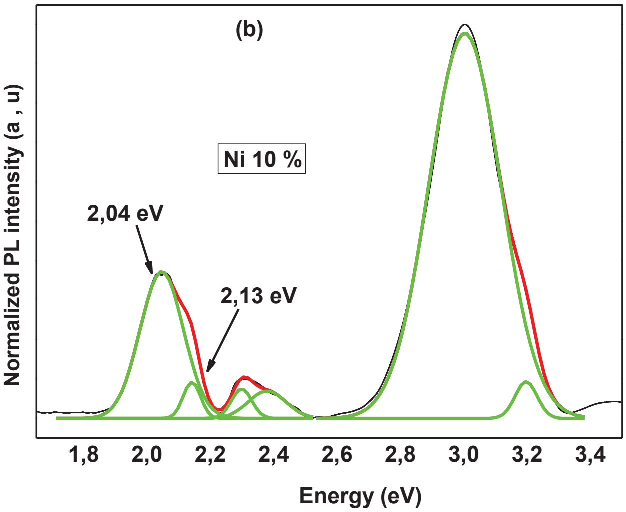

Figure 6. *Cont.*

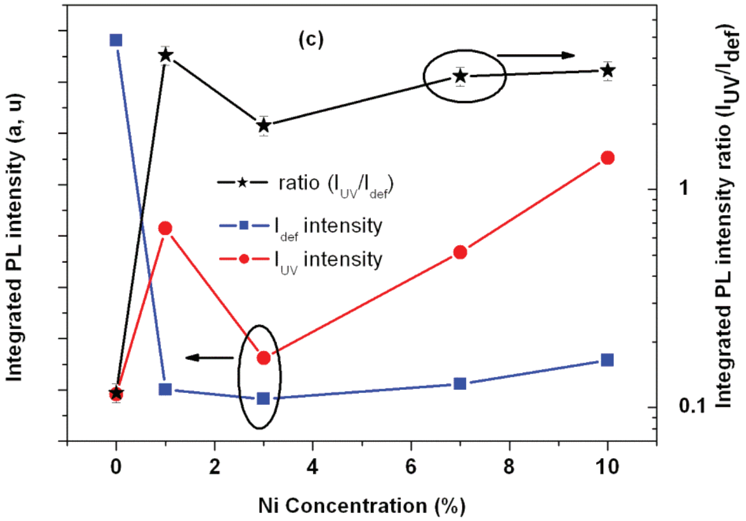

Figure 6. (**a**) Room temperature PL spectra of ZnNiO nanoparticles. (**b**) PL spectra of 10% ZnNiO along with the Gaussian fit. Luminescence arising from the pure bulk ZnO is shown as a reference. (**c**) Integrated PL intensity of the UV band (I_{UV}), the wide defect related band (I_{def}) and relative PL peak intensities ratio R (I_{UV}/I_{def}) vs Ni concentration.

Raman analysis is very useful for finding Ni^{2+} doping-related changes in ZnNiO crystalline structure, such as the formation of structural disorders, presence of vacancies, or defects in host lattice [32,33]. The host ZnO has a wurtzite structure belonging to P63mc space group symmetry [54]. Eight active normal vibrational modes are present in the wurtzite ZnO comprising of two acoustic modes and six optical modes, of which four optical modes are Raman active [55]. Before explaining the Raman spectra of ZnNiO, a brief description of expected vibrational modes is required. The major Raman modes of ZnO, in Group theory's Mulliken notations, are A_1, $2E_2$ and E_1. The A_1 mode is symmetric to principal rotation axis (c-axis) and shows a mode split in the form of A_1(TO) and A_1(LO) modes relative to transverse and longitudinal one-dimensional atomic vibration. The split is due to the macroscopic electric field of LO vibration increasing the restoring force and stiffness of the bond, thus increasing the split A_1 mode's energy. Similarly, the two-dimensional E_1 mode is perpendicular to the c-axis, with displacements of the O- and Zn sub-lattices also showing polarity-induced stiffness and manifesting in the E_1 mode's LO/TO splitting. However, the E_2 mode is asymmetric on the c-axis and the polarity-induced macroscopic field can be easily cancelled out due to asymmetric motion of the sub-lattices. Hence, the LO/TO splits do not take place and the mode remains non-polar. Nevertheless, the E_2 mode further shows two components, low (E_{2L}) and high (E_{2H}) energy modes due to atomic mass difference between the Zn and O atoms. Additionally, some higher-order difference modes and surface phonon modes are also expected in wurtzite ZnO. The usual Raman modes are often reported in the literature for the wurtzite phase of ZnO: E_{2L}-$E_{2H,}$ A_1(TO), E_{2H}, surface phonons and A_1(LO) [33,34]. Raman spectra recorded for ZnNiO samples are shown in Figure 7 and all the usual Raman peaks are appropriately marked. The positions of the marked Raman peaks in ZnNiO are generally in agreement with the available literature [30,33,34]. The presence of all the expected Raman modes in the figure indicates conservation of wurtzite phase in ZnNiO.

The highest intensity E_{2H} mode, related to two-dimensional doubly degenerate vibrations of O-atoms, is very sensitive to internal stresses [34]. Ni doping has been reported to introduce new stresses and disorder in the cationic sub-lattice reducing the overall wurtzite symmetry of ZnNiO [30,33]. Ni doping can also distort the local charge distributions in cationic sub-lattice leading to reduction in bond polarizability and reduced Raman intensity. E_{2H} mode intensity in ZnNiO is found to be reduced by ≈50% at 7% and 10% Ni content in comparison to other compositions. The reduced Raman intensity indicates introduction of internal stresses in material as a result of doping. Both the Raman analysis and the XRD structural analysis point towards the presence of higher stress in ZnNiO samples. Moreover, doping-induced stress is also expected in ZnNiO samples because of the possibility of differences in dopants' radii of Ni^{2+} and Ni^{3+} ions [56].

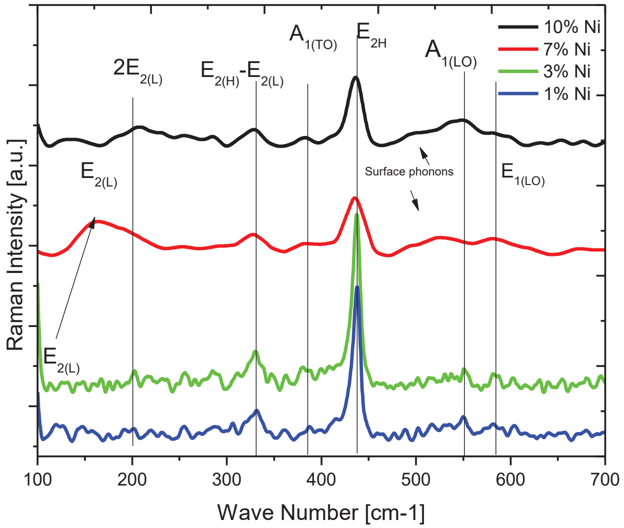

Figure 7. Room temperature micro Raman spectra for ZnNiO nanoparticles recorded in the confocal mode. Vertical lines show the positions of different normal modes of Raman vibrations. Ni content in the ZnNiO samples are written by Ni-1%, -3%, -7% and -10%, respectively, and the corresponding Raman spectra are plotted in blue, green, red and black colors.

The Raman modes, A_1(TO) and A_1(LO), are positioned at 380 and 550 cm^{-1}, respectively, and according to the Lyddane–Sachs–Teller (LST) rule the mode positions indicate the ionic character of ZnNiO [34,57]. The LST rule explains that the square of the ratio of LO and TO frequencies in the ionic lattice should be equal to ratio of static (8.5 for ZnO) to optical (4.1 for ZnO) dielectric constants. The A_1(TO) and A_1(LO) modes are also found to shift to higher frequencies with increasing Ni content in ZnO samples. The modes involve symmetric vibration of both Zn and O sub-lattices, and they are sensitive to the presence of Ni atoms in Zn sub-lattice. The ionic radii of Ni ions in octahedron coordination are 0.69 Å, 0.56 Å, and 0.48 Å for Ni^{2+}, Ni^{3+} and Ni^{4+} ions, which are lower in size than Zn^{2+}, 0.74 Å. Low ionic radii cause a reduced distance in between the two sub-lattices and that increases the force constant of bond and vibration frequency. The intensity of A_1(LO) mode was found to increase with Ni doping, which can be ascribed to the involvement of O-atoms only in the vibration, while the presence of vacancies can increase the mode intensity due to the change in bond polarizability.

The E_2 overtone and difference modes arise at different positions due to higher-order $2E_{2L}$ and difference E_{2H}-E_{2L} modes at peak positions 200 cm^{-1} and 330 cm^{-1}, respectively. Disorder modes are also present in the nanoparticles, as is clear from Figure 7, at 530 cm^{-1}, indicating the presence of either higher surface disorder, defect density or non-uniform strain, especially at 7% and 10% Ni doping percentages. The disorder modes have often been described as originating from the doping related structural defects and that results in manifestation of several broader line width phonons in doped ZnO [34].

XPS spectra for Ni_{2p}, O_{1s} and Zn_{2p} photoelectron binding energies (BE) in ZnNiO nanoparticles are shown in Figures 8–10, respectively, for assorted Ni doping concentrations. The Ni_{2p} spectrum shows a general feature of two distinct XPS peaks at BE values of 854.3 eV and 873.3 eV for Ni^{2+} oxidation state and correspondingly related to 3/2 and 1/2 spin-split components of Ni_{2p} electrons. Excluding the ZnNiO with 1% doping level, the Ni_{2p} XPS peaks, as shown in Figure 8, exhibit a general feature of blue shifted binding energy and XPS peak broadening. Typically, the BE shift increases with doping of ZnNiO, and the BE energy is blue shifted to 856.1 eV at the 10% Ni doping level, indicating the presence of both Ni^{2+} and Ni^{3+} oxidation states. A difference of ≈2.7 eV has been reported previously in between the Ni^{2+} and Ni^{3+} oxidation states [58]. The Ni_{2p} BE blue shift (−1.8 eV) indicates the presence of the additional Ni^{3+} oxidation state. Thus, the Ni_{2p} XPS results directly point towards substitution of multivalent Ni dopants, both Ni^{2+} as well as Ni^{3+}, in ZnNiO nanoparticles, especially in the ZnNiO-10 sample. Conversely, in the 1% Ni doped sample, ZnNiO-1, should only have the divalent Ni doping because of the absence of the BE shift. The aforementioned Burstein-Moss blue shifts can also be easily explained by using the observation of Ni^{3+} oxidation states in the ZnNiO-10 sample; the Ni atom is indeed behaving as a donor atom in ZnNiO nanoparticles at higher doping percentages ≥7%.

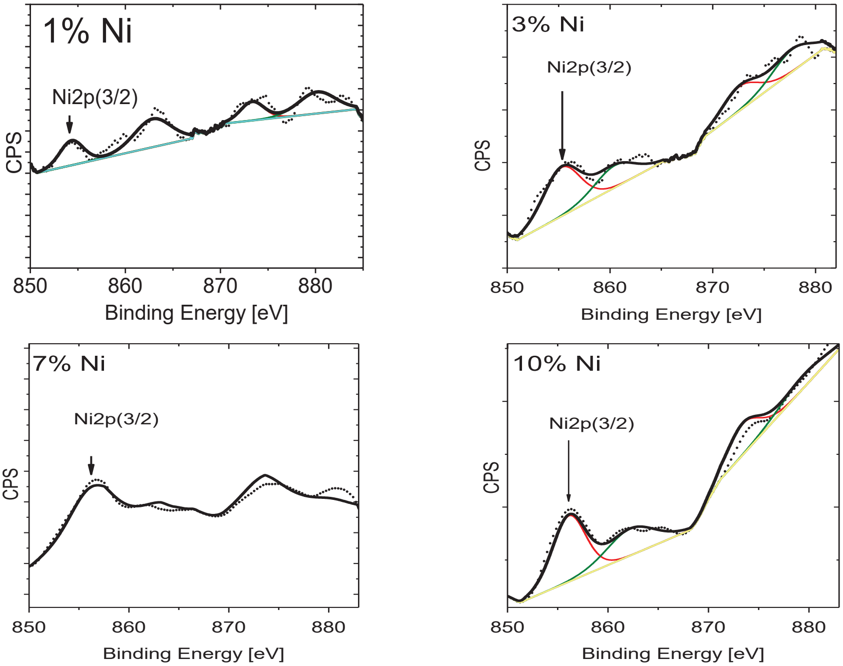

Figure 8. High-resolution XPS spectra are plotted for the Ni_{2p} photoelectrons. XPS is recorded for the ZnNiO samples containing 1%, 3%, 7% and 10% Ni weight percentages.

A deconvolution of the XPS peak of O_{1s} electrons in ZnNiO nanoparticles shows two peaks; the first peak is indicative of the native oxygen, and the second deconvoluted peak positioned at 532.5 eV is related to the oxygen defects [58]. Indeed, the oxygen defects are found to increase at higher Ni doping, since the second O_{1s} peak, as shown in Figure 9, becomes larger in area with doping, and that is also indicative of the formation of more oxygen defects due to Ni^{3+} substitution in the Zn^{2+} cationic sub-lattice. At higher Ni doping, the XPS spectra of the Zn_{2p} binding energy, see Figure 10, show relatively little change in the positions 1023 eV and 1046 eV of both types of 2p electrons of Zn ion. The Zn^{2+} oxidation state remains invariant to the doping.

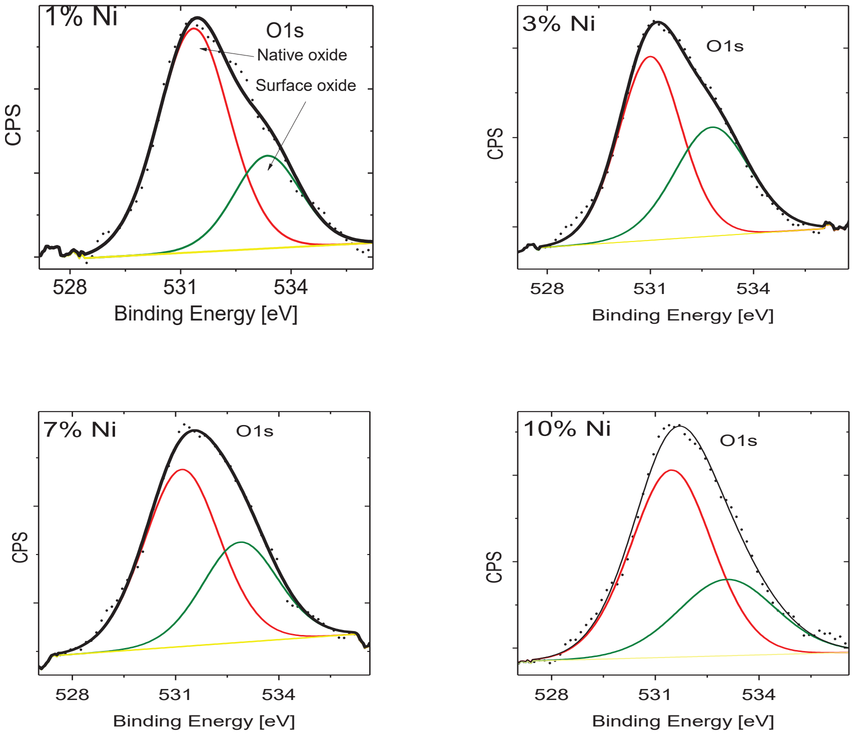

Figure 9. XPS recorded for the ZnNiO samples containing 1%, 3%, 7% and 10% Ni weight percentages. High-resolution XPS spectra are plotted for the O_{1s} photoelectrons.

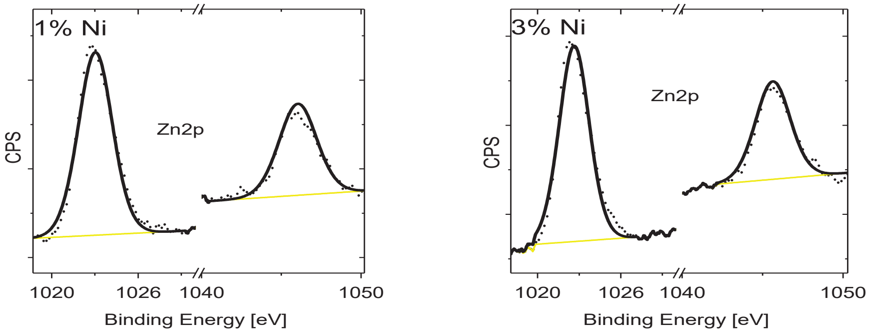

Figure 10. *Cont.*

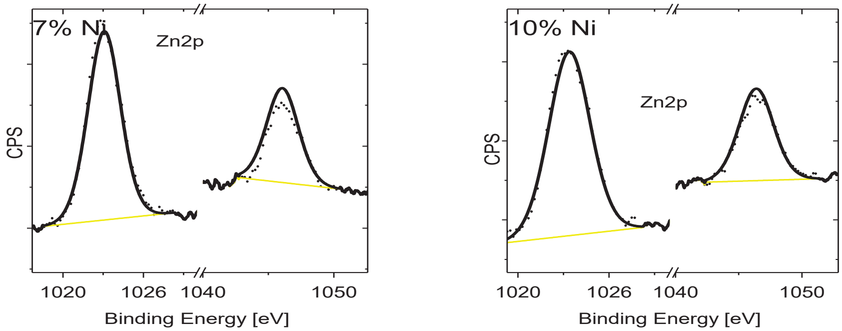

Figure 10. XPS recorded for the ZnNiO samples containing 1%, 3%, 7% and 10% Ni weight percentages. High-resolution XPS spectra are plotted for the Zn_{2p} photoelectrons.

4. Conclusions

A simple sol–gel method is used to prepare ZnNiO nanoparticles at assorted doping levels by increasing the Ni concentration to 10%. The dopant concentration was clearly found to significantly affect optical and structural properties of ZnNiO nanoparticles. XRD results indicate a substitutional solid solution phase among the ternary nanoparticles. No impurity phase is detected at all the assorted Ni doping percentages and all the observed XRD reflections can only be ascribed to wurtzite structural phase of ZnNiO. However, reduced structural symmetry, crystal strain and structural defects are detected during the XRD analysis of ZnNiO nanoparticles. XRD peak-shifting and -splitting become clear at higher Ni doping levels >7% and are attributed to the presence of crystal strain. Furthermore, the doping related decrease in Scherrer's particle size from 32 nm to 14 nm is also noted in ZnNiO nanoparticles. Spherical nanoparticle morphology is observed in SEM imaging with larger agglomerations of ZnNiO nanoparticles (≈52 nm) forming bigger clusters at higher doping. Kubelka-Munk function F(R) calculated from the DRS data is used to find the fundamental optical absorption onset. A small Burstein-Moss shift ≈0.1eV is observed in the linear-fit of KM function, which is credited to electrons transferred from the Ni dopant to the ZnNiO conduction band. Similarly, PL studies reveal intense UV luminescence in ZnNiO nanoparticles in comparison to pure ZnO, and the UV PL emission peak is also found to be blue-shifted ~0.15 eV with 10% Ni doping, further corroborating the Burstein-Moss effect. Raman analyses show a complete agreement with XRD structural studies. Doping-induced reduction in the Raman peak intensity of E-mode indicates a gradual decay of wurtzite character of ZnNiO nanoparticles. Additionally, polar Raman modes exhibit Ni doping related increased bond stiffness indicating presence of crystal strain in ZnNiO nanoparticles. Several disorder Raman modes are also observed in ZnNiO nanoparticles, confirming the presence of structural defects. Lastly, XPS studies show the presence of both Ni^{2+} and Ni^{3+} oxidation states at higher Ni doping. In this report, we have unequivocally shown the importance of multivalent Ni dopant states in the observed optical and structural changes of ZnNiO nanoparticles.

Author Contributions: Conceptualization, A.F.A.N. and J.M.; Data curation, A.H.F. and M.H.H.A.; Formal analysis, A.H.F., O.N. and M.H.H.A.; Funding acquisition, A.F.A.N.; Investigation, A.F.A.N. and J.M.; Methodology, A.H.F. and J.M.; Project administration, A.F.A.N.; Resources, A.F.A.N.; Software, A.F.A.N.; Supervision, J.M.; Validation, M.A. and O.N.; Visualization, M.A. and O.N.; Writing – original draft, J.M.; Writing – review & editing, J.M. All authors have read and agreed to the published version of the manuscript.

Funding: This research is funded by DSR, King Faisal University by grant number RGST-17122004 and the APC is funded by DSR-RGST-17122004.

Acknowledgments: The authors acknowledge the Deanship of Scientific Research at King Faisal University for the financial support received under the Research Group Support Track (Grant No. 17122004).

Conflicts of Interest: Herewith, the authors declare that there is no conflict of interests in this work.

References

1. Anandan, S.; Muthukumaran, S. Microstructural, crystallographic and optical characterizations of Cu-doped ZnO nanoparticles co-doped with Ni. *J. Mater. Sci. Mater. Electron.* **2015**, *26*, 4298–4307. [CrossRef]
2. Baruah, J.M.; Narayan, J. Dilute magnetic semiconducting quantum dots: Smart materials for spintronics. *Nonmagn. Magn. Quantum Dots* **2018**, 87–199. [CrossRef]
3. Li, J.; Haney, P.M. Optical spintronics in organic-inorganic perovskite photovoltaics. *Phys. Rev. B* **2016**, *93*, 155432. [CrossRef] [PubMed]
4. Lalieu, M.L.M.; Lavrijsen, R.; Koopmans, B. Integrating all-optical switching with spintronics. *Nat. Commun.* **2019**, *10*, 1–6. [CrossRef] [PubMed]
5. Gałązka, R.R.; Zawadzki, W. Magnetoreflection and magnetophotoluminescence in the dilute magnetic semiconductor Zn 1− x Mn x Te. *Phys. Rev. B* **2018**, *97*, 214435.
6. Pradhan, N.; Das Adhikari, S.; Nag, A.; Sarma, D.D. Luminescence, plasmonic, and magnetic properties of doped semiconductor nanocrystals. *Angew. Chem. Int. Ed. Engl.* **2017**, *56*, 7038–7054. [CrossRef]
7. Liu, S.; Chen, Y.J.; Cui, H.N.; Sun, S.N.; Wang, Z.H.; Wang, H.S. Native Defect Luminescence of Zinc Oxide Films and Its Potential Application as White Light Sources. *Guang Pu Xue Yu Guang Pu Fen Xi* **2016**, *36*, 1604–1614.
8. Tong, L.N.; Cheng, T.; Han, H.B.; Hu, J.L.; He, X.M.; Tong, Y.; Schneider, C.M. Photoluminescence studies on structural defects and room temperature ferromagnetism in Ni and Ni-H doped ZnO nanoparticles. *J. Appl. Phys.* **2010**, *108*, 023906. [CrossRef]
9. Chen, S.H.; Chen, W.C.; Yu, C.F.; Lin, C.F.; Kao, P.C. Influence of gallium-doped zinc-oxide thickness on polymer light-emitting diode luminescence efficiency. *Microsc. Res. Tech.* **2013**, *76*, 783. [CrossRef]
10. Song, G.L. Luminescence characteristics of terbium-doped nanocrystalline zinc oxide. *Guang Pu Xue Yu Guang Pu Fen Xi* **2007**, *27*, 2409–2412.
11. Gautam, U.K.; Imura, M.; Rout, C.S.; Bando, Y.; Fang, X.; Dierre, B.; Sakharov, L.; Govindaraj, A.; Sekiguchi, T.; Golberg, D.; et al. Unipolar assembly of zinc oxide rods manifesting polarity-driven collective luminescence. *Proc. Natl. Acad. Sci. USA* **2010**, *107*, 13588–13592. [CrossRef] [PubMed]
12. Khan, R.; Fashu, S. Effect of annealing on Ni-doped ZnO nanoparticles synthesized by the co-precipitation method. *J. Mater. Sci. Mater. Electron.* **2017**, *28*, 10122–10130. [CrossRef]
13. Xu, K.; Liu, C.; Chen, R.; Fang, X.X.; Wu, X.L.; Liu, J. Structural and room temperature ferromagnetic properties of Ni doped ZnO nanoparticles via low-temperature hydrothermal method. *Phys. B Condens. Matter.* **2016**, *502*, 155–159. [CrossRef]
14. Mihalache, V.; Negrila, C.; Bercu, V.; Secu, M.; Vasile, E.; Stan, G. Effect of dilute doping and non-equilibrium synthesis on the structural, luminescent and magnetic properties of nanocrystalline Zn1-xNixO (x= 0.0025–0.03). *Mater. Res. Bull.* **2019**, *115*, 37–48. [CrossRef]
15. Muller, S.; Zhou, M.; Li, Q.; Ronning, C. Intra-shell luminescence of transition-metal-implanted zinc oxide nanowires. *Nanotechnology* **2009**, *20*, 135704. [CrossRef]
16. Liu, Y.; Liu, H.; Chen, Z.; Kadasala, N.; Mao, C.; Wang, Y.; Zhang, Y.; Liu, H.; Liu, Y.; Yang, J.; et al. Effects of Ni concentration on structural, magnetic and optical properties of Ni-doped ZnO nanoparticles. *J. Alloy. Compd.* **2014**, *604*, 281–285. (In English) [CrossRef]
17. Chacko, L.; Shafeeq, K.M.; Anjana, R.; Jayaraj, M.K.; Aneesh, P.M. Room temperature ferromagnetism in Zn1- x Ni x O nanostructures synthesized by chemical precipitation method. *Mater. Res. Express* **2017**, *4*, 105905. [CrossRef]
18. Aydin, C.; El-sadek, M.S.A.; Zheng, K.B.; Yahia, I.S.; Yakuphanoglu, F. Synthesis, diffused reflectance and electrical properties of nanocrystalline Fe-doped ZnO via sol-gel calcination technique. *Opt. Laser Technol.* **2013**, *48*, 447–452. (In English) [CrossRef]
19. Fabbiyola, S.; Sailaja, V.; Kennedy, L.J.; Bououdina, M.; Vijaya, J.J. Optical and magnetic properties of Ni-doped ZnO nanoparticles. *J. Alloy. Compd.* **2017**, *694*, 522–531. (In English) [CrossRef]
20. Jlassi, M.; Sta, I.; Hajji, M.; Ezzaouia, H. Effect of nickel doping on physical properties of zinc oxide thin films prepared by the spray pyrolysis method. *Appl. Surf. Sci.* **2014**, *301*, 216–224. (In English) [CrossRef]
21. Reddy, I.N.; Reddy, C.V.; Shim, J.; Akkinepally, B.; Cho, M.; Yoo, K.; Kim, D. Excellent visible-light driven photocatalyst of (Al, Ni) co-doped ZnO structures for organic dye degradation. *Catal. Today* **2020**, *340*, 277–285. [CrossRef]

22. Reddy, I.N.; Reddy, C.V.; Sreedhar, A.; Shim, J.; Cho, M.; Yoo, K.; Kim, D. Structural, optical, and bifunctional applications: Supercapacitor and photoelectrochemical water splitting of Ni-doped ZnO nanostructures. *J. Electroanal. Chem.* **2018**, *828*, 124–136. (In English) [CrossRef]
23. Rauwel, P.; Salumaa, M.; Aasna, A.; Galeckas, A.; Rauwel, E. A Review of the Synthesis and Photoluminescence Properties of Hybrid ZnO and Carbon Nanomaterials. *J. Nanomater.* **2016**, *2016*, 19. (In English) [CrossRef]
24. Verma, K.C.; Bhatia, R.; Kumar, S.; Kotnala, R.K. Vacancies driven magnetic ordering in ZnO nanoparticles due to low concentrated Co ions. *Mater. Res. Express* **2016**, *3*, 076103. (In English) [CrossRef]
25. Asokan, T.; Freer, R. Characterization of Spinel Particles in Zinc-Oxide Varistors. *J. Mater. Sci.* **1990**, *25*, 2447–2453. (In English) [CrossRef]
26. Wu, M.S.; Chang, H.W. Self-Assembly of NiO-Coated ZnO Nanorod Electrodes with Core-Shell Nanostructures as Anode Materials for Rechargeable Lithium-Ion Batteries. *J. Phys. Chem. C* **2013**, *117*, 2590–2599. (In English) [CrossRef]
27. Carnes, C.L.; Klabunde, K.J. The catalytic methanol synthesis over nanoparticle metal oxide catalysts. *J. Mol. Catal. A Chem.* **2003**, *194*, 227–236. (In English) [CrossRef]
28. Hou, S.; Zhang, G.; Zeng, W.; Zhu, J.; Gong, F.; Li, F.; Duan, H. Hierarchical Core-Shell Structure of ZnO Nanorod@NiO/MoO2 Composite Nanosheet Arrays for High-Performance Supercapacitors. *ACS Appl. Mater. Interfaces* **2014**, *6*, 13564–13570. (In English) [CrossRef]
29. Mohapatra, J.; Mishra, D.K.; Kamilla, S.K.; Medicherla, V.R.R.; Phase, D.M.; Berma, V.; Singh, S.K. Ni-doped ZnO: Studies on structural and magnetic properties. *Phys. Status Solidi B Basic Solid State Phys.* **2011**, *248*, 1352–1359. (In English) [CrossRef]
30. Saravanan, S.; Silambarasan, M.; Soga, T. Structural, morphological and optical studies of Ag-doped ZnO nanoparticles synthesized by simple solution combustion method. *Jpn. J. Appl. Phys.* **2014**, *53*, 11RF01. (In English) [CrossRef]
31. Sharma, P.K.; Dutta, R.K.; Pandey, A.C. Effect of nickel doping concentration on structural and magnetic properties of ultrafine diluted magnetic semiconductor ZnO nanoparticles. *J. Magn. Magn. Mater.* **2009**, *321*, 3457–3461. [CrossRef]
32. Du, C.L.; Gu, Z.B.; Lu, M.H.; Wang, J.; Zhang, S.T.; Zhao, J.; Cheng, G.X.; Heng, H.; Chen, Y.F. Raman spectroscopy of (Mn, Co)-codoped ZnO films. *J. Appl. Phys.* **2006**, *99*, 123515. (In English) [CrossRef]
33. Wahab, H. Tuning the band gap, electronic polarizability and conduction mechanism of DyxZn1-xO nanostructures: The role of band tail states. *Mater. Res. Express* **2018**, *6*, 015034. [CrossRef]
34. Russo, V.; Ghidelli, M.; Gondoni, P.; Casari, C.S.; Bassi, A.L. Multi-wavelength Raman scattering of nanostructured Al-doped zinc oxide. *J. Appl. Phys.* **2014**, *115*, 073508. [CrossRef]
35. Dey, R.; Bhunia, R.; Hussain, S.; Chakraborty, B.R.; Bhar, R.; Pal, A.K. Structural and Optical Studies on Sol-gel Composites of Nickel-Doped Nanocrystalline Zinc Oxide/Polyvinylidene Fluoride. *Polym. Plast. Technol. Eng.* **2017**, *56*, 310–320. (In English) [CrossRef]
36. Dey, R.; Yadav, A.K.; Bhunia, R.; Jha, S.N.; Bhattacharyya, D.; Hussain, S.; Bhar, R.; Pal, A.K. Probing local structure of co doped polyvinylidene fluoride-ZnO thin films using X-ray absorption spectroscopy. *Spectrochim. Acta Part B At. Spectrosc.* **2017**, *131*, 115–123. (In English) [CrossRef]
37. Biesinger, M.C.; Payne, B.P.; Grosvenor, A.P.; Lau, L.W.M.; Gerson, A.R.; Smart, R.S. Resolving surface chemical states in XPS analysis of first row transition metals, oxides and hydroxides: Cr, Mn, Fe, Co and Ni. *Appl. Surf. Sci.* **2011**, *257*, 2717–2730. (In English) [CrossRef]
38. Lv, J.; Xu, J.; Zhao, M.; Sun, Y.; Jiang, Y.; He, G.; Zhang, M.; Sun, Z. Microstructure, surface morphology and optical properties of Na x Cu y Zn 1-x-y O thin films. *J. Mater. Sci. Mater. Electron.* **2016**, *27*, 4019–4025. [CrossRef]
39. Awan, S.U.; Hasanain, S.K.; Mehmood, Z.; Anjum, D.H.; Shah, S.A.; Aftab, M.; Abbas, T.A. Study of room temperature Raman scattering and XPS, high temperature electrical and low temperature magnetic properties of Zn1-yLiyO ($0.00 \leq y \leq 0.10$) nanoparticles. *Smart Mater. Struct.* **2015**, *24*, 115025. [CrossRef]
40. Norton, D.P.; Heo, Y.W.; Ivill, M.P.; Ip, K.; Pearton, S.J.; Chisholm, M.F.; Steiner, T. ZnO: growth, doping & processing. *Mater. Today* **2004**, *7*, 34–40.
41. Thota, S.; Dutta, T.; Kumar, J. On the Sol-Gel Synthesis and Thermal, Structural, and Magnetic Studies of Transition Metal (Ni, Co, Mn) Containing ZnO Powders. *J. Phys. Condens. Matter.* **2006**, *18*, 2473. [CrossRef]
42. Lafuente, B.; Downs, R.T.; Yang, H.; Stone, N. The power of databases: The RRUFF project. In *Highlights in Mineralogical Crystallography*; De Gruyter: Berlin, Germany, 2015; pp. 1–30.

43. Mazher, J.; Shrivastav, A.K.; Nandedkar, R.V.; Pandey, R.K. Strained ZnSe nanostructures investigated by x-ray diffraction, atomic force microscopy, transmission electron microscopy and optical absorption and luminescence spectroscopy. *Nanotechnology* **2004**, *15*, 572–580. (In English) [CrossRef]
44. Chen, J.L.; Devi, N.; Li, N.; Fu, D.J.; Ke, X.W. Synthesis of Pr-doped ZnO nanoparticles: Their structural, optical, and photocatalytic properties. *Chin. Phys. B* **2018**, *27*, 086102. (In English) [CrossRef]
45. Weast, R.C. *CRC Handbook of Chemistry and Physics*; CRC Press: Boca Raton, FL, USA, 1988.
46. Jenkins, F.A.; White, H.E. Fundamentals of optics. *Am. J. Phys.* **1958**, *26*, 272. [CrossRef]
47. Lopez, R.; Gomez, R. Band-gap energy estimation from diffuse reflectance measurements on sol–gel and commercial TiO 2: A comparative study. *J. Sol-Gel. Sci. Technol.* **2012**, *61*, 1–7. [CrossRef]
48. Thien, N.D.; Tu, N.N.; Viet, N.N.; Phuong, N.D.; Long, N.N. Hydrothermal Synthesis and Optical Properties of Undoped and Eu^{3+}-doped Zinc Stannate Nanocrystals. *Commun. Phys.* **2015**, *25*, 327. [CrossRef]
49. Nowak, M.; Kauch, B.; Szperlich, P. Determination of energy band gap of nanocrystalline SbSI using diffuse reflectance spectroscopy. *Rev. Sci. Instrum.* **2009**, *80*, 046107. (In English) [CrossRef]
50. Awan, S.U.; Hasanain, S.; Jaffari, G.H.; Anjum, D.H.; Qurashi, U.S. Defects induced luminescence and tuning of bandgap energy narrowing in ZnO nanoparticles doped with Li ions. *J. Appl. Phys.* **2014**, *116*, 083510. [CrossRef]
51. Srinet, G.; Kumar, R.; Sajal, V. Structural, optical, vibrational, and magnetic properties of sol-gel derived Ni doped ZnO nanoparticles. *J. Appl. Phys.* **2013**, *114*, 033912. [CrossRef]
52. Rajeh, S.; Barhoumi, A.; Mhamdi, A.; Leroy, G.; Duponchel, B.; Amlouk, M.; Guermazi, S. Structural, morphological, optical and opto-thermal properties of Ni-doped ZnO thin films using spray pyrolysis chemical technique. *Bull. Mater. Sci.* **2016**, *39*, 177–186. [CrossRef]
53. Rana, A.K.; Kumar, Y.; S, A.M.; Adarsh, K.; Sen, S.; Shirage, P.M. Enhancement of two photon absorption with Ni doping in the dilute magnetic semiconductor ZnO crystalline nanorods. *Appl. Phys. Lett.* **2015**, *107*, 231907. [CrossRef]
54. Downs, R.T.; Hall-Wallace, M. The American mineralogist crystal structure database. *Am. Mineral.* **2003**, *88*, 247–250.
55. Kroumova, E.; Aroyo, M.I.; Perez-Mato, J.M.; Kirov, A.; Capillas, C.; Ivantchev, S.; Wondratschek, H. Bilbao crystallographic server: Useful databases and tools for phase-transition studies. *Phase Transit.* **2003**, *76*, 155–170. (In English) [CrossRef]
56. Perry, N.H.; Bishop, S.R.; Tuller, H.L. Tailoring chemical expansion by controlling charge localization: In situ X-ray diffraction and dilatometric study of (La, Sr)(Ga, Ni) O 3- δ perovskite. *J. Mater. Chem. A* **2014**, *2*, 18906–18916. [CrossRef]
57. Lyddane, R.H.; Sachs, R.G.; Teller, E. On the polar vibrations of alkali halides. *Phys. Rev.* **1941**, *59*, 673. [CrossRef]
58. Lu, Q.H.; Huang, R.; Wang, L.S.; Wu, Z.G.; Li, C.; Luo, Q.; Zuo, S.Y.; Li, J.; Peng, D.L.; Han, G.L.; et al. Thermal annealing and magnetic anisotropy of NiFe thin films on n(+)-Si for spintronic device applications. *J. Magn. Magn. Mater.* **2015**, *394*, 253–259. (In English) [CrossRef]

materials

MDPI

Article

Out-of-Plane Magnetic Anisotropy in Ordered Ensembles of Fe_yN Nanocrystals Embedded in GaN

Andrea Navarro-Quezada [1,*], **Katarzyna Gas** [2], **Tia Truglas** [3], **Viola Bauernfeind** [3], **Margherita Matzer** [1], **Dominik Kreil** [4], **Andreas Ney** [1], **Heiko Groiss** [3], **Maciej Sawicki** [2] and **Alberta Bonanni** [1]

[1] Institute of Semiconductor and Solid-State Physics, Johannes Kepler University Linz, Altenberger Str. 69, 4040 Linz, Austria; margherita.matzer@jku.at (M.M.); andreas.ney@jku.at (A.N.); alberta.bonanni@jku.at (A.B.)
[2] Institute of Physics, Polish Academy of Sciences, Aleja Lotnikow 32/46, PL-02668 Warsaw, Poland; kgas@ifpan.edu.pl (K.G.); mikes@ifpan.edu.pl (M.S.)
[3] Christian Doppler Laboratory for Nanoscale Phase Transformations, Johannes Kepler University Linz, Altenberger Str. 69, 4040 Linz, Austria; Tia.truglas@jku.at (T.T.); viola.bauernfeind@speed.at (V.B.); heiko.groiss@jku.at (H.G.)
[4] Institute of Theoretical Physics, Johannes Kepler University Linz, Altenberger Str. 69, 4040 Linz, Austria; dominik.kreil@jku.at
* Correspondence: andrea.navarro-quezada@jku.at; Tel.: +43-732-2468-9622

Received: 6 July 2020; Accepted: 22 July 2020; Published: 24 July 2020

Abstract: Phase-separated semiconductors containing magnetic nanostructures are relevant systems for the realization of high-density recording media. Here, the controlled strain engineering of GaδFeN layers with Fe_yN embedded nanocrystals (NCs) *via* $Al_xGa_{1-x}N$ buffers with different Al concentration $0 < x_{Al} < 41\%$ is presented. Through the addition of Al to the buffer, the formation of predominantly prolate-shaped ε-Fe_3N NCs takes place. Already at an Al concentration $x_{Al} \approx 5\%$ the structural properties—phase, shape, orientation—as well as the spatial distribution of the embedded NCs are modified in comparison to those grown on a GaN buffer. Although the magnetic easy axis of the cubic γ'-$Ga_yFe_{4-y}N$ nanocrystals in the layer on the $x_{Al} = 0\%$ buffer lies in-plane, the easy axis of the ε-Fe_3N NCs in all samples with $Al_xGa_{1-x}N$ buffers coincides with the $[0001]$ growth direction, leading to a sizeable out-of-plane magnetic anisotropy and opening wide perspectives for perpendicular recording based on nitride-based magnetic nanocrystals.

Keywords: magnetic anisotropy; iron nitrides; III-nitrides; nanocrystals

---

1. Introduction

Iron nitrides (Fe_yN) have been widely studied for half a century due to their outstanding physical properties [1–7] and their application in magnetic recording media [4]. Particularly relevant are the high spin polarization and high Curie temperature (T_C) ferromagnetic compounds ε-Fe_3N with reported $T_C = 575$ K [5], and γ'-Fe_4N with $T_C = 767$ K [6–8]. Their implementation in combination with GaN into heterostructures is expected to serve for spin injection devices [9–11].

In this respect, the controlled fabrication of planar arrays of ferromagnetic γ'-$Ga_yFe_{4-y}N$ nanocrystals (NCs) embedded in a GaN matrix resulting from the epitaxy of GaδFeN layers, and whose size, shape and density can be adjusted through the fabrication conditions [12,13], becomes appealing for the realization of spin injection. The incorporation of Ga ions into the γ'-$Ga_yFe_{4-y}N$ NCs is expected to allow tuning the magnetic properties of the embedded NCs from ferromagnetic to ferrimagnetic [14] and weakly antiferromagnetic [15], opening wide perspectives for the implementation of these material systems into the field of antiferromagnetic spintronics [16]. The structural, magnetic and transport properties of thin GaδFeN layers deposited onto GaN buffers grown on *c*-sapphire (Al_2O_3) have been already studied in detail [12,13,17–19]. It was demonstrated that in GaδFeN layers, the face-centered cubic γ'-$Ga_yFe_{4-y}N$ nanocrystals have a preferential epitaxial relation $[001]_{NC} \| [0001]_{GaN}$ and $\langle 110 \rangle_{NC} \parallel \langle 11\bar{1}0 \rangle_{GaN}$, with a minimal fraction of NCs aligned according to $\langle 111 \rangle_{NC} \| \langle 0001 \rangle_{GaN}$ and adjusting to the hexagonal symmetry of the matrix. Co-doping with Mn leads to the reduction of the NCs size and to a quenching of the overall superparamagnetic character of the layers [18]. Recently, in ordered γ'-$Ga_yFe_{4-y}N$ nanocrystal arrays embedded in GaN, the transport of a spin-polarized current at temperatures below 10 K and an anisotropic magnetoresistance at room-temperature [19] larger than that previously observed for γ'-Fe_4N thin layers [20], were observed.

Further control over these embedded magnetic NCs can be achieved with the modification of their magnetic anisotropy through stress, by incorporating Al into the GaN buffer. The strain energies and piezoelectric effects at the GaN/$Al_xGa_{1-x}N$ interface are expected to alter the formation energies and thermodynamic equilibrium conditions of the nanocrystals. In this way, size and shape engineering and the modification of the magnetic anisotropy energy are expected to generate a switchable out-of-plane magnetic anisotropy in the nanocrystals.

In this work, the effect of strain, induced by adding Al to the GaN buffer—i.e., in GaδFeN/$Al_xGa_{1-x}N$ ($0 < x_{Al} < 41\%$) heterostructures—on the structural and magnetic properties of the Fe-rich nanocrystals embedded in GaδFeN thin layers is investigated. It is observed that already 5% of Al added to the GaN buffer layer modifies not only the structural properties—phase, shape, size and orientation—of the NCs in comparison to those grown on a pure GaN buffer, but it also leads to a sizeable out-of-plane magnetic anisotropy. Through the addition of Al into the buffer layer, additionally to the γ'-$Ga_yFe_{4-y}N$ NCs, the formation of ε-Fe_3N NCs is promoted. The crystallographic orientation and the distribution of the two phases in the GaN matrix point at the formation of ordered hexagonal ε-Fe_3N NCs elongated along the growth direction as the origin of the observed magnetic anisotropy.

2. Experimental Details

The layers considered in this work are grown in a metalorganic vapor phase epitaxy (MOVPE) Aixtron 200X horizontal reactor system (Aixtron, Achen, Germany) on *c*-plane [0001] Al_2O_3 substrates using trimethylgallium (TMGa), trimethylaluminium (TMAl), ammonia (NH_3) and ferrocene (Cp_2Fe) as precursors. The 1 µm $Al_xGa_{1-x}N$ buffers are deposited at 1000 °C on a 50 nm low-temperature (540 °C) $Al_xGa_{1-x}N$ nucleation layer annealed at 1000 °C. The Al concentration x_{Al} is varied between 0% and 41% over the sample series by adjusting the Ga/Al ratio for the growth of the buffer layer.

After deposition of the $Al_xGa_{1-x}N$ buffers, a 60 nm thick GaδFeN layer is grown at 810 °C following the δ-like procedure described in detail in Ref. [12] for GaδFeN fabricated onto GaN. The GaδFeN layers are covered by a nominally 20 nm thin GaN capping layer to avoid the segregation to the sample surface of α-Fe upon cooling [19,21]. A schematic representation of the samples is reproduced in Figure 1a.

Information on the layers' structure, on x_{Al} and on the nanocrystals' phases is obtained by high-resolution X-ray diffraction (HRXRD) carried out in a PANalytical X'Pert Pro Material Research Diffractometer (Malvern Panalytical, Nürnberg, Germany). The measurements have been performed in a configuration that includes a hybrid monochromator equipped with a 0.25° divergence slit, a PixCel detector using 19 channels for detection and a 11.2 mm anti-scatter slit. Rocking-curves acquired along the [0001] growth direction are employed to analyze the overall layer structure and the nanocrystals' crystallographic phase. From the integral breadth β of the $(000l)$ symmetric and of the $(20\bar{2}4)$ asymmetric diffraction planes, an estimation of the dislocation density in the $Al_xGa_{1-x}N$ buffer layers is obtained according to the procedure described by Moram et al. [22]. Reciprocal space maps (RSM) of the asymmetric $(10\bar{1}5)$ diffraction plane allow obtaining directly the in-plane *a* and out-of-plane *c* lattice parameters of the $Al_xGa_{1-x}N$ buffer and of the GaδFeN layers, as well as information on the strain state of the GaδFeN layers. The x_{Al} is then calculated from the lattice parameters by applying the Vegard's law [23].

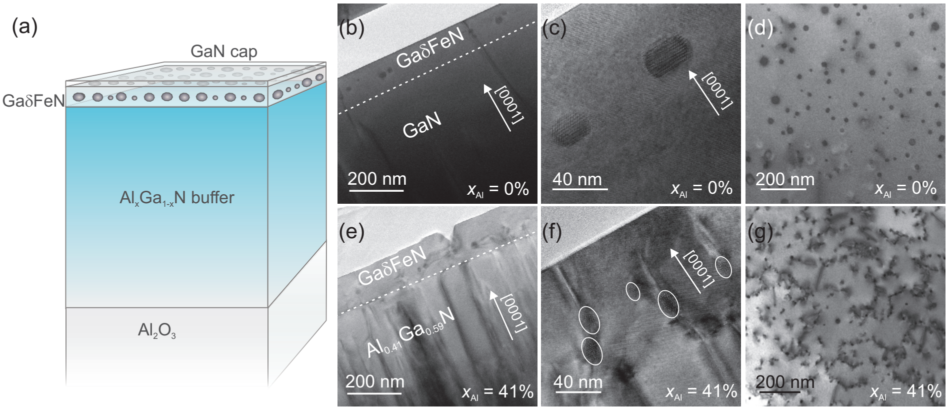

Figure 1. (**a**): Architecture of the investigated samples. Cross-section TEM micrographs of the samples grown (**b**,**c**): on GaN, and (**e**,**f**): on $Al_{0.41}Ga_{0.59}N$ buffers, showing the embedded nanocrystals distributed in the GaδFeN layer. (**d**,**g**): Plan-view TEM images of the two samples, revealing an increased dislocation network for the layer grown on the $Al_{0.41}Ga_{0.59}N$ buffer with respect to the layer grown on GaN.

The structural characterization has been completed by transmission electron microscopy (TEM) imaging using a JEOL JEM-2200FS TEM microscope (Jeol, Tokyo, Japan) operated at 200 kV in high-resolution imaging (HRTEM) mode. The TEM specimens are prepared in cross-section and plan-view by a conventional procedure including mechanical polishing followed by Ar^+ milling. The prepared samples are plasma cleaned before being inserted into the TEM. The elemental analysis is performed *via* energy dispersive X-ray spectroscopy (EDX) of the specimens while measuring the samples in scanning TEM mode (STEM).

The magnetic properties are investigated in a Quantum Design superconducting quantum interference device (SQUID) MPMS-XL magnetometer (Quantum Design, Darmstadt, Germany) equipped with a low field option at magnetic fields H up to 70 kOe in the temperature range between 2 K and 400 K. The samples are measured in perpendicular and in-plane orientation. The dominant diamagnetic response of the sapphire substrate is compensated by employing a recently developed method for the *in situ* compensation of the substrate signals in integral magnetometers [24]. For the magnetothermal properties, measurements are performed at weak static magnetic fields following the typically employed sequence of measurements: zero-field-cooled (ZFC), field-cooled (FC), and at remanence (TRM). Both ZFC and FC measurements are carried out at $H = 100$ Oe. Moreover, since the experimental magnetic signals are in the order of 10^{-5} emu, all magnetic measurements are carried out by strictly observing an experimental protocol for minute signals [25] elaborated to eliminate artifacts and to overcome limitations associated with integral SQUID magnetometry [26].

3. Results and Discussion

3.1. Structural Properties

The main structural differences between the GaδFeN layers grown on GaN and those deposited on the $Al_xGa_{1-x}N$ buffers are summarized in Figure 1, where the overall sample structure, including TEM cross-section and plan-view images for the reference sample ($x_{Al} = 0\%$) and for the sample with the highest Al concentration $x_{Al} = 41\%$ are reported. A comparison between the overview cross-section images presented in Figure 1b,e reveals a dislocation density in the $Al_{0.41}Ga_{0.59}N$ buffer larger than the one in GaN, affecting the nanocrystal distribution in the GaδFeN overlayer. As a consequence, the NCs are not all localized in one plane like those embedded in the layer grown on GaN, as demonstrated in the TEM micrographs reproduced in Figure 1c,f. It is further observed that the majority of the NCs in the GaδFeN/$Al_{0.41}Ga_{0.59}N$ sample form at the end of dislocations propagating from the buffer, in contrast to the NCs in the layer grown on GaN, which are embedded in the GaδFeN matrix volume. This is visualized in the plan-view images presented in Figure 1d,g, where NCs with a round-shaped contour, distributed homogeneously in the plane with an average distance of (20–100) nm between nanocrystals, are observed. The NCs density increases from $(5.0 \pm 0.2) \times 10^9$ NCs/cm^2 for the reference sample to $(5.0 \pm 0.3) \times 10^{10}$ NCs/cm^2 for the sample grown on the $Al_{0.41}Ga_{0.59}N$ buffer. Besides an increased NC density, there is a complex dislocation network connecting the NCs observed for the GaδFeN layer grown on the $Al_{0.41}Ga_{0.59}N$ buffer.

The nanocrystal phases are established from the HRXRD 2θ-ω scans collected along the [0001] growth direction and reported in Figure 2a for all samples. Besides the diffraction peaks from the GaδFeN layer, from the $Al_xGa_{1-x}N$ ($0 < x_{Al} < 41\%$) buffer and from the Al_2O_3 substrate, two additional diffraction peaks located around $(41.28 \pm 0.07)°$ and $(47.72 \pm 0.07)°$ are observed for all samples with Al in the buffer. The first diffraction peak is attributed to the (0002) plane of the hexagonal ε-Fe_3N phase, while the second one origins from the (200) plane of the fcc γ'-$Ga_yFe_{4-y}N$ phase. The calculated lattice parameters for the two Fe_yN phases are (0.437 ± 0.002) nm and (0.381 ± 0.002) nm, respectively. These values lie in the range of the reported literature values for both phases: the hexagonal ε-Fe_3N with $a = 0.469$ nm and $c = 0.437$ nm [27], and the fcc γ'-$Ga_yFe_{4-y}N$ with $a = 0.379$ nm [15]. For the reference sample, only the γ'-$Ga_yFe_{4-y}N$ phase is observed.

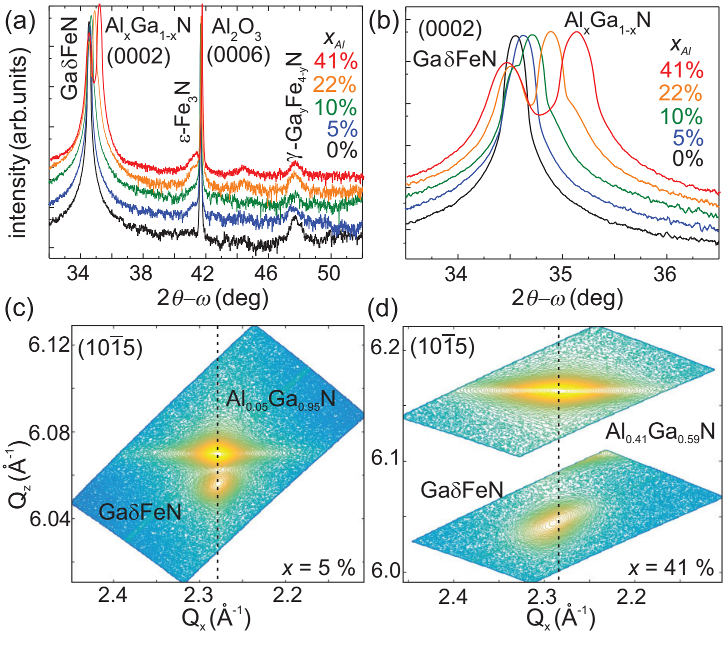

Figure 2. (**a**) Radial 2θ-ω scans collected along the [0001] growth direction with the diffraction peaks identified for the $Al_xGa_{1-x}N$ buffer, the GaδFeN layers and the embedded nanocrystal phases [28,29]. (**b**) Close-up of the (0002) diffraction peaks of the $Al_xGa_{1-x}N$ buffer and of the GaδFeN layers. (**c**,**d**) Reciprocal space maps of the $(10\bar{1}5)$ diffraction plane for the samples containing 5% and 41% Al in the buffer, respectively.

A close-up of the region around the (0002) diffraction peak of the GaδFeN overlayer and of the $Al_xGa_{1-x}N$ buffer is presented in Figure 2b, showing the shift of the buffer peak to higher diffraction angles with increasing Al concentration, pointing at a reduction in the *c*-lattice parameter. The position of the diffraction peak related to the GaδFeN thin layer remains unchanged for the buffers with

$x_{\mathrm{Al}} \leq$10% and shifts to lower angles for increasing Al concentrations, i.e., larger *c*-lattice parameter. This suggests that the GaδFeN layer is compressively strained on the Al$_x$Ga$_{1-x}$N buffers.

To analyze the strain state and to obtain the in-plane *a*-lattice parameter, reciprocal space maps at the (10$\bar{1}$5) diffraction plane are acquired. The RSM for the samples with buffers containing 5% and 41% of Al are shown in Figure 2c,d, demonstrating that while the GaδFeN layer grows fully strained on the Al$_{0.05}$Ga$_{0.95}$N buffer, it is partially relaxed on the Al$_{0.41}$Ga$_{0.59}$N one. The in-plane percentage of relaxation $R_{\%}$ of the GaδFeN thin layer with respect to the buffer is obtained directly from the respective in-plane *d*-lattice spacings as [30]:

$$R_{\%} = \frac{d_{\parallel}^{\mathrm{GaFeN(m)}} - d_{\parallel}^{\mathrm{AlGaN(m)}}}{d_{\parallel}^{\mathrm{GaN(0)}} - d_{\parallel}^{\mathrm{AlGaN(0)}}} \times 100\,, \tag{1}$$

where $d_{\parallel}$ refers to the in-plane lattice spacings d. The values in the numerator are the measured ones and those in the denominator are the values for free-standing GaN and Al$_x$Ga$_{1-x}$N according to the Vegard's law. The calculated $R_{\%}$ values for the samples considered here, are reported in Table 1, showing that for $x_{\mathrm{Al}} < 10\%$, the GaδFeN layers grow fully strained on the buffers and the onset of relaxation occurs at $x_{\mathrm{Al}} \geq 10\%$. This is also evident from the lattice parameters presented in Figure 3a,b as a function of x_{Al}, where the lattice parameter a for the GaδFeN layer is found to deviate from the one of the Al$_x$Ga$_{1-x}$N buffer with $x_{\mathrm{Al}} > 10\%$. The dashed lines in Figure 3a,b give the trend of the Vegard's law and the dashed-dotted lines indicate the literature values for the lattice parameters for GaN [31]. Although the *c*-lattice parameter for the GaδFeN layer is not significantly affected by increasing the Al concentration, a matches the one of the buffer until $x_{\mathrm{Al}} \approx$10% and then deviates significantly, confirming the relaxation of the GaδFeN thin layer. Considering that the GaδFeN thin layer has only biaxial in-plane strain, the strain $\epsilon_{xx}^{\mathrm{GaFeN}}$ and stress $\sigma_{xx}^{\mathrm{GaFeN}}$ tensors are calculated employing a linear interpolation between the value of the Young modulus E and the stiffness constants C_{ij} of GaN (E = 450 GPa, $2C_{13}/C_{33}$ = 0.509) and AlN (E = 470 GPa, $2C_{13}/C_{33}$ = 0.579) [31]. The values reported in Table 1 show that independent of the Al concentration, the GaδFeN layers are all under a comparable compressive strain.

Table 1. List of investigated samples and their relevant parameters: Al concentration x_{Al} in the buffer; R$_{\%}$ degree of relaxation; out-of-plane $\epsilon_{zz}^{\mathrm{GaFeN}}$ and in-plane $\epsilon_{xx}^{\mathrm{GaFeN}}$ strain and $\sigma_{xx}^{\mathrm{GaFeN}}$ stress in the GaδFeN thin layer. The Fe$_y$N nanocrystal phases identified by HRXRD and HRTEM are also listed.

x_{Al} (%)	R$_{\%}$ (%)	$\epsilon_{xx}^{\mathrm{GaFeN}}$ (%)	$\epsilon_{zz}^{\mathrm{GaFeN}}$ (%)	$\sigma_{xx}^{\mathrm{GaFeN}}$ (GPa)	Fe$_y$N NCs Phases
0	0	−0.012	0.063	−0.564	γ'-Ga$_y$Fe$_{4-y}$N
5	0	−0.012	0.063	−0.564	ε-Fe$_3$N/γ'-Ga$_y$Fe$_{4-y}$N
10	13	−0.016	0.081	−0.706	ε-Fe$_3$N/γ'-Ga$_y$Fe$_{4-y}$N
22	67	−0.018	0.093	−0.847	ε-Fe$_3$N/γ'-Ga$_y$Fe$_{4-y}$N
41	85	−0.012	0.063	−0.564	ε-Fe$_3$N/γ'-Ga$_y$Fe$_{4-y}$N

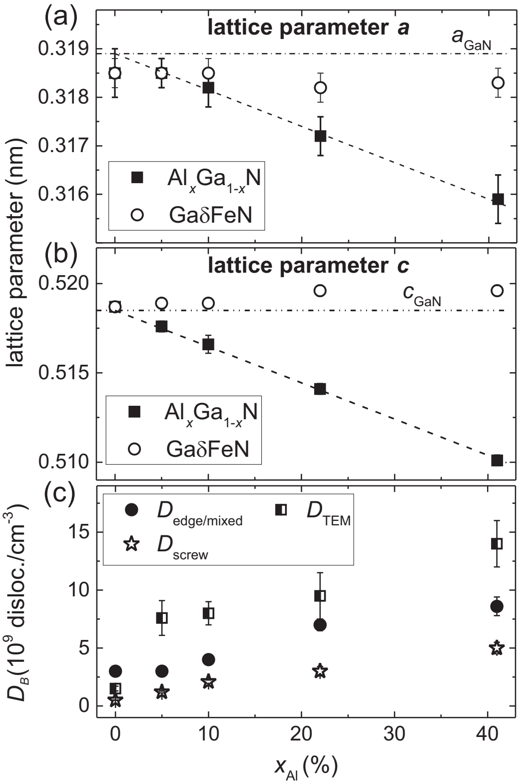

Figure 3. (**a**,**b**): Lattice parameters *a* and *c* of the $Al_xGa_{1-x}N$ buffer (full squares) and the Ga*δ*FeN layers (empty circles) *vs.* x_{Al}. The dashed line corresponds to the Vegard's law and the dashed-dotted line indicates the literature values of the lattice parameters *a* and *c* for GaN [31]. (**c**) Dislocation densities—edge-mixed (full circles) and screw (empty stars)—in the $Al_xGa_{1-x}N$ buffer layers estimated from XRD and TEM (half-filled squares) as a function of x_{Al}.

The (0002) diffraction peak of the $Al_xGa_{1-x}N$ buffers presented in Figure 2b broadens with increasing Al concentration, pointing at an increment of defects and dislocation density in the buffer layers. In [0001]-oriented III-nitride films, three main types of threading dislocations are commonly observed: edge-, mixed- and screw-type. The analysis of the integral breadth of the diffraction peaks originating from the (000*l*) planes allows estimating the density of screw dislocations, while the one in the $(20\bar{2}4)$ plane provides information on the density of edge and mixed type dislocations [22]. According to Dunn and Koch, the density of dislocations D_B is given by [32]:

$$D_B = \frac{\beta^2}{4.35b^2}, \tag{2}$$

where β is the integral breadth and b is the Burgers vector. This equation was previously employed to estimate the dislocation density in GaN thin films [33]. The dislocation densities obtained from HRXRD analysis for all buffer layers as a function of x_{Al} are reported in Figure 3c, where a linear increase is observed reaching values up to four times larger than those of the GaN buffer for both edge-mixed and screw dislocations in the buffer with the highest Al concentration. These results are consistent with the observations from the cross-section and plan-view TEM images shown in Figure 1. The dislocation density is also estimated from TEM micrographs, yielding larger values for the $Al_xGa_{1-x}N$ buffers than those obtained from the XRD analysis, but following the same trend: the greater the concentration of Al in the buffer, the higher the dislocation density.

The increased dislocation density in the $Al_xGa_{1-x}N$ buffers with $x_{Al} > 10\%$ leads to the relaxation of the GaδFeN thin layers. As observed in Figure 1f, a fraction of the dislocations from the $Al_{0.41}Ga_{0.59}N$ buffer runs throughout the entire GaδFeN layer, promoting the aggregation of Fe along the defects and, therefore, the preferential formation of nanocrystals. Interestingly, the nanocrystals stabilized at the dislocations are predominantly elongated along the [0001] growth direction.

A more detailed analysis of the NCs sizes is performed on cross-section and plan-view TEM images. The size of the NCs is determined with an accuracy of ±0.5 nm by measuring the size of the areas where Moiré patterns are visible with the Fiji software [34]. The results are presented in Figure 4a–e, where the size distribution of 200 measured NCs per sample is reported. For this evaluation, the NCs are treated as ellipsoids according to the schematic representation in Figure 4f with dimensions perpendicular (A) and parallel (C) to the [0001] growth direction for the different x_{Al} in the buffers. The solid line marks the aspect ratio (AR) equal to 1, i.e., $A = C$. From the size distributions presented in Figure 4, it is seen that the size of the NCs in the reference sample has a broader distribution and particularly a larger in-plane A than in the samples grown on the $Al_xGa_{1-x}N$ buffers. Although the size of the NCs in the reference sample tends to lie on or below the solid line, indicating an AR$\leq$1 and an oblate shape of the NCs—with their y-axis elongated in the plane of the layer—the size of the NCs in the layers grown on the $Al_xGa_{1-x}N$ buffers lies above the solid line, i.e., with an AR>1, pointing at prolate NCs elongated along the [0001] growth direction. From the measured dimensions of the NCs, the average sizes parallel and perpendicular to the growth direction [0001] are estimated, confirming the decrease in the size perpendicular to the growth direction for the nanocrystals embedded in the GaδFeN layers grown on the $Al_xGa_{1-x}N$ buffers.

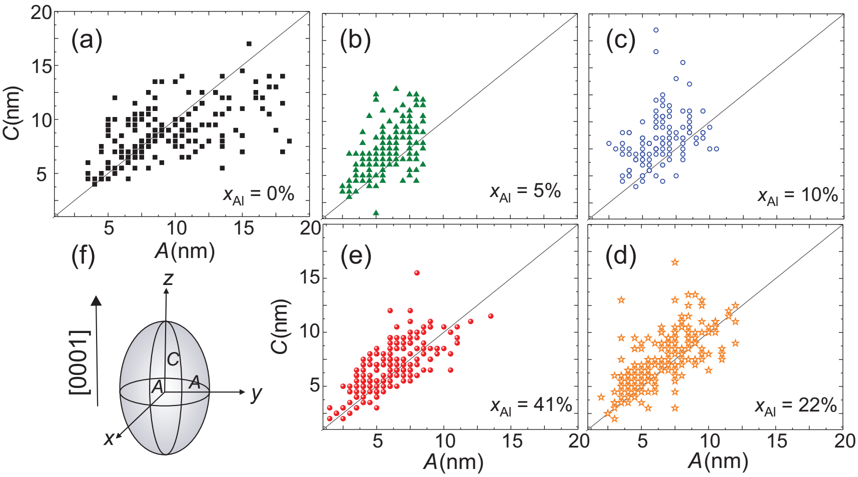

Figure 4. Size distribution of 200 NCs measured in cross-section HRTEM for x_{Al} in the buffers equal to: (**a**) 0%, (**b**) 5%, (**c**) 10%, (**d**) 22%, and (**e**) 41%. The dimensions A and C correspond to the schematic representation depicted in (**f**) and correspond to half the size perpendicular and parallel to the [0001] growth direction, respectively.

Furthermore, it is found that in all samples the nanocrystals located at dislocation sites are predominantly prolate. This suggests that the increase in dislocation density for the layers grown on the $Al_xGa_{1-x}N$ buffers promotes the formation of prolate NCs, which are mostly arranged in pairs aligned along dislocations, as shown in Figure 5a. In contrast, the oblate NCs are all located at the same depth in the layers.

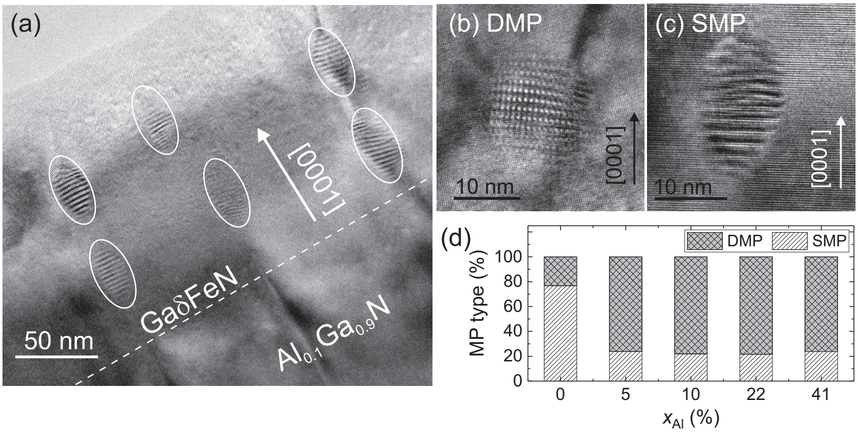

Figure 5. (**a**) Cross-section HRTEM image showing the distribution in pairs of prolate NCs along dislocations in the GaδFeN/Al$_{0.1}$Ga$_{0.9}$N sample. (**b**,**c**) HRTEM images of nanocrystals with double and single Moiré-patterns, respectively. (**d**) Fraction of NCs displaying SMP and DMP as a function of x_{Al}.

In addition to providing the size and phase, the characterization of the Moiré patterns (MPs) observed in the HRTEM micrographs yields further relevant information about the embedded NCs. The origin of MPs in general is the result of the overlap of two lattices with equal spacings that are rotated with respect to each other, or of the superposition of lattices with slightly different spacings. This leads to a pattern with Moiré fringe spacings with either single periodicity (line pattern) or double periodicity (grid-like pattern). Exemplary NCs showing a double and a single MP are presented in Figure 5b,c, respectively. The Moiré fringe spacings depend on the two underlying crystal structures, on their orientation relationship, and on the lattice strain. The fraction of nanocrystals displaying single MP (SMP) and double MPs (DMP) is shown in Figure 5d. Up to 78% of the NCs exhibit single MPs and 22% produce double MPs in the reference GaδFeN grown on GaN buffer, while for the films grown on the Al$_x$Ga$_{1-x}$N buffers this tendency is inverted. The double MP pattern is an indication of an in-plane misorientation of the NCs, which is related to the enhanced dislocation density in the underlying buffer layers and to the formation of the NCs along the dislocations, leading to slight distortions and strain within the GaN matrix.

The Fe$_y$N phases identified in the HRXRD spectra depicted in Figure 2a are confirmed by HRTEM analysis. In HRTEM micrographs showing NCs, the regions of interests are Fourier transformed by Fast Fourier Transformation (FFT) using the Gatan Digital Micrograph (Gatan Inc.) software. Micrographs of two NCs are shown in Figure 6a,d along with the corresponding FFTs in Figure 6b,e. The FFT images are used to determine the lattice parameters by measuring the spacings in the two directions of the diffraction pattern. To identify the NCs orientation with respect to the GaN matrix, a comparison with the diffraction patterns simulated by the JEMS software is performed [35]. Employing this procedure, the investigated NC in Figure 6a is identified as ε-Fe$_3$N oriented along the zone axis (ZA) $[110]_{\mathrm{NC}}$, which is parallel to the ZA $[210]_{\mathrm{GaN}}$, and therefore corresponds to an epitaxial relation $[11\bar{2}0]_{\mathrm{NC}} \| [10\bar{1}0]_{\mathrm{GaN}}$. A schematic representation of the epitaxial relation is sketched in Figure 6c, showing that the NC is 30° rotated with respect to the crystallographic axis of GaN, but parallel to the one of the sapphire substrate, similarly to the fcc NCs studied in GaδFeN/GaN layers [13]. The above procedure is applied to the NCs found in the reference sample and reproduced in Figure 6d, revealing the epitaxial relation $[110]_{\mathrm{NC}} \| [11\bar{2}0]_{\mathrm{GaN}}$ presented in Figure 6f and previously reported for γ'-Ga$_y$Fe$_{4-y}$N NCs in GaδFeN layers grown on GaN [13]. The majority of the NCs found in the GaδFeN layers grown on the Al$_x$Ga$_{1-x}$N buffers are identified as the hexagonal ε-Fe$_3$N phase, while those in the reference sample are associated with the cubic γ'-Ga$_y$Fe$_{4-y}$N phase oriented preferentially as $[001]_{\mathrm{NC}} \| [0001]_{\mathrm{GaN}}$, in agreement with the results from the XRD spectra presented in Figure 2a. From elemental composition analysis *via* EDX line-scans, the presence of Al in the GaδFeN layers is ruled out as shown in Figure S1 (Supplementary Materials) of the Suplemental Material.

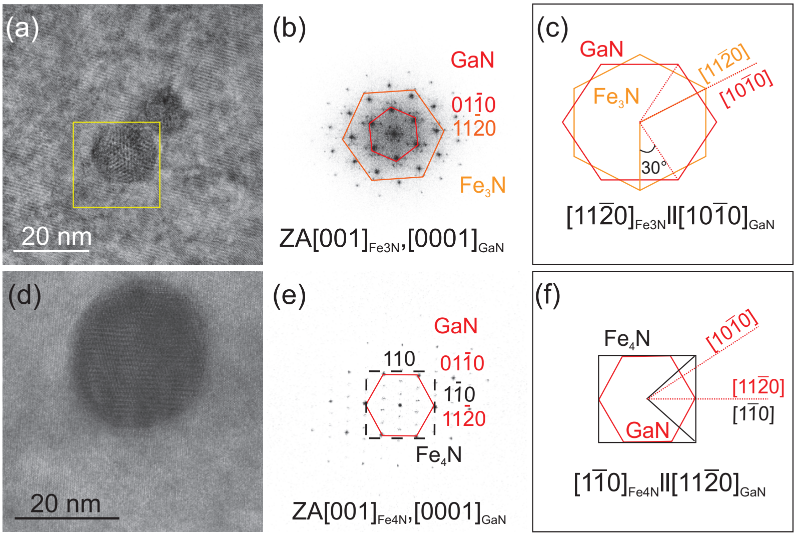

Figure 6. Plan-view HRTEM images of exemplary Fe$_y$N nanocrystals embedded in a GaδFeN layer grown on (**a**) an Al$_{0.1}$Ga$_{0.9}$N buffer, and (**d**) GaN. (**b**,**e**) FFT of the images presented in (**a**,**d**), respectively, showing the epitaxial orientation of the NCs with respect to the GaN matrix. The FFT in (**c**) corresponds to the NCs marked by the square in (**a**). (**c**,**f**): Schematic representation of the epitaxial relation in (**b**,**e**).

3.2. Magnetic Properties

In the previous section it has been demonstrated that the basic structural characteristics of the NCs change considerably with the incorporation of Al into the buffer layer. To shed light onto how the magnetic characteristics of the layers are modified by these structural changes, a comparative analysis of the magnetic properties of the reference GaδFeN/GaN and the GaδFeN/Al$_{0.1}$Ga$_{0.9}$N samples is performed. As indicated in Table 1 and depicted in Figure 2, the former contains mostly γ'-Ga$_y$Fe$_{4-y}$N NCs, which are characterized by a balanced distribution of prolate and oblate shapes, whereas in the latter, prolate ε-Fe$_3$N NCs prevail over the γ'-Ga$_y$Fe$_{4-y}$N ones.

The formation of the Fe-rich NCs in GaN is the direct consequence of the solubility limit of Fe in GaN being $(1.8 \times 10^{20})\,\mathrm{cm}^{-3}$ or 0.4% at the growth conditions considered here [36–38]. Therefore, when the doping level exceeds this concentration, the Fe ions are found both in Ga substitutional sites as Fe^{3+} and in the phase-separated NCs. The Fe-rich NCs form disperse ensembles of large ferromagnetic macrospins with specific size and shape distributions. In the absence of mobile carriers, the randomly distributed Fe^{3+} ions, despite their high spin state ($L = 0, S = 5/2$), do not interact in the relevant temperature range between 2 K and 400 K and exhibit paramagnetic properties. Due to the high diffusivity of transition metal ions in GaN, these paramagnetic ions are found diffusing a few hundreds of nanometres below the Fe-δ-doped layer [39]. This substantially increases the total amount of the dilute Fe^{3+}, making the intensity of the paramagnetic signal at low temperatures comparable to the one of the ferromagnetic NCs. Therefore, a dedicated experimental approach is required to distinguish between the two contributions.

The isothermal magnetization curves with the magnetic moment as a function of the applied magnetic field $m(H)$ for the reference sample ($x_{\mathrm{Al}} = 0\%$) are plotted for selected temperatures (solid symbols) in Figure 7. As mentioned, the bare magnetic signal consists of two distinct contributions. At temperatures above 50 K, the fast saturating response resembling a Langevin's $L(H)$ function at weak fields is attributed to the ferromagnetic NCs. However, the lack of a systematic T-dependency satisfying the H/T scaling [40] and the presence of a weak magnetic hysteresis indicate that the majority of the NCs is not in thermal equilibrium and their magnetic response is affected by the presence of energy barriers and governed by their distribution. At temperatures below 50 K, the $m(H)$ gains in strength and a slowly saturating contribution originating from the non-interacting Fe^{3+} ions retaining their own magnetic moment dominates [37,38,41,42].

The paramagnetism of the Fe^{3+} ions is described by the Brillouin function B_S for $S = J = 5/2$ [36,43,44], and the experimentally established difference $\Delta m(H)$ between $m(H)$ at, e.g., 2 K and 5 K permits the quantification of the ions' contribution by fitting $\Delta B_S(H, \Delta T) = B_S(H, 2\,\mathrm{K}) - B_S(H, 5\,\mathrm{K})$ to $\Delta m(H)$ with the procedure described in detail in Ref. [38]. The open circles in Figure 7 represent the experimental difference $\Delta m(H)$ between $m(H)$ at 2 K and 5 K, whereas the dotted line follows the magnitude of the expected change $\Delta B_{5/2}(H, \Delta T)$ corresponding to several ions $N_{\mathrm{PM}} = (1.8 \times 10^{15})$ cm^{-2}. The dashed line indicates the magnitude of the paramagnetic contribution corresponding to N_{PM} at 2 K.

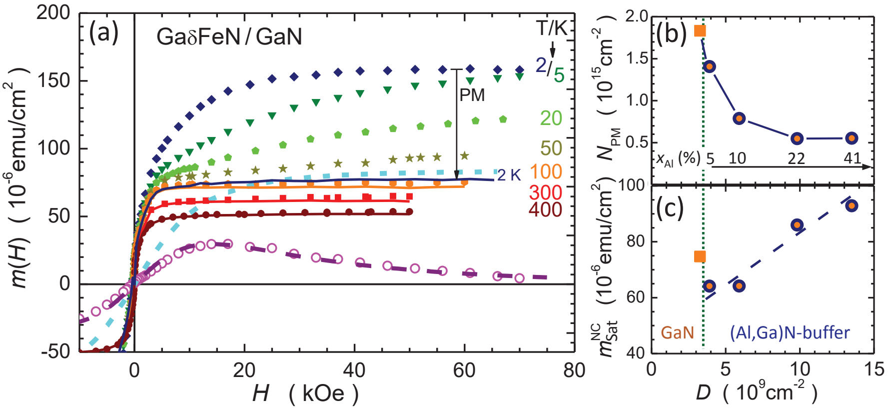

Figure 7. (**a**) (Solid symbols) Isothermal magnetization curves of the reference GaδFeN/GaN structure at selected temperatures. The open circles denote the difference $\Delta m(H)$, whereas the dashed line corresponds to the calculated difference of the respective Brillouin functions calculated for the paramagnetic Fe^{3+} ions with $N_{\mathrm{PM}} = (1.8 \times 10^{15})\,\mathrm{cm}^{-2}$. The solid lines mark the resulting magnitudes of $m_{\mathrm{NC}}(H)$ of the NCs, after subtracting the paramagnetic component. The solid down–arrow indicates the degree of the reduction of $m(H)$ due to the subtraction of the paramagnetic contribution. (**b**,**c**) N_{PM} and m_{NC}^{sat} plotted as a function of total dislocation density D. The squares represent the reference GaδFeN/GaN structure, the circles mark data for the layers grown on the $\mathrm{Al}_x\mathrm{Ga}_{1-x}\mathrm{N}$ buffers. The corresponding concentration of Al in the $\mathrm{Al}_x\mathrm{Ga}_{1-x}\mathrm{N}$ buffers is indicated in panel (**b**). Dashed lines in panels (**b**,**c**) are guide to the eye.

Having established N_{PM} in each of the investigated structures, the paramagnetic contribution $m_{\mathrm{PM}}(H) = g\mu_{\mathrm{B}}SN_{\mathrm{PM}}B_{5/2}(H, T)$—where g is the g-factor and μ_{B} the Bohr magneton—is calculated and subtracted from the experimental data to obtain the magnitude $m_{\mathrm{NC}}(H, T)$ of the magnetization corresponding to the NCs. The results are indicated by solid lines in Figure 7. It is worth noting that $m_{\mathrm{NC}}(H, T)$ saturates at all investigated temperatures for $H \geq 10\,\mathrm{kOe}$, confirming the ferromagnetic order within the NCs. The evolution of N_{PM} and m_{NC} as a function of the dislocation density is presented in Figure 7b,c, respectively. The former decreases, whereas the latter increases with the dislocation density, suggesting that the dislocations originating at the sapphire/$\mathrm{Al}_x\mathrm{Ga}_{1-x}\mathrm{N}$ interface serve as preferential sites for the aggregation of the Fe ions. This is substantiated by the fact that the magnitude of N_{PM} in the reference structure and related solely to the layer nominally containing Fe, i.e., (60–100) nm, corresponds to $(4 \times 10^{20})\,\mathrm{cm}^{-3}$ or $\simeq$ 1% of Fe ions, largely exceeding the Fe solubility limit in GaN. Thus, the Fe^{3+} ions are distributed across the entire depth in the structure of the reference sample, whereas in the layers grown on the $Al_xGa_{1-x}N$ buffers a significant fraction of the Fe ions migrates to the dislocations, where they aggregate into the hexagonal ε-Fe_3N NCs. Since the dislocation density is found to correlate with the Al content in the buffer, as presented in Figure 3c, the Al content in the $Al_xGa_{1-x}N$ buffer is instrumental to control both the substitutional Fe atoms concentration and the strength of the ferromagnetic signatures related to the NCs.

The temperature dependence of the saturation magnetization $m_{NC}^{sat}(T)$ of the ferromagnetic signal specific to the NCs for the layer grown on the $Al_{0.1}Ga_{0.9}N$ buffer (circles) and for the reference one (squares) is reproduced in Figure 8. These dependencies are established upon performing a $m(H)$ analysis similar to the one exemplified in Figure 7 (solid symbols), as well as from direct continuous sweeping of T at $H = 20\,\mathrm{kOe}$ (open symbols). This allows quantifying the temperature dependence of the saturation magnetization M_{sat} of the γ'-$Ga_yFe_{4-y}N$ and ε-Fe_3N present in the structures.

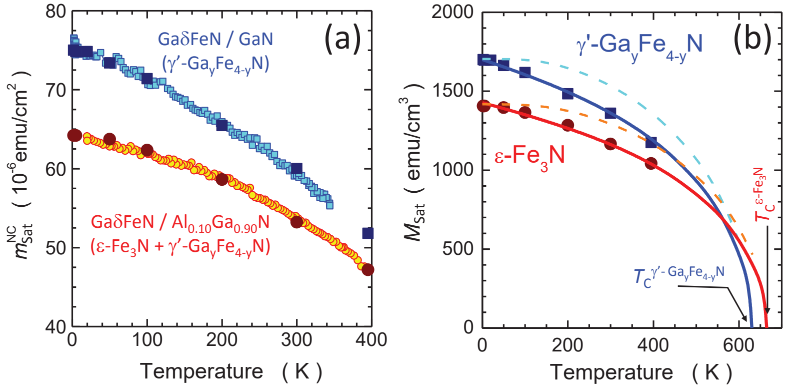

Figure 8. (**a**) Comparison of the temperature dependence of $m_{NC}^{sat}(T)$ in the studied GaδFeN layers grown on a GaN buffer (squares) and grown on a $Al_{0.1}Ga_{0.9}N$ buffer (circles). Solid symbols: m_{NC}^{sat} inferred from the $m_{NC}(H)$ isotherms. Open symbols: direct continuous sweeping of T at $H = 20\,\mathrm{kOe}$. (**b**) Temperature dependence of the saturation magnetization M_{Sat} of the two Fe_yN compounds formed due to the epitaxy of the GaδFeN layers. The solid lines mark two classical Langevin functions $L(T)$ rescaled to follow the corresponding experimental result for $2\,\mathrm{K} < T < 400\,\mathrm{K}$. The dashed lines are Brillouin functions $B_{5/2}(T)$ rescaled to reproduce the corresponding magnitudes of $m_{NC}^{sat}(0)$ and T_C.

To quantify the magnetization of the NCs, their average volume is estimated from the size distribution shown in Figure 4 and the average densities established from TEM by taking into account that (50-70)% of the prolate NCs in the GaδFeN/$Al_xGa_{1-x}N$ structures grow in pairs along the dislocations, as shown in Figure 5a. The estimated values of the NCs magnetization are $(1700 \pm 200)\,\mathrm{emu/cm^3}$ for the NCs in the reference sample containing γ'-$Ga_yFe_{4-y}N$ NCs, and $(1400 \pm 900)\,\mathrm{emu/cm^3}$ for the NCs present in the GaδFeN/$Al_{0.1}Ga_{0.9}N$ structure, where about 80% of the NCs are ε-Fe_3N and 20% are γ'-$Ga_yFe_{4-y}N$. These values are consistent with those estimated from ferromagnetic resonance measurements [17], shown in Figure S2 of the Suplemental Material, and in good agreement with the respective ranges of M_{sat} reported in the literature for these compounds. For γ'-Fe_4N, the M_{sat} ranges between $1500\,\mathrm{emu/cm^3}$ and $2000\,\mathrm{emu/cm^3}$ [2,45–47], so that the values obtained for the γ'-$Ga_yFe_{4-y}N$ NCs considered here point at high crystallinity and low dilution by Ga, i.e., $(y \ll 1)$. For the layer grown on the $Al_{0.1}Ga_{0.9}N$ buffer the M_{sat} established, taking into account a 20% contribution of γ'-$Ga_yFe_{4-y}N$ NCs, yields a corrected value of $M_{sat} = (1300 \pm 900)\,\mathrm{emu/cm^3}$ for the ε-Fe_3N NCs, consistent with previous studies [2,5,48–54].

The resulting magnitudes of $M_{\mathrm{Sat}}(T)$ for both compounds are represented as solid symbols in Figure 8b. The experimental trends of $M_{\mathrm{Sat}}(T)$ for both $\mathrm{Fe}_y\mathrm{N}$ compounds are compared with the spontaneous magnetization calculated as a function of T based on the molecular field theory in the classical limit and with the Langevin function $L(T)$, i.e., corresponding to a large magnetic moment of the NCs $J = S \rightarrow \infty$ (solid lines). It is observed that the low-T fast drop of $m_{\mathrm{FM}}(T)$ starting at $T \approx 50\,\mathrm{K}$, is indeed well captured by $L(T)$, and could not be reproduced by a Brillouin function. For comparison, the $B_{5/2}(T)$ functions are added to Figure 8b as dashed lines. The $L(T)$ is then extrapolated to assess the T_{C} of the NCs in each sample.

In the reference sample containing mostly γ'-$\mathrm{Ga}_y\mathrm{Fe}_{4-y}\mathrm{N}$ NCs a $T_{\mathrm{C}} = (630 \pm 30)\,\mathrm{K}$ is found, i.e., about 100 K lower than the values reported for Ga-free γ'-$\mathrm{Fe}_4\mathrm{N}$ of $T_{\mathrm{C}} = 716\,\mathrm{K}$ [47] and 767 K [6]. This is attributed to a partial replacement of the Fe ions by Ga, which leads to a magnetic dilution and randomization of spins breaking down the ferromagnetic order [15,55]. However, the Ga incorporation is minimal, since the ternary $\mathrm{GaFe_3N}$ is weakly antiferromagnetic [15]. The same extrapolation method yields $T_{\mathrm{C}} = (670 \pm 30)\,\mathrm{K}$ for the layer grown on the $\mathrm{Al_{0.1}Ga_{0.9}N}$ buffer, which contains predominantly ε-$\mathrm{Fe_3N}$ NCs and a limited amount of γ'-$\mathrm{Ga}_y\mathrm{Fe}_{4-y}\mathrm{N}$. No quantitative conclusion about the T_{C} of ε-$\mathrm{Fe_3N}$ NCs can be made, nevertheless it can be stated that its value is significantly greater than the previously reported 575 K [5] and (500–525) K [53,56]. This result is relevant, since despite the high potential of ε-$\mathrm{Fe_3N}$ for spintronics [5], the technological development of this material has been limited by its high chemical reactivity and by challenges in obtaining the required stoichiometry [57]. The magnitude reported here for ε-$\mathrm{Fe_3N}$ NCs points, on the other hand, to the possibility of stabilizing, in a controlled fashion, relevant $\mathrm{Fe}_y\mathrm{N}$ nanostructures in a GaN matrix.

The magnetothermal behavior of these ensembles of NCs traced for two orientations of H, i.e., $H_{\|}$ parallel (full symbols) and $H_{\perp}$ perpendicular (open symbols) to the film plane is shown in Figure 9a and follows a trend specific to ferromagnetic nanoparticle ensembles previously reported for Fe-rich NCs stabilized in GaN [18,37,38]. These features indicate that independently of the orientation, a specific distribution of energy barriers $E_B = K_{\mathrm{eff}}V_{\mathrm{NC}}$ for the ferromagnetic moment reversal determines the response in the whole temperature range. Here K_{eff} is the effective magnetic anisotropy energy density specific to a given NC with volume V_{NC}. The effect is particularly significant in the $\mathrm{Ga}\delta\mathrm{FeN/Al_{0.1}Ga_{0.9}N}$ layer for $H_{\perp}$. This finding demonstrates that the predominantly prolate character of the ε-$\mathrm{Fe_3N}$ NCs in the layers grown on the $\mathrm{Al}_x\mathrm{Ga}_{1-x}\mathrm{N}$ buffers dramatically affects the magnetic anisotropy (MA), which will be treated in detail later.

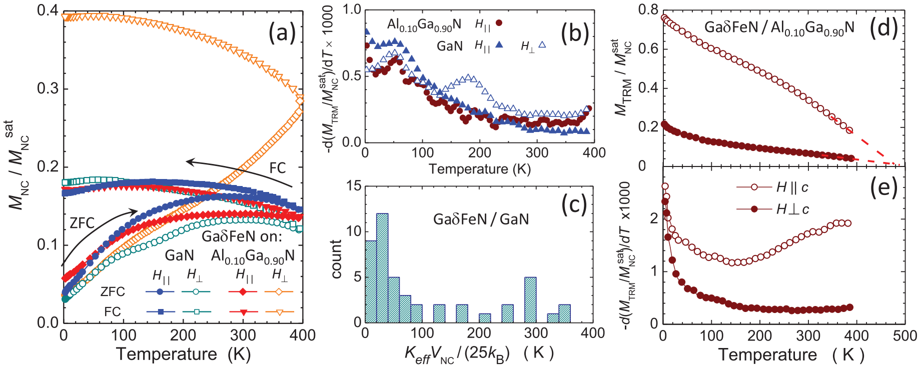

Figure 9. (**a**,**b**) ZFC, FC and the calculated temperature derivative of the thermoremanence magnetization (TRM): $-d(M_{\mathrm{FC}} - M_{\mathrm{ZFC}})dT$ in the studied GaδFeN structures grown either on GaN or on the $\mathrm{Al_{0.1}Ga_{0.9}N}$ buffer. (**c**) Superparamagnetic limit distribution in the GaδFeN/GaN structure calculated based on the size and shape distributions of the NCs taken from Figure 4a. (**d**) Direct measurement of TRM in $\mathrm{Ga}\delta\mathrm{FeN/Al_{0.1}Ga_{0.9}N}$ after cooling down in a saturating $H = 10\,\mathrm{kOe}$ and (**e**) its T–derivative. The dashed lines in (**d**) point to the superparamagnetic limit of about 500 K.

For an ensemble of non-interacting magnetic NCs the temperature derivative of the thermoremanence magnetization (TRM) provides qualitative information on the E_B distribution in the ensemble [58]. From $M_{\mathrm{TRM}} = M_{\mathrm{FC}} - M_{\mathrm{ZFC}}$, the $-d(M_{\mathrm{FC}} - M_{\mathrm{ZFC}})dT$ is calculated and displayed in Figure 9b, with non-zero values in the whole T-range and exhibiting a peak at around 50 K. From this, the magnitude of the superparamagnetic limit T_{SP} in the layers is quantified. Here, T_{SP} is the temperature above which a given magnetic NC or an ensemble of NCs is in thermal equilibrium and is defined by $E_B = 25k_{\mathrm{B}}T_{\mathrm{SP}}$ [59], where k_{B} is the Boltzmann constant and the numerical factor 25 corresponds to the typical magnetometry probing time of 100 s.

Due to the fact that all considered layers contain γ'-$Ga_yFe_{4-y}N$ NCs, their size distribution is taken into account. For each NC, the individual $K_{\mathrm{eff}} = K_{\mathrm{mcr}} + K_{\mathrm{sh}}$, where $K_{\mathrm{mcr}} = (3 \times 10^5)\,\mathrm{erg/cm^3}$ is the magnitude of the cubic magnetocrystalline anisotropy parameter of γ'-Fe_4N [60], is calculated. The positive sign indicates that the magnetic easy axes are directed along the [100] direction, which is parallel to the c-axis of GaN. The shape contribution to the MA for each NC:

$$K_{\mathrm{sh}} = (N_A - N_C)M_{\mathrm{sat}}^2/2\,, \tag{3}$$

is determined by the difference $N_A - N_C$ of the demagnetizing coefficients N of the considered nanocrystals according to the ellipsoid with semi-axes A and C [61]. The experimental magnitude of $M_{\mathrm{sat}} = 1700\,\mathrm{emu/cm^3}$ established here is employed, considering that the main crystallographic axes of the NCs and their axes of revolution are aligned with those of the host lattice. The magnitudes of K_{mcr} and K_{sh} can be added with the *caveat* that all NCs with negative values of K_{eff} are discarded. This is because for $K_{\mathrm{eff}} < 0$ the easy plane of the magnetization M rotates smoothly by 180^o to facilitate the reversal and the NCs are at thermal equilibrium at any T, thus not contributing to TRM. Based on the data presented in Figure 4a, as much as 50% of the NCs belong to this category, a decisive factor for understanding the magnetic softness of the ensembles of NCs [18,19,24,37,38]. The large number of NCs in equilibrium explains also the low magnitude of M_{FC} (and M_{TRM}), i.e., less than 20% of the total saturation value. Finally, for nearly spherical NCs ($C/A \simeq 1$), where the cubic K_{mcr} prevails, $E_B = K_{\mathrm{eff}}V_{\mathrm{NC}}/4$ is set, as expected for cubic anisotropy exhibiting magnetic easy axes oriented along the $\langle 100 \rangle$ family of directions ($K_{\mathrm{mcr}}^{\mathrm{cubic}} > 0$) [62]. The calculated T_{SP} distribution as a function of the $K_{\mathrm{eff}}\,V_{\mathrm{NC}}/(25k_{\mathrm{B}})$ is depicted in Figure 9c and is in agreement with the experimental data in Figure 9b. The calculated distribution peaks around 40 K, decreases at higher temperatures, and remains non-zero up to 400 K, as found experimentally.

The non-conventional behavior of M_{ZFC} and M_{FC} of the GaδFeN/$Al_{0.1}Ga_{0.9}N$ structure probed for $H_\perp$ indicates that even at $T = 400$ K the field of 100 Oe is too weak to overcome the energy barriers. Therefore, direct TRM measurements to establish the actual magnitude of the low–T M_{TRM} are performed. To this end, the sample is cooled down at a saturating field of 10 kOe to $T = 2$ K, then the field is quenched and at $H \simeq 0$ the TRM measurement is performed while warming up. For comparison, the same sequence is executed for $H_\parallel$. The results and their T-derivatives are presented in Figure 9d,e, respectively. The magnitude of the irreversible response increases for the perpendicular orientation (empty symbols) to about 80% of the total magnetic saturation. Taking into account the significant MA of hexagonal ε-Fe_3N and the much weaker one of cubic γ'-$Ga_yFe_{4-y}N$, the 80% level is taken as a coarse estimate of the relative content of the ε-Fe_3N NCs in the layer grown on the $Al_{0.1}Ga_{0.9}N$ buffer.

Both TRMs remain non-zero even at 400 K. By extrapolating the curves to zero, with the maximum value of T_{SP} located at 500 K. This procedure is valid because the derivatives dM_{TRM}/dT increase as $T \to 400$ K. Interestingly, the T-derivative of M_{TRM} for the in-plane configuration is featureless and larger than the one established at low fields in the ZFC and FC measurements, suggesting that in these two measurements two different subsets of NCs determine the response.

The normalized magnetization M/M_{sat} of the layers as a function of the magnetic field is presented in Figure 10a,b, where both $M(H_\perp)$ and $M(H_\parallel)$ show the sensitivity of the magnetization to the orientation of H for the reference structure and for the GaδFeN/$Al_{0.1}Ga_{0.9}N$ layer, respectively.

The measured $M(H)$ saturates beyond ± 10 kOe and does not significantly depend on H in the whole studied T-range, as demonstrated earlier in Figure 7a for the reference sample and in previous studies [19,24]. A similar behavior is observed for all the layers deposited on the $Al_xGa_{1-x}N$ buffers.

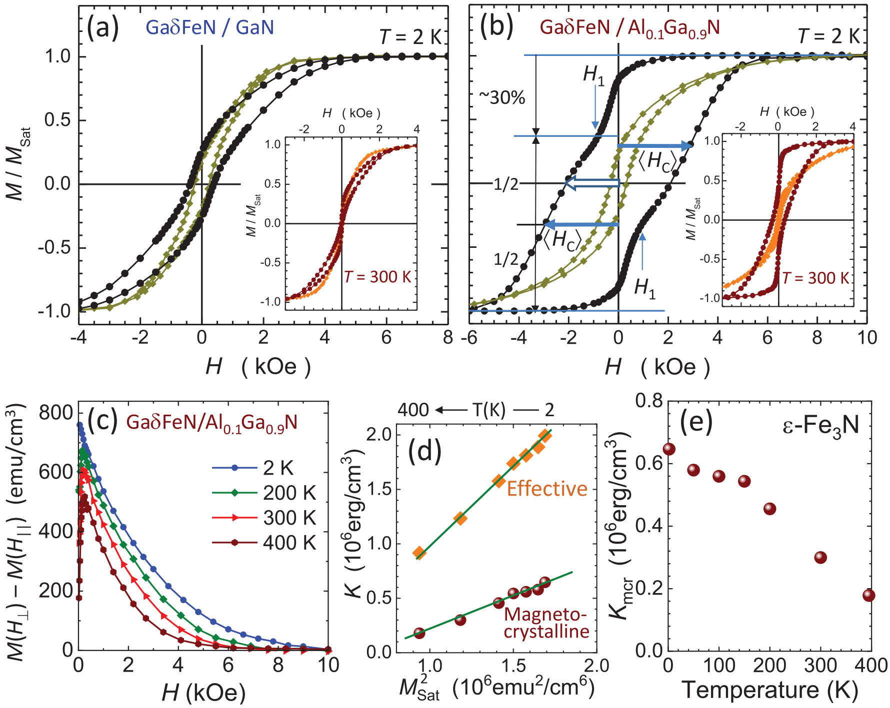

Figure 10. Normalized magnetization M/M_{sat} acquired at 2 K for the two magnetic field configurations $H_{\perp}$ (circles) and $H_{\parallel}$ (diamonds) for (**a**) the reference sample, and (**b**) GaδFeN/$Al_{0.1}Ga_{0.9}N$. The M/M_{sat} at 300 K as a function of the magnetic field is depicted in the insets. The vertical arrows mark an inflection point H_1 on $M(H_{\perp})$ separating two different contributions to M during its reversal. The empty arrow marks the coercive field of the whole ensemble, whereas the lengths of the two full arrows indicate the average coercive field $\langle H_C \rangle$ of the prolate part of the distribution. (**c**) Magnetic anisotropy $M(H_{\perp}) - M(H_{\parallel})$ obtained for the GaδFeN/$Al_{0.1}Ga_{0.9}N$ sample acquired at selected temperatures. (**d**) Magnitudes of K_{eff} established from the area under the curves in (**c**) plotted as the function of M^2_{Sat} (diamonds) and of K_{mcr} of ε-Fe_3N (bullets). Solid lines mark the proportionality of both K_{eff} and K_{mcr} to M^2_{Sat}. (**e**) Temperature dependence of K_{mcr} of ε-Fe_3N.

It is worth underlining that the main symmetry axes of the ε-Fe_3N NCs are fixed in the direction of the c-axis of GaN, i.e., perpendicular to the sample plane, which is essential for modelling the results. The uniaxial magnetocrystalline anisotropy (UMA) of the hexagonal ε-Fe_3N NCs was found to be between $(0.5\text{–}1 \times 10^6)$ emu/cm^3 [54] with the easy axis along the [0001]-direction. Due to preferential nucleation along the dislocations, the distribution of shapes of the ε-Fe_3N NCs is highly asymmetric, adding a sizeable shape contribution to the native crystalline UMA of ε-Fe_3N. The data presented in Figure 4c yield the average elongation $\langle C/A \rangle = 1.34$ for the prolate part of the distribution, what, according to Equation (3) and $M_{\mathrm{sat}} = 1300$ emu/cm^3, points to $\langle K_{\mathrm{sh}} \rangle = (1.2 \times 10^6)$ erg/cm^3, which represents the most relevant contribution to the overall MA of this ensemble.

The large UMA along the growth direction is the origin of the pronounced squareness and the resemblance of the experimental $m(H_{\perp})$ to the perpendicular magnetic anisotropy of bulk ferromagnets and layered structures. This is further demonstrated by the hard-axis-like shape of

$m(H_{\parallel})$. The magnitude of the UMA exerted by the considered ensemble of NCs is calculated by taking the experimental difference $\Delta M(H) = M(H_{\perp}) - M(H_{\parallel})$, plotted for selected temperatures in Figure 10c. By definition, the area under the $\Delta m(H)$ yields the magnitude of K_{eff}. The established magnitudes are plotted against the corresponding magnitudes of M_{sat}^2 in Figure 10d (diamonds). The nearly linear relationship $K_{\text{eff}} \propto M_{\text{sat}}^2$ confirms the significant UMA in this ensemble, allowing the direct determination from Equation 3 of K_{mcr} of ε-Fe_3N from the T–dependence of $m_{\text{NC}}^{\text{sat}}(T)$ (Figure 8). The resulting magnitudes of $K_{\text{mcr}} = K_{\text{eff}} - K_{\text{sh}}$ established at all the measured temperatures, are shown in Figure 10e (bullets). This is the first direct determination of the absolute magnitudes of K_{mcr} of ε-Fe_3N in such a broad and technologically relevant temperature range up to 400 K.

On the other hand, as indicated in Figure 10b, the magnetization process in the GaδFeN/$Al_xGa_{1-x}N$ structures is based on two rather independent switching processes. This is seen at the two temperatures exemplified in Figure 10b. The $T = 2$ K case, where the thermal activation contribution to $m(H)$ can be neglected, is considered in detail. Here, about a third of the total magnetization of the NCs switches at very weak fields. This process completes at weak negative fields, where a kink is seen in $m(H_{\perp})$ at about ±1 kOe, marked by the arrows at H_1. Up to H_1 about 30% of the total M has switched or rotated to the new direction of H. This is the result of a narrow band of weak switching fields brought about by the minority of the oblate NCs (which nominally reverse M at $H = 0$) and of several cubic γ'-$Ga_yFe_{4-y}N$ NCs, which reverse M at weak fields, as demonstrated in Figure 10a. For the remaining 70% NCs, the switching process begins after $H_{\perp}$ passes H_1 and these are the prolate ε-Fe_3N NCs, which, due to their generally high K_{eff} require larger magnitudes of H to overcome the individual anisotropy fields $H_A = 2K_{\text{eff}}/M_{\text{sat}}$. Since the majority of the NCs is in the single domain state, the different magnitudes of H_A contribute to a broad distribution of switching (coercive) fields H_C, resulting in the wide $m(H_{\perp})$ for $|H| > |H_1|$. From the magnitude of $\langle K_{\text{eff}} \rangle$, $\langle H_C \rangle = 3$ kOe at low temperatures is obtained and it is also extrapolated directly from the $m(H)$ curve in Figure 10b. Since the reversal process of M of the prolate fraction of the NCs ensemble in the GaδFeN/$Al_xGa_{1-x}N$ structures starts after the magnetically soft part of the ensemble has reversed, the H_C cannot be determined at $M = 0$. The $m(H)$ after H_1 is assigned to the prolate ε-Fe_3N, marked by the arrows in Figure 10b, from where the corresponding $\langle H_C \rangle$ can be obtained. It is worth noting that the difference in $\langle H_C \rangle$ between the two branches of $m(H_{\perp})$ corresponds to the magnitude of the soft part of M which switches within $|H| < |H_1|$, *i.e.* the magnetically hard part of $m(H_{\perp})$ corresponding to the prolate NCs is broken up by the magnetically soft component of the distribution.

4. Conclusions

Strained and partially relaxed GaδFeN thin layers grown on $Al_xGa_{1-x}N$ buffers by MOVPE reveal the formation of hexagonal ε-Fe_3N and fcc γ'-$Ga_yFe_{4-y}N$ nanocrystals epitaxially embedded in the GaN matrix. The GaδFeN layers are strained for an Al concentration in the buffer up to 10% and then relax up to 85% for an Al concentration of 41%. With increasing Al content, an increase in the dislocation density in the buffer layers is observed, together with a preferential aggregation of nanocrystals along the dislocations in the GaδFeN layers. The NCs have either oblate or prolate shape, with the majority of the NCs being prolate. Both nanocrystal phases are coherently embedded into the surrounding GaN matrix with an epitaxial relation: $[0001]_{\text{NC}} \parallel [0001]_{\text{GaN}}$ and $\langle 11\bar{2}0\rangle_{\text{NC}} \parallel \langle 10\bar{1}0\rangle_{\text{GaN}}$ for the ε-Fe_3N NCs, and $[001]_{\text{NC}} \parallel [0001]_{\text{GaN}}$ and $\langle 110\rangle_{\text{NC}} \parallel \langle 11\bar{2}0\rangle_{\text{GaN}}$ for the γ'-$Ga_yFe_{4-y}N$ NCs.

The magnetic response of the layers is consistent with the one previously found for phase-separated (Ga,Fe)N consisting of two components: a dominant paramagnetic low-T contribution from Fe^{3+} ions dilute in the GaN matrix and in the buffer volume, and a ferromagnetic one dominant above 50 K originating from the γ'-$Ga_yFe_{4-y}N$ and the ε-Fe_3N embedded NCs [37,38]. The low–T contribution of the Fe^{3+} ions to the total magnetization reaches magnitudes comparable to those of the NCs. The T_C of the reference layer containing solely γ'-$Ga_yFe_{4-y}N$ is found to be (630 ± 30) K, pointing at the inclusion of Ga into the NCs and therefore lowering the T_C with respect to one of γ'-Fe_4N [6]. Due to the formation of additional ε-Fe_3N in the GaδFeN/$Al_xGa_{1-x}N$ layers, T_C is increased to (670 ± 30) K, indicating a high crystalline and chemical quality of the NCs. Moreover, the calculated magnetization of the NCs is consistent with literature values. The magnetization process in the GaδFeN/Al$_x$Ga$_{1-x}$N structures is based on two substantially independent switching processes: a relatively fast switching of the oblate and γ'-Ga$_y$Fe$_{4-y}$N NCs at low fields, followed by the switching of the ε-Fe$_3$N NCs, which require larger magnitudes of H to overcome the individual anisotropy fields. All GaδFeN layers grown on the Al$_x$Ga$_{1-x}$N buffers exhibit a sizeable uniaxial magnetic anisotropy with the easy axis matching the c-axis of the hexagonal ε-Fe$_3$N NCs and the $[0001]$ growth direction of the layers. This suggests that the formation of ordered elongated hexagonal ε-Fe$_3$N NCs along the dislocations in the Al$_x$Ga$_{1-x}$N buffers is responsible for the observed out-of-plane magnetic anisotropy. The finding is substantiated by the value of H_C obtained directly from the normalized magnetization for $H_\perp$ that is well reproduced by the calculated value obtained considering the K_{eff} of the prolate ε-Fe$_3$N NCs. Significantly, this is the first direct determination of the absolute magnitudes of K_{mcr} of ε-Fe$_3$N in a broad and technologically relevant temperature range up to 400 K.

According to these findings, GaδFeN/Al$_x$Ga$_{1-x}$N heterostructures provide a controllable housing for stabilizing ordered arrays of ferromagnetic Fe$_y$N compounds, opening wide perspectives for spin injection in these phase-separated material systems and for the electric-field manipulation of the magnetization [63].

Supplementary Materials: The following are available at http://www.mdpi.com/1996-1944/13/15/3294/s1, Figure S1: EDX line-scans *vs.*depth, and Figure S2: Angular dependence of the FMR signal.

Author Contributions: Conceptualization, A.N.-Q.; Data curation, A.N.-Q.; Formal analysis, A.N.-Q., K.G., T.T., V.B., M.M., D.K., A.N., H.G. and M.S.; Funding acquisition, A.N.-Q., H.G., M.S. and A.B.; Investigation, A.N.-Q., K.G., T.T., V.B., M.M., D.K. and M.S.; Resources, A.N.-Q.; Visualization, A.N.-Q.; Writing—original draft, A.N.-Q., T.T., K.G. and M.S.; Writing—review and editing, A.N.-Q. and A.B. All authors have read and agreed to the published version of the manuscript.

Funding: The work has been funded by the Austrian Science Fund FWF Projects No. V478-N36, P26830 and P31423, and the Austrian Exchange Service (ÖAD) Project No. PL-01/2017 (DWM.WKE.183.72.2017). The financial support by the Austrian Federal Ministry for Digital and Economic Affairs, the National Foundation for Research, Technology and Development and the Christian Doppler Research Association is gratefully acknowledged.

Acknowledgments: The authors greatly acknowledge Werner Ginzinger for his extensive work in the sample preparation and on TEM measurements. Open Access Funding by the Austrian Science Fund (FWF).

Conflicts of Interest: The authors declare no conflict of interest.

References

1. Jack, K.H. The Iron-Nitrogen System: The Crystal Structures of ε-Phase Iron Nitrides. *Acta Cryst.* **1952**, *5*, 404. [CrossRef]
2. Eck, B.; Dronskowski, R.; Takahashi, M.; Kikkawa, S. Theoretical calculations on the structures, electronic and magnetic properties of binary 3d transition metal nitrides. *J. Mater. Chem.* **1999**, *9*, 1527–1537. [CrossRef]
3. Gölden, D.; Hildebrandt, E.; Alff, L. The film phase diagram of iron nitrides grown by molecular beam epitaxy. *J. Magn. Mag. Mater.* **2017**, *422*, 407–411. [CrossRef]
4. Coey, J.; Smith, P. Magnetic nitrides. *J. Magn. Magn. Mater.* **1999**, *200*, 405–424. [CrossRef]
5. Leineweber, A.; Jacobs, H.; Hüning, F.; Lueken, H.; Schilder, H.; Kockelmann, W. ϵ-Fe3N: magnetic structure, magnetization and temperature dependent disorder of nitrogen. *J. Alloy. Comp.* **1999**, *288*, 79–87. [CrossRef]
6. Shirane, G.; Takei, W.J.; Ruby, S.L. Mössbauer Study of Hyperfine Fields and Isomer Shifts in Fe$_4$N and (Fe,Ni)$_4$N. *Phys. Rev.* **1962**, *1*, 49–52. [CrossRef]
7. Kokado, S.; Fujima, N.; Harigaya, K.; Shimizu, H.; Sakuma, A. Theoretical analysis of highly spin-polarized transport in the iron nitride Fe$_4$N. *Phys. Rev. B* **2006**, *73*, 172410. [CrossRef]
8. Shirane, G.; Takei, W.J.; Ruby, S.L. Spin polarization of Fe$_4$N thin films determined by point-contact Andreev reflection. *Appl. Phys. Lett.* **2009**, *94*, 202502.
9. Tao, Z.K.; Cui, X.G.; Zhang, R.; Xiu, X.Q.; Xie, Z.L.; Zheng, Y.D. Ferromagnetic Fe$_3$N films grown on GaN(0002) substrates by MOCVD. *J. Cryst. Growth* **2010**, *312*, 1525–15258. [CrossRef]

10. Fang, H.; Zhang, R.; Liu, B.; Tao, Z.; Wang, X.; Xie, Z.; Xiu, X.; Zheng, Y. Magnetic and electrical properties of ϵ-Fe_3N on c-plane GaN. *J. Phys. D: Appl. Phys.* **2012**, *45*, 315002. [CrossRef]
11. Kimura, M.; Kasawara, S. Growth evolution of γ'-Fe_4N films on GaN(0001) and their interfacial structure. *Jap. J. Appl. Phys.* **2016**, *55*, 05FD02. [CrossRef]
12. Navarro-Quezada, A.; Devillers, T.; Li, T.; Bonanni, A. Tuning the Size, Shape and Density of γ'-$Ga_yFe_{4-y}N$ Nanocrystals Embedded in GaN. *Crystals* **2019**, *9*, 50. [CrossRef]
13. Navarro-Quezada, A.; Devillers, T.; Li, T.; Bonanni, A. Planar arrays of magnetic nanocrystals embedded in GaN. *Appl. Phys. Lett.* **2012**, *101*, 081911. [CrossRef]
14. Rebaza, A.V.G.; Desimoni, J.; Kurian, S.; abd Namdeo S. Gajbhiye, S.B.; y Blancá, E.L.P. Ab Initio Study of the Structural, Electronic, Magnetic and Hyperfine Properties of $Ga_xFe_{4-x}N$ ($0.00 \leq x \leq 1.00$) Nitrides. *J. Phys. Chem. C* **2011**, *115*, 23081–23089. [CrossRef]
15. Houeben, A.; Burghaus, J.; Dronskowski, R. The Ternary Nitrides $GaFe_3N$ and $AlFe_3N$: Improved Synthesis and Magnetic Properties. *Chem. Mater.* **2009**, *21*, 4332–4338. [CrossRef]
16. Jungwirth, T.; Martí, X.; Wadley, P.; Wunderlich, J. Antiferromagnetic spintronics. *Nat. Nanotech.* **2016**, *11*, 231. [CrossRef]
17. Grois, A.; Devillers, T.; Li, T.; Bonanni, A. Planar array of self-assembled $Ga_xFe_{4-x}N$ nanocrystals in GaN: magnetic anisotropy determined via ferromagnetic resonance. *Nanotechnology* **2014**, *25*, 395704. [CrossRef]
18. Bianco, L.D.; Spizzo, F.; Li, T.; Adhikari, R.; Bonanni, A. Influence of Mn co-doping on the magnetic properties of planar arrays of $Ga_xFe_{4-x}N$ nanocrystals in a GaN matrix. *Phys. Chem. Chem. Phys.* **2018**, *20*, 25411. [CrossRef]
19. Navarro-Quezada, A.; Aiglinger, M.; Faina, B.; Gas, K.; Matzer, M.; Li, T.; Adhikari, R.; Sawicki, M.; Bonanni, A. Magnetotransport in phase-separated (Ga,Fe)N with γ'-$Ga_yFe_{4-y}N$ nanocrystals. *Phys. Rev. B* **2019**, *99*, 085201. [CrossRef]
20. Nikolaev, K.; Krivorotov, I.; Dahlberg, E.; Vas'ko, V.; Urazdhin, S.; Loloee, R.; Pratt, W. Structural and magnetic properties of triode-sputtering Fe4N epitaxial films on SrTiO3(001) substrates. *Appl. Phys. Lett.* **2003**, *82*, 98. [CrossRef]
21. Li, T.; Simbrunner, C.; Navarro-Quezada, A.; Wegscheider, M.; Quast, M.; Litvinov, D.; Gerthsen, D.; Bonanni, A. Phase-dependent distribution of Fe-rich nanocrystals in MOVPE-grown (Ga,Fe)N. *J. Cryst. Growth* **2008**, *310*, 3294–3298. [CrossRef]
22. Moram, M.A.; Vickers, M.E. X-ray diffraction of III-nitrides. *Rep. Prog. Phys.* **2009**, *72*, 036502. [CrossRef]
23. Vegard, L. Die Konstitution der Mischkristalle und die Raumfüllung der Atome. *Z. Phys.* **1921**, *5*, 17–26. [CrossRef]
24. Gas, K.; Sawicki, M. In situ compensation method for high-precision and high-resistivity integral magnetometry. *Meas. Sci. Technol.* **2019**, *30*, 8. [CrossRef]
25. Sawicki, M.; Stefanowicz, W.; Ney, A. Sensitive SQUID magnetometry for studying nanomagnetism. *Semicond. Sci. Technol.* **2011**, *26*, 064006. [CrossRef]
26. Pereira, L.M.C. Experimentally evaluating the origin of dilute magnetism in nanomaterials. *J. Phys. D: Appl. Phys.* **2017**, *50*, 393002. [CrossRef]
27. Liapina, T.; Leinweber, A.; Mittemeijer, E.J.; Kockelmann, W. The lattice parameters of ϵ-iron nitrides: lattice strains due to a varying degree of nitrogen ordering. *Acta Mater.* **2004**, *52*, 173–180. [CrossRef]
28. Navarro-Quezada, A. Magnetic Nanostructures Embedded in III-Nitrides: Assembly and Performance *Crystals* **2020**, *10*, 359. [CrossRef]
29. Navarro-Quezada, A.; Truglas, T.; Bauernfeind, V.; Ginzinger, W.; Matzer, M.; Ney, A.; Groiss, H.; Bonanni, A. Perpendicular magnetic anisotropy in $Ga\delta FeN/Al_xGa_{1-x}N$ heterostructures. *arXiv* **2020**, arXiv:2001.07375.
30. Fewster, P.F.; Andrew, N.L. Strain analysis by X-ray diffraction. *Thin Solid Films* **1998**, *319*, 1–8. [CrossRef]
31. Morkoç, H. *Handbook of Nitride Semiconductors and Devices*; WILEY-VCH: Weinheim, Germany, 2008.
32. Dunn, C.G.; Koch, E.F. Comparison of dislocation densities of primary and secondary recrystallisation grains of Si-Fe. *Acta Metall.* **1957**, *5*, 548. [CrossRef]
33. Metzger, T.; Höpler, R.; Born, E.; Ambacher, O.; Stutzmann, M.; Stömmer, M.; Schuster, R.; Göbel, H.; Christiansen, S.; Albrecht, M.; Strunk, H. Defect structure of epitaxial GaN films determined by transmission electron microscopy and triple-axis X-ray diffractometry. *Acta Mater.* **2004**, *52*, 173–180. [CrossRef]
34. Schindelin, J.; Arganda-Carrera, I.; Frise, E. Fiji: an open-source platform for biological-image analysis. *Nat. Methods* **2012**, *9*, 676–682. [CrossRef] [PubMed]

35. Stadelmann, P.A. JEMS—A Software Package for Electron-Diffraction Analysis and Hrem Image Simulation in Material Science. *Ultramicroscopy* **1987**, *21*, 131–145. [CrossRef]
36. Przybylińska, H.; Bonanni, A.; Wolos, A.; Kiecana, M.; Sawicki, M.; Dietl, T.; Malissa, H.; Simbrunner, C.; Wegscheider, M.; Sitter, H.; et al. Magnetic properties of a new spintronic material — GaN:Fe. *Mater. Sci. Eng. B* **2006**, *126*, 222–225. [CrossRef]
37. Bonanni, A.; Kiecana, M.; Simbrunner, C.; Li, T.; Sawicki, M.; Wegscheider, M.; Quast, M.; Przybylinska, H.; Navarro-Quezada, A.; Jakieła, R.; et al. Paramagnetic GaN:Fe and ferromagnetic (Ga,Fe)N: The relationship between structural, electronic, and magnetic properties. *Phys. Rev. B* **2007**, *75*, 125210. [CrossRef]
38. Navarro-Quezada, A.; Stefanowicz, W.; Li, T.; Faina, B.; Rovezzi, M.; Lechner, R.T.; Devillers, T.; d'Acapito, F.; Bauer, G.; Sawicki, M.; et al. Embedded magnetic phases in (Ga,Fe)N: Key role of growth temperature. *Phys. Rev. B* **2010**, *81*, 205206. [CrossRef]
39. Jakieła, R.; Gas, K.; Sawicki, M.; Barcz, A. Diffusion of Mn in gallium nitride: Experiment and modelling. *J. Alloys Compd.* **2019**, *771*, 215–220. [CrossRef]
40. Bean, C.P.; Jacobs, I.S. Magnetic Granulometry and Super-Paramagnetism. *J. Appl. Phys.* **1956**, *27*, 1448–1452. [CrossRef]
41. Nielsen, M.D.; Levin, E.M.; Jaworski, C.M.; Schmidt-Rohr, K.; Heremans, J.P. Chromium as resonant donor impurity in PbTe. *Phys. Rev. B* **2012**, *85*, 045210. [CrossRef]
42. Sawicki, M.; Guziewicz, E.; Łukasiewicz, M.I.; Proselkov, O.; Kowalik, I.A.; Lisowski, W.; Dluzewski, P.; Wittlin, A.; Jaworski, M.; Wolska, A.; et al. Homogeneous and heterogeneous magnetism in (Zn,Co)O: From a random antiferromagnet to a dipolar superferromagnet by changing the growth temperature. *Phys. Rev. B* **2013**, *88*, 085204. [CrossRef]
43. Pacuski, W.; Kossacki, P.; Ferrand, D.; Golnik, A.; Cibert, J.; Wegscheider, M.; Navarro-Quezada, A.; Bonanni, A.; Kiecana, M.; Sawicki, M.; et al. Observation of Strong-Coupling Effects in a Diluted Magnetic Semiconductor $Ga_{1-x}Fe_xN$. *Phys. Rev. Lett.* **2008**, *100*, 037204. [CrossRef] [PubMed]
44. Malguth, E.; Hoffmann, A.; Phillips, M.R. Fe in III-V and II-VI semiconductors. *Phys. Status Solidi B* **2008**, *245*, 455. [CrossRef]
45. Xiao, J.Q.; Chien, C.L. Radio frequency reactive sputtered iron nitrides using ammonia gas: Structure and magnetic properties. *Appl. Phys. Lett.* **1994**, *64*, 384–386. [CrossRef]
46. Atiq, S.; Ko, H.S.; Siddiqi, S.A.; Shin, S.C. Effect of epitaxy and lattice mismatch on saturation magnetization of γ'-Fe_4N thin films. *Appl. Phys. Lett.* **2008**, *92*, 222507. [CrossRef]
47. Dirba, I.; Yazdi, M.B.; Radetinac, A.; Komissinskiy, P.; Flege, S.; Gutfleisch, O.; Alff, L. Growth, structure, and magnetic properties of γ-Fe_4N thin films. *J. Magn. Magn. Mater.* **2015**, *379*, 151–155. [CrossRef]
48. Bhattacharyya, S.; Shivaprasad, S.; Gajbhiye, N. Variation of magnetic ordering in ε-Fe_3N nanoparticles. *Chem. Phys. Lett.* **2010**, *496*, 122–127. [CrossRef]
49. Robbins, M.; White, J. Magnetic properties of epsilon-iron nitride. *J. Phys. Chem. Solids* **1964**, *25*, 717–720. [CrossRef]
50. Wu, X.; Zhong, W.; Tang, N.; Jiang, H.; Liu, W.; Du, Y. Magnetic properties and thermal stability of nanocrystalline ε-Fe_3N prepared by gas reduction-nitriding method. *J. Alloys Compd.* **2004**, *385*, 294–297. [CrossRef]
51. Siberchicot, B.; Vast, N.; Matar, S. Band-structure calculation of the magnetocrystalline anisotropy energy of Fe_3N. *Int. J. Mod Phys B* **1993**, *07*, 01n03. [CrossRef]
52. Yamaguchi, K.; Yui, T.; Yamaki, K.; Kakeya, I.; Kadowaki, K.; Suemasu, T. Epitaxial growth of ferromagnetic ε-Fe_3N films on Si(111) substrates by molecular beam epitaxy. *J. Cryst. Growth* **2007**, *301–302*, 597–601. [CrossRef]
53. Zieschang, A.M.; Bocarsly, J.D.; Dürrschnabel, M.; Molina-Luna, L.; Kleebe, H.J.; Seshadri, R.; Albert, B. Nanoscale Iron Nitride, ε-Fe_3N: Preparation from Liquid Ammonia and Magnetic Properties. *Chem. Mater.* **2017**, *29*, 621–628. [CrossRef]
54. Mamiya, M.; Nakatani, I.; Furubayashi, T.; Ohnuma, M. Analyses of Superparamagnetism - Magnetic Proprties of Isolated Iron-Nitride Nanoparticles. *Trans. Magn. Soc. Japan* **2002**, *2*, 36–48. [CrossRef]
55. Burghaus, J.; Sougrati, M.; Moechel, A.; Houben, A.; Hermann, R.P.; Dronskowski, R. Local ordering and magnetism in Ga0.9Fe3.1N. *J. Solid State Chem.* **2011**, *184*, 2315. [CrossRef]

56. Mukasyan, A.S.; Roslyakov, S.; Pauls, J.M.; Gallington, L.C.; Orlova, T.; Liu, X.; Dobrowolska, M.; Furdyna, J.K.; Manukyan, K.V. Nanoscale Metastable ε-Fe_3N Ferromagnetic Materials by Self-Sustained Reactions. *Inorg. Chem.* **2019**, *58*, 5583–5592. [CrossRef]
57. Gajbhiye, N.; Bhattacharyya, S. Spin-glass-like ordering in ε-$Fe_{3-x}Ni_xN$ ($0. \leq x \leq 0.8$) nanoparticles. *Mater. Chem. Phys.* **2008**, *108*, 201–207. [CrossRef]
58. Dormann, J.L.; Fiorani, D.; Tronc, E. Magnetic Relaxation in Fine-Particle Systems. *Adv. Chem. Phys.* **1997**, *98*, 283.
59. Bean, C.P.; Livingston, J.D. Superparamagnetism. *J. Appl. Phys.* **1959**, *30*, S120–S129. [CrossRef]
60. Coey, J. *Magnetism and Magnetic Materials*; Cambridge University Press: Cambridge, UK, 2010; p. 408.
61. Osborn, J.A. Demagnetizing Factors of the General Ellipsoid. *Phys. Rev.* **1945**, *67*, 351–357. [CrossRef]
62. Walker, M.; Mayo, P.I.; OGrady, K.; Charles, S.W.; Chantrell, R.W. The magnetic properties of single-domain particles with cubic anisotropy. I. Hysteresis loops. *J. Phys.: Condens. Matter* **1993**, *5*, 2779–2792. [CrossRef]
63. Sztenkiel, D.; Foltyn, M.; Mazur, G.; Adhikari, R.; Kosiel, K.; Gas, K.; Zgirski, M.; Kruszka, R.; Jakieła, R.; Li, T.; et al. Stretching magnetism with an electric field in a nitride semiconductor. *Nat. Commun.* **2016**, *7*, 13232. [CrossRef] [PubMed]

materials

MDPI

Article

Following the Martensitic Configuration Footprints in the Transition Route of Ni-Mn-Ga Magnetic Shape Memory Films: Insight into the Role of Twin Boundaries and Interfaces

Milad Takhsha Ghahfarokhi, Lucia Nasi, Francesca Casoli, Simone Fabbrici, Giovanna Trevisi, Riccardo Cabassi and Franca Albertini *

Institute of Materials for Electronics and Magnetism, National Research Council (IMEM-CNR), Parco Area delle Scienze 37/A, 43124 Parma, Italy; milad.takhsha@imem.cnr.it (M.T.G.); lucia.nasi@imem.cnr.it (L.N.); francesca.casoli@imem.cnr.it (F.C.); simone.fabbrici@imem.cnr.it (S.F.); giovanna.trevisi@imem.cnr.it (G.T.); riccardo.cabassi@imem.cnr.it (R.C.)

* Correspondence: franca.albertini@imem.cnr.it

Received: 22 March 2020; Accepted: 28 April 2020; Published: 1 May 2020

Abstract: Magnetic shape memory Heuslers have a great potential for their exploitation in next-generation cooling devices and actuating systems, due to their "giant" caloric and thermo/magnetomechanical effects arising from the combination of magnetic order and a martensitic transition. Thermal hysteresis, broad transition range, and twinning stress are among the major obstacles preventing the full exploitation of these materials in applications. Using Ni-Mn-Ga seven-modulated epitaxial thin films as a model system, we investigated the possible links between the phase transition and the details of the twin variants configuration in the martensitic phase. We explored the crystallographic relations between the martensitic variants from the atomic-scale to the micro-scale through high-resolution techniques and combined this information with the direct observation of the evolution of martensitic twin variants vs. temperature. Based on our multiscale investigation, we propose a route for the martensitic phase transition, in which the interfaces between different colonies of twins play the major role of initiators for both the forward and reverse phase transition. Linking the martensitic transition to the martensitic configuration sheds light onto the possible mechanisms influencing the transition and paves the way towards microstructure engineering for the full exploitation of shape memory Heuslers in different applications.

Keywords: martensitic transition; Heusler alloys; magnetic shape memory alloys; twin boundary; epitaxial Ni-Mn-Ga films; transmission electron microscopy

1. Introduction

Magnetic shape memory Heuslers provide new concepts for magnetic field-driven actuation [1,2], energy harvesting [3], and solid-state cooling technology [4] thanks to the magnetostructural martensitic phase transition and the giant magnetic field-induced strain, which has been reported in bulk single crystals as orders of magnitude higher than piezoelectric and magnetostrictive counterparts [5,6].

Ni-Mn-Ga films are a model system for magnetic shape memory materials. By exploiting epitaxial growth on different substrates, suitable growth conditions (including stress), and geometrical parameters (e.g., thickness) high quality and suitably oriented epitaxial films can be obtained. They allow accurate studies of structure and magnetism at the different length scales [7–9]. Despite their different martensitic configuration with respect to bulk materials, thin films also provide a suitable platform to study the role of intrinsic and extrinsic properties in the martensitic transformation process and formulate models that can be extended to bulk materials [10,11].

Being a type of thermoelastic material, epitaxial Ni-Mn-Ga films form interrelated 3D hierarchical patterns of twin boundaries in the martensitic phase to compensate the shear stress caused by the symmetry reduction during the martensitic phase transition from the cubic austenitic phase to the lower symmetry martensitic phase. The symmetry operator(s) for the twin boundaries connecting twin variants, is (are) rotation or (and) mirror [12–15]. The hierarchical nature of the originating from the self-accommodation occurring at the transition covers a broad range from nanoscale to macroscale [16].

For all the above-mentioned applications, the material cyclically undergoes one of the following phenomena.

(1) Martensitic phase transition induced by magnetic field, stress, or temperature.
(2) Magnetic field-induced reorientation of the twin variants in the martensitic phase.

The first phenomenon is based on the magnetostructural phase transition between the high-temperature austenitic and the low-temperature martensitic phases, while the latter only occurs in the low-temperature phase. It originates from the high magnetocrystalline anisotropy of the martensitic cells, which favors the alignment of the crystal cells in such a way that the magnetization easy axes of the cells are parallel to the external magnetic field [4]. It is well known that a few obstacles, stemming from both the intrinsic and extrinsic characteristics of the material, prevent the full exploitation of the aforementioned properties in applications. Among the obstacles are the thermal and magnetic hysteresis [17], broadness of the transition [18], and twinning stress [19], which are affected by several parameters, e.g., composition, chemical order, crystal structure, geometric compatibility of the martensite and austenite [20], dynamics of the transition [21], internal stress, and crystal defects. The two latter parameters are strongly linked to the configuration of the twin variants in the martensitic phase, which covers a long range from nano- to macro-scale [7,22,23].

Therefore, in order to find possible solutions to overcome these obstacles, it is necessary to gain a comprehensive view of the configuration of the twin variants at the different length scales and its evolution upon martensitic phase transition. In the literature, there are a few works focused on the crystallographic structures and the martensitic configurations of epitaxial Ni-Mn-Ga thin films through experiments and models [7–10,24–26]. However, the knowledge about the multiscale hierarchical self-accommodation of the twin variants in the martensitic phase and its possible links to the transition route is still limited, mainly due to lack of direct multiscale observation.

In this article, we report a multiscale study of martensitic Ni-Mn-Ga epitaxial films, characterized by a seven-fold incommensurate monoclinic superstructure with lattice modulation along the [001] crystallographic direction of the monoclinic setting [27]. In the martensitic phase, we directly visualize the crystallography of the epitaxial films, the symmetry relations between the twin boundaries and the interfaces between the different colonies of twin boundaries. We make use of various transmission electron microscopy (TEM) techniques with resolution from the atomic- to the micro-scale. This enables us to characterize the twin boundaries in a large-scale range. Our direct observations through TEM techniques in cross-sectional view are combined with atomic force microscopy (AFM) topography imaging vs. temperature. We propose a route for the martensitic forward and reverse transitions of the films, highlighting the major role played by the different martensitic interfaces.

2. Materials and Methods

2.1. Experimental

Epitaxial Ni-Mn-Ga films (200 nm) were prepared using radio frequency (RF) sputtering technique at elevated temperature (623 K) with a deposition rate of 0.1 nm s^{-1} and an Ar pressure of 1.5 Pa. The first sample (#1) was grown directly on (100) MgO followed by post-annealing (3600 s at 623 K in 10^{-3} mPa) and local mechanical stress (normal to the substrate, straining the film along the edge of MgO). The applied stress value was estimated to be >20 MPa, as described in [7], where complementary and detailed results on this sample can be found. The second sample (#2) was grown on 50 nm Cr underlayer, and in turn grown on the (100) MgO substrate. No post-growth treatment was performed for this sample. The composition measurement was performed using energy dispersive X-ray spectroscopy (EDS, EDAX detector, NJ, USA), obtaining $Ni_{52.7}Mn_{19.9}Ga_{27.4}$, $Ni_{53.0}Mn_{20.3}Ga_{26.7}$, for samples #1 and #2, respectively (uncertainty 1.0%). Atomic and magnetic force microscopy (Veeco Dimension 3100, CA, USA) imaging (supplementary material Figure S1) confirmed the X-type microstructure for the as-grown samples [26]. For sample #1, Y-type configuration stripes were induced by mechanical stress [7]. The details of X- and Y-microstructures are reported in Section 2.2. Different TEM techniques were performed with a JEOL 2200FS microscope (Tokyo, Japan) working at 200kV, i.e., high-angle angular dark-field scanning transmission electron microscopy (HAADF), high-resolution transmission electron microscopy (HR-TEM, Instrument), and selected-area electron diffraction (SAED). The lamellas for TEM observations were prepared parallel to [100] MgO (sample #1) and [1−10] MgO (sample #2) by focused ion beam lift-off technique using a Zeiss Auriga Compact scanning electron microscopy (Jena, Germany) equipped with Focused Ion Beam (FIB). Iso-field magnetic curves over temperature were measured by superconducting quantum interference device (SQUID) magnetometer (Quantum Design, CA, USA). In situ atomic force microscopy imagining versus temperature were measured by Dimension 3100 equipped with Nanoscope Veeco controller (Veeco Dimension 3100, CA, USA) using MESP-V2 tips.

2.2. Basic Concepts on the Crystallography of the Twin Boundaries

Figure 1a shows the martensitic cell in the monoclinic (red) and the austenitic setting (black) with respect to the MgO substrate directions. The martensitic seven modulation direction (MD) is along c′ in the monoclinic setting, whereas it is along one of the <110> directions in the austenitic setting. The easy magnetization direction in the two settings is b′ = c. In epitaxial Ni-Mn-Ga films, differently from the bulk single crystals, the six {101} planes of the cubic austenitic cells are not equivalent. As shown in Figure 1b, the two planes which are normal to the substrate plane are closely aligned to the martensitic twin boundaries called Y-type, where the magnetic easy axis alternates in the plane of the film (Figure 1c). The four remaining {101} planes of the austenitic cells, which are 45° inclined with respect to the substrate, are closely aligned to the martensitic twin boundaries called X-type. For these configurations, the easy magnetization axis of the martensitic cell alternates in and out of the plane of the film (Figure 1c) [9]. As shown in Figure 1b, the six orientations of twin boundaries in X- and Y-type regions are conjugated in three pairs, i.e., Y1–Y2, X1–X2, and X3–X4, and give rise to a typical microstructure characterized by twin variants only oriented at 45° or at 90° with respect to the substrate plane.

From the crystallographic point of view, X- and Y-type twin boundaries separate regions following strict twinning relations (Figure 1d). The twinning operators are mirror or (and) rotation. Therefore, based on theoretical models within the continuum theory of martensite, we introduce three atomically sharp crystallographic twin boundaries, which are observed in our epitaxial films (for the crystallographic description, see the Results section):

(1) Type I twin boundary, where the a and c axes of the martensitic cells (austenitic setting) alternate through a mirror plane (K1 is the twinning plane, left panels in Figures 2e and 3d).

(2) Type II twin boundary, in which the a and c axes of the martensitic cells (austenitic setting) alternate by a 180° rotation (around the η1 axis, middle panel in Figure 2e and right panel in Figure 3d).

(3) Modulation twin boundaries (MTB), where only the modulation direction of the martensitic cells alternates across the boundary (right panel in Figure 2e). In this type of boundary, both twinning symmetry relations are satisfied [12,28,29].

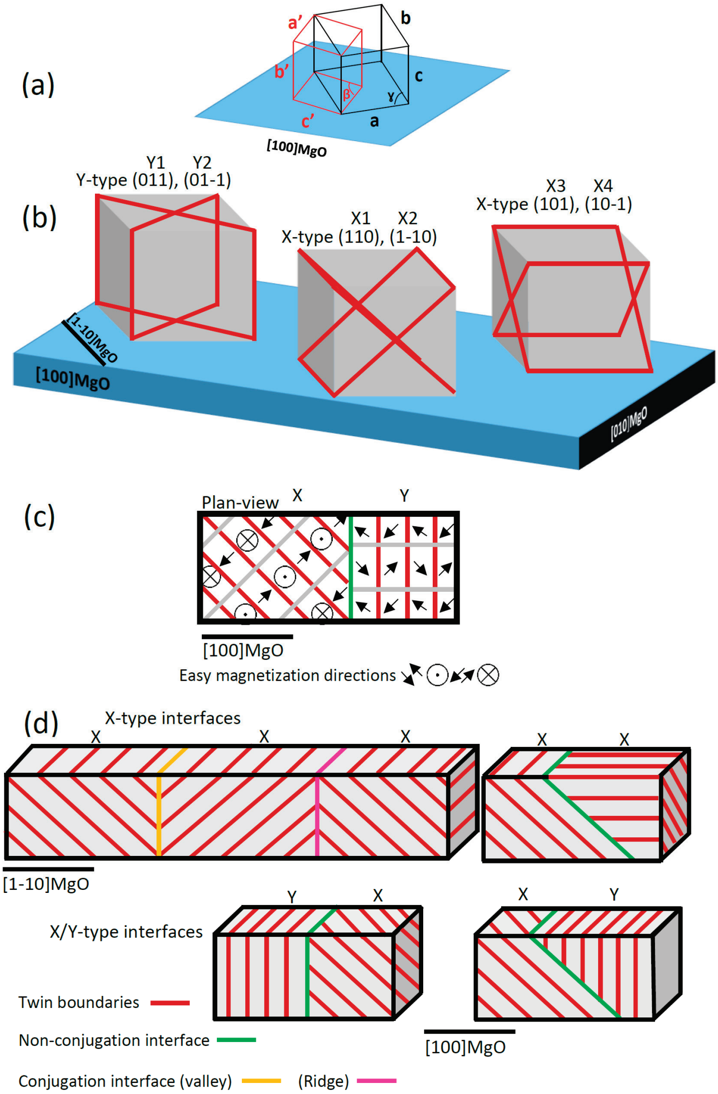

Figure 1. (**a**) Schematic representation of the relative orientations between the standard martensitic (red) and the austenitic setting (black) with respect to the MgO substrate directions. The indices show the three axes of the martensitic cell in the two represented settings. The martensitic seven modulation direction is along c′, whereas it is along one of the <110> directions in the austenitic setting. The easy magnetization direction in the two settings is b′ = c. The monoclinic non-right angle is β in the standard setting and γ in the austenitic setting; (**b**) Schematic representation of the {101} cubic planes in the Ni-Mn-Ga austenitic cell that are aligned with the twin boundaries in X-type and Y-type martensitic twin boundaries. (**c**) Top view of the X- and Y-type twin boundaries, showing the orientation of the magnetic easy axis in both the configurations. (**d**) Schematic representation of the martensitic interfaces in X-type and Y-type connecting the colonies of the twin boundaries nucleated from different twinning planes, color version is provided online.

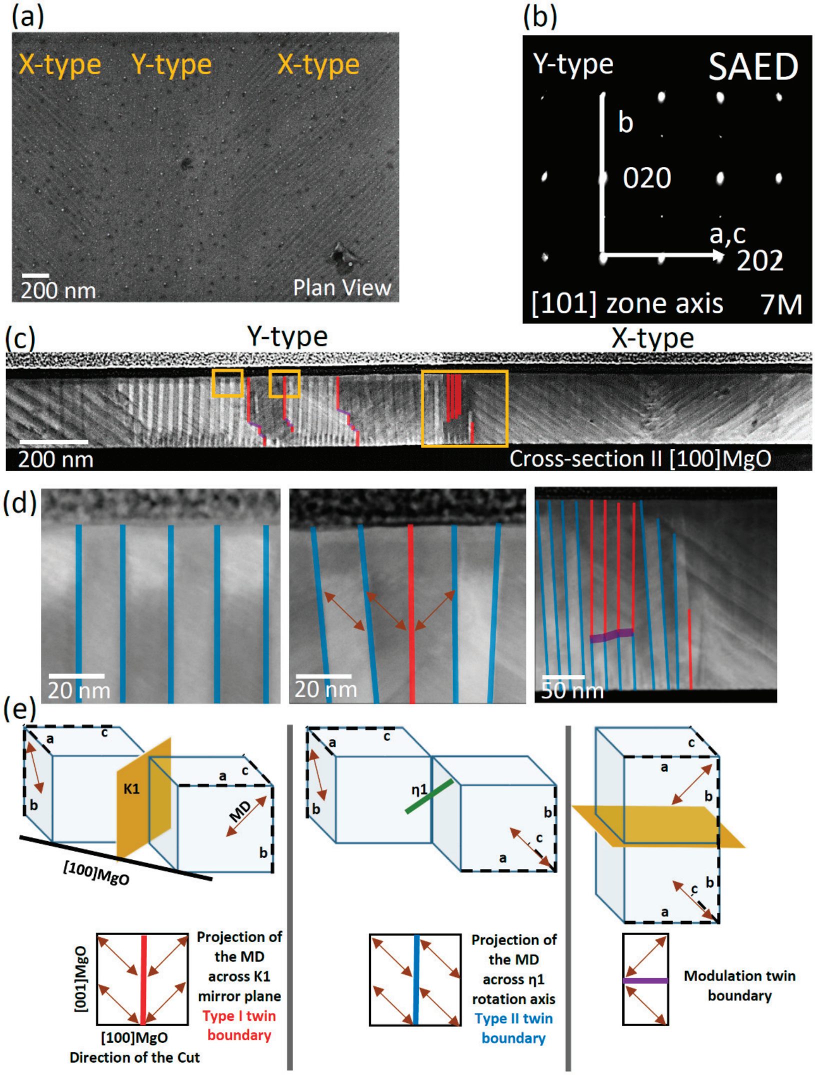

Figure 2. (**a**) SEM secondary electron image of sample #1 showing the coexistence of X-type and Y-type configurations; (**b**) selected-area electron diffraction (SAED) pattern of the Y-type region showing the parameters of the martensitic cell in the Y-type configuration, which have been fitted to 7M monoclinic cell and the orientation of each axis; (**c**) large-scale cross- section high-angle angular dark-field scanning transmission electron microscopy (HAADF) image of the sample; (**d**) magnified HAADF images of the marked areas in panel (**b**) showing the type of twins (red for type I, blue for type II and purple for modulation twin boundaries), the modulation directions are shown by double-headed arrows; (**e**) top: schematic representation of the martensitic cell axis and the modulation direction in Y-type across type I, type II and modulation boundaries (austenitic setting); bottom: the corresponding projection of the modulation direction in the plane of the lamella (FIB-cut along [100]MgO).

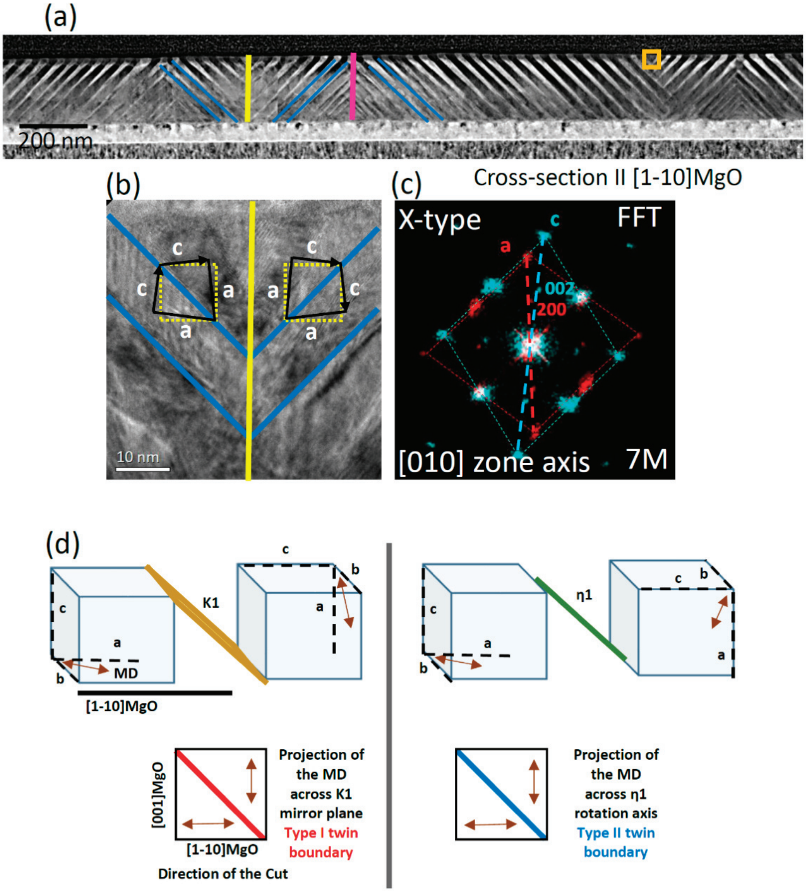

Figure 3. (**a**) Large-scale HAADF image of sample #2, the twin boundaries and the conjugation interfaces are marked by blue, pink, and yellow lines; (**b**) HR-TEM of the marked area in panel (**a**) showing the symmetry of the martensitic cells across the twin boundary and the conjugation interface; (**c**) FFT pattern taken at the twin boundary (shown in panel (**b**), left) showing the a and the c axes (black lines) alternating across the twin boundary, the yellow dashed lines aligned along the [001] and [1−10] directions of MgO are guides for the eyes to evidence the observed cell misorientation; cell parameters are fitted to the 7M monoclinic cell; (**d**) top: schematic representation of the martensitic cell axes and the modulation direction in X-type across type I, type II boundaries (austenitic setting), bottom: the corresponding projection of the modulation direction in the plane of the lamella (FIB-cut along [1−10]MgO).

Among the twinning systems, type I and type II and their related twinning stress are of special interest, as they alternate the easy magnetization axis in the martensitic cell.

In the literature about Ni-Mn-Ga, the twinning stress of type II twin boundaries is reported to be up to around twenty times lower than the type I counterpart, i.e., type II twin boundaries are considered highly mobile upon applying external magnetic field [19,30,31]. Therefore, in order to achieve giant magnetic field induced strain, type II twin boundaries are evidently desired.

In 2015, Yang et al. reported a combination of type I and type II twin boundaries for both X-type and Y-type configurations in 7M Ni-Mn-Ga epitaxial films [25]. In 2017, Niemann et al. reported a model for the X- and Y-type configurations, where combinations of eight compatible twin variants nucleate diamond-like enclosed volumes of martensite. The diamonds grow until they meet each other or (and) meet the substrate. The midribs of the diamonds serve as the twin boundaries (type I, type II, and modulation) [10].

In addition to the above twinning systems, there exist interfaces separating colonies of X- or Y-type twin boundaries in larger scale, for which the exact atomically sharp twinning relations are not fulfilled. These interfaces can be sorted into conjugation interfaces and non-conjugation interfaces, depending on whether they separate colonies of conjugated or non-conjugated planes (Figure 1d) [32–34].

Simplified schematic representations of the twin boundaries nucleated from different {101} planes and interfaces connecting the colonies of twin boundaries are provided in Figure 1d. The scheme shows the twin boundaries as the inclined and vertical red lines (X and Y, respectively). The pink line corresponds to a ridge and the yellow line corresponds to a valley [35], both can be categorized as conjugation interfaces. The green lines are assigned for the non-conjugation interfaces [32–34].

3. Results and Discussion

The epitaxial crystallographic relations of the MgO substrate, Cr under layer (for sample #2), and Ni-Mn- Ga cells were determined by TEM analysis as [100]Ni-Mn-Ga//(001)[110]MgO for sample #1 and (001) [100]Ni-Mn-Ga//(001)[100]Cr//(001)[110]MgO for sample #2. The crystal symmetry of the martensitic cells was characterized as sevenfold modulated monoclinic structure [27]. The crystallographic coordinates describing the martensitic cell are provided in Figure 1a. In order to keep the coherency and simplify the description, the martensitic cells will be described only in the austenitic setting (i.e., a, b and c, c is the shortest axis and the easy magnetization axis).

The cell parameters of the martensitic cells were measured by TEM and X-ray diffraction (Figure S3) for sample #1 as a = 0.608 nm, b = 0.578 nm, c = 0.552 nm, $\gamma = 91.5°$ and for sample #2 as a = 0.609 nm, b = 0.577 nm, c = 0.552 nm, $\gamma = 91.5°$.

3.1. Symmetry of the Twin Boundaries

To avoid the superposition of the twin boundaries across the TEM lamella, the cross section of the samples were prepared along [100] MgO (for observing Y-type in sample #1) and [1−10] MgO (for investigating X-type in sample #2).

Figure 2 shows the results obtained for sample #1, presenting the coexistence of X-type and Y-type configurations. The Y-type configuration was induced by a local mechanical stress applied after the growth (Figure 2a) [7]. The lamella for TEM investigation was prepared from the Y-type region. The diffraction pattern taken from the [101] zone axis of the Y-type region is shown in Figure 2b. Considering the orientation of the martensitic cells in the austenitic setting, the b axis of the cells lies out of plane, whereas the a and c axes alternate in the plane of the film (the c axis being the shortest axis and the easy magnetization axis). This is the typical pattern for the Y-type twinning configuration in 7M monoclinic martensitic phase. The HAADF image of the whole lamella is shown in Figure 2c; the three marked square areas are magnified and represented in Figure 2d. As can be seen, inside each variant there are tiny contrast variations with certain directions, which correspond to the 7M contrast modulation of the martensitic phase. The strategy we used to evaluate the type of twin boundaries in Y-type configuration is based on the observation of changes of contrast modulation direction across the boundaries, by HAADF and HR-TEM. This enables us to identify the types of twin boundaries on a large scale. Based on this approach, three types of twin boundaries can be identified, which have been marked with red, blue, and purple lines in Figure 2c,d. The direction of the modulation only changes across the red and purple boundaries. As an example, in the middle HAADF image of Figure 2d, the directions of the contrast variations across the boundaries are shown by double-headed arrows. A higher resolution version of the right image in Figure 2d can be found in the supplementary material (Figure S2a). In addition, in Figure 2e, the schematic explanation of the observed changes is provided. If we consider the martensitic monoclinic cell in the austenitic setting, the direction of the modulation always lies in the plane of the a and b axes (Figure 1b). For the top left scheme of Figure 2e, the K1 mirror plane (type I) serves as the twin boundary by alternating the orientation of the martensitic cell, while for the middle image, the η1 axis (type II) serves as the twin boundary by rotating the cell of about 180°. As for the top right scheme, only the modulation direction (MD) of the cell alternates across the twinning plane. In all the three schemes, double-headed arrows show the MD across the twin boundaries. In the bottom part of Figure 2e, the schemes show the relative (with respect to the top schemes) projection of these MD across the twin boundaries in the plane of the lamella (FIB-cut along [100] MgO), proving the types of twin boundaries in the Y-type configuration of the prepared lamella. We scanned the whole Y-type region to find the distribution of the types of twinning. Only the twin boundaries marked with red and purple in Figure 2c,d were found to have type I and modulation symmetry relations. The rest of the twin boundaries evidently show type II twin boundary. It is worth mentioning that close to the substrate interface (~50 nm), we observed a pronounced branching of the twins with type I boundaries, which are shown in the supplementary material (Figure S2). This represents an experimental evidence for the model proposed as the diamond model of the nucleation and growth of the martensitic nuclei in Y-type configuration [24].

Figure 3a shows the HAADF image of the lamella prepared from sample #2, alternating stripes with bright and dark contrasts, around 45° and −45° tilted with respect to the substrate, which are typical of X-type configuration.

Besides X-type twin boundaries (marked with blue lines), some conjugation interfaces connecting the colonies of differently inclined twin boundaries at the valley and ridges are marked with yellow and pink, respectively.

The square marked area in Figure 3a is magnified in HR-TEM (Figure 3b). The corresponding fast Fourier transform (FFT) (Figure 3c), taken at the top left twin boundary of Figure 3b, shows the alternation of the a- and c-axes in the out-of-plane direction; the b-axis always lies in the film plane, which is typically expected for X-type configuration. The FFT reveals a few degrees misorientation of the a- and c-axes with respect to the [001] and [1−10] directions of MgO (dashed yellow lines). In addition, a close inspection of HAADF and HR-TEM images enables us to determine the predominant variant in sample #2. These latter results are consistent with the results obtained by XRD. More details are reported in supplementary material, Figure S3.

For the X-type configuration, due to the orientation of the twin boundaries, as it is shown in Figure 3d, the projections of the resultant MDs for both the mirror and rotation symmetry operators in the plane of the lamella (FIB-cut along [1−10] MgO) are equal. In this case, the presence of the type II twinning system for a cross section along [1−10] MgO is proposed in Ref. [10].

3.2. Evolution of the Interfaces

Figure 4a shows the HAADF image of conjugation interfaces separating colonies of differently inclined twin boundaries. The conjugation interfaces highlighted in the HAADF image can be directly visualized in the AFM plan view topography shown in Figure 4b. Ridges and valleys are revealed by the height profile of the topography taken along the [1−10] direction of the MgO substrate (Figure 4d). The corresponding MFM image (Figure 4c) shows an inversion of contrast at the conjugation interfaces. The main source of MFM contrast is the variation of the stray field in the direction normal to the sample surface; this reveals that the out-of-plane easy magnetization axis of the martensitic variants inverts the direction across the conjugation interfaces. In order to schematize this effect in the atomic scale we inserted arrows in Figure 3b to evidence both the crystallographic orientations and the magnetization directions (i.e., c axis) across the conjugation interface.

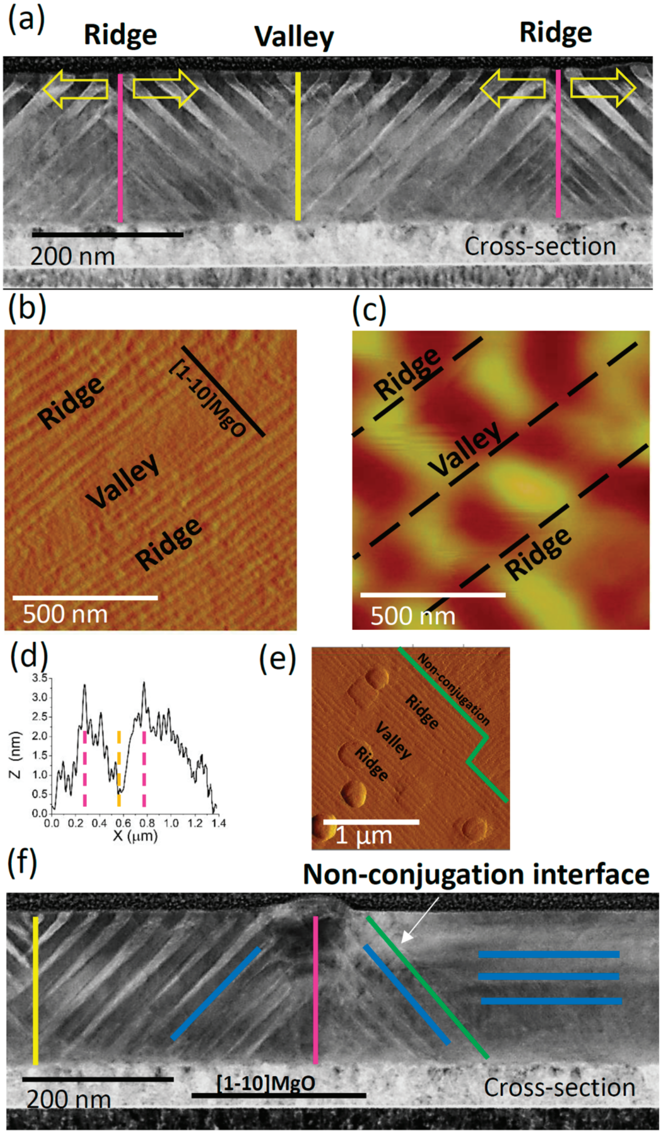

Figure 4. (**a**) HAADF image of sample #2 showing the ridges and valleys created by the conjugation interfaces (pink and yellow lines); (**b**,**c**) AFM/MFM images of sample #2 at RT showing the conjugation interfaces in plan-view (**b**) and the related disconnections in the magnetic domains (**c**); (**d**) height profile (Z) of the topography (**b**) taken along the [1−10] direction of MgO (X), showing the position of the two ridges and the valley; (**e**) topography image illustrating the conjugation and non-conjugation interfaces (green lines) in plan-view; (**f**) HAADF image of sample #2 showing the non-conjugation interface (green line) in cross section view, the geometry of the twins (blue lines) and the conjugation interfaces (pink and yellow).

Figure 4a also shows a variation of the spatial twinning periodicity throughout the film (Λ range ≈ 10–30 nm). It is evident that Λ decreases close the substrate for the twin boundaries that connect at the ridges, while Λ decreases close the surface for the twin boundaries that connect at the valleys. The twin boundaries with low twinning periodicity in the ridge position (pink line) do not reach the surface, while those in the valley position (yellow line) do not reach the Cr underlayer; evidently, because they meet each other before growing through the whole thickness of the film, therefore their further growth is hindered. In addition, more symmetric conjugation interfaces are observed in the lamella at the ridges rather than at the valleys (Figure 3a). Symmetric conjugation typically appears when the two sides of the conjugation system meet at the registry [34]. In the present case (i.e., Ni-Ni-Ga film), it could occur when the twins nucleate at the same point (or grow equally towards each other). All these observations are coherent with in situ AFM topography measurements vs. temperature, and can be explained by a transition route, in which the nucleation of the twin boundaries initiates from the ridges and proceeds until they meet at the valleys, at non-conjugation interfaces or they reach the substrate (Figure 4a). This route will be discussed in detail below.

The other type of martensitic interface, which was shown schematically in Figure 1d, is the non-conjugation interface. An example of this type of interface is shown in the topography plan view (Figure 4e) and HAADF cross section (Figure 4f). They show a blurred region on the right side of the image and a region with well distinguishable twin boundaries on the left side separated by an inclined green line. In the blurred region, the orientations of the twin boundaries are superimposed and parallel to the lamella, causing the observed blurredness. The relative orientations of the twin boundaries are highlighted by blue lines, while the ridge and valley by pink and yellow lines, respectively.

In the martensitic forward and reverse transitions, the interfaces play an important role. In thermoelastic materials, the martensitic forward transition starts with the formation of the phase boundaries and proceeds with moving the phase boundaries, propagating the martensitic phase at the expense of the austenitic phase. The nucleation of the lower symmetry phase is energy costly, a cost which needs to be compensated. To reduce the energy cost, the transition initiates by a heterogeneous nucleation of the low symmetry phase from the most vulnerable regions (e.g., defects, impurities, scratches, etc.). On the other hand, in the reverse transition (martensite to austenite) the material transforms back to the high symmetry austenitic phase [35]. Residuals of untransformed austenitic phase inside the martensitic phase have been suggested to serve as the starting points for the reverse transition. In the literature, the above-described martensitic interfaces are generally suggested to be the regions maintaining the residuals of the untransformed austenitic phase [36].

In this work, in order to clarify this point, we explored the X–Y interfaces (Figure 2) and X–X interfaces (Figure 3, both conjugation and non-conjugation) by HR-TEM. No trace of the austenitic phase was found at room temperature by FFT and SAED analysis.

To deepen the phenomenology of the transition, we measured the evolution of the interfaces (conjugation and non-conjugation) upon phase transition by in situ topography imaging vs. temperature (Figure 5) in sample #2 (all X-type). In X-type microstructure, the pronounced corrugation of surface can be clearly imaged through height contrast by means of atomic force microscopy measurements. In contrast, in the Y-type microstructure, the twin structure can be scarcely visualized by height contrast because of the very small surface corrugation it gives rise to [9]. Sample #2 was cooled down from 345 K to 300 K and subsequently heated up to 345 K, capturing the topography images in different stages of the forward and reverse transition. Figure 5a shows the status of the sample at 328 K (austenitic phase). As the temperature is decreased to 321 K (Figure 5b), the X-type twin boundaries nucleate in isolated regions (ridges, some of them are highlighted), which then continue to nucleate and grow towards each other. The highlighted areas in Figure 5c show the valleys and the non-conjugation interfaces, which are not yet transformed. Upon further decreasing temperature to 315 K (Figure 5d), the scanned area fully transforms to the martensitic phase.

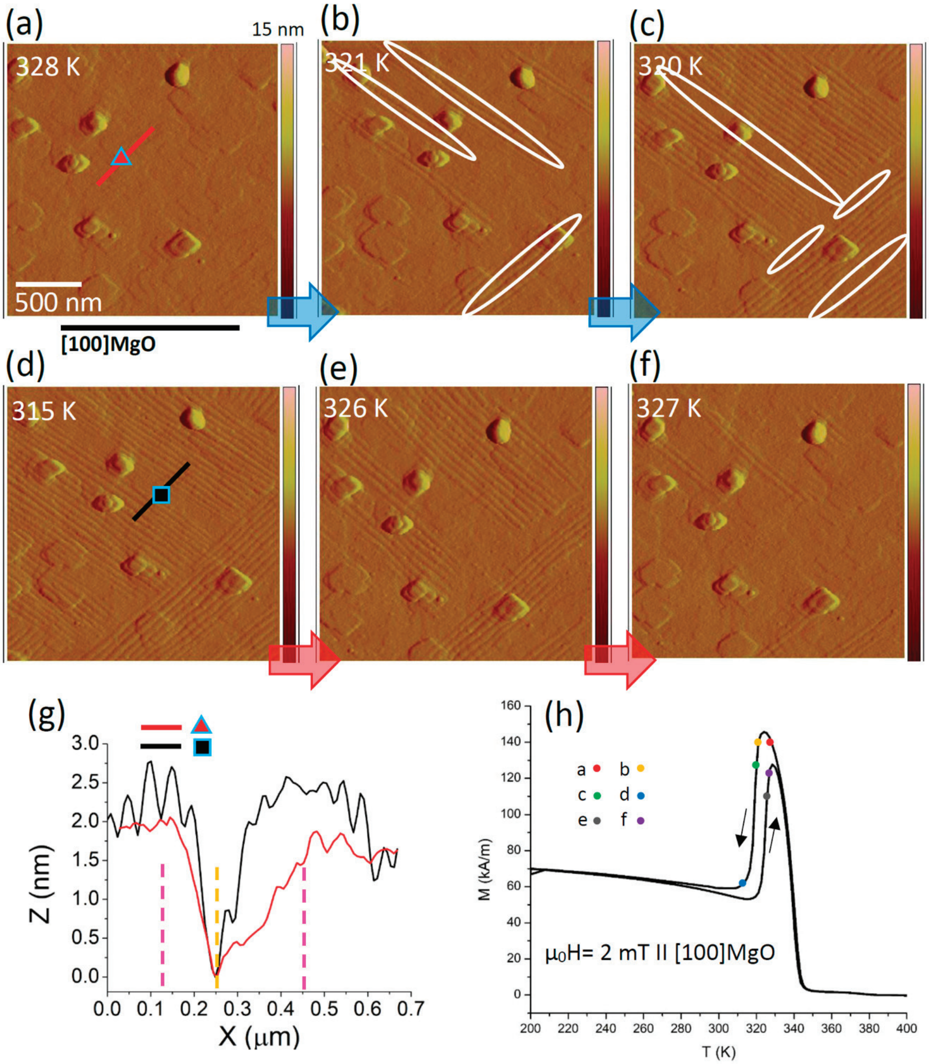

Figure 5. Tracing the formation and annihilation of the interfaces in sample #2 by means of in situ topography imaging vs. temperature. AFM images were captured in different stages of the forward and reverse transition (345K-300K-345K): (**a**) 328K, the film is in the austenitic phase; (**b**) 321K, nucleation of the martensitic phase starting from the ridges (conjugation interfaces), some are highlighted; (**c**) 320K, twin boundaries continue to nucleate and grow till they meet each other, the highlighted valleys and non-conjugation interfaces have not transformed yet; (**d**) 315K, the film is in the martensitic phase, the valleys and the non-conjugation interfaces have transformed as well; (**e**) 326K, the material transforms back to the austenitic phase starting from the valleys and the non-conjugation interfaces; (**f**) 327K, only the ridges are still untransformed; (**g**) height profile of the marked area (the two ridges and the valley are assigned by the pink and yellow dash-lines, respectively); (**h**) initial magnetization vs. temperature curve of the sample with schematic correspondence between the imaging temperatures and the curve.

One can trace the positions of the ridges, valleys, and the non-conjugation interfaces. Upon subsequent heating (to 326 K, Figure 5e), the reverse transition takes place, starting from the positions of the valleys and the non-conjugation interfaces. Figure 5f shows that the ridges degrade at the final stages of the reverse transition. In order to better visualize the positions of the interfaces, the height profile of the marked areas in Figure 5a,d are shown in Figure 5g. As it is shown in Figure 5g, a kind of nanometric surface relief evidently pre-exists close to the martensitic transition. Identifying the origin of this surface relief requires further investigation, taking into account different possibilities, e.g., short-range ordering [37] and the thermomagnetomechanical history of the sample [38]. Finally, for the same sample, the martensitic transition can be followed on the low field magnetization curves over temperature, which are reported in Figure 5h.

With these results, we propose that the nucleation of the martensitic phase in sample #2 starts from the positions of the ridges on the surface of the sample. The twin boundaries continue to nucleate and grow towards each other and towards the substrate, until they meet at the valleys and at the non-conjugation interfaces. However, for the reverse transition the non-conjugation interfaces and valleys transform to the austenitic phase at the initial stages of the transition, while the ridges are the last to transform.

In light of our experiments, we emphasize the primary role played by the interfaces in the transition route, and we can deny that it has to be related to residuals of the austenitic phase.

Ni-Mn-Ga cells on the surface of the film provide an additional degree of freedom compared to the cells at the interface with the substrate, which impose huge pinning constraint [39]. The surface of the film serves as the interface for the heat exchange, facilitating the transition [40]. Therefore, upon the forward transition, it is likely that the heat exchange favors the nucleation of the martensitic phase primarily on the surface and at the ridges having convex shape.

In addition, these coarse corrugations break the elastic homogeneity of the material, facilitating the heterogeneous nucleation of the martensitic phase. Upon the nucleation of the martensitic twin boundaries and their subsequent growth in the austenitic matrix, the created elastic strain energy typically dissipates in the form of heat and acoustic waves and partially stores in the material in the form of stored elastic energy. This energy is related to the irreversible steps of the transition, e.g., the obstacles stopping the growth, therefore it is thermodynamically irreversible [41]. The stored elastic energy works like a spring by partially storing the strain energy during the forward transition. Over the reverse transition, the stored energy is released back serving as a driving force; therefore, it could be mechanically reversible.

For a multivariant system, where the self-accommodation of the twin variants takes place by the coalescence of differently oriented equivalent boundaries, the dissipation and storage of the elastic strain typically occurs locally upon the nucleation as well as at pinning obstacles [41]. This makes conjugation and non-conjugation interfaces the critical regions of the sample (Figure 4).

The size of twin boundaries is expected to be directly proportional to the dissipated energy over the martensitic transition [22]. Thus, the stored elastic energy is expected to be inversely proportional the size of the twin boundaries. The low-twinning periodicity boundaries in Figure 4a,f, which do not grow across the whole thickness of the film, are expected to have a larger portion of stored elastic energy.

The stored elastic energy also regulates the sequence of the transition of the twin boundaries: in Figure 5, the first twin boundaries that appear at the forward transition are the last boundaries to disappear at the reverse transition, which is in agreement with the model proposed in [41,42] for thermoelastic martensites. In fact, the boundaries that appear first over the forward transition are typically the largest, which dissipate the largest energy in the form of heat and acoustic waves and store the lowest elastic energy. On the contrary, the boundaries that appear as the last over the forward transition are typically the smallest, which dissipate the lowest energy in the form of heat and acoustic waves and store the highest portion of elastic energy. These smaller boundaries annihilate first over the reverse transition (compare Figures 4 and 5).

Recently, the transition temperature of a 400 nm epitaxial Ni-Mn-Ga film was investigated by a nanolocalized scanning thermal microscopy, reporting a considerable temperature gradient (~20 K) for the reverse phase transition of different regions of the sample [43]. Based on the route provided in this study, the reported temperature gradient is likely to be linked also to the transition temperature difference for the martensitic interfaces (i.e., ridges and valleys).

In a system where the transition involves the nucleation and growth of a ferromagnetic phase in a paramagnetic matrix, such as our Ni-Mn-Ga thin film, surface topography and spatial distribution of nucleation sites may have an important influence on the magnetostatic energy. A quantitative evaluation in the specific case would require an accurate modeling, such as proposed for bulk La-Fe-Si [44], a system for which the preferential nucleation of the ferromagnetic phase at the convex areas has been experimentally demonstrated [40].

Our investigation provides a direct evidence of the major role played by the martensitic interfaces on the forward and the reverse transition in epitaxial Ni-Mn-Ga films (Figure 5). We propose that the forward transition initiates heterogeneously from the position of the conjugation interfaces, i.e., ridges on the surface of the film. The twin boundaries continue to nucleate and grow until they meet at the conjugation interfaces, i.e., valleys and the non-conjugation interfaces, where the growth is hindered. In these regions, the elastic strain energy created during the transition is partially stored. The stored energy in these regions serves as the driving force for the reverse transition by initiating the nucleation of the austenitic phase.

4. Conclusions

We investigated the crystallographic relations between the twin boundaries and interfaces in Ni-Mn-Ga epitaxial films from the atomic scale to the microscale and accompanied this investigation with the direct observation of the evolution of the martensitic interfaces vs. temperature.

Based on the symmetry relations between the twin variants, we identified the types of twin boundaries and the twinning interfaces, i.e., ridges, valleys, and non-conjugation interfaces.

Using the change of modulation direction across the boundary observed by HAAFD and HR-TEM, in Y-type regions we were able to determine the presence of type I, type II, and modulation twin boundaries with a dominant presence of type II.

Beyond these findings, we propose a transition route originating from the martensitic configuration, highlighting the major role played by the different martensitic interfaces. The forward transition starts with the heterogeneous formation of twin boundaries at the position of the ridges on the surface of the film and moves towards the substrate. The twin boundaries continue to nucleate and grow until they meet at the other kind of conjugation interfaces, i.e., valleys, or at non-conjugation interfaces, where the growth is hindered. In these regions, the elastic strain energy created during the transition is partially stored. This stored energy serves as the driving force for the reverse transition by initiating the nucleation of the austenitic phase.

In conclusion, this paper sheds light into the direct link between the martensitic configuration at the different length scales and the martensitic forward and reverse transitions. The present results represent a step forward in the understanding of the transition processes and pave the way to the possibility of tuning the characteristics of the transition, e.g., hysteresis and transition width, by microstructural engineering aimed at the full exploitation of martensitic Heuslers in cyclic applications.

Supplementary Materials: The following are available online at http://www.mdpi.com/1996-1944/13/9/2103/s1, Figure S1: (a,b) atomic force microscopy images and (c,d) magnetic force microscopy images at room temperature showing the typical X-type microstructure for the as-grown sample #1 and #2, Figure S2: Type of twin boundaries in the Y-type configuration of the lamella prepared out of sample #1: (a) HAADF image of the lamella, examples of different types of twins are highlighted. In addition, the observed branching of the Y-type twins close to the MgO interface is highlighted, (b) HR-TEM of an example of the type I twin boundaries alternating the modulation direction of the cells across the boundaries near the substrate and Figure S3: X-ray diffraction of sample #2 at 223 K, the dark blue shows the {h00} family of epitaxial peaks in a normal theta-2theta scan for 2theta = 58–70° and the purple shows the asymmetric scan (2° offset). The (400) and (004) martensitic peaks measured in the asymmetric scan are assigned for the a and c-axis of the martensitic cells out-of-plane of the film, respectively. The relative intensity counts of the two peaks is reported in the figure. Considering the possible errors of the measurement and the calculations, the values are in reasonable agreement with the relative intensity counts calculated from the STEM image of the lamella #2 for a and c-axis out-of-plane of the film (34% a-axis and 66% c-axis) As it was explained in the manuscript, the peaks related to the out-of-plane a and c-axis typically appear with slight misorientation with respect to the substrate normal plane due to the slight (CW or CCW) rotation of the martensitic cells around the b axis upon the formation.

Author Contributions: Conceptualization, Investigation, Writing—original draft, M.T.G.; Investigation, Writing—review G.T.; Investigation, Writing—review & editing, L.N.; Investigation, Writing—review S.F.; Investigation, Writing—review R.C.; Writing—review & editing, Supervision, F.C. and F.A. All authors have read and agreed to the published version of the manuscript.

Funding: This research received no external funding.

Acknowledgments: The authors thank Davide Calestani (IMEM-CNR, Parma) and Federica Celegato (INRIM, Turin) for the compositional characterization of the samples.

Conflicts of Interest: The authors declare no conflicts of interest.

References

1. Saren, A.; Smith, A.R.; Ullakko, K. Integratable magnetic shape memory micropump for high-pressure, precision microfluidic applications. *Microfluid. Nanofluid.* **2018**, *22*, 38. [CrossRef]
2. Yu, Y.; Zhang, C.; Zhou, M. Elman Neural Network-Based Identification of Krasnosel'skii-Pokrovskii Model for Magnetic Shape Memory Alloys Actuator. *IEEE Trans. Nanotechnol.* **2020**, *19*, 1–4. [CrossRef]
3. Kohl, M.; Gueltig, M.; Wendler, F. Coupled simulation of thermomagnetic energy generation based on NiMnGa Heusler alloy films. *Shape Mem. Superelasticity* **2018**, *4*, 242–255. [CrossRef]
4. Planes, A.; Mañosa, L.; Acet, M. Magnetocaloric effect and its relation to shape-memory properties in ferromagnetic Heusler alloys. *J. Phys. Condens. Mat.* **2009**, *21*, 233201. [CrossRef] [PubMed]
5. Sozinov, A.; Lanska, N.; Soroka, A.; Zou, W. 12% magnetic field-induced strain in Ni-Mn-Ga-based non-modulated martensite. *Appl. Phys. Lett.* **2013**, *102*, 021902. [CrossRef]
6. Kainuma, R.; Imano, Y.; Ito, W.; Sutou, Y.; Morito, H.; Okamoto, S.; Kitakami, O.; Oikawa, K.; Fujita, A.; Kanomata, T.; et al. Magnetic-field-induced shape recovery by reverse phase transformation. *Nature* **2006**, *439*, 957–960. [CrossRef] [PubMed]
7. Takhsha Ghahfarokhi, M.; Casoli, F.; Fabbrici, S.; Nasi, L.; Celegato, F.; Cabassi, R.; Trevisi, G.; Bertoni, G.; Calestani, D.; Tiberto, P.; et al. Martensite-Enabled Magnetic Flexibility: The Effects of Post-Growth Treatments in Magnetic-Shape-Memory Heusler Thin Films. *Acta Mater.* **2020**, *187*, 135–145. [CrossRef]
8. Ranzieri, P.; Fabbrici, S.; Nasi, L.; Righi, L.; Casoli, F.; Chernenko, V.A.; Villa, E.; Albertini, F. Epitaxial Ni–Mn–Ga/MgO (1 0 0) thin films ranging in thickness from 10 to 100 nm. *Acta Mater.* **2013**, *61*, 263–272. [CrossRef]
9. Ranzieri, P.; Campanini, M.; Fabbrici, S.; Nasi, L.; Casoli, F.; Cabassi, R.; Buffagni, E.; Grillo, V.; Magén, C.; Celegato, F.; et al. Achieving Giant Magnetically Induced Reorientation of Martensitic Variants in Magnetic Shape-Memory Ni-Mn-Ga Films by Microstructure Engineering. *Adv. Mater.* **2015**, *27*, 4760–4766. [CrossRef]
10. Niemann, R.; Backen, A.; Kauffmann-Weiss, S.; Behler, C.; Rößler, U.K.; Seiner, H.; Heczko, O.; Nielsch, K.; Schultz, L.; Fähler, S. Nucleation and growth of hierarchical martensite in epitaxial shape memory films. *Acta Mater.* **2017**, *132*, 327–334. [CrossRef]
11. Li, Z.B.; Yang, B.; Zhang, Y.D.; Esling, C.; Zhao, X.; Zuo, L. Crystallographic insights into diamond-shaped 7M martensite in Ni-Mn-Ga ferromagnetic shape-memory alloys. *IUCrJ* **2019**, *6*, 909–920. [CrossRef] [PubMed]
12. Müllner, P.; King, A.H. Deformation of hierarchically twinned martensite. *Acta Mater.* **2010**, *58*, 5242–5261. [CrossRef]
13. Saxena, A.; Wu, Y.; Lookman, T.; Shenoy, S.R.; Bishop, A.R. Hierarchical pattern formation in elastic materials. *Physical A* **1997**, *239*, 18–34. [CrossRef]
14. Sun, L.; He, X.; Lu, J. Nanotwinned and hierarchical nanotwinned metals: A review of experimental, computational and theoretical efforts. *NPJ Comput. Mater.* **2018**, *4*, 1–18. [CrossRef]
15. Zhou, L.; Schneider, M.M.; Giri, A.; Cho, K.; Sohn, Y. Microstructural and crystallographic characteristics of modulated martensite, non-modulated martensite, and pre-martensitic tweed austenite in Ni-Mn-Ga alloys. *Acta Mater.* **2017**, *134*, 93–103. [CrossRef]
16. Niemann, R.; Rößler, U.K.; Gruner, M.E.; Heczko, O.; Schultz, L.; Fähler, S. The role of adaptive martensite in magnetic shape memory alloys. *Adv. Eng. Mater.* **2012**, *14*, 562–581. [CrossRef]

17. Gutfleisch, O.; Gottschall, T.; Fries, M.; Benke, D.; Radulov, I.; Skokov, K.P.; Wende, H.; Gruner, M.; Acet, M.; Entel, P.; et al. Mastering hysteresis in magnetocaloric materials. *Philos. Trans. R. Soc. A* **2016**, *374*, 20150308. [CrossRef]
18. Cugini, F.; Porcari, G.; Fabbrici, S.; Albertini, F.; Solzi, M. Influence of the transition width on the magnetocaloric effect across the magnetostructural transition of Heusler alloys. *Philos. Trans. R. Soc. A* **2016**, *374*, 20150306. [CrossRef]
19. Peter, M. Twinning stress of type I and type II deformation twins. *Acta Mater.* **2019**, *176*, 211–219. [CrossRef]
20. Cui, J.; Chu, Y.S.; Famodu, O.O.; Furuya, Y.; Hattrick-Simpers, J.; James, R.D.; Ludwig, A.; Thienhaus, S.; Wuttig, M.; Zhang, Z.; et al. Combinatorial search of thermoelastic shape-memory alloys with extremely small hysteresis width. *Nat. Mater.* **2006**, *5*, 286–290. [CrossRef]
21. Gottschall, T.; Skokov, K.P.; Burriel, R.; Gutfleisch, O. On the S (T) diagram of magnetocaloric materials with first-order transition: Kinetic and cyclic effects of Heusler alloys. *Acta Mater.* **2016**, *107*, 1–8. [CrossRef]
22. Niemann, R.; Kopeček, J.; Heczko, O.; Romberg, J.; Schultz, L.; Fähler, S.; Vives, E.; Mañosa, L.; Planes, A. Localizing sources of acoustic emission during the martensitic transformation. *Phys. Rev. B* **2014**, *89*, 214118. [CrossRef]
23. Niemann, R.; Hahn, S.; Diestel, A.; Backen, A.; Schultz, L.; Nielsch, K.; Wagner, M.X.; Fähler, S. Reducing the nucleation barrier in magnetocaloric Heusler alloys by nanoindentation. *APL Mater.* **2016**, *4*, 064101. [CrossRef]
24. Campanini, M.; Nasi, L.; Fabbrici, S.; Casoli, F.; Celegato, F.; Barrera, G.; Chiesi, V.; Bedogni, E.; Magén, C.; Grillo, V.; et al. Magnetic Shape Memory Turns to Nano: Microstructure Controlled Actuation of Free-Standing Nanodisks. *Small* **2018**, *14*, 1803027. [CrossRef] [PubMed]
25. Yang, B.; Zhang, Y.; Li, Z.; Qin, G.; Zhao, X.; Esling, C.; Zuo, L. Insight into variant selection of seven-layer modulated martensite in Ni-Mn-Ga thin films grown on MgO (001) substrate. *Acta Mater.* **2015**, *93*, 205–217. [CrossRef]
26. Diestel, A.; Neu, V.; Backen, A.; Schultz, L.; Fähler, S. Magnetic domain pattern in hierarchically twinned epitaxial Ni–Mn–Ga films. *J. Phys. Condens. Mat.* **2013**, *25*, 266002. [CrossRef]
27. Righi, L.; Albertini, F.; Villa, E.; Paoluzi, A.; Calestani, G.; Chernenko, V.; Besseghini, S.; Ritter, C.; Passaretti, F. Crystal structure of 7M modulated Ni-Mn-Ga martensitic phase. *Acta Mater.* **2008**, *56*, 4529–4535. [CrossRef]
28. Christian, J.W.; Mahajan, S. Deformation twinning. *Prog. Mater. Sci.* **1995**, *39*, 1–157. [CrossRef]
29. Pitteri, M.; Zanzotto, G. *Continuum Models for Phase Transitions and Twinning in Crystals*; CRC: Boca Raton, FL, USA, 2003; pp. 107–300.
30. Straka, L.; Heczko, O.; Seiner, H.; Lanska, N.; Drahokoupil, J.; Soroka, A.; Fähler, S.; Hänninen, H.; Sozinov, A. Highly mobile twinned interface in 10 M modulated Ni-Mn-Ga martensite: Analysis beyond the tetragonal approximation of lattice. *Acta Mater.* **2011**, *59*, 7450–7463. [CrossRef]
31. Straka, L.; Soroka, A.; Seiner, H.; Hänninen, H.; Sozinov, A. Temperature dependence of twinning stress of Type I and Type II twins in 10M modulated Ni-Mn-Ga martensite. *Scr. Mater.* **2012**, *67*, 25–28. [CrossRef]
32. Szczerba, M.J.; Chulist, R. Detwinning of a non-modulated Ni–Mn–Ga martensite: From self-accommodated microstructure to single crystal. *Acta Mater.* **2015**, *85*, 67–73. [CrossRef]
33. Chulist, R.; Czaja, P.; Tokarski, T.; Kuksgauzen, I.; Chumlyakov, Y.I. Orthogonal shear process in Ni-Mn-Sn single crystal. *Int. J. Plast.* **2019**, *114*, 63–71. [CrossRef]
34. Muntifering, B.; Pond, R.C.; Kovarik, L.; Browning, N.D.; Müllner, P. Intra-variant substructure in Ni–Mn–Ga martensite: Conjugation boundaries. *Acta Mater.* **2014**, *71*, 255–263. [CrossRef]
35. Khachaturyan, A.G. *Theory of Structural Transformations in Solids, Courier Corporation*; Dover Publications INC.: Mineola, NY, USA, 2008; pp. 157–314.
36. Diestel, A.; Niemann, R.; Schleicher, B.; Nielsch, K.; Fähler, S. Reducing Hysteresis Losses by Heating Minor Loops in Magnetocaloric Ni-Mn-Ga-Co Films. *Energy Technol.* **2018**, *6*, 1463–1469. [CrossRef]
37. Guo, X.; Jin, Y.M.; Ren, Y.; Wang, Y.U. Quasi-Spin Ising Model and Monte Carlo Simulation of Ferroelastic Phase Transition: 3D Diffuse Scattering and Displacement Short-Range Ordering in Pre-Martensitic State. *arXiv* **2019**, arXiv:1912.10295. Available online: https://arxiv.org/abs/1912.10295 (accessed on 21 December 2019).
38. Reinhold, M.; Watson, C.; Knowlton, W.B.; Müllner, P. Transformation twinning of Ni–Mn–Ga characterized with temperature-controlled atomic force microscopy. *J. Appl. Phys.* **2010**, *107*, 113501. [CrossRef]
39. Buschbeck, J.; Niemann, R.; Heczko, O.; Thomas, M.; Schultz, L.; Fähler, S. In situ studies of the martensitic transformation in epitaxial Ni–Mn–Ga films. *Acta Mater.* **2009**, *57*, 2516–2526. [CrossRef]

40. Waske, A.; Lovell, E.; Funk, A.; Sellschopp, K.; Rack, A.; Giebeler, L.; Gostin, P.F.; Fähler, S.; Cohen, L.F. The impact of surface morphology on the magnetovolume transition in magnetocaloric $LaFe_{11. 8}Si_{1. 2}$. *APL Mater.* **2016**, *4*, 106101. [CrossRef]
41. Wollants, J.; Roos, R.; Delaey, L. Thermally- and stress-induced thermoelastic martensitic transformations in the reference frame of equilibrium thermodynamics. *Prog. Mater. Sci.* **1993**, *37*, 227–288. [CrossRef]
42. Tong, H.C.; Wayman, C.M. Characteristic temperatures and other properties of thermoelastic martensites. *Acta Metall.* **1974**, *22*, 887–896. [CrossRef]
43. Pereira, M.J.; Amaral, J.S.; Silva, N.J.; Amaral, V.S. Nano-localized thermal analysis and mapping of surface and sub-surface thermal properties using scanning thermal microscopy (SThM). *Microsc. Microanal.* **2016**, *22*, 1270–1280. [CrossRef]
44. Fujita, A.; Kondo, T.; Kano, M.; Yako, H. Shape-anisotropic heterogeneous nucleation and magnetic Gibbs-Thomson effect in itinerant-electron metamagnetic transition of La $(Fe_{0.88}Si_{0.12})_{13}$ magnetocaloric compound. *Appl. Phys. Lett.* **2013**, *102*, 041913. [CrossRef]

materials

MDPI

Article

Structural and Magnetic Properties of FePd Thin Film Synthesized by Electrodeposition Method

Gabriele Barrera [1,*], Federico Scaglione [2], Matteo Cialone [2,3], Federica Celegato [1], Marco Coïsson [1], Paola Rizzi [2] and Paola Tiberto [1]

[1] Istituto Nazionale di Ricerca Metrologica (INRiM), Advanced Materials Metrology and Life Sciences, Strada delle Cacce 91, I-10135 Torino, Italy; f.celegato@inrim.it (F.C.); m.coisson@inrim.it (M.C.); p.tiberto@inrim.it (P.T.)

[2] Dipartimento di Chimica e Centro Interdipartimentale NIS (Nanostructured Surfaces and Interfaces), University of Turin, Via Pietro Giuria 7, I-10125 Torino, Italy; federico.scaglione@unito.it (F.S.); matteo.cialone@uab.cat (M.C.); paola.rizzi@unito.it (P.R.)

[3] Departament de Física, Universitat Autònoma de Barcelona, 08193 Cerdanyola del Vallès, Spain

[*] Correspondence: g.barrera@inrim.it

Received: 7 February 2020; Accepted: 21 March 2020; Published: 23 March 2020

Abstract: Bimetallic nanomaterials in the form of thin film constituted by magnetic and noble elements show promising properties in different application fields such as catalysts and magnetic driven applications. In order to tailor the chemical and physical properties of these alloys to meet the applications requirements, it is of great importance scientific interest to study the interplay between properties and morphology, surface properties, microstructure, spatial confinement and magnetic features. In this manuscript, FePd thin films are prepared by electrodeposition which is a versatile and widely used technique. Compositional, morphological, surface and magnetic properties are described as a function of deposition time (i.e., film thickness). Chemical etching in hydrochloric acid was used to enhance the surface roughness and help decoupling crystalline grains with direct consequences on to the magnetic properties. X-ray diffraction, SEM/AFM images, contact angle and magnetic measurements have been carried out with the aim of providing a comprehensive characterisation of the fundamental properties of these bimetallic thin films.

Keywords: FePd alloy; electrodeposition technique; magnetic properties; structural characterisation

1. Introduction

Bimetallic nanomaterials, composed by a noble element and a magnetic metal, have attracted a growing interest in the scientific community because they show together the properties of both metals in addition to confinement effects [1–4]. Noble metals play a central role in the area of catalysis [5,6]; whereas the magnetic metal elements (Fe, Co, Ni) with specific magnetic properties offer the possibility to easily recover and reuse the bimetallic nanostructured catalysts after the completion of the reaction and/or the chemical processes [7,8]. In particular, the magnetic separation process provides a practical and useful technique for recycling the magnetic nanostructured catalysts [7,8].

Additionally, the magnetic–noble bimetallic nanomaterials exhibit not only a simple combination of the properties associated with their single elements but they perform enhanced catalyst activity, modified catalyst selectivity or improved catalyst stability with respect to the monometallic catalysts: Sun et al. [9] reveal that the addition of Fe significantly enhances the hydrodeoxygenation activity of Pd/C; Zhao and Gorte [10] found that the activity of Pd/ceria catalysts increases by as much as an order of magnitude upon the addition of a controlled amount of Fe for the water-gas shift; Mu at al. [11] demonstrated that the synergistic effect between Pt and Ni enhances the activity to CO oxidation;

additional enhanced catalyst activity by means of magnetic–noble nanomaterials can be found in literature [12–16].

In view of their applications, magnetic–noble bimetallic nanomaterials should be produced in large quantities and at low costs. While nanoparticles may relatively comply well to these constraints, other forms of nanomaterials, such as thin films, could be more difficult to adapt, as their preparation techniques often require large and complex setups with well-controlled vacuum conditions. Electrodeposition technique helps overcoming some of these constraints, being a relatively low-cost and scalable approach for growing metallic thin films, even in the form of bimetallic alloys [17].

Within this context, it is of great importance and scientific interest to design and develop new multifunctional magnetic–noble bimetallic nanomaterials and to study the interplay between the properties and their microstructure, synthesis technique or spatial confinement, as the multiple available degrees of freedom could be exploited to tailor the properties to the desired application [2,15,18–20]. In the case of thin films, both bulk (e.g., grain size) and surface (e.g., roughness, surface-to-volume ratio) characteristics turn out to play fundamental roles in determining the resulting properties of the nanomaterial and to define the catalytic activity, therefore an adequate control during the growth process or the subsequent chemical etching is strictly required [21,22].

In this manuscript, we deal with this large subject by focussing on bimetallic thin films combining the noble metal, Pd, with the magnetic transition metal, Fe [23–27]. The former is attracting a wide interest for its catalytic properties, whereas the second, among the magnetic ones, is the least expensive. The FePd bimetallic nanomaterials are prepared in thin films form by electrodeposition, which allows obtaining a Fe-rich composition, and offers the possibility to easily control the film thickness by simply picking the desired deposition time. The surface (e.g., roughness) and magnetic properties depend on the film thickness, as specific microstructure and morphological features develop as a function of deposition time. The Fe-rich composition of the alloy combined with the higher removal rate of the Fe atoms than the one of the Pd atoms through chemical etching in hydrochloric acid allow to refine the roughness on the thickest films and to help the decoupling their grains. Such changes resulted in the ability to fine tune the magnetic properties and increase the surface-to-volume ratio. X-ray diffraction, as well as roughness, contact angle and magnetic measurements have been carried out with the aim of providing a comprehensive characterisation of the fundamental properties of these magnetic–noble bimetallic thin film.

2. Materials and Methods

Binary FePd alloy was potentiostatically electrodeposited in a cylindrical electrochemical cell [28], in which a thin foil of platinum acts as counter electrode, a conductive substrate as working electrode and an Ag|AgCl electrode as a reference electrode ($V_{Ag|AgCl} = +0.239$ V vs. standard hydrogen electrode at 25 °C). The reference electrode and the working one were mounted into the electrochemical cell in a horizontal arrangement. The depositions were performed at room temperature without stirring the solution. According to the previous work of Konczak et al. [29], the electrolyte composition is 0.01 M $Pd(NH_3)_4Cl_2$, 0.06 M sulfosalicylic acid (SSA), 0.05 M $Fe_2(SO_4)_3$ $7H_2O$, 0.3 M $(NH_4)_2SO_4$ (pH = 5). The magnetic FePd thin film was deposited on the working electrode constituted by a Si/SiO_2 substrate made conductive by the deposition of an Au layer. The adhesion of Au layer on SiO_2 surface was ensured by a thin Ti layer deposited between them. Prior to the FePd electrodeposition, the substrates were cleaned consecutively with acetone, isopropanol and de-ionized water in an ultrasonic bath.

The deposition potential was fixed at $E_0 = -1.2$ V vs. $V_{Ag|AgCl}$ selecting three different deposition times: 500, 150 and 50 s; the three electrodeposited FePd thin film samples were labelled S500, S150 and S50, respectively.

Scanning Electron Microscopy (SEM) was used to study the morphology of the electrodeposited samples. A software analysis of SEM images enables to calculate the size distribution of the grains. SEM was equipped by energy dispersive x-ray spectrometer (EDS) in order to evaluate the stoichiometry of the FePd alloy.

Thickness and surface morphology of all samples were characterised by means of Atomic Force Microscopy (AFM) operating in intermittent contact mode with the oscillation frequency and amplitude set point achieved by the tuning of the cantilever.

The film thickness was evaluated measuring the height of a well-defined step obtained by a lithographic process between the FePd film and the underlying substrate, see Figure S2 in the Supplementary Materials; the measured thickness was 51, 400 and 631 nm for the S50, S150 and S500 sample, respectively.

From 2D AFM profiles, roughness parameters are calculated such as the root mean square roughness (R_q), the mean slope of the roughness motifs ($1/K_r$) and the steepness of the sample surface (R_q/ξ) [30–35]. The $1/K_r$ parameter is defined as: $K_r = AR/R$, where R is the mean depth of the roughness motifs and AR is the mean spacing of the roughness motifs [30]; whereas the ξ parameter is the correlation length that reflects the average distance between consecutive peaks on the surface [34].

In the manuscript, roughness (R_q) is reported as the average value and standard deviation of several measurements in different points of the sample surface.

The structure of the as deposited FePd thin films was investigated by grazing angle X-ray diffraction (XRD) with a Cu-K_α radiation. The incident X-ray beam was set at a constant grazing angle of 0.6° for all measurements. The moving detector, instead, was rotated around the sample with a step size of 0.02 degrees and an acquisition time of 40 s per step, which were found to provide a good signal-to-noise ratio. A substrate pattern got before electrodeposition was collected and used as a reference in the reflections assignment.

Wettability properties of the samples surface were investigated by means of contact angle measurements performed at room temperature in which a droplet, with a volume of approximately 1 µL, is released from the tip of a calibrated micropipette on the sample surface. Each contact angle value is calculated as the average of at least six measurements in different points of the sample surface.

Magnetic measurements were performed using an Alternating Gradient Field Magnetometer (AGFM) working in the field interval $-18\ \text{kOe} \leq H \leq 18\ \text{kOe}$ in the parallel configuration (applied magnetic field in the sample plane). Hysteresis loops were obtained at room temperature for all samples and the diamagnetic signal of sample holder and film substrate was adequately subtracted.

First Order Reversal Curves (FORC) [36–38] have been measured with the same AGFM instrument, with the aim of identifying reversible and irreversible magnetisation reversal processes in the samples, and their dependence on inter-grain coupling. Such measurement technique results in a FORC-distribution [39] that can be used to express the spreading of the irreversible magnetisation reversal mechanisms taking place in the sample, as a function of local coercive field H_C values and mutual magnetic interactions among grains, expressed in terms of a so-called bias field H_B. Therefore, the peak of the FORC distributions measured for all the studied samples will be analysed to identify the spreading of local coercive field values, due to the grain size distribution in the sample, and the presence of inter-grain interactions affecting the magnetisation reversal processes.

All as-deposited samples were chemically treated for 5 h in a 2 molar aqueous solution of hydrochloric acid without applying any external potential and labelled S500_5h, S150_5h and S50_5h, respectively.

The morphological and surface transformations and the magnetic variations induced by the chemical treatment were characterised by means of the aforementioned experimental techniques.

3. Results and Discussion

Current density (j) vs. time curves recorded during the potentiostatic deposition of FePd thin film samples are shown in Figure 1a. At the beginning of the electrodeposition process, the j(t) curves show a reduction of their absolute value reaching a minimum ($|j|_{min}$) at around 20 s (indicated by the grey vertical dashed line in Figure 1a); this first portion of curve corresponds to the accumulation of a capacitive charge at the interface between the electrode and the solution [40]. Later, the FePd deposition occurs at an increasingly negative current density, which stays approximately constant only in the time interval 25–60 s (time interval between the grey vertical dashed and dotted lines in Figure 1a).

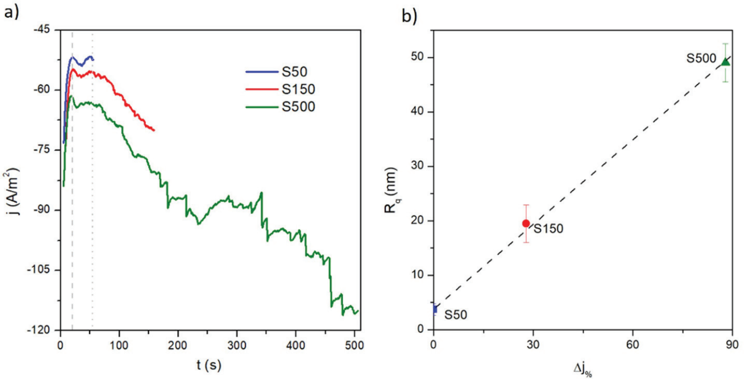

Figure 1. (**a**) Current density as a function of time recorded during the potentiostatic deposition of FePd thin film samples; (**b**) root mean square roughness (R_q) as a function of variation of current density values Δj (see text for details) over the deposition time.

After that, the strong increase in |j|(t) over time, observed for the deposition of S150 and S500 samples, indicates that the deposition conditions are changing and that the surface area of the working electrode is increasing [40,41]. As a consequence, the formation and growth of an increasingly rough film over deposition time is expected.

This hypothesis is corroborated by the results of surface analysis of the samples obtained by the AFM; representative images for all samples are reported in Figure 2. Indeed, the root-mean-square roughness (R_q) values measured from the AFM images turn out to monotonically increase as a function of electrodeposition time.

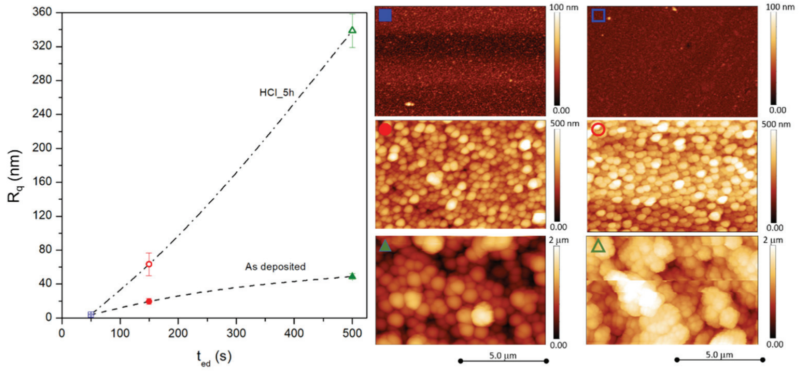

Figure 2. Root mean square roughness (Rq) for as-deposited and chemical etched samples as a function of electrodeposition time. At the right, the corresponding AFM images, identified by the same symbols and colours used in the graph.

In addition, the R_q increase is also linearly correlated with the $\Delta j = \left|\left(j_{stop} - j_{min}\right)/j\right|$ parameter (see Figure 1b), which takes into account the variation of current density values over the deposition time; j_{stop} is the current density value at which the electrodeposition process is stopped. This correlation indicates that the progressive increase of working electrode surface area is developed by means of an increasing of surface roughness. This behaviour makes the growth in thickness nonlinear as a function of the deposition time.

The grazing angle patterns of electrodeposited FePd thin films are reported in Figure 3. The contribution of the substrate is evident in all samples, independent of their thickness. Reflections peaks, labelled as black triangles in Figure 3, are associated to an α-(Fe, Pd) solid solution phase: however their position is shifted to lower angles at decreasing deposition time, meaning that a variation of stoichiometry and a different ratio of deposition are taking place. This issue, already reported in literature [42], is due to a local increase of pH of the near-electrode layer, that can cause the precipitation of iron hydroxide at quite negative potential, when the electrodeposition bath does not contain complexing agents: in this work, the addition of sulfosalicilic acid and Fe^{3+} ions as an iron source instead of Fe^{2+} avoids iron hydroxide precipitation [29] but not the local pH increase; as a consequence, a change in the pH occurs. Furthermore, the hydrogen evolution at the sample surface favours the inclusion of hydrogen into the deposit [42].

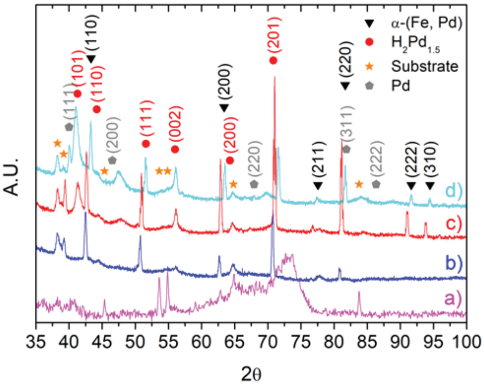

Figure 3. Grazing angle XRD pattern of: (a) substrate and electrodeposited FePd thin films (b) S50, (c) S150, (d) S500.

When deposition is performed for longer times (sample S500, cyan pattern in Figure 3), the fluctuation of the electrolyte composition in proximity of the working electrode becomes stronger, causing the deposition of a further phase identified as almost pure palladium [43].

A significant amount of a tetragonal $Pd_{1.5}H_2$ phase appears in all samples due to the high affinity between hydrogen and palladium [44,45]. The formation of this metal hydride usually induces a lattice distortion followed by surface cracking [46]; however, SEM images reported in Figure 4 do not show this evidence.

A shift of reflections of the $Pd_{1.5}H_2$ phase is observed on decreasing the time of deposition. This is possibly due to change in stoichiometry of the hydride phase as a consequence of the increase of pH and, therefore, the amount of Pd electrodeposited.

The ratio of Fe:Pd was determined using EDS resulting in $Fe_{68}Pd_{32}$, $Fe_{66}Pd_{34}$ and $Fe_{69}Pd_{31}$ for S50, S150 and S500 sample, respectively. However, these stoichiometry values of as-deposited FePd alloy are affected by a high error because the EDS technique is not able to detect the H atoms present in the samples ($Pd_{1.5}H_2$ phase observed by XRD) and, as a consequence, it is not possible to distinguish the correct fraction of the Pd atoms present in the FePd alloy from those in the $Pd_{1.5}H_2$ metal hydride. Therefore, these EDS data are only used as a reference value to obtain the variation of Fe content in each sample after the chemical etching, as discussed in the following.

If the R_q value (shown in Figure 2) mainly provides information on the change of the morphology along the vertical direction, the lateral growth of the grains as a function of electrodeposition time was studied by means of SEM measurements.

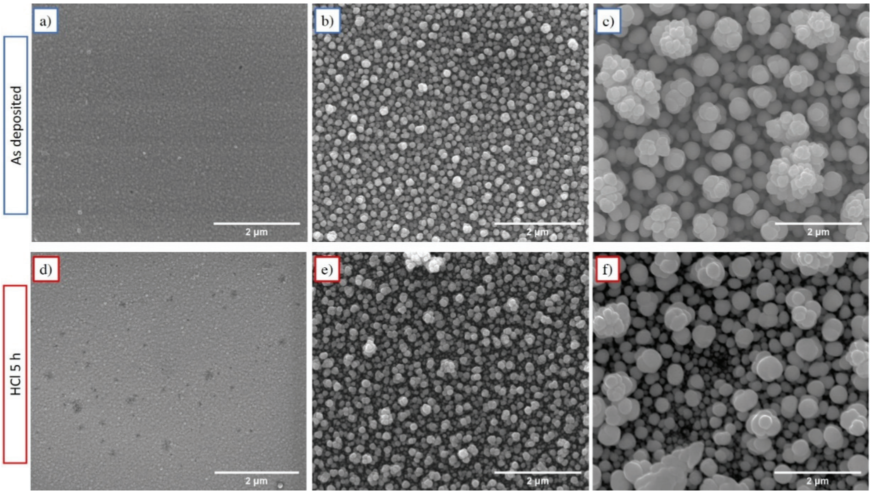

Figure 4. SEM images of as-deposited (**a**) S50, (**b**) S150, (**c**) S500 samples and etched (**d**) S50_5h, (**e**) S150_5h, (**f**) S500_5h samples in a 2 M aqueous solution of HCl for 5 h.

The surface of electrodeposited samples shows a rough granular morphology constituted by spherically shaped grains with different size as a function of deposition time (see Figure 4a–c). In particular, the grain size of FePd thin films is observed to increase significantly as a function of deposition time. In the early stages of the deposition, several nucleation centres on the Au substrate are localized and, for short deposition time intervals, the grains do not have a chance to grow and the film appears dense (see Figure 4a). As a consequence, the S50 sample displays small grains uniformly distributed over the substrate surface characterised by a narrow size distribution (Figure 5a) with a mean value < D > ≈ 85 nm, as shown in Figure 5c.

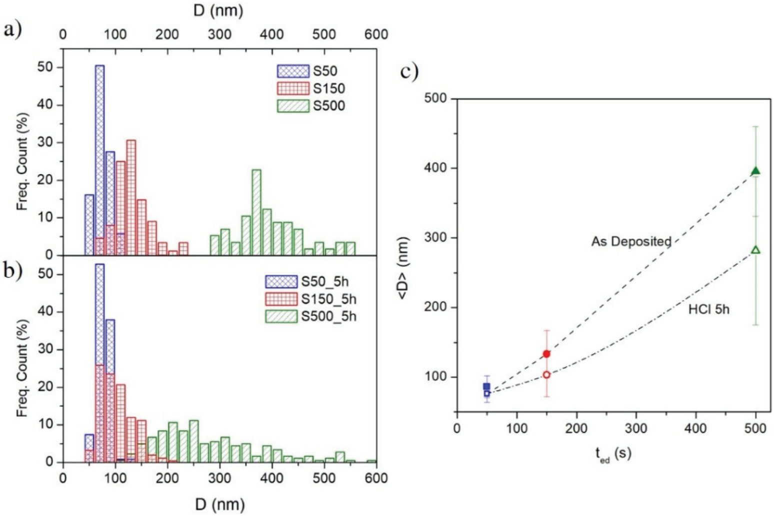

Figure 5. Grain size distributions of: (**a**) as-deposited samples and (**b**) etched samples in a 2 M aqueous solution of HCl for 5 h; (**c**) grain mean diameter < D > evolution as a function of electrodeposition time.

On increasing the deposition time, the grains are able to grow in spherical shape and their size distribution becomes wider (see Figure 5a) and the mean value increases to $< D > \approx 133$ and 395 nm for the S150 and S500 sample, respectively, as shown in Figure 5c. The observed simultaneous increase of surface roughness and of the grain size indicates a 3D growth in the films as a function of the electrodeposition time, and is probably related, as already mentioned above, to the current density variation $j(t)$ during the potentiostatic electrodeposition. The $|j(t)|$ increase over the deposition time (see Figure 1a) promotes an increasingly rapid growth of independent grains over the coalescence growth mechanism by inhibiting a compliant film deposition.

The electrodeposited FePd alloy samples were chemically treated for 5 h in a 2 molar aqueous solution of HCl acid in order to induce a free corrosion of the sample surface promoting a variation of its morphological and physical properties.

The measured FePd alloy stoichiometry after the chemical treatment is $Fe_{66}Pd_{34}$, $Fe_{63}Pd_{37}$ and $Fe_{60}Pd_{40}$ for S50_5h, S150_5h and S500_5h sample, respectively. The observed variation of the stoichiometry with respect to the initial values indicates that a selective dissolution of the FePd alloy occurs in which the removal rate of the Fe atoms is higher than the one of the Pd atoms in all samples. This effect is similar to a dealloying process [18,47–50] in which the less noble element of the alloy, Fe in FePd alloy, is selectively removed by the 2M HCl solution. The percentage reduction of Fe contained in the FePd alloy before and after chemical etching for each sample is shown in Figure 6.

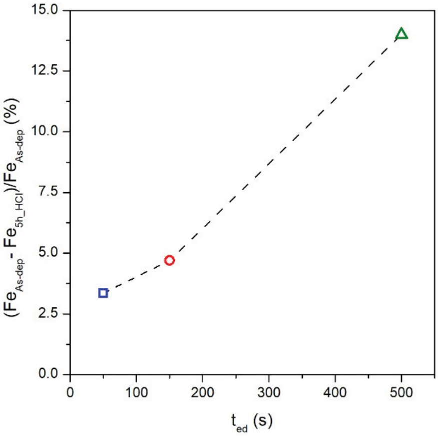

Figure 6. Percentage reduction of Fe contained in the FePd alloy before and after chemical etching as a function of the electrodeposition time.

The Fe reduction rate is not constant among samples, but it monotonically increases as a function of the electrodeposition time. This effect can be ascribed mainly to the different fraction of sample surface area exposed to the aggressive 2 M HCl solution. The previous characterisations of R_q and $< D >$ values indicate that the as-deposited S500 sample shows the biggest exposed surface area, in agreement with the highest Fe dissolution rate during the chemical process. On the other hand, the as-deposited S50 sample characterised by a low R_q and small grains size exposes a lower surface area to the acid solution making the chemical etching very slow.

The morphological transformations of the surface of FePd thin films induced by the chemical etching were characterised by the aforementioned AFM and SEM techniques. A primary consequence of the selective Fe dissolution is the increase of the average surface roughness (R_q) and of the associated standard deviation. This effect is substantially clear for the S150_5h and S500_5h samples whose R_q values increase to 63 and 340 nm, respectively, as shown in the Figure 2. On the contrary, the S50_5h sample keeps almost the same roughness properties as the as-deposited S50 sample indicating a different response to the chemical etching.

In addition to the effect on surface roughness, also the grain size is affected by the chemical etching. SEM images in Figure 4d–f show that the arrangement of the spherical grains in S150_5h and S500_5h sample appear less dense with a slightly higher separation among them. No significant change is visible in the S50 sample, where the structure does not seem to be altered by treatment in HCl acid (see Figure 4a,d).

In addition, Figure 5b shows the variation of grain size distribution induced by the chemical treatments. The grain size distribution of the S500_5h sample is uniform over a much wider dimensional range than the one of as-deposited S500 sample and with an average grain size reduced to $< D > \approx 282$ nm (see Figure 5c). In particular, this enlargement of the distribution induced by the chemical etching occurs completely towards smaller grain sizes while keeping the size of the larger grains unchanged. This change in the distribution shape indicates that the corrosion rate is not uniform on each grain but the as-deposited larger grains are more resistant. This evidence can be explained by assuming that the alloy stoichiometry of the as-deposited larger grains is richer in palladium or consists in pure palladium (as observed in XRD pattern), hindering the entire corrosion process.

The chemical treatment induces similar effects, but with less intensity, also on the grain size distribution of the S150_5h sample (see Figure 5b,c). The average size $< D >$ is slightly reduced and the distribution becomes slightly more asymmetric towards lower size while maintaining a rather narrow peak and a values dispersion comparable to the ones of as deposited S150 sample. On the contrary, the effects induced by the same chemical etching on the grain size distribution of the S50_5h sample are marginal since the average (see Figure 5b,c), the dispersion of the values and the distribution are comparable to those of the as-deposited sample. In agreement to the EDS characterisation (see Figure 6), the topographic and morphological features of the etched samples surface confirm that the etching rate of the surface is strongly correlated with the surface area induced of the as-deposited samples.

The surface morphology of the sample strongly influences its wettability properties [31–35,51] which are characterised by measuring the contact angle between a drop of water and the surface itself, see Figure 7a. The measured contact angle values are reported for all samples in Figure 7b where no significant differences are observed among as-deposited and etched samples. In particular, the contact angle values increase as a function of electrodeposition time indicating a more hydrophobic surface.

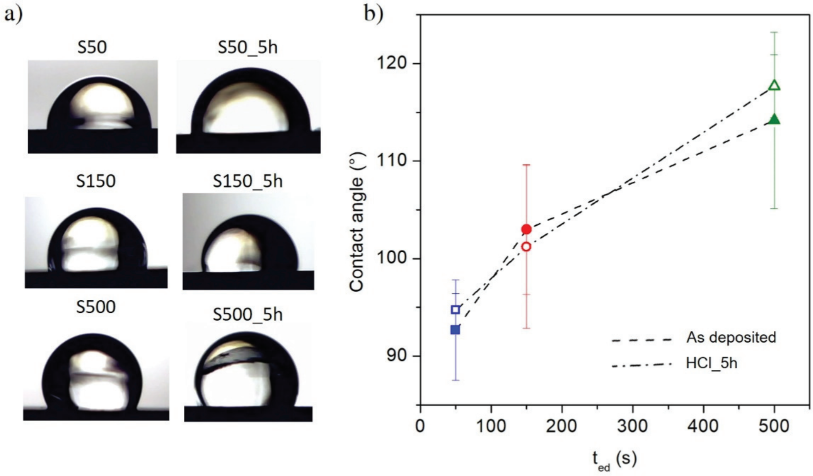

Figure 7. (**a**) Water drop on the samples surface; (**b**) contact angle evolution as a function of electrodeposition time for as-deposited and etched samples.

Several models describe the connection between the wettability behaviour of a surface and its roughness by means of some parameters calculated from 2D AFM profiles such as the mean slope of the roughness motifs ($1/K_r$) and the measure of the steepness of the sample surface (R_q) [30–35]. Both $1/K_r$ and R_q/quantities, defined in the experimental section, include information both on the horizontal distance and on the vertical profile of the peaks in order to give an overall description of the contact surface on which the drop is released.

The $1/K_r$ and R_q/parameters were calculated for all studied samples both before and after the etching treatment and their dependence on the measured contact angle is shown in Figure 8.

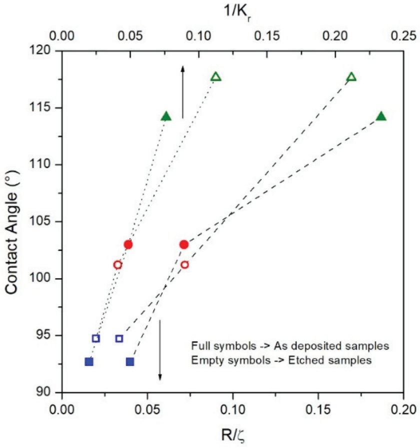

Figure 8. Contact angle values as a function of: 1/Kr parameter (dotted line) and R_q/ξ parameter (dashed line) for as-deposited (full symbols) and etched (empty symbols) samples.

The $1/K_r$ and R/parameters monotonically increase as a function of contact angle and, therefore, as a function of the deposition time (see Figure 7b) for both as-deposited and etched samples. This development indicates a surface evolution over the deposition time, in which the vertical growth of the peaks (expressed by R and R_q for Kr and R_q/ξ, respectively) is faster than the increase in their horizontal distance (expressed by AR and ξ for Kr and R_q/ξ, respectively). This behaviour disadvantages the spreading penetration of the droplet into the sharp local irregularities on the surface, increasing the volume of air between the solid surface and the droplet [30]; as a consequence, the contact angle value increases. Therefore, the wettability of the FePd sample surface decreases as a function of deposition time becoming more hydrophobic (> 90°). Similar wettability properties of film surface are observed after the chemical etching.

Room-temperature hysteresis loops of S50, S150 and S500 samples are shown in Figure 9. The magnetic field is applied in the FePd thin film plane and the curves are normalized to the magnetisation value at H = 10 kOe. The magnetisation reversal process of the S50 sample displays the typical features of a soft magnetic material [52]: a single irreversible magnetisation jump with a small coercive field ($H_c \approx 6.3$ Oe). This is also evident by analysing the FORC distribution as a function of the coercive field, reported in Figure 10: the S50 sample is characterised by a sharp coercivity distribution at low fields. By increasing the deposition time, the magnetisation reversal as observed in the hysteresis loops of Figure 9a takes place on an increasingly wider magnetic field range; the single irreversible magnetisation jump reduces its intensity whereas a reversible mechanism becomes clearly visible with a slow approach of magnetisation to saturation. In addition, the coercive field slightly increases to 11.7 Oe for the S150 sample and to 23.7 Oe for the S500 sample. This is reflected in the FORC distributions of Figure 10, whose intensities decrease as the deposition time increases, indicating a progressively reduced contribution of the irreversible processes to the magnetisation reversal, at the advantage of reversible rotation mechanisms, which do not contribute to the FORC curves intensity. At the same time, the FORC distribution becomes wider as a function of the coercive field as the deposition time increases, in agreement with hysteresis loops.

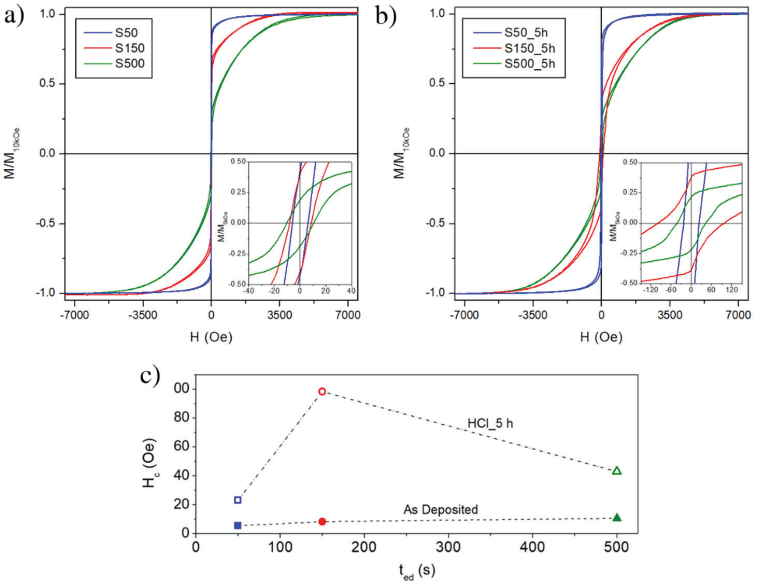

Figure 9. (**a**) Room temperature hysteresis loops of as-deposited samples; (**b**) room temperature hysteresis loops of etched samples in a 2 M aqueous solution of HCl for 5 h; (**c**) evolution of coercive field as a function of electrodeposition time for as-deposited and etched samples.

This evolution of magnetic properties is fully compatible with the morphology changes observed by AFM and SEM characterisation and previously discussed. In the case of the S500 sample, the large grain size and the consequent high roughness imply a dominant role of the grain shape and crystal anisotropy in orienting the magnetisation. Therefore, at remanence the magnetisation is mostly randomly oriented in space, following the local easy axes of individual grains; upon increasing the applied field, reversible rotation processes bring the sample magnetisation to saturation. The same picture holds for the S150 sample, where, however, the small grain size and roughness are responsible for a smaller shape and crystal anisotropy energies; as a consequence, the reversible rotation processes affect a smaller fraction of the total magnetisation and the saturation is approached in a narrower field range. The S50 sample, instead, is characterised by smaller grain size and roughness, and a more compact morphology; in this case, inter-grain interactions overcome the single-grain shape and crystal anisotropy energies, inducing the formation of domain structures that cover several grains; their anisotropies are then largely averaged out, resulting in a magnetically soft behaviour with a fast approach to saturation determined by the absence of significant local anisotropies hindering the domain wall motion and forcing magnetisation rotation.

The magnetic behaviour above described is isotropic in the film plane for all the as-deposited samples as confirmed by the prefect superposition of the hysteresis loops measured in two in-plane orthogonal direction, see Figure S1 in the Supplementary Materials.

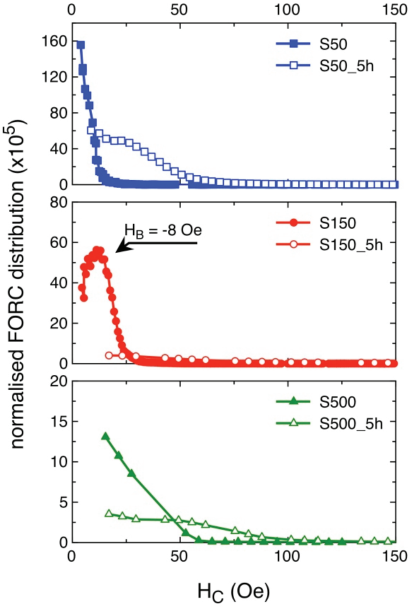

Figure 10. First Order Reversal Curves (FORC) distribution profiles as a function of the coercive field, taken at a bias field $H_B = 0$ for all samples, except S150. Full symbols correspond to as-deposited samples; the equivalent open symbols correspond to the samples submitted to chemical etching.

Once the samples are submitted to chemical etching, some important changes in the hysteresis loops take place, as shown in Figure 9b, as well as in FORC distributions vs. coercivity, depicted in Figure 10. Overall, the sample deposited for 50 s remains the softer and with the steeper approach to saturation, whereas for the other two samples the contribution of magnetisation rotation toward saturation seems to have increased even further. Indeed, while for all three deposition times the FORC distribution has a lower intensity after HCl etching, the decrease is way more pronounced for the S150_5h and S500_5h samples with respect to the S50_h one, indicating, for them, a predominant role of reversible rotation processes in the magnetisation reversal. However, the most significant change with respect to the non-etched samples is the large variation of coercive field, summarised in Figure 9c. As discussed earlier, the effect of the chemical etching process is to reduce and spread the grains size, make the grains more far apart, and increase the roughness. This is reflected by the FORC distribution of the three etched samples, that with respect to their as-deposited counterparts display a much larger spreading of coercive field values, that are due to the increased size distribution of the grains induced by exposition to HCl. As the grains are also more far apart, they also become more magnetically decoupled; as a result, their reciprocal interactions become weaker with respect to the as-deposited films. For the S50_5h sample this means that the mechanism of local averaging out of the magnetic anisotropy is less efficient, and the coercive field increases. However, inter-grains coupling is still largely present, due to the more compact morphology of this sample, that is little affected by the chemical etching. As a consequence, the hysteresis loop still displays a fast approach to saturation after the coercive field has been overcome, with just a slightly more pronounced contribution of magnetisation rotation toward saturation.

At the opposite end, the S500_5h sample incurs in a similar evolution with respect to its as-deposited counterpart: the coercive field increases, and the loop branches remain separated over a larger field interval, indicating that irreversible processes are spread over a larger portion of the hysteresis loop, in agreement with the much wider grains size distribution measured for this sample.

The effects of the chemical etching on the magnetic properties are particularly evident in the S150_5h sample, displaying the largest coercivity value and the most significant change of loop and FORC distribution shape with respect to the as-deposited specimen. While grains borders etching, spreading of grains size, and their magnetic decoupling are still responsible for the observed variations of loop shape and coercive field values, in the S150_5h sample their effects are enhanced. Indeed, while for the 50 s deposition time the etching process is not sufficient to decouple the grains, and for the 500 s deposition time they were already largely independent in the as-prepared state, the specimen deposited for 150 s incurs in a more complex evolution: in its as-prepared state, and differently from all the other samples, the FORC distribution as a function of coercivity has its peak at a bias field of -8 Oe, as indicated in Figure 10. The presence of such a bias field indicates that the S150 sample is in a state where the dominant ferromagnetic behaviour is attributed to the magnetic properties of the individual grains plus the effects of their mutual interactions; conversely, the S50 sample magnetic properties are attributed to a collective ferromagnetic behaviour of the grains, that lose their independence in favour of an averaging out of the local anisotropies, whereas for the S500 one the magnetic properties are mostly due to the sum of those of the individual grains. After chemical etching, the significant magnetic decoupling of the grains occurring in the S150_5h sample induces the disappearance of the bias field in the peak of the FORC distribution, that goes back to H_B = 0 Oe, and the particularly enhanced changes of loop and FORC distribution shapes.

After the chemical etching, the isotropic magnetic behaviour in the film plane of all sample is preserved, see Figure S1 in the Supplementary Materials.

4. Conclusions

Potentiostatically electrodeposited FePd alloy thin films are characterised by different morphological, structural and magnetic properties as a function of electrodeposition time.

In addition to the desired α-(Fe, Pd) solid solution phase, XRD structural analysis reveals the formation of a pure palladium phase in the S500 sample and a tetragonal $Pd_{1.5}H_2$ phase in all samples due to the high affinity between hydrogen and palladium.

The increase of $|j|(t)$ over deposition time indicates a progressive increase of surface area of the working electrode with direct and strong influence on the surface roughness and the grain size distribution of the FePd thin film. The FePd film surface appears dense and flat with small and uniformly distributed grains for deposition time of about 50 s; for longer deposition time, an increasingly rapid growth of independent spherical grains is observed favouring a reduction of film density with a strong increase of surface roughness and grain size.

Magnetic properties are fully compatible with the structural and morphological properties of the as-deposited samples. Soft magnetic features of hysteresis loop with a single irreversible magnetisation jump and small coercive field are observed in S50 sample indicating that the magnetic anisotropy on the film plane can be easily overcome. For longer deposition times, the increase of the roughness and of the grain size strongly affects the magnetisation processes in which reversible rotations appear to reach the magnetic saturation.

As-deposited samples show different response to chemical treatment (5 h in a 2 M aqueous solution of HCl). In general, the observed variation of the Fe:Pd ratio induced by the chemical etching indicates that a selective dissolution of Fe in the FePd alloy occurs in which the removal rate of the Fe atoms is higher than the one of the Pd atoms in all samples. However, differences arise among the different samples.

The flat and homogeneous surface of the S50 sample allows slow chemical etching and, as consequence, the roughness and the average grain size keep almost the same values after the treatment. On the contrary, the chemical etching is more efficient on the S500 sample surface characterised by the biggest exposed surface area. In this case, a huge increase of the surface roughness and a remarkable reduction of the grain size is observed with a slightly higher reciprocal distance; however, the corrosion rate is not uniform on each grain but the as-deposited larger grains appear more corrosion resistant. The most significant change in the magnetic properties of the etched samples with respect to the non-etched ones is the large increase of coercive field. This effect is due to the morphological evolution of grains that induce weaker inter-grain interactions with respect to the as-deposited films. Single-grain anisotropy (both shape and crystal) becomes more important over collective behaviour in the etched samples, thanks to the magnetic decoupling of the grains, that is particularly evident in the S150_5h sample. Even though the in-plane isotropic behaviour of all samples is not modified by the chemical treatment, etched samples develop a magnetic behaviour more dominated by single-grain properties, which results in an increased coercivity and a reduction of the irreversible contributions to the magnetisation reversal, in favour of reversible rotations.

A hydrophobic behaviour of the surface is observed in all FePd thin films. As a function of electrodeposition time, the $1/K_r$ and R/ parameters indicate that the vertical growth of the surface peaks develops faster than the increase in their horizontal distance disadvantaging the spreading penetration of the water drop into the sharp local irregularities on the surface and, as a consequence, the contact angle value is observed to increase. No significant differences on the wettability properties of film surface are observed after the chemical etching.

In conclusion, this work provides a comprehensive characterisation of the fundamental properties of these FePd metallic thin films and demonstrates the ability to fine tune these properties opening the way to further advanced studies focused on their possible use as catalysts with improved features of activity, selectivity and stability combined to the possibility to recover and reuse them thanks to their specific magnetic properties.

Supplementary Materials: The following are available online at http://www.mdpi.com/1996-1944/13/6/1454/s1, Figure S1: (a) Room temperature hysteresis loops of as-deposited samples; (b) room temperature hysteresis loops of etched samples in a 2 M aqueous solution of HCl for 5 h. 0° and 90° labels indicate the two orthogonal in-plane directions along which the hysteresis loops are measured, Figure S2: FM profiles of the step height between the substrate and the electrodeposited S500, S150 and S50 samples.

Author Contributions: Conceptualization, P.T. and P.R.; preparation of the samples, M.C. (Matteo Cialone), F.S. and F.C.; SEM characterisation and morphological data analysis, F.C. and G.B.; AFM characterisation and data analysis, F.C. and G.B.; XRD characterisation and structural data analysis, F.S., M.C. (Matteo Cialone) and P.R.; EDS characterisation and data analysis, F.C., G.B. and M.C. (Marco Coïsson); contact angle measurements and data analysis, F.C. and G.B.; magnetic measurements and magnetic data analysis, G.B., M.C., F.C. (Marco Coïsson) and P.T.; supervision, P.T. and P.R.; writing of the manuscript, G.B., M.C. (Marco Coïsson) and F.S. All authors have read and agreed to the published version of the manuscript.

Funding: This research received no external funding.

Conflicts of Interest: The authors declare no conflict of interest.

References

1. Gaudry, M.; Cottancin, E.; Pellarin, M.; Lermé, J.; Arnaud, L.; Huntzinger, J.R.; Vialle, J.L.; Broyer, M.; Rousset, J.L.; Treilleux, M.; et al. Size and composition dependence in the optical properties of mixed (transition metal/noble metal) embedded clusters. *Phys. Rev. B-Condens. Matter Mater. Phys.* **2003**, *67*, 1–10. [CrossRef]
2. Duan, S.; Wang, R. Bimetallic nanostructures with magnetic and noble metals and their physicochemical applications. *Prog. Nat. Sci. Mater. Int.* **2013**, *23*, 113–126. [CrossRef]
3. Kang, K.M.; Kim, H.W.; Shim, I.W.; Kwak, H.Y. Catalytic test of supported Ni catalysts with core/shell structure for dry reforming of methane. *Fuel Process. Technol.* **2011**, *92*, 1236–1243. [CrossRef]
4. Qin, L.; Zeng, Z.; Zeng, G.; Lai, C.; Duan, A.; Xiao, R.; Huang, D.; Fu, Y.; Yi, H.; Li, B.; et al. Cooperative catalytic performance of bimetallic Ni-Au nanocatalyst for highly efficient hydrogenation of nitroaromatics and corresponding mechanism insight. *Appl. Catal. B Environ.* **2019**, *259*, 118035. [CrossRef]
5. Guo, J.; Lin, C.; Jiang, C.; Zhang, P. Review on noble metal-based catalysts for formaldehyde oxidation at room temperature. *Appl. Surf. Sci.* **2019**, *475*, 237–255. [CrossRef]
6. Shi, Q.; Zhu, C.; Du, D.; Lin, Y. Robust noble metal-based electrocatalysts for oxygen evolution reaction. *Chem. Soc. Rev.* **2019**, *48*, 3181–3192. [CrossRef]

7. Riva, J.S.; Juárez, A.V.; Urreta, S.E.; Yudi, L.M. Catalytic properties of Fe–Pd ferromagnetic nanowires at liquid/liquid interfaces. *Electrochim. Acta* **2019**, *298*, 379–388. [CrossRef]
8. Shokouhimehr, M. Magnetically separable and sustainable nanostructured catalysts for heterogeneous reduction of nitroaromatics. *Catalysts* **2015**, *5*, 534–560. [CrossRef]
9. Sun, J.; Karim, A.M.; Zhang, H.; Kovarik, L.; Li, X.S.; Hensley, A.J.; McEwen, J.S.; Wang, Y. Carbon-supported bimetallic Pd-Fe catalysts for vapor-phase hydrodeoxygenation of guaiacol. *J. Catal.* **2013**, *306*, 47–57. [CrossRef]
10. Zhao, S.; Gorte, R.J. The activity of Fe-Pd alloys for the water-gas shift reaction. *Catal. Letters* **2004**, *92*, 75–80. [CrossRef]
11. Mu, R.; Fu, Q.; Xu, H.; Zhang, H.; Huang, Y.; Jiang, Z.; Zhang, S.; Tan, D.; Bao, X. Synergetic Effect of Surface and Subsurface Ni Species at Pt-Ni Bimetallic Catalysts for CO Oxidation. *J. Am. Chem. Soc.* **2011**, *133*, 1978–1986. [CrossRef]
12. Chen, J.; Wang, S.; Lu, L.; Zhang, X.; Liu, Y. Improved catalytic upgrading of simulated bio-oil via mild hydrogenation over bimetallic catalysts. *Fuel Process. Technol.* **2018**, *179*, 135–142. [CrossRef]
13. Tang, Y.; Cao, S.; Chen, Y.; Lu, T.; Zhou, Y.; Lu, L.; Bao, J. Effect of Fe state on electrocatalytic activity of Pd-Fe/C catalyst for oxygen reduction. *Appl. Surf. Sci.* **2010**, *256*, 4196–4200. [CrossRef]
14. Shen, L.; Li, H.; Lu, L.; Luo, Y.; Tang, Y.; Chen, Y.; Lu, T. Improvement and mechanism of electrocatalytic performance of Pd-Ni/C anodic catalyst in direct formic acid fuel cell. *Electrochim. Acta* **2013**, *89*, 497–502. [CrossRef]
15. Chen, L.; Guo, H.; Fujita, T.; Hirata, A.; Zhang, W.; Inoue, A.; Chen, M. Nanoporous PdNi bimetallic catalyst with enhanced electrocatalytic performances for electro-oxidation and oxygen reduction reactions. *Adv. Funct. Mater.* **2011**, *21*, 4364–4370. [CrossRef]
16. Yang, Y.; Fei, H.; Ruan, G.; Tour, J.M. Porous cobalt-based thin film as a bifunctional catalyst for hydrogen generation and oxygen generation. *Adv. Mater.* **2015**, *27*, 3175–3180. [CrossRef]
17. Jayakrishnan, D.S. *Electrodeposition: The Versatile Technique for Nanomaterials*; Woodhead Publishing Limited: Cambridge, UK, 2012.
18. Robbennolt, S.; Fornell, J.; Quintana, A.; Zhang, H.; Menéndez, E.; Pellicer, E.; Sort, J. Structural and Magnetic Properties of Fe_xCu_{1-x} Sputtered Thin Films Electrochemically Treated To Create Nanoporosity for High-Surface-Area Magnetic Components. *ACS Appl. Nano Mater.* **2018**, *1*, 1675–1682. [CrossRef]
19. Zhang, H.; Wang, Z.; Yang, M.; Deng, Q. The effect of an external magnetic field on the dealloying process of the Ni-Al alloy in alkaline solution. *Phys. Chem. Chem. Phys.* **2017**, *19*, 18167–18171. [CrossRef]
20. Hakamada, M.; Mabuchi, M. Fabrication, microstructure, and properties of nanoporous Pd, Ni, and their alloys by dealloying. *Crit. Rev. Solid State Mater. Sci.* **2013**, *38*, 262–285. [CrossRef]
21. Pečko, D.; Rožman, K.Ž.; McGuiness, P.J.; Pihlar, B.; Kobe, S. Temperature-driven microstructural, compositional, and magnetic changes in electrodeposited Fe-Pd thin films. *J. Appl. Phys.* **2010**, *107*. [CrossRef]
22. Zhang, Y.; Shamberger, P.J. Thick Film $Ni_{0.5}Mn_{0.5-x}Sn_x$ Heusler Alloys by Multi-layer Electrochemical Deposition. *Sci. Rep.* **2018**, *8*, 1–13. [CrossRef] [PubMed]
23. Lin, H.P.; Kuo, J.C. Texture and magnetic properties of electrodeposited FePd films. *Mater. Lett.* **2011**, *65*, 3537–3539. [CrossRef]
24. Soundararaj, A.; Mohanty, J. Magnetic properties of electrodeposited FePd alloy thin films. *AIP Conf. Proc.* **2017**, *1832*.
25. Haehnel, V.; Fähler, S.; Schultz, L.; Schlörb, H. Electrodeposition of Fe70Pd30 nanowires from a complexed ammonium-sulfosalicylic electrolyte with high stability. *Electrochem. Commun.* **2010**, *12*, 1116–1119. [CrossRef]
26. Tiberto, P.; Celegato, F.; Barrera, G.; Coisson, M.; Vinai, F.; Rizzi, P. Magnetization reversal and microstructure in polycrystalline $Fe_{50}Pd_{50}$ dot arrays by self-assembling of polystyrene nanospheres. *Sci. Technol. Adv. Mater.* **2016**, *17*, 462–472. [CrossRef]
27. Tiberto, P.; Barrera, G.; Celegato, F.; Coisson, M.; Olivetti, E.S.; Vinai, F. Microstructural evolution and magnetic properties in $Fe_{50}Pd_{50}$ sputtered thin films submitted to post-deposition annealing. *J. Alloys Compd.* **2014**, *615*, S236–S241. [CrossRef]
28. Iselt, D.; Gaitzsch, U.; Oswald, S.; Fähler, S.; Schultz, L.; Schlörb, H. Electrodeposition and characterization of Fe80Ga20 alloy films. *Electrochim. Acta* **2011**, *56*, 5178–5183. [CrossRef]

29. Konczak, C.; Haehnel, V.; Schultz, L.; Schlörb, H. Adjusting the phase structure of electrodeposited Fe-Pd films. *Mater. Chem. Phys.* **2016**, *174*, 150–155. [CrossRef]
30. Ourahmoune, R.; Salvia, M.; Mathia, T.G.; Mesrati, N. Surface morphology and wettability of sandblasted PEEK and its composites. *Scanning* **2014**, *36*, 64–75. [CrossRef]
31. Kubiak, K.J.; Mathia, T.G.; Wilson, M.C.T. Methodology for Metrology of Wettability Versus Roughness of Engineering Surfaces. *Measurement* **2009**.
32. Ostrovskaya, L.; Podestà, A.; Milani, P.; Ralchenko, V. Influence of surface morphology on the wettability of cluster-assembled carbon films. *Europhys. Lett.* **2003**, *63*, 401–407. [CrossRef]
33. Arora, H.S.; Xu, Q.; Xia, Z.; Ho, Y.-H.; Dahotre, N.B.; Schroers, J.; Mukherjee, S. Wettability of nanotextured metallic glass surfaces. *Scr. Mater.* **2013**, *69*, 732–735. [CrossRef]
34. Palasantzas, G.; de Hosson, J.T.M. Wetting on rough surfaces. *Acta Mater.* **2001**, *49*, 3533–3538. [CrossRef]
35. Foadi, F.; Ten Brink, G.H.; Mohammadizadeh, M.R.; Palasantzas, G. Roughness dependent wettability of sputtered copper thin films: The effect of the local surface slope. *J. Appl. Phys.* **2019**, *125*. [CrossRef]
36. Pike, C.R.; Roberts, A.P.; Dekkers, M.J.; Verosub, K.L. An investigation of multi-domain hysteresis mechanisms using FORC diagrams. *Phys. Earth Planet. Inter.* **2001**, *126*, 11–25. [CrossRef]
37. Muxworthy, A.R.; Dunlop, D.J. First-order reversal curve (FORC) diagrams for pseudo-single-domain magnetites at igh temperature. *Earth Planet. Sci. Lett.* **2002**, *203*, 369–382. [CrossRef]
38. Roberts, A.P.; Pike, C.R.; Verosub, K.L. First-order reversal curve diagrams: A new tool for characterizing the magnetic properties of natural samples. *J. Geophys. Res. Solid Earth* **2000**, *105*, 28461–28475. [CrossRef]
39. Bahamida, S.; Fnidiki, A.; Coïsson, M.; Laggoun, A.; Barrera, G.; Celegato, F.; Tiberto, P. Mixed exchange-coupled soft $α$-(Fe 80 Pd 20) and hard L1 0 FePd phases in Fe 64 Pd 36 thin films studied by first order reversal curves. *Mater. Sci. Eng. B* **2017**, *226*, 47–56. [CrossRef]
40. Cerisier, M.; Attenborough, K.; Celis, J.P.; Van Haesendonck, C. Structure and magnetic properties of electrodeposited Co films onto Si(100). *Appl. Surf. Sci.* **2000**, *166*, 154–159. [CrossRef]
41. Motoyama, M.; Fukunaka, Y.; Sakka, T.; Ogata, Y.H. Initial stages of electrodeposition of metal nanowires in nanoporous templates. *Electrochim. Acta* **2007**, *53*, 205–212. [CrossRef]
42. Gamburg, Y.D.; Zangari, G. *Theory and Practice of Metal Electrodeposition*, 1st ed.; Springer: Berlin/Heidelberg, Germany, 2011; ISBN 978-1-4419-9668-8.
43. Dislaki, E.; Sort, J.; Pellicer, E. Parametric aqueous electrodeposition study and characterization of Fe–Cu films. *Electrochim. Acta* **2017**, *231*, 739–748. [CrossRef]
44. Flanagan, T.B.; Oates, W.A. The palladium-hydrogen system. *Annu. Rev. Mater. Res.* **1991**, 269–304. [CrossRef]
45. Darren, P.B. *Hydrogen Storage Materials*, 1st ed.; Springer: Berlin/Heidelberg, Germany, 2011.
46. Baumgärtner, M.E.; Gabe, D.R. Palladium-iron alloy electrodeposition. Part II alloy plating systems. *Trans. Inst. Met. Finish.* **2000**, *78*, 79–85. [CrossRef]
47. Gan, Y.L.; Yang, Y.; Du, J.J.; Zhang, R.H.; Dai, Z.X.; Zhou, X.W. Studies on the synthesis, dealloying, and electrocatalytic properties of CoPd nanocatalysts. *J. Solid State Electrochem.* **2015**, *19*, 1799–1805. [CrossRef]
48. Hakamada, M.; Mabuchi, M. Preparation of nanoporous palladium by dealloying: Anodic polarization behaviors of Pd-M (M = Fe, Co, Ni) alloys. *Mater. Trans.* **2009**, *50*, 431–435. [CrossRef]
49. McCue, I.; Benn, E.; Gaskey, B.; Erlebacher, J. Dealloying and Dealloyed Materials. *Annu. Rev. Mater. Res.* **2016**, *46*, 263–286. [CrossRef]
50. Scaglione, F.; Rizzi, P.; Celegato, F.; Battezzati, L. Synthesis of nanoporous gold by free corrosion of an amorphous precursor. *J. Alloys Compd.* **2014**, *615*, S142–S147. [CrossRef]
51. Kubiak, K.J.; Wilson, M.C.T.; Mathia, T.G.; Carval, P. Wettability versus roughness of engineering surfaces. *Wear* **2011**, *271*, 523–528. [CrossRef]
52. Cullity, B.D.; Graham, C.D. *Introduction to Magnetic Materials*; John Wiley & Sons: Hoboken, NJ, USA, 2009; ISBN 9780471477419.

materials

MDPI

Article

Temperature Dependence of the Magnetic Properties of IrMn/CoFeB/Ru/CoFeB Exchange Biased Synthetic Antiferromagnets

Edoardo Albisetti *, Giuseppe Scaramuzzi, Christian Rinaldi, Matteo Cantoni, Riccardo Bertacco and Daniela Petti *

Dipartimento di Fisica, Politecnico di Milano, Via Giuseppe Colombo 81, 20133 Milano, Italy; giuseppe.scaramuzzi@mail.polimi.it (G.S.); christian.rinaldi@polimi.it (C.R.); matteo.cantoni@polimi.it (M.C.); riccardo.bertacco@polimi.it (R.B.)

* Correspondence: edoardo.albisetti@polimi.it (E.A.); daniela.petti@polimi.it (D.P.)

Received: 21 December 2019; Accepted: 9 January 2020; Published: 14 January 2020

Abstract: Synthetic antiferromagnets (SAF) are widely used for a plethora of applications among which data storage, computing, and in the emerging field of magnonics. In this framework, controlling the magnetic properties of SAFs via localized thermal treatments represents a promising route for building novel magnonic materials. In this paper, we study via vibration sample magnetometry the temperature dependence of the magnetic properties of sputtered exchange bias SAFs grown via magnetron sputtering varying the ferromagnetic layers and spacer thickness. Interestingly, we observe a strong, reversible modulation of the exchange field, saturation field, and coupling strength upon heating up to 250 °C. These results suggest that exchange bias SAFs represent promising systems for developing novel artificial magnetic nanomaterials via localized thermal treatment.

Keywords: synthetic antiferromagnet; exchange bias; interlayer exchange coupling; vibrating sample magnetometry; CoFeB; thermally assisted magnetic scanning probe lithography; magnetron sputtering

---

1. Introduction

Synthetic antiferromagnets (SAFs) comprise ferromagnetic layers coupled antiferromagnetically through a non-magnetic spacer, by interlayer exchange coupling (IEC), which is essentially a Ruderman-Kittel-Kasuya-Yosida (RKKY) electronic coupling.

Starting from the first observation of the IEC in 1986 [1] and the subsequent study of the oscillatory behavior of IEC as a function of the spacer thickness [2,3], SAF systems played a fundamental role in the foundation of modern spintronics.

As in natural antiferromagnets, compensated SAFs present almost zero stray field and high stability. Furthermore, the interlayer coupling is typically orders of magnitude weaker than the exchange coupling between neighboring atoms in antiferromagnets, so that the manipulation of the magnetic order in SAF is easier. Some of the features that makes SAFs extremely interesting for applications is their wide applicability to in-plane as well out-of-plane magnetized materials, their large tunability via layer thickness and material composition, and the possibility to combine SAF and exchange bias by adding an antiferromagnetic layer to the stack. Throughout the years, SAFs were successfully used in spin-valves [4,5] and magnetic tunnel junctions [6–9] as reference layers, with applications as read heads in magnetoresistive [10,11] hard drives [12], magnetic random access memories (MRAM) [13–15], microwave oscillators [16] and magnetic biosensors [17–22]. More recently, SAFs have been proposed as base materials for racetrack memories [23], due to the higher domain wall velocity with respect to single ferromagnetic layers [24], and their capability to host a range of topological spin-textures [25]. SAFs have also raised considerable interest in the growing field of magnonics [26,27], due to the peculiar properties of spin-waves propagating in antiferromagnetically coupled bilayers [28,29]. Furthermore, recently it has been demonstrated that localized thermal treatments in combination with magnetic fields can be effectively used for manipulating the static and dynamic magnetic properties of exchange bias systems [30–32]. In this framework, studying the temperature dependence of their magnetic properties is of crucial importance. In this work, we perform a systematic study of the magnetic properties of exchange biased SAF systems grown via magnetron sputtering, varying the ferromagnetic layers thickness (from 25 nm to 45 nm) and the spacer layer thickness (from 0.6 nm to 0.7 nm). In particular, we use vibration sample magnetometry (VSM), for measuring quantitatively the hysteresis loops as a function of the in-plane field angle and temperature, ranging from room temperature up to 250 °C. Then, from the hysteresis loops we extract the exchange field, saturation field, saturation magnetization and exchange constant, and study their dependence on temperature. This work sheds light on the temperature behavior of exchange biased synthetic antiferromagnets, allowing the design and implementation of novel methodologies for the thermally assisted control of their magnetic properties.

2. Materials and Methods

The samples were grown on Si/SiO_2 (100 nm) substrates by employing an AJA Orion8 magnetron sputtering system (AJA International, Scituate, MA, USA) with a base pressure below 1×10^{-8} Torr. All the materials were sputtered in the DC mode from single stoichiometric targets, using the parameters listed in Table 1. Note that two different conditions were employed for Ru: 3 mTorr for Ru films exploited as a capping layer and 5 mTorr for Ru films used as interlayer in the synthetic antiferromagnet. Indeed, the lower deposition rate at a pressure of 5 mTorr allows a better control on the Ru thickness, fundamental to obtain a sizable interlayer exchange coupling of the two ferromagnets.

Table 1. Magnetron sputtering parameters.

Material	Power (W)	Ar Pressure (mTorr)
Ru	50	3
Ru SAF	50	5
$Co_{40}Fe_{40}B_{20}$	58	4
$Ir_{22}Mn_{78}$	50	3

Before the deposition, the substrates underwent a soft etch in the same chamber at an Argon pressure of 3 mTorr and an RF power of 20 W for 5′, in order to clean the surface. During the growth, a 30 mT magnetic field (H_G) was applied in the sample plane for setting the magnetocrystalline uniaxial anisotropy direction in the $Co_{40}Fe_{40}B_{20}$ layer and the exchange bias direction in the as-grown sample.

After the growth, the samples underwent an annealing at 250 °C for 5 min, which promoted the crystallization of the amorphous CoFeB and the IrMn layers.

Different sets of samples were studied, consisting of the stacks shown in Figure 1a, namely Si/SiO_2/$Co_{40}Fe_{40}B_{20}$ t/Ru d/$Co_{40}Fe_{40}B_{20}$ t/IrMn 10/Ru 2 (dimensions in nm) varying the thickness of the CoFeB ferromagnetic layers (t) and that of the non-magnetic interlayer Ru (d). The specific CoFeB and IrMn stoichiometry was chosen because of their widespread use in magnetic tunnel junctions, the low spin-wave damping in $Co_{40}Fe_{40}B_{20}$ and the high exchange bias strength. The exact composition of the studied samples is reported in Table 2, using the same coding which will be used in the subsequent discussion.

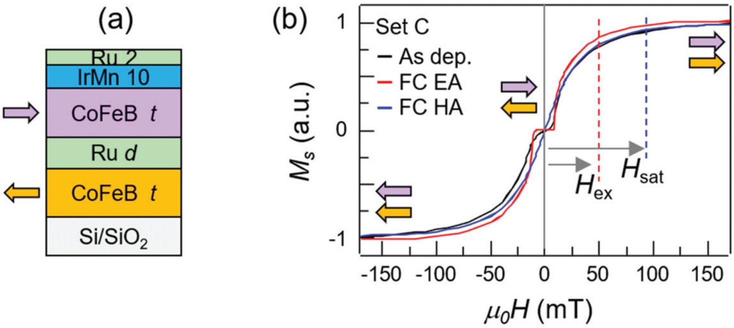

Figure 1. (**a**) Sketch of the CoFeB/Ru/CoFeB/IrMn/Ru synthetic antiferromagnet stacks grown via magnetron sputtering. *t* indicates the thickness of the CoFeB layers, ranging from 25 nm to 45 nm. *d* indicates the thickness of the Ru coupling layer, ranging from 0.6 to 0.7 nm; (**b**) room-temperature vibrating sample magnetometer hysteresis loop of sample C (CoFeB 35 nm, Ru 0.6 nm) in the as deposited sample measured along the easy axis (black line) and the sample after a field cooling at 250 °C measured along the easy axis (red line) and hard axis (blue line). The colored arrows indicate the direction of the magnetization of top (purple) and bottom (orange) layers. H_{ex} and H_{sat} indicate the exchange field and saturation field related to the annealed sample, respectively.

Table 2. List of the studied sample sets and corresponding stack compositions.

Set Name	Stack Compositions (Dimensions in nm)
A	Si/SiO$_2$/CoFeB 25/Ru 0.7/CoFeB 25/IrMn 10/Ru 2
B	Si/SiO$_2$/CoFeB 35/Ru 0.7/CoFeB 35/IrMn 10/Ru 2
C	Si/SiO$_2$/CoFeB 35/Ru 0.6/CoFeB 35/IrMn 10/Ru 2
D	Si/SiO$_2$/CoFeB 45/Ru 0.6/CoFeB 45/IrMn 10/Ru 2

The hysteresis loop of the films was measured via a vibrating sample magnetometer (VSM; EZ-9, Microsense, Lowell, MA, USA) as a function of the sample temperature, from RT to 250 °C, and of the direction of the magnetic field in the film plane. The VSM was used also for performing the initial annealing and field cooling of the samples.

3. Results and Discussion

3.1. Room-Temperature Magnetic Characterization and Angular Hysteresis Loops

Figure 1b shows the VSM hysteresis loops along the easy axis acquired at room temperature of set C (35 nm CoFeB, 0.6 nm Ru) for the as deposited sample, black line, and after the field cooling, red line. The field cooling was performed by heating the sample up to 250 °C and subsequently cooling it down to room temperature while applying a static 400 mT external magnetic field in the sample plane, in the same direction of the field applied during the growth, H_G. The field cooling sets the direction of the exchange bias, and therefore the pinning direction of the magnetization of the top CoFeB layer. The direction of the magnetization of the top (bottom) CoFeB layers as a function of the external field is indicated by the purple (orange) arrows. The hysteresis loop displays the characteristic plateau at low field, which is a signature of robust antiferromagnetic coupling between the two CoFeB layers, induced by the interlayer exchange coupling across the thin Ru layer. The plateau is also a signature of the presence of the anisotropy of the film, which is further confirmed by the angle-dependent measurement of Figure 2. The two main contributions are the magnetocrystalline anisotropy and the exchange bias set during the growth. The two lobes of the loop are related to the rotation of the top (negative fields) and bottom (positive fields) CoFeB layer. The saturation field H_{sat} and the exchange field H_{ex} are indicated in figure for the measurement after field cooling. In particular, H_{ex} was extracted from the measurement as the halfway point between the end of the low-field plateau and the saturation field. In high external fields, the antiferromagnetic coupling is overcome by the Zeeman field, which saturates the magnetization in the direction of the applied field. Upon decreasing the magnetic field, the magnetizations rotate coherently and gradually reach the antiparallel alignment. The well-defined plateau in the annealed samples, with respect to the as-deposited samples, mainly arises from setting the unidirectional anisotropy of exchange bias via field cooling.

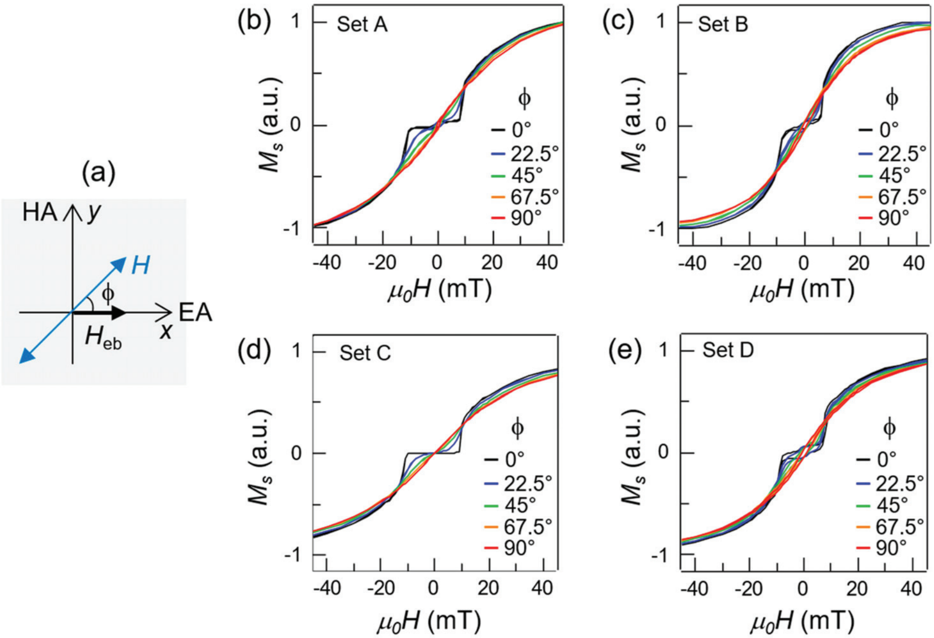

Figure 2. Room temperature hysteresis loops as a function of the field angle. (**a**) Sketch of the experimental configuration for the measurements. The thick arrows indicate the direction of the exchange bias field, set during field cooling (H_{eb}) along the x axis direction. ϕ indicates the angle of the external applied field (H) with respect to the exchange bias direction, in the plane of the film. (**b**–**e**) Hysteresis loops measured via vibration sample magnetometry (VSM) at room temperature as a function of the angle ϕ (color-coded) for set A, B, C, and D respectively.

Figure 2 shows the room temperature hysteresis loops after field cooling as a function of the angle of the external field applied in the plane of the sample. Panel (a) shows the geometry of the measurement. In particular, ϕ is the angle between the direction of the exchange bias H_{eb}, set during the field cooling, and the direction of the external field applied during the measurement H. Specifically, the easy magnetization axis (EA) is given by $\phi = 0°$ and the hard axis (HA) is for $\phi = 90°$. The measurements were performed in the same conditions on all the sets with a step of 22.5° from $\phi = 0°$ to $\phi = 90°$, color-coded. In all the sets, the loops feature the characteristic two lobes and low-field plateau along the EA, and the elongated loop along the HA. For intermediate angles, the loops assume a mixed EA and HA character, with the low field plateau progressively tilting to higher derivatives. Some samples show at low field a small hysteresis loop, probably due to slightly non-compensated ferromagnetic structures. The origin of non-compensation can be ascribed to the small variation of the CoFeB deposition conditions, or possibly to the influence of the surface roughness of one of the two ferromagnetic layers [33,34].

3.2. Temperature Dependence of the Magnetic Properties

Figure 3 shows the hysteresis loops of sets C and D along the easy axis (ϕ = 0°, panels (a–b)) and hard axis (ϕ = 90°, panels (c–d)), as a function of temperature, ranging from room temperature up to 250 °C, color-coded. Regarding the EA loops, three main effects of temperature are observed. First, a reduction of the plateau field with increasing temperature, from ~9 mT at room temperature down to ~4 mT at 250 °C in set C, and from ~7 mT at room temperature down to ~4 mT at 250 °C in set D. The decrease of the plateau was mainly due to the weakening of the unidirectional anisotropy set by the exchange bias while approaching the blocking temperature, combined with a reduction of the interlayer coupling strength, as the dependence of the magnetocrystalline anisotropy on the temperature in this ranges is much weaker [35]. Second, a reduction of the saturation field H_{sat} and exchange field H_{ex}, which was consistent with a reduction in the interlayer coupling with temperature. Third, as expected [36,37] we observe a slight reduction of the saturation magnetization M_s with increasing temperature. All these effects were however reversible, provided that the same exchange bias direction and strength was retrieved at the end of the heating process, e.g., (as performed in our experiments) by applying an external saturating field in the direction of the exchange bias during the cooling process.

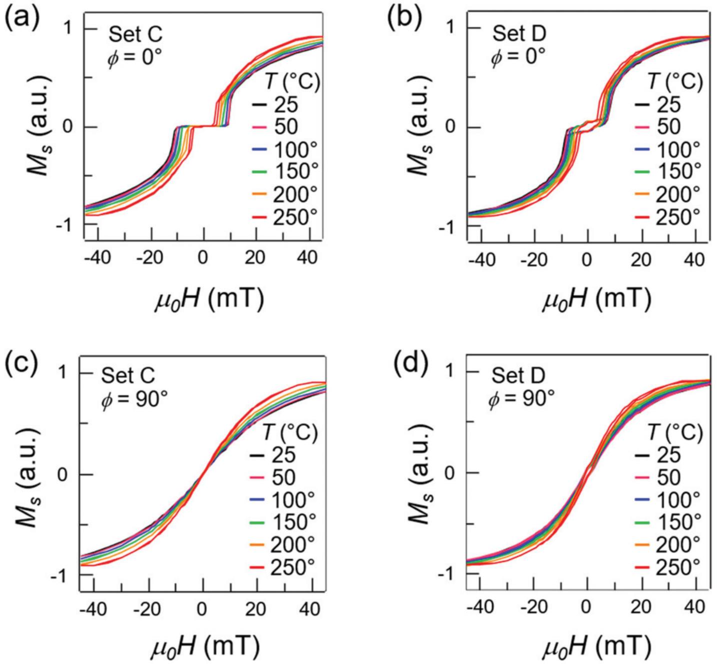

Figure 3. (**a**,**b**) Hysteresis loops of set C and set D along the easy-axis (ϕ = 0°) measured as a function of temperature (color-coded) ranging from 25 °C to 250 °C; (**c**,**d**) Hysteresis loops of set C and set D along the hard-axis (ϕ = 90°) measured as a function of temperature (color-coded) ranging from 25 °C to 250 °C.

For analyzing quantitatively the characteristics of the hysteresis loops, in Figure 4 we plotted the exchange field H_{ex} (a) and saturation field H_{sat} (b) as a function of the temperature for all the sample sets (A–D). From the room temperature data (at T = 25 °C) of both panel (a) and panel (b), we observed higher H_{ex} around 45 mT and H_{sat} around 85 mT in sets C–D, and lower H_{ex} around 20 mT and H_{sat} around 40 mT in sets A–B. This was consistent with the oscillatory nature of the interlayer coupling as a function of the Ru thickness, which was 0.6 nm in sets C–D and 0.7 nm in sets A–B. It is worth noting that, the Ru thickness being equal, slightly higher exchange and saturation fields were observed in the sets characterized by thinner CoFeB layers (set A, 25 nm and set C, 35 nm). This is coherent with the interfacial nature of the antiferromagnetic interlayer coupling, which is inversely proportional to the film thickness.

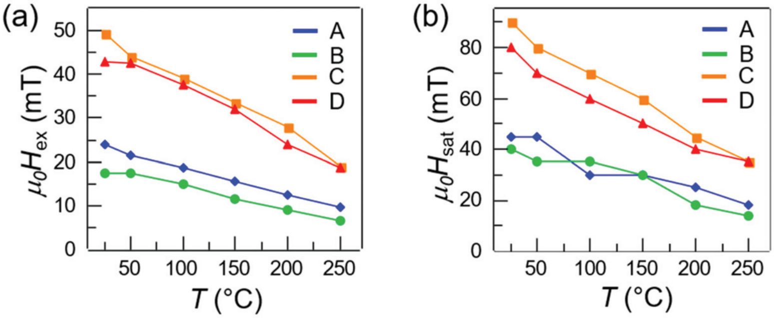

Figure 4. (**a**,**b**) Exchange field $\mu_0 H_{ex}$ and saturation field $\mu_0 H_{sat}$ as a function of temperature for sets A–D (color-coded).

Regarding the temperature dependence of the exchange and saturation fields, we observed an overall reduction of both parameters with increasing temperature, in all sample sets. In particular, both H_{ex} and H_{sat} displayed a reduction of about 60% from room temperature to 250 °C. This behavior is particularly interesting in the framework of thermally assisted magnetic writing schemes, such as TAMR (thermally assisted magnetic recording) or tam-SPL (thermally assisted magnetic scanning probe lithography), where local heating in combination with external fields is used for writing magnetization patterns. Note that, at the same time, the reduction of the plateau field was around 50%.

In Figure 5, we studied the saturation magnetization (a) and the interlayer coupling strength (b) as a function of temperature. M_s measured at room temperature is 0.9–1.1 × 10^6 A/m in all sets, which is in agreement with values found in the literature [38,39] for CoFeB films with the same stoichiometry. The M_s, which lowers with increasing temperature due to magnon excitation [40], was calculated normalizing the quantitative VSM measurements by the magnetic volume of each sample. The slight variations observed across different samples are due to non-idealities in the sample shape. In order to study the dependence of the coupling coefficient on the temperature, we calculated the total effective coupling strength $J_{eff} = H_{ex}M_st$, where H_{ex} is the exchange field (see Figure 1b), M_s is the saturation magnetization and t is the sample thickness. The physical origin of such dependence can be ascribed to both interfacial effects, spacer-related mechanisms or effects arising in the magnetic layers [41]. In panel (b) we plot J_{eff} as a function of temperature for all the sets. As previously noted, sets A and B (Ru 0.7 nm thick) feature a lower J_{eff}~ 1.25 mJ/m^2 with respect to sets C and D (Ru 0.6 nm thick), which feature J_{eff}~ 3.5 mJ/m^2 at room temperature, due to the different Ru interlayer thickness, consistently with the expected oscillatory behavior [2]. Noteworthy, J_{eff} was reduced reversibly by 60–65% from room temperature to 250 °C with only slight variations across different sets, suggesting that even mild heating treatment could significantly and temporarily alter the SAF coupling strength, with high potential for applications. These results were consistent with those found in similar system, namely synthetic antiferromagnets based on thin ferromagnetic layers with in plane and perpendicular to the plane magnetic anisotropies [35,42]. The theoretical explanation of the decrease of interlayer exchange coupling with the temperature can be found in [41].

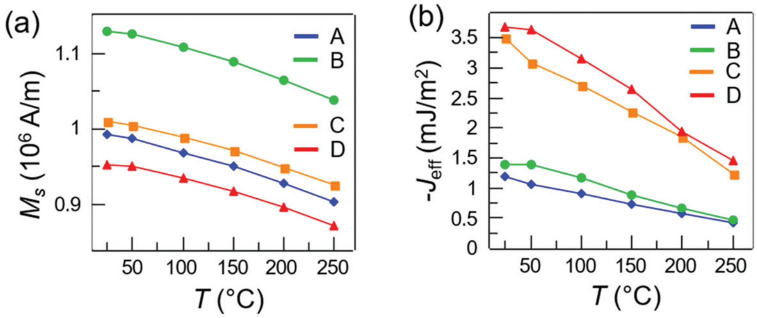

Figure 5. (**a**) Saturation magnetization M_s as a function of temperature for set A–D (color-coded); (**b**) Coupling strength J_{eff} as a function of temperature for set A–D (color-coded).

4. Conclusions

In this work, we studied the temperature and angular dependence of the magnetic properties of exchange biased synthetic antiferromagnets, in the case of compensated in-plane magnetized layers with thickness ranging from 25 nm to 45 nm. Noteworthy, we observed a strong reversible reduction of the exchange field, saturation field and antiferromagnetic coupling strength with a mild heating treatment (up to 250 °C). These results are particularly interesting in the framework of heat-assisted magnetic writing methods such as thermally assisted magnetic scanning probe lithography (tam-SPL), where localized heating in combination with external fields were used for reversibly writing the magnetic properties of thin-film materials. These results suggest that SAFs represent promising systems for developing novel artificial magnetic nanomaterials via localized thermal treatment.

Author Contributions: Conceptualization, data analysis and writing E.A., D.P.; Experiments E.A., G.S., C.R., M.C., D.P. Supervision, R.B. All authors have read and agreed to the published version of the manuscript.

Funding: The research leading to these results has received funding from the European Union's Horizon 2020 research and innovation program under grant agreements no. 705326, project SWING.

Conflicts of Interest: The authors declare no conflict of interest.

References

1. Grünberg, P.; Schreiber, R.; Pang, Y. Layered Magnetic Structures: Evidence for Antiferromagnetic Coupling of Fe Layers across Cr Interlayers. *Phys. Rev. Lett.* **1986**, *57*, 2442–2445. [CrossRef] [PubMed]
2. Parkin, S.S.P.; More, N.; Roche, K.P. Oscillations in exchange coupling and magnetoresistance in metallic superlattice structures: Co/Ru, Co/Cr, and Fe/Cr. *Phys. Rev. Lett.* **1990**, *64*, 2304–2307. [CrossRef] [PubMed]
3. Bruno, P.; Chappert, C. Oscillatory coupling between ferromagnetic layers separated by a nonmagnetic metal spacer. *Phys. Rev. Lett.* **1991**, *67*, 1602–1605. [CrossRef] [PubMed]
4. Dieny, B.; Speriosu, V.S.; Gurney, B.A.; Parkin, S.S.P.; Wilhoit, D.R.; Roche, K.P.; Metin, S.; Peterson, D.T.; Nadimi, S. Spin-valve effect in soft ferromagnetic sandwiches. *J. Magn. Magn. Mater.* **1991**, *93*, 101–104. [CrossRef]
5. Kerr, E.; van Dijken, S.; Coey, J.M.D. Influence of the annealing field strength on exchange bias and magnetoresistance of spin valves with IrMn. *J. Appl. Phys.* **2005**, *97*, 093910. [CrossRef]
6. Yuasa, S.; Djayaprawira, D.D. Giant tunnel magnetoresistance in magnetic tunnel junctions with a crystalline MgO(0 0 1) barrier. *J. Phys. D. Appl. Phys.* **2007**, *40*, R337–R354. [CrossRef]
7. Zaleski, A.; Skowronski, W.; Czapkiewicz, M.; Kanak, J.; Stobiecki, T.; Macedo, R.; Cardoso, S.; Freitas, P.P. Reduction of critical current in magnetic tunnel junctions with CoFeB/Ru/CoFeB synthetic free layer. *J. Phys. Conf. Ser.* **2010**, *200*, 052035. [CrossRef]
8. Cuchet, L.; Rodmacq, B.; Auffret, S.; Sousa, R.C.; Prejbeanu, I.L.; Dieny, B. Perpendicular magnetic tunnel junctions with a synthetic storage or reference layer: A new route towards Pt- and Pd-free junctions. *Sci. Rep.* **2016**, *6*, 21246. [CrossRef]

9. Lee, Y.M.; Hayakawa, J.; Ikeda, S.; Matsukura, F.; Ohno, H. Giant tunnel magnetoresistance and high annealing stability in CoFeB/MgO/CoFeB magnetic tunnel junctions with synthetic pinned layer. *Appl. Phys. Lett.* **2006**, *89*, 87–90. [CrossRef]
10. Baibich, M.N.; Broto, J.M.; Fert, A.; Van Dau, F.N.; Petroff, F.; Etienne, P.; Creuzet, G.; Friederich, A.; Chazelas, J. Giant Magnetoresistance of (001)Fe/(001)Cr Magnetic Superlattices. *Phys. Rev. Lett.* **1988**, *61*, 2472–2475. [CrossRef]
11. Binasch, G.; Grünberg, P.; Saurenbach, F.; Zinn, W. Enhanced magnetoresistance in layered magnetic structures with antiferromagnetic interlayer exchange. *Phys. Rev. B* **1989**, *39*, 4828–4830. [CrossRef] [PubMed]
12. Childress, J.R.; Carey, M.J.; Wilson, R.J.; Smith, N.; Tsang, C.; Ho, M.K.; Carey, K.; Macdonald, S.A.; Ingall, L.M.; Gurney, B.A. IrMn Spin-Valves for High Density Recording. *IEEE Trans. Magn.* **2001**, *37*, 1745–1748. [CrossRef]
13. Parkin, S.; Jiang, X.; Kaiser, C.; Panchula, A.; Roche, K.; Samant, M. Magnetically engineered spintronic sensors and memory. *Proc. IEEE* **2003**, *91*, 661–680. [CrossRef]
14. Bhatti, S.; Sbiaa, R.; Hirohata, A.; Ohno, H.; Fukami, S.; Piramanayagam, S.N. Spintronics based random access memory: A review. *Mater. Today* **2017**, *20*, 530–548. [CrossRef]
15. Smith, N.; Maat, S.; Carey, M.J.; Childress, J.R. Coresonant Enhancement of Spin-Torque Critical Currents in Spin Valves with a Synthetic-Ferrimagnet Free Layer. *Phys. Rev. Lett.* **2008**, *101*, 247205. [CrossRef]
16. Hrkac, G.; Keatley, P.S.; Bryan, M.T.; Butler, K. Magnetic vortex oscillators. *J. Phys. D. Appl. Phys.* **2015**, *48*, 453001. [CrossRef]
17. Search, H.; Journals, C.; Contact, A.; Iopscience, M.; Address, I.P.; Freitas, P.P.; Ferreira, R.; Cardoso, S.; Cardoso, F. Magnetoresistive sensors. *J. Phys. Condens. Matter* **2007**, *19*, 165221.
18. Gaster, R.S.; Xu, L.; Han, S.-J.; Wilson, R.J.; Hall, D.A.; Osterfeld, S.J.; Yu, H.; Wang, S.X. Quantification of protein interactions and solution transport using high-density GMR sensor arrays. *Nat. Nanotechnol.* **2011**, *6*, 314–320. [CrossRef]
19. Donolato, M.; Sogne, E.; Dalslet, B.T.; Cantoni, M.; Petti, D.; Cao, J.; Cardoso, F.; Cardoso, S.; Freitas, P.P.; Hansen, M.F.; et al. On-chip measurement of the Brownian relaxation frequency of magnetic beads using magnetic tunneling junctions. *Appl. Phys. Lett.* **2011**, *98*, 073702. [CrossRef]
20. Sharma, P.; Albisetti, E.; Monticelli, M.; Bertacco, R.; Petti, D. Exchange Bias Tuning for Magnetoresistive Sensors by Inclusion of Non-Magnetic Impurities. *Sensors* **2016**, *16*, 1030. [CrossRef]
21. Sharma, P.P.; Albisetti, E.; Massetti, M.; Scolari, M.; La Torre, C.; Monticelli, M.; Leone, M.; Damin, F.; Gervasoni, G.; Ferrari, G.; et al. Integrated platform for detecting pathogenic DNA via magnetic tunneling junction-based biosensors. *Sens. Actuators B Chem.* **2017**, *242*, 280–287. [CrossRef]
22. Albisetti, E.; Petti, D.; Damin, F.; Cretich, M.; Torti, A.; Chiari, M.; Bertacco, R. Photolithographic bio-patterning of magnetic sensors for biomolecular recognition. *Sens. Actuators B Chem.* **2014**, *200*, 39–46. [CrossRef]
23. Parkin, S.S.P.; Hayashi, M.; Thomas, L. Magnetic Domain-Wall Racetrack Memory. *Science* **2008**, *320*, 190–194. [CrossRef] [PubMed]
24. Yang, S.H.; Ryu, K.S.; Parkin, S. Domain-wall velocities of up to 750 m s-1 driven by exchange-coupling torque in synthetic antiferromagnets. *Nat. Nanotechnol.* **2015**, *10*, 221–226. [CrossRef]
25. Legrand, W.; Maccariello, D.; Ajejas, F.; Collin, S.; Vecchiola, A.; Bouzehouane, K.; Reyren, N.; Cros, V.; Fert, A. Room-temperature stabilization of antiferromagnetic skyrmions in synthetic antiferromagnets. *Nat. Mater.* **2019**, *19*, 34–42. [CrossRef]
26. Chumak, A.V.; Vasyuchka, V.I.; Serga, A.A.; Hillebrands, B. Magnon spintronics. *Nat. Phys.* **2015**, *11*, 453–461. [CrossRef]
27. Lenk, B.; Ulrichs, H.; Garbs, F.; Münzenberg, M. The building blocks of magnonics. *Phys. Rep.* **2011**, *507*, 107–136. [CrossRef]
28. Sluka, V.; Schneider, T.; Gallardo, R.A.; Kákay, A.; Weigand, M.; Warnatz, T.; Mattheis, R.; Roldán-Molina, A.; Landeros, P.; Tiberkevich, V.; et al. Emission and propagation of 1D and 2D spin waves with nanoscale wavelengths in anisotropic spin textures. *Nat. Nanotechnol.* **2019**, *14*, 328–333. [CrossRef]
29. Albisetti, E.; Tacchi, S.; Silvani, R.; Scaramuzzi, G.; Finizio, S.; Wintz, S.; Wintz Rinaldi, C.; Cantoni, M.S.; Raabe, J.; Carlotti, G.; et al. Optically-inspired nanomagnonics with nonreciprocal spin waves in synthetic antiferromagnets. *Adv. Mater.* **2020**. [CrossRef]

30. Albisetti, E.; Petti, D.; Pancaldi, M.; Madami, M.; Tacchi, S.; Curtis, J.; King, W.P.; Papp, A.; Csaba, G.; Porod, W.; et al. Nanopatterning reconfigurable magnetic landscapes via thermally assisted scanning probe lithography. *Nat. Nanotechnol.* **2016**, *11*, 545–551. [CrossRef]
31. Albisetti, E.; Petti, D.; Sala, G.; Silvani, R.; Tacchi, S.; Finizio, S.; Wintz, S.; Calò, A.; Zheng, X.; Raabe, J.; et al. Nanoscale spin-wave circuits based on engineered reconfigurable spin-textures. *Commun. Phys.* **2018**, *1*, 56. [CrossRef]
32. Albisetti, E.; Calò, A.; Spieser, M.; Knoll, A.W.; Riedo, E.; Petti, D. Stabilization and control of topological magnetic solitons via magnetic nanopatterning of exchange bias systems. *Appl. Phys. Lett.* **2018**, *113*, 162401. [CrossRef]
33. Desai, M.; Misra, A.; Doyle, W.D. Effect of interface roughness on exchange coupling in synthetic antiferromagnetic multilayers. *IEEE Trans. Magn.* **2005**, *41*, 3151–3153. [CrossRef]
34. Varvaro, G.; Laureti, S.; Peddis, D.; Hassan, M.; Barucca, G.; Mengucci, P.; Gerardino, A.; Giovine, E.; Lik, O.; Nissen, D.; et al. Co/Pd-Based synthetic antiferromagnetic thin films on Au/resist underlayers: Towards biomedical applications. *Nanoscale* **2019**, *11*, 21891–21899. [CrossRef] [PubMed]
35. Wiese, N.; Dimopoulos, T.; Rührig, M.; Wecker, J.; Reiss, G.; Sort, J.; Nogués, J. Strong temperature dependence of antiferromagnetic coupling in CoFeB/Ru/CoFeB. *Europhys. Lett.* **2007**, *78*, 67002. [CrossRef]
36. Callen, H.B.; Callen, E. The present status of the temperature dependence of magnetocrystalline anisotropy, and the power law. *J. Phys. Chem. Solids* **1966**, *27*, 1271–1285. [CrossRef]
37. Sato, H.; Chureemart, P.; Matsukura, F.; Chantrell, R.W.; Ohno, H.; Evans, R.F.L. Temperature-dependent properties of CoFeB/MgO thin films: Experiments versus simulations. *Phys. Rev. B* **2018**, *98*, 214428. [CrossRef]
38. Chen, Y.-T.; Xie, S.M. Magnetic and Electric Properties of Amorphous Co40Fe40B20 Thin Films. *J. Nanomater.* **2012**, *2012*, 29. [CrossRef]
39. Conca, A.; Greser, J.; Sebastian, T.; Klingler, S.; Obry, B.; Leven, B.; Hillebrands, B. Low spin-wave damping in amorphous Co 40 Fe 40 B 20 thin films. *J. Appl. Phys.* **2013**, *113*, 213909. [CrossRef]
40. Bloch, F. Zur Theorie des Ferromagnetismus. *Z. Phys. A Hadron. Nucl.* **1930**, *61*, 206–219. [CrossRef]
41. Schwieger, S.; Nolting, W. Origin of the temperature dependence of interlayer exchange coupling in metallic trilayers. *Phys. Rev. B* **2004**, *69*, 224413. [CrossRef]
42. Li, Y.; Jin, X.; Pan, P.; Tan, F.N.; Lew, W.S.; Ma, F. Temperature-dependent interlayer exchange coupling strength in synthetic antiferromagnetic $[\mathrm{Pt/Co}]_2/\mathrm{Ru}/[\mathrm{Co/Pt}]_4$ multilayers. *Chin. Phys. B* **2018**, *27*, 127502. [CrossRef]

MDPI
St. Alban-Anlage 66
4052 Basel
Switzerland
Tel. +41 61 683 77 34
Fax +41 61 302 89 18
www.mdpi.com

Materials Editorial Office
E-mail: materials@mdpi.com
www.mdpi.com/journal/materials

MDPI
St. Alban-Anlage 66
4052 Basel
Switzerland

Tel: +41 61 683 77 34
Fax: +41 61 302 89 18

www.mdpi.com

ISBN 978-3-0365-3105-2